Supramolecular routes to a bio-inspired synthesis of micro- and nano-structured materials

Bartosz Marzec

A thesis submitted to the University of Dublin for the degree of

Doctor of Philosophy

February 2013

Trinity College Dublin

School of Chemistry

I declare that this thesis has not been submitted as an exercise for a degree at this or any other university and it is entirely my own work, except where otherwise cited, referenced, acknowledged or accredited.

I agree to deposit this thesis in the University's open access institutional repository or allow the library to do so on my behalf, subject to Irish Copyright Legislation and Trinity College Library conditions of use and acknowledgement. I agree that the Library may at their discretion lend or copy this thesis upon request.

……

(*date and signature*)

Summary

This thesis presents a contribution to the research field of coordination chemistry and synthesis of hybrid, organic-inorganic materials. The weak, non-covalent interactions that occur between the synthesised metal complexes gives rise to hierarchical supramolecular assemblies and allow the study of the self-assembly and self-organisation processes that may be used in the future bottom-up' approaches to design intelligent materials or functional nanodevices. Fourteen new coordination compounds that contain iminodiacetic acid based ligands were characterised using a variety of analytical techniques, including single crystal X-ray diffraction in order to determine their coordination environments and solid-state packing modes. The structures and constitution of related non- crystalline materials were compared to those of the crystalline materials and were primarily characterised by electron microscopy approaches and other supplemental analytical techniques.

Attention was directed to the elucidation of suramolecular packing arrangements of the molecular subunits. It was observed that hydrophobic, alkyl substituents generally promote the formation of layered, lamellar structures with clearly defined hydrophobic 'organic' and hydrophilic 'inorganic' areas. In a consecutive step the compounds were thermolysed and the morphology of the residues was investigated using electron microscopy in an attempt to establish links between the supramolecular packing structure and the morphology of the precursor material and the morphology of the residues. In several cases existence of flat, plate-like, almost two-dimensional crystals of copper(II) oxide, copper(II) oxide, calcium oxide and calcium carbonate was confirmed; these observations and layered imprints may be attributable to the initial pre-arrangement of the starting materials within 3D supramolecular networks. Furthermore the amphiphilic iminodiacetic acid-based pheniolic ligands were employed as habit modifiers for $CaCO_3$ crystals.

Chapter I introduces the reader to the subject area of supramolecular chemistry and highlights relevant compounds that contain related ligands. This chapter also summarises aspects relevant to biomimetic crystallisation of calcium carbonate.

Chapter II outlines the aims of the research project.

Chapter III describes coordination complexes and supramolecular packing structures containing iminodiacetic-acid based phenolic ligands, Cu(II) and Zn(II) ions. The solid-state structures are discussed along with the thermal degradation pathways and the morphologies of the residual CuO and ZnO materials. A reaction between the C_2vda ligand and Cu^{2+} ions yielded the formation of $[Cu(C_2vda)(H_2O)]\cdot 2H_2O\cdot 2MeOH$ (**1**), when TEA was used as a base, or $[Cu_3(\mu\text{-}Cl)_2(\mu\text{-}C_2vda)(C_2vda)(H_2O)_4]\cdot H_2O$ (**2**), when KOH was added to deprotonate the ligand. Complexation of the C_6vda ligand with Cu^{2+} ions resulted in the generation of two new

complexes: [Cu(C_6vda)(H_2O)$_2$] (**3**), which forms in the presence of TEA, and K_2[Cu_2(μ-Cl)$_2$(C_6vda)$_2$]·4H_2O (**4**) that forms in the presence of KOH. The utilisation of the C_{10}vda ligand in a reaction with Cu^{2+} resulted in [Cu(C_{10}vda)(H_2O)$_2$] (**5**). Compounds **1** and **2** form H-bonded layers, sandwiched between layers of constitutional solvent molecules, while compounds **3**-**5** display a layered lamellar packing arrangements. The final compound discussed in this chapter, [Zn(Me_2hda)(H_2O)$_2$]·H_2O (**6**), forms when the Me_2hda ligand is reacted with Zn^{2+} ions and also adopts a layered lamellar packing motif. **1**-**6** formed single-crystalline phases.

Chapter IV contains the description of 8 new Ca-containing coordination complexes and studies on the morphology of their thermal degradation products. Calcium carbonate gained much attention in materials science as it is used as the main building material for exoskeletons of many marine organisms; it also plays a major role in the formation of hard tissues in higher organisms, including humans. The global carbon cycle depends on the abilities of sea organisms such as coral reefs or algae to capture CO_2 and bind it in the form of $CaCO_3$. It is commonly used as a model material to study biomineralisation processes. Compound [Ca_2(Chnida)$_2$(H_2O)$_2$]·4H_2O (**7**) adopts a three dimensional network structure. The utilisation of the Me_2hda ligand in this reaction results in the formation of [Ca(Me_2hda)(H_2O)$_3$]·½H_2O·½MeOH (**8**), while a ligand of similar amphiphilicity, C_2vda, gives [Ca(C_2vda)(H_2O)$_2$]·H_2O (**9**). Compounds **8** and **9** adopt layered lamellar packing motifs. Further extension of the hydrophobic part of the ligands resulted in the formation of self-assembled, non-crystalline compounds [Ca(C_6vda)(H_2O)$_2$]·H_2O (**10**), [Ca(C_{10}vda)(H_2O)$_2$] (**11**) and [Ca(C_{12}hda)(H_2O)$_2$]·H_2O (**12**),. These amorphous phases were confirmed by TEM to adopt hierarchical, lamellar arrangements. The *t*-Bu_2hda and Bc_2hda ligands stabilise [Ca(*t*-Bu_2hda)(H_2O)$_2$]·3H_2O (**13**) and K_2(H_2O)$_5$[Ca(H_2Bc_2hda)(HBc_2hda)(H_2O)$_4$]Cl·H_2O (**14**) complexes. **13** forms an amorphous phase, while **14** is a crystalline forming a potassium-ion mediated network structure.

Another research aspect presented in this thesis relates to the control over morphology of calcium carbonate crystals as described in chapter V. The aforementioned hda and vda ligands were introduced into the crystallising system in low concentration (when compared with the synthesis of supramolecular compounds) in order to disturb the crystal nuclei formation or inhibit the growth of a specific crystal face. Spherical $CaCO_3$ assemblies with the resemblance to the naturally occurring coccospheres were obtained when the C_{12}hda ligand was employed as habit modifier; these and other resulting morphologies of the $CaCO_3$ crystals are different to the rhombohedral blocks that are obtained under conventional crystallisation conditions highlighting the ability of the used hda and vda complexing agents to act as habit modifiers.

Chapter VI provides the conclusions based on the research results and provides directions for future work. Finally, chapter VII contains the experimental details for the synthesis of the organic ligands and the complexes along with the details of the applied analytical techniques and equipment.

Acknowledgements

The PhD programme at Trinity College was a wonderful, mind-blowing and life-changing experience. I would like to use the opportunity to say a big 'THANK YOU' to all of the people, who have helped me for the last 4 years. Without you guys this thesis would not exist and all of the exciting experiments described in it would not have been done.

First and foremost I would like to thank my supervisor, **Prof. Wolfgang Schmitt** – you are a brilliant scientist and I have learned a lot when I was working in the group. I appreciate your constructive criticism and commitment to high standards in research.

Another 'Thank you' goes to the current and past members of the Schmitt's group, who contributed to the research described in this thesis, especially:

- **Dr. Giuseppe La Spina** – practical introduction to the synthesis of the hda-type ligands and basic crystallisation techniques
- **Dr. Lei Zhang** – help with the single crystal X-Ray diffraction experiments and refinement of the obtained models
- **Dr. David Walsh**, **Annemarie O'Toole**, **Gerard Tobin**, **Adam Paterson** – proof-reading

Experimental staff members of the TCD School of Chemistry, School of Physics, CRANN, School of Engineering and Dublin Dental Hospital, who contributed to the findings described in this thesis:

- **Dr. Clive Dawling, Dr. Markus Böese, Dr. Tarek Lutz** – electron microscopy
- **Dr. Thomas McCabe, Dr Karsten Rode** – crystallography
- **Dr. John O'Brien** and **Dr. Manuel Ruther** – NMR spectroscopy
- **Dr. Bernard Jean-Denis** and **Dr. Martin Feeney** – mass spectrometry
- **Prof. Biqong Chen, Prof. Garry Fleming, Dr. Adam Dowling** – mechanical tests

External academics, who were happy to provide a positive feedback about the results and research methodologies described in this work:

- **Prof. Lia Addadi** (Weizmann Institute, Israel)
- **Prof. Fiona Meldrum** (University of Leeds, UK)

I would like to thank my mother, **Zofia Marzec** and my fiancée, **Małgorzata Nowostawska**, for their love, support and encouragement throughout past four years.

The research project along with my stay in Ireland was founded by **Dublin Region Higher Education Alliance (DRHEA)**, **Science Foundation Ireland (SFI)** and **Trinity College Dublin**. I would like to thank these institutions for their financial support.

Abbreviations

ACN – Acetonitrile

Ar –Aromatic

Bc_2hda - 2,2'-((2-hydroxy-3,5-bis(2-phenylpropan-2-yl)benzyl)azanediyl)diacetic acid

BVSA – Bond valence sum analysis

C_2vda – 2,2'-(5-(ethoxycarbonyl)-2-hydroxy-3-methoxybenzylazanediyl)diacetic acid

C_6vda – 2,2'-(5-(hexyloxycarbonyl)-2-hydroxy-3-methoxybenzylazanediyl)diacetic acid

$C_{10}vda$ – 2,2'-(5-(decyloxycarbonyl)-2-hydroxy-3-methoxybenzylazanediyl)diacetic acid

$C_{12}hda$ – 2,2'-(5-dodecyl-2-hydroxy-3-methylbenzylazanediyl)diacetic acid

Chnida – 2,2'-((3-carboxy-2-hydroxynaphthalen-1-yl)methylazanediyl)diacetic acid

DMF – N,N'-dimethylformamide

EDX – Energy-dispersive X-ray spectroscopy

ESI-MS – Electrospray ionization mass spectrometry

EtOH – Ethanol

HCnida – 2,2'-((6-carboxy-2-hydroxynaphthalen-1-yl)methylazanediyl)diacetic acid

HeIM – Scanning helium ion microscopy

HMBC – Heteronuclear multiple-bond correlation spectroscopy

HSQC – Heteronuclear single-quantum correlation spectroscopy

Hvda – 2,2'-(5-carboxy-2-hydroxy-3-methoxybenzylazanediyl)diacetic acid

IR – Infrared spectroscopy

Me_2hda - 2,2'-(2-hydroxy-3,5-dimethylbenzylazanediyl)diacetic acid

MeOH – Methanol

MOF – Metal-organic framework

m/z – Mass to charge ratio

NMR – Nuclear magnetic resonance spectroscopy

SBU – Secondary building unit

SEM – Scanning electron microscope

***t*-Bu_2hda** – 2,2'-(3,5-di-*tert*-butyl-2-hydroxybenzylazanediyl)diacetic acid

TEM – Transmission electron microscopy

TGA – Thermogravimetric analysis

UV-Vis – Ultraviolet – visible spectroscopy

Table of Contents

Summary iii

Acknowledgements v

Abbreviations vi

Table of Contents vii

--- CHAPTER I --- Introduction 1

1.1. Supramolecular chemistry 1

1.1.1. Supramolecular interactions 1

1.1.2. Hybrid materials 3

1.1.3. Iminodiacetic acid-based coordination compounds 8

1.2. Bio-inspired strategies towards the control over the $CaCO_3$ crystal morphology 17

1.2.1. Calcium carbonate – a brief insight 17

1.2.2. Influencing the morphology of $CaCO_3$ crystals 18

--- CHAPTER II --- Objectives of the project 28

--- CHAPTER III --- Supramolecular coordination compounds containing selected *d*-block metals and amphiphilic vda-type ligands 31

3.1. The synthesis and characterization of the organic ligands 31

3.1.1. A general mechanism of the Mannich reaction 31

3.1.2. Special case – Ligands based on the vanillic acid (vda-type ligands) 33

3.1.3. Crystal structure of the C_2vda monohydrate 34

3.2. Compound $[Cu(C_2vda)(H_2O)]\cdot 2H_2O\cdot 2MeOH$ (**1**) 41

*3.2.1. Characterization of compound **1*** 41

3.2.2. Additional analyses 47

*3.2.3. Formation of copper(II) oxide by the thermolysis of compound **1*** 48

3.3. Compound $[Cu_3(\mu\text{-}Cl)_2(\mu\text{-}C_2vda)(C_2vda)(H_2O)_4]\cdot H_2O$ (**2**) 52

*3.3.1. Characterization of compound **2*** 52

*3.3.2. Additional characterization of **2*** 60

*3.3.3. Thermogravimetric analysis **2*** 60

3.4. Compound $[Cu(C_6vda)(H_2O)_2]$ (**3**) 64

*3.4.1. Characterization of compound **3*** 64

*3.4.2. Thermogravimetric analysis of **3*** 71

3.5. Compound $K_2[Cu_2(\mu\text{-}Cl)_2(C_6vda)_2]\cdot 4H_2O$ (**4**) 74

*3.5.1. Characterization of compound **4*** 74

*3.5.2. Thermolysis of **4** and the formation of copper(II) oxide.* 81

3.6. Compound $[Cu(C_{10}vda)(H_2O)_2]$ (**5**) 85

*3.6.1. Characterization of compound **5*** 85
*3.6.2. Thermolysis of **5*** 92
3.7. Compound $[Zn(Me_2hda)(H_2O)_2]\cdot H_2O$ (**6**) 95
*3.7.2. Formation of copper(II) oxide by the thermolysis of **6**.* 101
--- CHAPTER IV --- Ca-containing coordination networks as templates for the synthesis of calcium carbonate **104**
4.1. Compound $[Ca_2(Chnida)_2(H_2O)_2]\cdot 4H_2O$ (**7**) 106
4.1.1. Characterization of the structure 106
*4.1.2. Thermolysis of **7*** 111
4.2. Compound $[Ca(Me_2hda)(H_2O)_3]\cdot ½H_2O\cdot ½MeOH$ (**8**) 114
*4.2.1. Characterization of compound **8*** 114
4.2.2. Additional characterization 121
*4.2.3. Compound **8** as a precursor for the formation of calcium carbonate* 123
4.3. Compound $[Ca(C_2vda)(H_2O)_2]\cdot H_2O$ (**9**) 128
*4.3.1. Characterization of **9*** 128
*4.3.2. Self-assembly of **9*** 135
*4.3.3. **9** as a template for the formation of calcium carbonate* 139
4.4. Compound $[Ca(C_6vda)(H_2O)_2]\cdot H_2O$ (**10**) 144
4.4.1. Characterization 144
*4.4.2. Thermal decomposition of **10** and the formation of calcium carbonate* 149
4.5. Compound $[Ca(C_{10}vda)(H_2O)_2]$ (**11**) 154
4.5.1. Characterization 154
4.5.2. Results of the thermal degradation 160
4.6. Compound $[Ca(C_{12}hda)(H_2O)_2]\cdot H_2O$ (**12**) 164
4.6.1. Characterization of the compound 164
*4.6.2. **12** as a template for the formation of calcium carbonate* 175
4.7. $[Ca(t\text{-}Bu_2hda)(H_2O)_2]\cdot 3H_2O$ (**13**) 181
4.7.1. Characterization 181
4.7.2. Results of the calcification 186
4.8. Compound $K_2(H_2O)_5[Ca(H_2Bc_2hda)(HBc_2hda)(H_2O)_4]Cl\cdot H_2O$ (**14**) 194
--- CHAPTER V --- Morphogenesis of calcium carbonate crystallised in the presence of the hda- and vda- type ligands **203**
5.2. Me_2hda as the habit modifier for the crystallisation of $CaCO_3$ 206
5.3. Calcium carbonate crystals templated using the $C_{12}hda$ ligand 210
5.3.1. Ligand/metal ratio dependence 210
5.3.2. Temperature dependence 213
5.3.3. Time dependence 215
5.3.4. Spherical aggregates 216
5.4. Templating effect of the vda-type ligands family 221

5.4.1. Calcium carbonate crystals grown in the presence of the C_2vda ligand 221
5.4.2. Calcium carbonate crystals grown in the presence of the C_6vda ligand 223
5.4.3. Calcium carbonate crystals grown in the presence of the C_{10}vda ligand 225

--- CHAPTER VI --- Conclusions and future work **227**

6.1. Conclusions 227
6.2. Recommended directions of future research 231

--- CHAPTER VII --- Experimental procedures **234**

7.1. Materials and methods 234
7.1.1. Reagents 234
7.1.2. Nuclear magnetic resonance spectroscopy. 234
7.1.3. Mass spectrometry 234
7.1.4. Elemental analysis 234
7.1.5. Infrared spectroscopy. 235
7.1.6. Thermogravimetric Analysis (TGA). 235
7.1.7. P-XRD analysis 235
7.1.8. Single X-ray diffraction. 235
7.1.9. SEM Microscopy. 236
7.1.10. Helium Ion Microscopy (HeIM) 236
7.1.11. TEM Microscopy. 236
7.2. Synthesis of the ligands 237
7.2.1. Synthesis of 2,2'-(2-hydroxy-3,5-dimethylbenzylazanediyl)diacetic acid (Me_2hda) 237
7.2.2. Synthesis of 2,2'-((3,5-di-tert-butyl-2-hydroxybenzyl)azanediyl)diacetic acid (t-Bu_2hda) 237
7.2.3. Synthesis of 2,2'-((2-hydroxy-3,5-bis(2-phenylpropan-2-yl)benzyl)azanediyl)diacetic acid (Bc_2hda) 238
7.2.4. Synthesis of 2,2'-((3-carboxy-2-hydroxynaphthalen-1-yl)methylazanediyl)diacetic acid (Chnida) 238
7.2.5. Synthesis of ethyl 4-hydroxy-3-methoxybenzoate (ethyl vanillate) 239
7.2.6. Synthesis of 2,2'-(5-(ethoxycarbonyl)-2-hydroxy-3-methoxybenzylazanediyl)diacetic acid (C_2vda) 239
7.2.7. Synthesis of hexyl 4-hydroxy-3-methoxybenzoate (hexyl vanillate) 240
7.2.8. Synthesis of 2,2'-(5-(hexyloxycarbonyl)-2-hydroxy-3-methoxybenzylazanediyl)diacetic acid (C_6vda) 240
7.2.9. Synthesis of decyl 4-hydroxy-3-methoxybenzoate (decyl vanillate) 241
7.2.10. Synthesis of 2,2'-(5-(decyloxycarbonyl)-2-hydroxy-3-methoxybenzylazanediyl)diacetic acid (C_{10}vda) 242
7.2.11. Synthesis of 2,2'-((5-dodecyl-2-hydroxy-3-methylbenzyl)azanediyl)diacetic acid (C_{12}hda) 242
7.3. Synthesis of the complexes 244
*7.3.1. Synthesis of $[Cu^{II}(C_2vda)(H_2O)]\cdot 2H_2O\cdot 2MeOH$ (**1**)* 244
*7.3.2. Synthesis of $[Cu^{II}_3(\mu\text{-}Cl)_2(\mu\text{-}C_2vda)(C_2vda)(H_2O)_4]\cdot H_2O$ (**2**)* 244
*7.3.3. Synthesis of $[Cu^{II}(C_6vda)(H_2O)_2]$ (**3**)* 244

*7.3.4. Synthesis of $K_2[Cu_2(\mu\text{-}Cl)_2(C_6vda)_2]\cdot 4H_2O$ (**4**)* 245
*7.3.5. Synthesis of $[Cu^{II}(C_{10}vda)(H_2O)_2]$ (**5**)* 245
*7.3.6. Synthesis of $[Zn(Me_2hda)(H_2O)_2]\cdot H_2O$ (**6**)* 245
*7.3.7. Synthesis of $[Ca_2(Chnida)_2(H_2O)_2]\cdot 4H_2O$ (**7**)* 245
*7.3.8. Synthesis of $[Ca(Me_2hda)(H_2O)_3]\cdot ½H_2O\cdot ½MeOH$ (**8**)* 246
*7.3.9. Synthesis of $[Ca(C_2vda)(H_2O)_2]\cdot H_2O$ (**9**)* 246
*7.3.10. Synthesis of $[Ca(C_6vda)(H_2O)_2]\cdot H_2O$ (**10**)* 246
*7.3.11. Synthesis of $[Ca(C_{10}vda)(H_2O)_2]$ (**11**)* 247
*7.3.12. Synthesis of $[Ca(C_{12}hda)(H_2O)_2]\cdot H_2O$ (**12**)* 247
*7.3.13. Synthesis of $[Ca(t\text{-}Bu_2hda)(H_2O)_2]\cdot 3H_2O$ (**13**)* 247
*7.3.14. Synthesis of $K_2(H_2O)_5[Ca(H_2Bc_2hda)(HBc_2hda)(H_2O)_4]Cl\cdot H_2O$ (**14**)* 248
7.4. $CaCO_3$ morphogenesis 249
7.4.1. General synthetic procedure 249
7.4.2. Sample preparation and methods 249
References **250**
Appendixes **256**
A.1. 2D NMR results 256
A.2.1. HMBC spectrum of 2,2'-(5-(ethoxycarbonyl)-2-hydroxy-3-methoxybenzylazanediyl)diacetic acid (C_2vda) 256
A.2.2. HMBC spectrum of 2,2'-(5-(hexyloxycarbonyl)-2-hydroxy-3-methoxybenzylazanediyl)diacetic acid (C_6vda) 257
A.2.3. HSQC and HMBC spectra of 2,2'-(5-(decyloxycarbonyl)-2-hydroxy-3-methoxybenzylazanediyl)diacetic acid ($C_{10}vda$) 258
A.2. Mechanical measurements results 260
*A.2.1. The nanoindentation experiment on compound **12*** 260
7.5. Content of the attached CD 261

–– CHAPTER I ––

Introduction

1.1. Supramolecular chemistry

Supramolecular chemistry is often described as 'the chemistry beyond a single molecule'.[1] The area of interest of this discipline of science is widespread and ranges from studying weak, non-covalent interactions between at least two molecules, to the understanding of principles which allow biological systems to work and fulfil designated roles in living organisms.[2] This variety of research topics results in many developed or potential applications associated with supramolecular chemistry concepts, involving for instance, the syntheses of new drug delivery systems, improvements in materials science, contributions to crystallography or even nanotechnology, where bottom-up approaches become increasingly important for the design of modern nanomachines and nanodevices.[3] A deep understanding of processes like molecular recognition or self-assembly of matter is necessary to model and mimic evolved natural phenomena and synthesis concepts. Those processes that unfold in living matter usually result in the creation of materials characterised by outstanding mechanical properties, which are in direct relation to their molecular structure. Such materials are very often hybrids and their inorganic parts contain ions of the following metals or metalloids: calcium, magnesium, iron, silicon, zinc, strontium and barium. Typical inorganic anionic components can be carbonates, sulphates or phosphates.[4,5] Anionic components can also be provided by simple organic molecules, like oxalates, alcohols or amino acids[6], or more advanced compounds, such as proteins, lipids[7] or polymers.[8] Supramolecular chemistry can contribute to science in many different ways as it leads to the formation of functional materials. Interesting examples of possible applications of this discipline include synthesis of single molecule magnets[9], metal-organic frameworks[10-12], porous materials for gas separation[13] or self-assembled materials for regenerative medicine.[14-16]

1.1.1. Supramolecular interactions

There are several interactions that are beneficial to supramolecular chemistry due to their abilities to link neighbouring molecules into more complex structures. These are coordination bonds[17] and other non-covalent interactions, such as electrostatic ion-ion, ion-dipole and dipole-dipole interactions[18-20], hydrogen bonds, π - π stacking interactions[21-24], van der Waals forces[25-27] and hydrophobic effects[28,29]. The existence of these intermolecular forces gives rise to the processes of molecular recognition and self-assembly, which are highly selective and a key role in the development of supramolecular systems.

Hydrogen bonds

Hydrogen bonds are the dominant type of interactions that prevail in many polar reaction systems and significantly influence the structures of supramolecular coordination assemblies described in this thesis. Hydrogen bonding occurs between a hydrogen atom, which is typically linked *via* a covalent bond to another atom, and an electronegative atom, such as fluorine, chlorine, nitrogen or oxygen.[30,31] The typical O-O distance of a H-bond donor and acceptor pair depends on the exact geometry of the bonding partners and typically varies between 2.6 and 3.0 Å.[32] Distances smaller than 2.5 Å are rarely observed and indicate a very strong hydrogen bond interaction.[33] The energy of a hydrogen bond between two uncharged groups usually ranges from 4 kJ·mol^{-1} to 6 kJ·mol^{-1}, whereas that involving a charged group is slightly higher, 6 kJ·mol^{-1} to 12 kJ·mol^{-1}. The energy of a hydrogen bond between a charged donor and a charged acceptor may reach *ca.* 17 kJ·mol^{-1}.[34]

Hydrogen bonds are ubiquitous in nature. DNA is a prominent example of a naturally occurring material that is stabilised by hydrogen bond interactions to adopt its 3D structure.[35] This compound is a polymer composed of two anti-parallel strands and the monomeric units of each strand are called nucleotides. They consist of a backbone comprising of a phosphorylated deoxyribose unit, and a heterocyclic base belonging either to the purine or pyrimidine class. The strands self-assemble into the well-known double helix by forming hydrogen bonds between pairs of complementary bases.[36] As presented in Fig. 1.1, adenine (A) binds to thymine (T) *via* two hydrogen bonds while guanine (G) interacts with cytosine (C) *via* three hydrogen bonds.[37] Due to the geometrical restrictions, which involve the precise and fixed location of the hydrogen atoms and the electron lone pairs, other combinations of bases are not allowed.[38] The particular sequence of the bases encodes genetic information.[39]

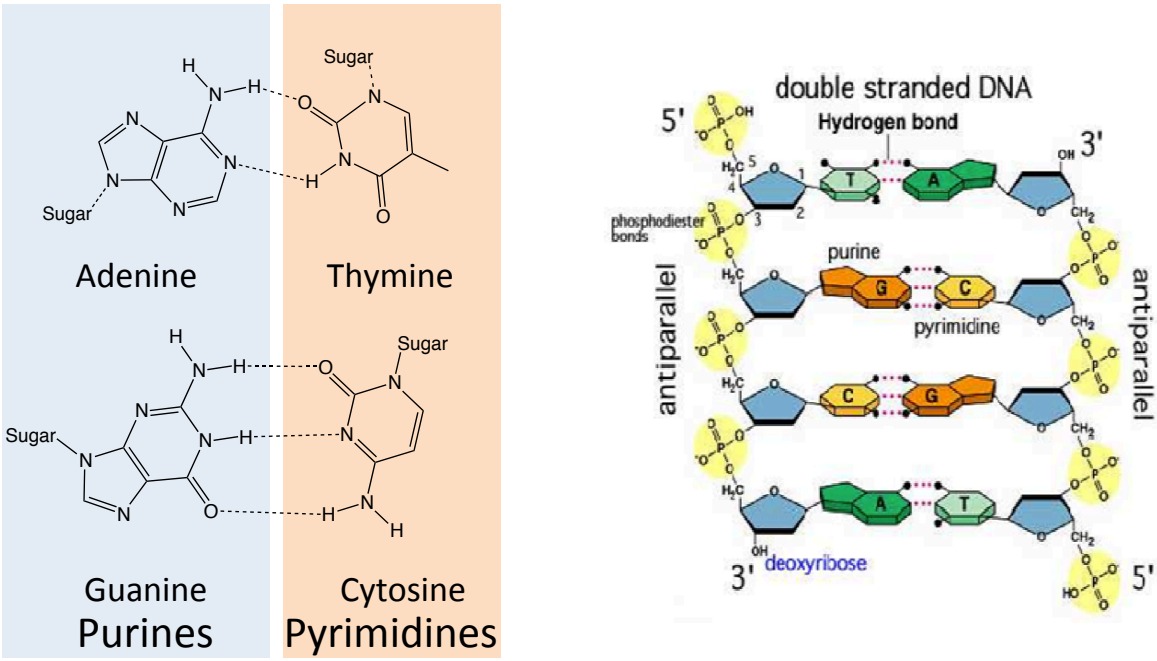

Fig. 1.1 | (**left**) Pairs of complementary bases observed in DNA bound with hydrogen bonds; (**right**) the hydrogen bonds contribute to the self-assembly of a double helix structure.[40]

1.1.2. Hybrid materials

The supramolecular interactions and coordinative bonds have the ability to combine inorganic moieties with organic moieties, for instance with small organic molecules or macromolecular proteins. The underlying synthetic methodology is widely explored in nature, where evolutionary refined processes are responsible for the construction of hybrid, organic-inorganic materials characterised by unique properties and functions. Examples of such materials are crustacean carapaces or mollusc shells and bone or teeth tissues in vertebrates.[41] Hybrid materials can generally be defined as nanocomposites, where the inorganic and organic components are intimately mixed. The properties of these materials are often not simply a sum of the individual attributes of both components. The physicochemical, electronic and mechanical characteristics are influenced by the overlapping orbitals, electron transfer processes and geometrical arrangements observed on the inner interface between the organic and inorganic moieties.[42]

Depending on the involved bonds that link the organic and inorganic parts of the composite, hybrid materials can be divided into two classes. In the first class, the inorganic phase is immersed within the organic 'matrix' or *vice versa* and only weak, non-covalent bonds link both phases. A good example of a material that belongs to this class is the Maya Blue pigment, which has been extensively used by ancient and medieval societies.[43] It consists of molecules of the natural blue indigo that are encapsulated within the channels of clay. The resulting composite combines the colour of the organic dye and the mechanical resistance of the inorganic host.[44]

Within the second class of hybrid materials, the organic and inorganic phases are connected *via* stronger chemical bonds. These materials are in particular being considered for advanced and innovative applications in many fields, including optics, electronics, ionics, mechanics, membranes, protective coatings, catalysis, gas storage, sensors and biology.[41] The chemical strategy for the construction of the second class of materials relies on the formation of relatively stable chemical linkages that associate the different components. As presented in Fig. 1.2, there are several pathways that allow the preparation of materials of this class. One approach, path A, relies on sol-gel approaches and solvothermal/hydrothermal conditions under which metal ions and bridging and polyfunctional precursors react.[45]

Path B corresponds to the assembling or the dispersion of well-defined nanobuilding blocks (NBB) which consist of well defined preformed objects or units that maintain their integrity in the final material.[46-48]

Path C is a popular synthetic approach to hybrid materials. It relies on the intentional design and synthesis of building blocks that have the ability to self-assemble.[49] In contrast to path B, additional non-covalent interactions prevail between these building units giving rise to specific affinities, molecular recognition processes or template effects, allowing further self-organisation of the material. These interactions have the potential to influence the morphology and the topology of the resulting hybrid composites.[50-52]

Hybrid materials can be further sub-divided into rigid, hard and soft, flexible materials. This division relates to the composition and structure at the molecular level, which is further reflected in the macroscopic properties of the material.[53] Good examples of the rigid materials include metal-organic frameworks, in which a directed construction of defined building units results in distinct topologies with vast empty spaces giving rise to highly porous materials.[54]

In contrast, soft materials usually contain amphiphilic moieties within their structures and their formation is driven by less directed self-assembly processes.[42,55-57]

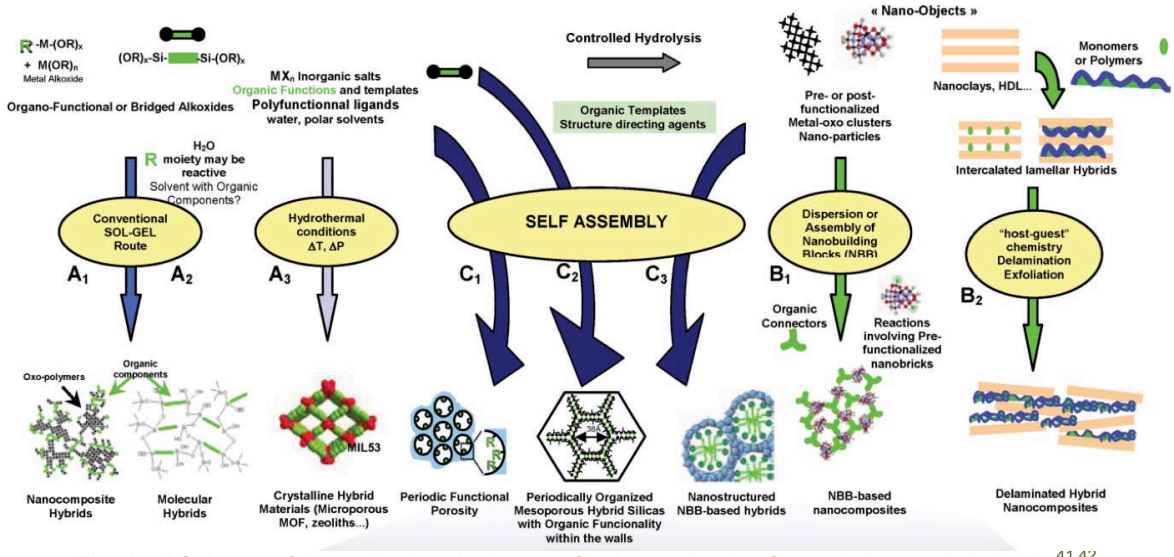

Fig. 1.2 | Scheme of the main chemical routes for the synthesis of organic-inorganic hybrids.[41,42]

Metal-organic frameworks

Metal-organic frameworks (MOFs) are important crystalline, hybrid materials consisting of clusters, complexes or metal ions linked by organic ligands and resulting in microporous networks. The interest in these compounds is a result of their advantageous characteristics which include facile synthesis, high porosity and being amenable to chemical modifications for targeted purposes.[58,59] MOFs and other hybrid network structures have potentially excellent H_2 storage capabilities and research activities are aiming to provide scientific preconditions to initiate a shift towards more sustainable energy concepts.[32,60,61]

Recent examples of important discoveries in this field include the synthesis and characterisation of MOF-5 and new MOF-505 structures reported by Yaghi *et al.*[54,62] The methodology applied by this group takes advantage of predefined secondary building units (SBUs) that link *via* coordination bonds to give default topologies (reticular synthesis concept). It was observed that guest solvent molecules present inside the structures can be easily removed by increasing the temperature while the network retains its structural integrity. Moreover, it was demonstrated that some high-surface area networks can effectively absorb gases like nitrogen or hydrogen, however**,** for industrial applications the temperature difference between absorption and desorption has to be adjusted to a reasonable scale. For MOF-5 the reaction was carried out between $Zn(NO_3)_2$ and terephtalic acid (BDC) and the formation of tetranuclear Zn building units $\{Zn_4O(CO_2)_2\}$ with octahedral topology resulted in

a stable, rigid framework with octahedral topology. MOF-55 contains $\{Cu_2(CO_2)_4\}$ paddle wheel complexes and the 3,3',5,5'-biphenyltetracarboxylic acid (H_4bptc) as organic linkers. The molecular structures of MOF-5 and MF-505 are shown Fig. 1.3.

Yaghi *et al*. demonstrated that by reacting $Zn(NO_3)_2$ with extended carboxylate ligands one can systematically increase the surface area whilst maintaining a given topology (isoreticular structures). Different ligand structures and functionalities may give different topologies that are often related to those purely inorganic solid states structures.[58]

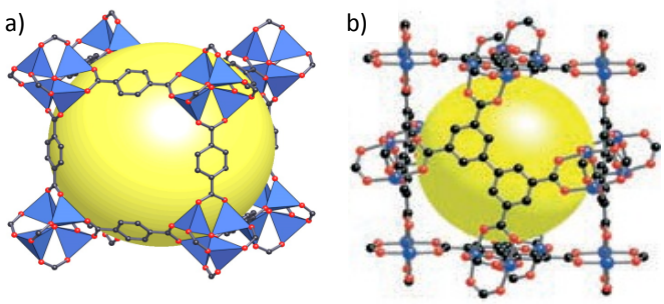

Fig. 1.3 | a) – Primitive cubic topology of $[Zn_4O(BDC)_3]\cdot(DMF)_8(C_6H_5Cl)$, MOF-5, framework. The yellow sphere represents the largest sphere that would occupy the cavity without contacting the internal van der Waals surface; **b)** - Structure of MOF-505. The chemical formula of this compound is $[Cu_2(bptc)(H_2O)_2]$. Solvent molecules were omitted for clarity. Cu: blue; C: black; O: red.[54,62]

When using H_3bte and H_2bpdc ligands (Fig. 1.4) it is possible to synthesise a metal-organic framework (MOF-210) which is characterised by an extremely high surface area of 6240 $m^2 \cdot g^{-1}$. Theoretical calculations indicate that MOF-210 should have excellent hydrogen storage capabilities with the gravimetric H_2 density of 176 $mg \cdot g^{-1}$. The reported chemical formula of this compound is $Zn_4O(BTE)_{4/3}(BPDC)$ and the structure consists of aforementioned $\{Zn_4O(CO_2)_2\}$ units which are connected by the organic ligands.[63]

MOFs and other hybrid organic-inorganic materials containing biologically relevant elements such as Ca and Zn may also be viewed in relation to biomimetic synthetic concepts.[64] Calcium cations are the basic ingredient of any living creature's skeleton. In the form of carbonate, oxalate or phosphate it crystallises in a biological matrix and creates various types of tissues: shells, teeth and bones.[65] Zinc is one of the microelements, which are necessary for humans to live. It is included in the active centre of over 200 enzymes present in all developed organisms (i.e. carbonic anhydrase, histone deacetylases or angiotensin converting enzyme).[66]

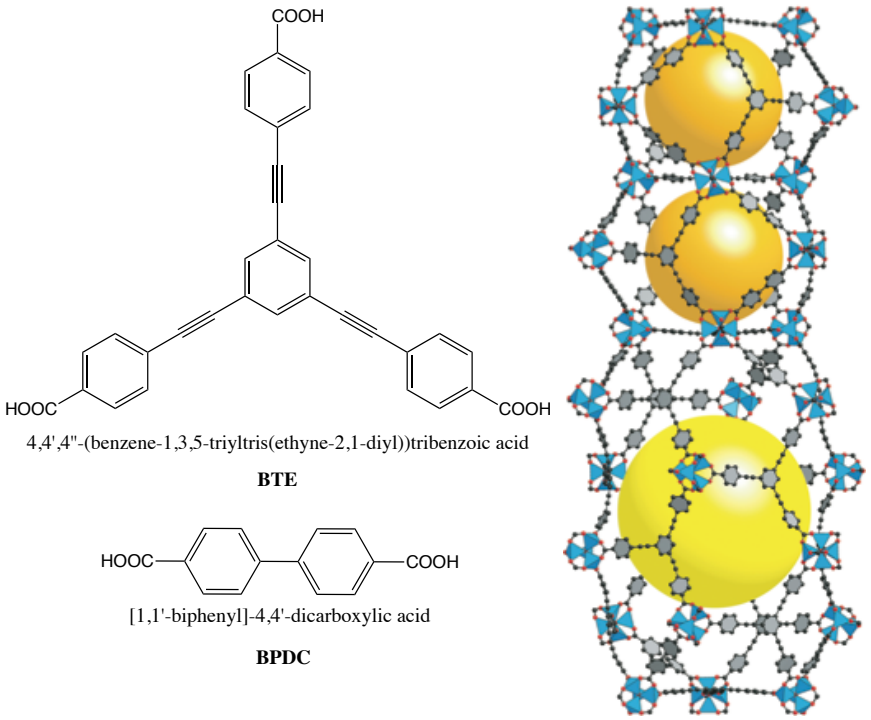

Fig. 1.4 | (**left**) Structure of the BTE and BPDC ligands used for the synthesis of MOF-210; (**right**) network structure in MOF-210; the yellow spheres represent the largest volumes that would occupy the cavity without contacting the internal van der Waals surface.[63]

Soft materials

Supramolecular chemistry concepts apply several different approaches to create different types of functional materials. These approaches include self-assembly (process where highly disordered system changes into an ordered structure as a result of specific, local interactions of molecules[67,68]) and molecular recognition (specific non-covalent interactions between two molecules, where the first molecule acts as a host, and the second – as a guest[69]).

In the age of nanotechnology, self-assembly processes seem to play the key role in the development of bottom-up methodologies towards the synthesis of modern materials. According to central objectives of this underlying concept, molecules can assemble into hierarchical materials or useful nanodevices, while traditional manufacturing based on the top-down methodology may fail to produce small and resolved structures due to physical restrictions or technical limits (like in electron lithography).[70] Self-assembled structures are present in many biological systems. Numerous successful bio-inspired approaches for materials synthesis use amphiphiles to provide well defined and confined spaces in which**,** for instance**,** mineralisation and condensations of inorganic phases can occur.[71-73]

Certain self-assembled materials were proven to be biocompatible and might play a key role in the development of nanotechnology and material science concepts, especially in the field of regenerative medicine. For instance, the self-assembly of the specific group of compounds known as peptide amphiphiles (PA) leads to the formation of bioactive nanofibres. They were shown *in vivo* to accelerate the regeneration of damaged nervous systems in mice, however**,** their full potential in human treatments has not been studied yet.[74] An example of a functional PA is presented in Fig. 1.5. The compound consists of a long alkyl chain which has a gradually changing amphilicity: from the hydrophobic alkane to the amine-enriched end. The

lone pairs of electrons present on the nitrogen and oxygen atoms may act as donors and bind to metal ions or other organic molecules, e.g. proteins. Moreover, the structure presented below can be considered as biocompatible as it contains peptide part found in biogenic proteins.

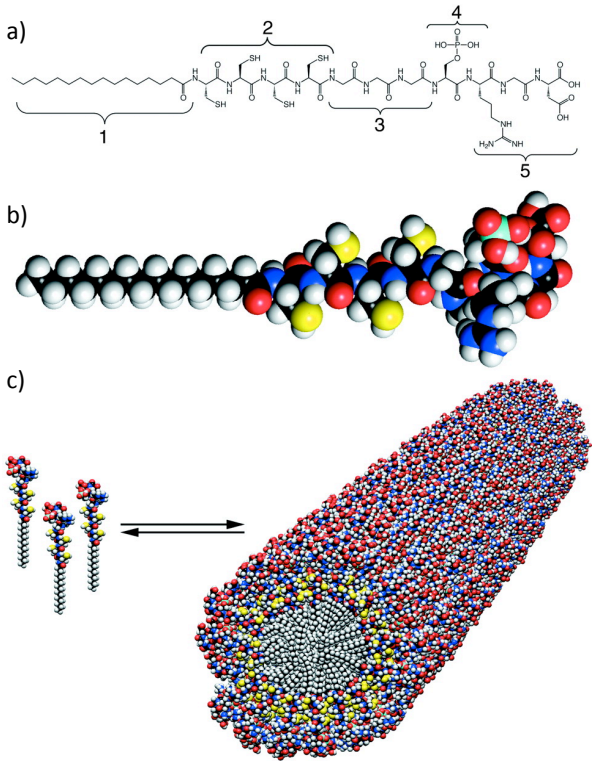

Fig. 1.5 | a) Chemical formula of heparin-binding peptide amphiphile. The polarity changes gradually along the chain; **b)** a ball-and-stick model representing the peptide amphiphile; **c)** the self-assembly process leads to the formation of fibres that express the hydrophilic parts towards the surface while their core is composed of hydrophobic aliphatic chains.[74]

PA molecules have the ability to self-assemble into fibres with diameters varying from a few to several hundreds of nanometres**,** while the length of one individual fibre may reach micrometre dimensions. Fig. 1.6 shows an example of self-assembled PAs.

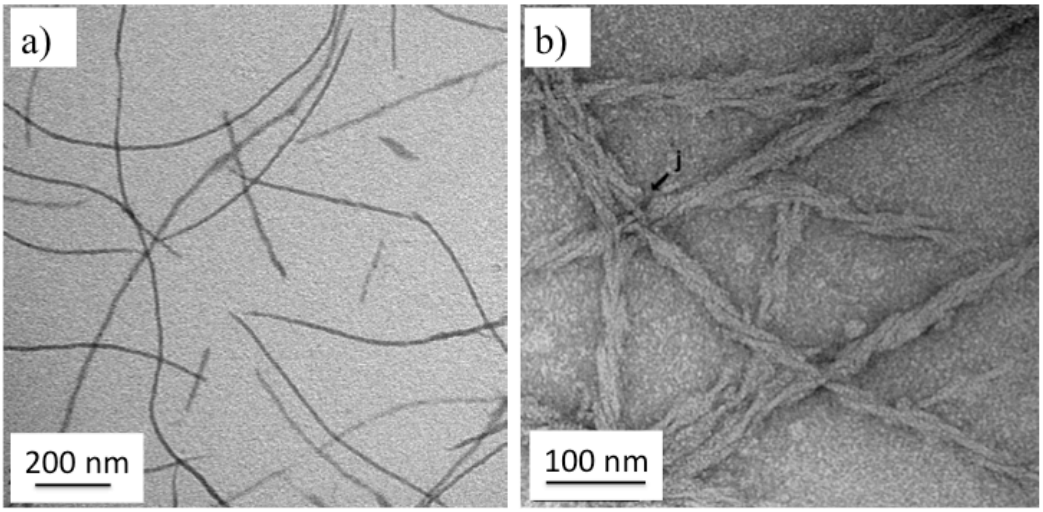

Fig. 1.6 | Fibres that form upon self-assembly of PA molecules. **a)** - TEM image; **b)** – magnification which reveals the helical nature of the resulting fibrous assembly.[75]

The same material has been proven to act as an excellent scaffold for the *in vivo* growth of stem cells derived from mononuclear bone-marrow cells. This is a promising solution for the treatment of acute and chronic myocardial infarction and peripheral arterial disease.[76]

This use of self-assembled structure to stimulate cell growth has not been exploited greatly, however, recently published results are promising and seem to indicate improvements in the treatment of diverse systems, including the nervous and immune systems.[76-80]

Self-assembled fibres of peptide amphiphiles may also act as a gel matrix which can be a template for the biomineralisation of hydroxyapatite. It was shown, that enzymatically mediated harvesting of phosphate ions combined with nanofibre surface nucleation can lead to a spatially selective and biomimetic mineralisation in a 3D environment. This work suggests that both spatial and temporal elements are necessary to achieve biomimetic mineralisation in synthetic materials.[81]

1.1.3. Iminodiacetic acid-based coordination compounds

This thesis describes supramolecular coordination complexes that are based on iminodiacetic acid-containing ligands. As presented in Sch. 1.1 iminodiacetic acid (ida) is an organic acid that consists of two acetic acid moieties bound to a secondary amine group. This compound and its derivatives have been extensively used in coordination chemistry to generate a vast number of coordination complexes. The resulting compounds range from small, mononuclear complexes to large multinuclear clusters.

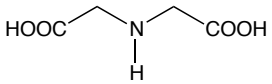

Sch. 1.1. | The structure of iminodiacetic acid (ida).

Mononuclear complexes

In a typical case, the reaction between the unsubstituted ida molecule and a *d*-block metal ion results in the formation of a mononuclear complex, where the ligand provides two O-donors and one N-donor.[82-88] The resulting coordination sphere surrounding the metal ion can be often described as a distorted octahedron, where each ida molecule provides two O-donors and one N-donor.[82, 89-91] The complexes containing the Fe^{III} and Al^{III} ions, $[Fe(ida)_2]^-$ and $[Al(ida)_2]^-$, which were reported by Schmitt *et al.*, illustrate the binding characteristic of this ligand (see Fig. 1.7).[92]

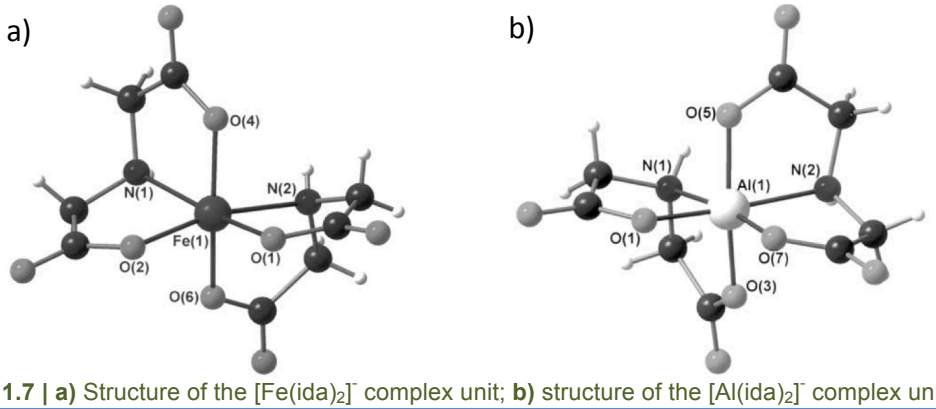

Fig 1.7 | a) Structure of the $[Fe(ida)_2]^-$ complex unit; **b)** structure of the $[Al(ida)_2]^-$ complex unit.[92]

Substituting the hydrogen atom of the amine group with diverse aliphatic functionalities provides a convenient way of modifying iminodiacetic acid through introduction of additional O- and N-donors that change the chelating ability. For instance, Heath *et al.* presented an interesting report concerning the behaviour of the Heidi ligand in reactions with Fe^{3+} ions in an aqueous environment.[93] Heidi, 2,2'-((2-hydroxyethyl)azanediyl)diacetic acid, is an organic complexing agent that consists of the iminodiacetic acid moiety that is N-substituted with a hydroxyethyl residue (Fig. 1.8). The reported reactions were carried out using two different sets of experimental conditions. When the 1:1 molar ratio of Heidi to Fe^{III} was used, the reaction resulted in the formation of dinuclear species with the chemical formula $[Fe^{III}(Heidi)(H_2O)_2]$ (Fig. 1.8b). Within these complexes, the iminodiacetic acid moiety provides two O-donors and one N-donor, while the O-donors of the hydroxyl groups form μ_2-type bridges between two neighbouring metal ions. Water molecules occupy the remaining sites of the octahedral coordination spheres.

It was noted that when the Heidi/Fe^{III} molar ratio is changed to 1:2, the reaction yielded in Fe_{17} and Fe_{19} coordination clusters (see Fig. 1.8c), $[Fe_{17}(\mu_3\text{-}O)_4(\mu_3\text{-}OH)_6(\mu_2\text{-}OH)_{10}(Heidi)_8(H_2O)_{12}]^{3+}$ and $[Fe_{19}(\mu_3\text{-}O)_6(\mu_3\text{-}OH)_6(\mu_2\text{-}OH)_8(Heidi)_{10}(H_2O)_{12}]^{+}$ respectively. Within these clusters, the oxo- and hydroxo-bridges are observed. The most striking feature is that these clusters stabilise brucite-type mineral cores. The organic ligand moieties are located on the periphery adopting coordination modes that are closely related to that observed in the dinuclear units.

Similar complexes can also be isolated from the corresponding Al^{III}/Heidi system.[94]

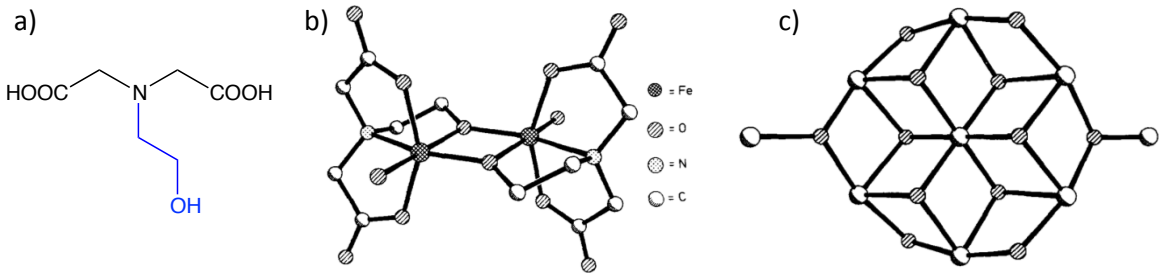

Fig. 1.8 | a) Structure of the Heidi ligand; **b)** crystal structure of the alkoxo-bridged dinuclear complex $[Fe(Heidi)(H_2O)_2]_2$; **c)** the core unit of the Heidi-containing Fe_{17} and Fe_{19} clusters.[93]

The iminodiacetic acid moiety can be attached to a phenol moiety, giving rise to structurally modified organic ligands which are closely related to Heidi and retain the ida coordinating properties. Again, two Fe^{III}-containing compounds $[Fe(t\text{-}Bu_2hda)(H_2O)_2]\cdot 3H_2O$ and $[Fe(Bc_2hda)(H_2O)(EtOH)]\cdot 4H_2O$ reported by Schmitt *et al.* illustrate the coordination behaviour of this class of hda-ligands. As presented in Fig. 1.9, both complexes contain an octahedrally coordinated metal ion. Each iminodiacetic acid moiety provides two O-donors and one N-donor and the oxygen atom of the aromatic hydroxyl group contributes to the coordination sphere which is further completed by coordination water molecules. The structure packing diagrams (Fig. 1.9c-d,h-i) show that in both cases the mononuclear complexes self-assemble into a layered, lamellar material, where the hydrophilic, mainly metal-containing layers sandwich between the hydrophobic parts, composed of the ligand molecules. These

hydrophobic regions are stabilised by dispersion forces and π - π stacking interactions between the aromatic substituents.

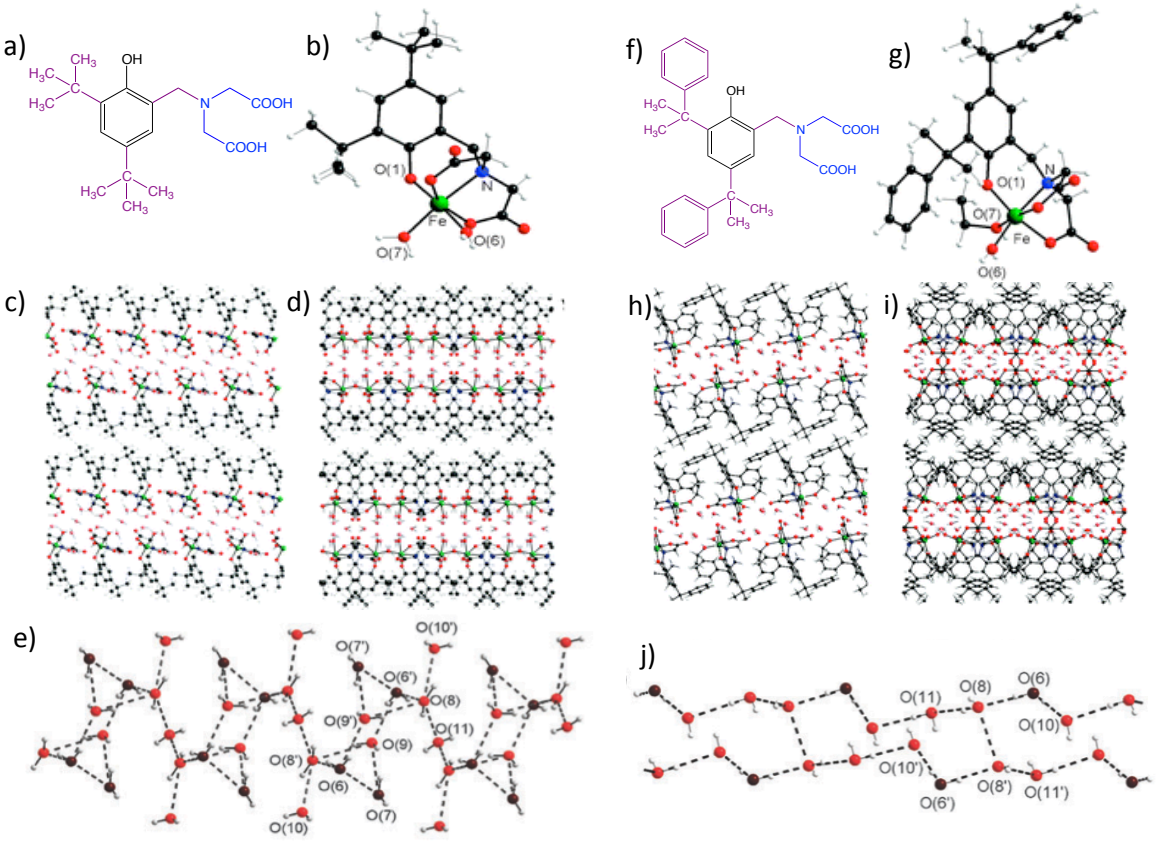

Fig. 1.9 | Examples of layered lamellar arrangement in compounds consisting of *t*-Bu_2hda (**a**-**e**) and Bc_2hda (**f**-**j**) ligands bound to the Fe^{3+} ion. **a)** – structure of the *t*-Bu_2hda ligand; **b)** mononuclear complex in [Fe(*t*-Bu_2hda)$(H_2O)_2$]·$3H_2O$ and its packing diagrams viewed along the crystallographic *b*-axis (**c**) and *c*-axis (**d**); **e)** hydrogen bonded network of constitution (red) and coordination (black) water molecules in the hydrophilic region; **f)** structure of the Bc_2hda ligand; **g)** mononuclear complex in [Fe(Bc_2hda)(H_2O)(EtOH)]·$4H_2O$ and its packing diagrams viewed along the crystallographic *b*-axis (**h**) and *c*-axis (**i**); **j)** hydrogen bonded network of constitution and coordination (brown) water molecules in the hydrophilic area.[95]

It was observed that the coordination and constitutional water molecules that occupy the confined hydrophilic regions within the supramolecular assemblies form H-bound networks (see Fig. 1.9e and j). In case of [Fe(*t*-Bu_2hda)$(H_2O)_2$]·$3H_2O$, the network formed by the water molecules shows some resemblance to the structure of the ice phase I_h.[95]

McKeogh *et al.* exploited the C_{12}hda ligand, which consists of the iminodiacetic acid moiety linked to a phenol ring that contains a dodecyl substituent in *para* position to the hydroxyl functionality (Fig. 1.10a).[95] A reaction between C_{12}hda and Fe^{III} ions results in the formation of compound [Fe^{III}(C_{12}hda)$(H_2O)_2$]·nH_2O that is structurally related to the previously discussed compounds. Due to the presence of the long aliphatic substituent, obtaining single crystals suitable for a single crystal X-ray diffraction experiment proved challenging and was not achieved. As presented in Fig. 1.10b-c, SEM images of the compound show that the complexes self-assemble into spheres and vesicles. Further TEM investigations revealed that the assemblies display a highly ordered, lamellar structure (Fig. 1.10d) similar to that of the parent crystalline complexes. The authors concluded, that the introduction of the dodecyl chain does not affect the coordinating mode of the ligand and results in the formation of a

layered structure where the distance separating the hydrophilic areas equals *ca.* 3.5 nm corresponding well with the extend of the alkyl chain.[95]

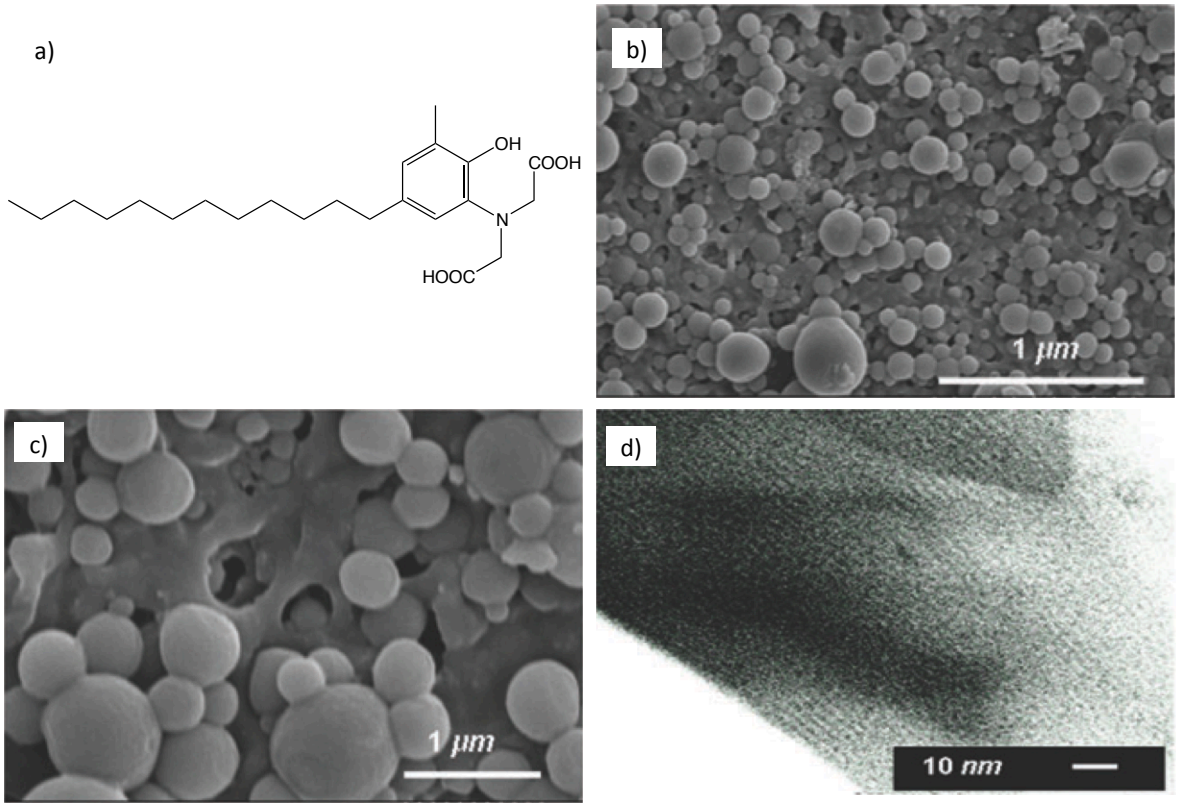

Fig. 1.10 | a) structure of the C_{12}hda ligand; **b-c)** SEM images of the self-assembled spheres of $[Fe^{III}(C_{12}hda)(H_2O)_2]\cdot nH_2O$; **d)** TEM image identifies a layered, lamellar arrangement of the Fe^{III} complexes.

Dinuclear complexes

The control over the nuclearity of the hda-based coordination complexes is realised by changing the reaction conditions. For instance, the reaction between the Bc_2hda ligand and Fe^{III} ions performed in neutral conditions, results in the previously described mononuclear complex in $[Fe(Bc_2hda)(H_2O)(EtOH)]\cdot 4H_2O$, while in the presence of $KHCO_3$ a dinuclear complex $K_4[(Bc_2hda)_2(\mu\text{-}CO_3)_2Fe^{III}_2]\cdot 6H_2O\cdot 2EtOH$ forms.[96] Within this complex, the mononuclear ligand-stabilised {Fe(Bc_2hda)} units are dimerisied through bridging carbonate functionalities. A remarkable feature of this compound is the presence of a potassium counter-ion that interacts with the aromatic substituents of the phenyl ring *via* π-cation interactions. As presented in Fig. 1.11, this interaction provides additional stabilisation to the dinuclear complex.

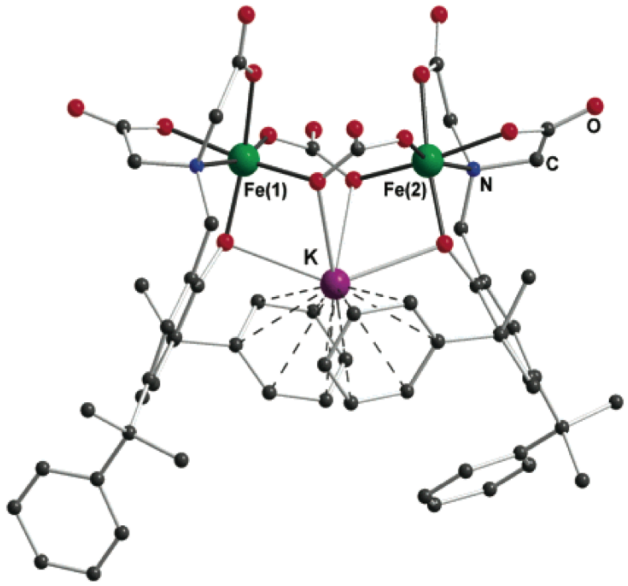

Fig. 1.11 | π-cation binding of a potassium ion in $K_4[(Bc_2hda)_2(\mu\text{-}CO_3)_2Fe^{III}_2]\cdot 6H_2O\cdot 2EtOH$.[96]

The presence of potassium hydroxide in the reaction mixture also affects the reaction between *t*-Bu_2hda and Fe^{III} ions, giving rise to the dinuclear complex $K_3[Fe_2(t\text{-}Bu_2hda)(\mu\text{-}OH)(\mu\text{-}CO_3)]\cdot 3H_2O\cdot EtOH$, where the mononuclear {Fe(*t*-Bu_2hda)} units are connected through carbonate and hydroxo bridges. The packing structure of both dinuclear Fe^{III} complexes is very similar to the packing diagrams of the corresponding mononuclear complexes (see Fig. 1.9). Both compounds display a hierarchical, lamellar structure, where the hydrophobic and hydrophilic layers are clearly separated.[96]

Later investigations revealed that the solid-state packing motifs of the dinuclear Fe^{III} complexes containing iminodiacetic acid moieties are affected by the introduction of additional functional groups to the phenolic or naphtoic ring. As presented in Fig. 1.12, when the aromatic ring is substituted with aliphatic residues occupying the *ortho* and/or *para* positions (with respect to the hydroxyl group), the resulting complexes adopt a layered, lamellar arrangements, similar to the packing motifs presented in Fig. 1.9. However, when the naphtoic ring is substituted with a carboxylate group located next to the hydroxyl group, the self-organisation of the complexes leads to the formation of dense networks, which display a hexagonal honeycomb motif. Finally, when the additional O-donors are located in the *para* position (again, with respect to the hydroxyl group), the complexes self-assemble into an open-framework structures in which dinuclear units pillar between hydrophilic areas of the structure.[61]

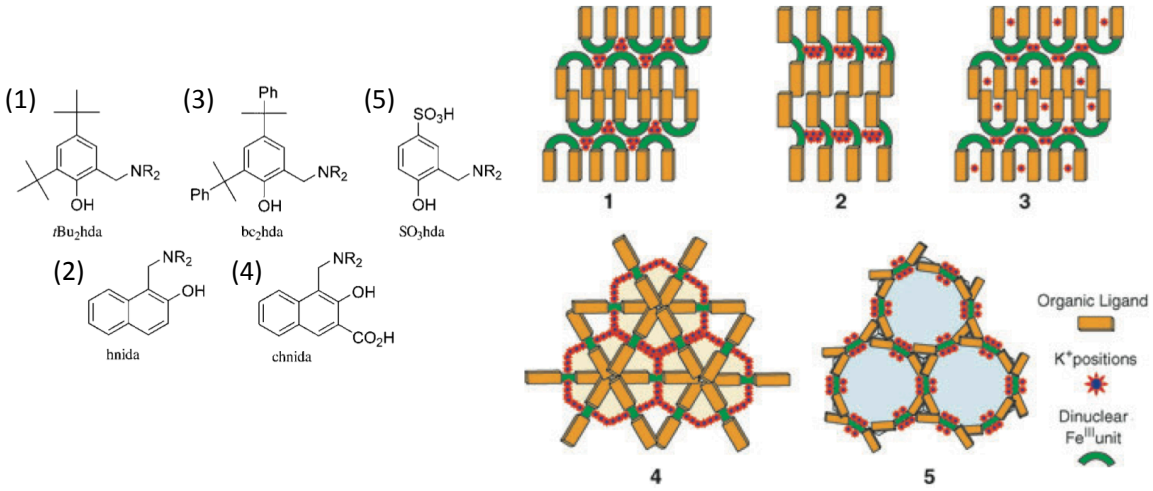

Fig. 1.12 | (left) The protonated *hda*-based organic ligands used in the studies; (right) pictograms of structural motifs in the supramolecular coordination networks. The numbers in brackets correspond to the observed supramolecular packing motif.[61]

Good examples of complexes that self-assemble to give the honeycomb-like packing structures are the dinuclear compounds $[Fe_2(\mu\text{-}O)(\mu\text{-}CO_3)(Chnida)_2]^{6-}$ and $[Fe_2(\mu\text{-}O)(\mu\text{-}CO_3)(SO_3\text{-}hda)_2]^{6-}$ reported by Schmitt *et al.*[61] As presented in Fig. 1.13, both dinuclear complexes contain two mononuclear [Fe(hda)] untis that are bridged through oxo and carbonate anions. In case of the Chnida-containing complex, the packing of the dinuclear units gives rise to the formation of a hexagonal, honeycomb-like structure, where the large pores are occupied by the hydrophobic moieties of the ligand molecules and the dinuclear complex penetrate the walls of the supramolecular architecture. The packing motif observed for the complex containing the SO_3-hda ligand is different - the walls within the hexagonal honeycomb-like structure are formed by the complexes, which are precisely aligned and give rise to an open framework assembly.

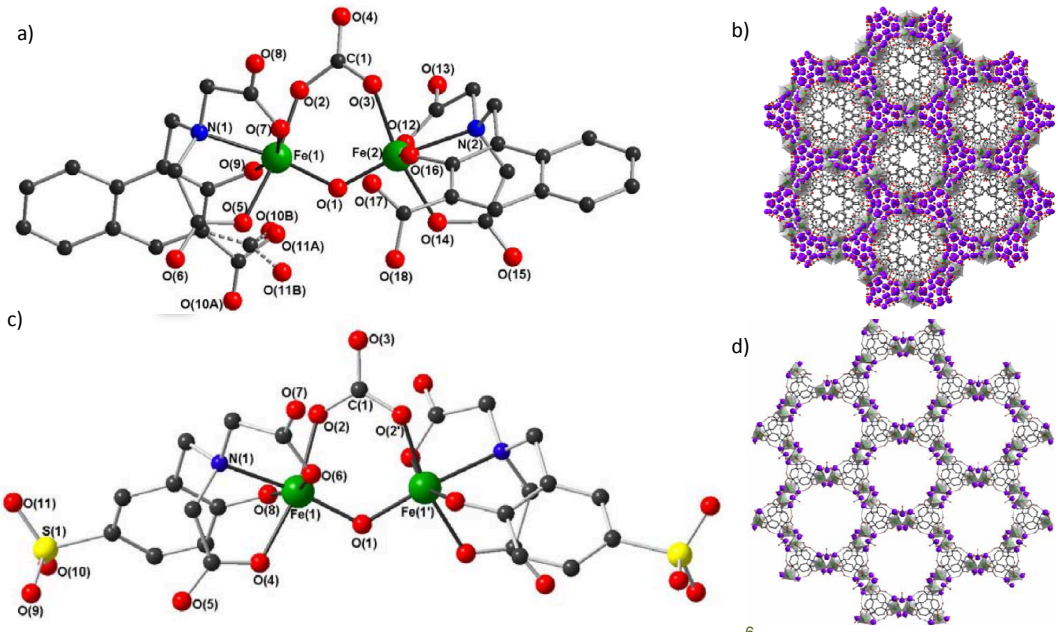

Fig. 1.13 | a) The structure of the dinuclear unit $[Fe_2(\mu\text{-}O)(\mu\text{-}CO_3)(\textit{chnida})_2]^{6-}$ and the corresponding packing structure (**b**); **c)** structure of the $[Fe_2(\mu\text{-}O)(\mu\text{-}CO_3)(SO_3\text{-}hda)_2]^{6-}$ unit and the corresponding packing diagram (**d**).[61]

The dinuclear complex $[Fe_2(\mu\text{-}O)(\mu\text{-}CO_3)(Chnida)_2]^{6-}$ also forms when the reaction between Fe^{III} ions and Chnida is preformed in the presence of NaOH.[97] The resulting compound, with the chemical formula $Na_6[Fe_2(\mu\text{-}O)(\mu\text{-}CO_3)(Chnida)_2]\cdot 12H_2O$ adopts a similar, dense honeycomb-like packing motif than the previously discussed potassium-stabilised compound. The Na-analogue was used as a template for the mineralisation of Na_2CO_3. After heating single crystals in the temperature range between 250°C and 350°C the material starts decomposing with the thermal degradation products being iron oxide and fibres of sodium carbonate (Fig. 1.14). The diameter of these Na_2CO_3 fibres is approximately 50-100 nm. This result confirms that the framework acts as a template for Na_2CO_3 crystal growth.[97]

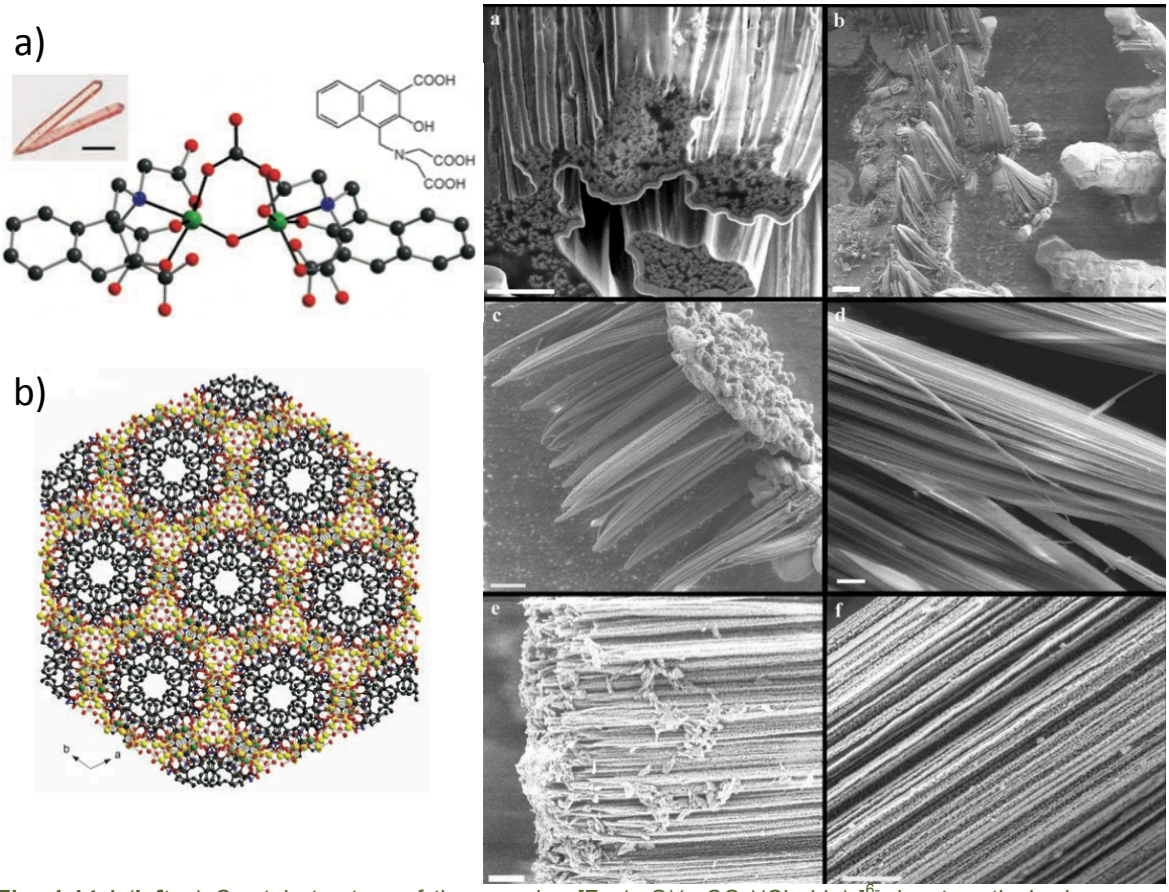

Fig. 1.14 | (**left a**) Crystal structure of the complex $[Fe_2(\mu\text{-}O)(\mu\text{-}CO_3)(Chnida)_2]^{6-}$, inset: optical microscope images of the single crystals; (**left b**) packing diagram of the compound $Na_6[Fe_2(\mu\text{-}O)(\mu\text{-}CO_3)(Chnida)_2]$; **(right)** – SEM images of thermolysed samples of $Na_6[Fe_2(\mu\text{-}O)(\mu\text{-}CO_3)(Chnida)_2]\cdot 13.5H_2O$; **a)** a crystal cut perpendicular to the crystallographic *c*-axis using FIB (scale bar: 2 μm); **b-c)** coagulated bundles of fibres after thermolysis at 370 °C (scale bar: 20 μm) and their magnification (**d-f**), scale bar: 2 μm).[97]

As it was demonstrated by La Spina *et al.*, a similar synthetic methodology can be applied to other metal ions, for example Cu^{II} ions.[98] When the iminodiacetic acid moiety-containing ligand H_3hnida (Fig. 1.15a) reacts with Cu^{2+} ions in the presence of KOH, it forms a dinuclear compound with the chemical formula $K_2[Cu^{II}(Hnida)]_2\cdot 2H_2O$. As presented in Fig. 1.15b, the arrangement of the dinuclear units within this compound results in a honeycomb-like structural motif closely related to that of the discussed Fe^{III} compound and where hydrophilic and hydrophobic areas are separated. The $[Cu^{II}(Hnida)]_2^{2-}$ complexes are arranged about a six-fold screw axis that runs parallel to the crystallographic *c*-axis and is localised in

the centres of the hydrophobic cavities. The hydrophobic part of the resulting tubular cavities has a cross-sectional diameter of *ca.* 11 Å.

The introduction of the additional carboxylic acid functional group located opposite to the aromatic hydroxyl group disturbs the formation of the honeycomb-like structure and can also in the Cu^{II} system be used to produce open-framework structures. When this modified H_4chnida ligand is reacted with Cu^{II} ions, the reaction yields in a dinuclear complex $K_4[Cu^{II}(Chnida)]_2 \cdot 4H_2O \cdot 4MeOH$ (Fig. 1.15d). As presented in Fig. 1.15c, the compound forms a structure with alternating hydrophobic organic and hydrophilic inorganic regions whereby ligand moieties now pillar between hydrophilic regions giving rise to a porous network structure. The change of the packing motif and slight changes of the coordination environments around the Cu^{II} centres is associated with further changes of the physical properties of both Cu^{II} compounds. The authors discovered that the Cu^{2+}/Hnida compound displays antiferromagnetic interactions between the Cu^{2+} centres stabilising an $S_T = 0$ spin ground state while interactions in the Cu^{2+}/Chnida compound are predominantly ferromagnetic resulting in an $S_T = 1$ ground state.[98]

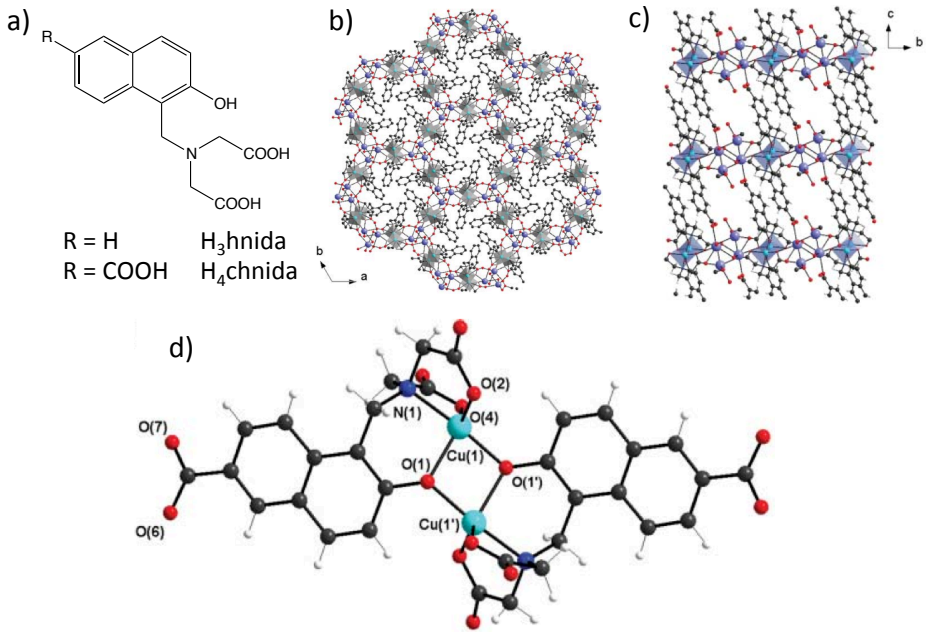

Fig. 1.15 | a) Structure of the naphthol-based iminodiacetic acid-containing ligands; **b)** supramolecular structure of $K_2[Cu^{II}(hnida)]_2 \cdot 2H_2O$; **c)** supramolecular structure of $K_4[Cu^{II}(chnida)]_2 \cdot 4H_2O \cdot 4MeOH$; **d)** structure of the $[Cu^{II}(chnida)]_2^{4-}$ complex in $K_4[Cu^{II}(chnida)]_2 \cdot 4H_2O \cdot 4MeOH$.

Complexes characterised by higher nuclearities

Consecutive studies using the iminodiacetic acid-containing hda ligands revealed that the nature of the substituents occupying the *ortho* and *para* positions of the phenolic ring can also affect the nuclearity of the resulting compound. For example, a reaction between the Me_2hda ligand (Fig. 1.16, left), which consists of the iminodiacetic acid moiety linked to a phenolic ring substituted with two methyl groups, and Fe^{III} ions results in a dinuclear compound $Na_2(H_2O)_4[Fe_2(Me_2hda)_2(\mu\text{-}OH)(\mu\text{-}CO_3)] \cdot 2H_2O \cdot 2EtOH$ that is very similar to the other previously discussed dinuclear Fe^{III} compounds. Surprisingly, when both of the methyl groups are substituted by chlorine atoms, the reaction with Fe^{III} that is performed in the same

conditions results in the formation of a trinuclear compound [{(Cl_2hda)Fe}$_2$(μ-OH)$_2$ Fe(H_2O)$_4$](NO_3)·4H_2O. The trinuclear complex, which is presented in Fig. 1.16 (right) consists of two {Fe(Cl_2hda)} units that are linked via μ-H_2O bridges to a central {Fe(H_2O)$_4$} centre. Within this complex, all three metal ions adopt an octahedral coordination geometry.[186]

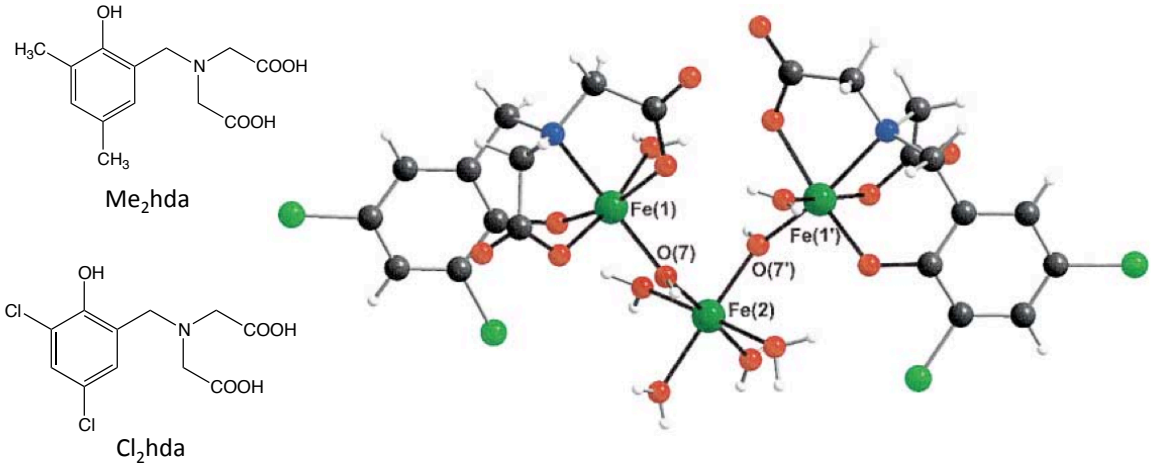

Fig. 1.16 | (left) Structures of the Me_2hda and Cl_2hda ligands; (**right**) the trinuclear complex [Fe_2(Cl_2hda)$_2$(μ-H_2O)$_2$Fe(H_2O)$_4$]$^+$.[186]

Further investigations into this system resulted in the formation of larger, octanuclear Fe^{III} coordination cluster. This cluster, [Fe_8(allyl,OMe-hda)$_4$(μ_3-O)$_4$(μ-OH)$_4$(*en*)$_4$], is stabilised by the allyl,OMe-hda ligand, which contains an additional methoxy group in the *ortho* position and a prop-2-en-1-yl substituent in the *para* position (with respect to the aromatic hydroxyl group), and ethylenediamine co-ligands. As presented in Fig. 1.17, this cluster contains eight metal centres that form a tetragonally compressed cube. The Allyl,OMe-hda ligands form an organic shell that surrounds the inorganic core. Four metal centres constitute the basis of the cube. Three of them are bridged by μ_3-O oxo ligands. The fourth metal centre is connected by a μ-bridging hydroxide anion to one Fe^{III} centre of the previously discussed three metal centres.[186]

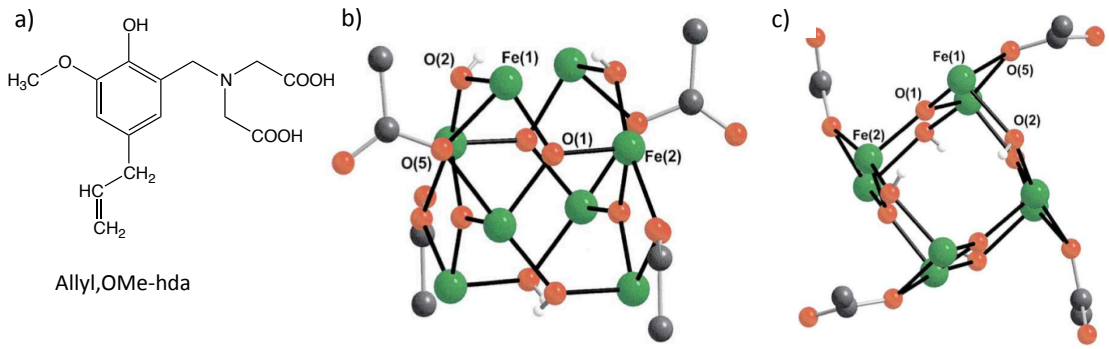

Fig. 1.17 | a) Structure of the allyl,OMe-hda ligand; **b-c)** The Fe_8(μ_3-O)$_4$(μ-OH)$_4$ core of [Fe_8(allyl,OMe-hda)$_4$(μ_3-O)$_4$(μ-OH)$_4$(en)$_4$] – a perspective view (**b**) and a view down a 4-fold symmetry axis (**c**). The diagrams also show iminodiacetic carboxylic acid functionalities of the allyl,OMe-hda ligand that stabilise the cluster.[186]

1.2. Bio-inspired strategies towards the control over the $CaCO_3$ crystal morphology

Biomineralisation is a process in which living organisms form hard tissues, such as bones or teeth, which are further used to construct their bodies.[99] It was discovered that living organisms grow crystals in ways fundamentally different from commonly applied chemical laboratory methods. The natural crystallisation process starts with creation of a transient amorphous, colloidal phase, which then turns into a crystalline material.[100-102] This phenomenon is observed for almost all classes of organisms: from single-cell algae species to primates, including humans.[103] In all cases biomineralisation is a complex process that has been refined over 500 million years of evolution and involves a proper phase selection, control over the shape, size and morphology of a growing crystal and transporting a crystal into a right position within the body. Such biominerals and their composites often offer enhanced mechanical properties when compared with their synthetic analogues. Some of them also display interesting additional features, such as electric conductivity or optic fibre behaviour.[104]

The most widespread naturally occurring biominerals are calcium salts: carbonates and phosphates. This can be explained by the high abundance of calcium ions dissolved in seawaters, originating from slowly dissociating rock sediments. According to the global carbon cycle, the excess of atmospheric CO_2 dissolves in ocean waters and forms bicarbonate anions, HCO_3^-. Almost all marine organisms take advantage from the availability of Ca^{2+} cations and HCO_3^- anions in the external environment. Marine organisms have developed and evolutionary refined several strategies allowing to uptake these ions and process them into calcium carbonate – the construction material, which is used to grow hard tissues. [105,106]

1.2.1. Calcium carbonate – a brief insight

Calcium carbonate is a naturally occurring compound that exists in five different crystalline phases: ikaite, vaterite, aragonite, monohydrocalcite and calcite. Only the last phase (calcite) is thermodynamically stable.[107] Ikaite forms only at low temperatures, close to the freezing point of water.[108-110] Vaterite is a transient phase that forms as a kinetically favourable product of $CaCO_3$ crystallisation, however, it rapidly rearranges to calcite in an aqueous environment.[111,112] Aragonite and monohydrocalcite are relatively stable, their rearrangement to calcite is significantly slower than the vaterite to calcite transformation.[113-117] Aragonite crystallises in an orthorhombic crystal system and the crystals usually adopt a needle-like morphology (Fig. 1.18a-b).[118,119]

Calcite is the predominant phase of $CaCO_3$ that is encountered in biogenic and synthetic samples.[120] It crystallises in the hexagonal space group $R\bar{3}c$ and forms rhombohedral, block-like crystals (Fig. 1.18c-d).[121,122] Unless grown in an impurities-free environment, these rhombohedral particles appear defected. The majority of these defects are attributed to twinning effects or the formation of inter-grown crystallites.[123,124]

Calcite crystals of biological origin adopt more complex morphologies. Fig. 1.19 presents two examples of calcite crystals that were produced by living organisms. Fig. 1.19a shows a coccosphere – a spherical aggregation of calcite disks that is produced by several species of marine algae. Each individual disk of the sphere consists of several single crystals that aggregate in an incredibly precise manner.[125]

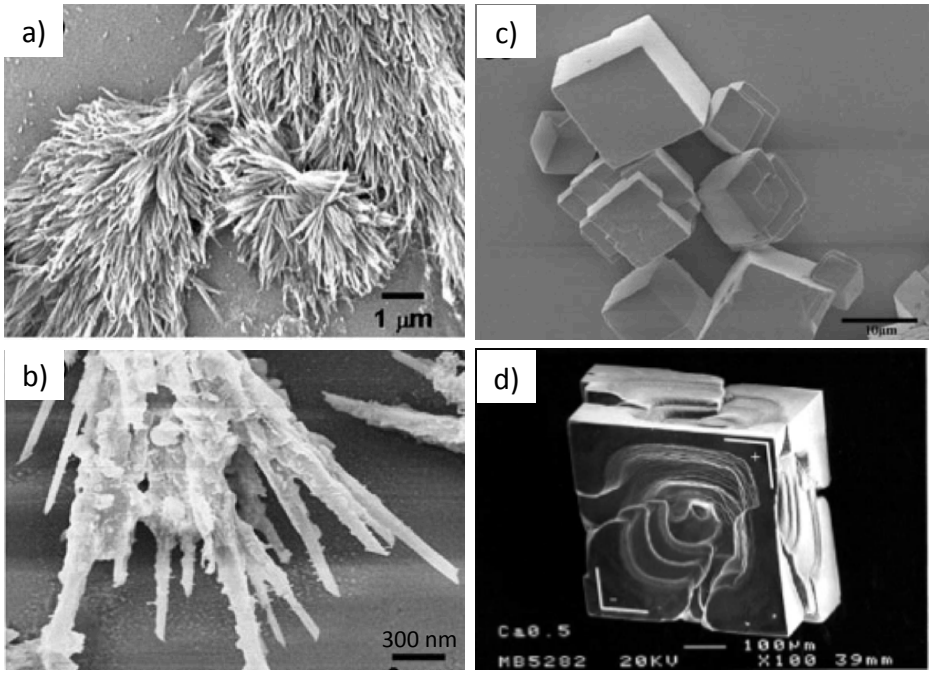

Fig. 1.18 | SEM images of $CaCO_3$ crystals. **a-b)** aggregates of needle-like crystals of aragonite; **c-d)** rhombohedral, block-shaped crystals of calcite.[125]

The second micrograph (Fig. 1.19b) shows a cross-section of a spine of sea urchin – a small marine animal. Despite being a polycrystalline material composed of several calcite crystals, this material scatters X-rays similarly to single crystals. This is possible due to unique shape and mutual orientation of the individual building blocks, which would not be achievable without the assistance of the evolutionary refined self-assembly and self-organisation processes.[126,127]

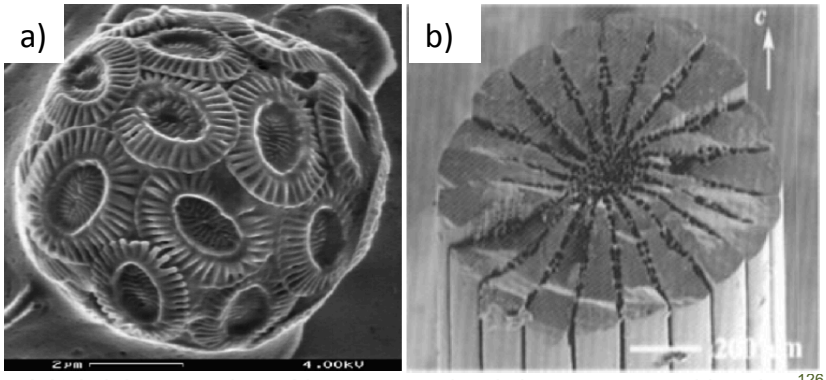

Fig. 1.19 | a) A coccosphere; **b)** a cross-sectional view on a sea urchin spine.[126,127]

1.2.2. Influencing the morphology of $CaCO_3$ crystals

Several attempts were made to mimic the morphologies of biogenic crystals in a synthetic environment. These kind of experiments provide scientists with a better

understanding of the biomineralisation phenomena and may be helpful in determining the mechanisms associated with the non-classical crystallisation processes.[128] Calcium carbonate, $CaCO_3$, is the main subject of the studies on biomineralisation due to its widespread occurrence in nature and various roles that it fulfils in living organisms (from being used as a building material for exoskeletons to a mediator in the nervous system). A vast number of possible applications for templated inorganic crystals exist as they can be used as reinforcing nanoadditives for composite materials to components of modern electronic nanodevices.[129]

This thesis describes an attempt to control the morphology of $CaCO_3$ crystals by performing the crystallisation in the presence of small, amphiphilic molecules. As the most prominent results are associated with calcite crystals adopting a hollow spherical morphology, the following examples of other reported templating effects focus on obtaining particles characterised by a spherical shape.

Stabilisation of amorphous calcium carbonate

It is clear that $CaCO_3$ mineralisation in living organisms disobeys the classical mechanism of ionic crystallisation. Thus research activities of several groups are directed towards the stabilisation of amorphous calcium carbonate (ACC) or the assembly of single crystals from pre-organised templates.[130-135] Similar mechanistical approaches are commonly observed in biological systems.[99,136]

ACC is a kinetically favoured phase of calcium carbonate. It means, that it is the first phase that forms during the mineralisation process. However, from the thermodynamic point of view ACC may be stable when dried, but in solutions it rearranges within minutes to more persistent forms, calcite or aragonite.[137,138] Stabilisation of ACC is a challenging task of great importance as this is the only phase flexible enough to be transported within living tissues and directed to crystallise in a desired phase and form.[139] These features make ACC an important material for future applications, especially in the field of regenerative medicine and tissue engineering, where it could act as a transient precursor for the growth of hard tissues.[140] Several groups of organic molecules have been confirmed to inhibit the phase transformation of ACC in biological samples. These are mainly macromolecules containing hydroxyaminoacids, polysaccharide groups, glycine, glutamine and phosphate moieties and inorganic magnesium ions.[141]

There are only a few synthetic methods that allow stabilisation of ACC over a longer periods of time. The first one relies on the utilisation of poly(propylene imine) dendrimers modified with long hydrocarbon chains and single chain surfactants. This system has been proven to stabilise ACC for 14 days.[142] Another method reported by Cölfen *et al.* takes advantage from the ability of phosphate groups to strongly adsorb onto ionic crystals and preferentially interact with kinks on the crystal nucleus surface, efficiently inhibiting crystal growth.[140] The authors performed synthetic mineralisation of $CaCO_3$ in the presence of phytic acid (Fig. 1.20a) applying a gas diffusion method in which ammonium carbonate was used as a

source of CO_2. The resulting material consists of amorphous calcium carbonate, which adopts an unusual morphology of hollow spheres (Fig. 1.20b).[135]

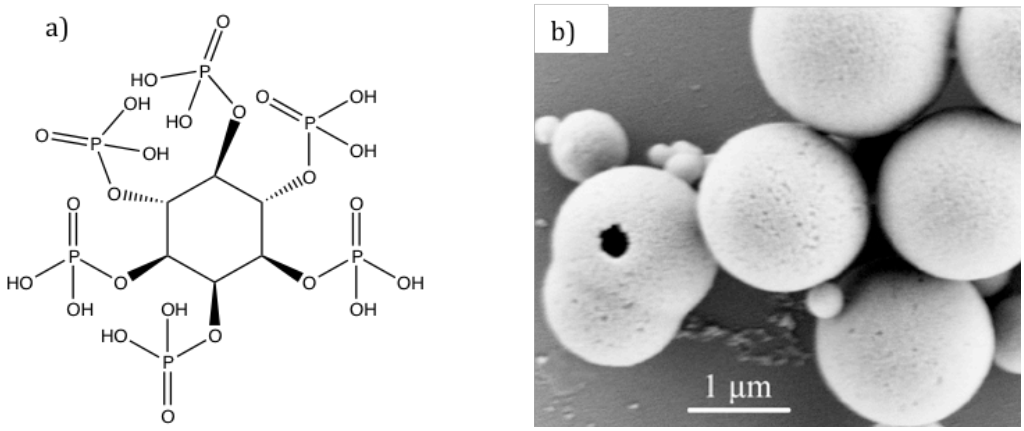

Fig. 1.20 | a) Chemical structure of phytic acid; **b)** SEM image of hollow ACC sphere obtained in the presence of phytic acid[135]

The TEM imaging was applied to determine the mechanism of formation of these particles. The authors discovered that during the process, anhydrous ACC is formed in the first place. Then at the solid-liquid interface the ACC phase becomes hydrated. This hydrated form is known to be more stable than the anhydrous form. This transformation occurs on the particle exterior whereby the hydrated ACC phase grows at the expense of the dissolving anhydrous ACC phase. The centre of the sphere acts as a sacrificial material source and after some time becomes depleted.[135]

Ostwald ripening

The mechanism described above resembles to some extend a well known process denoted as Ostwald ripening.[143] The process explains how larger crystals grow at the expense of smaller ones involving the diffusion of atoms, ions or molecules within an ensemble of a crystalline material.[144] Typically, this process begins when an amorphous material is deposited (precipitated from the solution). Although kinetically favoured during the nucleation stage, it becomes metastable in respect to more thermodynamically stable polymorphs as the originally supersaturated solution becomes less concentrated with time. As a result, the amorphous solid particles become coated with an ultra thin shell of a less-soluble crystalline phase until the system reaches equilibrium, with respect to the surface layer. Unlike the external crystalline layer, however, the amorphous core remains out of equilibrium with the surrounding solution due to its higher solubility and so, provided there is a diffusion pathway through the outer crystalline shell, the core dissolves. As a consequence, the supersaturation increases in the solution above the solubility of the product of the crystalline exterior layer, and secondary nucleation of the crystalline polymorph on the external surface occurs. In this way the crystalline shell increases in thickness as the amorphous core becomes progressively depleted to produce intact hollow microspheres without significant modification in the bulk particle morphology.[145]

As an example Mann *et al*. reported hollow $CaCO_3$ particles that form *via* the Ostwald ripening mechanism.[145] The authors performed an experiment, where the crystallisation of calcium carbonate occurred in the presence of poly(4-styrenesulfonate) (PSS). Calcium chloride was used as the source of Ca^{2+} ions and sodium carbonate provided the CO_3^{2-} anions. The reaction was performed in water containing a small addition of PSS. The reaction was carried out at room temperature, however, after mixing the reagents samples were placed in an oven and heated at 70°C for 2 hours. The resulting phase was confirmed to be vaterite, which adopted a spherical morphology (Fig. 1.21). The exact mechanism of its formation was confirmed using TEM.

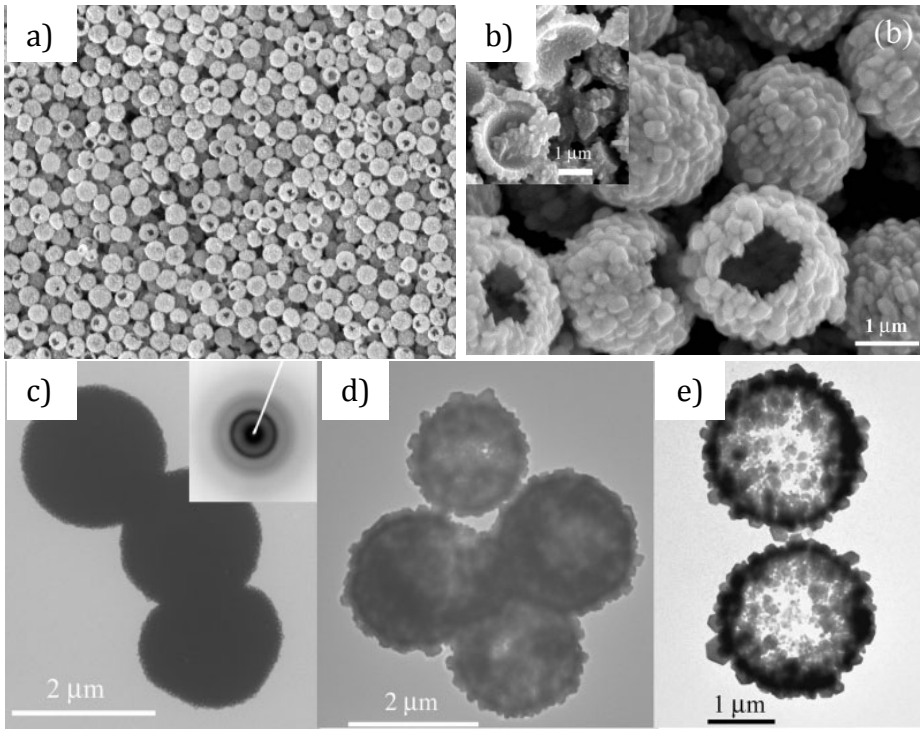

Fig. 1.21 | a) Low, and **b)** - high magnification SEM images of hollow vaterite spheres prepared in the presence of PSS; **c-e)** TEM images of $CaCO_3$ particles, **c** - 30 min. after the reagents were mixed, showing solid particles of amorphous calcium carbonate, **d** – after 2 h, showing vaterite crystallisation on the particle surface and reduced core density and **e** – after 24 h, showing intact hollow vaterite microspheres.[145]

The TEM images confirm that the initially precipitating solid is an ACC phase. After *ca.* two hours the deposition of vaterite was observed on the surface of the amorphous solid. After 24 hours the core is completely dissolved and crystals of vaterite grow at the surface. The rate of formation of the hollow particles depends strictly on the synthetic procedure (time, temperature) and environmental parameters (pH). The authors speculate that the high sulfate-group density along the PSS backbone provides high surface binding and stabilisation of primary clusters of ACC which initially nucleate from the solution. Furthermore, reduction in the surface charge of these primary clusters by polymer adsorption facilitates secondary aggregation.[145]

Double hydrophilic block copolymers (DHBC)

A similar mechanism, reported by Cölfen *et al.*, is responsible for the formation of hollow calcite spheres.[146] The researchers investigated the influence of double hydrophilic block copolymers (DHBC)[147] on the morphology of calcium carbonate.[148] A block copolymer poly(ethylene glycol)-*block*-poly(methacrylic acid) (PEG-*b*-PMAA) was dissolved in water along with $CaCl_2$ and this sample was closed in a bottle, which contained solid ammonium carbonate. $CaCO_3$ crystals precipitated due to the slow diffusion of CO_2 into the mixture. SEM was used to determinate their morphology. These studies revealed that primarily, polymer-stabilised ACC forms and aggregates into amorphous solid assemblies, which are *ca.* 300 nm in diameter. In the next step, spherical vaterite precursors form from the ACC particles. The final phase transition occurs when Ostwald-ripening leads to the dissolution of the vaterite spheres and to the nucleation of calcite crystals on the vaterite-solvent interface (Fig. 1.22a-e). This transition ends when the metastable vaterite core is depleted and a hollow calcite assembly is formed; the calcite-based material does not undergo any further rearrangements under the applied reaction conditions (Fig. 1.22f,g).[146]

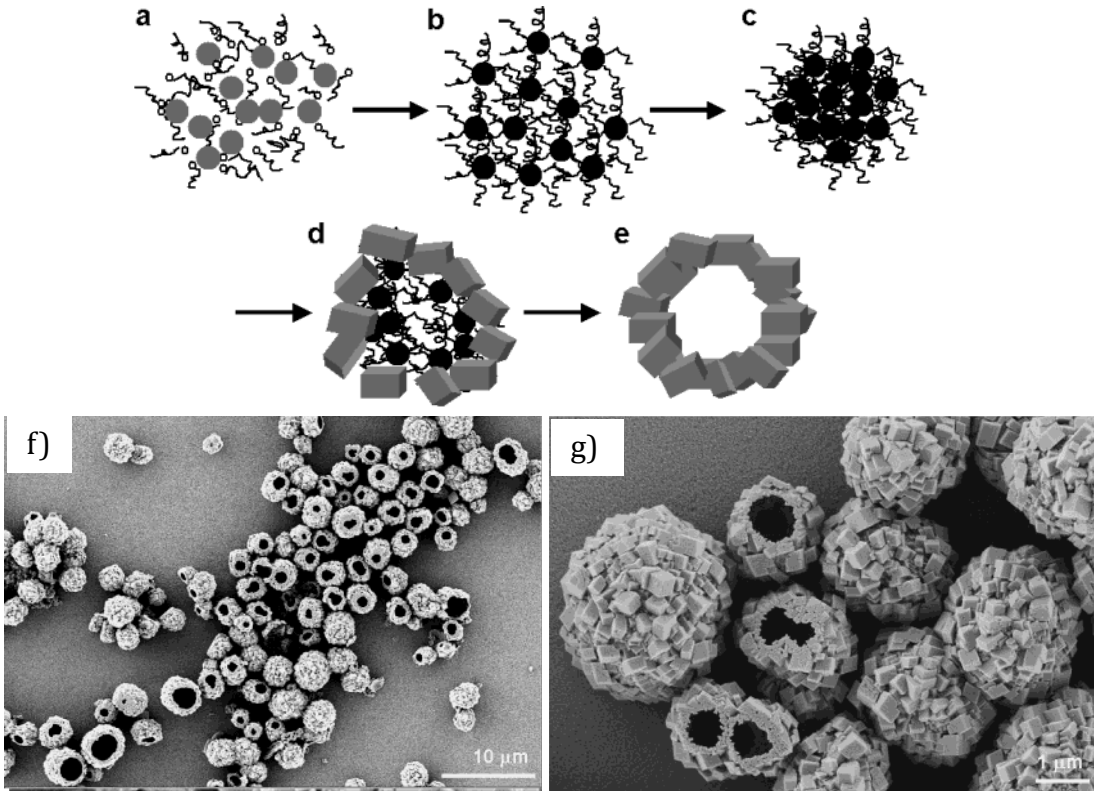

Fig. 1.22 | The mechanism of formation of the hollow calcite particles. **a)** The polymer-stabilised amorphous particles; **b)** formation of spherical vaterite precursors; **c)** aggregation of vaterite nanoparticles; **d)** vaterite-calcite transformation starting on the outer sphere of the particle; **e)** formation of calcite hollow spheres under consumption of the vaterite precursors; **f-g)** SEM images of hollow calcite spheres – overview (**f**) and magnification (**g**).[146]

There are several other methods that allow material scientists to modify the crystal growth, without involving direct Ostwald ripening processes. All of them rely on non-classical crystallisation pathways and the most prominent examples of these processes are described below.

Aggregation-mediated crystallisation

Aggregation-mediated crystallisation describes a process where ordered structures are constructed and/or transformed from larger, preformed units/species instead from single ions. Antonietti *et al.* demonstrated that this phenomenon finds application in $CaCO_3$ chemistry.[144] In this research vaterite mesocrystals with hexagonal symmetry were formed by vapour diffusion in the presence of a N-trimethylammonium derivative of hydroxyethyl cellulose (Fig. 1.23a). Vaterite can crystallise in either an orthorhombic or a hexagonal structure. It was confirmed that the polymer promotes the formation of hexagonal plates of vaterite (Fig. 1.23b).

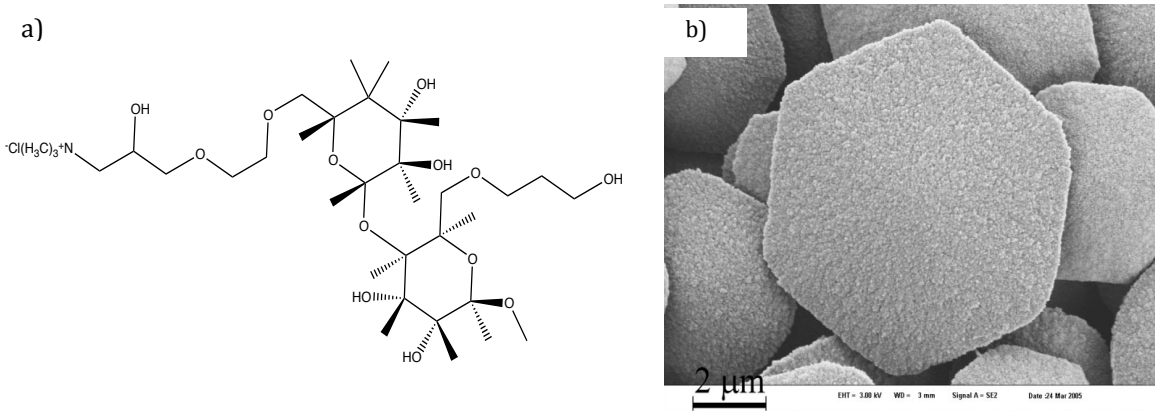

Fig. 1.23 | a) Structure of an N-trimethylammonium derivative of hydroxyethyl cellulose; **b)** hexagonal plate of vaterite[144]

TEM imaging suggests that firstly nearly spherical ACC particles stabilised by the polymer were deposited. Secondly, the vaterite phase was formed by phase transformation and crystallisation. The authors show that the vaterite crystals are exposed on the (001) face which is highly unusual for this mineral. The (001) face is composed of only CO_3^{2-} or Ca^{2+} ions in a hexagonal orientation, what makes it charged.[149] Moreover, in absence of the growth modifiers the (001) face has a high surface energy. It is suggested that the positively charged trimethylammonium moiety has a high affinity to the negative $[00\bar{1}]$ plane and thus it is able to reduce the surface energy. When the crystal grows, the (001) face is inhibited what results in a domination of this particular face in the final product.[144]

The most interesting observation is that the hexagonal vaterite plates have the ability to form highly ordered superstructures involving an aggregation-mediated crystallisation process. The plates tend to aggregate and form a 3D structure, which was confirmed to be a single-crystalline phase (Fig. 1.24). The tendency of these micromaterials to lower the surface area could be the driving force for this rearrangement.

The aggregation mediated crystallisation was reported for various types of organic habit modifiers, mainly polymers bearing charged phosphate or sulfonate groups.[138,150,151,152] The described N-triethylammonium system is quite complex and it was noted, that the aggregation-mediated crystallisation may not be the only pathway which leads to vaterite mesocrystals.[153]

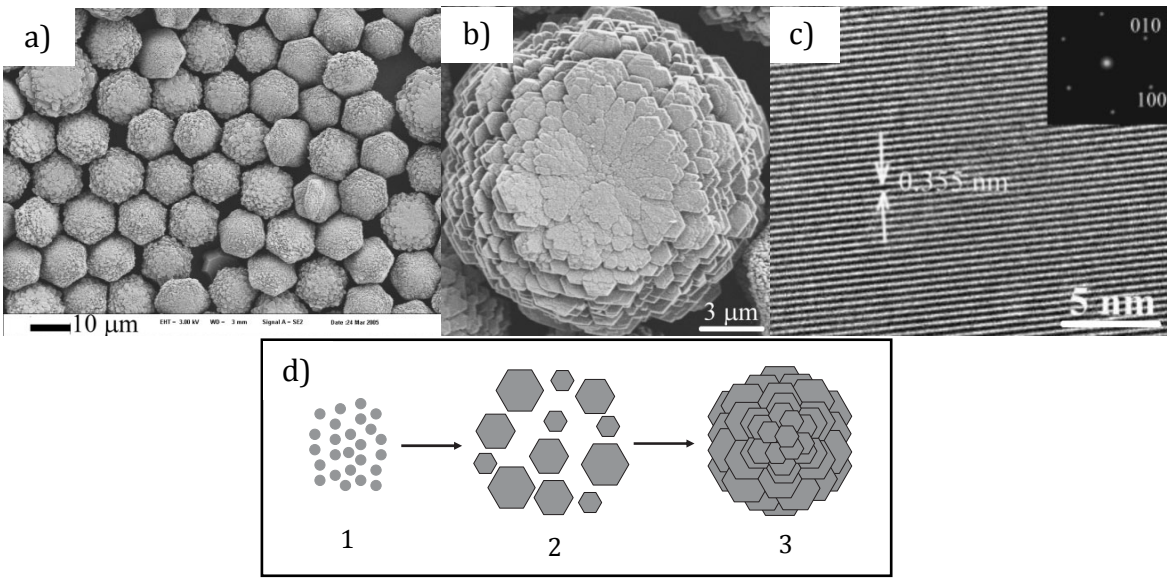

Fig. 1.24 | a-b) SEM images of vaterite mesocrystals; **c)** A TEM taken from primary thin disc of vaterite mesocrystals with clearly resolved lattice fringes of the [110] planes; **d)** proposed formation mechanism of hexagonal vaterite mesocrystals, 1 – nearly spherical ACC nanoparticles, 2 – The polymer-stabilised preformed hexagonal vaterite thin plates, 3 – The formation of hexagonal, large vaterite particles *via* aggregation-mediated crystallisation.[153]

Orientated Attachment Crystallisation

Orientated attachment crystallisation occurs when the amorphous particles coexist in the solution with a crystallising phase of one specific polymorph. This mechanism was initially reported for transition metal systems[154] and it appears feasible that it can also be applied to $CaCO_3$ mineralisation processes.

When calcium carbonate crystals grow in the slow diffusion experiment involving $(NH_4)_2CO_3$, NH_4^+ ions bind to the negatively charged $[00\bar{1}]$ plane and inhibit the growth in the (001) direction. It was shown that the observed hierarchical structures form by a mesoscale assembly process, in which in a first step, (001) oriented, NH_4^+-stabilised vaterite nanosheets are stacked to hexagonal superplates that subsequently slowly fuse to give single crystals by oriented attachment processes. Exceeding a critical size, the stacks can also attract primary ACC nanoparticles, which then undergo lock-in crystallisation toward a common single crystalline reference system.[153]

Experimental attempts to control of the crystal morphology are not limited to the utilisation of organic additives. Several experiments prove that a change in experimental conditions (e.g. variation of solvent system or temperature) influences the morphology or directs the crystallisation into a desired phase.

Crystallisation in microemulsions

The $CaCO_3$ mineralisation process may be performed under reversed microemulsion conditions, where crystallisation occurs in the droplets of supersaturated polar solutions in oil. Walsh *et al.* demonstrated that a sonicated mixture of octane, sodium dodecyl sulfate (SDS) and calcium bicarbonate reacts to produce vaterite materials characterised by a microsponge morphology (Fig. 1.25).[155]

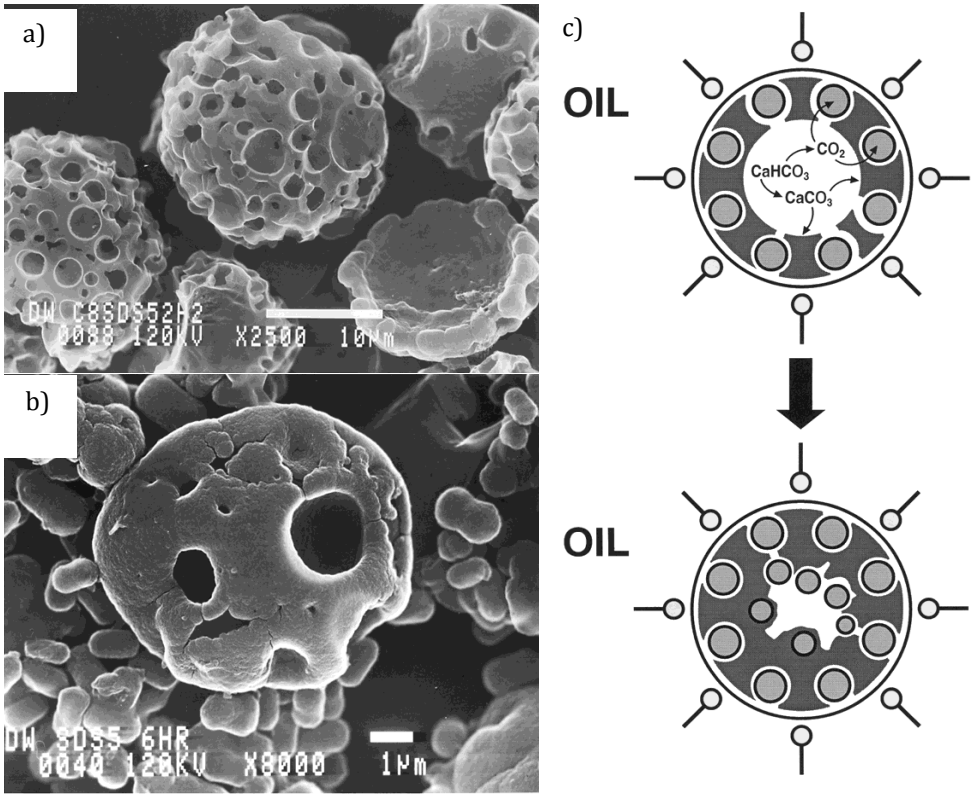

Fig. 1.25 | a-b) SEM images of vaterite crystals adopting the sponge morphology; **c)** proposed mechanism of formation.[155]

The mechanism of formation of these morphologies was resolved with the assistance of SEM and TEM imaging. The spheroids are formed by nucleation of vaterite at the anionic head groups of SDS molecules present at the oil/water droplet interface. Further patterning involves microbubbles of CO_2 entrapped within and at the surface of the water droplets.[155]

Crystallisation under Langmuir monolayers

Another interesting approach applied to modify the habit of $CaCO_3$ crystals involves the crystallisation in the presence of Langmuir monolayers. This was achieved by organising a monolayer of amphiphilic organic molecules on the air/water interface. The crystallisation occurs when Ca^{2+} and CO_3^{2-} ions present in the solution bind to the hydrophilic part of the monolayer. The specific binding process in combination with the particular arrangement of the organic monolayer regulates the morphology of the growing crystal (Fig. 1.26).[156]

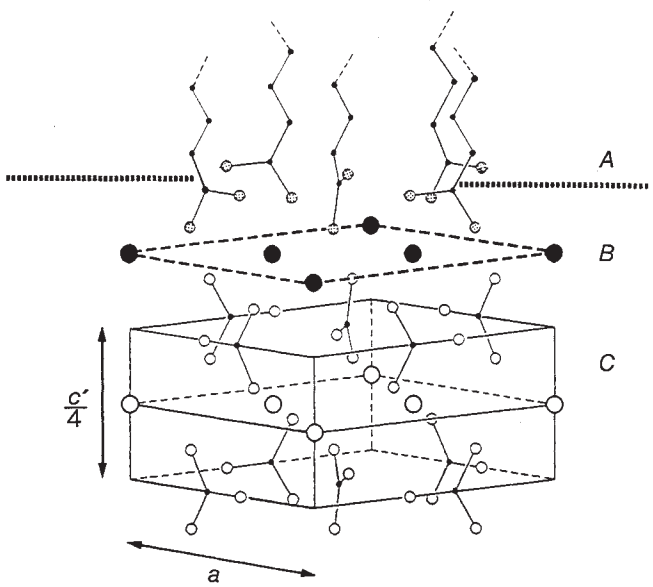

Fig. 1.26 | Organisation of the interface between stearic acid monolayer and nascent vaterite nuclei. **a)** Monolayer surface showing carboxylates aligned perpendicular to the air/water interface; **b)** Stern layer of headgroup-bound Ca^{2+} ions, the uni-charged layer is electrostatically equivalent to the (0001) face of vaterite; **c)** vaterite sub-cell showing the stereochemical arrangement of carbonates perpendicular to the (0001) face.[156]

The crystals are formed in this process at the air/water interface. Several classes of organic molecules have been explored for this purpose, including stearic acid[156], poly(aspartic acid) with octadecylamine[157], 5-hexadecylooxyisophtalic acid[158] and even protein sheets.[159]

Utilisation of solid templates

There have been other attempts to template the $CaCO_3$ crystallisation process, which rely on using solid templates rather than supramolecular recognition approaches involving specific molecules. Mann *et al.*, who used polystyrene spheres to prepare hollow particles of aragonite, presented an interesting example of this approach.[160] At first the authors performed a microemulsion-based crystallisation of $CaCO_3$. The crystallising solution was composed of calcium hydrogen carbonate, didodecyldimethyl ammonium bromide (DDAB, surfactant) and tetradecane, and the formation of the of the aragonite phase was initiated by the addition of a small amount of $MgCl_2$.[161] The resulting morphology was described as porous, cellular framework structure (Fig. 1.27a). Additionally the authors used Au-coated, spherical polystyrene (PS) particles with diameter of 1.09 μm that they added to the micoremulsion. The aragonite nucleation occurred on the relatively hydrophobic gold surface. Finally, the polystyrene core was removed by washing the material with an acetone/ethanol mixture and heating the material to 400˚C. The SEM analysis revealed that the product consists of hollow particles of aragonite that show a cellular surface pattern (Fig. 1.27b).[160]

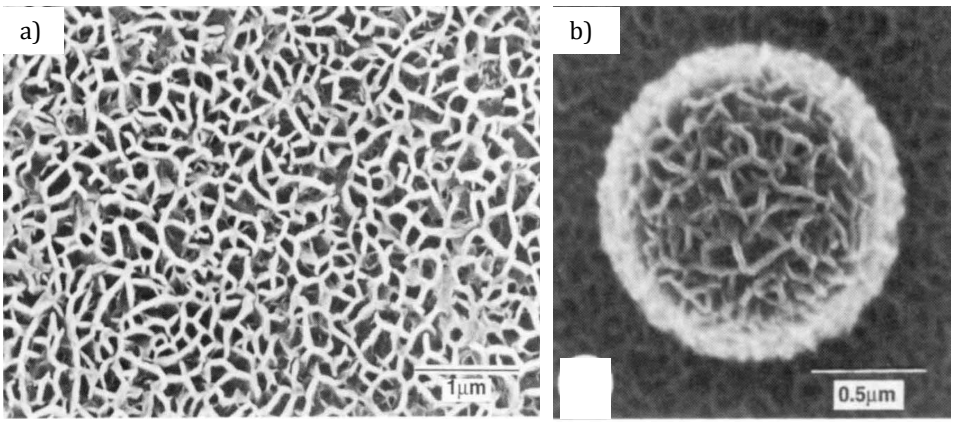

Fig. 1.27 | a) SEM picture of cellular frameworks of aragonite formed in a microemulsion consisting of tetradecane, DDAB and water; **b)** a hollow sphere of aragonite obtained by Mann *et al*.[60]

This very unusual morphology exhibits hierarchical order: the particles are crystalline and ordered at a molecular level, cellular on the mesoscopic/submicrometre scale, and spheroidal at the micrometer and macroscopic level, respectively. It was also noted, that the morphology of the spheres resembles the shape of a naturally occurring biomineral – a coccosphere, produced by a marine algae *Thoracosphaera*.[160]

--- CHAPTER II ---

Objectives of the project

The initial aim of this research project was the synthesis and characterization of new hybrid, organic-inorganic coordination compounds based on iminodiacetic-acid containing amphiphilic ligands (Sch. 2.1). As outlined in chapter I, the *hda*-type ligands react with different metal ions to give hybrid, organic-inorganic coordination compounds, that adopt hierarchical arrangements. By reacting these ligands with selected *d*-block metal ions (namely, Cu and Zn ions) and calcium ions we aimed to expand the known library of such hierarchical materials. An important objective of this research project was to explore the self-assembly process that occurred when the organic ligands were reacted with the afore-mentioned metal ions. The project focussed on understanding the structure of the resulting crystalline coordination complexes, investigating the supramolecular connectivity between their building units and describing the solid-state packing and network structures of the coordination compounds. The influence of ligand substituents on supramolecular assemblies was studied. The principal analytical technique used for these studies was single crystal X-ray diffraction.

A secondary objective of the project was to generate non-crystalline hierarchical materials based on the iminodiacetic acid-substituted ligands using molecular self-assembly approaches. The synthesis of these amorphous materials was achieved by altering the amphiphilic properties of the ligand system by introducing alkyl chains in the *para* position with respect to the aromatic hydroxyl group. The principal analytical technique used to investigate the morphology and structure of these materials was electron microscopy, i.e. SEM and TEM. The systematic studies required us to develop a methodology, whereby the alkyl chain length and thus the amphiphilicity of the phenolic ligands could systematically be varied. In order to achieve this, we used the vanillic acid molecule as a starting material for the ligand preparation. The carboxylic acid functionality of vanillic acid provided an opportunity to introduce the alkyl chains through esterification reactions (see *vda*-type ligands, Sch. 2.1, 3rd row).

Coordination complexes and their network structures have proven to have a templating effect on the morphology of inorganic residues, which form upon heating of the initial coordination compounds.[97] The next objective of this project was to study the thermal degradation of the Cu-, Zn- and Ca-containing coordination compounds in order to investigate if the molecular and solid-state packing structure of these precursor compounds imparts a templating effect on the morphology of the post-thermolytic or post-pyrolytic ceramic residues (carbonates and oxides).

This project addressed the question of how the molecular architectures which contain the starting components, e.g. for the mineralisation of $CaCO_3$, in a prearranged 3D form, influence the structures of the resulting phases that form within confined spaces of the hydrophilic parts of the coordination assemblies. The shape and morphology of the resulting inorganic materials were investigated using SEM, while P-XRD was applied to determine their chemical identity and phase purity.

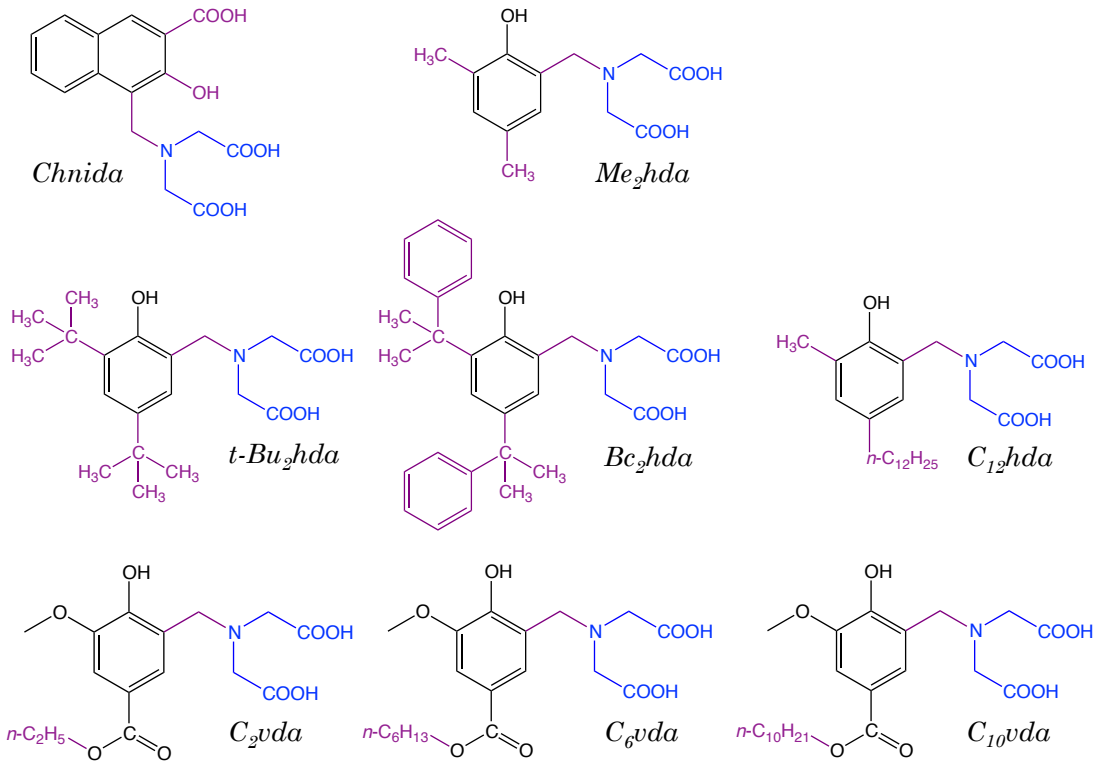

Sch. 2.1 | The iminodiacetic acid-based ligands used in this work. The iminodiacetic acid moiety and the phenol ring substituents have been highlighted for clarity.

The last aspect of this work utilizes a well-established approach to influence the crystal growth of $CaCO_3$ phases using organic molecules as habit modifiers.[162, 163] The *hda*- and *vda*-type ligands were added to a reaction mixture, which contained calcium cations and carbonate anions, in order to disturb the nucleation process or modify the crystal growth mechanism. Aliphatic ligands containing the iminodiacetic acid moiety have previously been confirmed to have a habit modifying effect on the growth of calcite crystals.[164] However, iminodiacetic acid substituted phenols have not been explored as habit modifiers before. It was expected that the ligands would interact with the hydrophilic faces of growing carbonate crystals and consequently influence the crystal morphology. The shape and morphology of the resulting $CaCO_3$ crystals were studied using SEM. P-XRD experiments were applied to investigate the $CaCO_3$ phase while TEM along with electron diffraction provided information with respect to the crystal growth mechanisms.

Specific aims of this study

In order to accomplish our objectives we set out to attain the following:

1. Prepare and characterise relevant hda-type ligands. Synthesize and fully characterize a new class of organic ligands that would be structurally similar to the *hda*-type ligands and could be easily modified using an esterification reaction.
2. React the ligands with Cu(II), Zn(II) and Ca(II) ions in the presence of different bases (organic bases and alkali hydroxides). Determine the crystal structures of these complexes to characterise the coordination ability of the ligands and the supramolecular structures of the resulting coordination assemblies.
3. Characterize the resulting coordination complexes using other relevant analytical techniques including elemental analysis, X-ray powder diffraction or IR spectroscopy.
4. Use the amphiphilic coordination complexes for molecular self-assembly purposes to give hierarchical nanomaterials. Investigate using electron microscopy approaches how ligand-substituents influence the observed morphologies and attributes of the resulting soft materials. Develop approaches to characterise the molecular structure and composition of these nanomaterials.
5. Investigate the thermal degradation pathways of the coordination complexes and the assembled materials.
6. Explore the possibility to use these supramolecular coordination assemblies as potential templates for nanomaterials that form upon thermolysis or pyrolysis. Characterise the thermal decomposition products. Determine morphology of the ceramic residues using SEM. Investigate potential links between the solid-state structure of the preceding coordination networks and the residual carbonate (or oxide) materials.
7. Use the iminodiacetic acid-substituted phenols as habit modifiers in the $CaCO_3$ crystallization process. Study the phase (using P-XRD) and morphology (using SEM) of the obtained crystals.

--- CHAPTER III ---

Supramolecular coordination compounds containing selected *d*-block metals and amphiphilic vda-type ligands

3.1. The synthesis and characterization of the organic ligands

Previously, within the Schmitt group, the hda-type ligands have been successfully employed to synthesise a variety of very interesting coordination compounds. With this in mind we decided to investigate the synthesis of a series of novel, aromatic iminodiacetic acid based (hda - type) ligands that, when reacted with metal ions, have the potential to form amphiphilic coordination compounds.

In initial investigations we used commercially available starting materials to synthesise the aromatic hda-type ligands. These ligands were prepared *via* the Mannich reaction.[165, 166]. This process utilised phenols and amines or amino acids to produce iminodiacetic acid based ligands. The starting materials were easily accessible and allowed us to elaborate a simple synthetic route and to develop an extensive library of hda–type compounds.

3.1.1. A general mechanism of the Mannich reaction

The Mannich reaction involves three main steps: In the first step a formaldehyde molecule accepts a proton to form a positively charged carbocation (Sch. 3.1).

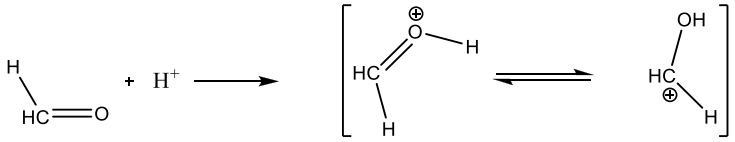

Sch. 3.1 | First step of Mannich reaction

Upon addition of an amine functionalised compound the lone pair of electrons on the nitrogen atom nucleophilically attacks the carbocation, to generate an imminium ion (Sch. 3.2)

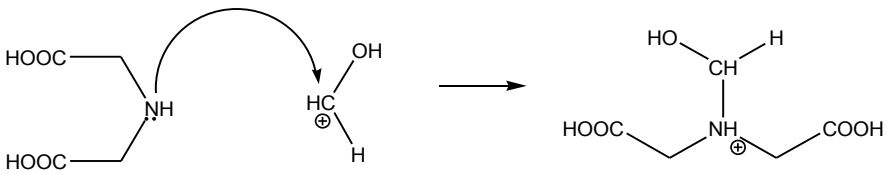

Sch. 3.2 | Mannich reaction - formation of a positively charged imminium ion

The imminium ion then undergoes an internal rearrangement whereby the lone pair of electrons of the hydroxy- oxygen atom migrates towards the amine functionality and a water molecule is eliminated (Sch. 3.3).

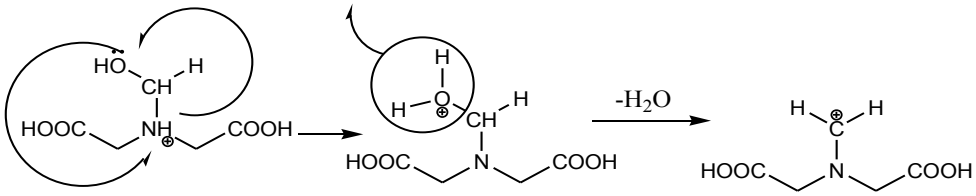

Sch. 3.3 | Mannich reaction - internal rearrangement

In the third step, an electrophilic substitution reaction occurs upon addition of the positively charged carbocation, shown in Sch. 3.3, to an aromatic ring. The phenolic hydroxyl group of the aromatic ring directs electrophiles into the *ortho* or the *para* positions. For the purpose of these investigations it was desirable to avoid the formation of doubly substituted phenols. In order to achieve this we chose aromatic phenolic reactants that contained blocking residues in the *para* and *ortho* positions of one side of the phenol ring. The Mannch reaction introduces a methylene group between the nitrogen atom and the phenolic ring (Sch. 3.4).

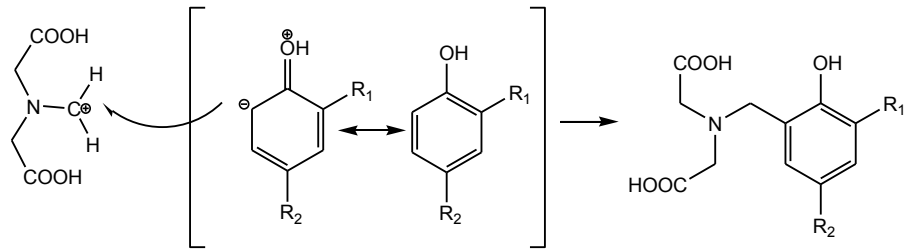

Sch. 3.4 | The last step of the Mannich reaction - electrophilic attack on the phenol molecule

The first two steps in the Mannich reaction can also occur under alkaline conditions. In this case the lone pair of electrons located on the iminodiacetic acid nitrogen atom attacks the formaldehyde to form an enol (Sch. 3.5).

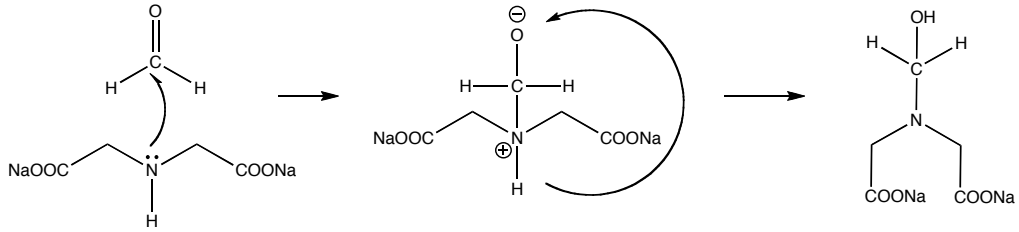

Sch. 3.5 | The first step in the Mannich reaction performed in basic conditions

The next step requires the presence of a proton. This is the rate-limiting step in the reaction as it is carried out under alkaline conditions. Upon protonation a carbocation is generated (as seen in Sch. 3.6). In the last stage the carbocation reacts with the phenol in an electrophilic substitution reaction as presented in Sch. 3.4. This results in the formation of a ligand molecule and a proton.

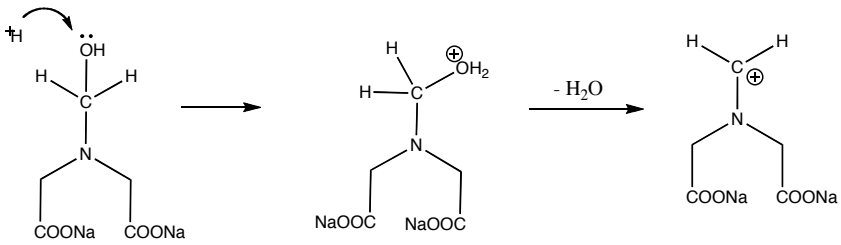

Sch. 3.6 | In the second step the previously formed enol undergoes a dehydratation

3.1.2. Special case – Ligands based on the vanillic acid (vda-type ligands)

The modification of the amphiphilicity of the hda-type ligands relies on exchanging the substituents located in the *ortho* and *para* positions (with respect to the aromatic hydroxyl group). However, the more sophisticated these substituents are, the more expensive is the commercially available phenol, which is used as the starting material in the Mannich reaction. Therefore, we have been exploring a new approach towards the synthesis of the hda-type ligands, which would allow us to control precisely the amphiphilicity of the ligand molecules by introducing another step into the synthesis process.

Vanillic acid was chosen as a starting material for this new class of ligands. It is an adventitious reagent as it contains a carboxylic acid group in the *para* position (with respect to the aromatic hydroxyl group) that can undergo a series of condensation reactions to form esters or amides. A wide selection of primary alcohols that are commercially available and reasonably priced enabled us to utilise aliphatic esters of vanillic acid as the starting material in the Mannich reaction. The methoxy moiety blocks one of the *ortho* positions and therefore prevents the formation of di-substituted products or polymeric resins in the subsequent reactions with formaldehyde. The remaining *ortho* site is the active site for electrophilic addition reactions. In addition to the ability to control the amphiphilicity of these ligands, these Vanillic acid based ligands contain an additional three oxygen atoms, which potentially can act as coordination sites.

In order to distinguish these new class of ligands from the well-established hda-type ligands they are referred to as vda-type ligands. The general structures of the vda-type ligands and their corresponding abbreviations can be seen in Sch. 3.7.

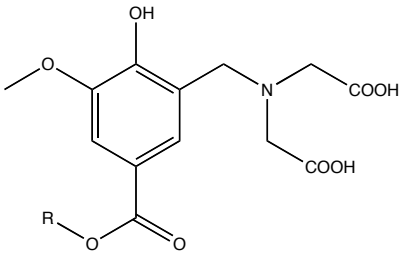

-R functionality	Ligand's name
H	Hvda
***n*-C_2H_5**	C_2vda
***n*-C_6H_{13}**	C_6vda
***n*-$C_{10}H_{21}$**	C_{10}vda
***n*-$C_{14}H_{29}$**	C_{14}vda
***n*-$C_{18}H_{37}$**	C_{18}vda
n-$C_{22}H_{45}$	C_{22}vda

Sch. 3.7 | Structure of the vda-type ligands

The synthesis of this class of ligands involves two major steps: the esterification of vanillic acid and the subsequent Mannich reaction between the ester, formaldehyde and the iminodiacetic acid.

For the esterification reaction (Sch. 3.8) the desired alcohol may be used as a solvent and as a reagent in the same time. We used sulfuric acid as a catalyst. Several esters were prepared in this way, including the ethyl (C_2), hexyl (C_6), decyl (C_{10}), myristyl (C_{14}), stearyl (C_{18}) and behenyl (C_{22}) derrivates.

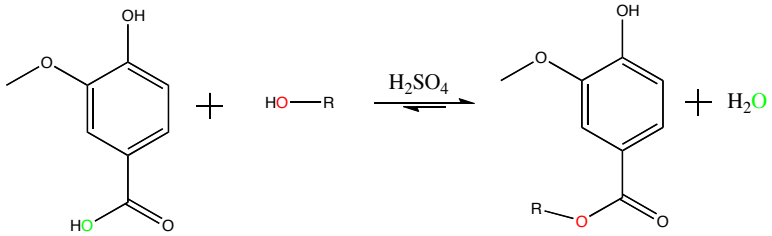

Sch. 3.8 | Estrification of vanillic acid with a primary alcohol

As water is a by-product of the esterification process, all the reactions with hexanol and higher alcohols were carried out at a temperature above 100°C. These reaction conditions not only enabled us to perform the reaction in a liquid state, where an excess of the alcohol was simultaneously used as a reagent and a solvent, but also facilitated the removal of water from the reaction mixture and shifted the equilibrium towards the products.

The second step involves the Mannich reaction between the ester, the formaldehyde and the iminodiacetic acid. The mechanism is the same as that seen for the hda-type ligands (Sch. 3.9). A typical mixture of reagents was stirred in acetic acid for 2 hours at 85°C followed by the addition of a 2% aqueous solution of hydrochloric acid. This caused the slow precipitation of the ligand.

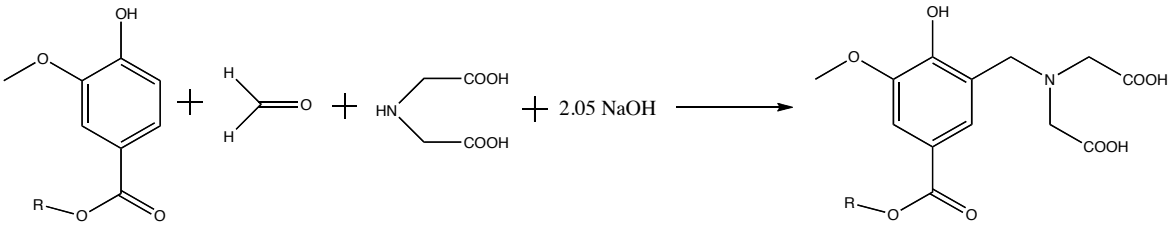

Sch. 3.9 | The Mannich reaction between an ester of the vanillic acid and iminodiacetic acid

An alternate approach for the synthesis of vda-type ligands, where the Mannich reaction was performed on Vanillic acid prior to the esterification reaction, was also investigated. However, this synthetic pathway was abandoned due to the formation of several impurities, mainly containing esterified carboxylic acid groups of the iminodiacetic acid moiety.

3.1.3. Crystal structure of the C_2vda monohydrate

During the studies on the synthesis of the vda-class ligands it was possible to obtain single crystals suitable for the single crystal X-Ray diffraction experiment. This analytical technique provided us with a detailed knowledge about the asymmetric unit, connectivity and

solid-state packing structure of the ligand molecules. Additionally, the single crystal structure undoubtedly confirms that the vda-class of ligands can be successfully synthesised according to the procedures presented above.

C_2vda monohydrate forms in the solid state a 3D network involving hydrogen bonds and π-π stacking interactions.

Asymmetric unit

C_2vda crystallises from a methanol/ethanol mixture in the form of colourless blocks in the orthorhombic space group *P*bcn (no. 60). The asymmetric unit presented in Fig. 3.1 consists of one C_2vda ligand molecule and one constitutional water molecule.

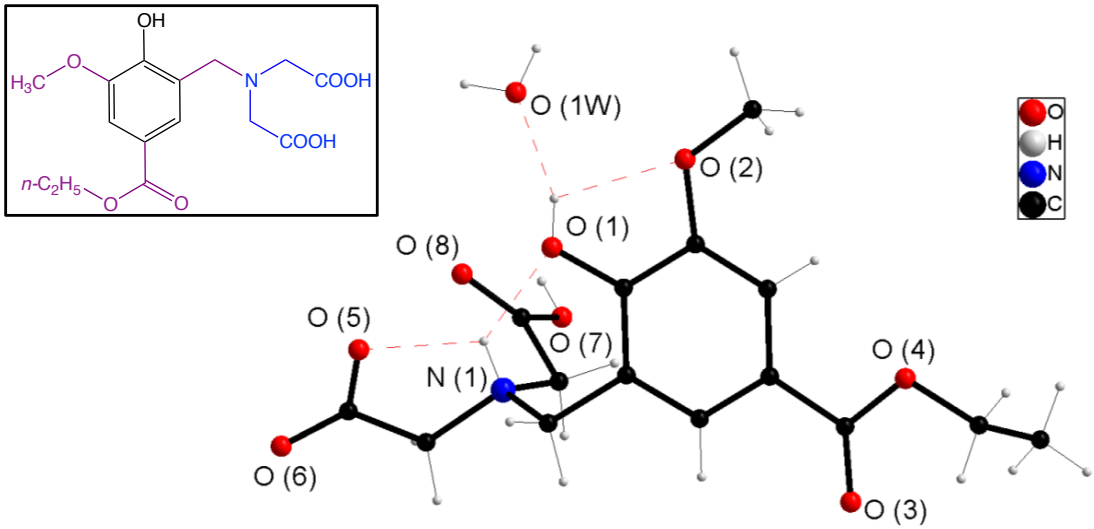

Fig. 3.1 | The asymmetric unit of the C_2vda monohydrate crystals. Intermolecular hydrogen bonds are highlighted with a red dotted line. Inset: the C_2vda ligand molecule

All of the hydrogen atoms were located in the electron density map and refined. The aromatic hydroxyl group, which contains the oxygen atom O(1), remains protonated. The same applies to one of the iminodiacetic acid carboxyl groups which contain the oxygen atoms O(7) (protonated) and O(8). The second iminodiacetic acid carboxylate group that contains the oxygen atoms O(5) and O(6) is deprotonated; the charge of C_2vda is balanced due to the presence of a proton on the nitrogen atom N(1).

As presented in Fig. 3.1, there are four intramolecular hydrogen bonds present within the asymmetric unit of C_2vda·H_2O. The proton of the nitrogen atom is involved in two hydrogen bond interactions. The first one occurs between the oxygen atom O(5) of the iminodiacetic acid carboxylate group and N(1). Both atoms are located 2.677(3) Å from each other. The second hydrogen bond interaction links the nitrogen atom N(1) to the oxygen atom O(1) of the aromatic hydroxyl group. The bond distance is 2.757(4) Å.

The oxygen atom O(1) of the aromatic hydroxyl group binds to the oxygen atom O(1W) of the constitutional water molecule and to the oxygen atom O(2) of the methoxy group. The bond lengths are 2.561(4) Å and 2.680(3) Å, respectively.

Connectivity

Each asymmetric unit is linked *via* hydrogen bond interactions with three other symmetry-equivalent units. As presented in Fig. 3.2, two of these interactions involve the constitutional water molecule, which interacts with the oxygen atom O(6^{I}) of the carboxylate group and the oxygen atom O(3^{II}) of the ester functional group. The bond distances are 2.715(4) Å and 2.893(4) Å, respectively. The third hydrogen bond interaction occurs between the oxygen atom O(7) of the carboxylic acid functional group and the symmetry generated oxygen atom O(5^{III}), which originates from the iminodiacetic acid carboxylate functionality. The bond length is 2.495(3) Å.

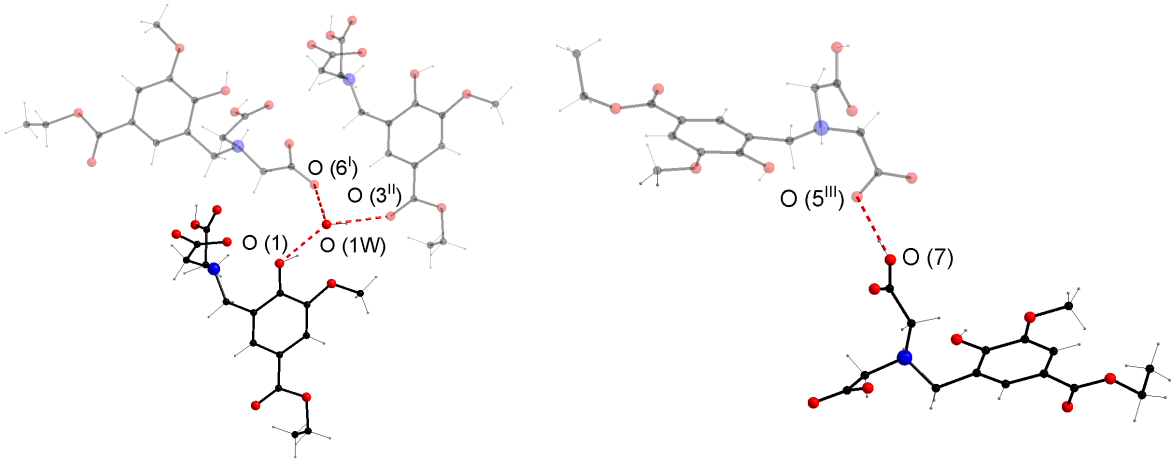

Fig. 3.2 | Supramolecular hydrogen bond interactions in C_2vda·H_2O. Three hydrogen bond interactions link the asymmetric unit to three different symmetry equivalent units. Two of these interactions involve the oxygen atom O(1W) of the constitutional water molecule (left) and the remaining one connects directly the oxygen atom O(7) of the carboxylic acid group to the oxygen atom O(5^{III}) of the iminodiacetic acid carboxylate group (right). Symmetry codes: (I): 0.5-x, -0.5+y, z; (II): x, -1+y, z; (III): 0.5-x, 1.5-y, 0.5+z.

As mentioned before, the protonated oxygen atom O(7) interacts with the neighbouring oxygen atom O(5^{I}). This H-bond interaction, presented in Fig. 3.3, connects each consecutive molecule to form 1D motifs that extend parallel to the crystallographic *c*-axis. The consecutive organic molecules are rotated by 180° and are shifted by a half of the *c*-vector length due to the 2_1 screw axis that is present within the unit cell.

As presented in Fig. 3.4, the constitutional water molecules bridge between two different symmetry equivalent asymmetric units. The O(1W) atom links neighbouring units into 1D assemblies that extend parallel to the crystallographic *b*-axis. The formation of these structural motifs is related to a glide plane, located between symmetry equivalent organic molecules, which creates a mirror image of each unit and shifts it by a half of the length of the *b* vector (again, see Fig. 3.4 for reference).

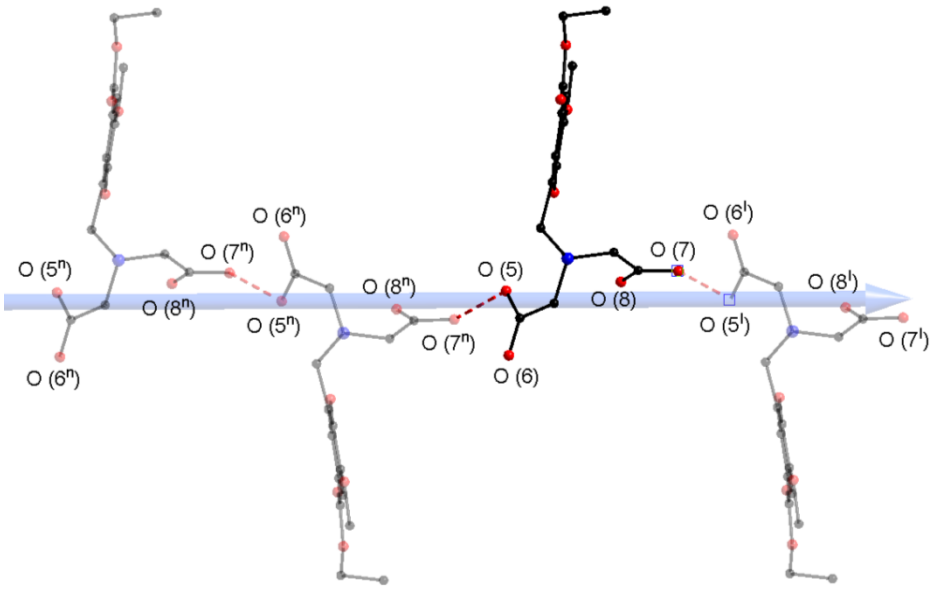

Fig. 3.3 | Hydrogen bonding in the C_2vda monohydrate crystals. The blue vector points in the direction of the crystallographic *c*-axis and corresponds to a 2_1 screw axis present within the unit cell. Hydrogen atoms were omitted for clarity. Symmetry codes: (I): 0.5-x, 1.5-y, 0.5+z.

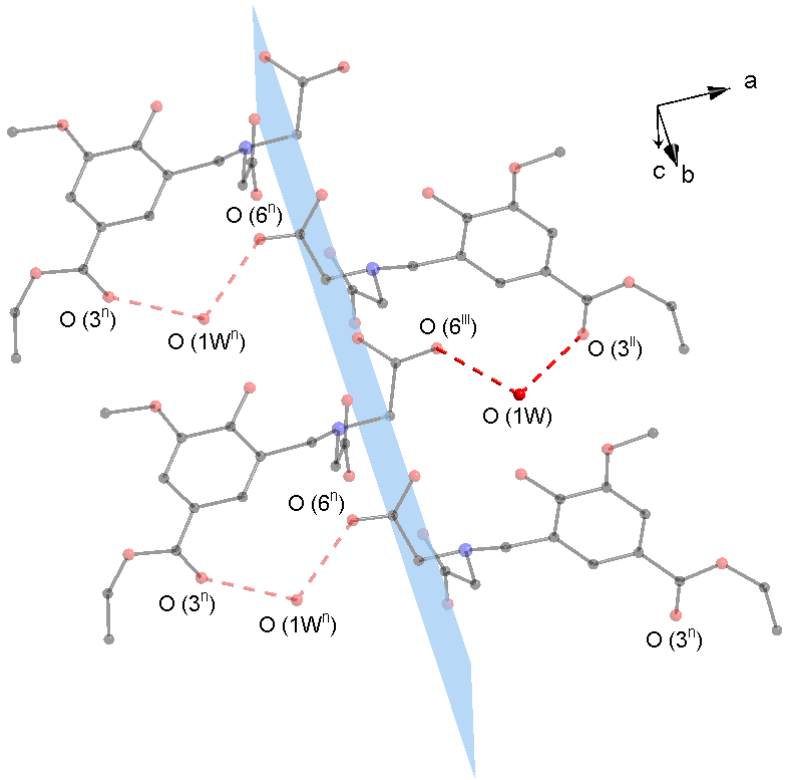

Fig. 3.4 | Hydrogen bonding in C_2vda monohydrate. The picture presents only the hydrogen bonds formed by the constitutional water molecule O(1W). Hydrogen atoms were omitted for clarity. The blue plane corresponds to the [400] glide plane present within the unit cell. Symmetry codes: (II): x, -1+y, z; (III): 0.5-x, -0.5+y, z.

A second type of non-covalent interaction is observed in the C_2vda monohydrate crystals. It is a weak π-π stacking that occurs between the symmetry equivalent aromatic rings (Fig. 3.5). The average distance between these aromatic moieties is equal to 3.7 Å.

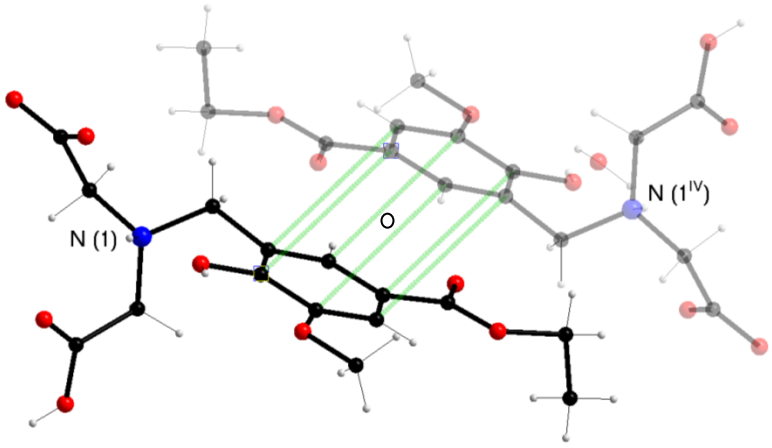

Fig. 3.5 | π-π stacking between the aromatic rings in the C_2vda monohydrate crystals. Symmetry codes: (IV): 1-x, 2-y, z.

The symmetry equivalent organic molecules that interact through π-π interactions are related by inversion symmetry with the symmetry centre located between each of the stacking aromatic rings.

Solid-state packing structure

The previously discussed hydrogen bonds and π-π stacking interactions are the driving forces that facilitate the self-organisation of the organic molecules into a three-dimensional structure. As presented in Fig. 3.6, the organic molecules form a structural motif in the *ac*-plane, where the stacking aromatic rings sandwich between the more hydrophilic, H-bound, iminodiacetic acid moieties and ester functional groups.

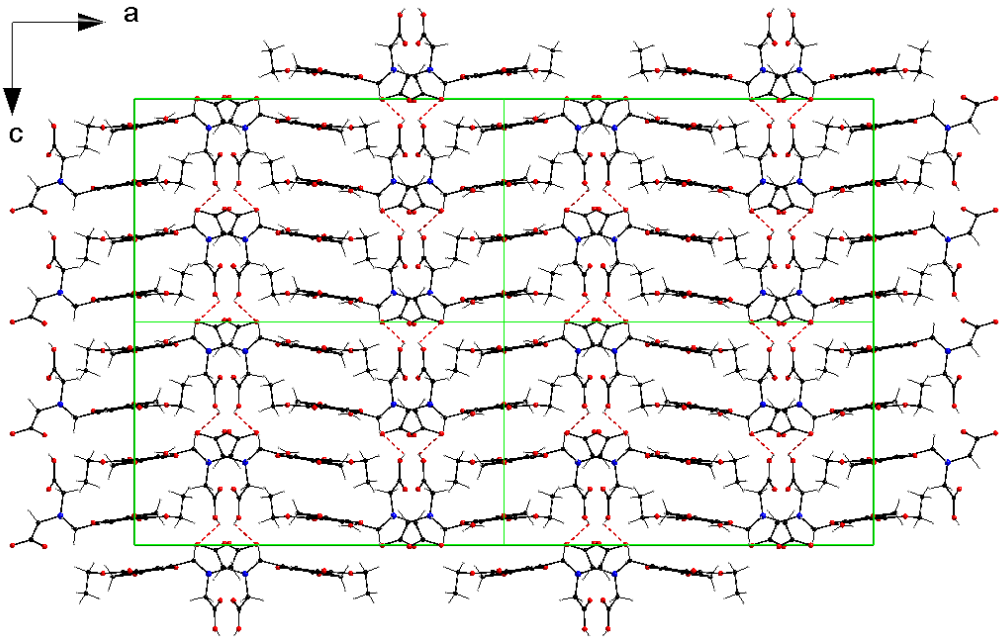

Fig. 3.6 | Packing structure of the C_2vda monohydrate crystals viewed along the crystallographic *b*-axis.

When the structure is viewed along the crystallographic *c*-axis (Fig. 3.7), it is possible to notice that the aromatic rings are almost on the top of each other. The iminodiacetic acid moieties belong to the H-bound parts of the structure and symmetry operations generate small cavities, which are occupied by the constitutional water molecules.

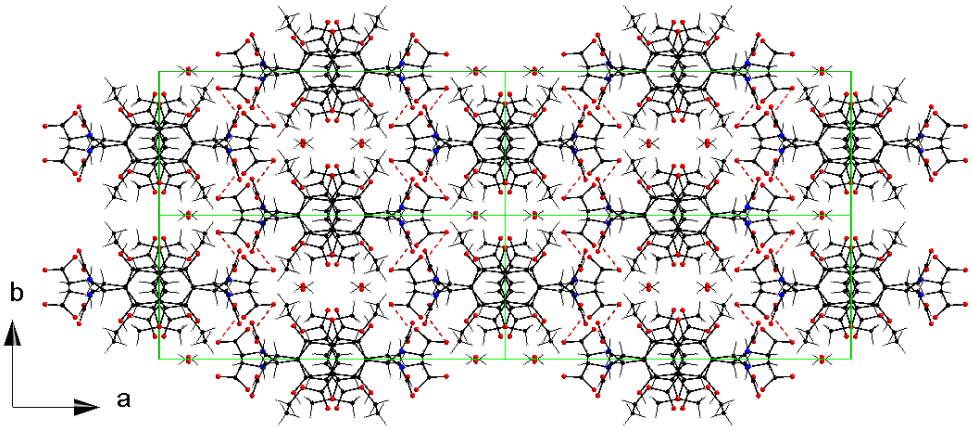

Fig. 3.7 | Packing structure of the C_2vda monohydrate viewed along the crystallographic *c*-axis.

Refinement details

Crystallographic parameters for the refined model of ethyl vanillate monohydrate are presented in Tab. 3.1

Tab. 3.1 | Crystallographic parameters of the refined model of ethyl vanillate monohydrate.

Identification code	Ethyl vanillate monohydrate	
Empirical formula	$C_{15}H_{21}NO_9$	
Formula weight	359.33 g/mol	
Temperature	150(2) K	
Wavelength	0.71073 Å	
Crystal system	Orthorombic	
Space group	*P*bcn	
Unit cell dimensions	a = 23.563(5) Å	α = 90°.
	b = 9.797(2) Å	β = 90°.
	c = 14.222(3) Å	γ = 90°.
Volume	3283.0(11) $Å^3$	
Z	8	
Density (calculated)	1.454 Mg/m^3	
Absorption coefficient	0.121 mm^{-1}	
F(000)	1520	
Crystal size	0.5 x 0.4 x 0.3 mm^3	
Theta range for data collection	1.73 to 24.99°.	
Index ranges	-28<=h<=28, -11<=k<=11, -16<=l<=16	
Reflections collected	24264	
Independent reflections	2901 [R(int) = 0.0790]	
Completeness to theta = 24.99°	100.0 %	
Refinement method	Full-matrix least-squares on F^2	
Data / restraints / parameters	2901 / 6 / 237	
Goodness-of-fit on F^2	1.101	

Final R indices [I>2sigma(I)]	R1 = 0.0780, wR2 = 0.1785
R indices (all data)	R1 = 0.0978, wR2 = 0.1898
Largest diff. peak and hole	0.562 and -0.363 e.Å^{-3}

Additional characterization

In order to confirm the phase purity and accuracy of the refined model, a P-XRD pattern was recorded. As expected, the results presented in Fig. 3.8 confirm that the solid-state model is accurate and there were no crystalline impurities within the sample.

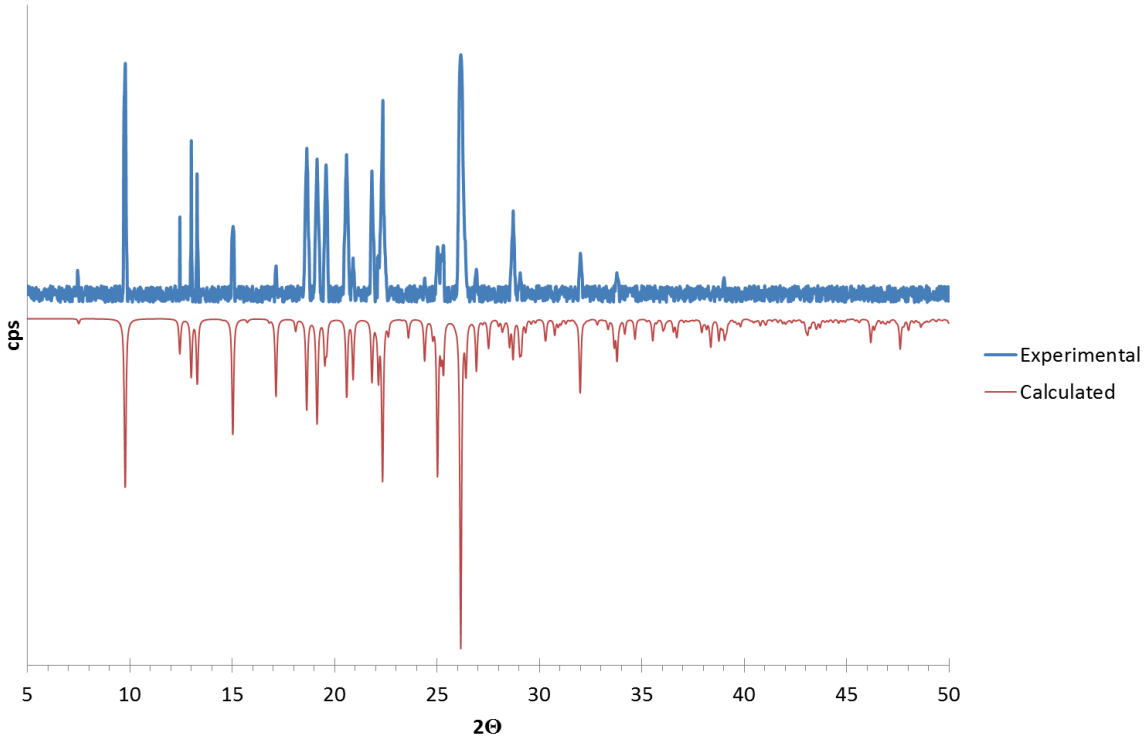

Fig. 3.8 | P-XRD pattern obtained for the crystals of ethyl vanillate monohydrate (blue) compared with a pattern simulated for the model based on the single crystal X-ray diffraction results (red).

3.2. Compound $[Cu(C_2vda)(H_2O)] \cdot 2H_2O \cdot 2MeOH$ (1)

After the vda-type ligands were successfully synthesised and characterised, it was decided to react them with copper(II) ions in an attempt to generate coordination complexes. It was anticipated that these compounds would form single-crystalline material that could be extensively analysed using the single crystal X-ray diffraction method. Important characteristic features, such as the coordination geometry, connectivity between the complexes and their solid-state packing structure could be determined in this way.

3.2.1. Characterization of compound 1

Compound **1** with the chemical formula $[Cu(C_2vda)(H_2O)] \cdot 2H_2O \cdot 2MeOH$ forms when the C_2vda ligand is reacted with copper(II) chloride in methanol. Blue needle-like crystals form after *ca.* 2 weeks of slow evaporation (Fig. 3.9). **1** crystallises in a monoclinic space group $P2_1/c$. The reactants form mononuclear units that are linked *via* coordination bonds to give 1D chains, which extend parallel to the crystallographic *c*-axis. Hydrogen interactions and dispersion forces link the chains into 2D sheets in the *bc* plane. The sheets further assemble in the direction of the crystallographic *a*-axis, which leads to the formation a lamellar material, consisting of sheets and layers of constitutional solvent molecules.

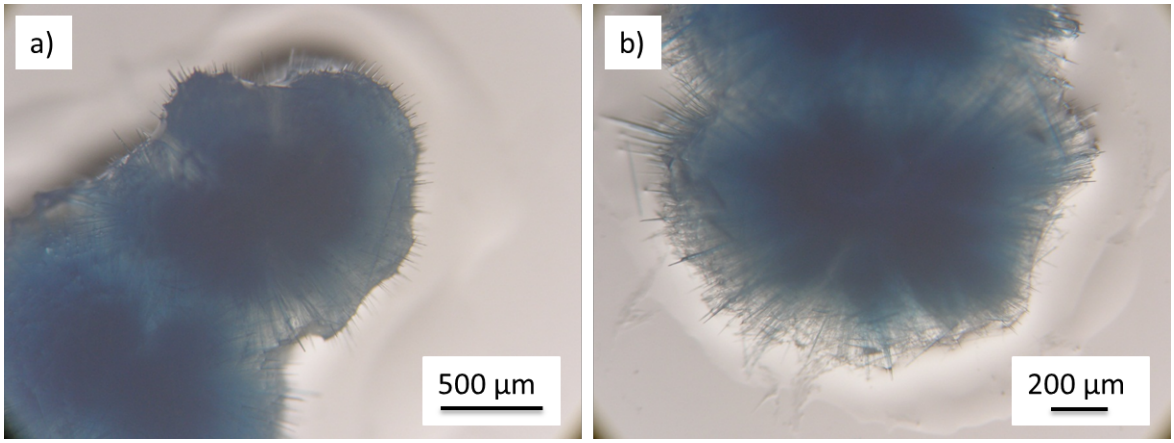

Fig. 3.9 | Optical microscope images of compound **1**. The needle-like blue crystals grow from a common centre.

Asymmetric unit

The mononuclear unit of **1** is presented in Fig. 3.10. The asymmetric unit additionally contains two constitutional water molecules and two methanol molecules. The coordination environment of the metal ion can be described as a distorted octahedron. The organic ligand provides three O-donors (O(2), O(3), O(6)) and one N-donor, N(1). The remaining sites of the octahedron are occupied by the oxygen atom O(5) of a coordinating water molecule and a symmetry generated O-donor O(8^{I}), that is a part of the ester carbonyl group of a neighbouring mononuclear unit.

The equatorial plane, presented in Fig. 3.11, is formed by the carboxylic acid O-donors (O(2), O(3)), the oxygen atom O(5) from a coordinating water molecule and the N-donor N(1). The carboxylate O-donors occupy the *trans* position within the plane. The apexes of the

octahedron are occupied by the oxygen atom O(6) of the protonated aromatic hydroxyl group (the proton was located in the electron density map and refined) and the symmetry generated carbonyl donor O(8^{I}).

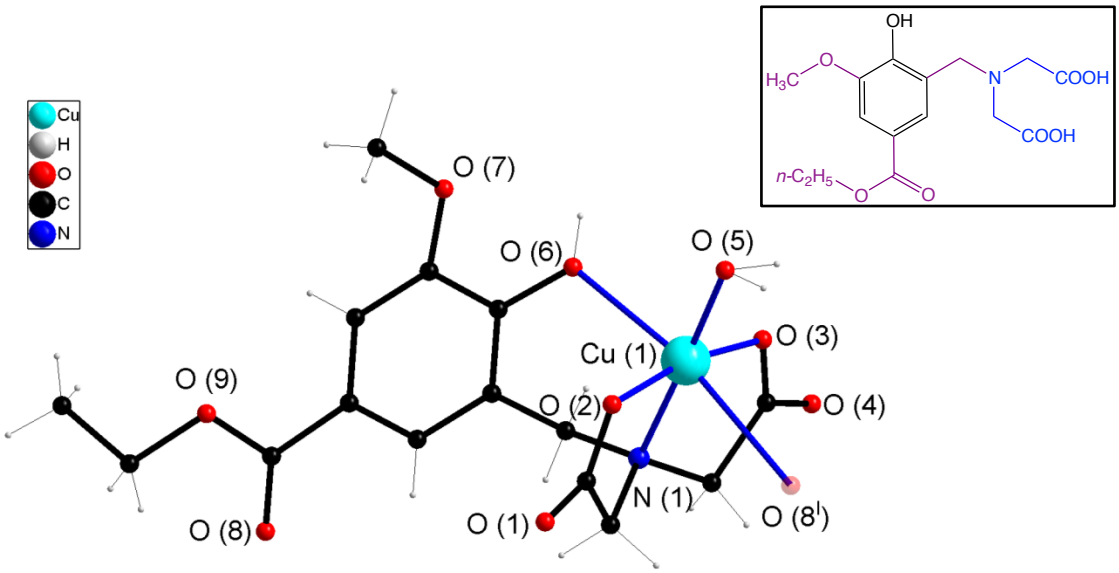

Fig. 3.10 | Mononuclear complex in **1**. Symmetry codes: (I): x, 0.5-y, 0.5+z. Inset: the C_2vda ligand molecule.

The bond distance between the metal ion and the hydroxyl O-donor O(6) is 2.477(3) Å while the carbonyl donor O(8^{I}) is located 2.734(5) Å from the copper ion. The tetragonal elongation of the octahedron can be explained by the Jahn-Teller effect.

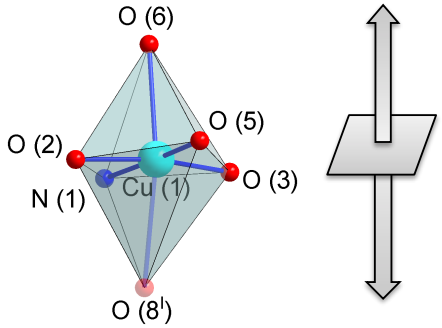

Atom 1	Atom 2	Symmetry code for atom 2	Bond lenght [Å]
Cu(1)	O(2)	x, y, z	1.920(4)
Cu(1)	O(3)	x, y, z	1.928(4)
Cu(1)	O(5)	x, y, z	1.944(4)
Cu(1)	N(1)	x, y, z	2.039(4)
Cu(1)	O(6)	x, y, z	2.477(3)
Cu(1)	O(8^{I})	x, 0.5-y, 0.5+z	2.734(5)

Fig. 3.11 | Coordination environment in **1**. The octahedron displays typical distortion due to the Jahn-Teller effect. The table presents the corresponding bond distances.

Connectivity

As the O-donor O(8^{I}) belongs to a symmetry generated mononuclear complex, **1** forms a 1D coordination chain that extends parallel to the crystallographic *c*-axis. The formation of these chains is supported by hydrogen bond interaction that occurs between the oxygen atom O(5) of a coordinating water molecule and the non-coordinating oxygen atom O(1), which belongs to one of the carboxylic acid functionalities (Fig. 3.12). The H-bond is characterised by an O-O distance of 2.676(6) Å.

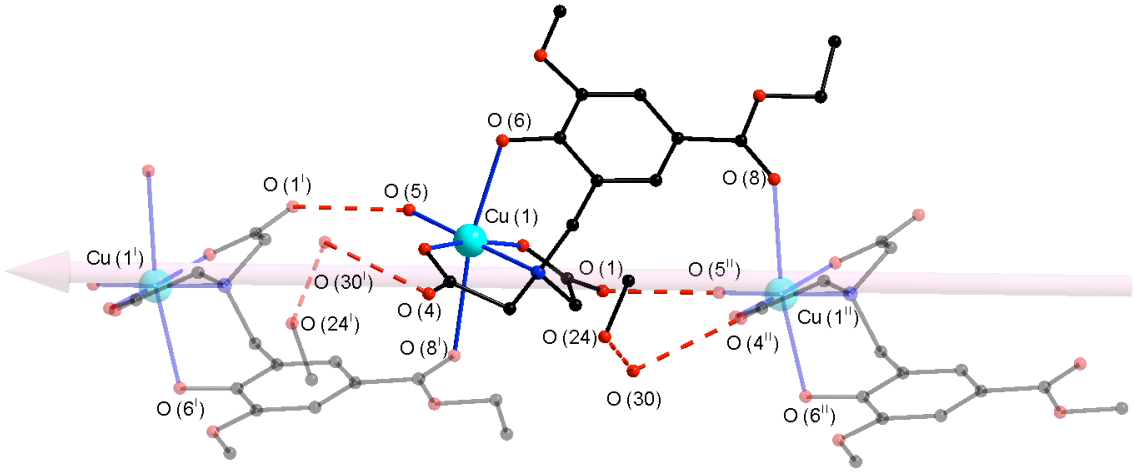

Fig. 3.12 | A 1D coordination chain in **1**. The rose vector points in the crystallographic *c*-direction and indicates the location of a glide plane. Hydrogen atoms and constitutional water molecules were omitted for clarity. Symmetry codes: (I): x, 0.5-y, 0.5+z; (II): x, 0.5-y, -0.5+z.

The two hydrogen bonds that occur between the constitutional solvent molecules can also be seen in Fig. 3.12. One of the bonds link the oxygen atom O(30) of a constitutional water molecule with the non-coordinating oxygen atom O(4^{II}), which is a part of an iminidiacetate group. The O-O distance of this H-bond is equal to 2.750(7) Å. The same oxygen atom (O(30)) is connected *via* a hydrogen bond to the oxygen atom O(24) of a constitutional methanol molecule. These O atoms are located 2.762(8) Å from each other.

As presented in Fig. 3.13, the constitutional solvent molecules mediate between the symmetry equivalent mononuclear units, which are located parallel to the crystallographic *a*-axis. A hydrogen bond interaction occurs between the O-donor O(2) of the iminodiacetic acid carboxylate group and the oxygen atom O(24) of the constitutional methanol molecule. A distance of 2.979(6) Å separates both atoms. The oxygen atom of the methanol molecule, O(24), is involved in another hydrogen bond, which links it with the oxygen atom O(28) of the constitutional water molecule. In this case the bond length is 2.941(6) Å.

Finally, the oxygen atom O(28) is connected to the non-coordinating oxygen atom O(4^{II}) that originates from a symmetry generated iminodiacetic acid carboxylate group. The bond distance is 2.843(7) Å.

The hydrogen bond interactions that occur between the constitutional solvent molecules are presented in Fig. 3.14. Although one might expect that these molecules form a 2D layer, a precise analysis confirms that they assemble into 1D units that do not grow into a 2D sheet or 3D network.

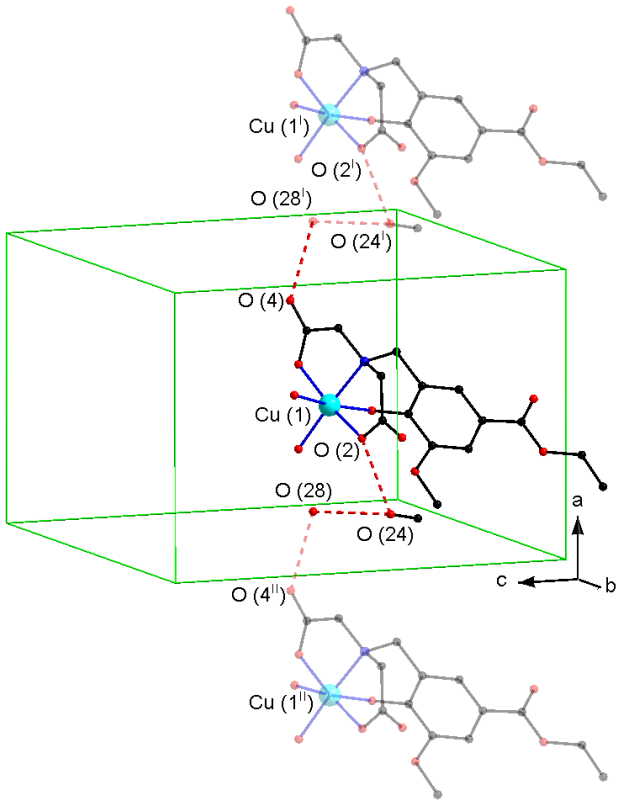

Fig. 3.13 | Hydrogen bonding in **1**. The constitutional solvent molecules mediate between the metal-organic complexes. Symmetry codes: (I): 1+x, y, z; (II): -1+x, y, z.

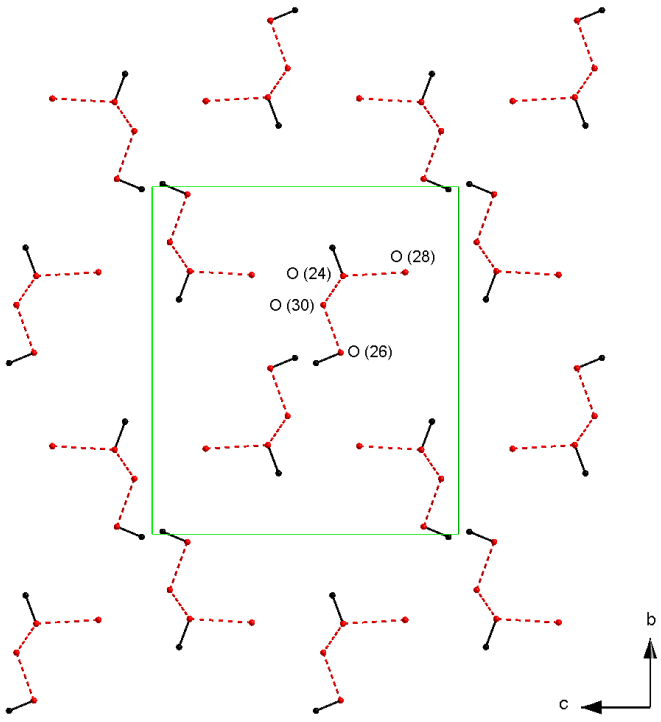

Fig. 3.14 | Hydrogen bond interactions between the constitutional solvent molecules in **1**. For clarity, the mononuclear units are omitted. View along the crystallographic *a*-axis.

The hydrogen bond distances for the constitutional solvent molecules are as follows: O(28)-O(24): 2.941(6) Å, O(24)-O(30): 2.762(8) Å, O(30)-O(26): 2.670(9) Å.

Another supramolecular interaction that occurs within **1** is a weak π-π stacking interaction between the aromatic ring of the ligand molecule and its symmetry equivalent. The distance between the stacking rings is 3.793(8) Å. The is an inversion centre located in the middle between the two rings. This interaction, which is presented in Fig. 3.15, can be considered as a weak to moderately strong π-π interaction.[24]

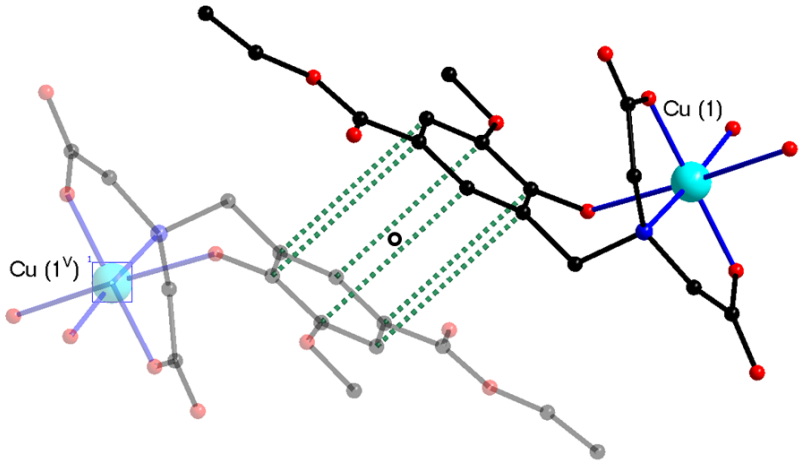

Fig. 3.15 | π-π stacking in **1**. Hydrogen atoms were omitted for clarity. Symmetry codes: (V): 1-x, 1-y, z.

Packing

The previously described intermolecular interactions link the mononuclear units into sheet-like layers (Fig. 3.16) that extend in the crystallographic *bc*-plane. These layers stack in the direction of the crystallographic *a*-axis. The stacking is further mediated by constitutional solvents molecules that are sandwiched between the sheets and link them *via* H-bonding interactions (Fig. 3.17). The thickness of the sheets containing the complexes does not exceed 9 Å in the *ab*- and *ac*-planes.

The layered structure of **1** is composed of 2D sheets of the complexes and layers of constitutional solvent molecules. The aliphatic ethyl chains do not interact with other moieties. This may suggest that a longer chain is required to enable pronounced van der Waals forces between the moieties located in the *para* position (with respect to the aromatic hydroxyl group).

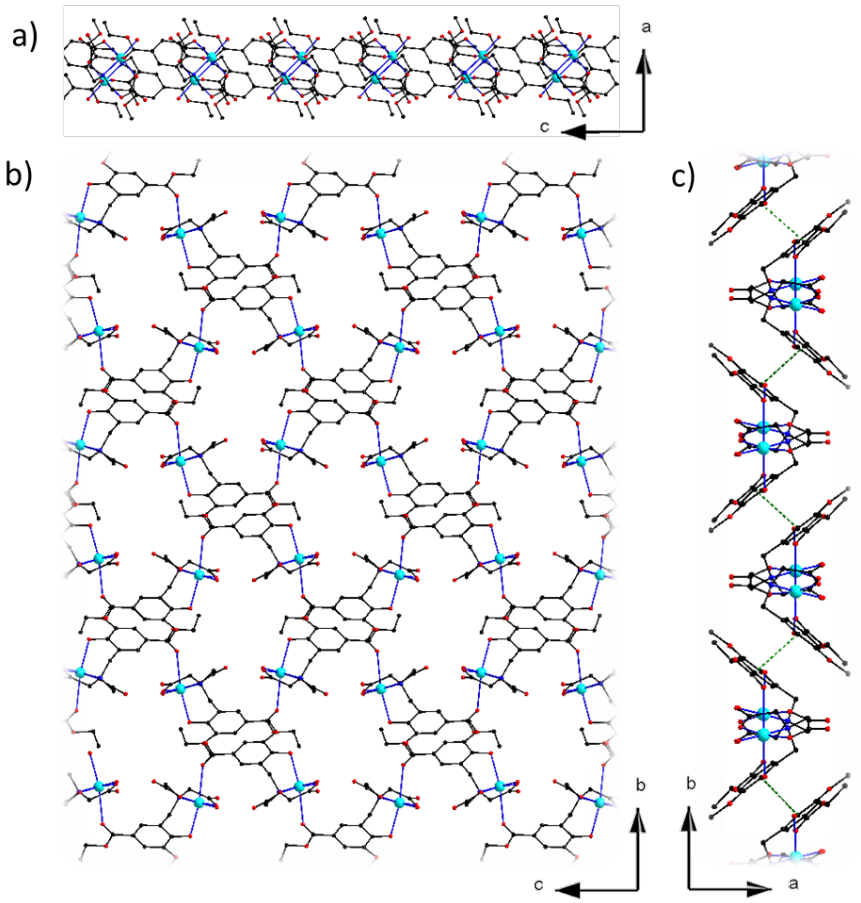

Fig. 3.16 | Sheet-like assemblies composed of mononuclear units in **1**. View along the crystallographic *b*-axis (**a**), *a*-axis (**b**) and *c*-axis (**c**). Hydrogen atoms were omitted for clarity.

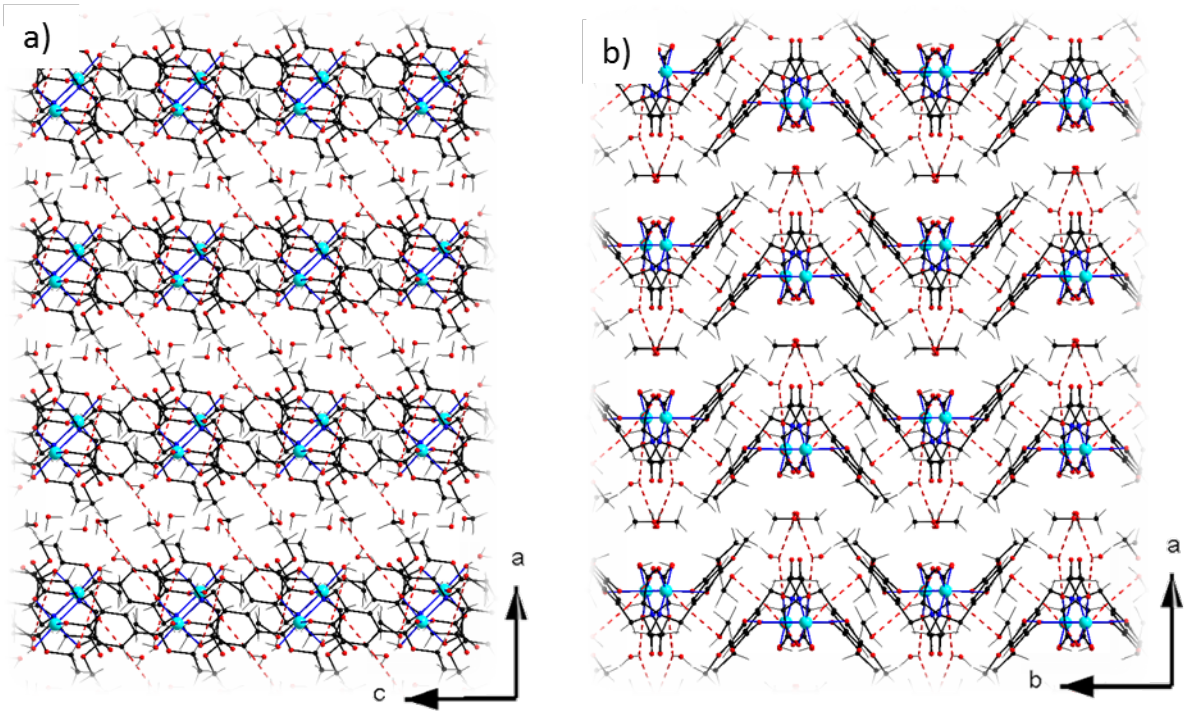

Fig. 3.17 | Packing diagram of compound **1** viewed along the crystallographic *b*-axis (**a**) and *c*-axis (**b**).

Refinement details

The refinement parameters and crystal data for the crystal structure of **1** are presented in Tab. 3.2.

Tab. 3.2 | Refinement details for compound **1**.

Identification code	**1**
Empirical formula	$C_{17}H_{31}CuNO_{13}$
Formula weight	520.98 g/mol
Temperature	150(2) K
Wavelength	0.71073 Å
Crystal system	Monoclinic
Space group	$P2_1/c$
Unit cell dimensions	a = 10.105(2) Å α = 90°. b = 16.349(3) Å β = 90.41(3)°. c = 14.425(3) Å γ = 90°.
Volume	2383.0(8) $Å^3$
Z	4
Density (calculated)	1.452 Mg/m^3
Absorption coefficient	6.602 mm^{-1}
F(000)	1530
Crystal size	0.7 x 0.1 x 0.1 mm^3
Theta range for data collection	1.25 to 25.00°.
Index ranges	-12<=h<=11, -12<=k<=17, -13<=l<=19
Reflections collected	8905
Independent reflections	6277 [R(int) = 0.0456]
Completeness to theta = 25.00°	74.8 %
Refinement method	Full-matrix least-squares on F^2
Data / restraints / parameters	6277 / 0 / 582
Goodness-of-fit on F^2	1.183
Final R indices [I>2sigma(I)]	R1 = 0.0868, wR2 = 0.2221
R indices (all data)	R1 = 0.0958, wR2 = 0.2312
Largest diff. peak and hole	1.306 and -0.518 $e.Å^{-3}$

3.2.2. Additional analyses

Crystals of **1** were collected and crushed using a mortar. This caused the colour of the crystals to change from a deep blue (as presented in Fig. 3.9) to pale green. The powder was analysed using the P-XRD. The resulting pattern was then compared with the simulated pattern generated from the single crystal X-ray diffraction data. The comparison presented in Fig. 3.18 clearly shows that the patterns do not fit. This result suggests that **1** is unstable at

room temperature; it readily loses the constitutional solvent molecules promoting a phase transition.

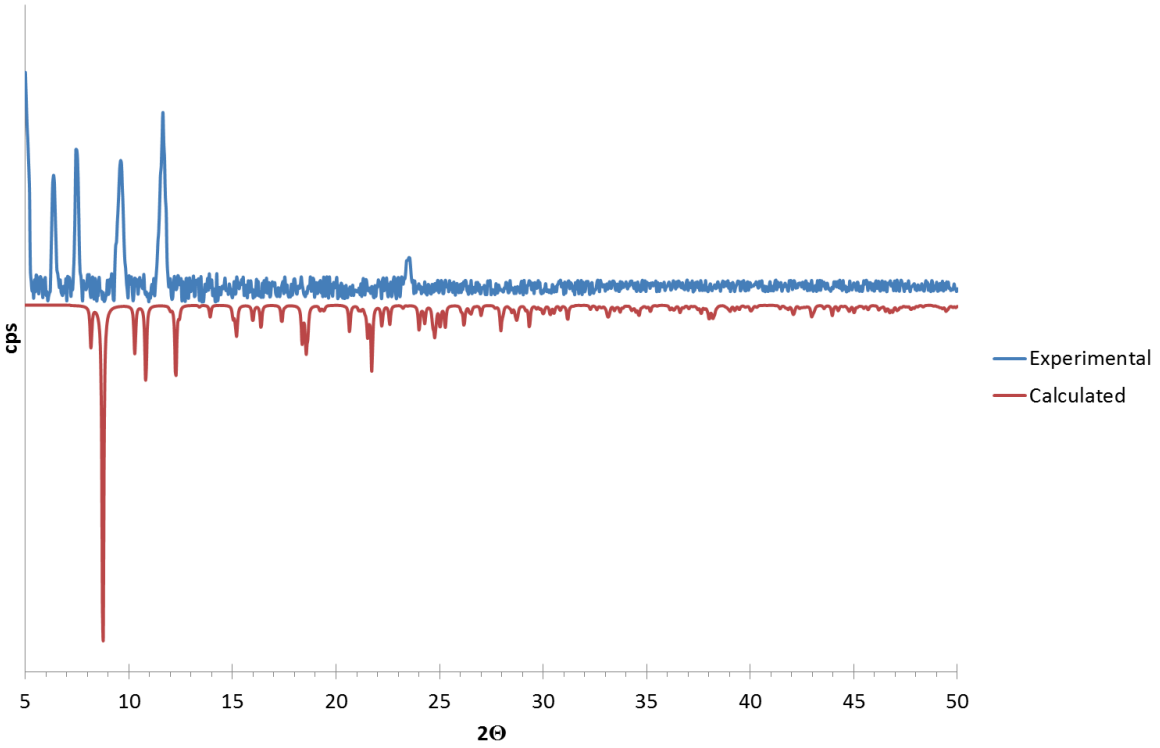

Fig. 3.18 | Comparison between the P-XRD pattern simulated for the refined structure of **1** (red) and the experimental pattern obtained for desolvated crystals of **1** (blue).

3.2.3. Formation of copper(II) oxide by the thermolysis of compound **1**

Thermogravimetric analysis (TGA) of the microcrystalline powder of **1** (see Fig. 3.19) confirms that the constitutional methanol molecules have already been lost at room temperature. At *ca*. 70 °C, the constitutional and coordinated water molecules have also been lost. Above 140 °C, the organic moieties in **1** undergo oxidative degradations. Finally, at *ca*. 340 °C, CuO has formed. Calculations suggest that other compounds are present at this temperature, but that at temperatures of 830 °C and higher, only CuO remains. The theoretical percentage masses of the proposed decomposition products were calculated as a percentage of the mass of $[Cu(C_2vda)(H_2O)] \cdot 2H_2O$. These are reported in Tab. 3.3 below and are in good agreement with the experimentally observed values.

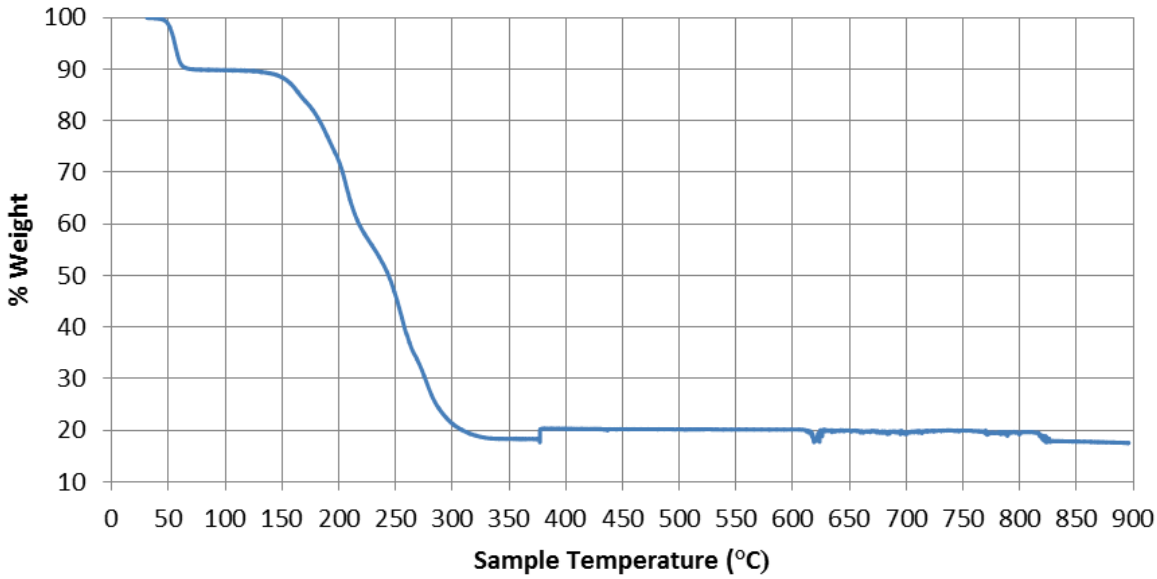

Fig. 3.19 | TGA analysis of compound **1**.

Tab. 3.3 | Results of the TGA experiment on **1**.

Formula	Theoretical mass [%]	Observed mass [%]	Sample Temperature (°C)
$[Cu(C_2vda)(H_2O)]\cdot 2H_2O$	100	100	30 (initial)
$Cu(C_2vda)$	88.15	89.66	70
CuO + other products	17.31 (CuO)	18.38	340
CuO	17.31	17.53	830

The chemical identity of this black powder was confirmed using the P-XRD pattern experiment. The resulting pattern fits the reference CuO pattern obtained from a database (Fig. 3.20).

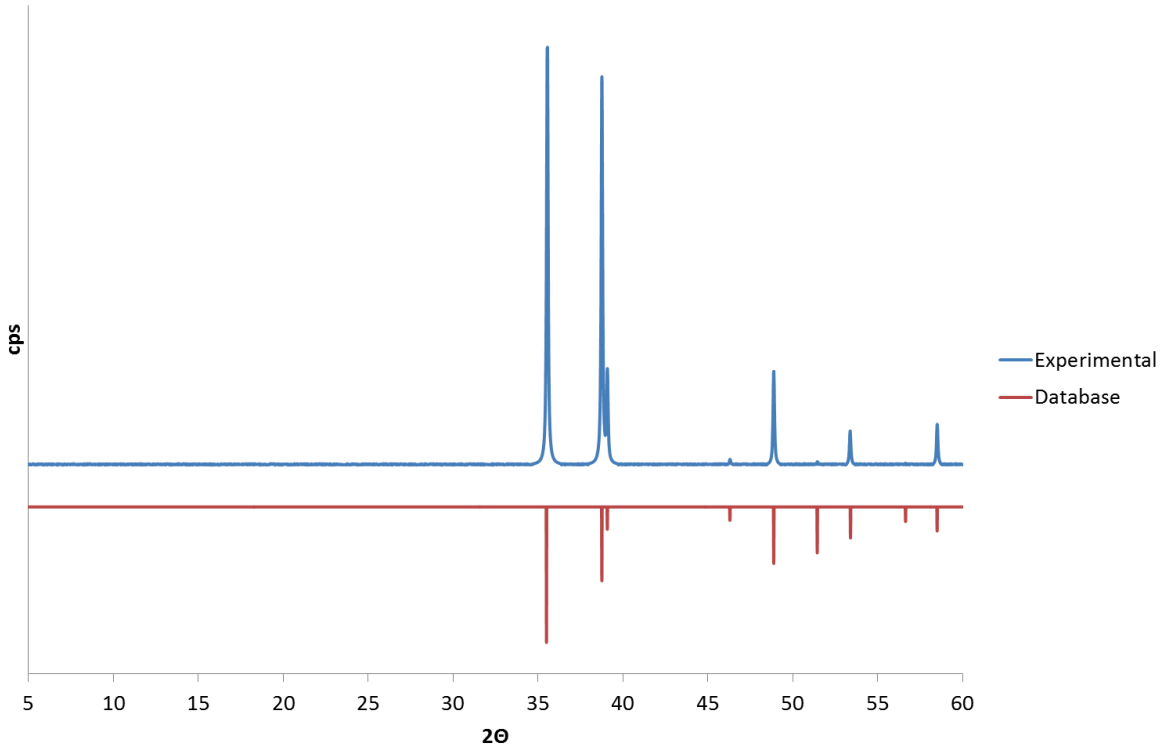

Fig. 3.20 | P-XRD pattern of the CuO particles obtained by a slow thermolysis of **1** (blue) and a reference pattern of copper(II) oxide (red).[178]

The decomposition residues were also imaged using a HeIM microscope. In order to prepare a sample for the analysis the black powder was suspended in methanol and two drops of the suspension were placed on a silicon surface. The Si surface was then coated with a thin (~2.5 nm) layer of a gold/palladium alloy. The images presented in Fig. 3.21 show that the obtained solid consists of an agglomeration of small particles with smooth edges. Their diameter does not exceed 3 μm. Imaging the sample at a higher magnification reveals that each small particle of CuO displays a layered imprint. This observation is highly unusual for copper(II) oxide crystals. The small crystals consist of flat, almost 2D layers, which adopt a uniform orientation and their thickness various between 5 and 50 nm.

This layered imprint may suggest that the lamellar morphology of the coordination network **1** is reflected in the layered morphology of the residual crystals of copper oxide. The thickness of the 2D CuO layers is significantly larger than the lattice separation distance of the layers observed in the *ac*-plane in **1**, which equals 10.11 Å. However, the resolution of the scanning electron microscopy technique is limited and further high resolution TEM analysis of suitable samples may elucidate the structural and morphological relationship between precursors and thermolysis products.

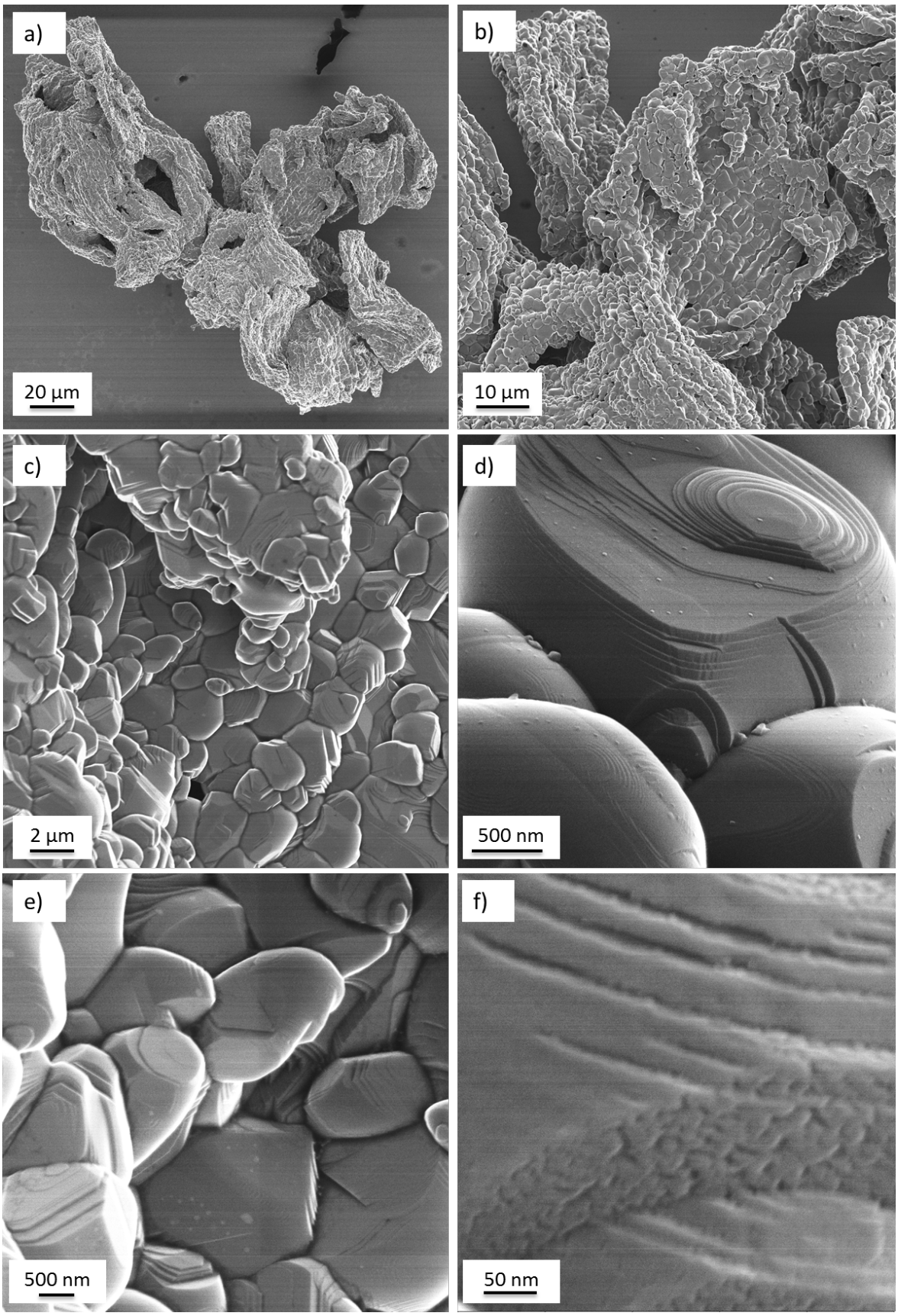

Fig. 3.21 | HeIM micrographs of the final product of the thermolysis of **1**. **a-b)** overview, **c-f)** higher magnification showing a layered imprint of the copper(II) oxide crystals.

3.3. Compound $[Cu_3(\mu\text{-}Cl)_2(\mu\text{-}C_2vda)(C_2vda)(H_2O)_4]\cdot H_2O$ (**2**)

In an attempt to further explore the reaction system containing the C_2vda ligand, it was decided to replace triethylamine with potassium hydroxide during the synthesis of **1**. This slight alteration in the conditions of the reaction resulted in the formation of a new coordination complex with the chemical formula $[Cu_3(\mu\text{-}Cl)_2(\mu\text{-}C_2vda)(C_2vda)(H_2O)_4]\cdot H_2O$ (**2**). Within this coordination compound the ligand and copper ions form a trinuclear complex.

3.3.1. Characterization of compound **2**

2 crystallises after *ca.* 14 days of slow evaporation from a water/ethanol mixture (1:9 v/v) to give the blue plate-like crystals presented in Fig. 3.22. The crystals were suitably sized for a single crystal X-ray diffraction experiment.

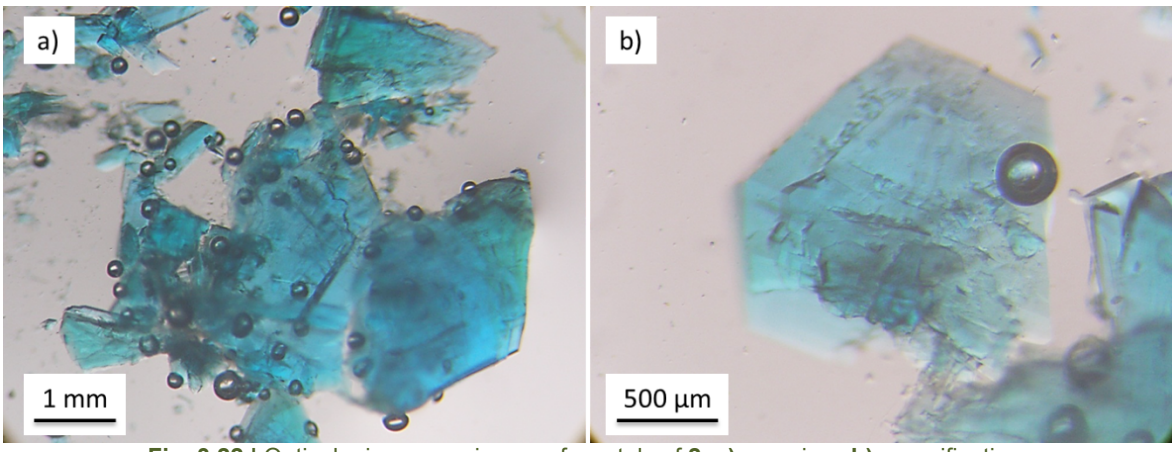

Fig. 3.22 | Optical microscope image of crystals of **2**. **a)** overview; **b)** magnification.

The X-ray data obtained from the experiments confirms that **2** crystallises in the monoclinic space group $P2_1/n$. It forms a trinuclear complex, where all three copper ions adopt three distinct coordination environments. These complexes interact through hydrogen bonds and π-π stacking interactions to give 2D layers that extend in the crystallographic *ab*-plane. These layers further self-assemble *via* hydrogen bonds to give rise to a complicated network structure.

Trinuclear complex

The trinuclear complex presented in Fig. 3.23 is formed by two symmetry equivalent units. The copper ions Cu(1) and Cu(2^I) are connected through a µ-type bridge formed by the two chlorine atoms Cl(1) and Cl(2). The bond lengths are 2.240(1) Å for the Cu(1)-Cl(1) bond, 2.789(1) Å for Cu(1)-Cl(2), 2.811(1) Å for Cu(2)-Cl(1) and 2.242(1) Å for the Cu(2)-Cl(2) bond. The octahedral coordination sphere in the case of the Cu(1) and Cu(2) ions is completed by three O-donors and one N-donor which are provided by the C_2vda ligand molecules.

The coordination environment of the Cu(3) ion is significantly different to that of the other Cu ions. It binds to four water molecules and the two remaining coordination sites are occupied by two O-donors that originate from one of the carboxylate groups of the C_2vda molecule.

The oxygen atom O(5) of the iminodiacetic acid carboxylate functionality bridges between the Cu(1) and Cu(3) copper ions and the corresponding distances are 2.005(3) Å for the O(5)-Cu(1) and 2.728(2) Å for the O(5)-Cu(3) bond. The remaining O-donor of this carboxylate functionality, O(6), is located 2.001(3) Å from the Cu(3) ion.

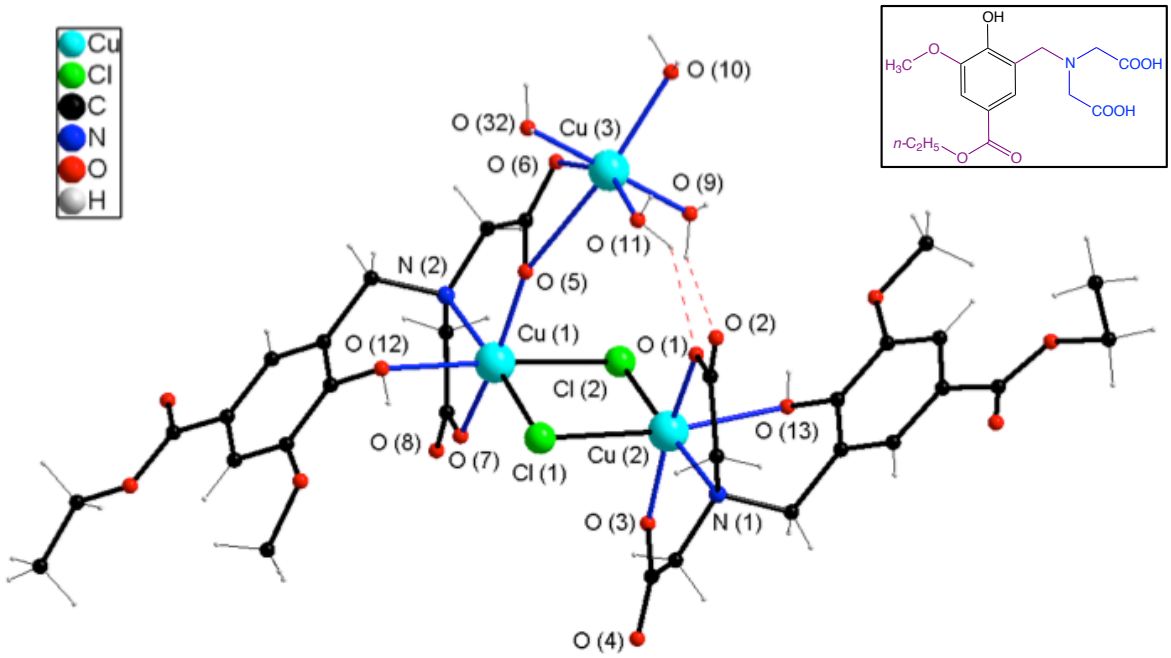

Fig. 3.23 | Trinuclear complex in **2**. Symmetry codes: (I): 0.5-x, -0.5+y, 0.5-z. Inset: the C_2vda ligand molecule.

The formation of the complex is further promoted by two intramolecular hydrogen bonds, which link the oxygen atom O(11) of a coordinating water molecule with the O-donor O(1) and the oxygen atom O(9) of a coordinating water molecule with the non-coordinating oxygen atom O(2). The bond lengths are 2.993(2) Å and 2.909(3) Å, respectively. The oxygen atoms O(1) and O(2) belong to the same carboxylate functionality that coordinates to Cu(2).

The coordination spheres around all three copper ions can be described as distorted octahedrons. The influence of the Jahn-Teller effect is observed for each metal ion. Details of the coordination environments and the coordination bond distances are presented in Fig. 3.24.

The copper ion Cu(1) is located 3.517(1) Å from the Cu(2) and 4.670(1) Å from the Cu(3) ion. The distance between the Cu(2) and Cu(3) ions is 5.397(1) Å. The angle formed by the O(5) donor bridging between the Cu(1) and Cu(3) ions (Cu(1)-O(5)-Cu(3)) is 161.17(11)°.

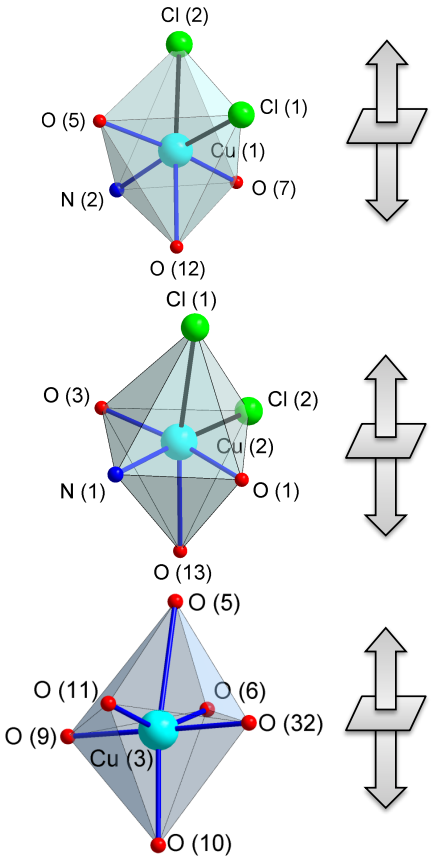

Atom 1	Atom 2	Symmetry code for atom 2	Bond lenght [Å]
Cu(1)	O(7)	x, y, z	1.956(2)
Cu(1)	O(5)	x, y, z	2.005(2)
Cu(1)	N(2)	x, y, z	2.021(3)
Cu(1)	Cl(1)	x, y, z	2.240(1)
Cu(1)	O(12)	x, y, z	2.546(3)
Cu(1)	Cl(2)	x, y, z	2.786(1)

Atom 1	Atom 2	Symmetry code for atom 2	Bond lenght [Å]
Cu(2)	O(1)	x, y, z	1.978(2)
Cu(2)	O(3)	x, y, z	1.981(2)
Cu(2)	N(1)	x, y, z	2.007(3)
Cu(2)	Cl(2)	x, y, z	2.242(1)
Cu(2)	O1(3)	x, y, z	2.561(3)
Cu(2)	Cl(1)	x, y, z	2.811(1)

Atom 1	Atom 2	Symmetry code for atom 2	Bond lenght [Å]
Cu(3)	O(11)	x, y, z	1.944(3)
Cu(3)	O(32)	x, y, z	1.957(3)
Cu(3)	O(9)	x, y, z	1.975(3)
Cu(3)	O(6)	x, y, z	2.001(3)
Cu(3)	O(10)	x, y, z	2.246(2)
Cu(3)	O(5)	x, y, z	2.728(2)

Fig. 3.24 | Coordination environments of the copper(II) ions in **2**. The corresponding bond distances are listed in the tables.

Connectivity

Intermolecular interactions play an important role in **2**. The aromatic rings are involved in weak π-π stacking interactions, which link the trinuclear complexes with their neighbouring symmetry equivalents. This type supramolecular bond connects the complexes resulting in 1D assemblies, which propagate in the direction of the crystallographic *a*-axis (Fig. 3.25). The average distance between the stacking rings is 3.712(5) Å.

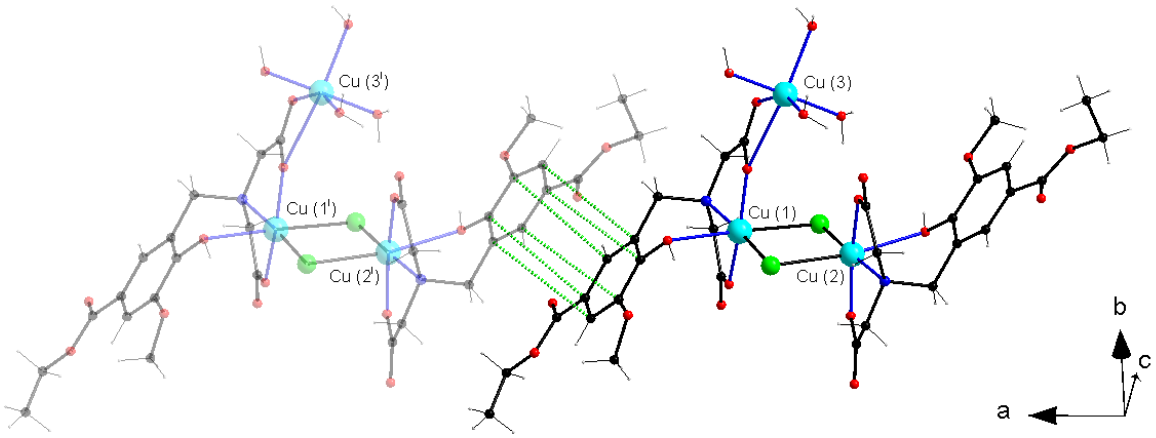

Fig. 3.25 | π-π stacking in **2**. Symmetry codes: (I): 1+x, y, z.

There are eight symmetry independent intermolecular hydrogen bonds within **2**. These bonds link the trinuclear complex to four different symmetry equivalents. The first set of hydrogen bonds is presented in Fig. 3.26 and shows the connectivity of the complex to its symmetry equivalent units in the direction of the crystallographic *c*-axis.

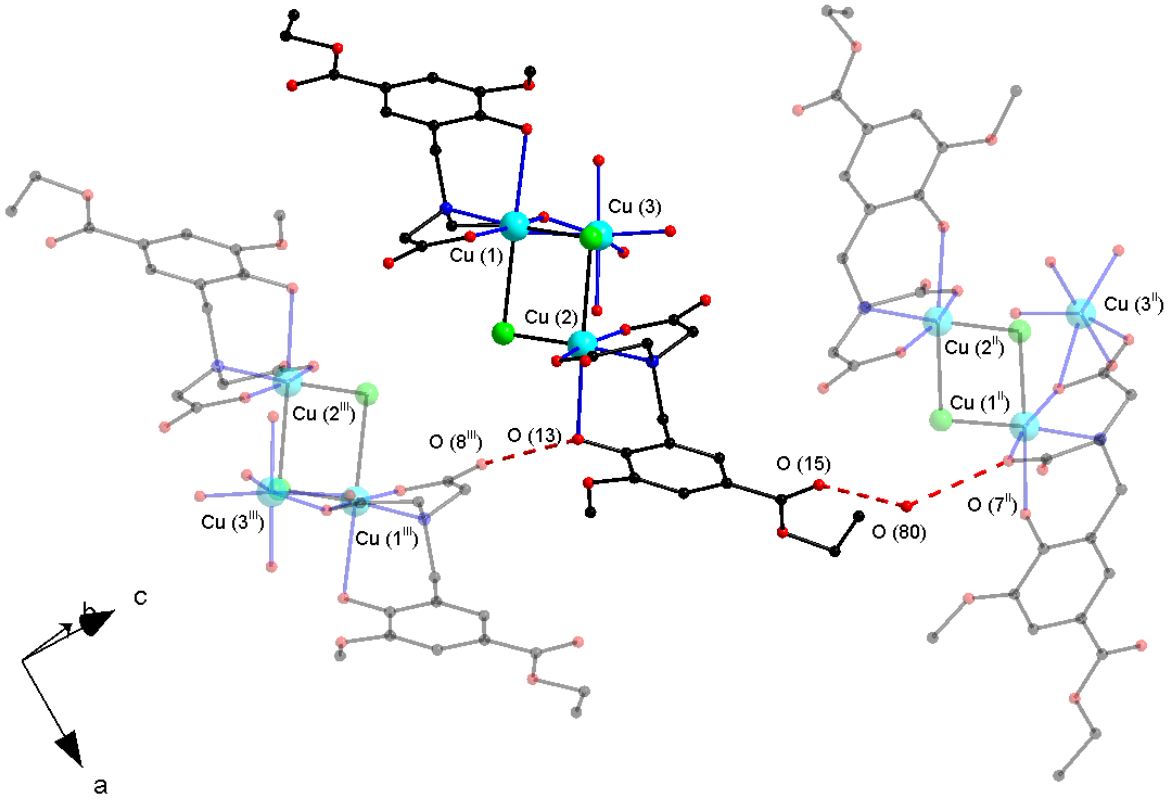

Fig. 3.26 | Hydrogen bonding in **2**. Hydrogen atoms were omitted for clarity. Symmetry codes: (II): x, 1+y, z; (III): -x, 1-y, -z.

A hydrogen bond occurs between the hydroxyl O-donor O(13) and the non-coordinating oxygen atom O(8^{III}), which belongs to a carboxylate functionality. The O-O distance is 2.874(4) Å. Fig. 3.26 presents also a hydrogen bond interaction between the oxygen atom O(15), which is a part of the ester group, and the oxygen atom O(80) of a constitutional water molecule. Both atoms are located 2.859(4) Å from each other. The constitutional solvent molecule binds to the oxygen donor O(^{II}), with originates from a carboxylate group. Both O-atoms reside 2.868(4) Å for each other. The bond angle formed by the constitutional water molecule and connected complexes (O(15)-O(80)-O(7^{II})) is 123.01(13)°.

The second set of hydrogen bonds presented in Fig. 3.27 connects the trinuclear complex to its second symmetry equivalent. The oxygen atom O(32) of a coordinating water molecule binds to the non-coordinating oxygen atom O(8^{IV}), which is a part of a carboxylate functionality. The H-bond is characterised by an O-O distance of 2.773(3) Å.

The O-donor O(8^{IV}) is a part of a neighbouring trinuclear complex. The second ligand molecule of this neighbouring trinuclear complex binds to the copper ion Cu(3) with two additional hydrogen bonds. The oxygen atom O(10) of a coordinating water molecule is linked to the O-donor O(3^{IV}), and the oxygen atom O(11) of a water molecule binds to the non-coordinating oxygen atom O(4^{IV}).

The O-O distances of these bonds are 2.769(3) Å and 2.569(4) Å, respectively. The oxygen atoms O(3^{IV}) and O(4^{IV}) belong to the same iminodiacetic acid carboxylate group.

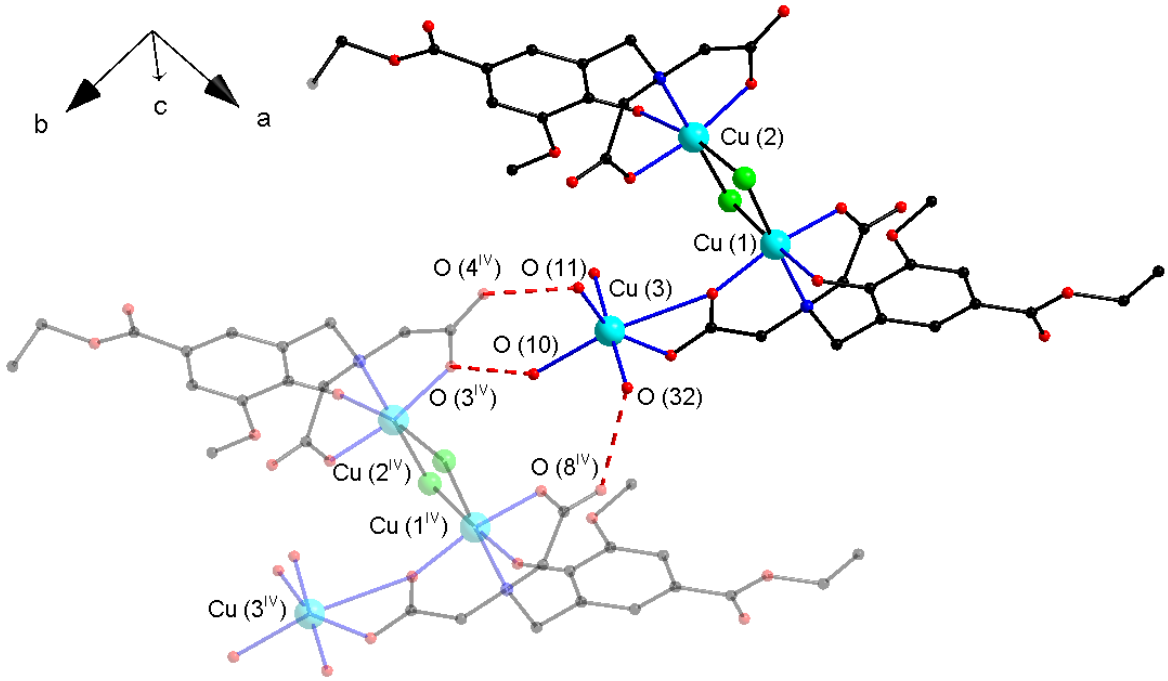

Fig. 3.27 | Hydrogen bonding in **2**. Hydrogen atoms were omitted for clarity. Symmetry codes: (IV): 0.5-x, 0.5+y, 0.5-z.

The oxygen atom O(9) of a coordinating water molecule is involved in one more hydrogen bond. In an interaction presented in Fig. 3.28 it H-bonds to a symmetry generated O-donor O(6^{V}) of the carboxylate group; the H-bond is characterised by an O-O distance of 2.783(4) Å.

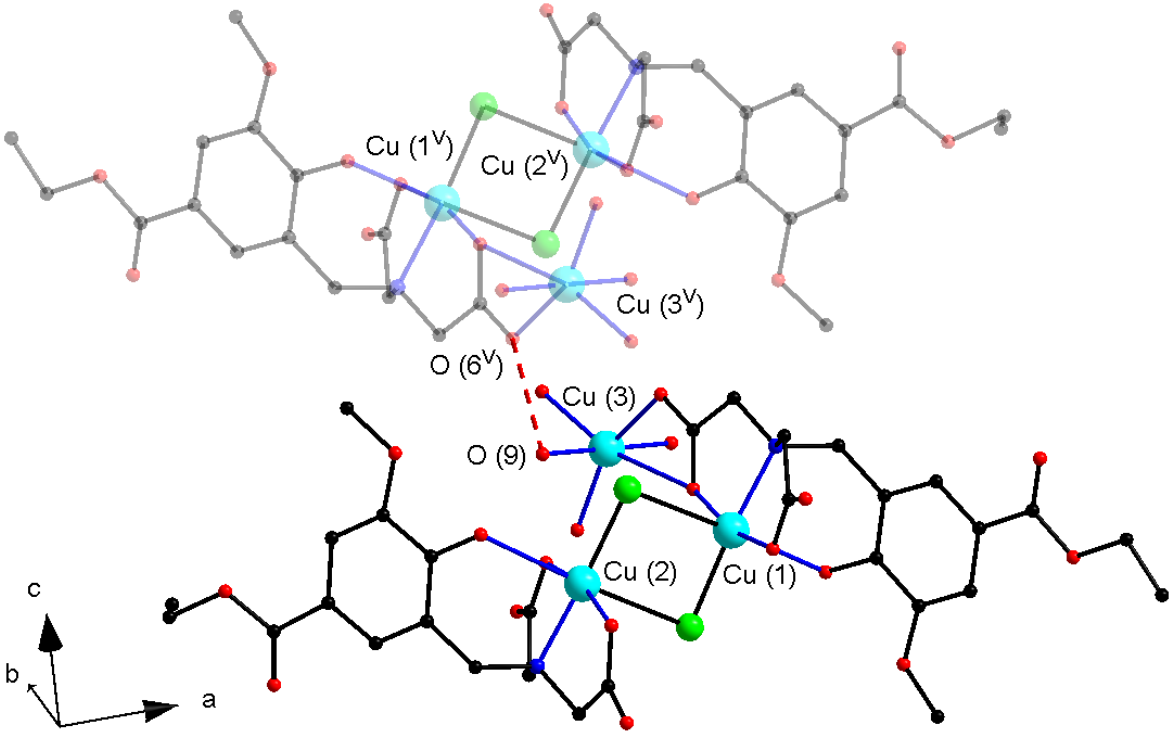

Fig. 3.28 | Hydrogen bonding in **2**. Hydrogen atoms were omitted for clarity. Symmetry codes: (V): 1-x, 1-y, 1-z.

Packing

The π-π stacking interactions as well as the hydrogen bonds are responsible for the formation of a 2D layer in the crystallographic *ab*-plane. Fig. 3.29 shows these forces and indicates that within the layer it is possible to observe a clear separation between the hydrophilic and hydrophobic parts. The hydrophilic area is *ca.* 7.1 Å thick in [100] and contains mainly metal ions, chlorine anions and carboxylic acid functionalities. The hydrophobic area contains the ligand molecules and its average thickness is 6.4 Å in [100].

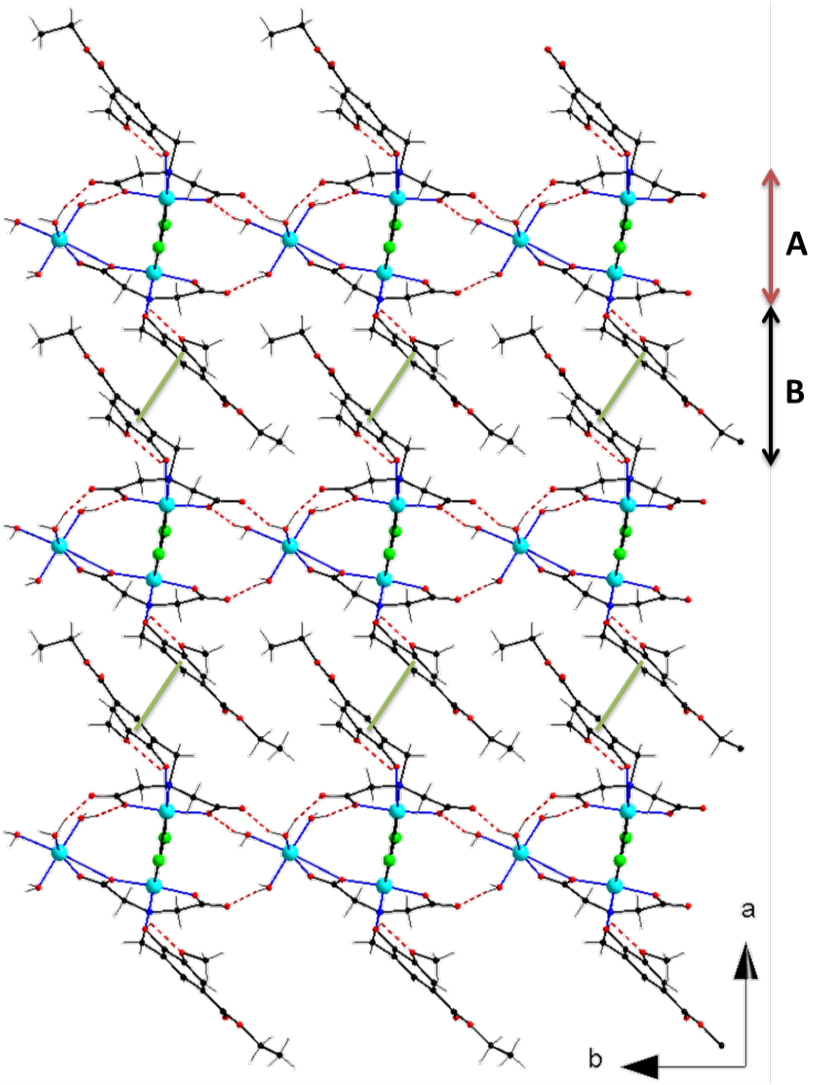

Fig. 3.29 | Trinuclear complexes interact via the π-π stacking and hydrogen bonds to form a layer in the crystallographic *ab*-plane. A – hydrophilic part; B- hydrophobic part. Constitutional solvent molecules were omitted for clarity.

Further assembly of the layers presented above is enabled by the hydrogen bonds, which occur almost parallel to the crystallographic *c*-axis. Fig. 3.30 shows the packing diagrams viewed along the *a*- and *b*-axis. An average separation distance between the layers is 3.7 Å.

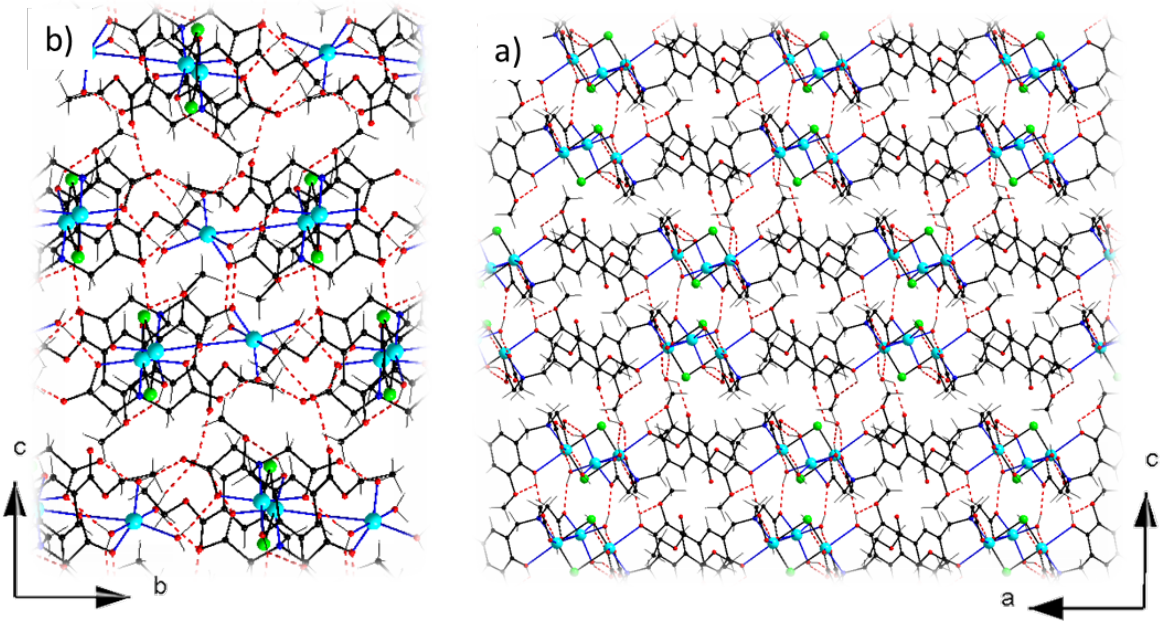

Fig. 3.30 | Packing structure of **2** viewed along the crystallographic *a*-axis (a) and *b*-axis (b).

Although the layers that form in the crystallographic *ab*-plane appear to display a separation between the hydrophilic and hydrophobic areas, the 2_1 screw axis, that is characteristic of the $P2_1/n$ space group, rotates each consecutive layer by 180° in the crystallographic *ab*-plane. As a result of these symmetry operations, a separation between the areas of different amphiphilicity is not observed in the complete packing structure of **2** (Fig. 3.31).

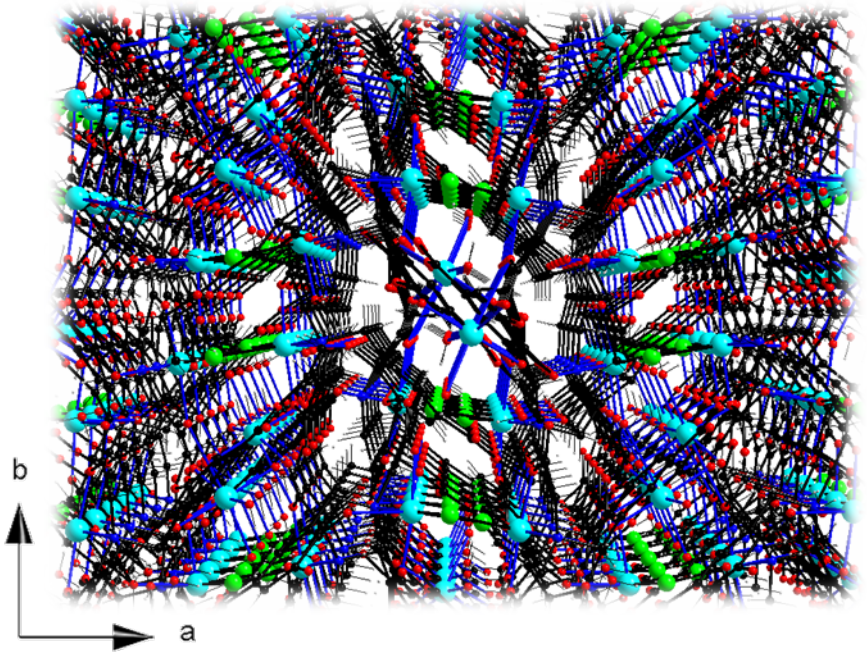

Fig. 3.31 | Perspective view on the packing of **2** along the crystallographic *c*-axis.

Refinement details

The refinement parameters and crystal data for the crystal structure of **2** are summarised in Tab. 3.4.

Tab. 3.4 | Refinement details for compound **2**

Identification code	**2**
Empirical formula	$C_{30}H_{44}Cl_2Cu_3N_2O_{21}$
Formula weight	1030.22 g/mol
Temperature	150(2) K
Wavelength	0.71073 Å
Crystal system	Monoclinic
Space group	$P2_1/n$
Unit cell dimensions	a = 14.194(3) Å α = 90°. b = 10.673(2) Å β = 91.00(3)°. c = 25.614(5) Å γ = 90°.
Volume	3879.6(13) $Å^3$
Z	4
Density (calculated)	1.764 Mg/m^3
Absorption coefficient	1.855 mm^{-1}
F(000)	2108
Crystal size	0.5 x 0.5 x 0.2 mm^3
Theta range for data collection	1.59 to 25.00°.
Index ranges	-16<=h<=15, -12<=k<=12, -29<=l<=30
Reflections collected	28815
Independent reflections	6715 [R(int) = 0.0228]
Completeness to theta = 25.00°	98.3 %
Refinement method	Full-matrix least-squares on F^2
Data / restraints / parameters	6715 / 15 / 530
Goodness-of-fit on F^2	1.069
Final R indices [I>2sigma(I)]	R1 = 0.0383, wR2 = 0.1282
R indices (all data)	R1 = 0.0475, wR2 = 0.1690
Largest diff. peak and hole	1.497 and -1.230 $e.Å^{-3}$

3.3.2. Additional characterization of **2**

In order to confirm that the solid-state structure of a bulk sample of **2** corresponds to the model based on the single crystal X-ray diffraction experiment, P-XRD was used. The pattern recorded for the bulk material was compared with a pattern simulated for the single crystal X-ray diffraction data. As presented in Fig. 3.32, there is a good correlation between both patterns, which confirms that the refined model of the solid-state structure of **2** is accurate.

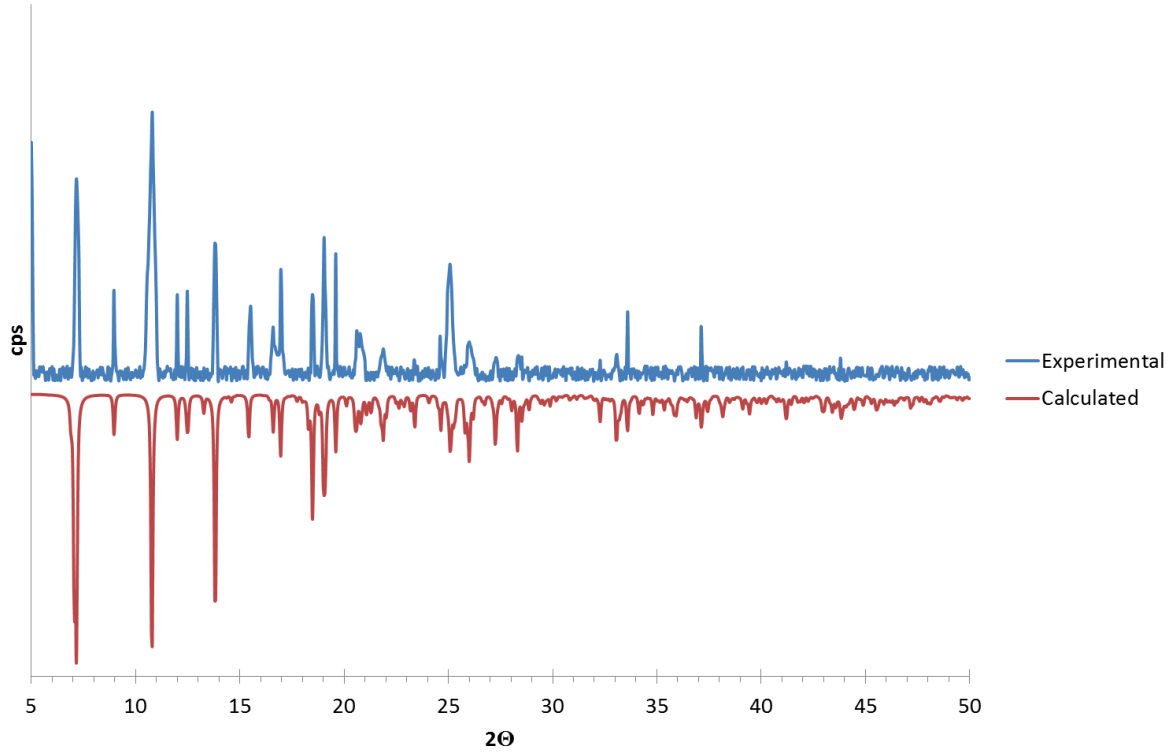

Fig. 3.32 | Comparison between the experimental P-XRD pattern obtained for the crystals of **2** (blue) and a calculated pattern based on the single crystal X-ray data of **2** (red).

3.3.3. Thermogravimetric analysis **2**

The thermogravimetric analysis of **2** was performed in air in the temperature range between 30 and 900 °C. The heating rate was set to 0.5 K/min. The results presented in Fig. 3.33 show that the compound starts to decompose at *ca.* 90 °C. At this temperature the dehydration process occurs, resulting in the loss of one constitutional and four coordinating water molecules of the trinuclear complex. The completely dehydrated product forms at 115 °C (*experimental weight loss*: 6.6%, *theoretical*: 7.0%). After a *plateau* on the TGA curve, the oxidation of the organic ligand starts at 135 °C. The final product of the thermal degradation is copper(II) oxide, which forms as a black powder at 415 °C (*experimental weight loss*: 77.8%, *theoretical*: 76.8%). This temperature is about 100 °C higher than the temperature observed for compound **1**. The results suggest that the presence of chloride ions elevates the temperature of the CuO formation.

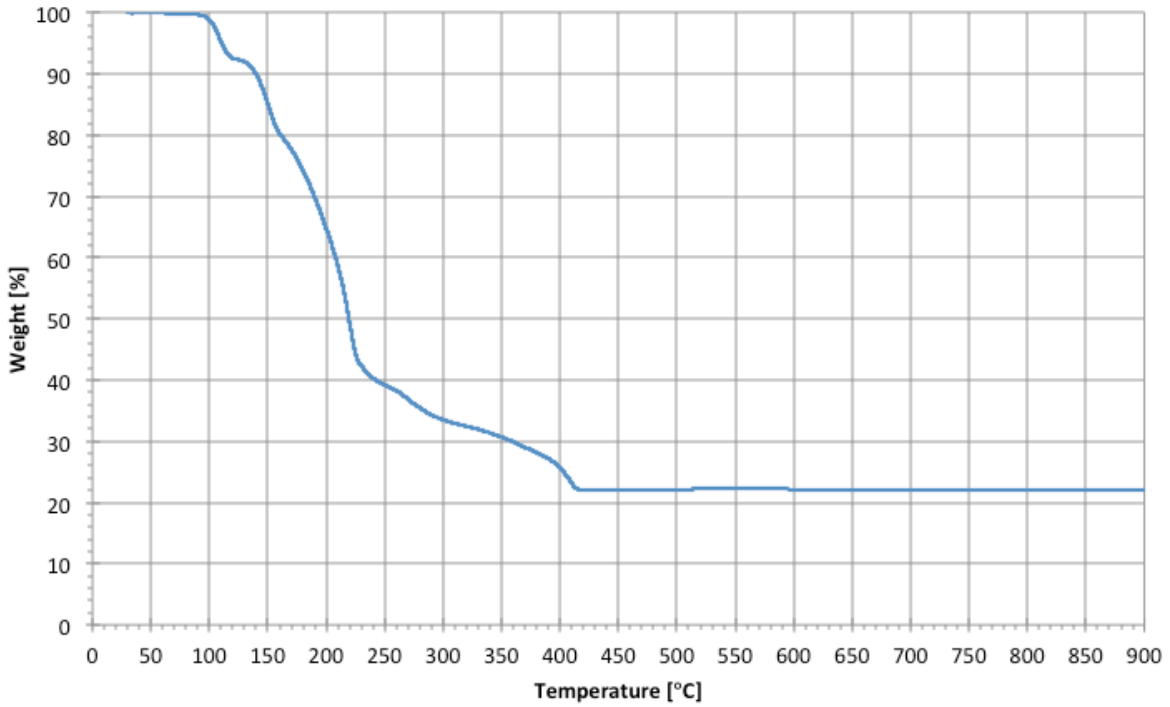

Fig. 3.33 | TGA analysis of compound **2**.

The identity of the residues was confirmed by P-XRD analysis. The experimental pattern was compared with a CuO reference pattern obtained from a database. The results presented in Fig. 3.34 show a correlation between both patterns thus proving, as expected, that the residues are composed of copper(II) oxide.

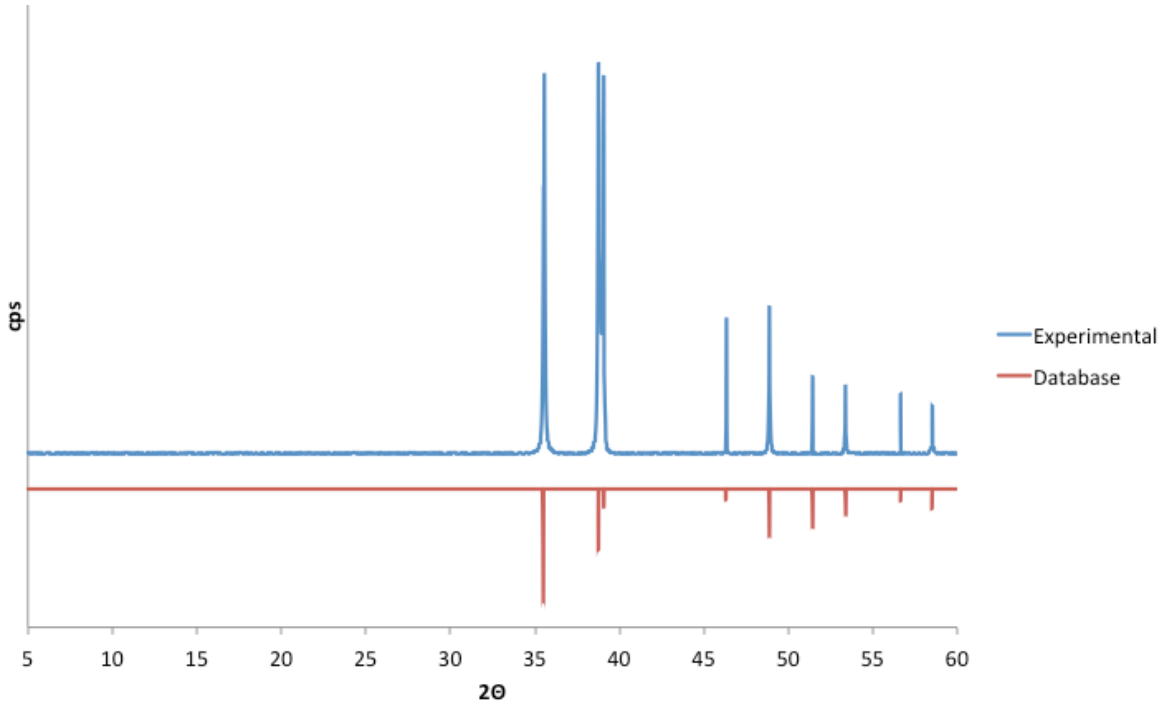

Fig. 3.34 | P-XRD pattern obtained for the residues remaining after the thermolysis of **2** (blue) and a reference pattern for copper(II) oxide (red).[178]

The morphology of the residues was studied using SEM. An overview picture (Fig. 3.35a,b) shows that the shape of the residues does not resemble the shape of the crystals the precursor coordination compound. The higher magnification images (Fig. 3.35c,d) reveal that

the solid consists of small, almost spherical crystals, which aggregate. Their average diameter is *ca.* 1 µm. On the nanoscale each small crystal displays a layered hierarchical organisation (Fig. 3.35e-f). This layered imprint may be a sign of the templating effect that the initial pre-arrangement of the starting materials has on the residual ceramic material.

The SEM imaging enabled us to perform EDX analysis on the CuO residues. Fig. 3.36 presents the EDX spectrum obtained for the sample. It confirms the presence of copper and oxygen and excludes the presence of chlorine that was observed within the coordination compound **2**. It also excludes the presence of potassium, which was used during the synthesis of **2** (KOH). The analysis was performed on a carbon-coated sample placed on a silicon surface. This explains the occurrence of signal arising form C and Si in the EDX spectrum. The quantitative analysis of the signals showed 17.3% composition for oxygen (*theoretically*: 20.1%) and 82.7% for copper (*theoretically*: 79.9%).

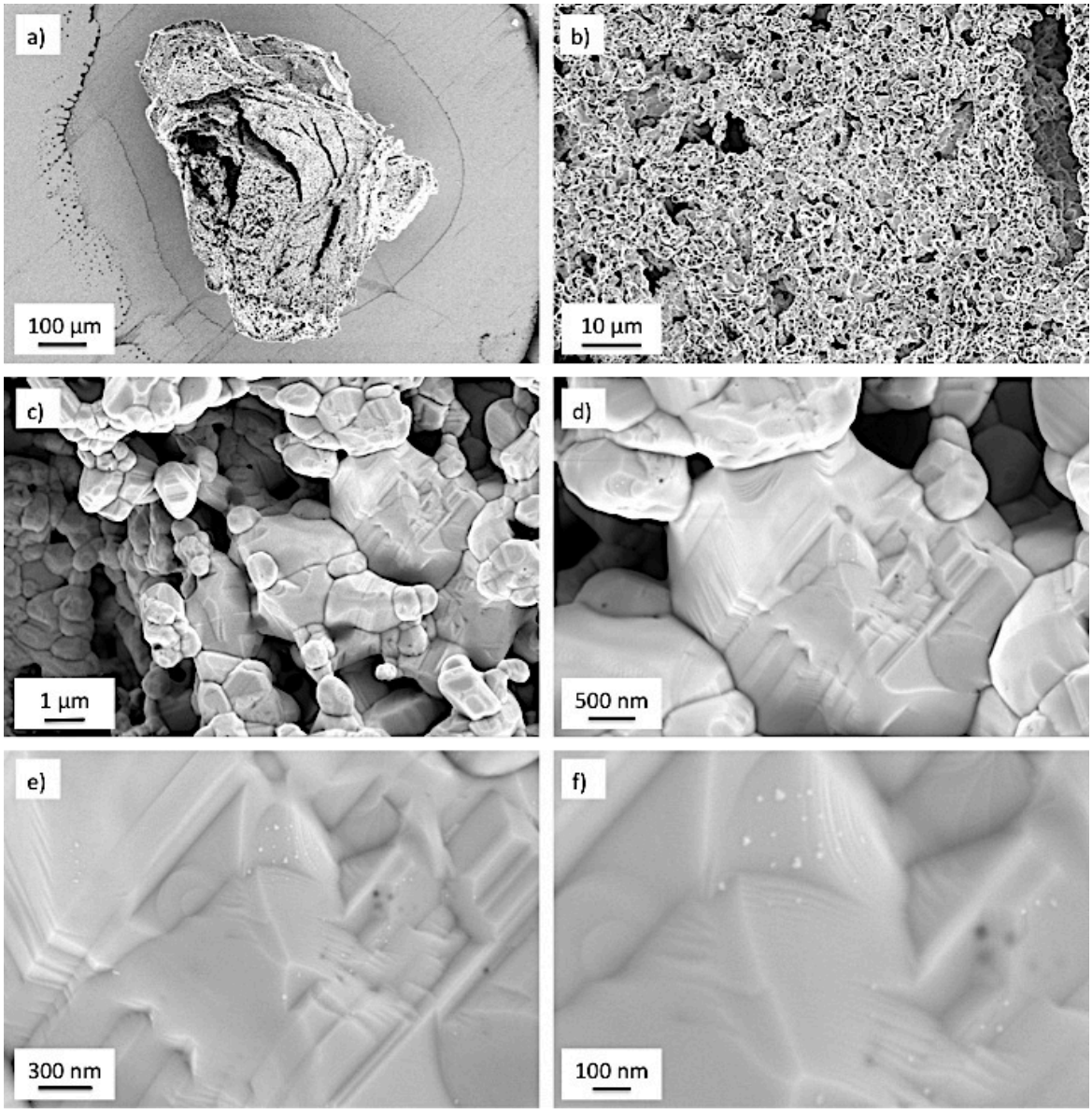

Fig. 3.35 | SEM micrographs of the residual copper(II) oxide remaining after the thermolysis of **2**. **a,b)** overview; **c-d)** magnification showing crystalline particles; **e-f)** higher magnification reveals the layered morphology of the nanoparticles.

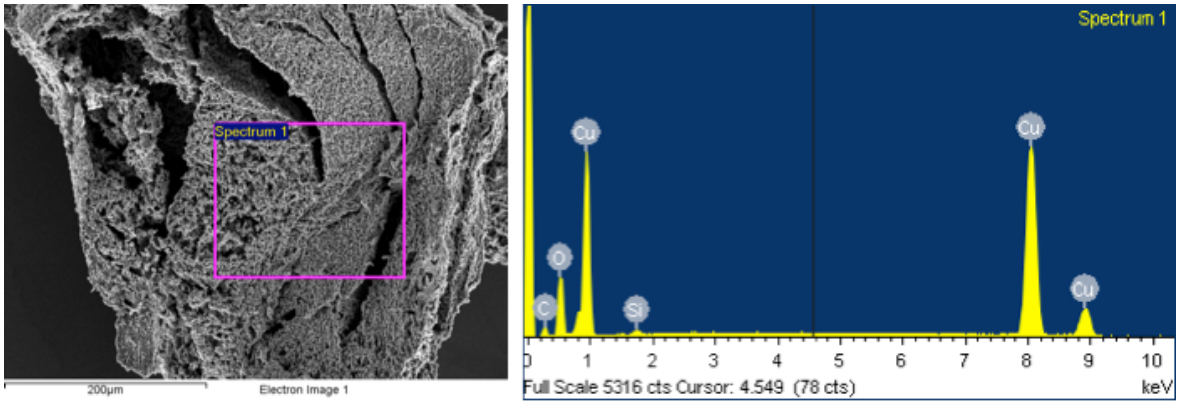

Fig. 3.36 | EDX analysis performed on the residual CuO particles remaining after the thermolysis of **2**. The carbon signals correspond to the carbon coating and the silicon signal is associated with the silicon surface.

3.4. Compound [Cu(C$_6$vda)(H$_2$O)$_2$] (**3**)

In the next step of the research it was decided to utilise the n-hexyl chain-containing C$_6$vda ligand in a reaction with copper(II) chloride. It was anticipated that the introduction of a longer hydrophobic chain would influence the packing structure of the resulting coordination compound due to increased dispersion forces that may influence intermiolecular interactions.

3.4.1. Characterization of compound **3**

Compound **3** with the chemical formula [Cu(C$_6$vda)(H$_2$O)$_2$] crystallises in a monoclinic *C*2/c space group when the C$_6$vda ligand is reacted with a stoichiometric amount of copper(II) chloride in methanol. Block-shaped blue crystals were obtained after *ca.* 5 days of slow evaporation of the solvent (Fig. 3.37).

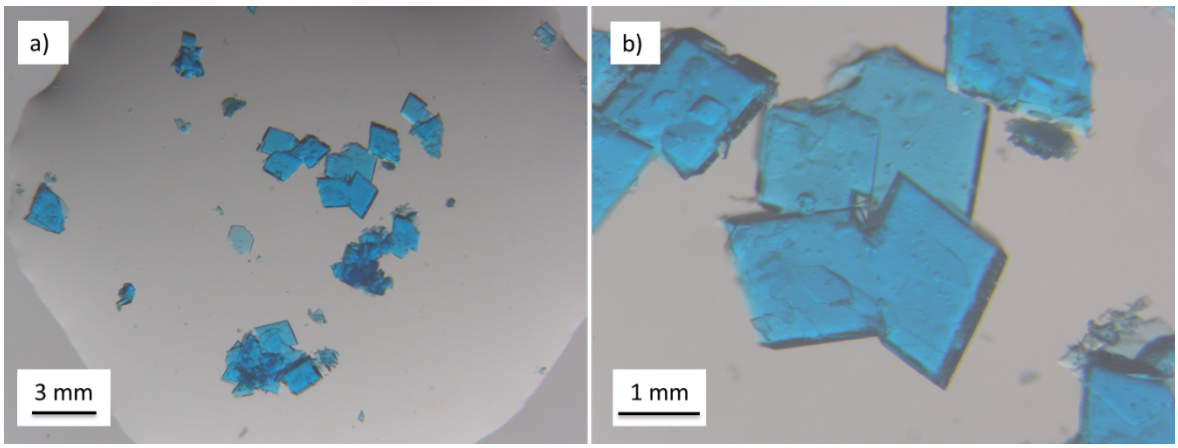

Fig. 3.37 | Optical microscope images of **2**. **a)** overview; **b)** magnification showing single crystals.

3 forms mononuclear complexes (Fig. 3.38) and the hydrogen bond interactions link the neighbouring complexes into 1D chains, which extend parallel to the crystallographic *b*-axis. Further assembly of these chains is realised *via* dispersion forces and hydrophobic interactions and leads to the formation of a layered, sandwich-like material that packs in the direction of the *a*-axis.

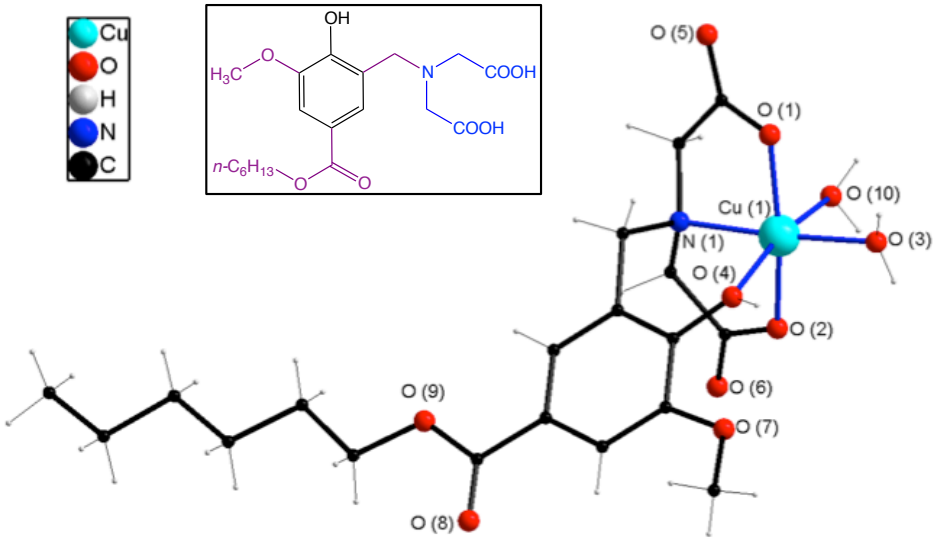

Fig. 3.38 | The mononuclear complex in **3**. Symmetry code: (I): 0.5-x, 0.5-y, 1-z. Inset: The C$_6$vda ligand molecule.

Asymmetric unit

The mononuclear complex in **3** consists of one metal ion, one ligand molecule and two coordinating water molecules. The ligand provides one N-donor and three O-donors. Two of the O-donors, O(1) and O(2), belong to two different carboxylate groups of the same iminodiacetic acid moiety. The third O-donor, O(4), originates from the hydroxyl group located on the aromatic ring. It remains protonated and binds to the metal ion with the distance of 2.329(2) Å. The coordination environment is completed by two O-donors of the coordinating water molecules, O(3) and O(10), which occupy the *cis* position within the octahedron.

Within **3** the coordination sphere of the metal ion adopts a distorted octahedral geometry (presented in Fig. 3.39). The equatorial plane is formed by the iminodiacetic acid O-donors O(1) and O(2) along with the N-donor N(1) and the O-donor O(3) of a coordinating water molecule. The apexes are occupied by the hydroxyl O-donor O(4) and the O-donor O(10) of a water molecule.

The octahedron is clearly elongated along the apexes in agreement with the Jahn-Teller effect, which is characteristic for Cu(II) systems.

The oxidation state of the Cu(1) ion was confirmed to be +II by the bond valence sum calculations, which gave 2.13 as the result.

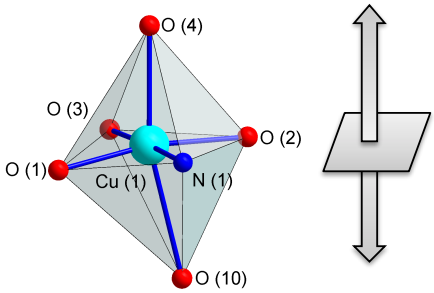

Atom 1	Atom 2	Symmetry code for atom 2	Bond lenght [Å]
Cu1	O3	x, y, z	1.937(2)
Cu1	O1	x, y, z	1.954(9)
Cu1	O2	x, y, z	1.955(6)
Cu1	N1	x, y, z	2.001(2)
Cu1	O4	x, y, z	2.329(2)
Cu1	O10	x, y, z	2.698(4)

Fig. 3.39 | Coordination environment in **3**.The table presents corresponding bond distances.

Connectivity

The oxygen atom O(3) of a coordinating water molecule is involved in the formation of a complementary hydrogen bond that links it to a symmetry generated O-donor O(2^{I}), which is a part of the iminodiacetic acid functionality. This bond, presented in Fig. 3.40, is 2.633(3) Å long and contributes to the formation of a hydrogen-bound dimer, which consists of two metal ions, two ligand molecules and four coordinating water molecules.

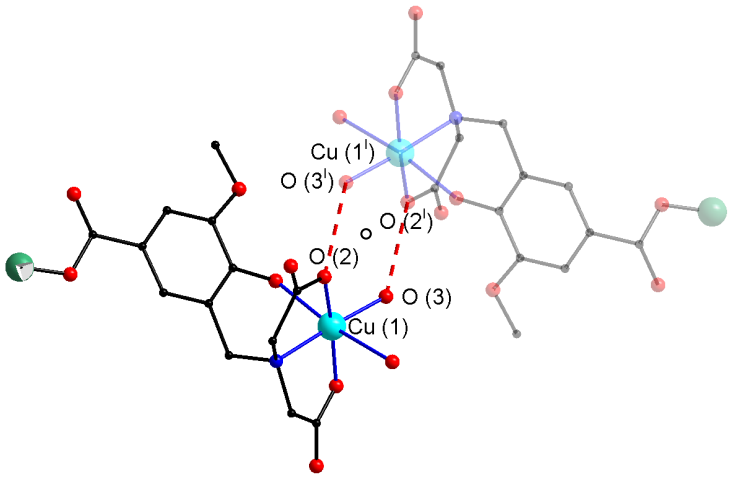

Fig. 3.40 | Complementary hydrogen bonding in **3**. The artificial green atoms correspond to the *n*-hexyl chains. Symmetry codes: (I): 0.5-x, 0.5-y, 1-z.

Another hydrogen bond, presented in Fig. 3.41, occurs between the O-donor O(4) of the aromatic hydroxyl group and the symmetry generated oxygen atom O(5^{II}) that originates from an iminodiacetic acid carboxylate functionality. The bond length is 2.480(3) Å. This hydrogen bond interaction is responsible for the formation of a 1D H-bound chain motif that extends in the crystallographic *c*-direction.

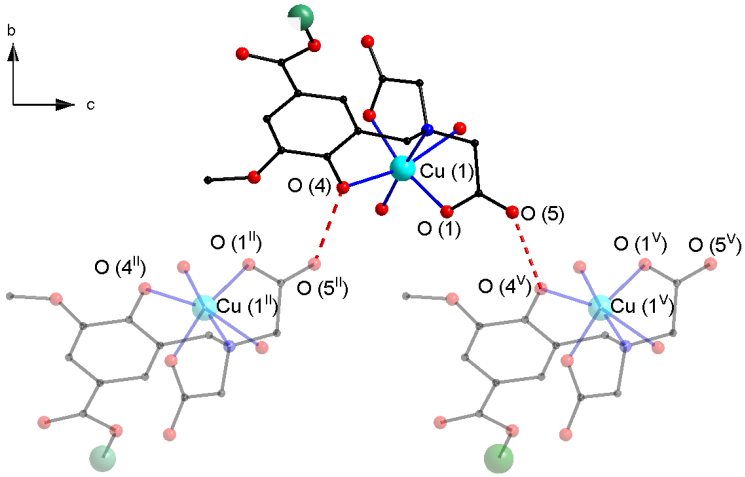

Fig. 3.41 | Hydrogen bonding in **3**. The artificial green atoms correspond to the *n*-hexyl chains. Symmetry codes: (II): x, -y, -0.5+z; (V): x, -y, 0.5+z.

The oxygen atom O(10) of the second coordinating water molecule is involved in two hydrogen bond interactions. The first one links it to the carboxylate O-donor O(1^{III}) of a neighbouring symmetry equivalent unit. This interaction is presented in Fig. 3.42 and the corresponding bond distance is 2.985(3) Å.

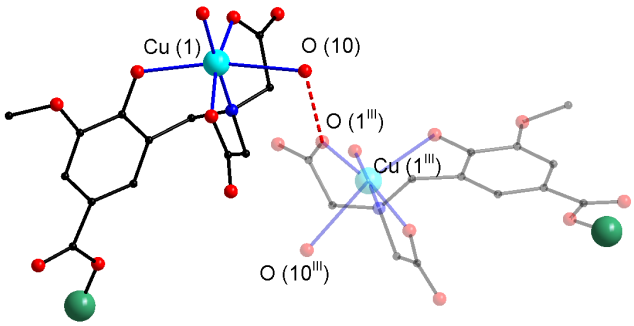

Fig. 3.42 | Hydrogen bonding in **3**. The *n*-hexyl chains have been replaced with the artificial green atoms for clarity. Symmetry codes: (III): 0.5-x, 0.5+y, 1.5-z.

The second hydrogen bond interaction that involves the O-donor O(10) of a coordinating water molecule connects it to the non-coordinating oxygen atom O(6^{IV}), which belongs to a symmetry generated iminodiacetic acid carboxylate functional group (see Fig. 3.43). The bond distance is 2.768(3) Å.

As presented in Fig. 3.43, the hydrogen bond connectivity that involves the O-donor O(10) contributes to the formation of a H-bound 1D chain motif and to the extension of this motif in the direction of the crystallographic *b*-axis. The angle formed by the hydrogen bonds O(6^{VI})-O(10)-O(1^{III}) is 138.35(9)°

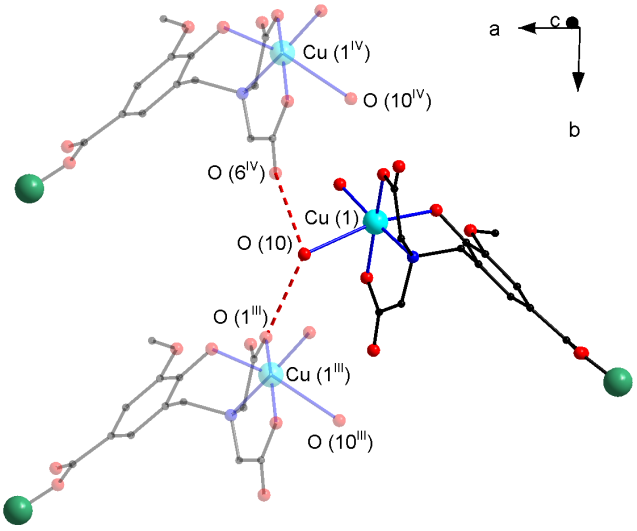

Fig. 3.43 | Hydrogen bonding in **3**. The aliphatic *n*-hexyl chains have been substituted with the artificial green atoms for clarity. Symmetry codes: (III): 0.5-x, 0.5+y, 1.5-z; (IV): 0.5-x, -0.5+y, 1.5-z.

The hydrogen bond interactions described above link the mononuclear complexes with their symmetry equivalents in the directions of the crystallographic *b*- and *c*-axes. This leads to the formation of 2D sheets that extend in the crystallographic *bc*-plane (see Fig. 3.44).

The thickness of each 2D sheet is *ca.* 2.6 nm. Its core is hydrophilic; it accommodates the metal ions, the coordinating water molecules and the organic O-donors. The average thickness of the core is 8 Å. The outer parts of the sheet contain the *n*-hexyl chains, which are aligned in a 'zigzag' motif due to the symmetry operations characteristic for the *C*2/c space group (namely glide planes and 2_1 screw axes).

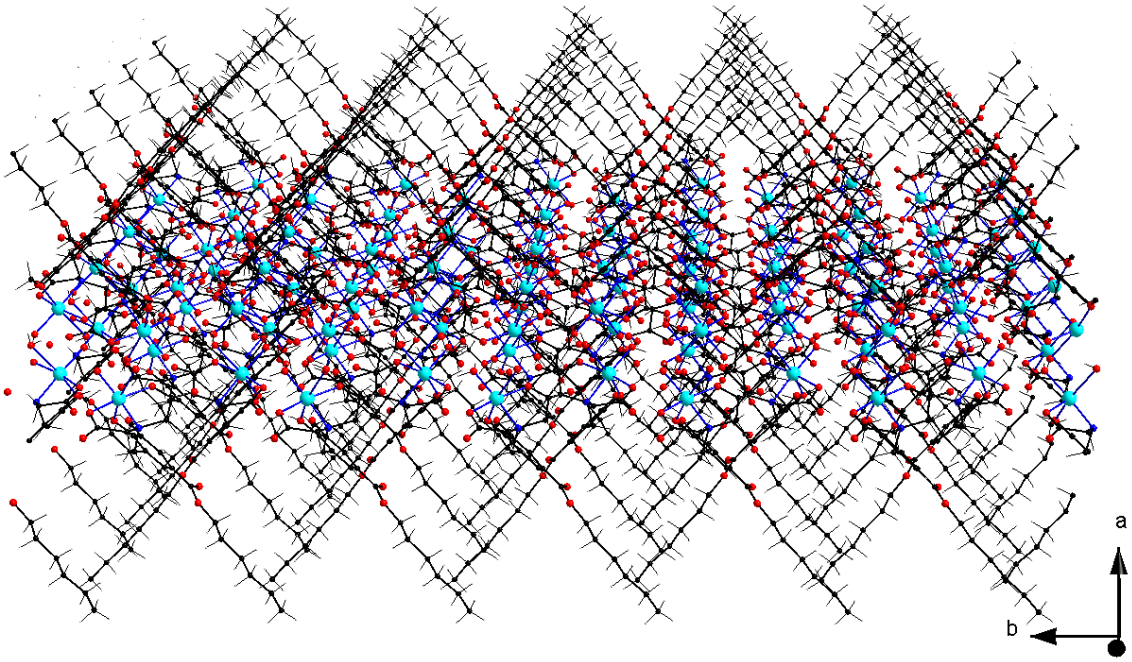

Fig. 3.44 | Perspective view along the crystallographic *c*-axis on a fragment of a single 2D sheet in **3**.

Packing

The 2D sheets described above self-assemble in the direction of the crystallographic *a*-axis *via* van der Waals forces and hydrophobic interactions that occur between the hydrophobic *n*-hexyl chains of symmetry equivalent sheets.

The plan view in the *ac*- and *ab*-planes (Fig. 3.45) shows that the packing structure of **3** contains separated hydrophilic and hydrophobic areas. The hydrophilic areas are constituted by the hydrophilic cores of the 2D sheets. The hydrophobic sections of the structure are *ca.* 12 Å thick and accommodate the remaining hydrophobic parts of the organic ligand molecules.

The lattice separation distance in **3** (calculated as a sum of the thickness of the hydrophobic and hydrophilic areas) is *ca.* 20 Å. This value is *ca.* 6 Å smaller than the thickness of a single 2D sheet and it indicates that the *n*-hexyl chains interdigitate with their symmetry equivalents.

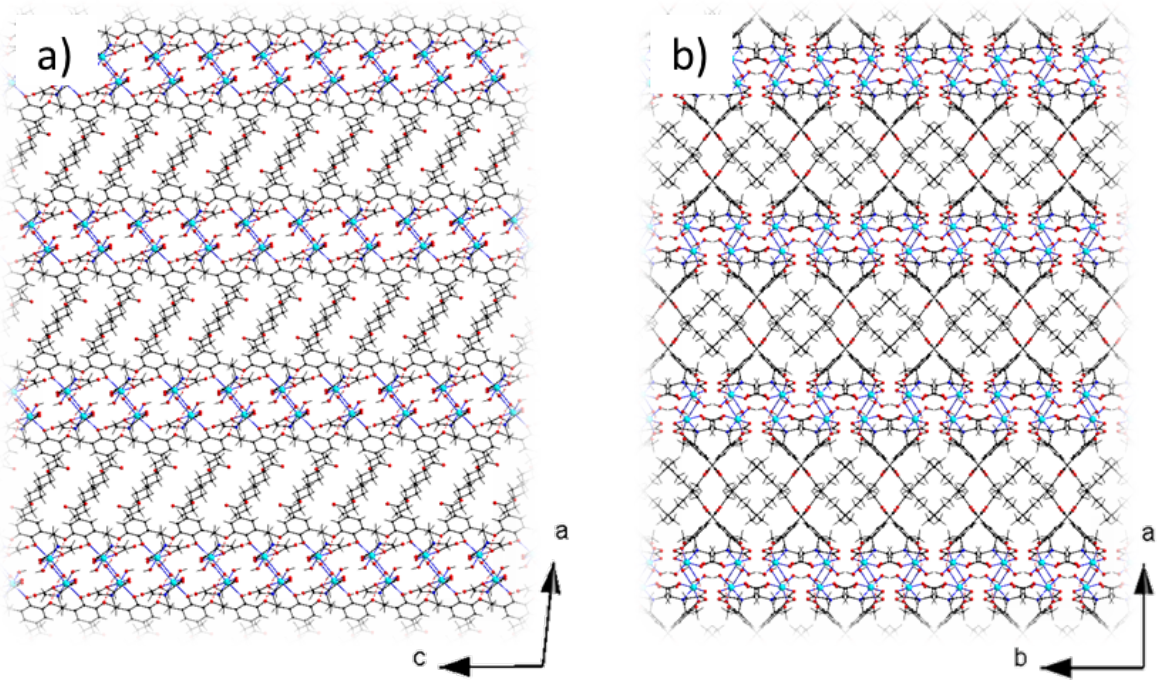

Fig. 3.45 | Packing diagrams for compound **3**. **a)** view along the crystallographic *b*-axis; **b)** view along the crystallographic *c*-axis.

The perspective view presented in Fig. 3.46 shows the assembly of the sheets into a layered, lamellar material.

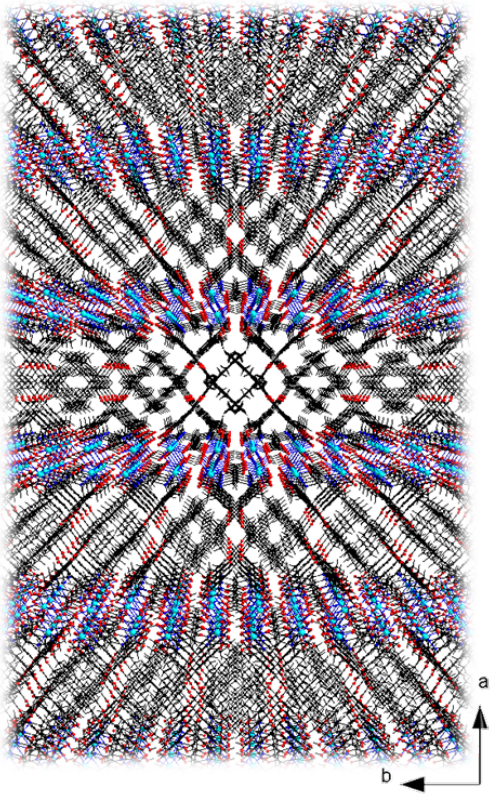

Fig. 3.46 | Perspective view on the packing structure of **3** shows the layered arrangement in the *bc*-plane.

The packing structure of **3** is different to the previously described compounds **1** and **2**. The layered lamellar packing motif forms due to the interactions between the hydrophobic chains. One may speculate that the ethyl moiety present in **1** and **2** is too short to enable this type of supramolecular structure.

Refinement details

Tab. 3.5 presents the refinement parameters for the crystal structure of **3**.

Tab. 3.5 | Refinement details for compound **3**.

Identification code	**3**
Empirical formula	$C_{19}H_{29}CuNO_{10}$
Formula weight	989.96 g/mol
Temperature	150(2) K
Wavelength	0.71073 Å
Crystal system	Monoclinic
Space group	*C*2/c
Unit cell dimensions	a = 37.350(8) Å α = 90°. b = 9.850(2) Å β = 96.50(3)°. c = 11.980(2) Å γ = 90°.
Volume	4379.0(15) $Å^3$
Z	2
Density (calculated)	2.210 Mg/m^3
Absorption coefficient	5.749 mm^{-1}
F(000)	2800
Crystal size	0.5 x 0.5 x 0.3 mm^3
Theta range for data collection	2.14 to 24.99°.
Index ranges	-44<=h<=44, -11<=k<=11, -14<=l<=11
Reflections collected	17018
Independent reflections	3840 [R(int) = 0.0338]
Completeness to theta = 24.99°	99.3 %
Refinement method	Full-matrix least-squares on F^2
Data / restraints / parameters	3840 / 7 / 299
Goodness-of-fit on F^2	1.065
Final R indices [I>2sigma(I)]	R1 = 0.0386, wR2 = 0.0894
R indices (all data)	R1 = 0.0398, wR2 = 0.0901
Largest diff. peak and hole	0.342 and -0.331 $e.Å^{-3}$

Additional characterization

P-XRD pattern was obtained for the bulk crystals of **3** and it was compared with a simulated pattern based on the refined single crystal structure. The results (presented in Fig. 3.47) demonstrate that bulk material of **3** is phase pure and confirm that the provided structural model is correct.

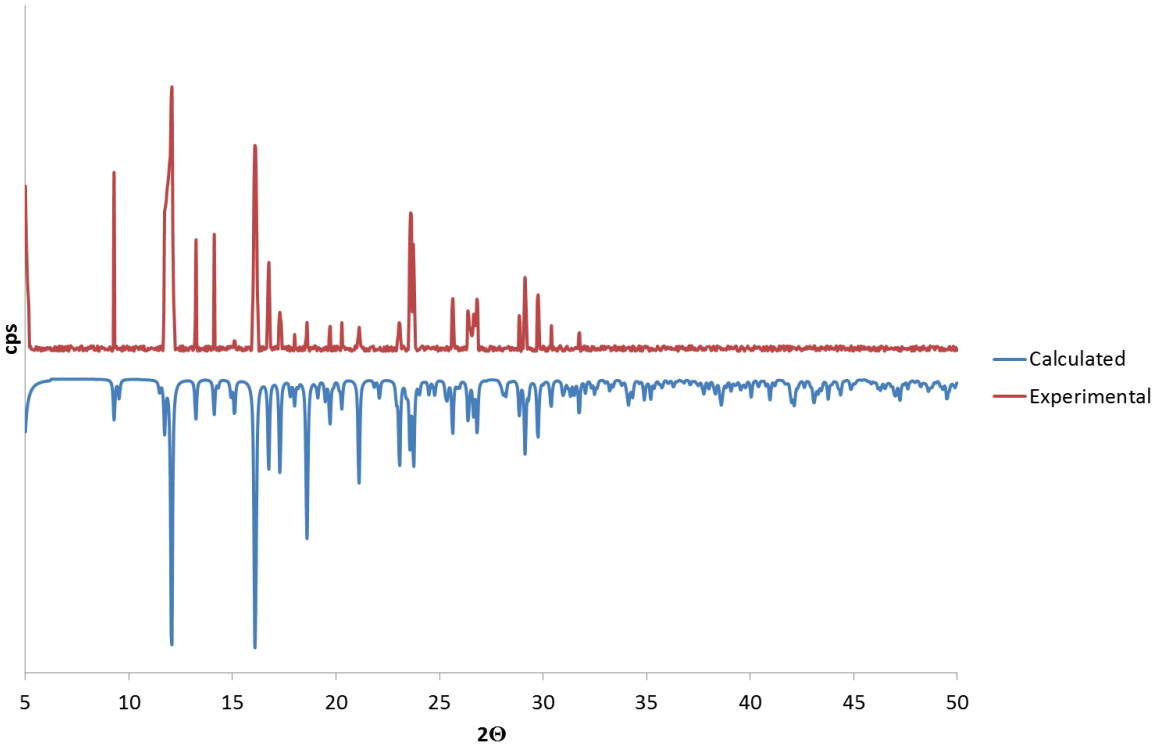

Fig. 3.47 | P-XRD pattern obtained for crystals of **3** (red) and a pattern simulated for the refined single crystal structure (blue).

3.4.2. Thermogravimetric analysis of **3**

The crystals of **3** were slowly (0.65 K/min) heated in an air atmosphere in the temperature range between 30 and 900°C. The degradation pathway is presented in Fig. 3.48. During the heating process the compound loses the two coordinating water molecules (*experimental weight loss*: 6.9%, *theoretical*: 7.3%). This dehydration is observed between 70 °C and 80 °C and results in a compound that was stable up to 180 °C. Above this temperature a rapid oxidation of the organic ligand occurred. The final product of the thermolysis is copper(II) oxide, which forms at *ca.* 300 °C (*experimental weight loss*: 83.5%, *theoretical*: 83.9%).

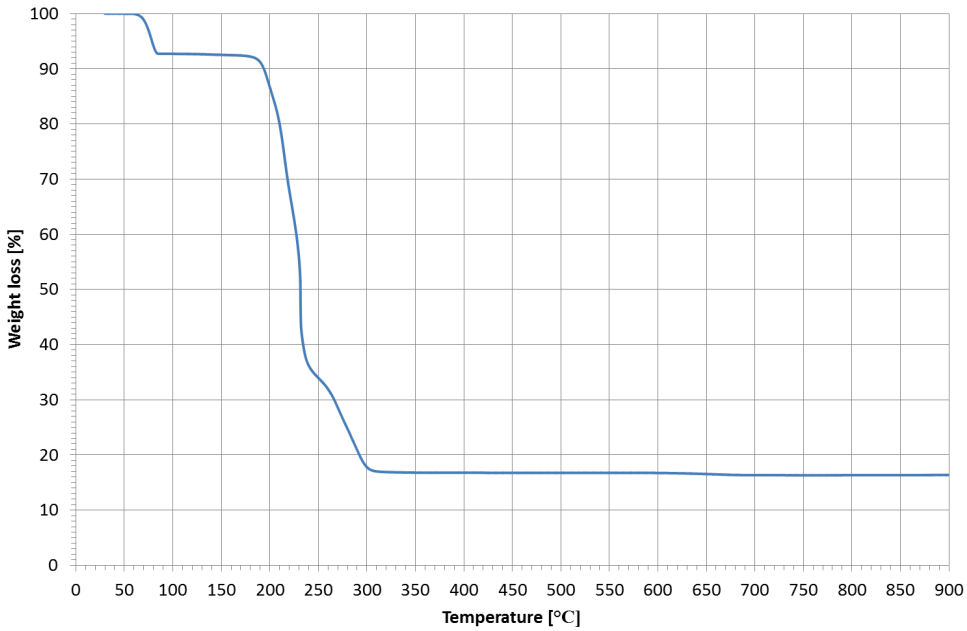

Fig. 3.48 | TGA analysis of compound **3**.

The residual black powder was collected and analysed using P-XRD in order to confirm its chemical identity and to determine the phase purity. The obtained data were compared with a reference pattern for copper(II) oxide. Fig. 3.49 shows that there is an agreement between both patterns thus confirming the composition and purity of the residues.

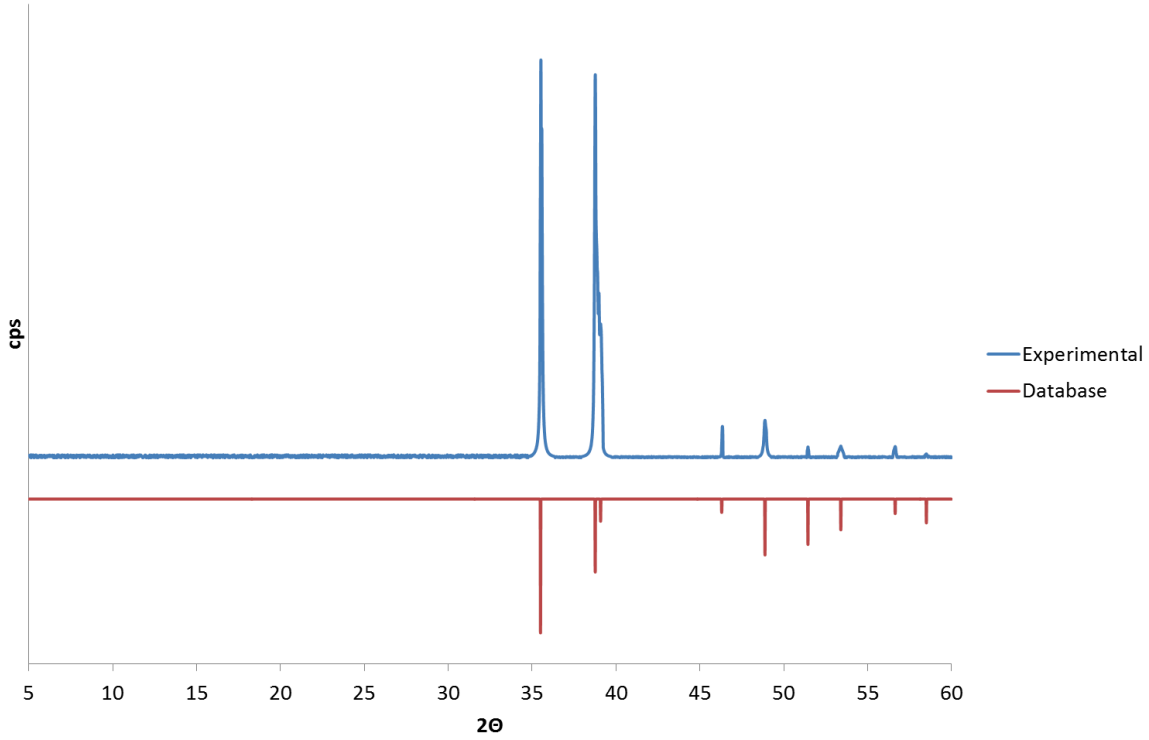

Fig. 3.49 | P-XRD pattern obtained for the residues resulting from the thermolysis of **3**.[178]

In a consecutive experiment the SEM technique was employed to examine the morphology of the CuO particles. Fig. 3.50a shows that the shape of the residues is similar to the plate-like crystals of **3**. Higher magnification imaging (Fig. 3.50b-d) reveals that the plates

are composed of small, almost spherical particles, which agglomerate to form a dense solid. The diameters of these particles ranges between 400 nm and 4 μm.

At high magnification (Fig. 3.50e-h) it is possible to notice that the small particles display layered structural imprints and arrangements. The thickness of the observed layered imprints varies between 5 and 100 nm. This specific morphology may be strongly influenced by the layered, lamellar molecular structure of the precursor compound.

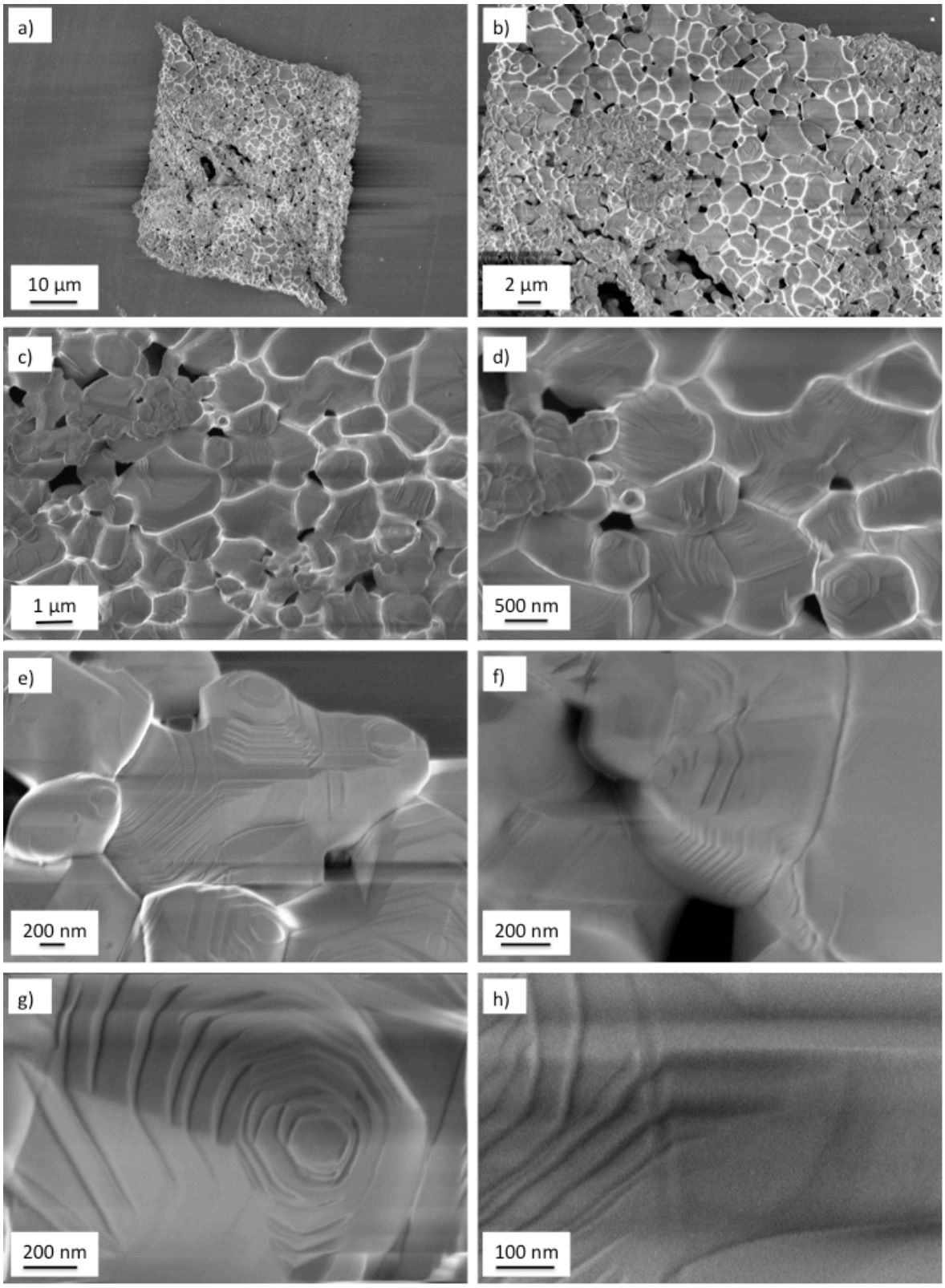

Fig. 3.50 | SEM images of the residual copper(II) oxide crystallites remaining after the thermolysis of **3**.

3.5. Compound $K_2[Cu_2(\mu\text{-}Cl)_2(C_6vda)_2] \cdot 4H_2O$ (4)

After compound **3** was fully characterised, it was decided to test if it is possible to change the nature of the coordination complex by altering reaction conditions. Therefore triethylamine, which was previously used to adjust the pH and deprotonate ligand molecules, was replaced with potassium hydroxide. This change had a significant effect on the binding mode as observed in the crystal structure of the newly formed complex. However, the applied chemical modification did not influence the overall solid-state packing structure resulting in a layered lamellar supramolecular arrangement.

3.5.1. Characterization of compound 4

Compound **4** with the chemical formula $K_2[Cu_2(\mu\text{-}Cl)_2(C_6vda)_2] \cdot 4H_2O$ crystallises in the monoclinic ***C***2/c space group from a water/methanol mixture after *ca.* 7 days of slow evaporation of the solvent to give blue crystals. Their shape varies from elongated, needle-like crystallites to thin, regular plates (Fig. 3.51). The size and quality of these plates were suitable for single crystal X-Ray diffraction experiments.

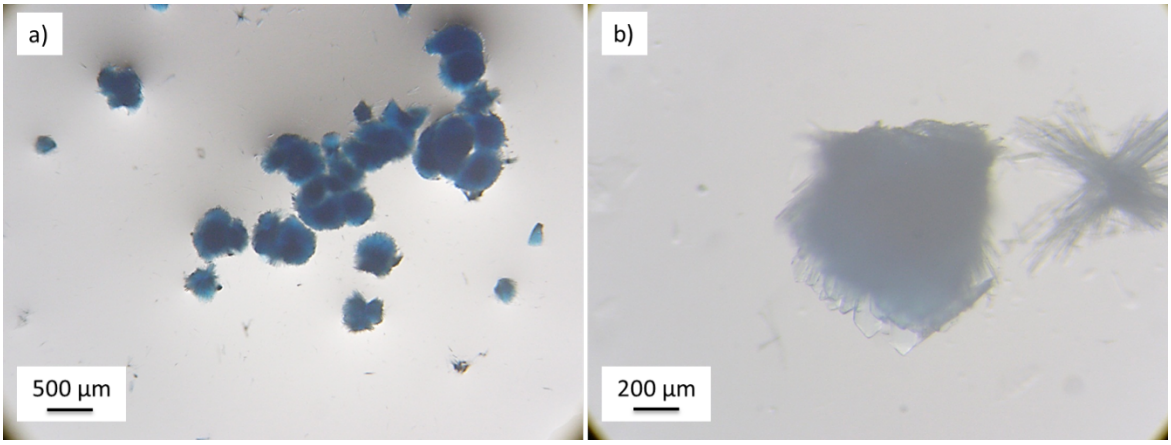

Fig. 3.51 | Optical microscope images of **4**. **a)** overview; **b)** a higher magnification image showing some thin plates sticking together along with thin needle-like crystals.

Coordination environment of the Cu^{2+} ion

The mononuclear sub-unit in **4** is presented in Fig. 3.52. The organic ligand binds to the metal ion *via* three O-donors – O(1) and O(2) originating from the deprotonated carboxylate groups of the iminodiacetic acid moiety, and O(5) from the protonated hydroxyl group attached to the aromatic ring. N- and carboxylate O-donor atoms of the iminodiacetic acid moiety adopt a meridional conformation.

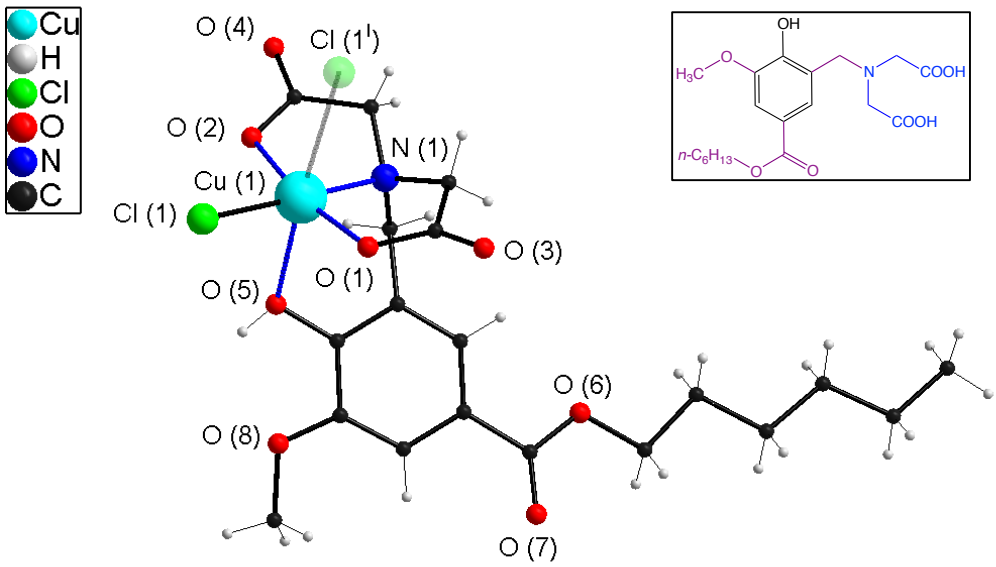

Fig. 3.52 | Mononuclear sub-unit in **4**. Inset: the C_6vda ligand molecule.

The d^9 Cu(II) coordination sphere again demonstrates Jahn-Teller distortion along the *z*-axis. As presented in Fig. 3.53, the equatorial plane of the octahedron is formed by the chlorine ion Cl(1) and the iminodiacetic acid N- and O-donors (N(1), O(1), O(2)). The apexes are occupied by the aromatic hydroxyl donor O(5) and the symmetry equivalent chlorine ion, Cl(1^I).

The Cu(1)-O bond distances range between 1.927(6) and 2.506(7) Å. The N(1) donor is located 2.014(7) Å from the metal ion, while the Cu(1)-Cl(1) and Cu(1)-Cl(1^I) bond distances are 2.261(2) Å and 2.951(3) Å, respectively. The bond distances are in good agreement with those described in the literature for similar Cu(II) complexes.[167]

The symmetry equivalent chlorine ions Cl(1) and Cl(1^I) are separated by the distance of 3.762(3) Å.

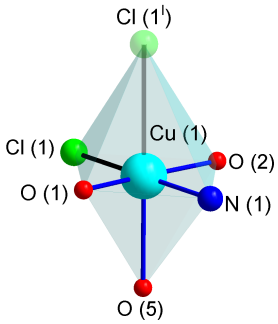

Atom 1	Atom 2	Symmetry code for atom 2	Bond lenght [Å]
Cu(1)	O(1)	x, y, z	1.927(6)
Cu(1)	O(2)	x, y, z	1.982(7)
Cu(1)	N(1)	x, y, z	2.014(7)
Cu(1)	Cl(1)	x, y, z	2.261(2)
Cu(1)	O(5)	x, y, z	2.506(7)
Cu(1)	Cl(1^I)	0.5-x, 0.5-y, 1-z	2.951(3)

Fig. 3.53 | Coordination environment in **4**. The table summarises the corresponding bond distances.

Formation of a dimeric unit

The chlorine atoms act as μ-type bridging ligands and are shared between two neighboring metal ions. This leads to the formation of a dimer in which the Cu(II) centres are doubly bridged (Fig. 3.54). Within the dimer the copper ions Cu(1) and Cu(1^I) are separated by a distance of 3.673(2) Å. Due to the presence of an inversion centre in the middle of the dimer, both mononuclear sub-units are symmetrically related.

The dinuclear complex carries a charge of -2, which is balanced by two potassium counter ions. These ions are chelated by one of the iminodiacetic acid carboxylate group (O(1)

and O(3)), while the second carboxylate group of the same iminodiacetic acid moiety binds to the K(1) counterion *via* one oxygen atom, O(2).

In addition, each potassium ion binds to three constitutional water molecules (O(1W), O(2W), O(1W^{I})) by ion-dipole forces. It is worth noticing that the iminodiacetic acid O-donors O(1) and O(2) bridge between the copper ions Cu(1) and the potassium counterions K(1) (see Fig. 3.54).

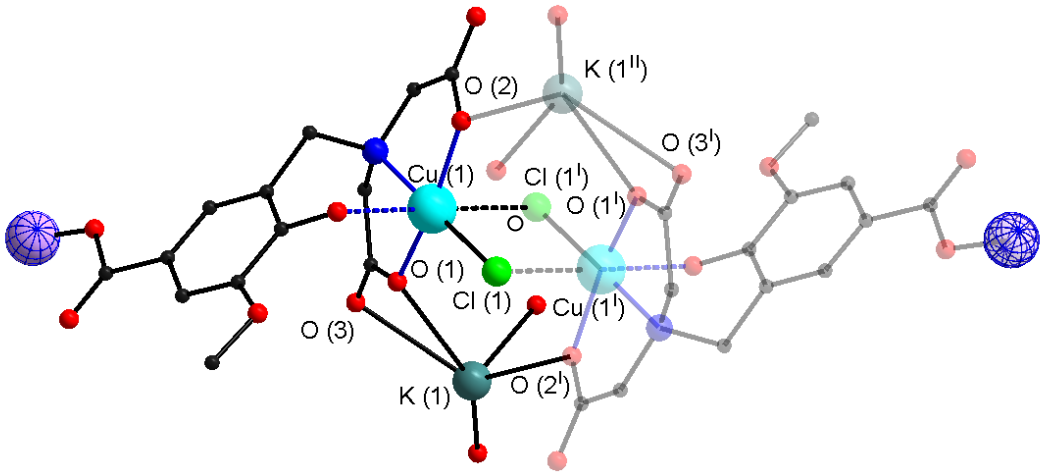

Fig. 3.54 | The mononuclear sub-units are bridged by two chlorine ions. Two potassium counter ions facilitate the formation of a dimer. The artificial pink atoms represent the *n*-hexyl chains. Hydrogen atoms are omitted for clarity. Symmetry codes: (I): 0.5-x, 0.5-y, 1-z; (II): 0.5-x, 1.5-y, 1-z.

The distance between the two symmetry equivalent potassium counterions K(1) and K(1^{II}) is 8.176(5) Å. The potassium counter ion K(1) is located 5.032(4) Å from the chlorine anion Cl(1) and 3.896(4) Å from its symmetry equivalent, Cl(1^{I}).

Role of the potassium counter ions

As presented in Fig. 3.55, the constitutional water molecule O(1W) creates a μ-type bridge between two symmetry equivalent potassium counterions K(1) and K(1^{I}). The bond distance between the O(1W) and K(1) atoms is 2.711(12) Å. A symmetry generated molecule O(1W^{I}) forms a second μ-type bridge between these two counter ions, this leads to the formation of another double-bridged dimer structure, which is composed of two constitutional water molecules and two equivalent potassium counter ions (Fig. 3.55). Both units of the dimer are symmetrically dependent due to the presence of an inversion centre located in the middle of the dimer. The bond distance between the symmetry generated potassium counterion K(1^{I}) and the water molecule O(1W) is 3.098(10) Å. The symmetry equivalent potassium counterions, which are involved in this structural motif, are located 4.807(4) Å from each other.

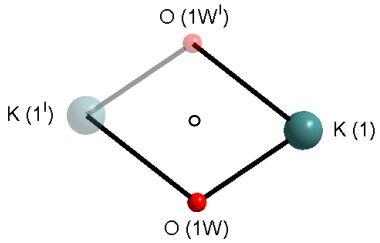

Fig. 3.55 | A dimer unit composed of the potassium counterions and constitutional water molecules. Symmetry codes: (I): 0.5-x, 1.5-y, 1-z.

As presented in Fig. 3.56, the counterion-containing dimer motifs link the copper-containing complexes into a 1D chain, which extends in the direction of the crystallographic *b*-axis. Within the chain, the iminodiacetic acid O-donors O(1) and O(2), which originate from two different carboxylate groups of the iminodiacetic acid moiety, form bridges between the Cu(1) ion and two different symmetry equivalent K(1) counterions. These counterions further bind through the bridging constitutional water molecule O(1W) to neighbouring symmetry equivalent complexes.

The predominant interactions responsible for the formation of this chain motif are the coordination bonds observed between the iminodiacetic acid O-donors and Cu(1) ions and the ion-dipole forces, which link the constitutional water molecule O(1W) with the potassium counterions.

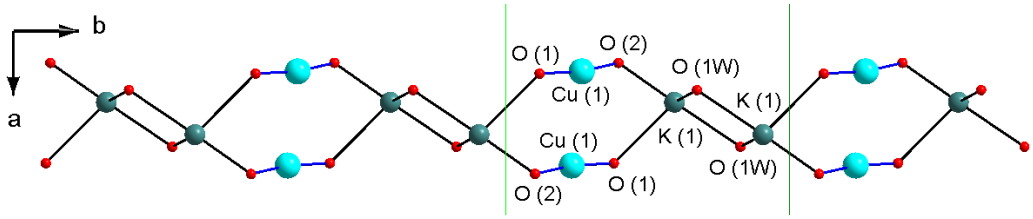

Fig. 3.56 | The copper-containing dimers are linked to the potassium-containing dimers and form a chain that propagates in the direction of the crystallographic *b*-axis. For clarity, the organic ligand molecules are not shown.

Hydrogen bonding

The hydrogen bonding interactions in **4** involve the carboxylate groups of the iminodiacetic acid moiety, the hydroxyl and methoxy groups attached to the aromatic ring, and the constitutional water molecules bound to the potassium ion. Hydrogen bond distances (O-O distance) range between 2.630(10) Å and 3.122(15) Å. The primary role of these bonds is to crosslink the previously discussed chains in the direction of the crystallographic *c*-axis to form neutral layers, which extend in the crystallographic *bc*-plane.

The most important hydrogen bond interactions are presented in Fig. 3.57. The protonated hydroxyl group located directly on the aromatic ring is linked *via* a hydrogen bond to a symmetry generated non-coordinating oxygen atom O(4^{I}), which belongs to one of the iminodiacetic acid carboxylate groups. The distance between these atoms is 2.630(10) Å.

The next interactions involve the oxygen atoms O(1W) and O(2W) of the constitutional water molecules, which are bound by the ion-dipole forces to the potassium counter ion K(1). The non-coordinating oxygen atom O(4^{III}) interacts *via* a hydrogen bond with the oxygen atom O(1W) of the constitutional water molecule, while the oxygen atom O(2W) of the second

constitutional water molecule binds to the oxygen atom O(8^{II}) of the aromatic methoxy group. The bond distances are 2.842(15) Å and 3.122(15) Å, respectively.

Although the hydrogen bond interactions are not aligned precisely along the crystallographic *c*-axis, their presence is the driving force for the growth of the structure in this crystallographic direction.

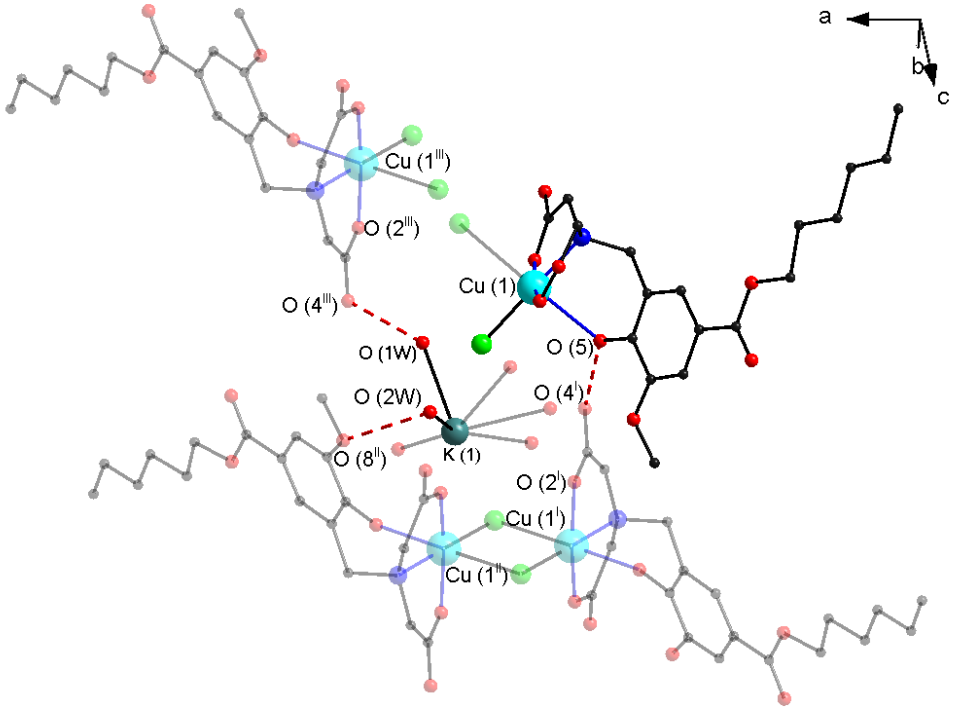

Fig. 3.57 | Three intermolecular hydrogen bonds give rise to a neutral layer in the *bc*-plane. Symmetry codes: (I): x, 1-y, 0.5+z; (II): 0.5-x, 0.5+y, 0.5-z; (III): 0.5-x, 0.5+y, 1.5-z.

The neutral layer, which grows in the crystallographic *bc*-plane, is presented in Fig. 3.58. The hydrophilic core of the layer, which is *ca.* 6.9 Å thick, consists mainly of the copper ions, potassium counter ions, water molecules and the iminodiacetic acid moieties. The hexyl chains of the ligand molecules point away from the core of the layer, thus making the *bc* 'surface' of the layer hydrophobic. This enables further self-assembly in the crystallographic *a*-direction *via* van der Waals forces and hydrophobic interactions. The thickness of the layer (measured from one end of the hexyl chain to the symmetry equivalent carbon atom) is *ca.* 25 Å.

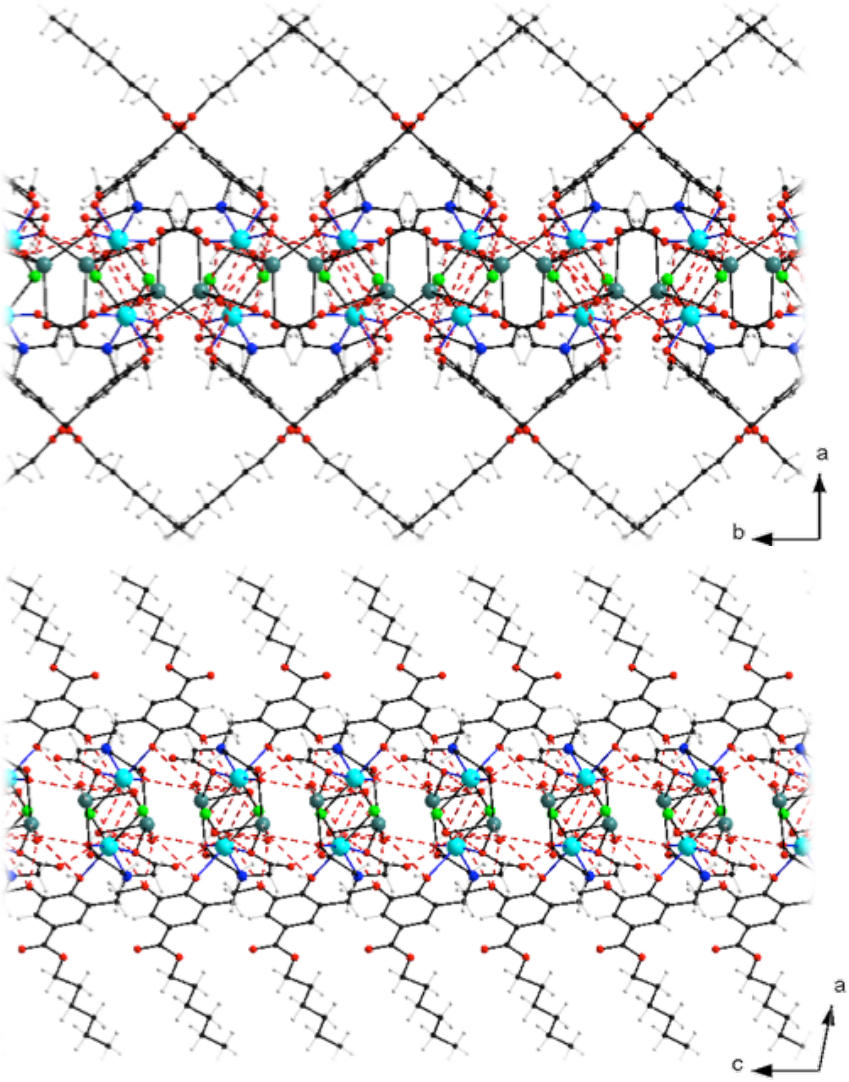

Fig. 3.58 | Cross-sectional view on a neutral layer in compound **4**. View in the direction of the crystallographic *c*-axis (top) and *b*-axis (bottom).

Packing

The afore-mentioned layers assemble in the direction of the crystallographic *a*-axis to give a 3D sandwich-like lamellar material, where the hydrophilic and hydrophobic parts are clearly separated. This packing motif may be observed when the structure is viewed along the crystallographic *b*- and *c*-axes (see Fig. 3.59). The thickness of the hydrophilic layers corresponds to the thickness of the hydrophilic core within a single neutral layer (*ca.* 6.9 Å), while the hydrophilic layers are *ca.* 12.1 Å thick. This value confirms that the hexyl chains of two neighbouring neutral layers are not completely separated but interact which each other.

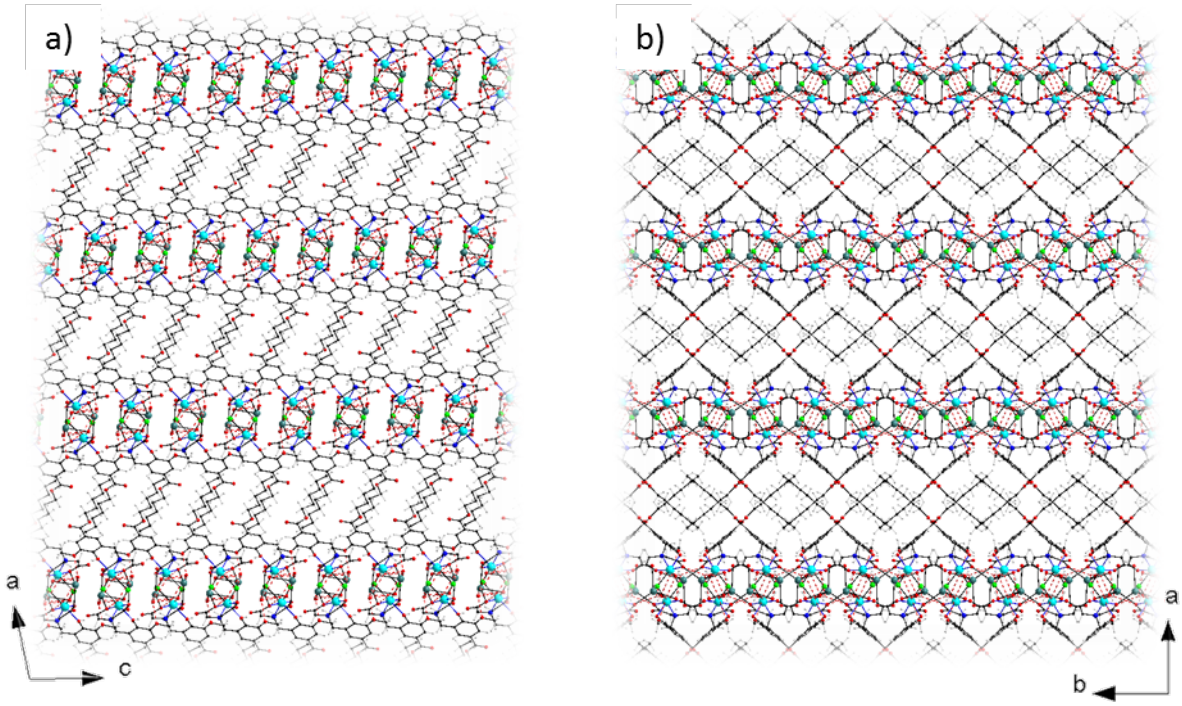

Fig. 3.59 | Packing of compound **4** viewed along the crystallographic *b*-axis (a) and *c*-axis (b).

Refinement details

The refinement parameters for the refined solid-state structure model of compound **4** based on the single crystal X-ray diffraction experiment are presented in Tab. 3.6.

Tab. 3.6 | Refinement details for compound **4**.

Identification code	**4**
Empirical formula	$C_{19}H_{29}ClCuKNO_{10}$
Formula weight	569.53 g/mol
Temperature	150(2) K
Wavelength	0.71073 Å
Crystal system	Monoclinic
Space group	*C*2/c
Unit cell dimensions	a = 38.096(8) Å α = 90°. b = 10.786(2) Å β = 100.93(3)°. c = 12.099(2) Å γ = 90°.
Volume	4881.7(17) $Å^3$
Z	8
Density (calculated)	1.550 Mg/m^3
Absorption coefficient	1.227 mm^{-1}
F(000)	2360
Crystal size	0.6 x 0.1 x 0.1 mm^3
Theta range for data collection	1.09 to 25.00°.
Index ranges	-45<=h<=38, -12<=k<=12, -14<=l<=14
Reflections collected	19323

Independent reflections	4284 [R(int) = 0.0741]
Completeness to theta = 25.00°	99.5 %
Refinement method	Full-matrix least-squares on F^2
Data / restraints / parameters	4284 / 7 / 317
Goodness-of-fit on F^2	1.325
Final R indices [I>2sigma(I)]	R1 = 0.0981, wR2 = 0.2909
R indices (all data)	R1 = 0.1215, wR2 = 0.3372
Largest diff. peak and hole	1.635 and -1.826 e.Å^{-3}

Additional characterization

In order to confirm the phase purity and the accuracy of the refined model, a P-XRD experiment was performed and the obtained pattern was compared with a theoretical pattern, which was based on the single crystal X-ray diffraction experiment. The results, presented in Fig. 3.60, confirm that **4** is phase pure and that all crystals within the bulk sample have the same crystal structure.

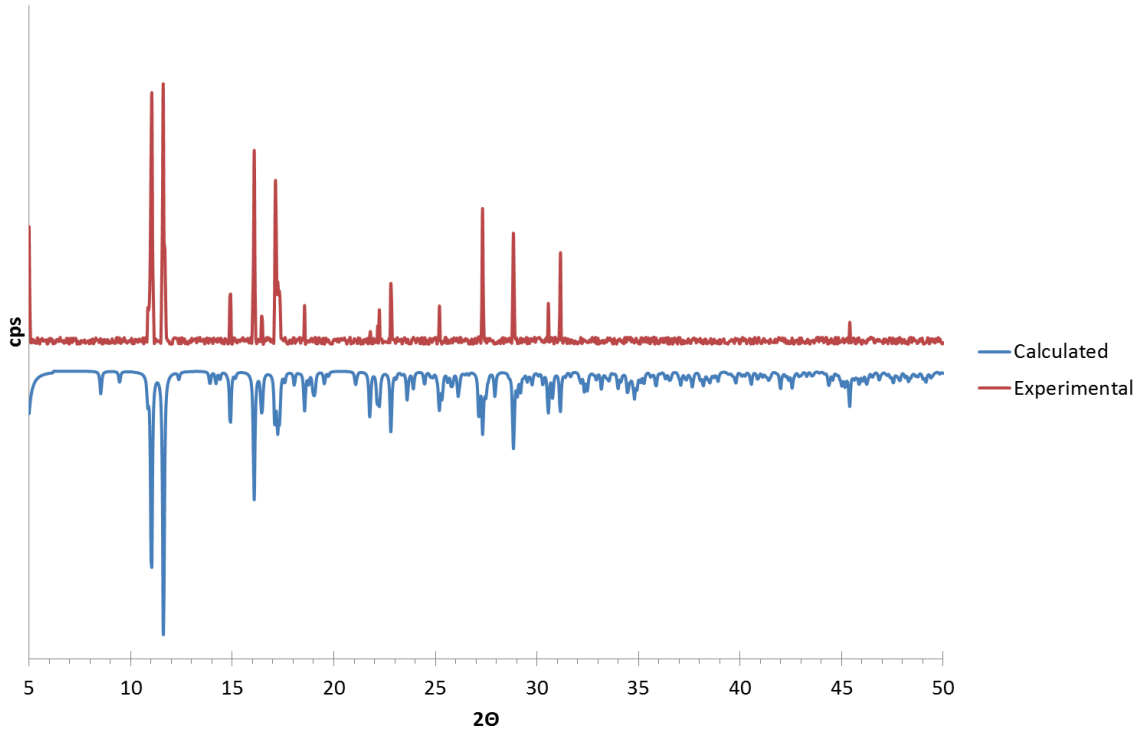

Fig. 3.60 | Comparison between an experimental P-XRD pattern of **4** (red) and a theoretical pattern calculated for the model based on the single crystal refinement results.

3.5.2. Thermolysis of 4 and the formation of copper(II) oxide.

The TGA analysis of compound **4** (see Fig. 3.61) was performed in air on a fresh crystalline sample and the heating rate was fixed at 0.5°C/min. The initial loss of weight observed between 70 and 80°C is associated with the loss of constitutional moisture (*experimental weight loss:* 3.9%, *theoretical:* 6.3%). **4** is thermally stable up to 160°C. Above this temperature a rapid oxidation occurs. In contrast to compounds **1** and **3**, crystals of **4** contain two additional elements: potassium and chlorine. Due to this fact the thermal

degradation is not so evident. The final product of the oxidation is copper(II) oxide (*experimental weight loss*: ~85%, *theoretical*: 86.1%) and its chemical identity was confirmed using the P-XRD (Fig. 3.62) and the EDX spectrometry (Fig. 3.63). It is assumed that CuO forms around 330°C, as it was observed in the previous structures, especially in **3**. The *plateau* on the TGA curve observed between 310 and 360°C may be associated with this process. The additional steps may correspond to the oxidation of potassium. This element is known to form various types of oxides, peroxides and superoxides that eventually sublimate and leave the TGA crucible.[168] This would explain why the presence of potassium was not confirmed in the final residues.

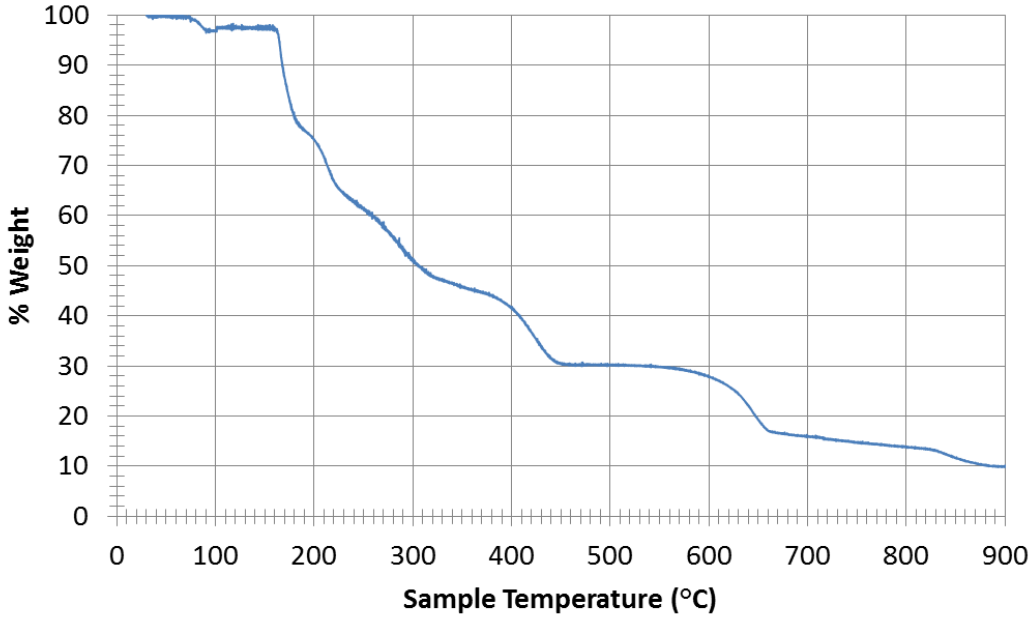

Fig. 3.61 I TGA analysis of compound **4**.

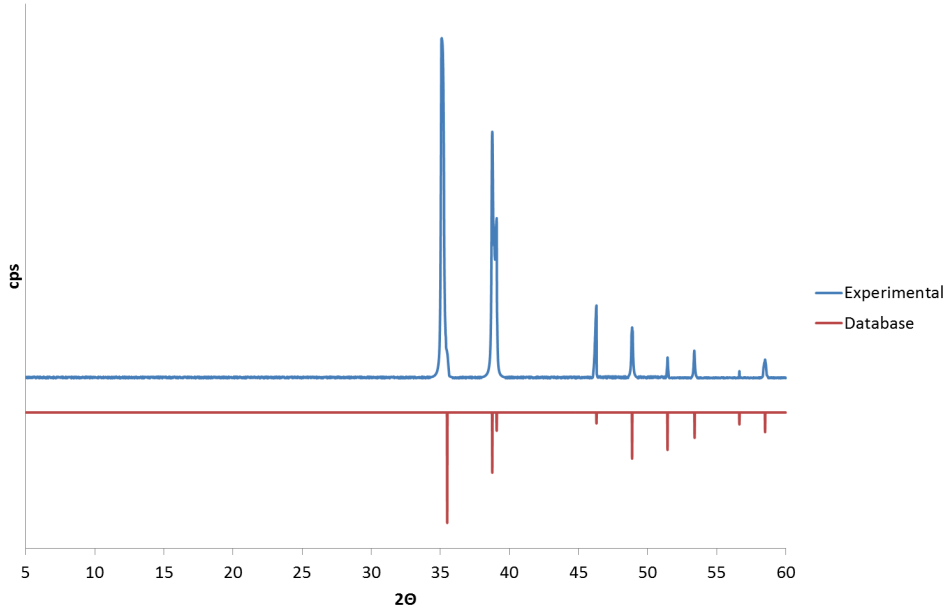

Fig. 3.62 | P-XRD pattern obtained for the residual black powder, which remained after the thermolysis of **4** (blue) compared with a reference pattern of copper(II) oxide from a database (red).[178]

The morphology of the residues was determined using SEM imaging. Fig. 3.64 shows SEM micrograpahs of the copper(II) oxide crystals that were formed during the thermolysis.

The macroscopic shape of the residual CuO particles (Fig. 3.64a) resembles the shape of the agglomerates of the needle-like crystals of compound **4** (Fig. 3.51). Copper(II) oxide seems to form thin fibres that grow from a common centre. When the image is magnified (Fig. 3.64b) it becomes clear that the fibres are composed of small crystals, which stick together. Further increase of the magnification (Fig. 3.64c-h) shows that similarly to the nanocrystals of CuO remaining after the thermolysis of **3**, these small crystalline particles display ordered hierarchical morphology. They seem to be composed of thin, 2D layers. The thickness of a single layer cannot be accurately measured with the SEM, however it appears to be less than 20 nm.

The layered imprint observed in the nanocrystals of CuO may be a result of the templating effect, which the initial pre-organisation of staring materials has on the crystallisation process.

SEM imaging was performed on an uncoated sample of the residues and this raised an opportunity to perform the EDX analysis. The spectrum presented in Fig. 3.63 shows that copper and oxygen are the only elements that were present in the analysed sample. The experimental Cu/O weight ratio is 3.59 (*theoretical*: 3.42).

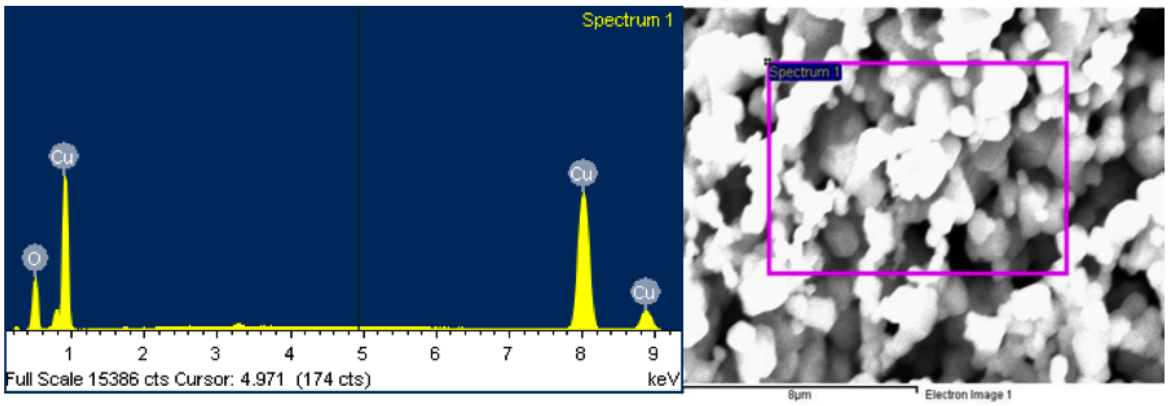

Fig. 3.63 | EDX analysis of the residues that remain after the thermolysis of **4** in 900°C.

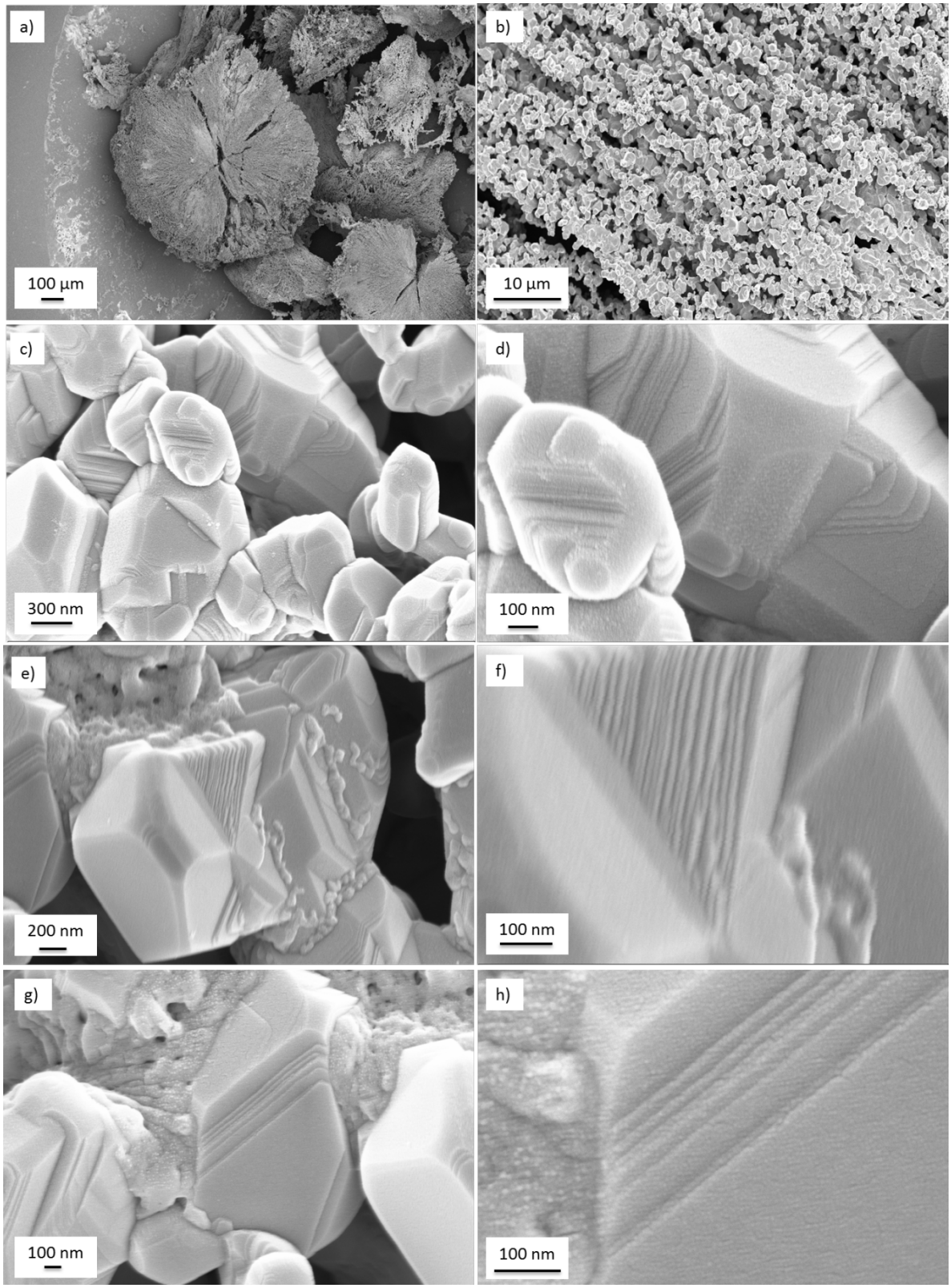

Fig. 3.64 | SEM images of the copper(II) oxide that forms during the thermolysis of **4**. **a,b)** overview, **d-h)** magnification showing layered structure of the nanoparticles

3.6. Compound $[Cu(C_{10}vda)(H_2O)_2]$ (**5**)

After the characterization of compounds **1**-**4** it became clear that the length of the hydrophobic chain in the vda-type ligands is the crucial parameter, which directs the self-assembly process by influencing the unit cell dimensions. In order to further investigate this phenomenon, it was decided to utilise the C_{10}vda ligand, containing a decyl chain in *para* position (with respect to the phenolic O- atom), in a reaction with copper(II) ions.

3.6.1. Characterization of compound **5**

Compound **5,** with the chemical formula $[Cu(C_{10}vda)(H_2O)_2]$, forms when the C_{10}vda ligand is reacted with a stoichiometric quantities of copper(II) chloride in methanol. Well-defined, blue, plate-like crystals of **5** form after *ca.* 5 days of slow evaporation of the solvent. As presented in Fig. 3.65, some of these plates grow separately while others appear to aggregate.

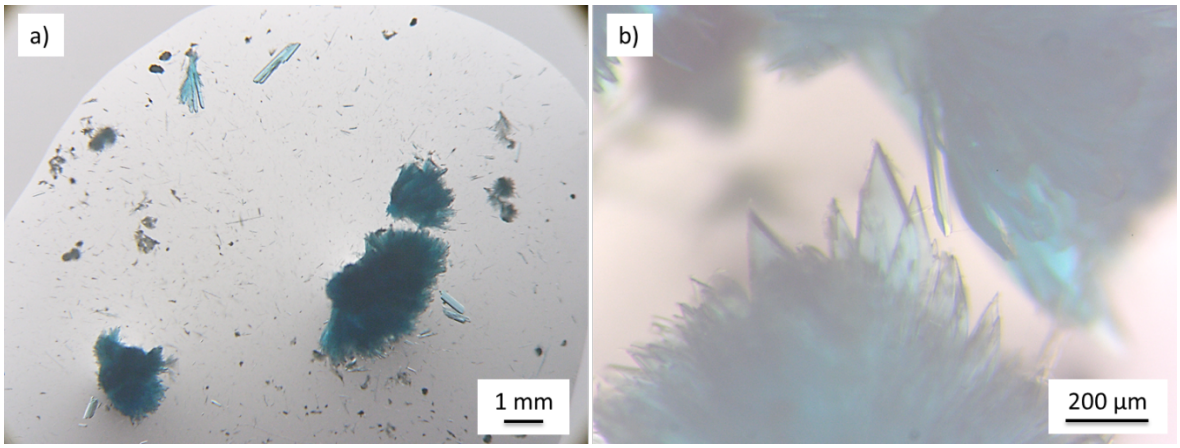

Fig. 3.65 | Optical microscope images of **5**. **a)** overview image showing separated single-crystalline plates and aggregates of plates; **b)** a higher magnification image confirms that the bunches are composed of plate-like single crystals.

The compound crystallises in the monoclinic space group ***C***2/c and contains the mononuclear complex presented in Fig. 3.66. Hydrogen bonds link this mononuclear unit with its symmetry equivalents in the directions of the crystallographic *b*- and *c*-axes resulting in the formation of 2D sheet-like assemblies in the (100) plane. Further self-organisation of these assemblies in the direction of the crystallographic *a*-axis is driven by the van der Vaals forces and hydrophobic interactions that occur between the *n*-decyl aliphatic chains of the C_{10}vda ligand molecules. **5** is a layered, lamellar material, where the hydrophobic areas sandwich between the hydrophilic parts of the solid-state structure.

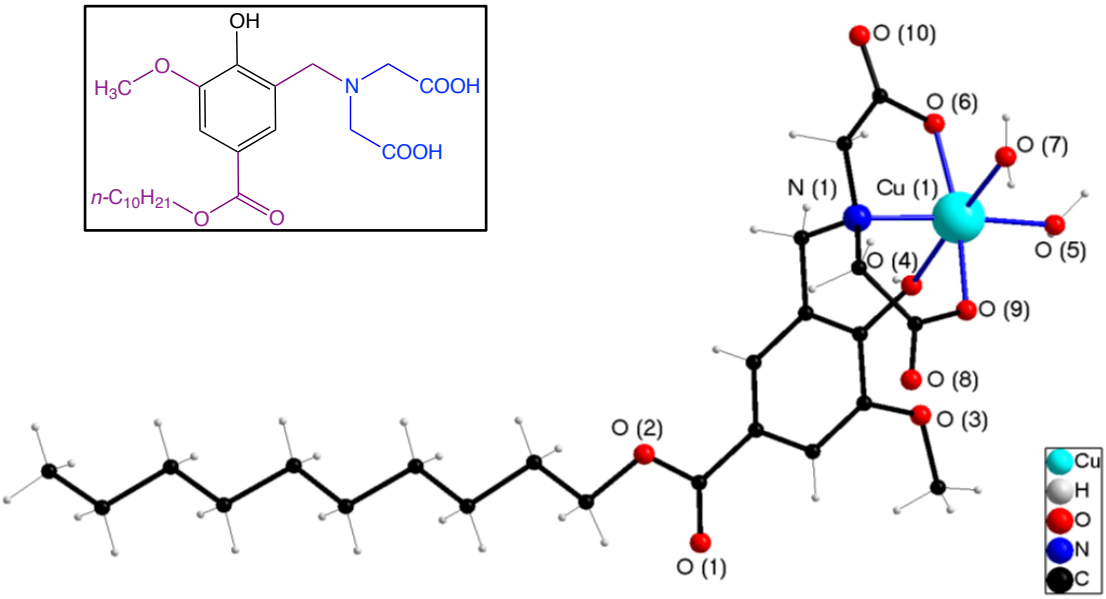

Fig. 3.66 | Mononuclear complex in **5**. Inset: the C_{10}vda ligand molecule.

Asymmetric unit

The asymmetric unit in **5** contains one copper ion, one ligand molecule and two coordinating water molecules. The octahedral coordination environment of the metal ion in **5** is presented in Fig. 3.67. The ligand provides three O-donors and one N-donor. Two of these O-donors, O(6) and O(9), which originate from two different iminodiacetic acid carboxylate groups, along with the N-donor N(1) bind to the metal ion in the *meridional* conformation mode. The equatorial plane of the octahedron is shown in Fig. 3.67 and consists of the N-donor N(1), the iminodiacetate O-donors O(6) and O(9) and the O-donor O(5) of a coordinating water molecule. The apexes are occupied by the oxygen atom O(7) of a second coordinating water molecule and the O-donor O(4), which belongs to the protonated hydroxyl group of the aromatic ring moiety. Both oxygen atoms of the coordinating water molecules, O(5) and O(7), are located in the *cis* position within the octahedron.

The average bond distance between the metal ion and the equatorial donors is 1.967 Å, while for the donor atoms located on the apexes this value is equal to 2.463 Å. The elongation may be explained by the Jahn-Teller effect commonly observed in the octahedral copper(II) complexes.

The bond valence sum for the copper ion is equal to 2.17 confirming the oxidation state of +II.

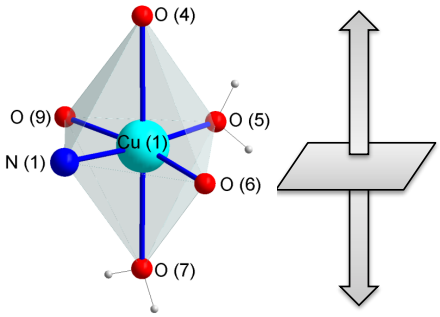

Atom 1	Atom 2	Symmetry code for atom 2	Bond lenght [Å]
Cu1	O6	x, y, z	1.947(5)
Cu1	O5	x, y, z	1.948(5)
Cu1	O9	x, y, z	1.965(5)
Cu1	N1	x, y, z	2.009(6)
Cu1	O7	x, y, z	2.401(6)
Cu1	O4	x, y, z	2.524(4)

Fig. 3.67 | Coordination environment of the metal ion in **5**. The octahedral coordination sphere is elongated along the axis marked with the arrows. The table shows corresponding bond lengths.

Connectivity

The two coordinating water molecules are involved in four hydrogen bond interactions. As presented in Fig. 3.68, the coordinating oxygen atom O(5) interacts with two symmetry generrated oxygen atoms: the O-donor O(6^{I}) of the iminodiacetic acid carboxylate functionality and the non-coordinating oxygen atom O(8^{II}) of another neighbouring carboxylate group. The bond distances are 2.700(7) Å and 2.715(8) Å, respectively. These two interactions generate a 1D H-bound chain motif, which extends in the direction of the crystallographic *c*-axis.

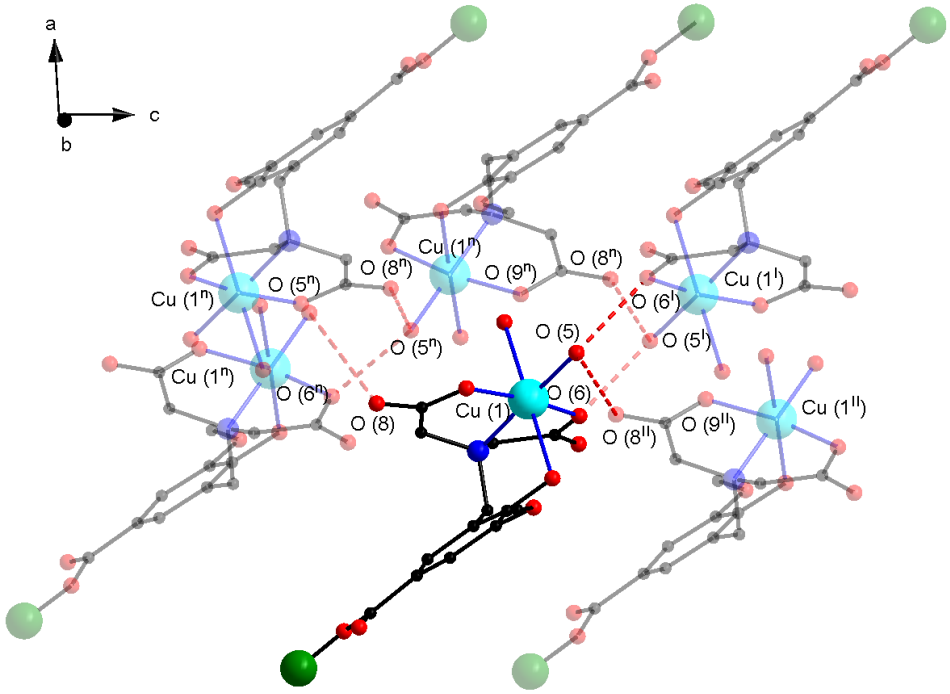

Fig. 3.68 | Hydrogen bonding in **5**. The *n*-hexyl chains have been replaced with the green artificial atoms for clarity. Symmetry codes: (I): 0.5-x, 0.5-y, 2-z; (II): x, 1-y, 0.5+z.

It is worth to notice that the hydrogen bonds that occur between the O-donor O(5) of the water molecule and the carboxylate O-donor O(6^{I}) form a complementary set. These interactions lead to the formation of a H-bound dimer, which is presented in Fig. 3.69. An inversion centre is located between both molecules.

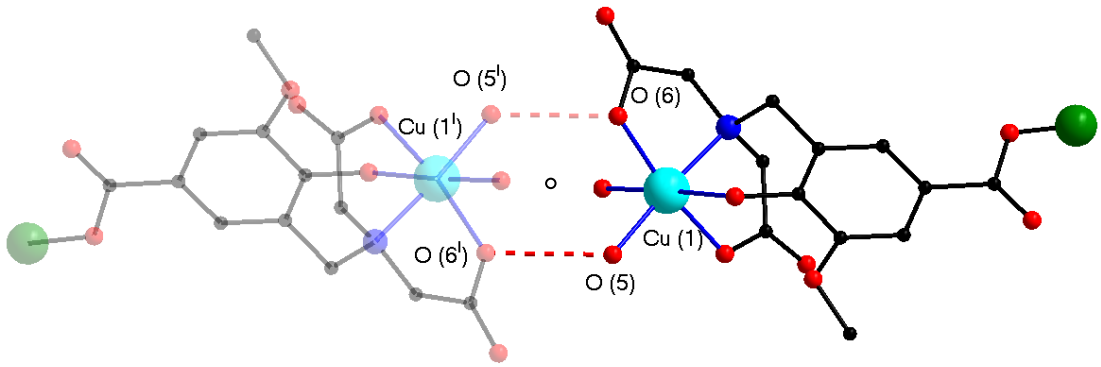

Fig. 3.69 | Complementary hydrogen bonding in **5**. The *n*-hexyl chains have been replaced with the green artificial atoms for clarity. Symmetry codes: (I): 0.5-x, 0.5-y, 2-z.

The oxygen donor of the second coordinating water molecule, O(7), is involved in a similar type of interactions that were encountered in the case of O(5). It links the mononuclear

unit *via* two hydrogen bonds with two symmetry independent complexes. As presented in Fig. 3.70, the O-donor O(7) binds to the symmetry generated O-donor O(9^{III}) of an iminodiacetic acid carboxylate functionality. The bond distance is 3.034(7) Å. The O-donor O(7) binds also to another symmetry generated non-coordinating oxygen atom O(8^{IV}) of an iminodiacetic acid carboxylate group. In this case the bond length is 2.893(8) Å. These two interactions lead to the formation of a H-bound chain motif that extends in the crystallographic *b*-direction.

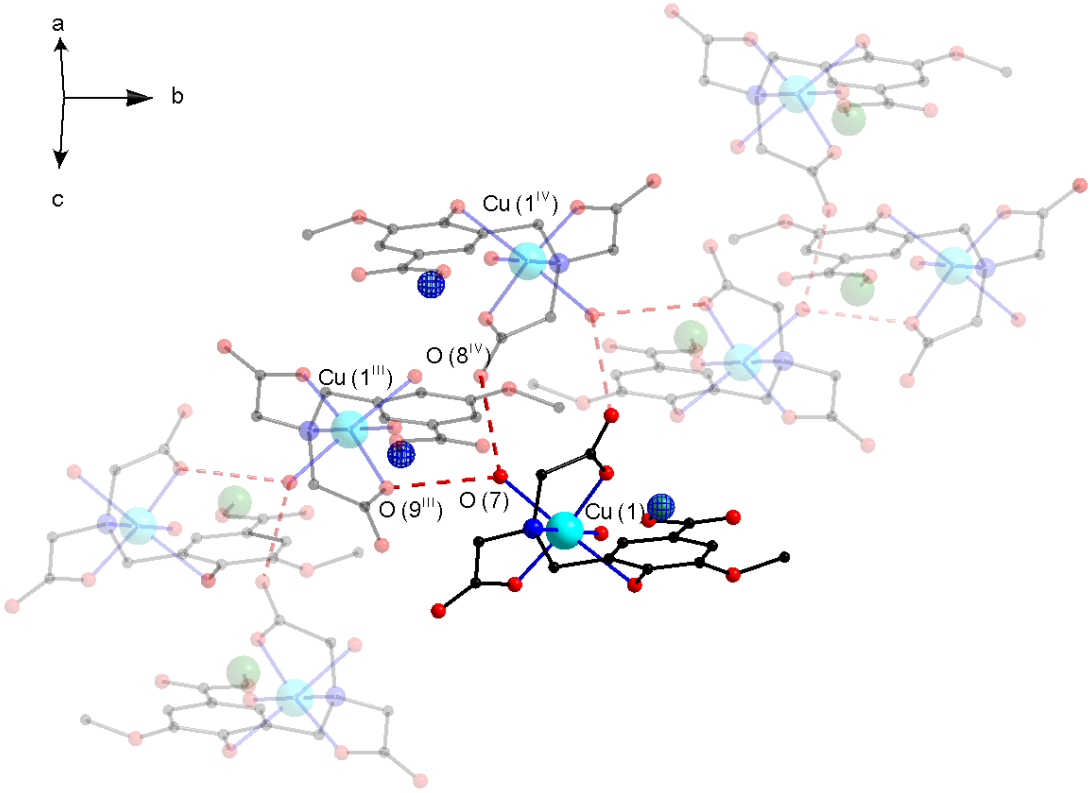

Fig. 3.70 | Hydrogen bonding in **5**. The *n*-hexyl chains have been replaced with the green artificial atoms for clarity. Symmetry codes: (III): 0.5-x, -0.5+y, 1.5-z; (IV): 0.5-x, 0.5-y, 1-z.

Similarly to O(5), the hydrogen bond involving the O-donor O(7) of a coordinating water molecule constitutes a set of complementary hydrogen bonds, which is presented in Fig. 3.71. An inversion centre is located between both molecules.

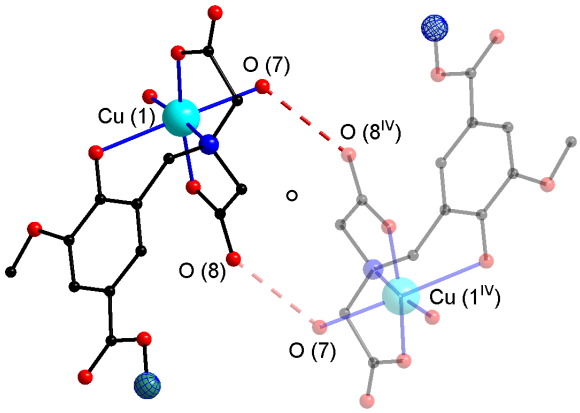

Fig. 3.71 | Complementary hydrogen bonding in **5**. The *n*-hexyl chains have been replaced with the green artificial atoms for clarity. Symmetry codes: (IV): 0.5-x, 0.5-y, 1-z.

In summary, the hydrogen bond interactions discussed above promote the formation of two 1D chain-like motifs that extend in two perpendicular directions. Therefore, these 1D

chains cross-link with their symmetry equivalents and form a two-dimensional, H-bound layer, which extends in the crystallographic *bc*-plane. This structural motif is visualised in Fig. 3.72.

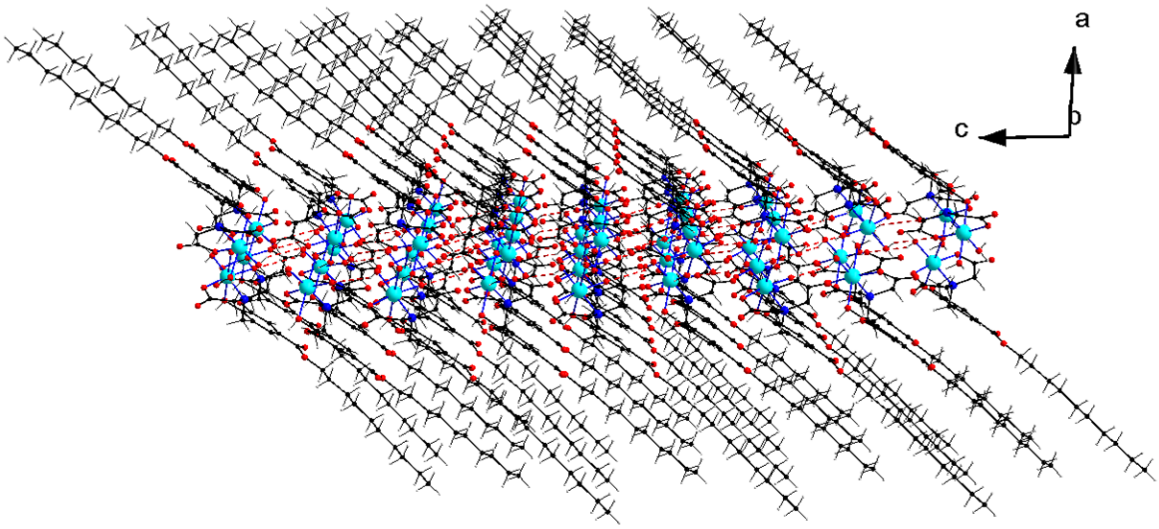

Fig. 3.72 | Perspective view on a fragment of a 2D layer in **5**, which extends in the crystallographic *bc*-plane.

The core of the 2D layer is composed of copper ions, coordinating water molecules and the N- and O-donors originating from the C_{10}vda ligand molecules. The thickness of the core, measured in the crystallographic a-direction, is *ca.* 8.8 Å. The shortest distance between two symmetry equivalent metal ions (Cu(1)-Cu(1^{I})) is 6.254(2) Å. The aromatic rings of the organic ligands of the complexes are parallel aligned to each other in [001] and their mean planes are located 5.622(10) Å from each other.

As presented in Fig. 3.73, the outer parts of the layered motif are composed mainly of the *n*-decyl chains, which form a characteristic 'zigzag' motif in the crystallographic *ab*-plane (see Fig. 3.73, right). Therefore, the *bc*-surface of the 2D layer is highly hydrophobic. The dimension of the layer in [100] does not exceed 29 Å.

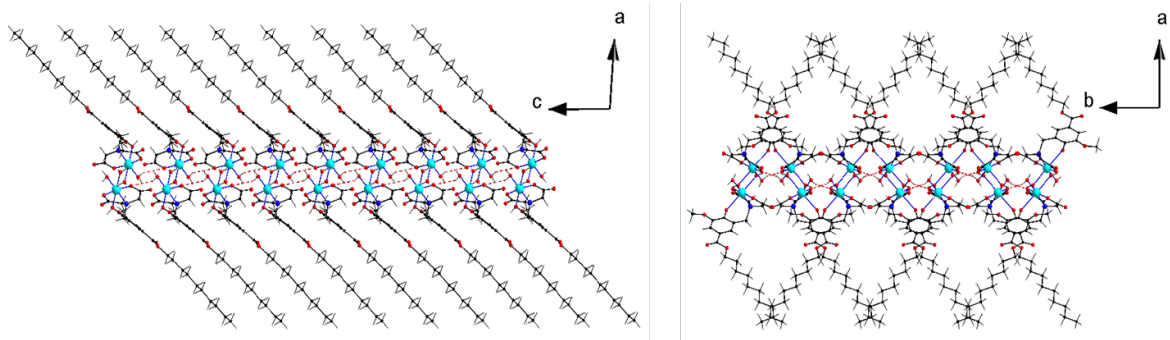

Fig. 3.73 | A 2D, H-bound layer in **5**. View along the crystallographic b-axis (left) and c-axis (right).

Packing

The overall packing structure of compound **5** is similar to the packing structure of the previously described copper-containing compounds **3** and **4**. Further self-assembly in the direction of the crystallographic *a*-axis is realised *via* van der Waals forces and hydrophobic interactions that occur between the symmetry equivalent *n*-decyl chains of the C_{10}vda ligand

molecules. As presented in Fig. 3.74, the H-bound, 2D layers stack in the crystallographic [100] direction to form a lamellar material with distinct areas of different polarity.

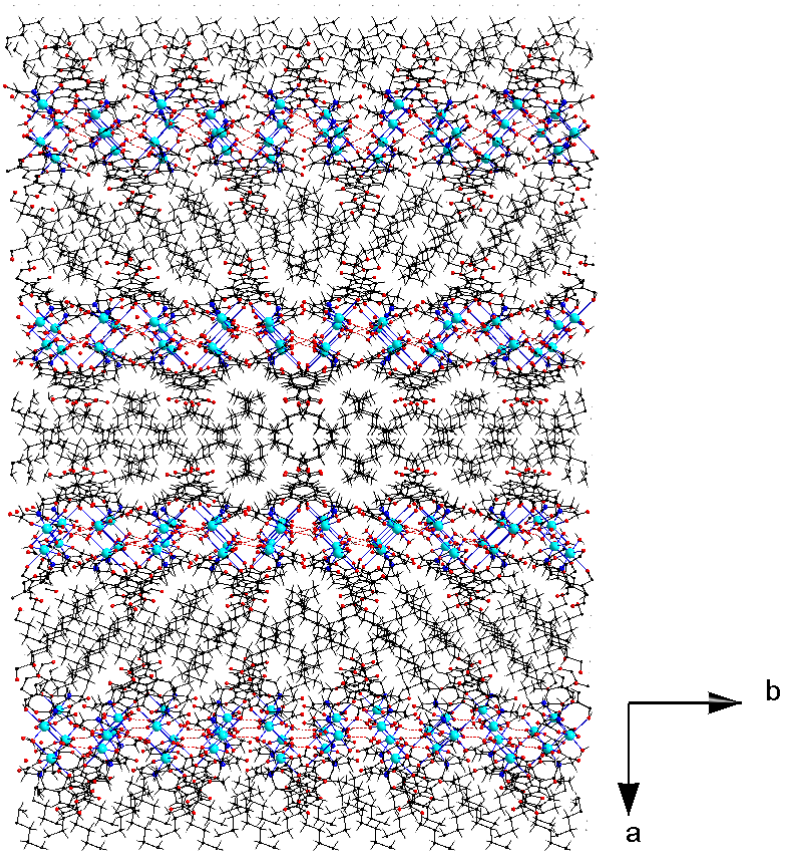

Fig. 3.74 | Packing of compound **5**. Perspective view in the direction of the crystallographic *c*-axis.

The view on the packing structure of **5**, which is presented in Fig. 3.75, provides additional insights into the assembly. The *n*-decyl chains interact in the direction of the *a*-axis, however, they are not aligned exactly parallel to this direction, but, as visualised in Fig. 3.75, they interdigitate in the crystallographic *a*-direction. Moreover, complex hydrophobic interactions lead to the formation of a grid-like motif that is visible in the *ab*-plane (Fig. 3.75b). The length of the chains is 12.569(11) Å, that is 5.071 Å longer than the lengths observed in **3** and **4**. When measured along the *a*-axis, the thickness of the hydrophilic part of the structure corresponds directly to the thickness of the hydrophilic cores of the 2D layers, while the hydrophobic section in **5** is *ca.* 14 Å thick. This value is nearly 2 Å longer when compared to that observed for **3** and **4** in the direction of the corresponding crystallographic *a*-axes.

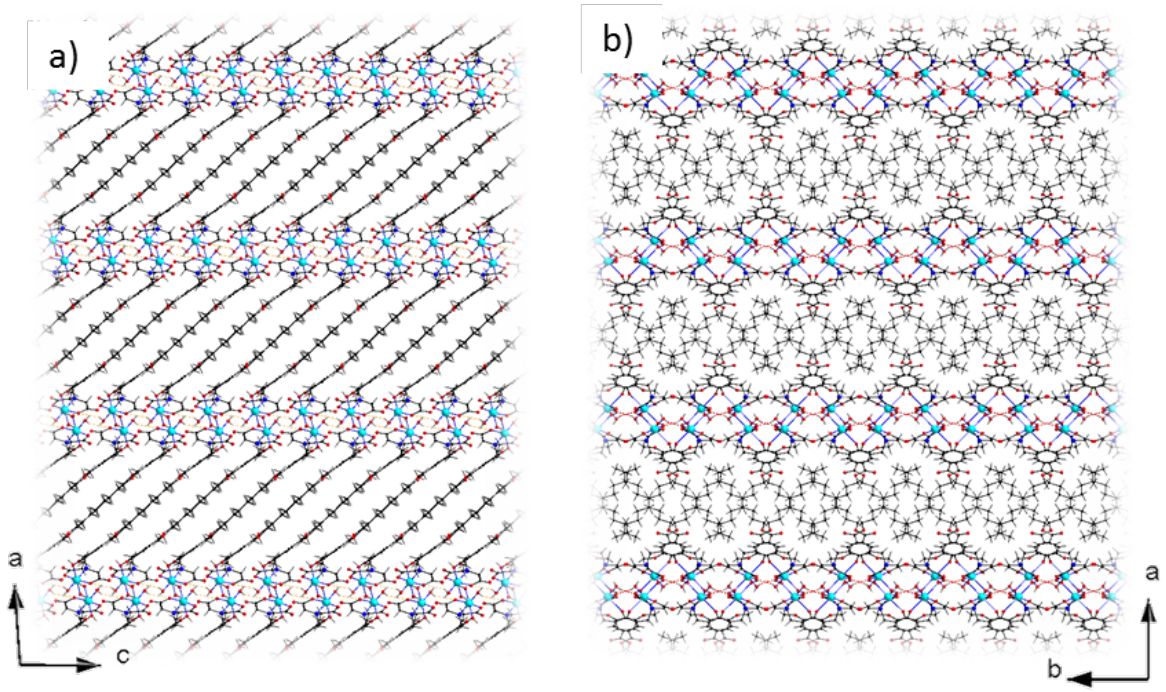

Fig. 3.75 | Packing structure of **5**. View along the crystallographic *b*-axis (**a**) and *c*-axis (**b**).

Refinement details

The refinement parameters for the crystal structure of **5** are presented in Tab. 3.7.

Tab. 3.7 | Refinement parameters for compound **5**.

Identification code	**5**
Empirical formula	$C_{23}H_{37}CuNO_{10}$
Formula weight	551.09 g/mol
Temperature	150(2) K
Wavelength	0.71073 Å
Crystal system	Monoclinic
Space group	*C*2/c
Unit cell dimensions	a = 40.150(8) Å α = 90°. b = 11.174(2) Å β = 94.33(3)°. c = 11.225(2) Å γ = 90°.
Volume	5021.6(16) $Å^3$
Z	8
Density (calculated)	1.458 Mg/m^3
Absorption coefficient	0.926 mm^{-1}
F(000)	2328
Crystal size	0.5 x 0.2 x 0.1 mm^3
Theta range for data collection	1.02 to 24.99°.
Index ranges	-47<=h<=47, -13<=k<=13, -13<=l<=11
Reflections collected	19593
Independent reflections	4390 [R(int) = 0.1104]

Completeness to theta = 24.99°	99.3 %
Refinement method	Full-matrix least-squares on F^2
Data / restraints / parameters	4390 / 7 / 334
Goodness-of-fit on F^2	1.408
Final R indices [I>2sigma(I)]	R1 = 0.0851, wR2 = 0.2701
R indices (all data)	R1 = 0.1160, wR2 = 0.3201
Largest diff. peak and hole	1.549 and -2.449 e.Å^{-3}

The goodness of fit value of 1.408 and the difference between the largest peak and the deepest hole on the Fourier map appear to be relatively large when compared with other refined structures. However, the presence of a decyl chain within **5** may introduce an additional thermal motion into the crystal structure and therefore elevate the GoF value. A similar phenomenon has been reported in the literature for aliphatic chain-containing compounds.[169]

Additional characterization

A P-XRD pattern was obtained for the bulk material of **5**. The pattern was then compared with a pattern that was simulated for the single crystal X-ray diffraction data. The results, presented in Fig. 3.76, prove that the described preparation method results in a phase pure material and confirm the accuracy of the structural model.

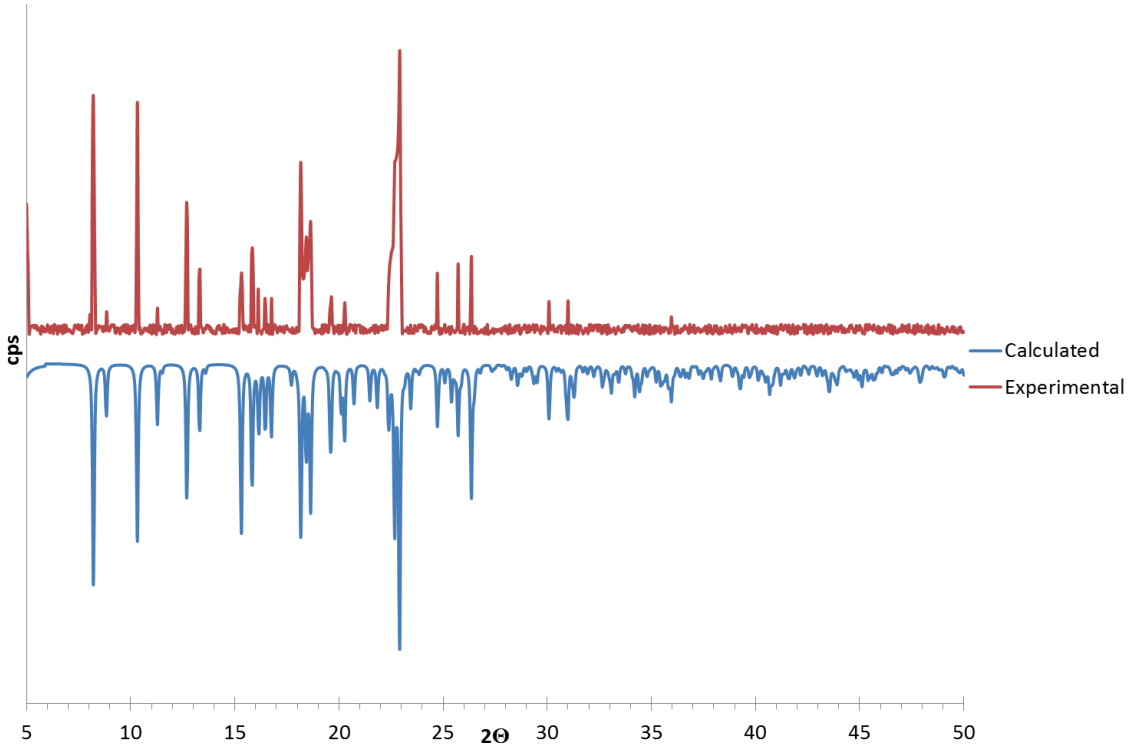

Fig. 3.76 | P-XRD pattern of **5** compared with a pattern simulated for the single crystal XRD data.

3.6.2. Thermolysis of **5**

The thermogravimetic analysis of compound **5** (Fig. 3.77) shows that initially, during the heating process, **5** undergoes a dehydration process resulting in the loss of the

coordinating water molecules. This process occurs between 50 °C and 70 °C (*experimental weight loss:* 6.2%, *theoretical:* 6.5%). The dehydrated compound is thermally stable up to 170°C. Above this temperature a rapid oxidation of the organic ligand occurs. The process is accompanied by the formation of copper(II) oxide at 330°C (*experimental weight loss:* 84.8%, *theoretical:* 85.5%).

The degradation pathway of **5** is similar to that of compound **3**. The formation of CuO occurs here at lower temperatures in comparison to the thermolysis process of **4**.

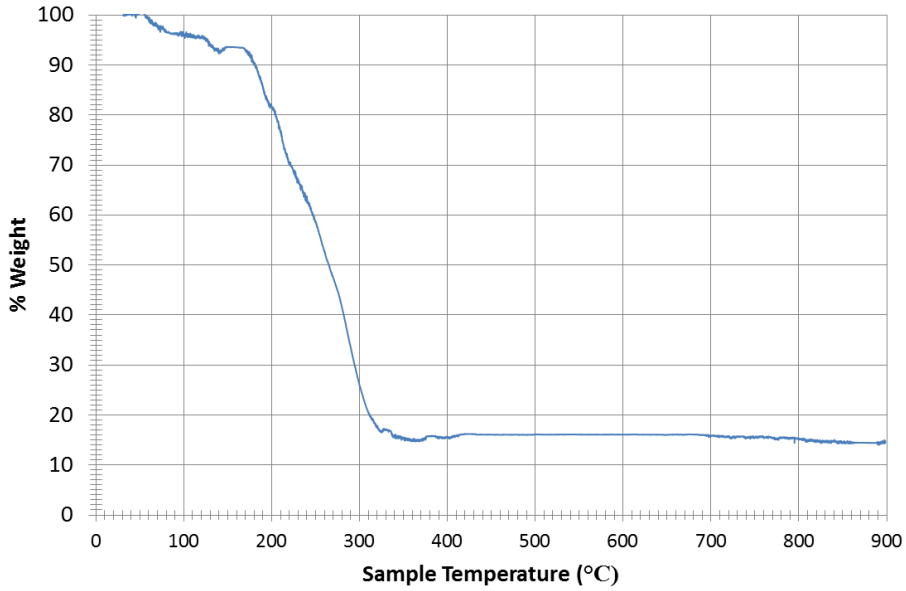

Fig. 3.77 | TGA analysis of compound **4**

The residues that remained after the TGA analysis were characterised using the P-XRD. The results, presented in Fig. 3.78, were compared with a database and it was confirmed that copper(II) oxide is the final product of the thermal degradation of **5**.

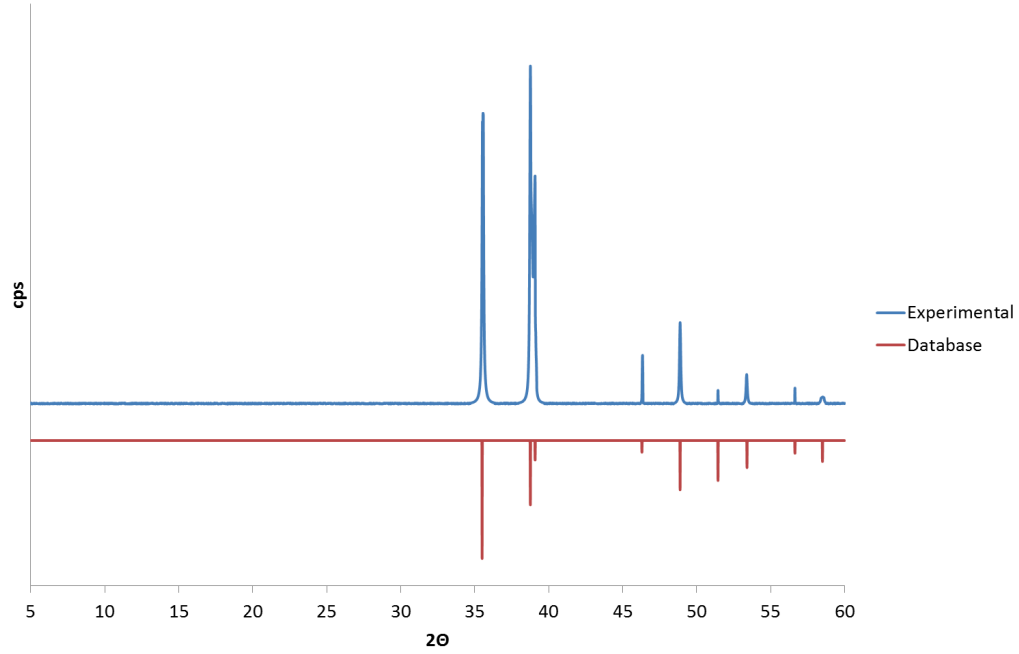

Fig. 3.78 | P-XRD pattern of the residues remaining after thermolysis of **5** (blue) compared with a reference P-XRD pattern of copper(II) oxide (red).[178]

The morphology of the residues was studied using SEM. The imaging revealed that the original macroscopic shape of the plate-like crystals is not reflected in the residual CuO (Fig. 3.79a,b). The observed morphology of the inorganic oxide is highly irregular and resembles a dense network of thin, tangled fibres that agglomerate together (again, see Fig. 3.79a,b). Higher magnification images, presented in Fig. 3.79c, show that the agglomerates are composed of small particles, which adopt a highly unsymmetrical shape. Their diameters vary between 200 nm and 3 μm. The images presented in Fig. 3.79d-f reveal that these small particles display layered imprints which may originate from the structural and morphological features of the organic-inorganic precursor.

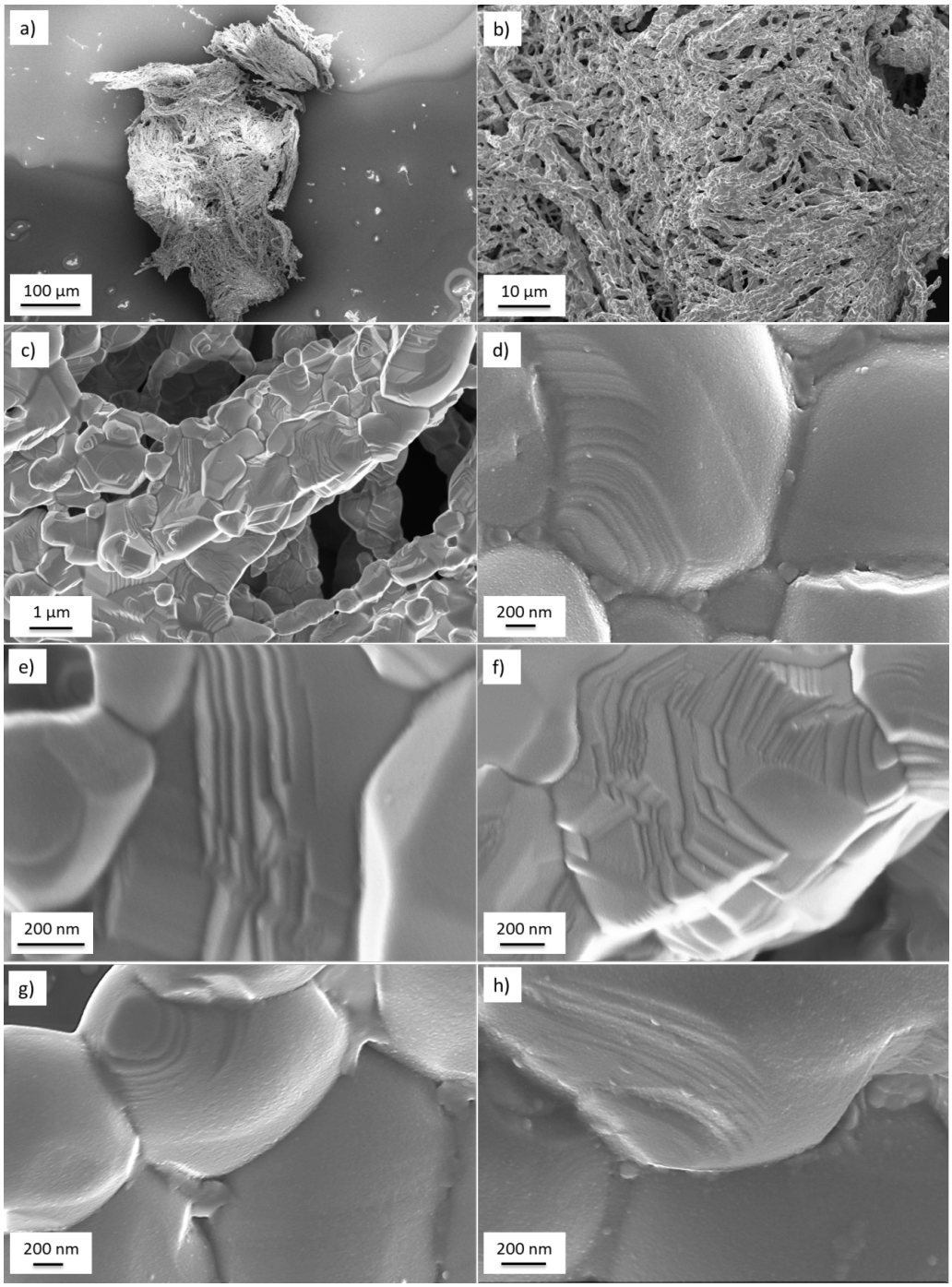

Fig. 3.79 | SEM micrographs of copper(II) oxide particles that formed during the thermolysis of compound **5** at 900 °C.

3.7. Compound $[Zn(Me_2hda)(H_2O)_2]\cdot H_2O$ (**6**)

For comparison with the Cu(II) systems it was decided to investigate how the hda-type ligands would bind to zinc(II) ions. The coordination environment and geometry of the obtained complex were studied in details. Also the self-assembly process and the thermal degradation pathway were explored in order to investigate if the initial pre-organisation has a templating effect on the formation of ceramic, Zn-containing residues.

Characterization of compound 6

Compound $[Zn(Me_2hda)(H_2O)_2]\cdot H_2O$ (**6**) forms when the Me_2hda ligand reacts with zinc perchlorate in a mixture of water and methanol. **6** crystallises as colourless needle-like crystals (Fig. 3.80) in the monoclinic space group $P2_1/c$ (No.14). Some of the crystals were suitably sized for XRD analyses.

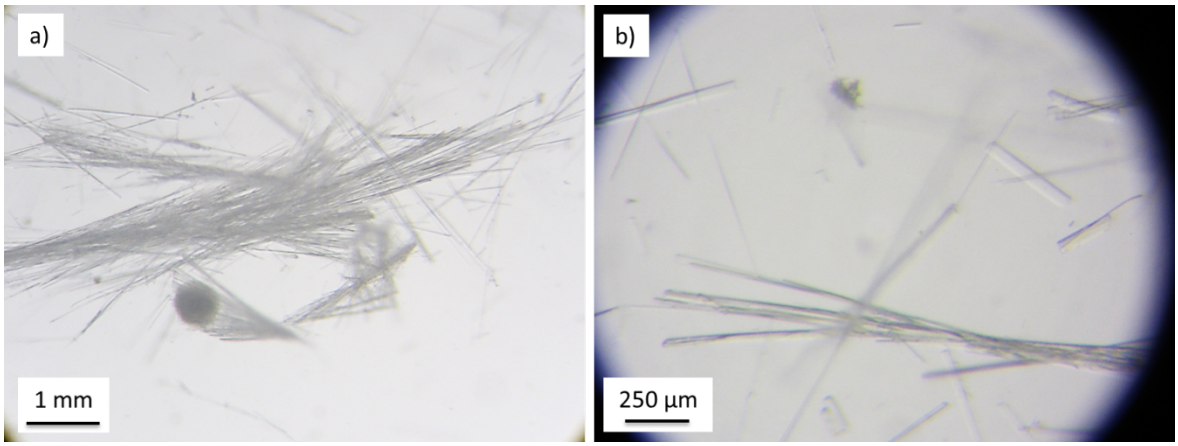

Fig. 3.80 | Optical microscope images of **6**. **a)** overview; **b)** magnification.

6 contains partially hydrated mononuclear complexes. The complexes are linked through hydrogen bonds forming layers that extend in the crystallographic *bc*-plane. These layers self-assemble in the direction of the crystallographic *a*-axis to give a layered lamellar material.

Asymmetric unit

The asymmetric unit in **6** (Fig. 3.81) consists of a mononuclear complex formed by the metal ion, the ligand molecule and two coordinating water molecules along with one molecule of constitutional water. The zinc atom Zn(1) has a distorted octahedral coordination geometry. It is coordinated by five O-donors (three of these derive from the Me_2hda ligand and the two remaining O-donors originate from water ligands) and one N-donor. The phenolic hydroxyl group located directly on the benzene ring remains protonated and binds to the zinc atom with a bond distance Zn(1)-O(3) of 2.114(2) Å to the central ion.

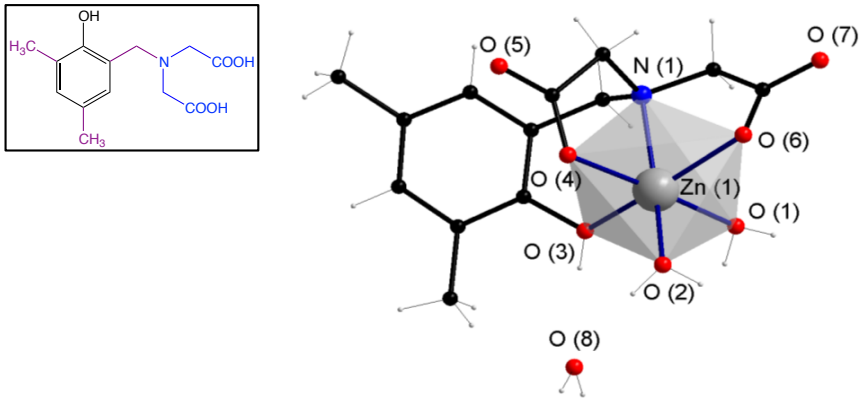

Fig. 3.81 | The asymmetric unit in **6**. Inset: the Me_2hda ligand molecule.

Both carboxylic acid groups of the iminodiacetic acid functionality are deprotonated and bind together with the N-donor in a *facial* arrangement to the metal cation. The bond distances between the carboxylate O-atoms O(4) and O(6) and Zn(1) are 2.119(2) Å and 2.162(2) Å, respectively. The distance between N-donor and the metal atom is 2.137(3) Å. The distorted octahedral coordination sphere of Zn(1) is completed by two *cis* coordinating water molecules. The Zn-O bond lengths of the water ligands are 2.101(2) Å for Zn(1)-O(1) and 2.013(2) Å for Zn(1)-O(2) bond.

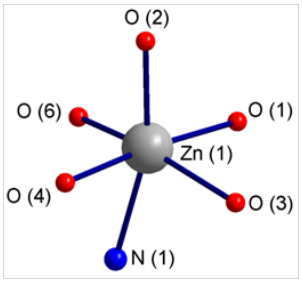

Atom 1	Atom 2	Symmetry code for atom 2	Bond distance [Å]
Zn(1)	O(2)	x, y, z	2.013(2)
Zn(1)	O(1)	x, y, z	2.101(2)
Zn(1)	O(4)	x, y, z	2.119(2)
Zn(1)	N(1)	x, y, z	2.137(3)
Zn(1)	O(3)	x, y, z	2.140(2)
Zn(1)	O(6)	x, y, z	2.162(2)

Fig. 3.82 | Coordination environment of the zinc ion in **6**. The table presents corresponding bond distances.

The [Ar] $3d^{10}$ electron configuration of the Zn^{2+} ion does not result in ligand field stabilisation effects in comparison to transition metal ions and the observed distortion of the coordination environment may be due to sterical restraints of the hda-type ligand. The difference between the longest and the shortest bond involving the Zn(II) ion in **6** is only 0.149(4)Å and the angle created by the N-donor and the O-donor O(2) (N(1)-Zn(1)-O(2)) located on the apexes of the octahedron (as presented in Fig. 3.82) is equal to 163.88(10)°.

Connectivity

The hydrogen bonds play an important role in the connectivity of **6**. They link the mononuclear complex with four neighbouring symmetry-equivalent complexes in the directions of the crystallographic *b*- and *c*-axes.

The first set of hydrogen bonds, which is presented in Fig. 3.83, has a double function: it is responsible for the formation of a 1D chain motif that extends in the crystallographic [010] direction and it contributes to linking this chain motif with its anti-parallel symmetry equivalent.

The growth in the crystallographic *b*-direction is realised *via* two hydrogen bonds that involve the oxygen atom O(8) of a constitutional water molecule, which forms a μ-type bridge

between the O-donor O(2) of a coordinating water molecule and the non-coordinating oxygen atom O(7^{I}) of a symmetry generated carboxylate functional group. The bond distances are 2.693(4) Å for the O(2)-O(8) bond and 2.797(3) Å for the O(8)-O(7^{I}) bond. The symmetry equivalent zinc ions (Zn(1)-Zn(1^{I})) are located 9.532(4) Å from each other.

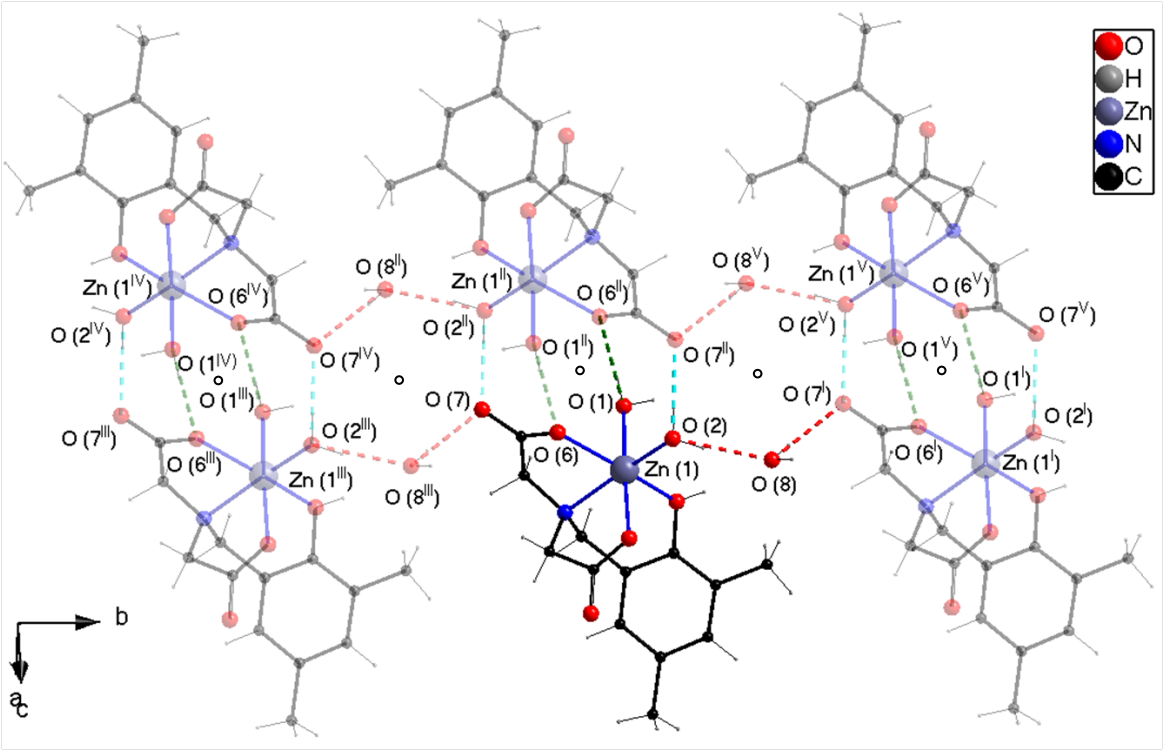

Fig. 3.83 | Hydrogen bonding in **6**.Hydrogen bonds highlighted in the red colour contribute to the growth of a 1D chain motif, while the remaining complementary interactions (green and blue) link mononuclear complexes with their neighbouring symmetry equivalents. Symmetry codes: (I): x, 1+y, z; (II): -z, -y, -z; (III): x, -1+y, z; (IV): -x, -1-y, -z; (V): -x, 1-y, -z.

As presented in Fig. 3.83, there are two pairs of complementary hydrogen bonds that directly link the hydrophilic parts of two symmetry equivalent mononuclear complexes. The first bond connects the O-donor O(2) of a coordinating water molecule with the non-coordinating oxygen atom O(7^{II}) of a symmetry generated carboxylate group. The O-O bond length is 2.614(3) Å. The second hydrogen bond links the O-donor O(1) of a coordinating water molecule to the O-donor O(6^{II}) of a neighbouring symmetry generated carboxylate functionality. The bond distance is 2.938(4) Å. The symmetry equivalent zinc ions Zn(1) and Zn(1^{II}) are located 5.686(2) Å from each other.

Symmetry operations generate H-bound, 6-membered oxygen rings within **6** (again, see Fig. 3.83). Inversion centres are located in the middle of each ring and in the middle between the Zn(1) and Zn(2) ions.

As presented in Fig. 3.84, the mononuclear complex in **6** is connected to its symmetry equivalent in the crystallographic [001] direction through two hydrogen bond interactions. The first interaction occurs between the O-donor O(1) of a coordinating water molecule and the O-donor O(4^{VI}) of a symmetry generated carboxylate group. The bond distance is 2.791(3) Å.

The non-coordinating oxygen atom O(5^{VI}) of the same carboxylate functionality binds to the protonated O-donor O(3) of the aromatic hydroxyl group. A distance of 6.016(2) Å

separates the symmetry equivalent zinc ions Zn(1) and Zn(1^{VI}). The average distance between the aromatic rings in this 1D, H-bound chain motif is *ca.* 5.8 Å and it cannot be considered as a π-π interaction.

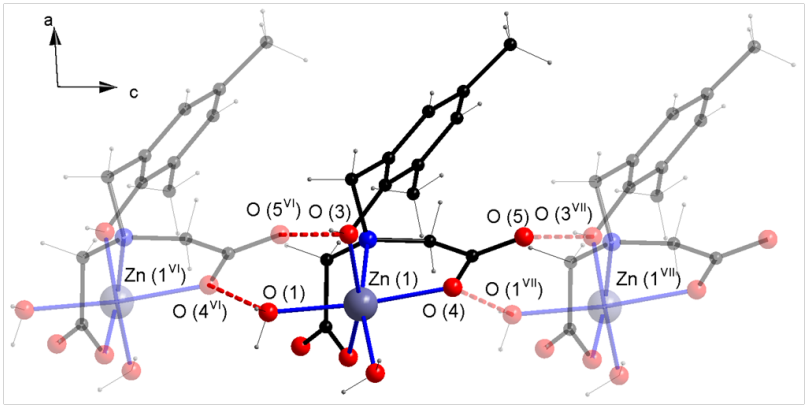

Fig. 3.84 | Hydrogen bonding in **6**. Hydrogen bonds contribute to the formation of a 1D chain motif that extends in the crystallographic *c*-direction. Symmetry codes: (VI): x, -0.5+y, -0.5+z; (VII): x, 0.5-y, 0.5+z.

In summary, the hydrogen bonds link the mononuclear complexes in the crystallographic (010) and (001) directions into a 2D layer that extends in the [100]-plane. This layer, which is presented in Fig. 3.85, is *ca.* 18 Å thick in (100). The thickness of the hydrophilic, H-bound core does not exceed 9 Å (again, in (100)).

The (100) surface of the layer is hydrophobic; it consists mainly of the aromatic rings and methyl substituents of the ligand molecules. The outlook of the layer is similar to the 2D, H-bound layer motifs observed in the copper-containing compounds **3** and **5**.

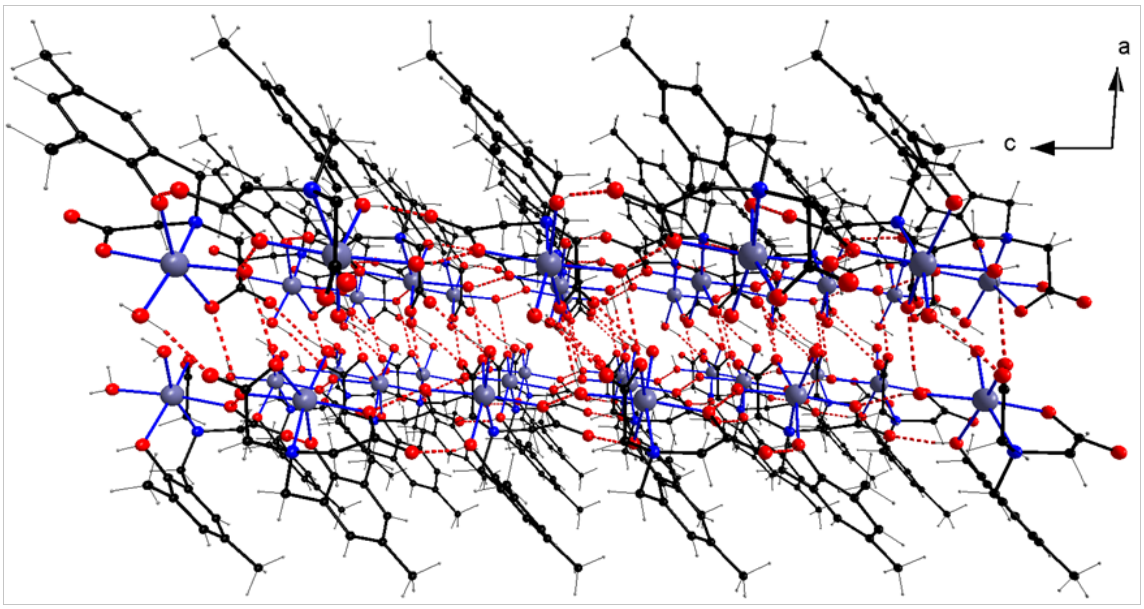

Fig. 3.85 | A H-bound, 2D layer in **6**. Perspective view along the crystallographic *b*-axis.

Packing

The resulting 2D layers in **6** pack in the direction of the crystallographic *a*-axis. The methyl and aromatic moieties of the ligands point in [100] direction and interact with adjacent layers through van der Walls forces and hydrophobic interactions. The layered lamellar structure in **6** is shown in Fig. 3.86 and in Fig. 3.87.

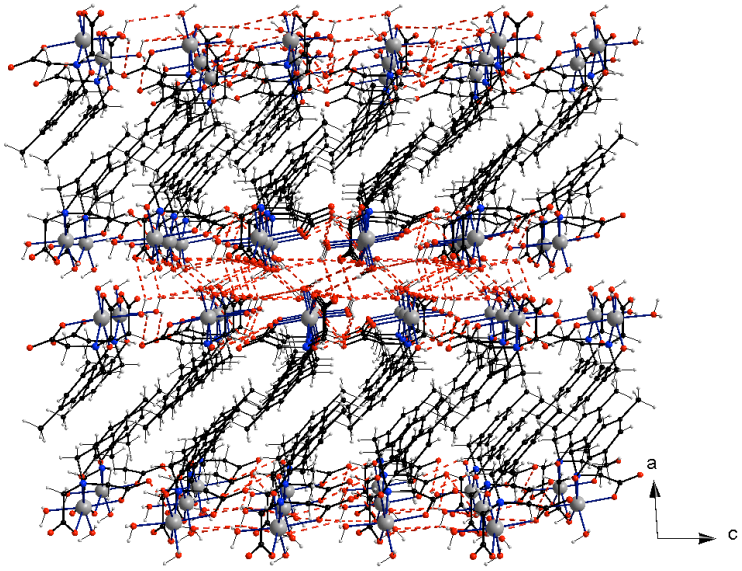

Fig. 3.86 | The perspective view on the packing of compound **6** along the crystallographic *b*-axis shows the assembly of the layers in the direction of the *a*-axis.

The thickness of the hydrophilic areas does not exceed 9 Å and corresponds to the thickness of the hydrophilic cores of each single layer measured in the [100] direction. The hydrophobic areas have a thickness of *ca.* 9 Å (again, measured in the [100] direction). The view on the packing diagram of **6** along the crystallographic *b*-axis (Fig. 3.87a) suggests that the hydrophobic parts of the structure interdigitate with their symmetry equivalents. By viewing the packing diagram in the direction of the *c*-axis (Fig. 3.87b) it is evident that the hydrophobic moieties form a 'zigzag' motif in the *ab*-plane.

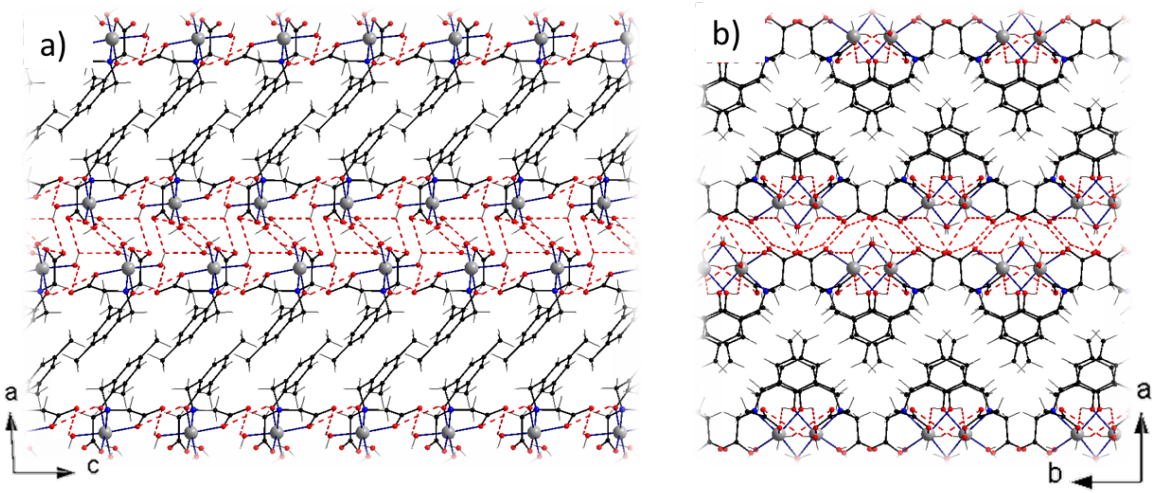

Fig. 3.87 | Packing diagram of compound **6**. **a)** view along the crystallographic *b*-axis; **b)** view along the crystallographic *c*-axis, where the structure forms a characteristic 'zigzag' motif in the *ab*-plane.

The packing structure of **6** is different to the arrangements observed for the previously discussed copper-containing structures. In the case of structures **1**-**5**, the final packing structure has depended on the length of the aliphatic chain of the aromatic ligand; when the chain was too short, compounds adopted a 2D arrangement that was sandwiched between 2D layers of H-bound solvent molecules. Longer hydrophobic chains have enabled hydrophobic interactions and the resulting structures adopt a 3D layered lamellar arrangement. In case of

the Zn-containing structure **6**, a 3D lamellar arrangement is observed despite the fact that the methyl substituent of the aromatic ring, which is located in the *para* position (with respect to the hydroxyl group), is even shorter than the ethyl chain of the C_2vda ligand.

The change in the behaviour of complex **6** arises from the substantial difference between the hda- and vda-type ligands. The hda-type ligands are deprived of the two potential O-donors of the ester functionality, which is present in the vda-type ligands. These oxygen atoms can link the organic ligand with other entities, i.e. metal ions (*via* coordination bonds) or constitutional solvent molecules (*via* hydrogen bonds). In **6** the Me_2hda ligand molecules cannot interact with other molecules in this way, therefore the overall packing structure adopts this layered lamellar arrangement.

Refinement details

The parameters of the refined model of the solid-state structure of **6** based on the single crystal X-ray diffraction experiment are presented in Tab. 3.8.

Tab. 3.8 | Refinement details for compound **6**

Identification code	**6**
Empirical formula	$C_{13}H_{21}NO_8Zn$
Formula weight	384.70 g/mol
Temperature	118(2) K
Wavelength	0.71075 Å
Crystal system	Monoclinic
Space group	$P2_1/c$
Unit cell dimensions	a = 14.779(7) Å α = 90°. b = 9.532(4) Å β = 93.952(6)°. c = 11.047(5) Å γ = 90°.
Volume	1552.5(12) $Å^3$
Z	4
Density (calculated)	1.646 Mg/m^3
Absorption coefficient	1.624 mm^{-1}
F(000)	800
Crystal size	0.6 x 0.1 x 0.1 mm^3
Theta range for data collection	1.38 to 31.06°.
Index ranges	-21<=h<=21, -13<=k<=13, -15<=l<=15
Reflections collected	17246
Independent reflections	4593 [R(int) = 0.0528]
Completeness to theta = 31.06°	92.4 %
Refinement method	Full-matrix least-squares on F^2
Data / restraints / parameters	4593 / 10 / 232
Goodness-of-fit on F^2	0.975
Final R indices [I>2sigma(I)]	R1 = 0.0398, wR2 = 0.0966

R indices (all data)	R1 = 0.0587, wR2 = 0.1520
Largest diff. peak and hole	0.816 and -0.941 e.Å^{-3}

Additional characterization

The P-XRD pattern presented in Fig. 3.88 shows a good correlation (particularly in the low 2Θ range) between the experimental data and the simulated pattern (based on the single crystal X-ray diffraction experiment). This confirms that **6** forms phase pure and that the refined model based on the single crystal measurements is accurate.

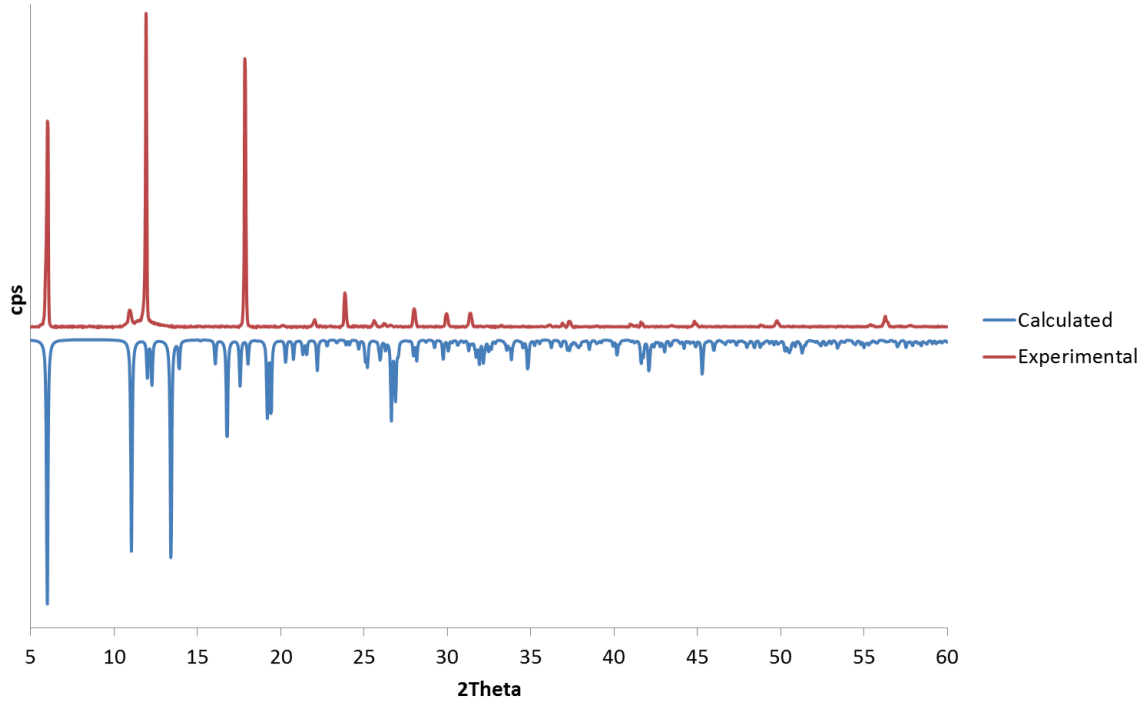

Fig. 3.88 | P-XRD pattern obtained for the crystals of **6** (red) and the simulated pattern calculated for the solid-state structure described above (blue).

3.7.2. Formation of zinc(II) oxide by the thermolysis of **6**.

The thermogravimetric analysis presented in Fig. 3.89 was performed in air at the heating rate of 0.5 °C/min. The thermal degradation starts with the loss of the constitutional water molecule, which occurs immediately after the compound is placed on a balance (due to the constant flow of dry air). This is followed by the loss of two coordinating water molecules forming a completely dehydrated sample at 110 °C (*experimental weight loss:* 12.5%, *theoretical:* 14.0%). The resulting material is stable up to 210 °C and above this temperature a rapid oxidation of the organic ligand occurs. The final product of the decomposition of **6** is zinc oxide, which forms at *ca.* 425 °C (*experimental weight loss: 77.1%, theoretical: 78.8%*)

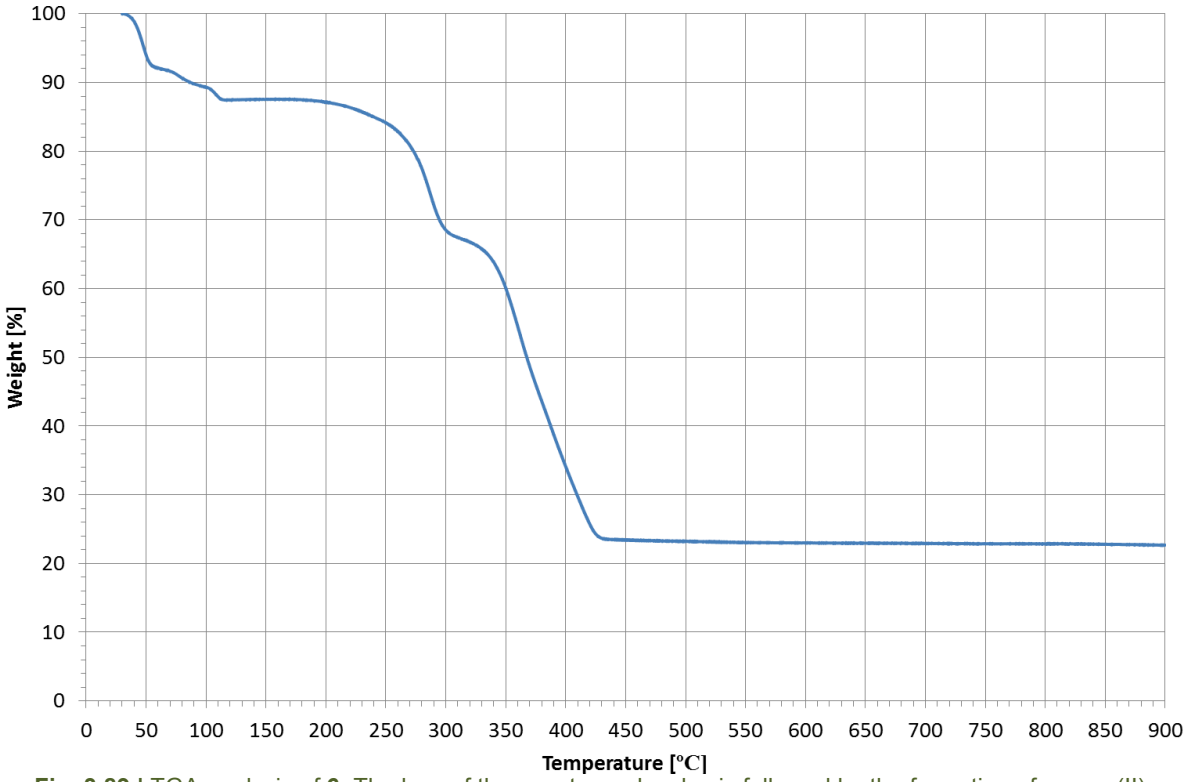

Fig. 3.89 | TGA analysis of **6**. The loss of three water molecules is followed by the formation of copper(II) oxide.

The morphology of the residues was studied using SEM. The images presented in Fig. 3.90 show that during the thermolysis the needle-like crystals of **6** retain their shape and subsequently form fibrous morphologies of zinc oxide. Higher magnification imaging reveals that the fibres are built up from small nanocrystals. Unlike the copper oxide crystals formed during the thermolysis of the coordination compounds **1**-**5**, the diameter of the zinc oxide nanocrystals ranges between 50 and 200 nm. A selection of these nanocrystals displays layered imprints (layers thicknesses vary between 5 and 20 nm). However, this feature is not as for the ZnO crystals.

The EDX analysis (Fig. 3.91) confirms that the residues consist of zinc oxide. The content of zinc is 78.1% (*theoretically*: 80.3%) and for oxygen is equal to 17.9% (theoretically: 19.7%).

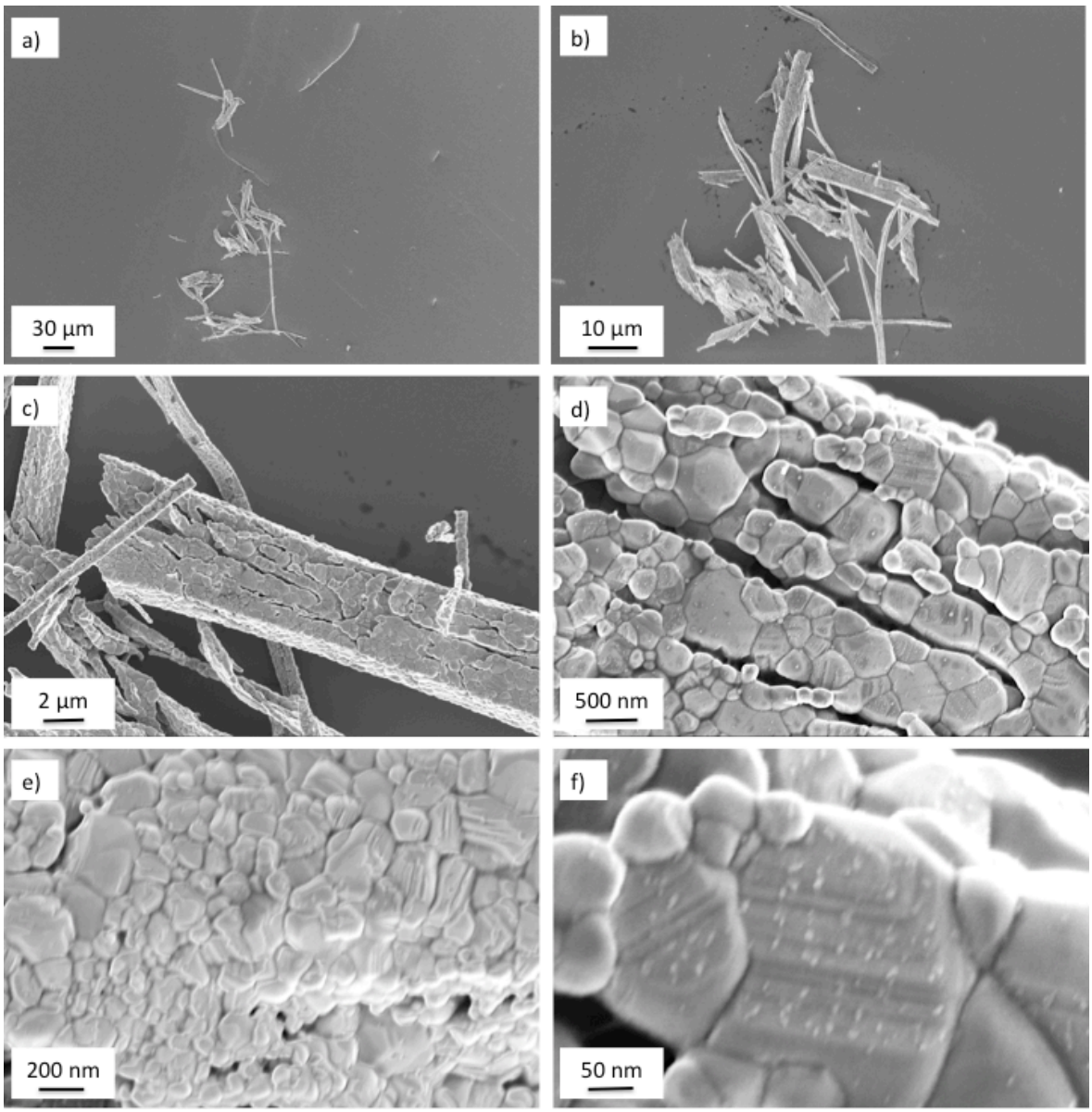

Fig. 3.90 | SEM images of the residual ZnO particles formed during the thermolysis of **6**.

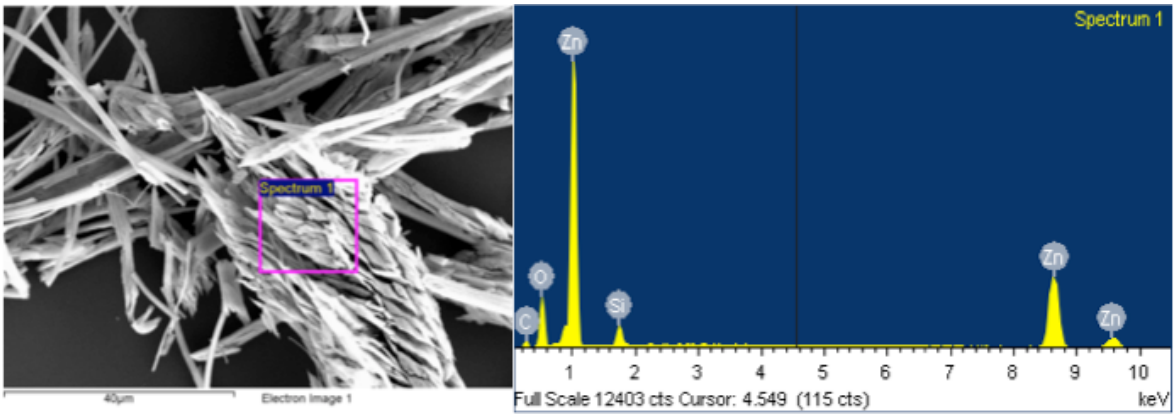

Fig. 3.91 | EDX analysis of the residues that remained after the thermolysis of **6**. Analysis was performed on a carbon-coated sample placed on a silicon surface.

–– CHAPTER IV ––

Ca-containing coordination networks as templates for the synthesis of calcium carbonate

Successful synthesis, characterization and thermal degradation of the coordination compounds described in Chapter III provided us with the motivation and inspiration to explore calcium-containing supramolecular compounds. Calcium is an alkaline earth metal, it belongs to the *s*-block of the periodic table. It is the fifth most abundant element in Earth's crust and its salts, mainly carbonates and phosphates, form hard tissues in a vast array of species.[170] It also plays a major role in the global carbon cycle, in its carbonate form it is used by nature to store excess atmospheric carbon dioxide.[171]

Tissues that form a skeleton are usually composite materials. They are considered to be organic-inorganic hybrids, where the hierarchical organisation and displayed level of order are beyond any man-made material synthesised so far. Deposition of the inorganic phase within these tissues is a genetically controlled process, which has been refined for 500 million years of evolution. It determines the transport mechanisms of amorphous materials (i.e. amorphous calcium carbonate), proper phase selection and nucleation mechanisms.[172] In all of these processes calcium ions interact with proteins, which facilitate or prevent crystallisation or phase change.[173, 174]

The electron configuration of a calcium atiom is [Ar] $4s^2$. The absence of the *d*-subshell means that all of the interactions between a Ca^{2+} ion and a chelating ligand are exclusively of electrostatic nature. There are no additional stabilising effects that could be associated with the ligand field theory.[175]

The hda-type ligands had not previously been reacted with calcium. This was also the case for the new vda-type ligands. The fact that zinc(II), which does not benefit from the crystal field stabilisation, forms the coordination complex with the Me_2hda ligand suggests that the doubly positive calcium ions should behave in a similar manner.

As previously established, *d*-block metal ions react with the hda- and vda-type ligands to form layered, sandwich-like materials, with defined hydrophobic and hydrophilic areas. This formation of a sandwich-like packing structure appears to be directed by the ligands and is independent of the nature of specific element used in a reaction.[61, 176, 177]

Calcium-containing coordination networks based on the hda- and vda-type ligands should display a behaviour similar to the *d*-block metals and self-assemble into layered, lamellar materials. The thickness of the hydrophobic parts of these structures could be controlled by the nature of the aliphatic substituents located on the aromatic ring of a ligand molecule. Upon heating the calcification should be promoted within the hydrophilic parts of

the sandwich-like structures. Thermolysis of these compounds performed in air should result in the calcium carbonate formation followed by the final oxidation to calcium oxide.

It is possible, that similarly to the copper(II) oxide particles described in Chapter III, the $CaCO_3$ crystals obtained in a slow thermolysis process would display a hierarchical organisation, which could be related to the solid state packing structure of the preceding coordination compound. The diversity of possible morphologies is not limited to the layered arrangement, but includes all of the motifs which can be observed within the pre-arranged coordination networks (i.e. honeycombs, 1D fibres, cages, etc.).

4.1. Compound $[Ca_2(Chnida)_2(H_2O)_2] \cdot 4H_2O$ (7)

The first example of a successful formation of a metal-organic compound, which incorporates calcium ions and a hda-type ligand is $[Ca_2(Chnida)_2(H_2O)_2 \cdot 4H_2O$ (**7**). The Chnida ligand was used with the aim to obtain a honeycomb-like structure, similar to the one observed when the ligand was reacted with iron (III) ions (see Fig. 1.13 on page 13).[97] It was anticipated that the theromolysis of the calcium analogue of the interesting compound could lead to the formation of fibrous calcium carbonate nanomaterials that form within single crystals.

4.1.1. Characterization of the structure

The compound $[Ca_2(Chnida)_2(H_2O)_2] \cdot 4H_2O$ (**7**) crystallises as thin, fragile, yellow plates in the monoclinic space group $P2_1/c$. The self-assembly process leads to a complex structure where the calcium ions adopt two distinct coordination environments. The coordination geometries of the metal ions are presented in Fig. 4.1.

Each calcium ion adopts a distorted octahedral coordination environment, where oxygen atoms are supplied by the deprotonated carboxylic acid functions of the Chnida ligands. The N-donor of the iminodiacetic acid moiety is protonated and does not bind to the calcium ions. The hydroxyl group located on the naphthalene ring also remains protonated. These H-atoms were located in the Fourier map and refined.

Compound **7** contains a complicated 3D coordination network, where the Ca^{2+} ions are linked *via* coordination bonds that extend the structure in the direction of the *a*-, *b*- and *c*-axes.

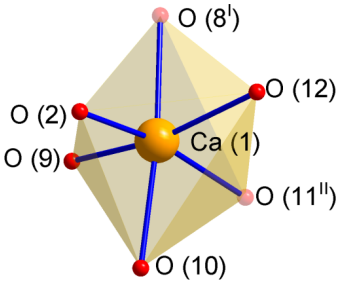

Atom 1	Atom 2	Symmetry code for atom 2	Bond lenght [Å]
Ca(1)	O(9)	x, y, z	2.294(3)
Ca(1)	O(11^{II})	-x, -0.5+y, 1.5-z	2.301(3)
Ca(1)	O(12)	x, y, z	2.322(3)
Ca(1)	O(2)	x, y, z	2.327(3)
Ca(1)	O(10)	x, y, z	2.355(3)
Ca(1)	O(8^{I})	-x, -y, 1-z	2.375(3)

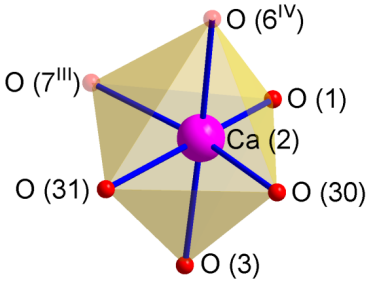

Atom 1	Atom 2	Symmetry code for atom 2	Bond lenght [Å]
Ca(2)	O(3)	x, y, z	2.282(3)
Ca(2)	O(6^{IV})	1-x, -y, 1-z	2.289(3)
Ca(2)	O(7^{III})	1+x, y, z	2.382(3)
Ca(2)	O(31)	x, y, z	2.383(3)
Ca(2)	O(1)	x, y, z	2.388(3)
Ca(2)	O(30)	x, y, z	2.407(3)

Fig. 4.1 | Coordination geometries of the calcium ions in **7**. The tables show the corresponding bond distances.

In case of the Ca(1) ion all O-donors originate from the organic ligand molecules, while for the Ca(2) ion the *cis*-coordinating oxygen atoms O(30) and O(31) are provided by water molecules. The difference between the length of the longest and the shortest bond is equal to 0.081(6) Å for the Ca(1) ion and 0.125(6) Å for Ca(2). The angles formed by the O-donors

located parallel to the elongated apexes of the octahedra are equal to 171.68(10)° for the O(8^{I})-Ca(1)-O(10) and 170.32(10)° for O(6^{IV})-Ca(2)-O(3).

Connectivity

Ca(1) binds to six different organic ligands through six O-donors; each ligand connects three different symmetry related Ca(1) ions through oxygen atoms which originate from carboxylic acid groups of the iminodiacetic acids and the acid group on the naphthalene ring (Fig. 4.2).

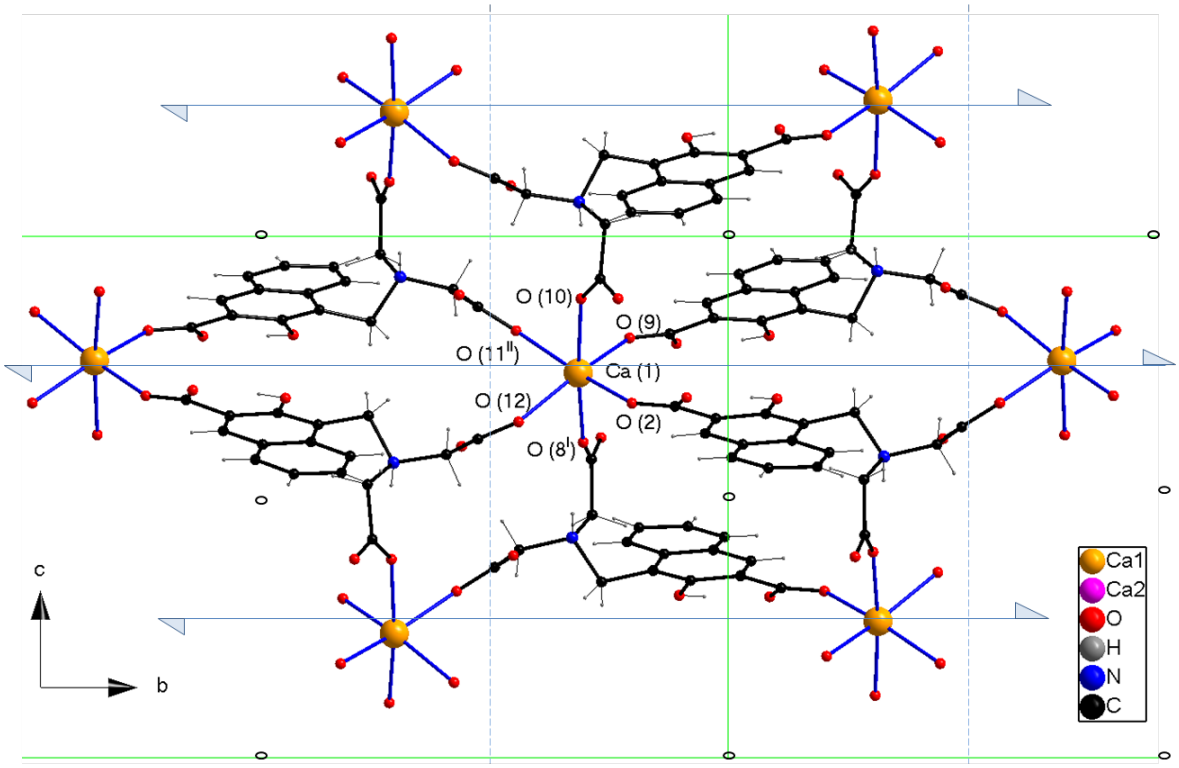

Fig. 4.2 | Coordination environment of Ca1 in compound **7**. The symmetry operations characteristic for the $P2_1/c$ space group are presented for clarity. Symmetry codes: (I) –x, -y, 1-z; (II) -x, -0.5+y, 1.5-z. Green lines correspond to the unit cell walls.

One of the oxygen atoms from each carboxylic groups is involved in these coordination bonds. Bond distances are as follows: Ca(1)-O(9): 2.294(3) Å, Ca(1)-O(11^{II}): 2.301(3) Å, Ca(1)-O(12): 2.322(3) Å, Ca(1)-O(2): 2.327(3) Å, Ca(1)-O(10): 2.355(3) Å, Ca(1)-O(8^{I}): 2.375(3) Å. The distance between two Ca(1) atoms separated parallel to the *b*-axis is 13.249(3) Å. A glide plane is responsible for the shift of half of the unit cell content in [001] direction and 2_1 screw axes, which run parallel to the *b*-axis, turn the positions by 180° and shift the coordinates by half a unit cell length.

There are inversion centres on each corner of the unit cell, in the centre of each cell vector and in the centre of the cell. These symmetry operations create a structure that extends in 2 dimensions parallel to the *bc* plane. The 2D structure can be visualised as two different types of macrocyclic rings which link Ca(1) to six Ca symmetry equivalents. The macrocycles that extend parallel to the *bc*-plane contain each two calcium ions and two ligand moieties. The separation distance between nitrogen atoms in [001] direction is N(1)-N(2): 6.127(5)Å.

The average distance between almost parallel-aligned aromatic rings in this motif is about 4 Å; weak π-π stacking effects may facilitate this arrangement. The packing structure showing the connectivity of Ca(1) and its symmetry equivalents is presented in Fig. 4.2.

Ca(2) binds to four organic ligands through O-donors and to two water molecules situated in *cis* positions (Fig. 4.3). The distances between calcium ions and water ligands are as follows: Ca(2)-O(30): 2.407(3) Å, Ca(2)-O(31): 2.383(3) Å.

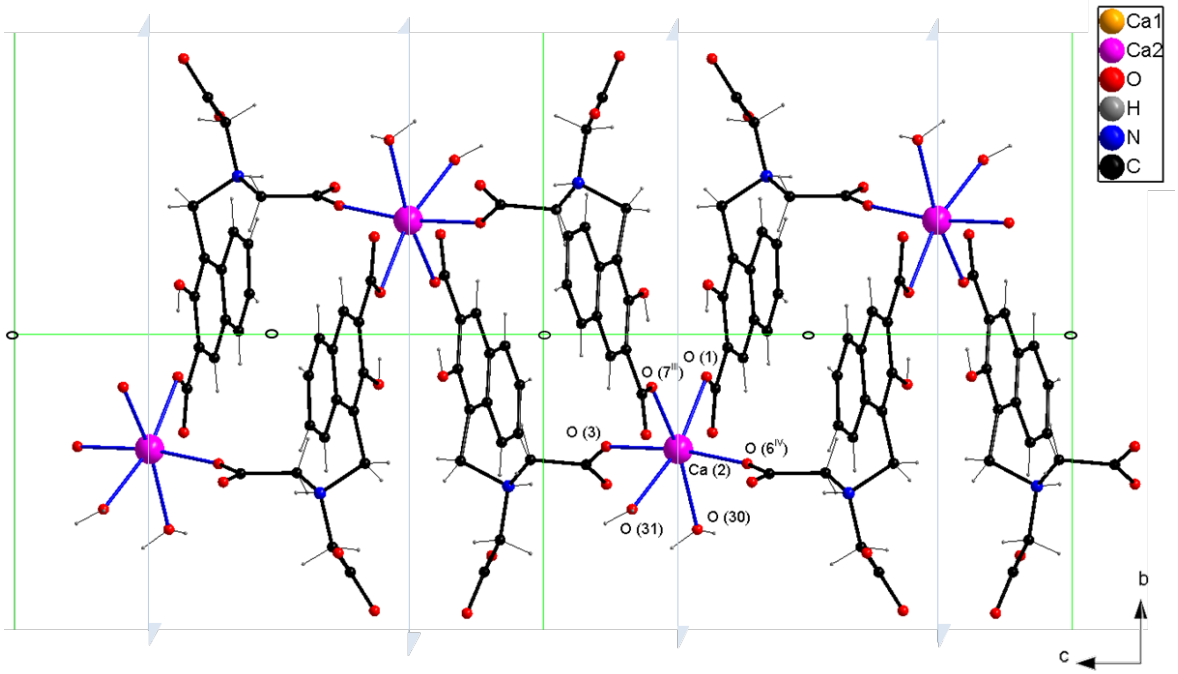

Fig. 4.3 | Coordination environment and connectivity of Ca(2) ions in **7**. View in the direction of the crystallographic *a*-axis. Symmetry codes: (III): 1+x, y, z; (IV) 1-x, -y, 1-z.

The aromatic carboxylate functionality binds through O(1) to Ca(2) and bridges in a μ_2-*syn, syn* bidentate bridging mode between Ca(1) and Ca(2). The same bridging mode is also observed by one of the iminodiactetate carboxylates containing the O atoms O(6) and O(8). O(8) binds to Ca(1) and O(6) binds to Ca(2) whereby bond distances are 2.375(3) Å and 2.289(3) Å, respectively. In a second iminodiacetic acid moiety a similar binding motif is observed. Oxygen atom O(10) binds to Ca(1) with the distance of 2.355(3) Å while O(3) binds to Ca(2) at a bond length of 2.382(3) Å. The remaining carboxylate functionality of the ligand binds through O(2) to Ca(1).

Two ligand molecules and two Ca(2) ions create a macrocycliclic ring-motif which links to its symmetry equivalent ring-motif through Ca(2). The connectivity of Ca(2) is shown in Fig. 4.3. The ligands and the Ca(2) ions form 1D coordination chains that extend parallel to the crystallographic *c*-axis.

Packing

The complete packing structure of **7** is presented. The overall network structure of **7**, presented in Fig. 4.4, is complex and can be considered as layers that extend in the *bc*-plane and contain the Ca(1) ions. These 2D sub-structures are linked through 'Ca(2) bridges' in [100] direction resulting in a 3D network structure. The total charge is balanced by the protonation

of the nitrogen atom on the iminodiacetic acid moiety. The protonation of the N-donor has previously been observed in similar structures.[98] A protonated N-donor cannot bind to Ca^{2+} ions and the ligand cannot chelate as observed in structures **1**-**6.** The protonation of the amino function might be the driving force for the formation of this complicated 3D structure.

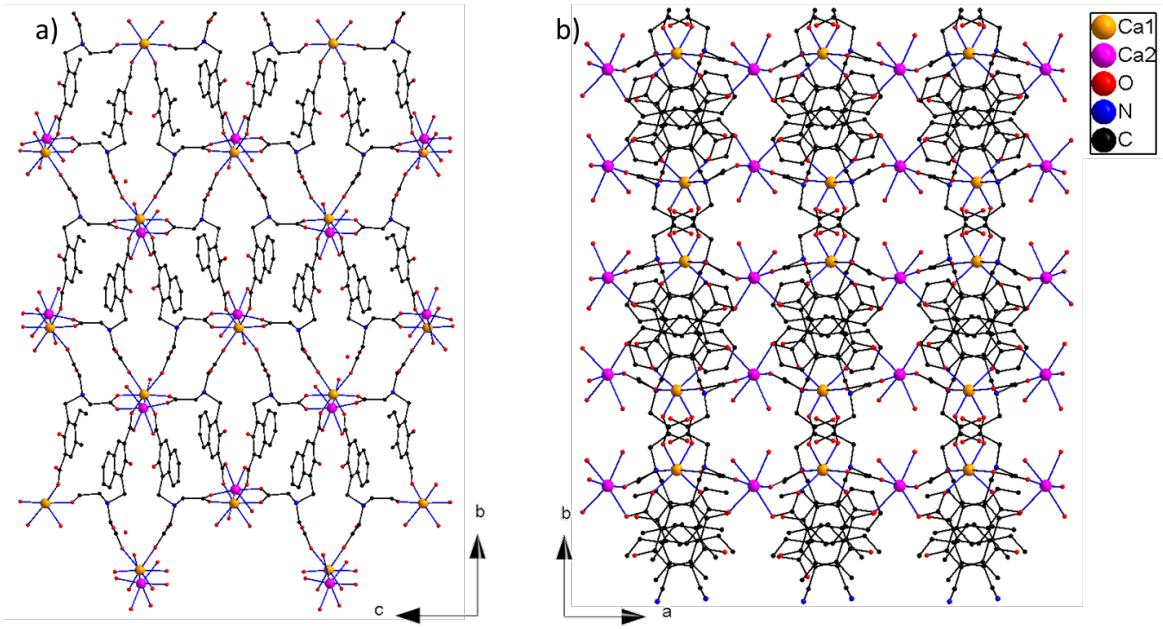

Fig. 4.4 | Packing structure of compound **7**. View along the crystallographic *a*-axis (a) and *c*-axis (b). Hydrogen atoms and solvent water molecules are omitted for clarity.

The packing and network structure in **7** is different to previously observed copper- and zinc-containing sandwich-like structures **1**-**6**. Moreover, the solid-state structure of **7** is different to the Fe(III) honeycomb structure stabilised by this ligand, which was used as a template for the formation of sodium carbonate fibres.[97] The reasons for structural difference can be attributed to the afore-mentioned protonation of the iminodiacetic acid N-donor and the presence of the additional carboxylic acid functionality, located on the naphthalene ring, that forces the ligand molecules to bridge between neighbouring metal ions.

The single crystal X-ray diffraction analysis of **7** proved that the preparation of ordered calcium- iminodiacetic-acid based structures, which display a clearly demarked separation between the hydrophobic and hydrophilic areas, is more challenging than the synthesis of transition metals based assemblies of this type.

Refinement details

The refinement parameters for compound **7** are presented in Tab. 4.1.

Tab. 4.1 | Refinement parameters for compound **7**.

Identification code	**7**
Empirical formula	$C_{32}H_{24}Ca_2N_2O_{20}$
Formula weight	836.69 g/mol
Temperature	150(2) K
Wavelength	0.71075 Å
Crystal system	Monoclinic
Space group	$P2_1/c$
Unit cell dimensions	a = 9.2963(19) Å α = 90.00° b = 26.467(5) Å β = 93.95(3)° c = 14.281(3) Å γ = 90.00°
Volume	3505.4(12) $Å^3$
Z	4
Density (calculated)	1.585 g/cm^3
Absorption coefficient	0.417 mm^{-1}
F(000)	1720.0
Crystal size	0.5 x 0.4 x 0.02 mm^3
Theta range for data collection	1.54 to 24.99°
Index ranges	-6<=h<=11, -31<=k<=31, -15<=l<=15
Reflections collected	25185
Independent reflections	5975 [R(int) = 0.0672]
Completeness to theta = 31.06°	97.0%
Refinement method	Full-matrix least-squares on F^2
Data / restraints / parameters	5975 / 0 / 507
Goodness-of-fit on F^2	1.131
Final R indices [I>2sigma(I)]	R1 = 0.0620, wR2 = 0.1786
R indices (all data)	R1 = 0.0712, wR2 = 0.2017
Largest diff. peak and hole	0.936 and -1.045 $e.Å^{-3}$

Additional characterization

A P-XRD experiment was performed to confirm the phase purity of the bulk sample of **7**. The results were compared with the pattern based on the single crystal data of **7**. The results, presented in Fig. 4.5, confirm that crystals of **7** are phase pure and the refined structural model is accurate. Some reflections are not present in the P-XRD pattern; this can be explained by reminding that **7** forms thin, plate-like crystals, where some particular crystal faces may be not present. The TGA results, presented in Fig. 4.6, show that **7** is relatively unstable and the dehydration processes commence immediately upon exposing the sample to ambient conditions. The loss of constitutional and coordinating water molecules results in the loss of crystallinity and in weakening of the X-ray reflections intensity.

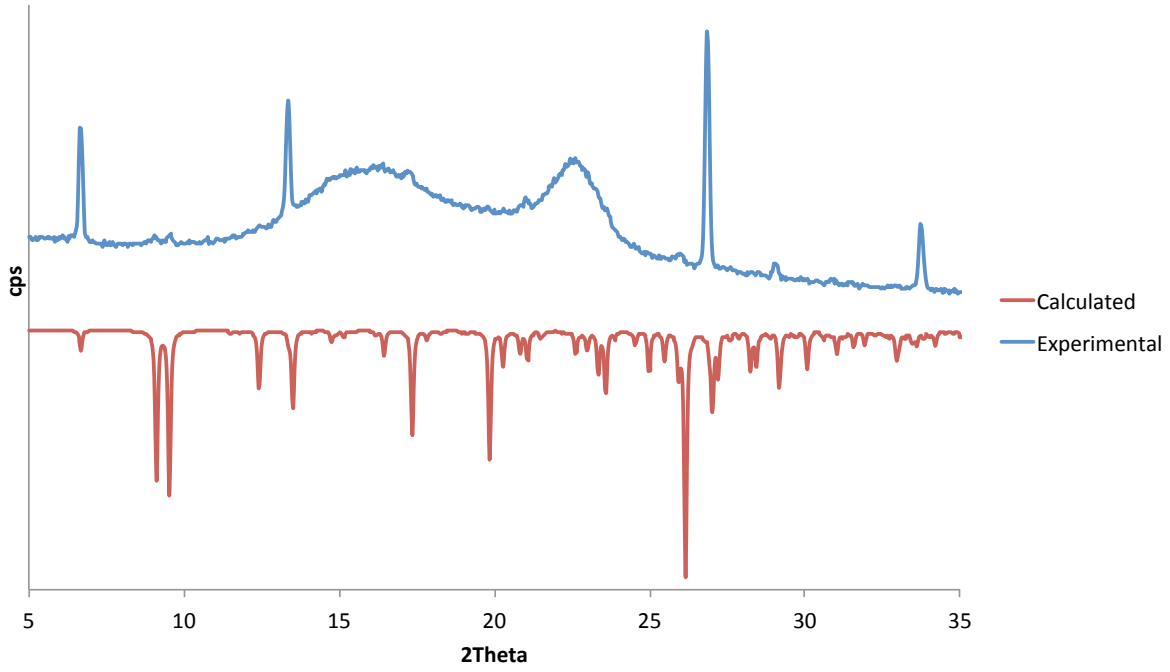

Fig. 4.5 | P-XRD pattern of **7** compared with a pattern calculated based on the single crystal XRD data. The background of the experimental pattern was not subtracted due to a low intensity of several reflections.

4.1.2. Thermolysis of **7**

The thermogravimetric analysis of compound **7** is presented in Fig. 4.6 and was performed in air at the heating rate of 0.5 °C/min. The thermal degradation starts almost instantly following the introduction of the sample into the balance (this is due to the flow of dry air). The loss of constitutional and coordinating water molecules leads to a dehydrated material, which forms at 65 °C and is stable up to 250 °C (*experimental weight loss*: 12.3%, *theoretical:* 12.9%). The dehydration is followed by a slow oxidation of the organic ligand, which occurs between 250 and 670 °C. The final product of the decomposition is calcium oxide, which represents the loss of 93.6% of the original mass (*theoretical*: 93.3%). Theoretical mass loss that would correspond to the formation of $CaCO_3$ is 88.0%, however there are no thermogravimateric steps in the TGA curve that could be associated with this process.

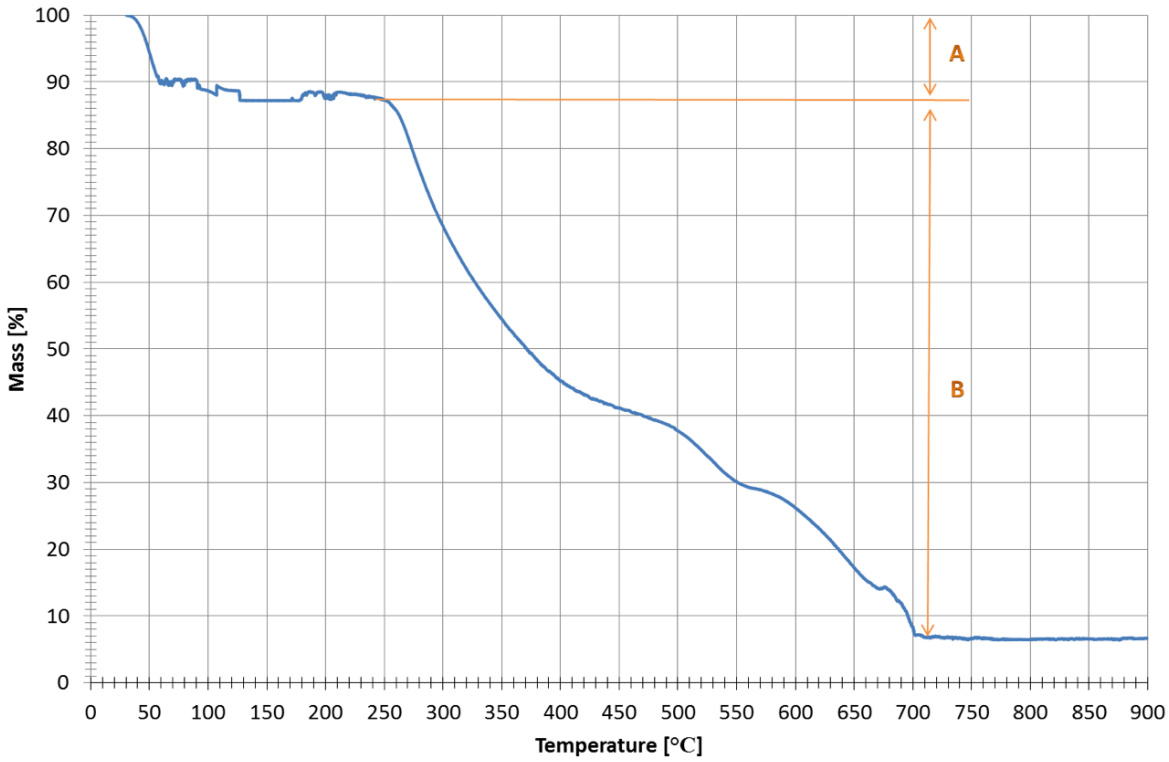

Fig. 4.6 | TGA of compound **7**. A – Loss of the constitutional and coordinating water molecules, B – further degradation of the organic ligand, leading to the formation of calcium oxide.

The residual crystals of calcium oxide were collected and kept under argon to prevent their reaction with water or atmospheric carbon dioxide. A SEM sample was prepared and the crystals were imaged in order to determinate their morphology (Fig. 4.7). The shape of the CaO crystals resembles the plate-like crystals of the original coordination network. They form solid, dense, flat plates, and their dimensions are *ca.* 300 x 200 μm. Higher magnification imaging reveals that the surface of the plates is highly defected and displays many cracks that propagate in random directions. Imaging performed on a nanometer scale shows that the plates are composed of block-like crystals, with dimensions that do not exceed 200 nm. These crystals aggregate in a random manner to give rise to three-dimensional solid assemblies.

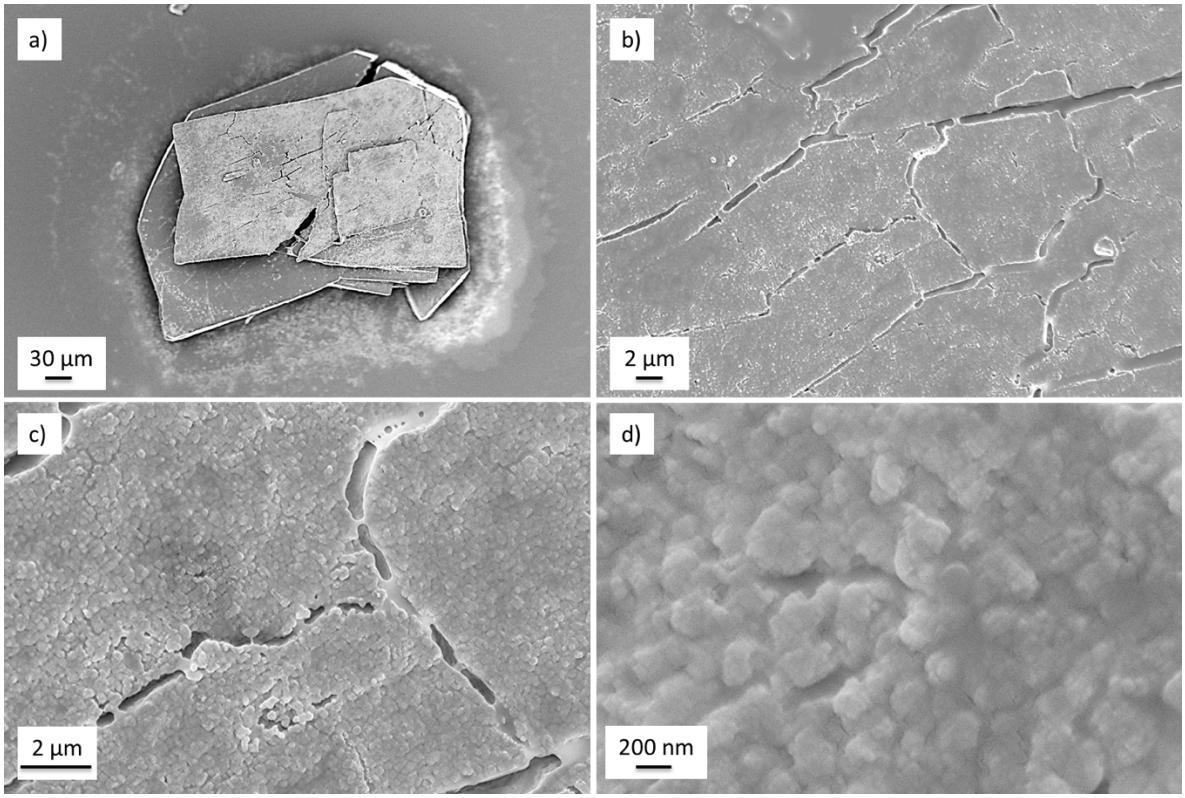

Fig. 4.7 | SEM images of the residual CaO particles that remained after the thermolysis of **7**. **a**) overview picture showing flat, plate-like crystals; **b-c**) higher magnification shows the irregular texture of the surface; **d**) nanocrystals of calcite are visible on the nanoscale.

4.2. Compound [Ca(Me$_2$hda)(H$_2$O)$_3$] ·½H$_2$O ·½MeOH (**8**)

The structural characterization of **7** demonstrated that the Chnida ligand has the ability to form a complicated, three dimensional coordination network when reacted with calcium ions. In an attempt to generate a structure, which would display a separation between the hydrophobic and hydrophilic regions, it was decided to use the Me$_2$hda ligand. This simple complexing agent contains an iminodiacetic acid moiety and a phenolic O-donor, however in contrast to Chnida the additional aromatic carboxyl group is missing.

4.2.1. Characterization of compound **8**

[Ca(Me$_2$hda)(H$_2$O)$_3$] ·½H$_2$O ·½MeOH (**8**) results from the reaction between calcium chloride and the Me$_2$hda ligand. The compound crystallises from a water/methanol reaction mixture to form rectangular plates. **8** crystallises in the triclinic space group $P\bar{1}$. It forms a mononuclear complex, which is linked into one-dimensional coordination chains extending parallel to the crystallographic *a*-axis. Intermolecular hydrogen bonds link the chains into 2D layers that extend in the *ab*-plane. Dispersion forces and hydrophobic interactions promote the assembly of these layers in the direction of the crystallographic *c*-axis to form a 3D sandwich-like lamellar material, where the distinct hydrophobic and hydrophilic areas are clearly separated.

Asymmetric unit

The asymmetric unit of **8** consists of two mononuclear complexes of [Ca(Me$_2$hda)(H$_2$O)$_3$], one free water molecule and one constitutional methanol molecule. Both metal ions adopt a similar coordination environment; the Me$_2$hda ligand provides three O-donors and one N-donor and the irregular coordination sphere is completed by three coordinating water molecules. Only one of these mononuclear complexes, containing the metal ion Ca(1), is described in details below. The second complex, which contains the Ca(2) ion, is crystallographically similar to the first one and does not display any additional features that would be helpful in understanding the overall structure.

The binding mode within the complex is presented in Fig. 4.8, and the coordination geometry around the metal ion is visible in Fig. 4.9.

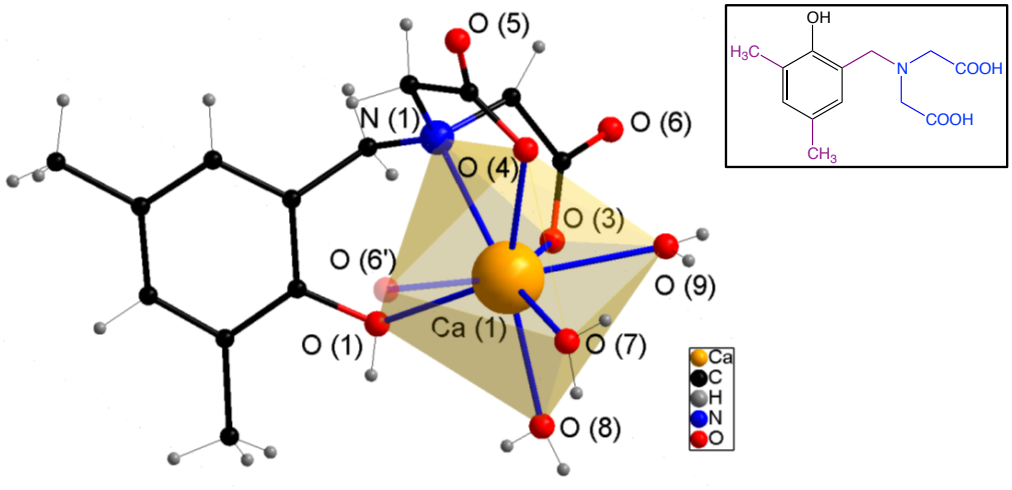

Fig. 4.8 | The mononuclear complex in **8**. Symmetry codes: (I): -1+x, y, z. Inset: the Me_2hda ligand molecule.

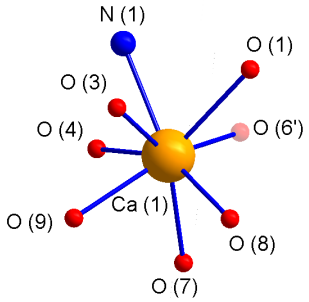

Atom 1	Atom 2	Symmetry code for atom 2	Bond lenght [Å]
Ca(1)	O(6^{I})	-1+x, y, z	2.281(3)
Ca(1)	O(8)	x, y, z	2.392(2)
Ca(1)	O(3)	x, y, z	2.400(3)
Ca(1)	O(4)	x, y, z	2.412(2)
Ca(1)	O(9)	x, y, z	2.498(2)
Ca(1)	O(7)	x, y, z	2.539(3)
Ca(1)	N(1)	x, y, z	2.600(3)

Fig. 4.9 | Coordination environment of the calcium ion Ca(1) in compound **8**. The table presents corresponding bond distances.

The Ca(1) ion adopts an 8-coordinated, irregular coordination environment. The organic ligand binds to the metal ion *via* two O-donors originating from the iminodiacetic acid moiety: O(3) and O(4). The bond distances are equal to 2.400(3) Å and 2.412(2) Å, respectively. The nitrogen atom N(1) is located 2.600(3) Å from the calcium ion. The hydroxyl group attached to the aromatic ring remains protonated (this hydrogen atom was located in the electron difference map and refined) and binds to the metal ion with the distance of 2.698(3) Å. Within the inner octahedral coordination environment, all three coordinating water molecules (O(7), O(8), O(9)) are located in the *facial* position. The bond lengths are as follows: Ca(1)-O(7): 2.539(3) Å, Ca(1)-O(8): 2.392(2) Å, Ca(1)-O(9): 2.498(2) Å.

The symmetry generated oxygen donor O(6^{I}), which belongs to the iminodiacetic acid carboxyl group, is located 2.281(3) Å from the metal ion. As the O-donors O6 and O3 are part of the same carboxylic functionality, they bridge between two neighbouring calcium ions in the μ_2 bridging mode.

Connectivity

The binding mode of one of the iminodiacetic acid carboxylate groups is responsible for the formation of a one-dimensional polymeric chain that extends parallel to the crystallographic *a*-axis (Fig. 4.10).

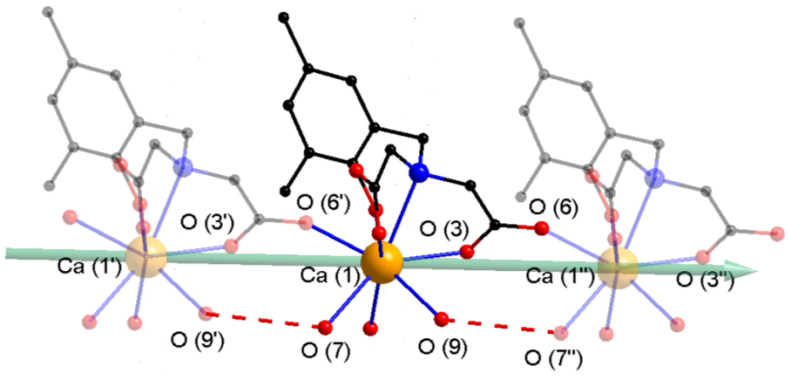

Fig. 4.10 | A 1D coordination chain within **8**. The hydrogen atoms and constitutional solvent molecules were omitted for clarity. Symmetry codes: (I): -1+x, y, z; (II): 1+x, y, z. The green vector points into the crystallographic [100] direction.

The distance between the symmetry equivalent calcium ions Ca(1)-Ca(1^{I}) is 6.265(2) Å. A weak hydrogen interaction that occurs between O(7) of the coordinating water molecule and O(9^{I}) of a symmetry generated coordinating water molecule further stabilises the coordination chain. The distance between the O-donors O(7)-O(9^{I}) equals 3.194(3) Å and may be considered as a weak hydrogen bonding.

There are several additional hydrogen bond interactions within compound **8**, that link each mononuclear complex with two symmetry generated complexes and a constitutional solvent molecule. These interactions are presented in Fig. 4.11.

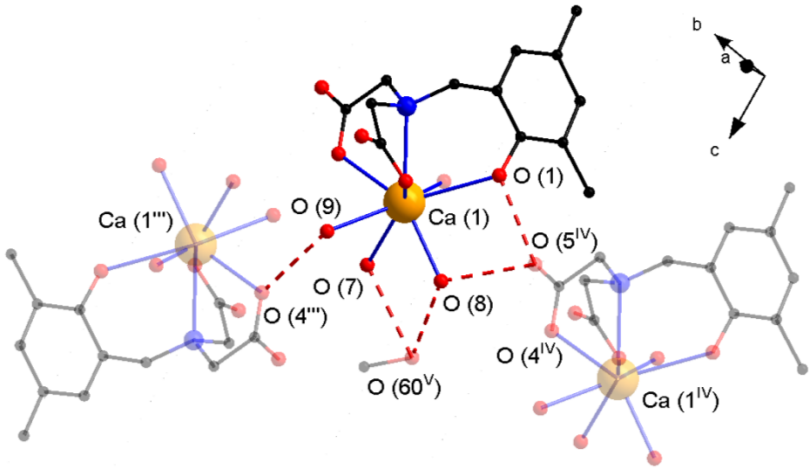

Fig. 4.11 | Hydrogen interactions in **8**. Hydrogen atoms were omitted for clarity. Symmetry codes: (III): 2-x, 1-y, 1-z; (IV): x, -1+y, z; (V): 1-x, -y, 1-z.

O(7) and O(8) of coordinating water molecules bind to a symmetry generated oxygen atom O(60^{V}), which belongs to the constitutional methanol molecule. The bond distances are 2.781(7) Å and 2.784(4) Å, respectively. The O donor of a coordinating water molecule O(8) also binds to the symmetry generated oxygen atom O(5^{IV}) from the non-bridging carboxyl group of the iminodiacetic acid moiety. The bond distance is 2.665(3) Å. The same oxygen atom O(5^{IV}) is linked *via* a hydrogen bond interaction with the hydroxyl O-donor O(1). Both atoms are located 2.648(4) Å from each other.

The final hydrogen bonding occurs between the O-donor of a coordinating water molecule O(9) and a symmetry generated O-donor O(4^{III}), which is a part of the non-bridging iminodiacetic acid carboxylate group. The bond distance is 2.674(3) Å.

The mutual orientation of the two mononuclear complexes within the same asymmetric unit is presented in Fig. 4.12.

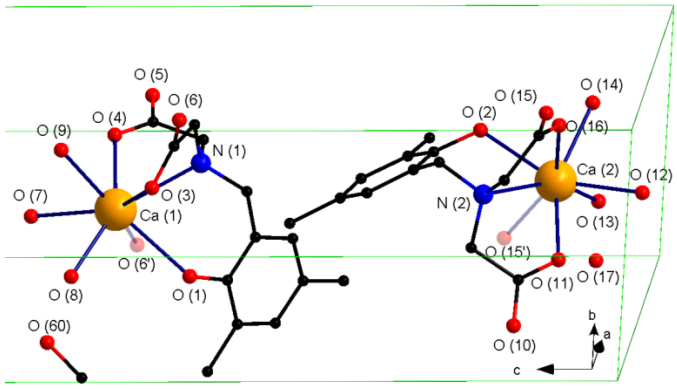

Fig. 4.12 | The asymmetric unit of **8**. Hydrogen atoms were omitted for clarity. Symmetry codes: (I): -1+x, y, z.

The shortest distance between both aromatic rings is 5.402(6) Å and, as anticipated, it cannot be considered to be a weak π-π stacking interaction. Also the angle between the aromatic moieties (equal to 133.73(27)°) does not favour this kind of bonding. However, the aromatic rings may interact through weak hydrophobic interactions to form hydrophobic layers within the packing structure of **8** (see 'Packing').

The coordination sphere that surrounds the Ca(2) ion and the connectivity of the Ca(2)-containing mononuclear complex are very similar to the previously discussed Ca(1)-containing complex. As presented in Fig. 4.13, it consists of three O-donors and one N-donor provided by the ligand, three coordinating water molecules and one O-donor that originates from a symmetry generated iminodiacetic acid carboxyl group (O15^{I}).

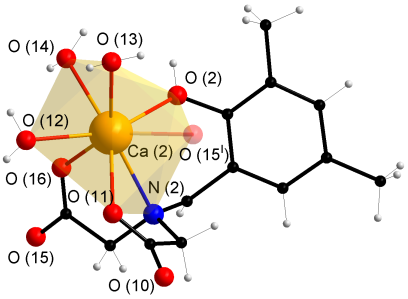

Atom 1	Atom 2	Symmetry code for atom 2	Bond lenght [Å]
Ca(2)	O(15^{I})	-1+x, y, z	2.352(2)
Ca(2)	O(16)	x, y, z	2.396(2)
Ca(2)	O(12)	x, y, z	2.428(3)
Ca(2)	O(14)	x, y, z	2.457(2)
Ca(2)	O(13)	x, y, z	2.461(3)
Ca(2)	O(11)	x, y, z	2.472(2)
Ca(2)	N(2)	x, y, z	2.621(3)

Fig. 4.13 | The second mononuclear complex within the asymmetric unit of **8**.

Hydrogen interactions link the previously discussed 1D coordination chains in the direction of the crystallographic *b*-axis. These bonds, presented in Fig. 4.14, occur between the neighbouring oxygen atoms.

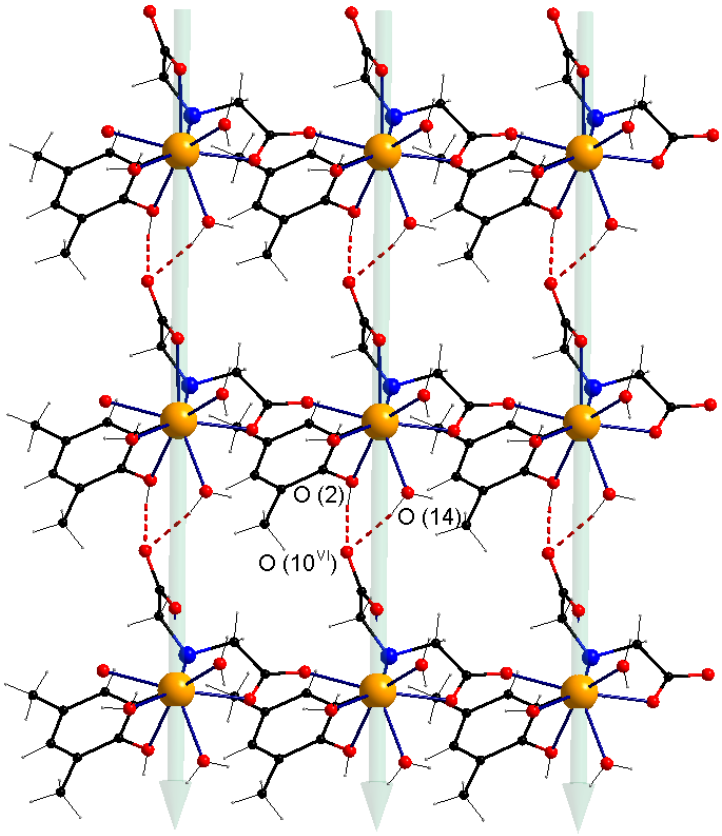

Fig. 4.14 | Hydrogen bonding in **8**. Interactions between symmetry equivalent coordination chains lead to the formation of a layer in the *ab*-plane. The green vectors point in the direction of the crystallographic *b*-axis. Constitutional solvent molecules were omitted for clarity. Symmetry codes: (VI): x, 1+y, z.

The aromatic O-donor O(2) binds to a symmetry generated non-coordinating oxygen atom O(10^{VI}), which belongs to the iminodiacetic acid carboxyl functionality. The bond distance is 2.697(4) Å. The oxygen atom O(10^{VI}) is also connected with the O-donor O(14) from the coordinating water molecule. In this case the bond length equals 2.725(4) Å. These interactions are responsible for the formation of a two dimensional single layer of **8** in the *ab*-plane.

Fig. 4.15 presents the last set of hydrogen interactions that prevail in **8**. The O-donor O(7), which is a part of one of the coordinating water molecules binds to the oxygen atom O(60^{VII}), which belongs to the constitutional methanol molecule. The bond length is 2.781(7) Å. The same oxygen atom (O(60^{VII}) is involved in another interaction with the symmetry generated O-donor O(3^{VIII}), which originates from the iminodiacetic acid functionality. The bond distance equals 2.628(7) Å and the angle between the O(7)-O(60^{VII})-O(3^{VIII}) molecules is 145.32(24)°. Meanwhile the O-donor O(8), which is a part of a coordinating water molecule binds *via* hydrogen interaction to its symmetry equivalent - the oxygen atom O(8^{VII}). These interactions bind two single layers, which were discussed previously, into one double layer that extends in the crystallographic *ab*-plane. The inner hydrophilic area of the layer is 11.073(4) Å thick (measured as a distance between the N(1) and N(1^{VIII}) atoms), while the thickness of the whole double layer, calculated as a distance between the C(8) and C(8^{VII}) atoms located on the outer edge of the structure is 18.660(8) Å.

The distance between the neighboring aromatic rings is 6.265(6) Å. The methyl substituents point towards the outer edge of the layer.

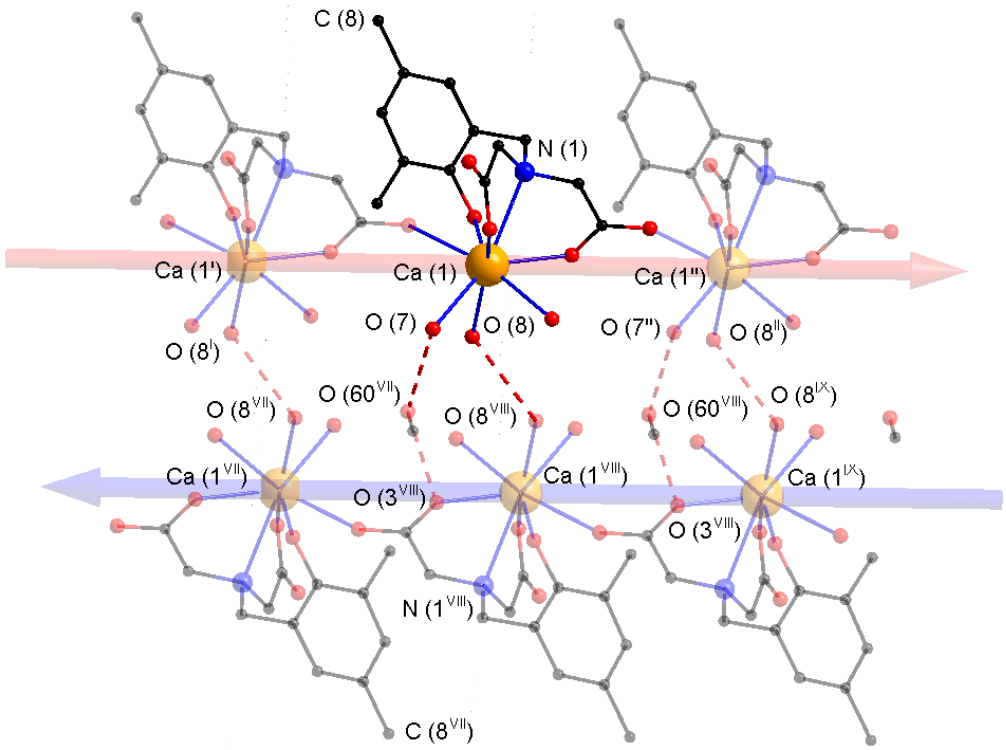

Fig. 4.15 | Two anti-parallel coordination chains linked through hydrogen bonds in **8**. The red vector points in the crystallographic [100] direction, while the blue vector indicates the [$\bar{1}$00] direction. Hydrogen atoms were omitted for clarity. Symmetry codes: (I): -1+x, y, z; (II): 1+x, y, z; (VII): 1-x, -y, 1-z; (VIII): 2-x, -y, 1-z; 3-x, -y, 1-z.

Packing

The two-dimensional double layers that extend in the crystallographic *bc*-plane further self-assemble in the direction of the *c*-axis *via* hydrophobic and van der Waals interactions that occur between the aromatic rings and methyl substituents. This process leads to the formation of a lamellar, hierarchical structure, where the hydrophilic, calcium-containing areas sandwich between the hydrophobic, carbon-enriched parts (Fig. 4.16)

The packing diagram presented in Fig. 4.17 shows the mutual arrangement of the hydrophobic areas of the structure, which is visible in the (100) and (010) planes. While the thickness of the hydrophilic areas is the same as discussed for the double layer, the hydrophobic parts are ca. 9 Å thick.

The solid-state packing structure observed in **8** shows a clear separation between the hydrophilic and hydrophobic areas. This result indicated that **8** may template the formation of calcium carbonate upon thermolysis. Although it is highly unlikely that the observed packing motif gives rise to fibrous $CaCO_3$ material, it is possible that the carbonate residues will display a layered imprint, similar to the one observed in copper-containing compounds **1**-**5**.

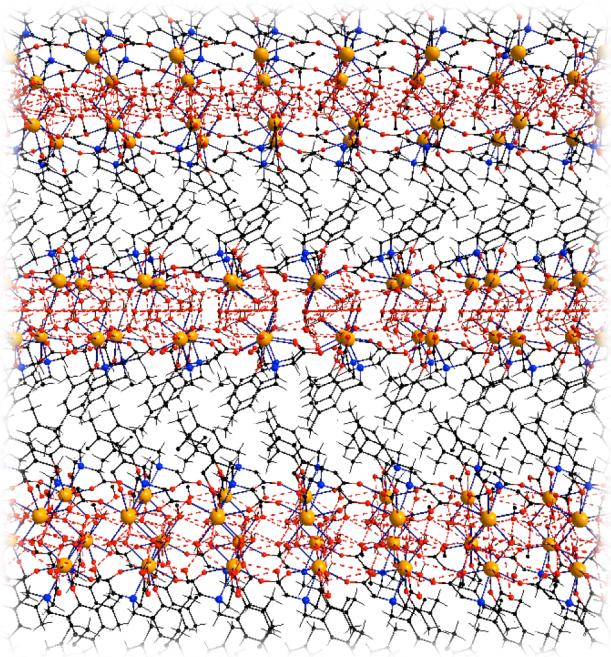

Fig. 4.16 | Layered lamellar structure in **8**. Perspective view along the crystallographic *a*-axis.

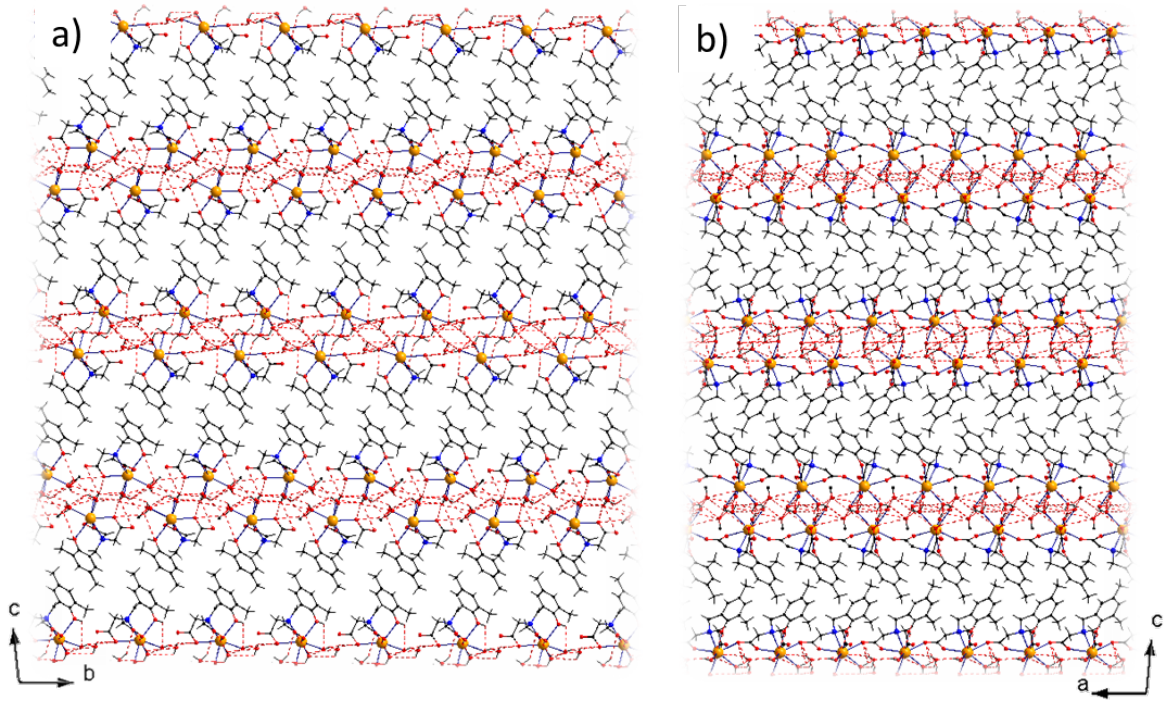

Fig. 4.17 | Packing diagrams of **8**. **a)** View along the crystallographic *a*-axis; **b)** view along the crystallographic *b*-axis.

Refinement details

Tab. 4.2 presents the refinement parameters for compound **8**.

Tab. 4.2 | Refinement parameters for compound **8**.

Identification code	**8**
Empirical formula	$C_{27}H_{42}Ca_2N_2O_{18}$
Formula weight	762.79 g/mol
Temperature	150(2) K
Wavelength	0.71075 Å
Crystal system	Triclinic
Space group	*P*-1
Unit cell dimensions	a = 6.2649(11) Å α = 96.657(4)° b = 8.2062(14) Å β = 94.771(4)° c = 33.649(6) Å γ = 92.072(4)°
Volume	1710.5(5) $Å^3$
Z	2
Density (calculated)	1.481 g/cm^3
Absorption coefficient	0.414 mm^{-1}
F(000)	804
Crystal size	0.80 x 0.05 x 0.05 mm^3
Theta range for data collection	2.45 to 25.86°.
Index ranges	-7<=h<=7, -10<=k<=10, -41<=l<=41
Reflections collected	19742
Independent reflections	6602 [R(int) = 0.0947]
Completeness to theta = 31.06°	99.6%
Refinement method	Full-matrix least-squares on F^2
Data / restraints / parameters	6602 / 17 / 432
Goodness-of-fit on F^2	1.022
Final R indices [I>2sigma(I)]	R1 = 0.0615, wR2 = 0.1629
R indices (all data)	R1 = 0.0767, wR2 = 0.1690
Largest diff. peak and hole	0.749 and -0.858 e.Å-3

4.2.2. Additional characterization

To confirm that the bulk material is phase pure, a P-XRD experiment was conducted and the results were compared with a pattern based on the single crystal X-ray data of **8**. The results presented in Fig. 4.18 confirm that the bulk sample of **8** is phase pure and that the refined structural model is accurate. The absence of certain reflections may be explained by the shape of the crystals (long and thin needles) and the loss of crystallinity due to the drying process, which commences when the bulk sample is exposed to ambient conditions.

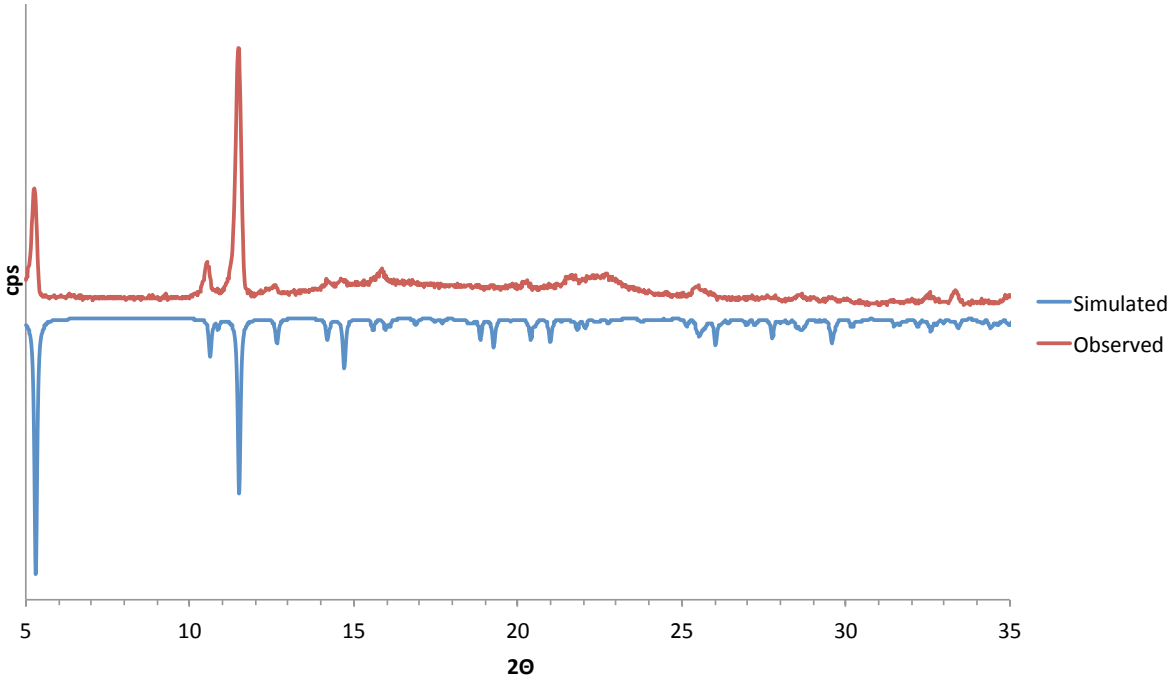

Fig. 4.18 | Comparison between the experimental P-XRD pattern obtained for crystals of **8** (red) and a simulated pattern based on the single crystal X-ray diffraction data (blue).

In a consecutive step, the crystals of **8** were filtrated, rinsed with deionised water and imaged using SEM. As presented in Fig. 4.19, crystals of **8** adopt two distinct morphologies. Most of the crystals form thin (*ca.* 300 nm) and long (above 100 μm) needles that further agglomerate into bunches. As visualised in Fig. 4.19b, all crystals belonging to the same bunch are aligned in the same direction.

The second type of morphology observed for the crystals of **8** is shown in Fig. 4.19c. The coordination compound forms block-shaped crystals that are *ca.* 50 μm long, 5 μm thick and 1 μm high. These crystals also agglomerate; however, the orientation of each individual crystal is random. It is possible that the block-shaped crystals form from the needle-like particles in the Ostwald ripening process.

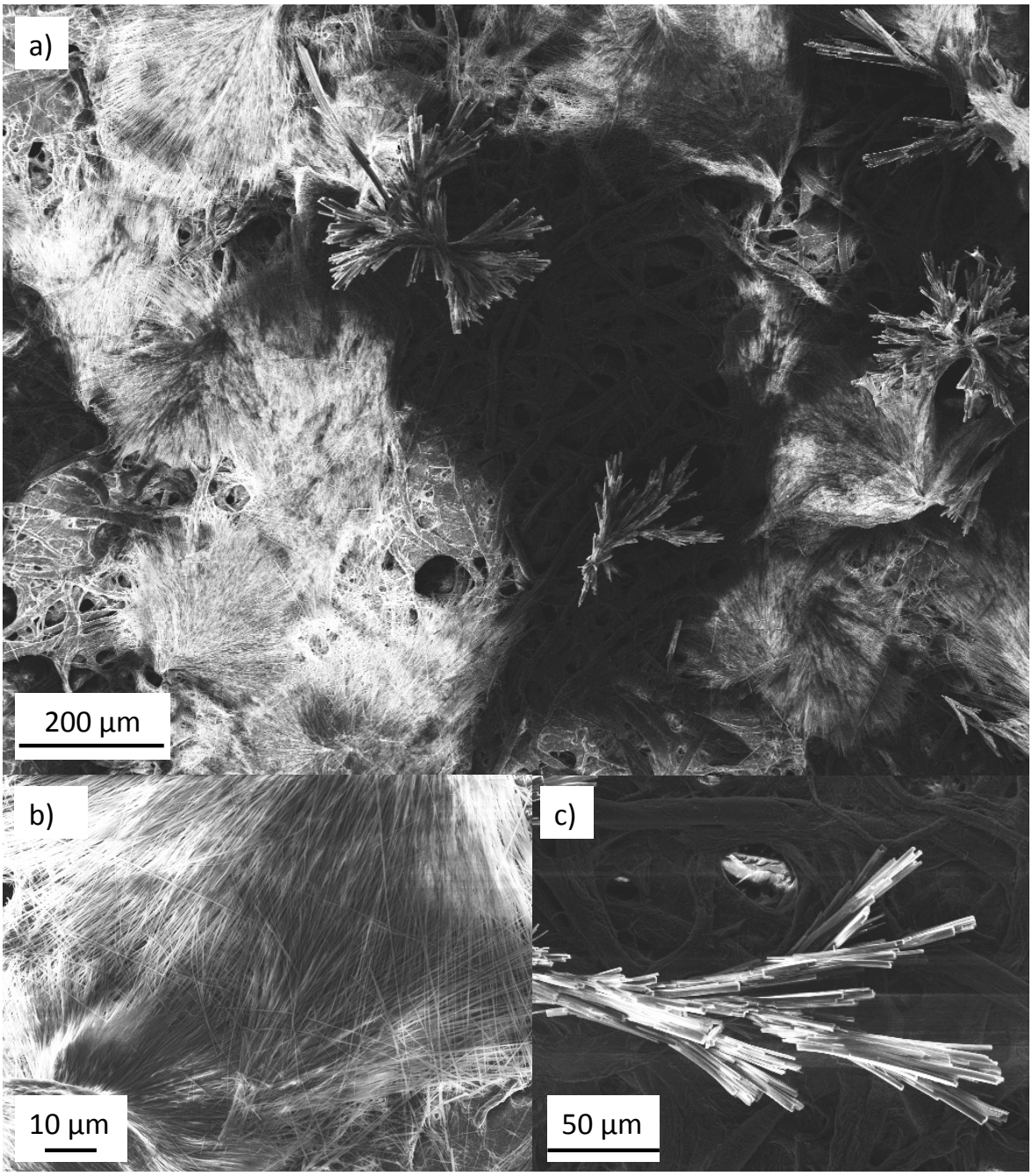

Fig. 4.19 | SEM images of the crystals of **8** located on a filter paper. **a)** An overview picture; **b)** a magnification showing the thin, elongated crystals; **c)** a magnification showing agglomerates of the block-shaped crystals.

4.2.3. Compound **8** as a precursor for the formation of calcium carbonate

The TGA analysis of compound **8** is in agreement with the constitutional assignment and elucidates its thermal degradation pathway. The main transformations are visible in Fig. 4.20. The sample was heated in air with the heating rate of 0.5 °C/min.

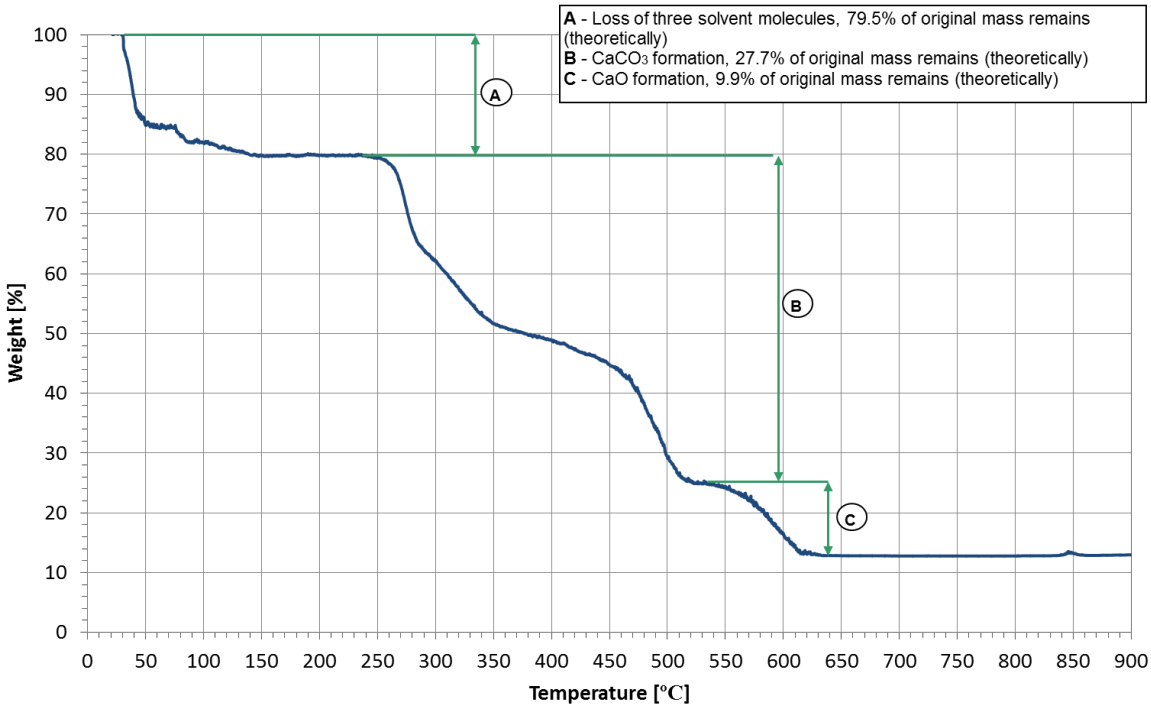

Fig. 4.20 | TGA analysis of compound **8**

The initial step of the thermal decomposition process is the loss of the constitutional solvent molecules, which commences upon exposing the crystals to the flow of dry air. This step is instantly followed by the loss of the coordinating water molecules, leading to a fully dehydrated product. The number of coordinating water molecules calculated from the TGA curve is in agreement with the model based on the single crystal X-ray diffraction experiment. The dehydrated material is observed at 140 °C (*theoretical weight loss*: 20.5%, *experimental*: 20.1%) and is stable up to 260°C. Above this temperature a further loss of mass is observed; this can be associated with a partial decomposition of the organic ligand. The plateau between 350 and 420 °C corresponds to the iminodiacetate calcium salt (*theoretical weight loss*: 55.5%, *experimental*: ~55 %). Further heating results in calcium carbonate crystals which form at 510 °C and which are stable up to 550 °C (*theoretical weight loss*: 74.0%, *experimental*: 73.6%). The final oxidation product is calcium oxide observed above 610 °C (*theoretical weight loss*: 85.4%, *experimental*: 85.8%).

A second sample of **8** was heated in air at 520 °C. The heating rate was decreased to 0.25 °C/min and the residual calcium carbonate was collected and analysed further using P-XRD and SEM techniques. The P-XRD pattern presented in Fig. 4.21 confirms that calcite is the only phase present within the sample.

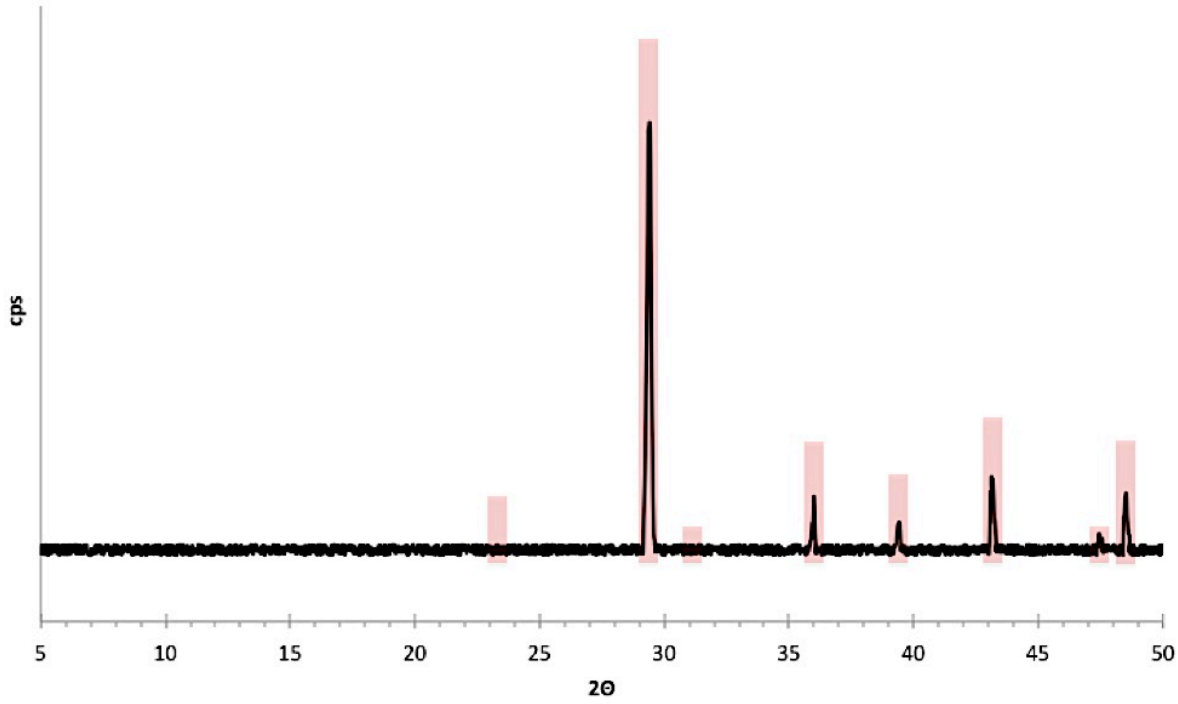

Fig. 4.21 | P-XRD pattern recorded for the residues obtaining by heating **8** in air at 520 °C. The heating rate was 0.25 °C/min. The highlighted areas correspond to the typical positions and intensities of calcite reflections.[178]

SEM micrographs of the residues presented in Fig. 4.22 show that the thermolysed crystals retain their macroscopic shape. On a nanometer scale they are composed of small, irregular nanoparticles (Fig. 4.22d-f, typical diameter *ca.* 100 nm), which aggregate to form elongated, needle-shaped polycrystalline particles. These assemblies are *ca.* 150 μm long and 750 nm thick and further aggregate into bunches. Within these bunches the polycrystalline needles are aligned in the same direction.

The layered imprint noted within the solid-state structure of **8** is not observed for the nanoparticles (Fig. 4.22f). One may speculate that the thickness of the hydrophobic part observed within the packing structure of **8** is not large enough to provide the necessary separation, which could result in the formation crystals with layered morphology, similar to these observed for the residues remaining after the thermolysis of compounds **1**-**6**.

Another experiment was performed, where the coordination compound **8** was pyrolysed by heating to 520 °C in the nitrogen atmosphere. The heating rate was set to 0.35 °C/min. During this process the organic ligand decomposed to form amorphous carbon and calcium carbonate. The residues were analysed by P-XRD which confirmed that calcite is the only crystalline phase present within the sample (Fig. 4.23). The quantity of amorphous carbon within the residues was calculated from the TGA curve that was recorded during the pyrolysis process (Fig. 4.23 right). The weight of the sample at 520 °C is equal to 35.8% of the original mass. As the theoretical weight of $CaCO_3$ is 27.7%, the difference of 8.1% is attributable to amorphous carbon. Further calculations suggest that the amorphous carbon constitutes 22.6% (by mass) of the residues. The results of the elemental analysis confirm these calculations.

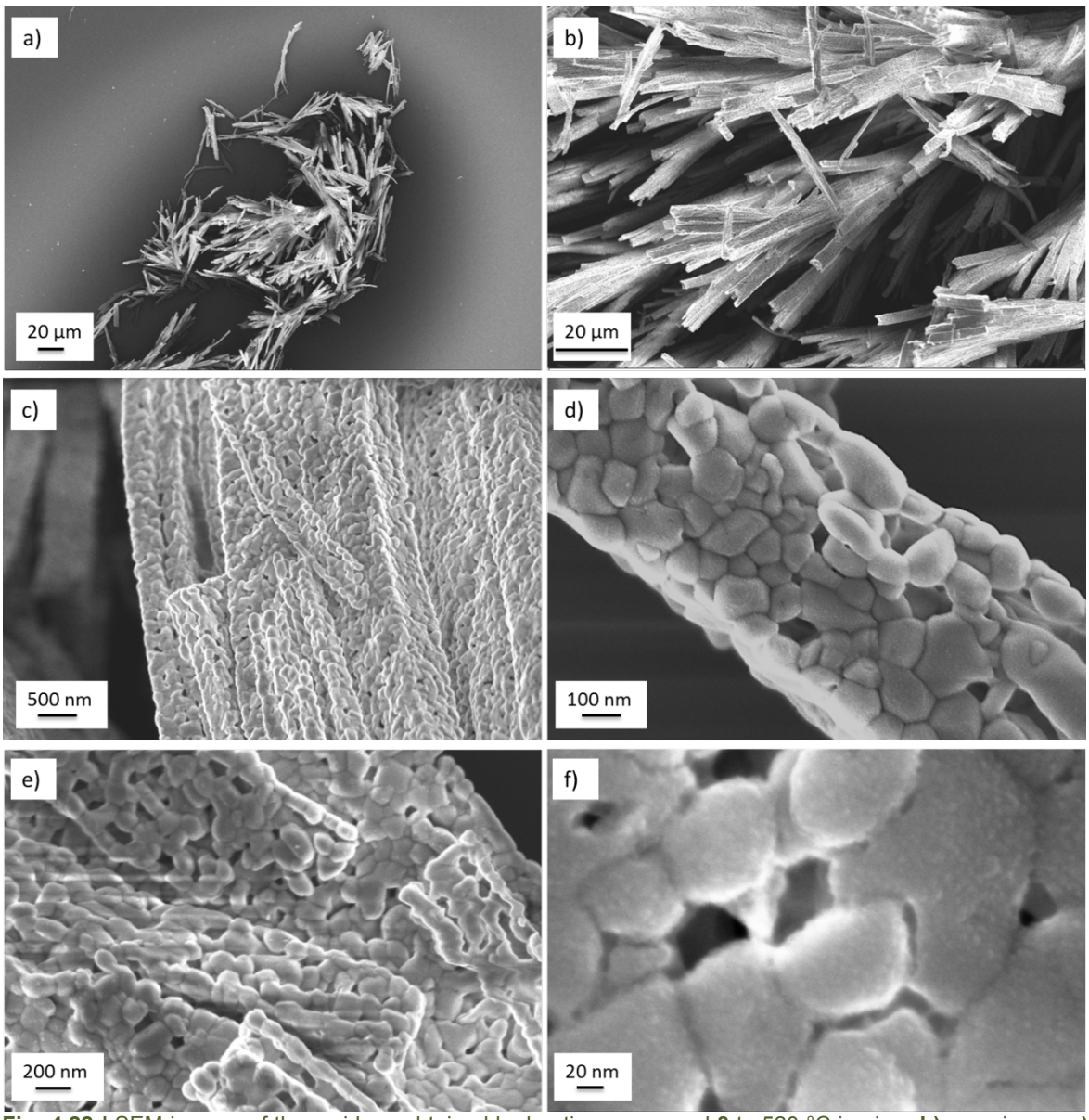

Fig. 4.22 | SEM images of the residues obtained by heating compound **8** to 520 °C in air. **a-b)** overview; **c-e)** higher magnification shows the small nanocrystals, **f)** HR SEM shows the shape of individual crystals. The sample was coated with a 4 nm thick layer of gold prior to imaging.

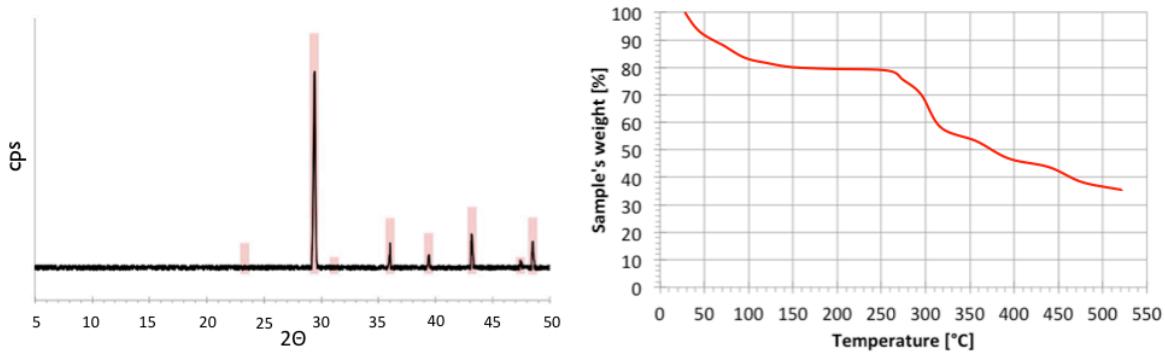

Fig. 4.23 | (**left**) P-XRD pattern of the calcite crystals obtained by pyrolysis of **8** in a N_2 atmosphere. The highlighted areas show the typical position of calcite reflections[178]; (**right**) the TGA curve of **8** recorded in a nitrogen atmosphere.

SEM imaging (Fig. 4.24) confirmed that the needle-like morphology of the calcite crystals obtained under these conditions is similar to that of the agglomerates obtained in air.

The main difference is that the small aggregating nanoparticles, which were randomly orientated to form elongated needle-like polycrystalline assemblies are in this case more aligned. Although in some areas of the sample the agglomerates seem to form a hierarchical arrangement, in most parts of the sample their orientation is rather unidirectional (Fig. 4.24e-f).

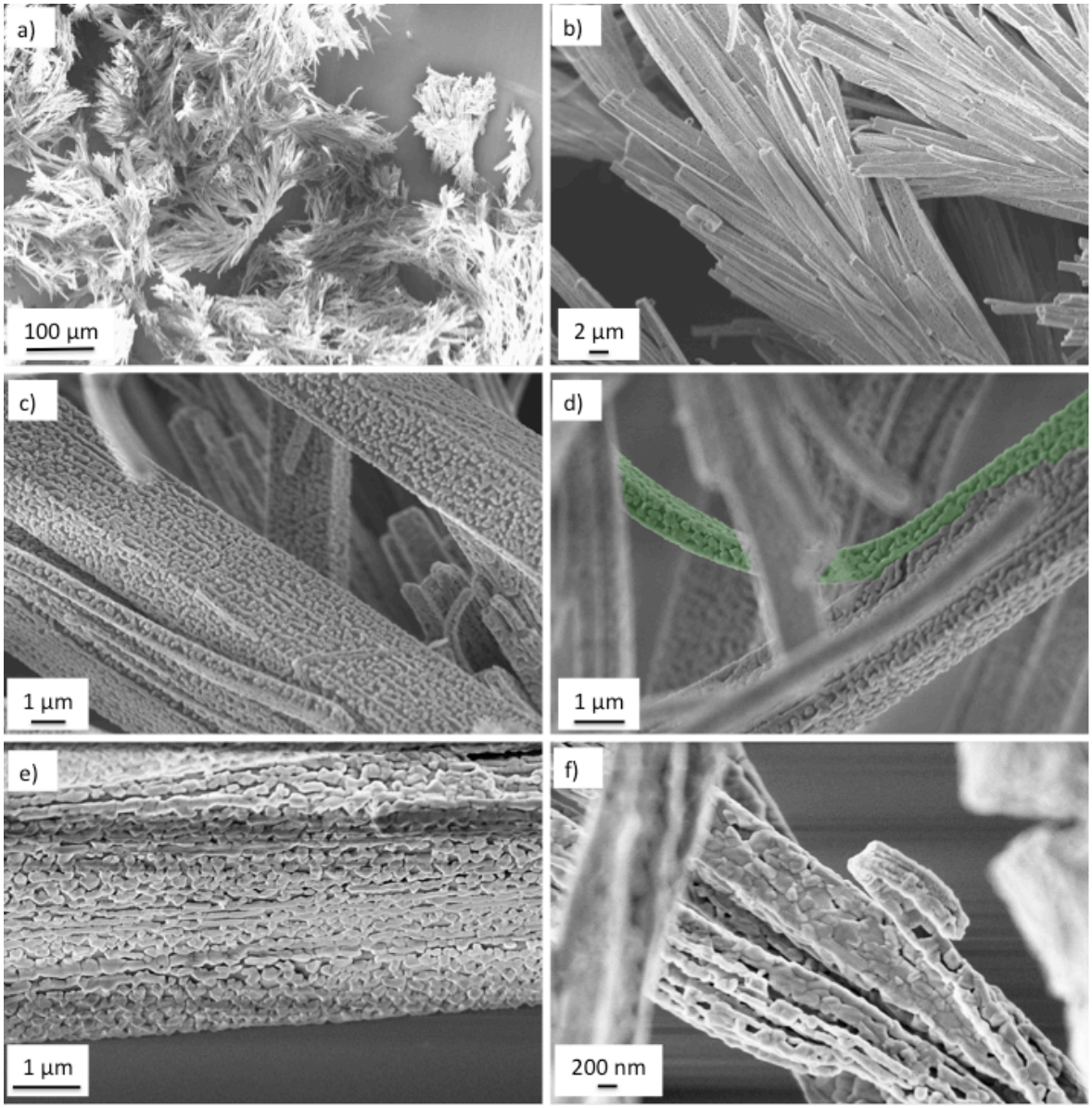

Fig. 4.24 | SEM micrographs showing the calcium carbonate (calcite) crystals, which formed during the pyrolysis of **8** performed in nitrogen upon heating to 520 °C. **a-b)** overview; **c-f)** higher magnification images showing ordered arrangement of the nanoparticles. Image (**d**) highlights the flexibility of this material. Imaging performed on an uncoated sample.

4.3. Compound $[Ca(C_2vda)(H_2O)_2]\cdot H_2O$ (**9**)

Compounds containing the vda-type ligands have not been previously described in the literature. Although their binding mode and packing structure of their mononuclear complexes is expected to be similar to the hda-type ligands, one may anticipate distinct differences as the additional ester group may contribute to the coordination environment, providing additional O-donors. The additional oxygen atoms may be also involved in the formation of intermolecular hydrogen bonds.

4.3.1. Characterization of **9**

Compound $[Ca(C_2vda)(H_2O)_2]\cdot(H_2O)$ (**9**) forms when the C_2vda ligand is reacted with a stoichiometric quantity of calcium chloride in a water/methanol mixture. Slightly yellow block-type crystals form after *ca.* 14 days upon slow evaporation of the solvent. **9** crystallises in a monoclinic space group *C*2/c. The 7-coordinate mononuclear complex of **9** is presented in Fig. 4.25 and consists of one ligand molecule, one calcium ion and two water molecules (O(1), O(2)) that coordinate to the metal ion. The ligand molecules form coordination bridges between neighbouring units to give a 1D chain that extends in parallel to the crystallographic *b*-axis. In addition to this, each asymmetric unit is connected to its symmetry equivalent and extends parallel to the crystallographic *c*-direction *via* hydrogen bonds. These interactions give rise to the formation of a neutral layer of **9** in the *bc*-plane. Further self-assembly along the *a*-axis into 3D sandwich-like lamellar material is facilitated by dispersion forces and hydrophobic interactions between the neighbouring hydrophobic moieties.

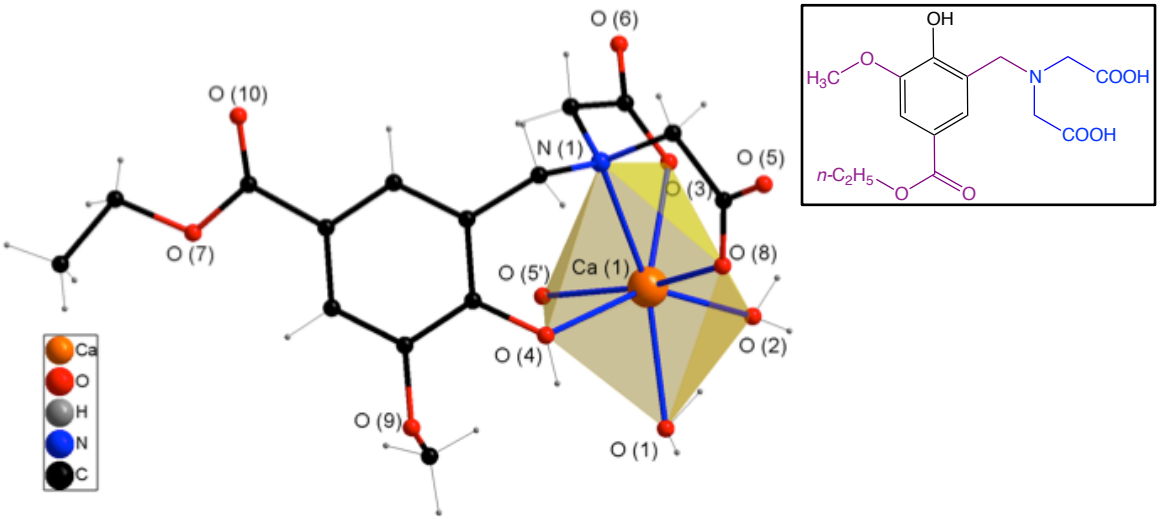

Fig. 4.25 | The mononuclear complex in **9**. Symmetry codes: (I): x, 1+y, z. The coordination environment of the metal ion includes also a symmetry generated O-donor O(5^{I}) that originates from one of the carboxylate groups, which belong to the iminodiacetic acid moiety. The bond distance is equal to 2.274(6)Å. Inset: the C_2vda ligand molecule.

Asymmetric unit

The asymmetric unit in **9** consists of the mononuclear complex and one constitutional water molecule O(1W). The coordination sphere surrounding the metal ion can be described as a pentagonal bipyramide, where the O-donors O(8) and O(5^{I}) are located on the apexes and the remaining N- and O-donors form the equatorial plane (Fig. 4.26).

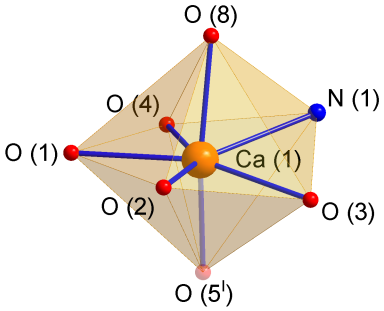

Atom 1	Atom 2	Symmetry code for atom 2	Bond lenght [Å]
Ca(1)	O(5^{I})	x, 1+y, z	2.274(6)
Ca(1)	O(8)	x, y, z	2.324(6)
Ca(1)	O(2)	x, y, z	2.382(6)
Ca(1)	O(1)	x, y, z	2.404(6)
Ca(1)	O(3)	x, y, z	2.436(5)
Ca(1)	O(4)	x, y, z	2.576(6)
Ca(1)	N(1)	x, y, z	2.593(7)

Fig. 4.26 | The coordination environment of the calcium ion Ca(1) in **9**. The table shows the corresponding bond lengths.

The calcium ion binds to the ligand *via* four coordination bonds. Each carboxylate group of the iminodiacetic acid moiety provides one O-donor. The O(8) and O(3) oxygen atoms are located 2.324(6) Å and 2.436(5) Å from the metal ion, respectively. The O-donor of the hydroxyl group, O(4), remains protonated and coordinates the calcium ion with a distance of 2.576(6) Å. The N-donor N(1) is located 2.593(7) Å from the metal ion.

O(1) and O(2) of two coordinating water molecules occupy the *cis* position in the coordination sphere and bind to the central ion with distances of 2.404(6) Å and 2.382(6) Å respectively.

Connectivity

The single crystal XRD experiment provided us with an understanding of the coordination and hydrogen bonds in **9**. These supramolecular interactions are responsible for the formation of ordered assemblies. The most important intermolecular bonds are presented in Fig. 4.27 on page 131.

One of the carboxylate groups originating from the iminodiacetic acid moiety provides two O-donors: O(5) and O(8). While the oxygen atom O(5) binds to the Ca(1) ion, the oxygen atom O(8) binds to a symmetry generated (x, -1+y, z) metal ion. This particular carboxylic group creates a μ_2 bridge that links the symmetry equivalent calcium ions into a 1D coordination chain, which extends parallel to the crystallographic *b*-axis. The angle formed by the carboxylate O-donor O(8), the metal ion and the symmetry generated oxygen atom O(5^{I}) is 161.2(2)°.

As presented in Fig. 4.27, hydrogen bonds that occur between the O-donors and constitutional water molecules link two symmetry equivalent coordination chains into a double-chain. The symmetry generated coordination chain is located anti-parallel to the former one; the 1D assemblies are structurally related by inversion centres located between symmetry equivalent complexes. These symmetry operations generate a hydrophilic layer involving these 1D chain motifs. The resulting double layer arrangement is stabilised by a

number hydrogen bond interactions between neighbouring 1D chain motifs. The average thickness of the hydrophilic layer is *ca.* 8.5 Å (calculated as the distance between the hydroxyl group donor O(4) and its symmetry equivalent O(4^{III}: 0.5-x, -0.5-y, 1-z))

O(2) of the coordinating water molecule is linked *via* a hydrogen bond to the oxygen atom O8(III), which belongs to the coordination bridge-forming carboxylate group. The bond length is 2.732(10) Å. The constitutional water molecule O($1W^{II}$: x, -1+y, z) is involved in two hydrogen bond interactions: the first interaction is directed towards the coordinating water molecule O(2) (distance: 2.769(9) Å) and the second interaction points to the O-donor O(3), which is part of the non-bridging carboxylate group of the iminodiacetic acid moiety. The distance between the O($1W^{II}$) and the O(3) atoms is 2.819(8) Å.

The coordinating water molecules O(1) and O(2) are connected *via* an intramolecular hydrogen interaction. In this case the bond length is 2.908(9) Å (for clarity this bond is not visible in Fig. 4.27).

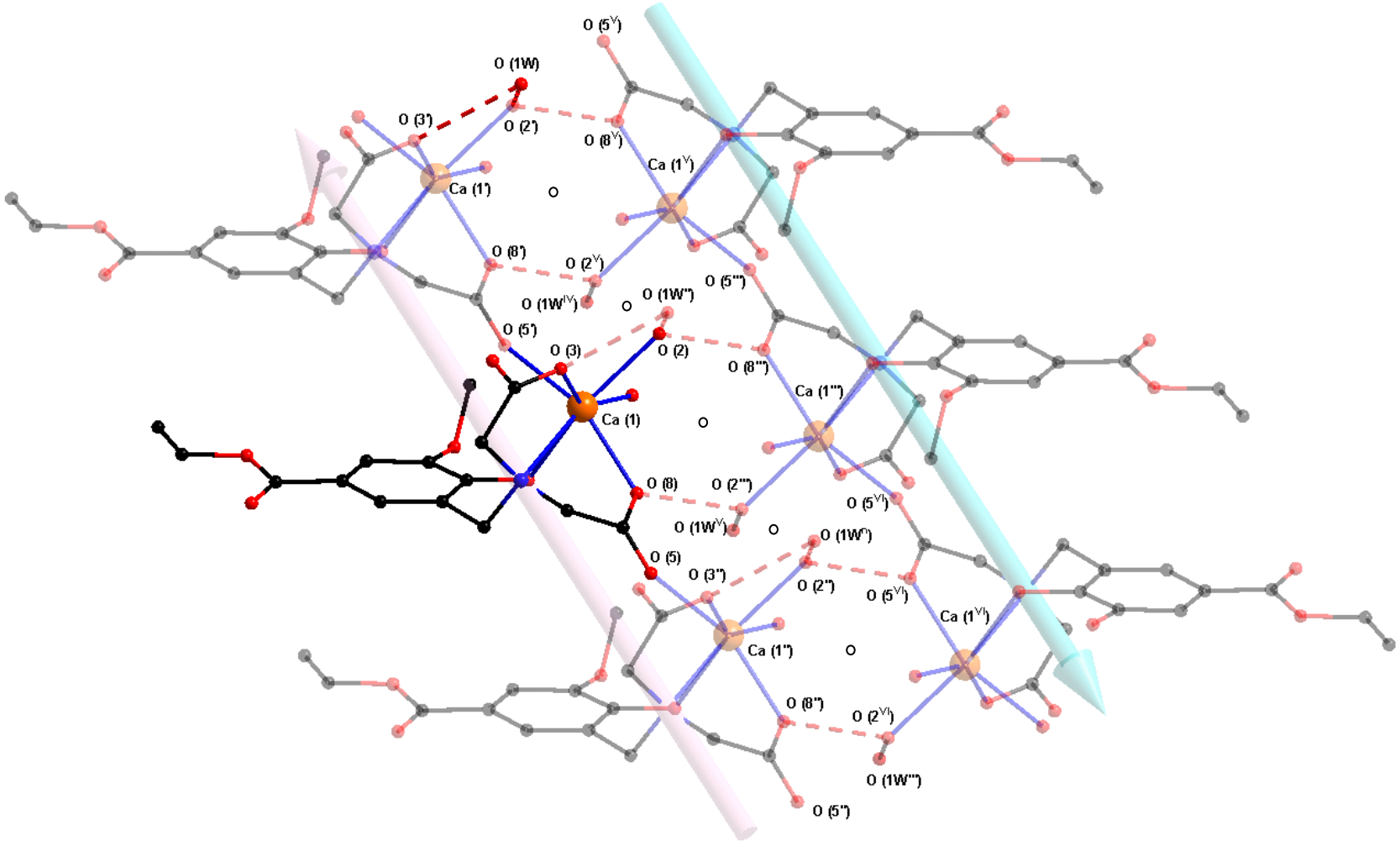

Fig. 4.27 | Coordination bonds and hydrogen bond interactions in **9**. The vectors indicate the crystallographic (010) (rose) and (0$\bar{1}$0) (blue) directions. Symmetry codes: (I);

The next set of hydrogen bond interactions in **9** is responsible for the
hydrogen-bonded chain that extends parallel to the crystallographic *c*-axis
non-coordinating oxygen atom O(6), which belongs to the non-bridging carb
the iminodiacetic acid moiety, binds the symmetry generated coordinating
O(1^{VII}: x, -y, 0.5+z). The O(6)-O($1V^{II}$) bond length is 2.742(7) Å. O(6) is
formation of a hydrogen bond with O(4) of the hydroxyl group. This group re
despite its contribution to the calcium ion coordination sphere (the hydroge
binds to the oxygen atom O(4) was found and refined on the electron density
(O(4)-O($6V^{III}$)) is 2.632(9) Å long.

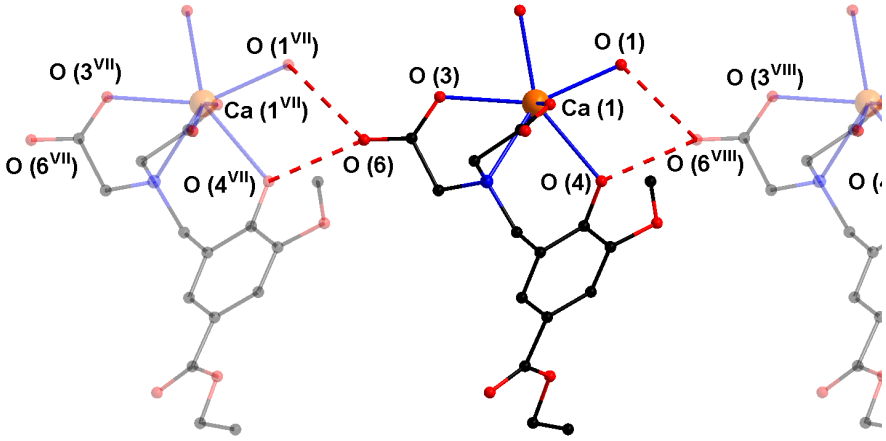

Fig. 4.28 | Hydrogen bonds link mononuclear units into a 1D assembly that exte
crystallographic *c*-axis. Hydrogen atoms were omitted for clarity. Symmetry codes:
(VIII): x, -y, -0.5+z.

The hydrogen-bound chain, presented in Fig. 4.28, displays a symmet
for the *C*2/c space group. The view along the crystallographic *a*-axis reveals t
which is parallel to the [001] direction, forms a mirror image of the preced
complex and shifts it by ½ of the *c*-vector length to form a subsequent unit
Fig. 4.29.

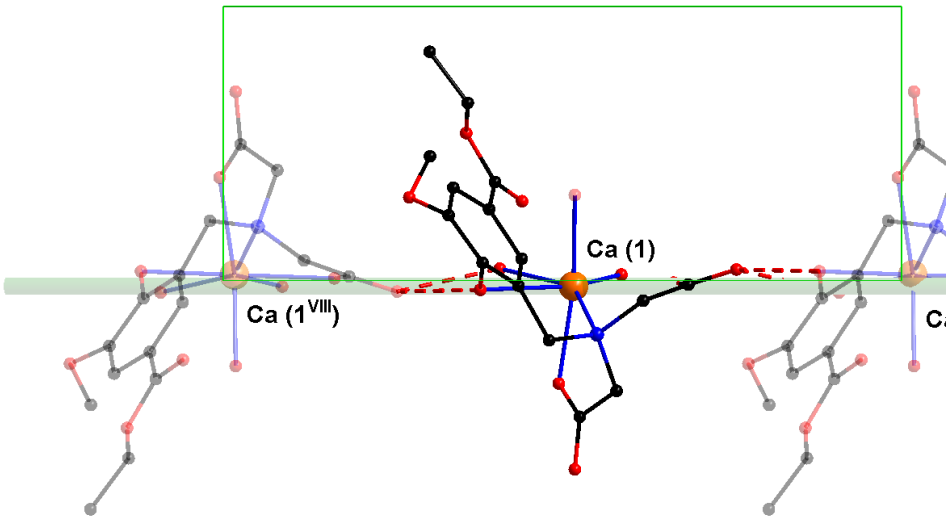

Fig. 4.29 | The hydrogen-bonded chain viewed along the crystallographic *a*-axis. The gr
the [101] glide plane. Symmetry codes: (VII): x, -y, 0.5+z; (VIII): x, -y, -0.5+z.

Packing

The packing of **9** is complex due to the coordination bonds and hydrogen interactions. The crystallographic studies show that **9** assembles into a lamellar material, where the hydrophilic and hydrophobic parts are well separated.

The initial assembly is realised *via* coordination bonds, which link mononuclear complexes into 1D chains that extend in the direction of the crystallographic *b*-axis. The previously discussed hydrogen bonds enable further assembly in the direction of the *c*-axis, which results in the formation of neutral 2D layers in the crystallographic *bc*-plane. The core of these layers contains metal ions, water molecules and hydrophilic O-donors, while the outer areas are composed mainly of hydrophobic parts of the ligand molecules.

The final assembly process occurs in the direction of the crystallographic *a*-axis, where the hydrophobic edges of the neutral layers interact *via* hydrophobic and van der Waals forces. This leads to the formation of a lamellar material, where the hydrophilic, metal containing layers are sandwiching between the hydrophobic, carbon-containing areas (see Fig. 4.30 and Fig. 4.31).

The average thickness of the hydrophobic layers is 12 Å, while the lattice separation distance is *ca.* 24 Å long.

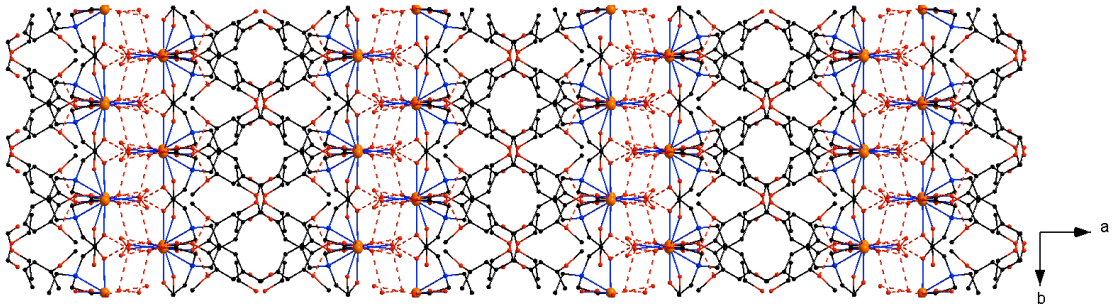

Fig. 4.30 | Packing structure of **9** viewed along the crystallographic *c*-axis. Hydrogen atoms were omitted for clarity.

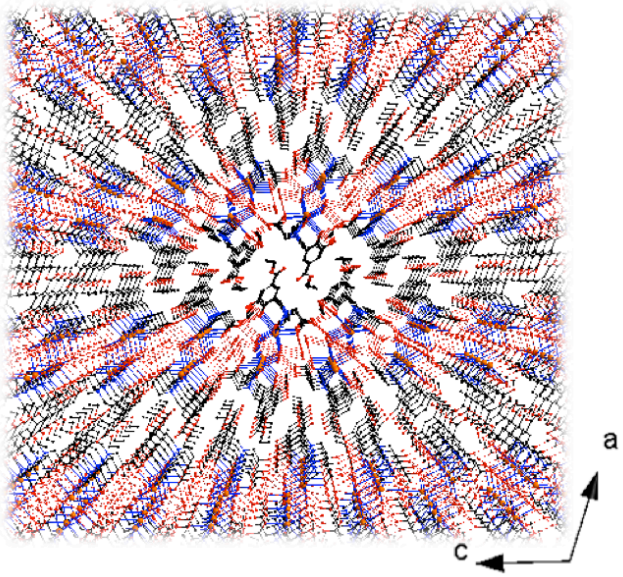

Fig. 4.31 | Perspective view on the packing structure of **9** viewed along the crystallographic *b*-axis. The neutral layers are visible on the *bc*-plane.

Refinement details

The refinement parameters for **9** are presented in Tab. 4.3.

Tab. 4.3 | Refinement parameters for compound **9**.

Identification code	**9**
Empirical formula	$C_{15}H_{23}CaNO_{11}$
Formula weight	433.42 g/mol
Temperature	150(2) K
Wavelength	0.71073 Å
Crystal system	Monoclinic
Space group	*C*2/c
Unit cell dimensions	a = 36.174(7) Å α = 90°. b = 6.4649(13) Å β = 108.60(3)°. c = 16.863(3) Å γ = 90°.
Volume	3737.6(12) $Å^3$
Z	8
Density (calculated)	1.540 Mg/m^3
Absorption coefficient	0.397 mm^{-1}
F(000)	1824
Crystal size	0.5 x 0.4 x 0.3 mm^3
Theta range for data collection	1.19 to 25.00°.
Index ranges	-42<=h<=42, -7<=k<=7, -20<=l<=19
Reflections collected	15019
Independent reflections	3273 [R(int) = 0.1013]
Completeness to theta = 25.00°	99.4 %
Absorption correction	Semi-empirical from equivalents
Max. and min. transmission	0.826 and 0.888
Refinement method	Full-matrix least-squares on F^2
Data / restraints / parameters	3273 / 22 / 255
Goodness-of-fit on F^2	1.320
Final R indices [I>2sigma(I)]	R1 = 0.1152, wR2 = 0.3003
R indices (all data)	R1 = 0.1487, wR2 = 0.3470
Largest diff. peak and hole	0.951 and -1.248 $e.Å^{-3}$

Additional characterization

P-XRD diffraction experiments were performed to confirm the phase purity of the bulk material. The results were compared with a pattern simulated based on the single crystal X-ray diffraction data. As presented in Fig. 4.32, most of the strongest calculated reflections are present in the experimental P-XRD pattern. This result suggests that the bulk sample is phase pure. The absence of certain reflections can be related to the loss of constitutional water

molecules, which occurs instantly after a fine powder is prepared for the powder X-ray diffraction experiment.

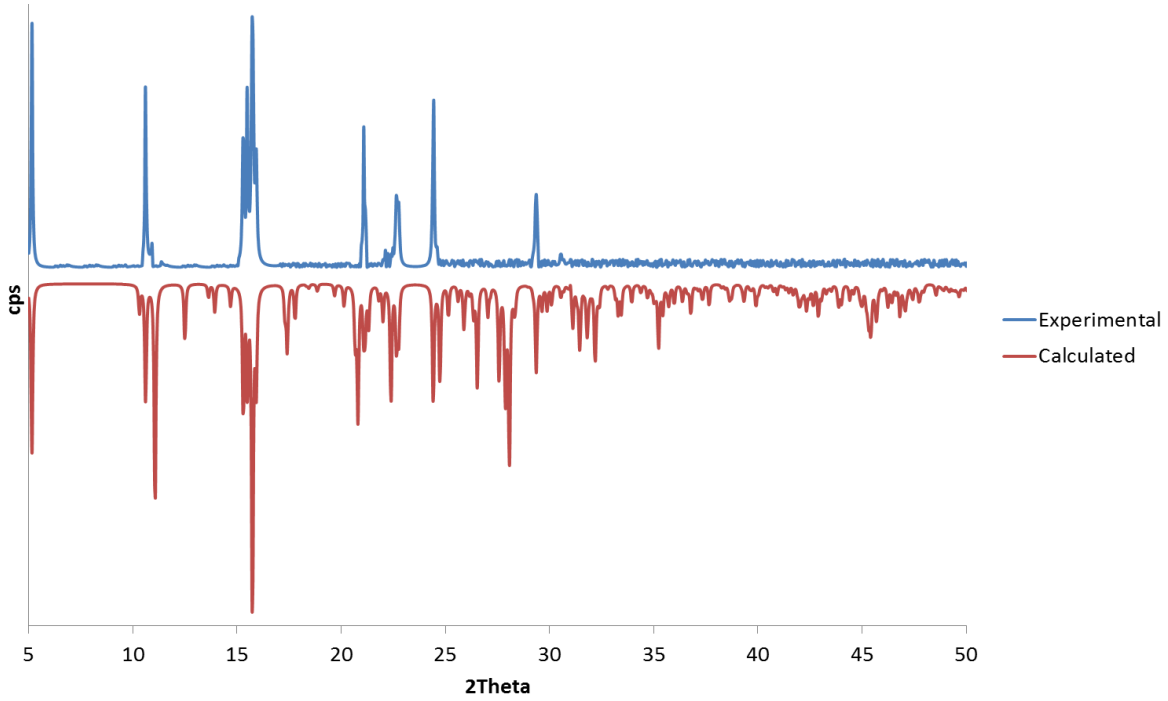

Fig. 4.32 | P-XRD pattern obtained for crystals of **9** (blue) compared with a simulated pattern based on the single crystal X-ray measurements (red).

4.3.2. Self-assembly of **9**

The chemical reaction between the C_2vda ligand and calcium ions is sensitive to molar concentrations of the reagents as well as such reaction parameters as the pH or temperature. Single crystals of **9** can be grown when the solvent mixture consists of 5 ml of methanol and 5 ml of water and the pH is slightly above neutral (~7.5, adjusted with TEA). When the ratio between two solvents is changed to 2:8 (methanol/water) the morphology of the material can be altered and the molecules of **9** self-assemble into fibrous, almost amorphous material.

Due to the weak X-ray diffraction of the fibrous assemblies it was not possible to obtain a good quality P-XRD pattern, which could be further compared with the pattern of the crystalline phase. It was necessary to confirm the chemical composition of the fibres by other methods.

Elemental analysis

Tab. 4.4 presents the comparison between the elemental analyses of the crystalline phase and the fibrous assemblies. The experimental values confirm that the materials have the same composition and are in agreement with the composition of **9**.

Tab. 4.4 | Comparison between the results of the elemental analyses of the assembles and the crystalline phase of **9**.

Element	Theoretical abundance [%]	Experimental result for the crystalline phase [%]	Experimental result for the assemblies [%]
C	43.37	43.24	43.11

H	5.10	5.17	5.21
N	3.37	3.32	3.26
Ca	9.65	9.61	9.58

Thermogravimetric analysis

Thermolysis of the assemblies was performed in air. The heating rate was set to 1 °C/min and the obtained results are presented in Fig. 4.33. After the sample was exposed to the flow of dry air, the initial weight loss resulted in the formation of anhydrous product (*experimental weight loss*: 8.0%, *theoretical*: 8.7%). This anhydrous product was stable between 80 °C and 280 °C. Above this temperature a rapid weight loss occurred, leading to a meta-stable *plateau* observed between 350 and 460 °C. The latter process might be associated with the oxidation of a major section of the organic ligand and the formation of calcium iminodiacetate (*experimental weight loss*: ~58%, *theoretical*: 60.5%).

In the following step this organic salt decomposed to give calcium carbonate at 520 °C (*experimental weight loss*: 75.6%, *theoretical*: 76.9%). The ultimate stable product was calcium oxide, observed above 680 °C (*experimental weight loss*: 84.6%, *theoretical*: 87.1%).

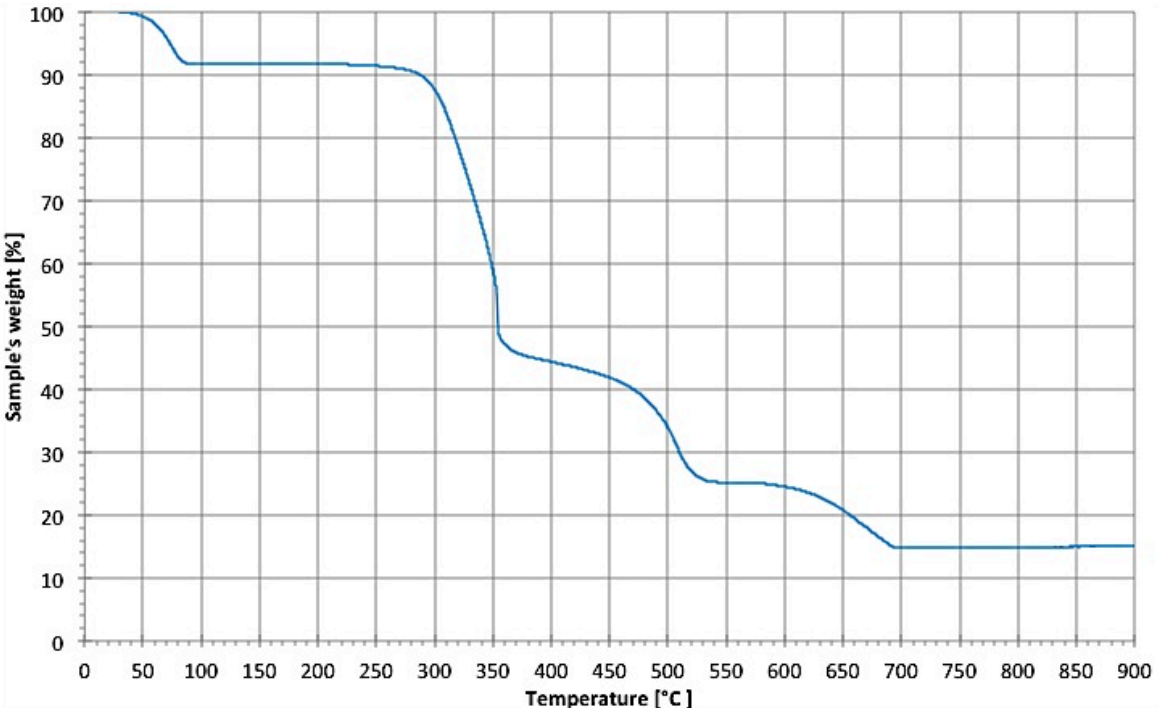

Fig. 4.33 | TGA analysis of compound **9** performed in air at 1 °C/min.

IR spectroscopy

With the aim to confirm that the molecular structure of the assemblies of **9** is identical with that of the crystalline phase, IR spectra of both phases were compared. As presented in Fig. 4.34, both spectra are identical, what proves that the crystalline phase of **9** and the self-assembled fibres are the same material.

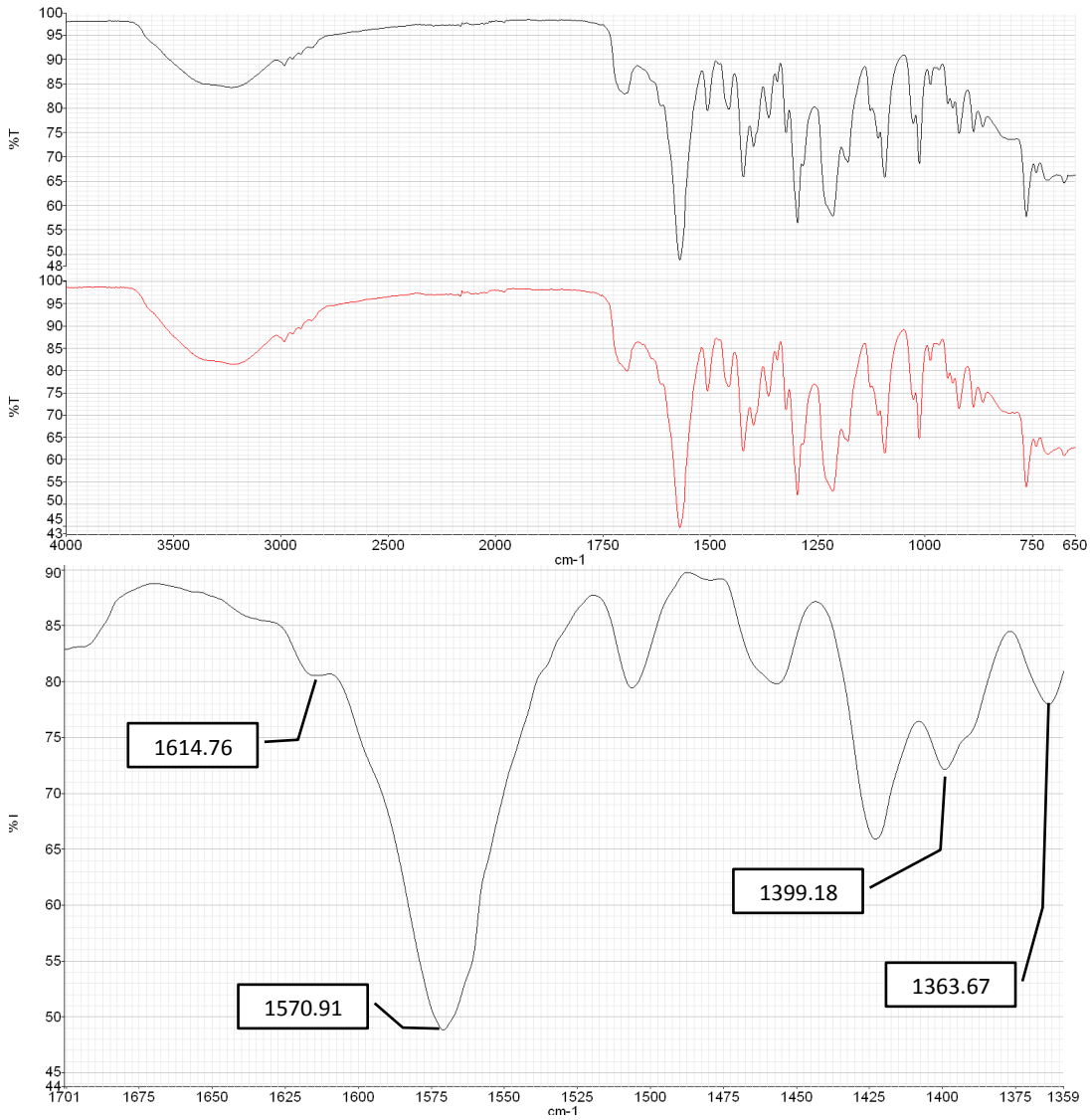

Fig. 4.34 | (**top**) Comparison between the IR spectra of the crystalline phase of **9** (black) and the fibrous assemblies (red); (**bottom**) magnification on the range characteristic for carboxylate stretching signals.

The most important vibrations observed in the IR spectra of both compounds are the asymmetric stretching vibrations of the carboxylic acid functional groups (ν_{as} (COO)) at 1614.76 cm^{-1} and 1570.91 cm^{-1}. The symmetric stretching vibrations of the same functionalities (ν_{s} (COO) are observed at 1363.67 cm^{-1} and 1399.18 cm^{-1}. The difference between the asymmetric and symmetric stretching frequency may be supportive in determining the binding mode within the metal-organic complex.

The carboxylic acid functional groups of the hda and vda-type ligands may coordinate to metal ions to form unidentate, bidentate or bridging coordination modes (see Sch. 4.1 for reference).

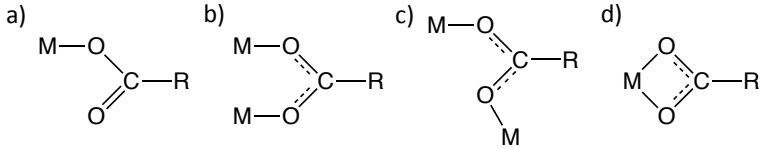

Sch. 4.1 | Possible coordination modes of a carboxylic acid functional group to a metal ion. a) *unidentate*; b) *syn-syn bridging*; c) *syn-anti bridging*; d) bidentate (chelating).

Deacon *et al.* have analysed a series of carboxylate complexes by infrared spectroscopy and established the following rules about the difference in the shift (Δν) between the asymmetric and symmetric carboxylate group C-O stretching frequencies.[179]

1) *Unidentate* complexes typically exhibit Δν values well above 200 cm^{-1}
2) For *bidentate* complexes the Δν values are significantly lower than 200 cm^{-1}, typically between 40 cm^{-1} and 100 cm^{-1}
3) Bridging carboxylate groups show Δν values greater than bidentate complexes; typically around 200 cm^{-1}.

Two different Δν values can be calculated for the crystalline phase and the assemblies of **9** (as two different asymmetric and symmetric stretching vibrations are observed in the IR spectra). They equal 251.09 cm^{-1} and 171.73 cm^{-1}. This observation confirms that both carboxylic acid functionalities adopt different coordination modes. The first one forms a *unidentate* complex (through O-donor O(3), while the second oxygen atom of this functionality, O(6), does not bind to any metal ion). The second carboxylate group adopts a *bridging* mode and binds to one calcium ion through the oxygen donor O(8), while the second oxygen atom of this group, O(5), binds to a symmetry equivalent metal ion (see Fig. 4.25 on page 128 for reference).

Electron microscopy

SEM was used to determine the morphology of the materials. The images, presented in Fig. 4.35a-d, show that **9** self-assemble into a fibrous material. The length of a single fibre can exceed 100 μm, while the average thickness is *ca.* 200 nm. Although most of the fibres are randomly orientated, some of the fibres tend to aggregate into bundles that are about 5 μm thick and *ca.* 60-100 μm long. The material appears to be soft; as seen in Fig. 4.35e-f, the assemblies may easily be twisted, folded or bent.

TEM imaging on a sample of the assemblies was attempted. Unfortunately, the fibrous material was sensitive to the energy of the electron beam and melted instantly after exposure (Fig. 4.35g-h).

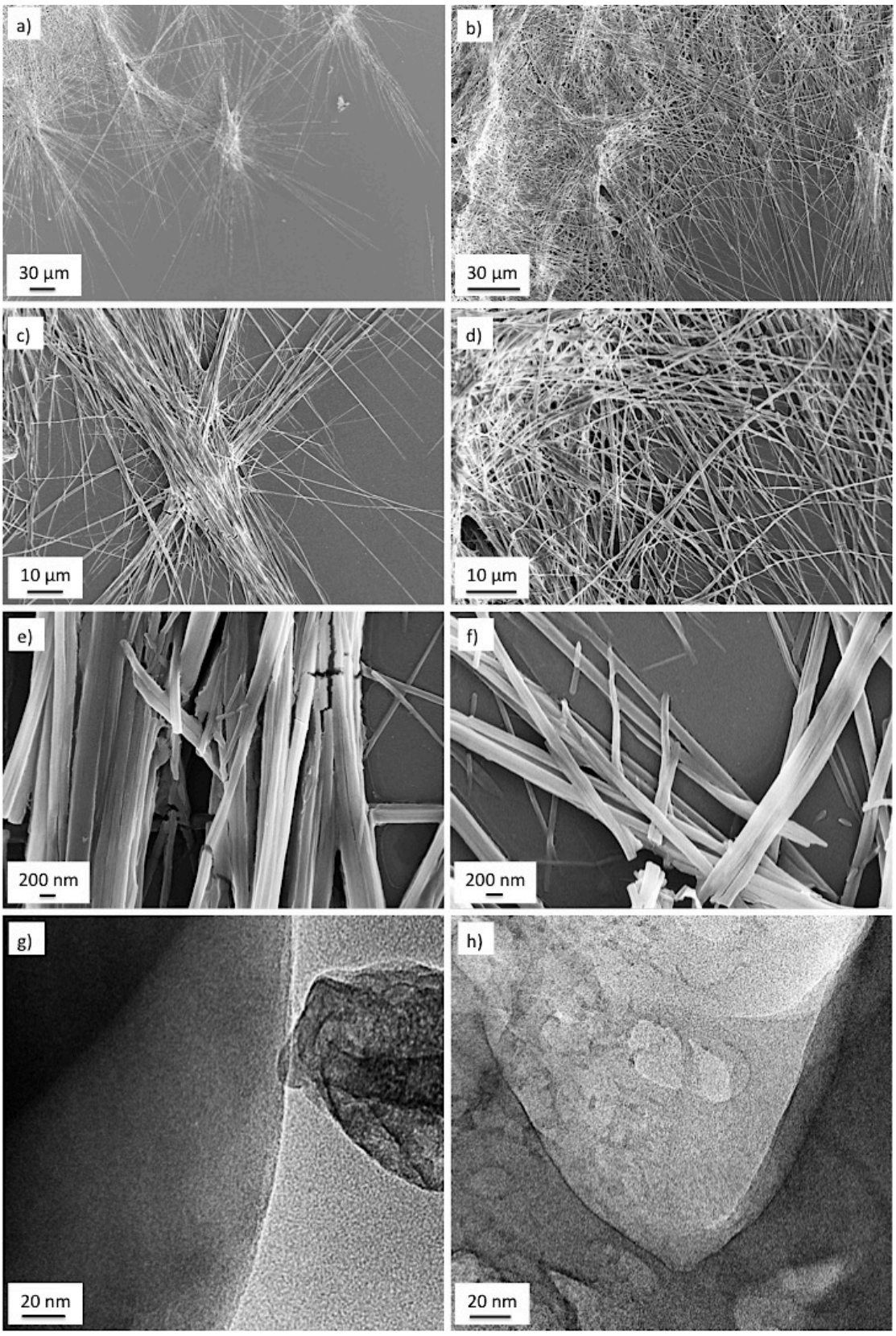

Fig. 4.35 | a-f) SEM pictures of the assemblies of **9**. **a,b)** overview; **c-d)** the fibres aggregate to form bundles; **e-h)** higher magnification images showing fibrous assemblies. **g-h)** HR TEM images of **9** immediately (**g**) and *ca.* 15 seconds (**h**) after exposure to the electron beam.

4.3.3. **9** as a template for the formation of calcium carbonate

As it was discussed before, when **9** is heated, it decomposes to give calcium carbonate at 520 °C. The thermal degradation experiment was repeated and the heating rate was

decreased to 0.35 °C/min. When the temperature of the sample reached 520 °C, the source of heat was disengaged and the residues were allowed to cool in ambient conditions. Then they were collected and analysed using powder X-ray diffraction and SEM techniques.

The P-XRD pattern presented in Fig. 4.36 confirms that calcite is the only crystalline phase present within the residues.

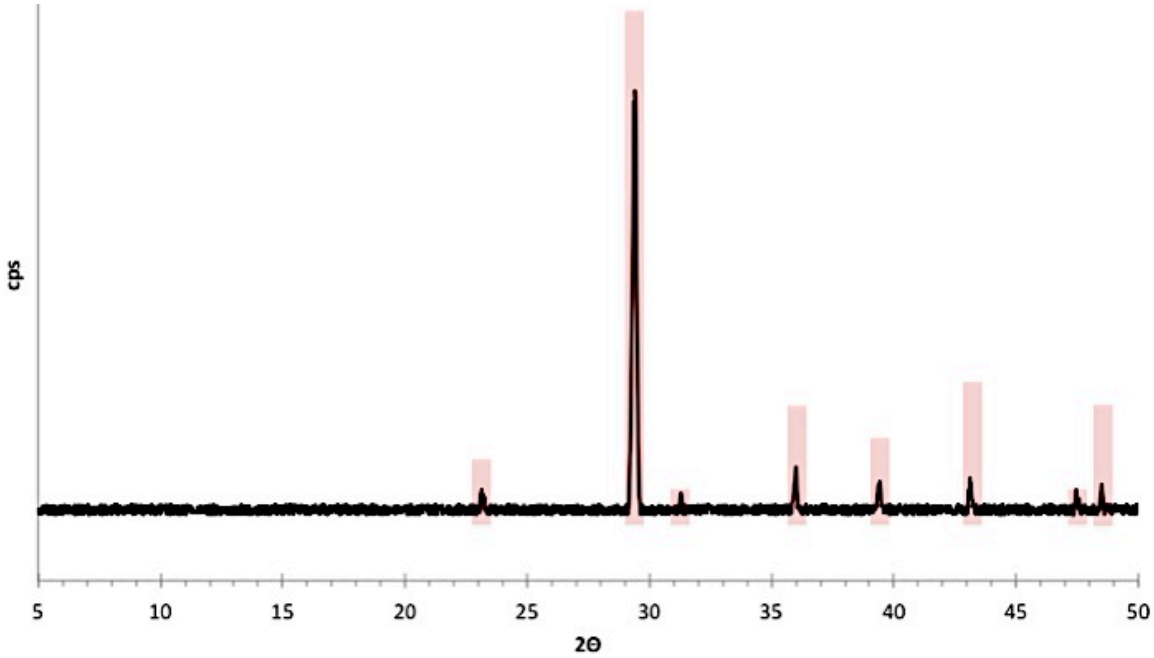

Fig. 4.36 | P-XRD pattern obtained for the residual crystals of calcium carbonate, obtained during the thermolysis of **9** to 520 °C in air. The highlighted areas mark positions of reflections that are attributable to calcite.[178]

SEM studies

The morphology of the residues was analysed using SEM. The overview images (Fig. 4.37a-b) show that $CaCO_3$ forms fibrous polycrystalline material. The length of a single fibre varies between 10 and 50 μm, while the thickness ranges from 100 to 400 nm. The fibres are aligned in the same direction and have a tendency to aggregate into bundles, which are about 200 μm long and 25 μm thick. Higher magnification images, presented in Fig. 4.37c-f, reveal that each fibre is composed of small (30 – 150 nm) crystals, which aggregate to form a dense solid. These small crystals appear to aggregate into a layered architecture, which may be influenced by the microscopic structure and macroscopic morphology of **9**. The morphology of the residues looks similar to the calcite crystals that were obtained by thermolysis of **8** in the air atmosphere. High-resolution imaging (Fig. 4.37g-h) confirms that the nanocrystals do not exhibit the layered imprint that was observed for the similar copper-containing structures **1** and **2**.

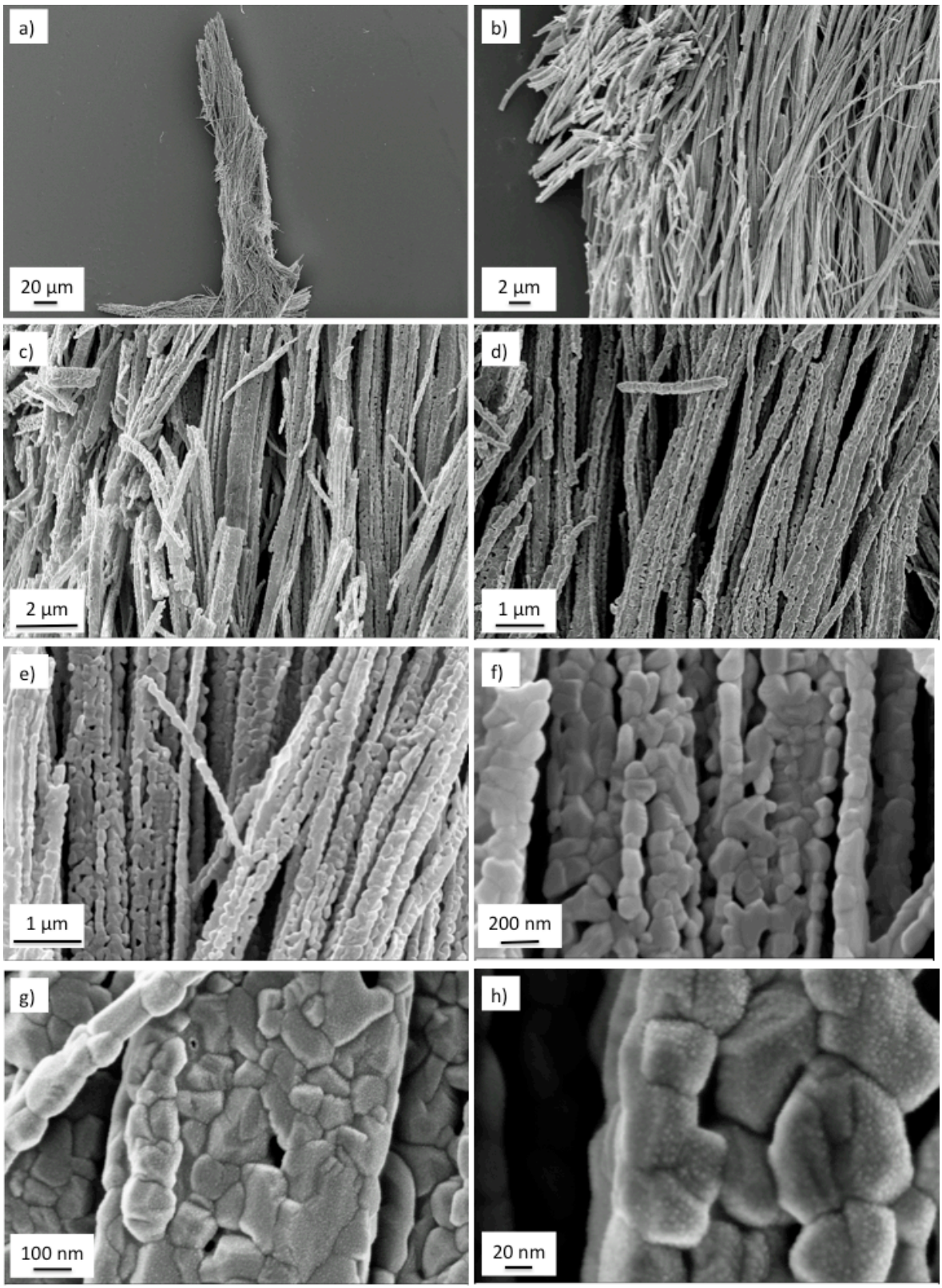

Fig. 4.37 | SEM images of the residual calcite crystals remaining after the thermolysis of **9**. **a-b)** overview pictures; **c-e)** higher magnification; **f)** high resolution imaging shows that the nanoparticles do not exhibit the layered imprint. Samples coated with a *ca.* 4 nm thick Au/Pd alloy.

The thermolysis experiment was reproduced in the nitrogen atmosphere and the resulting morphology of $CaCO_3$ was further studied and compared with the previously obtained data. An analytical sample of **9** was placed in a ceramic crucible and pyrolysed. The heating rate was set to 0.35 °C/min and the sample was heated from 30 °C to 520 °C. After this

the residues were allowed to cool down in ambient conditions and then they were analysed using the P-XRD and SEM.

The P-XRD pattern, presented in Fig. 4.38 (left), confirmed that calcite is the only crystalline phase present within the sample. The corresponding TGA curve (Fig. 4.38 right) indicates that the mass of the residues is 34.2% of the original sample. As the calculated mass of $CaCO_3$ is equal to 24.9%, the difference of 9.3% corresponds to the amorphous carbon. Further calculations show that the mass content of carbon within the residues is equal to 27.2%. These calculations were confirmed by the elemental analysis results.

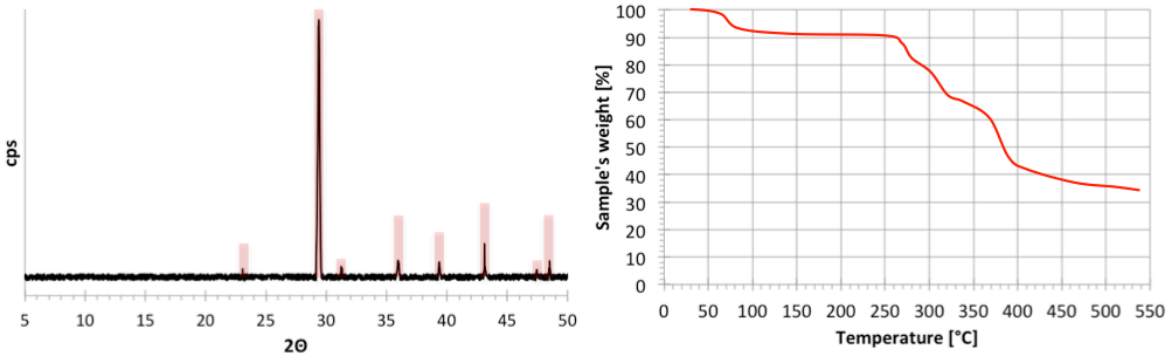

Fig. 4.38 | Pyrolysis of **9** in the nitrogen atmosphere. (**left**) the P-XRD pattern of the residues; the highlighted areas correspond to the calculated positions and intensities of calcite crystals[178]; (**right**) the corresponding TGA curve.

The SEM imaging (Fig. 4.39) revealed that in the nitrogen atmosphere **9** degrades to a fibrous polycrystalline material. The average length of a single fibre is 150 μm, while the thickness ranges between 250 and 700 nm.

Each single fibre is composed of small nanocrystals, which do not display the layered imprint. Due to the presence of the amorphous carbon the nanoparticles appear smoother than their analogues obtained in air (Fig. 4.39g-h). The fibres tend to aggregate into bundles, in which they are aligned in the same direction and display a residual hierarchical arrangement (Fig. 4.39d-e).

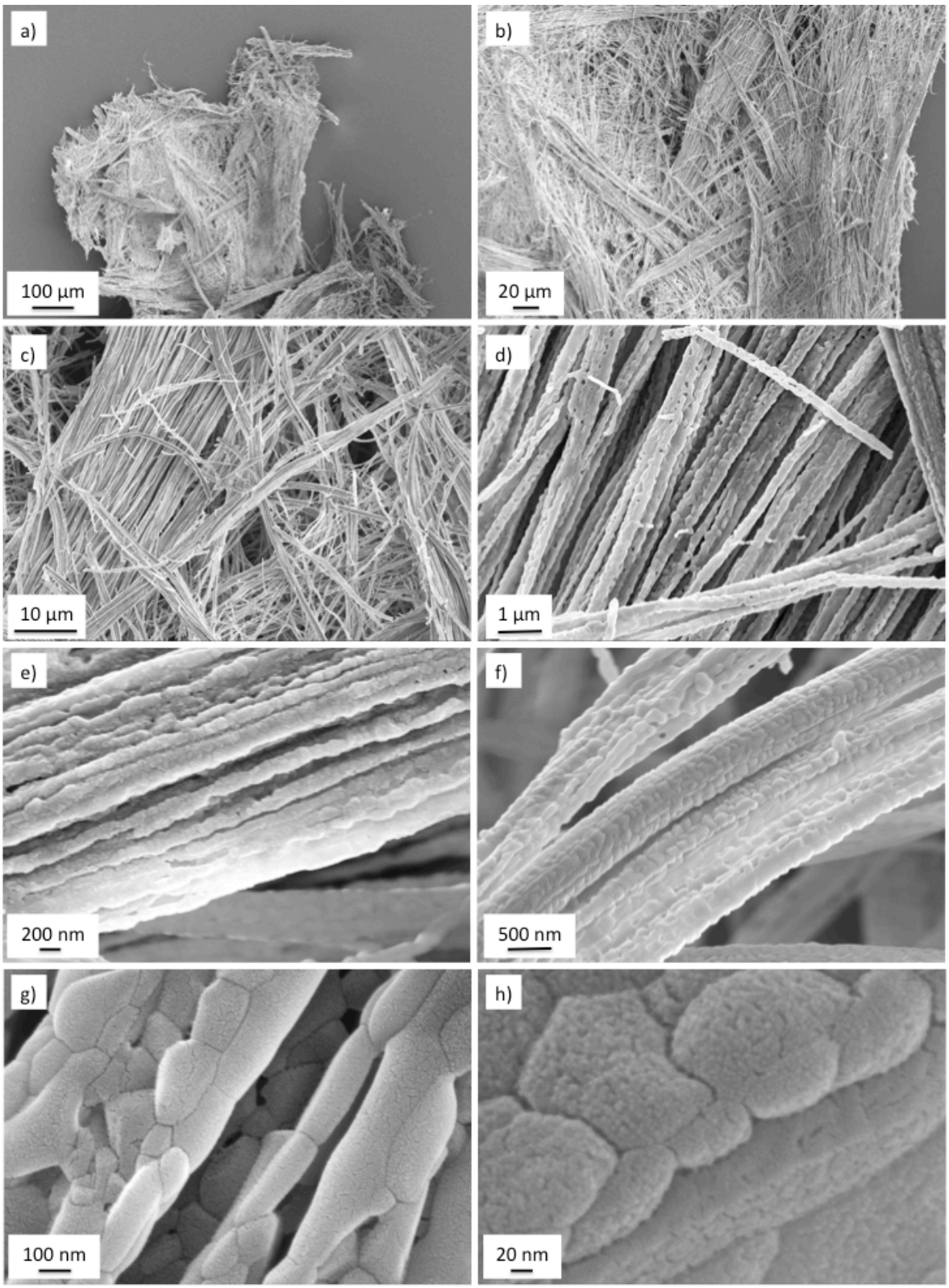

Fig. 4.39 | Crystals of calcite obtained by heating **9** in the nitrogen atmosphere at 520°C. **a-c)** overview; **d-f)** higher magnification showing layered lamellar architecture; **g-h)** high-resolution images of the nanoparticles. Imaging was performed on a Au/Pd alloy coated sample.

4.4. Compound $[Ca(C_6vda)(H_2O)_2] \cdot H_2O$ (**10**)

Successful synthesis and characterization of the calcium-containing coordination networks **7** – **9** containing the hda- and vda-type ligands provided the motivation to explore ligand variations equipped with a longer hydrophobic chain in the *para* position (in respect to the aromatic hydroxyl group). This modification was expected to increase the amphiphilicity of the ligand molecules and to result in a sandwich-like packing structure.

The main intention of this modification was to answer the question of how the increased length of the hydrophobic chain alters the self-assembly process, which occurs when the C_6vda ligand reacts with calcium ions. Although the solid-state structure was predicted to be similar to the previously described compounds, it was thought that the thickness of the hydrophobic regions would be larger. The length of the aliphatic chain should also be sufficient to enable the hydrophobic interactions within the hydrophobic parts of the structure.

The other question which was intended to answer was if the increased length of the alkyl chain could be used to generate non-crystalline products of the self-assembly process.

The secondary objective was to observe if the increased thickness of the hydrophobic areas within the solid-state packing structure of the new compound had a templating effect on the morphology of the ceramic residues, which remained after the thermolysis and pyrolysis processes.

4.4.1. Characterization

Compound **10** with the chemical formula $[Ca(C_6vda)(H_2O)_2] \cdot H_2O$ forms when the C_6vda ligand reacts with $CaCl_2$ in a 1:1 water/methanol mixture in the presence of triethylamine. White precipitate of **10** is observed *ca.* 2 minutes after the combination of the ingredients. Despite several attempts and modifications to the reaction procedure, there was no success in obtaining a single crystalline material. In order to confirm the structure of **10**, a combination of analytical methods was applied.

Elemental analysis

It was predicted that **10** forms a 1D coordination chain motif and the mononuclear unit in **10** is similar to the ones observed in compounds **8** and **9**. In this model three deprotonated carboxylic acid groups coordinate the calcium ion; two of them originate from the iminodiacetic acid functionality of the C_6vda ligand molecule and the third one belongs to a neighbouring mononuclear unit. Therefore, two carboxylate groups act as bridging moieties that link together neighbouring calcium ions into a 1D coordination chain.

The iminodiacetic acid N-donor, the aromatic hydroxyl O-donor and two water molecules occupy the vacant coordination sites. Therefore, the calcium ion is surrounded by seven N- and O-donors (as it was observed in compounds **8** and **9**).

For the purposes of the elemental analysis experiment it was assumed that each mononuclear unit is accompanied by one constitutional water molecule, which may take part in the hydrogen bond interactions.

According to the assumed model of **10**, the afore-mentioned 1D coordination chain is linked *via* hydrogen bond interactions to its neighbouring structural motifs, what results in the formation of a neutral layer, similar to these observed in **3**, **8** and **9**. The core of this layer is formed by the metal ions and hydrophilic functional groups, while the outer areas, are composed of the remaining aromatic parts of the ligand molecules and the *n*-hexyl chains. It is expected that the layers interact with each other through hydrophobic and van der Waals forces and self-assemble to give three-dimensional sandwich-like material, where the hydrophobic and hydrophilic areas are separated. This layered lamellar topology of coordination networks is characteristic for the previously described compounds that contain the hda- and vda-type ligands.

For this predicted structure a theoretical elemental composition was calculated and it was further compared with the results of the elemental analysis experiment. As presented in Tab. 4.5, there is a good correlation between the theoretical and experimental values, what confirms that the predicted molecular formula of **10** is correct.

Tab. 4.5 | Elemental analysis of compound **10**.

Element	Theoretical abundance [%]	Elemental analysis result [%]
C	48.40	**47.95**
H	6.20	**6.31**
N	2.97	**2.93**
Ca	8.50	**8.44**

Thermogravimetric analysis

The quantity of constitutional and coordinating water molecules was further confirmed using the TGA analysis. This method also allowed us to trace the thermal degradation pathway of **10**. An analytical sample was heated (heating rate: 3 °C/min) in an air atmosphere and the corresponding weight loss was recorded. The results, presented in Fig. 4.40, show that the initial loss of the constitutional and coordinating water molecules occur immediately after exposing the sample to the flow of dry air. The completely dehydrated product forms at 110 °C (*experimental weight loss*: 10.4%, *theoretical*: 11.0%) and is stable up to 180 °C. Above this temperature a rapid oxidation of the organic ligand begins. At 350 °C the aromatic and aliphatic parts of the ligand are completely oxidised and the residues are composed of iminodiacetic acid calcium salt (*experimental weight loss*: 64.5%, *theoretical*: 65.0%). This quasi-stable compound undergoes further oxidation leading to the formation of calcium carbonate at ~500 °C (*experimental weight*: 79.8%, *theoretical*: 79.6%). The final product of the thermal degradation is calcium oxide, which forms at 670 °C (*experimental weight loss*: 90.1%, *theoretical*: 91.3%).

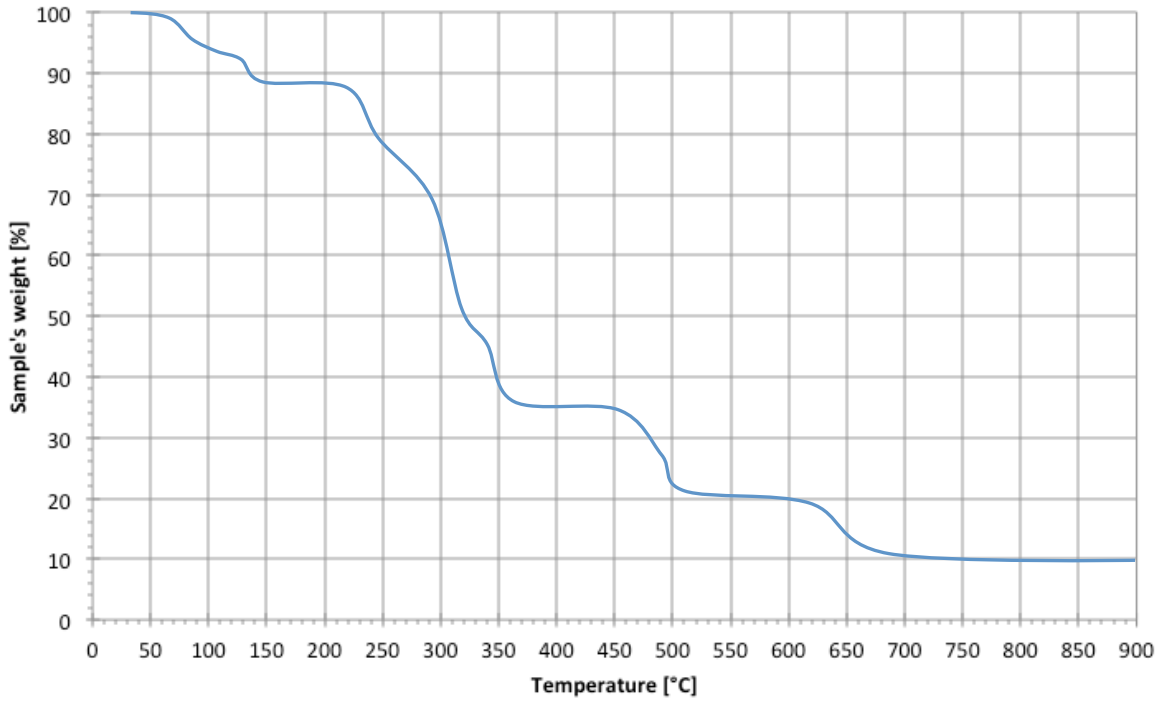

Fig. 4.40 | TGA analysis of **10**. An analytical sample was heated in air at 3 °C/min.

IR spectroscopy

After the chemical formula of **10** was correctly established, IR spectroscopy was used to investigate the binding mode of the C_6vda ligand molecules. As presented in Fig. 4.41, three different frequencies may be associated with the carboxylate groups of the C_6vda ligand in **10**. The first ones, which are observed at 1639.05 cm^{-1} and 1604.15 cm^{-1}, may be attributed to the asymmetric stretching. Two other frequencies, noted at 1404.84 cm^{-1} and 1336.12 cm^{-1} represent the symmetric stretching of the carboxylate functionality. The presence of two separated signals that can be attributed to the asymmetric (and symmetric) stretching suggests that each carboxylate group of the iminodiacetic acid functionality in **10** adopts a different binding mode.

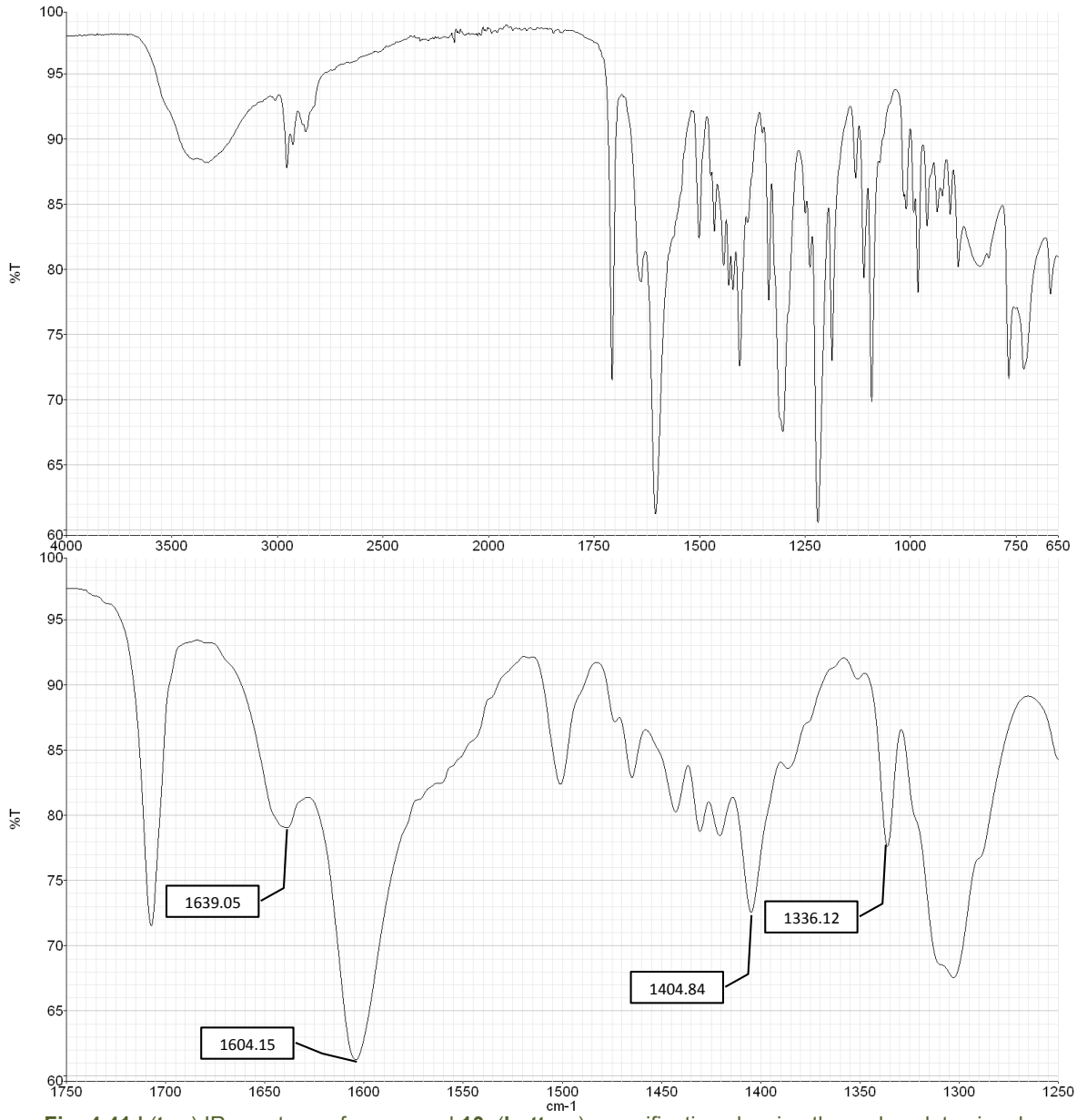

Fig. 4.41 | (**top**) IR spectrum of compound **10**; (**bottom**) magnification showing the carboxylate signals.

The differences between the asymmetric and symmtertic stretching frequencies (Δν) in **10** are: $\Delta\nu_1$ = 302.93 cm^{-1} and $\Delta\nu_2$ = 199.31 cm^{-1}. These values suggest that one of the carboxylate groups (the one that displays the symmetric stretching frequency of 1404.80 cm^{-1}) definitely binds to the metal ion in the *unidentate* mode. The second carboxylate group, which shows a difference of 199.35 cm^{-1}, adopts a bridgng mode and therefore links two symmetry equivalent calcium ions (see p. 137 for reference).

The IR spectroscopy experiments confirmed that the coordination environment in **10** is indeed similar to the previously described Ca-containing compounds **8** and **9**.

Electron microscopy and EDX analysis

SEM was used to investigate the morphology of **10**. The micrographs, presented in Fig. 4.42, show that **10** forms bunches of sheet-like assemblies that are *ca.* 20 μm long and contain several hundreds of virtually flat single crystallites. Although this material has a crystalline appearance, it does not scatter X-ray or an electron beam.

Higher magnification imaging (Fig. 4.42e,f) reveals that the thickness of the sheets of **10** ranges between 200 nm and 1 µm. When compared with the previously described compound **9**, it becomes apparent that **10** does not form long, thin fibres, but rather exhibits a tendency to form flatten agglomerates, which further assemble into bunches.

The SEM imaging of **10** was challenging due to observed charging effects, which could not be compensated for even when the sample was gold-coated. This is not surprising for a compound, which has a surface full of cracks, edges and breaks.

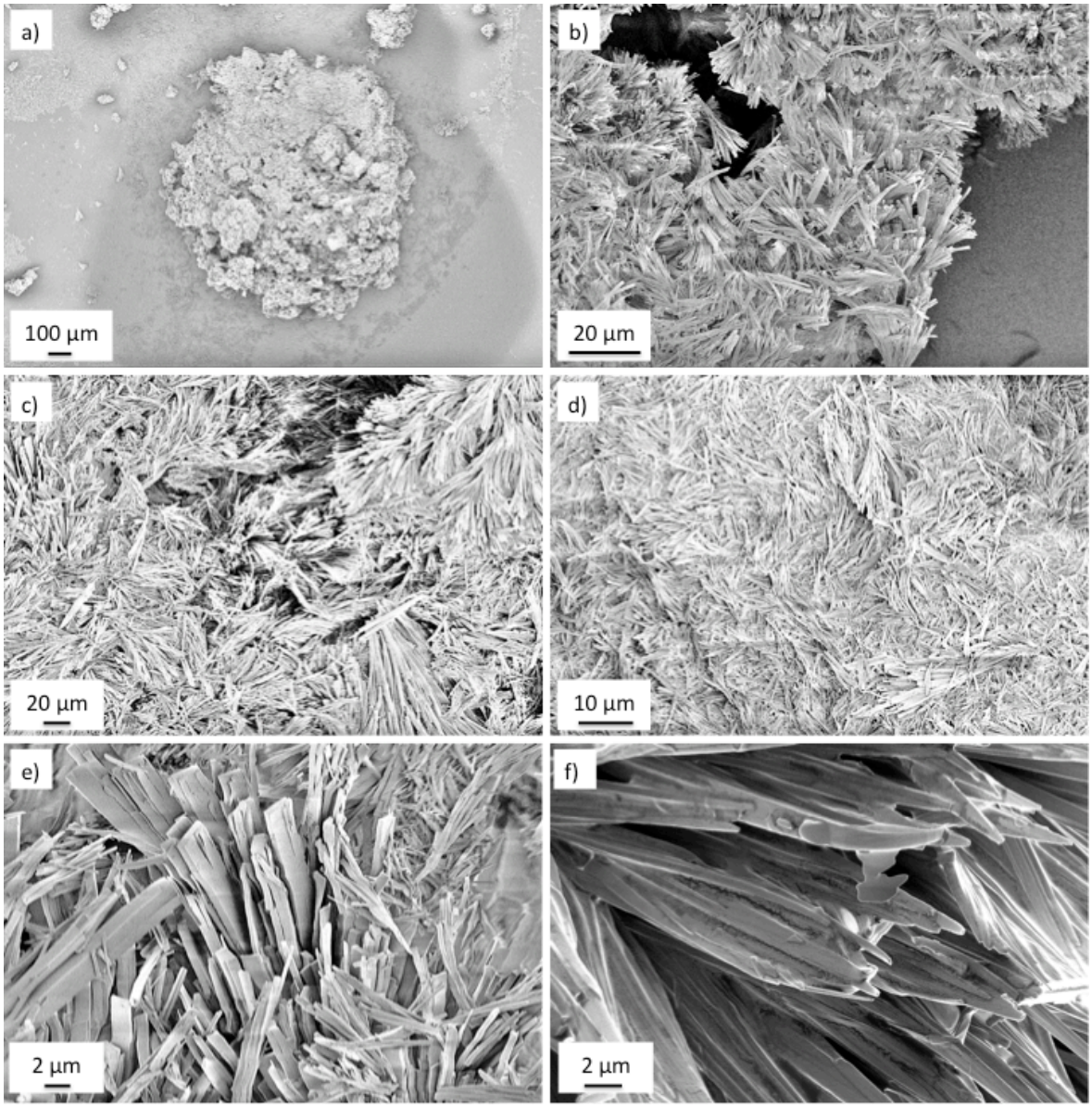

Fig. 4.42 | SEM images of the assemblies of **10**. **a,b)** overview; **c-d)** magnification showing crystalline assemblies; **e-f)** thin, plate-like assemblies.

The SEM imaging allowed us to perform the EDX analysis on the assemblies of **10**. The obtained spectrum, presented in Fig. 4.43, has confirmed that **10** is composed of calcium and other basic elements common for organic compounds (carbon, oxygen, nitrogen). Due to the low electron density, the presence of hydrogen could not be confirmed using this method.

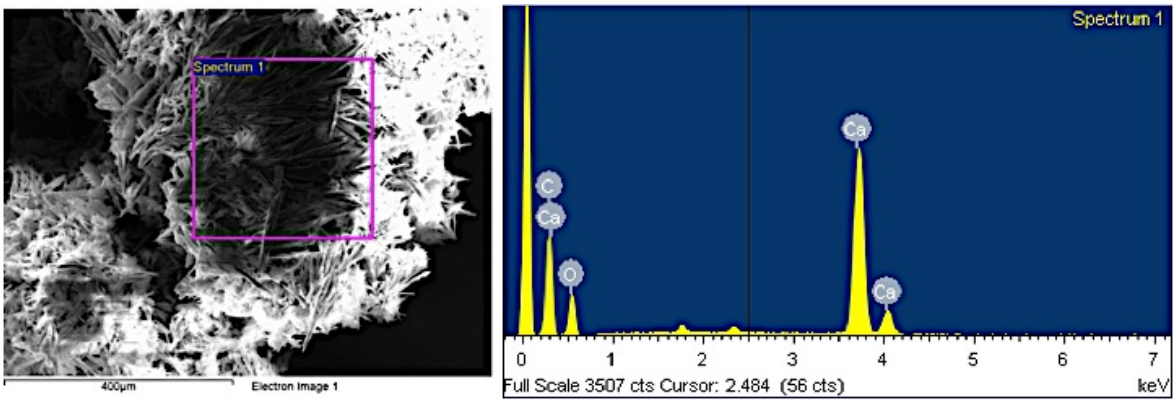

Fig. 4.43 | EDX analysis of compound **10**. Electron image (left) and the recorded energy spectrum (right).

As **10** form thin, sheet-like assemblies, it was possible to perform TEM imaging in search for a higher-ordered arrangement within their structure. **10** was more stable, when exposed to the electron beam than the ethyl ester containing compound **9**. Fig. 4.44 shows an assembly, which displays layered lamellar organisation. The lattice separation distance is 1.89 (±0.15) nm. This value is similar to the lattice separation distance observed in the copper-containing compound **3** (2.0 nm) and strongly suggests that the packing structure of **10** and **3** are similar.

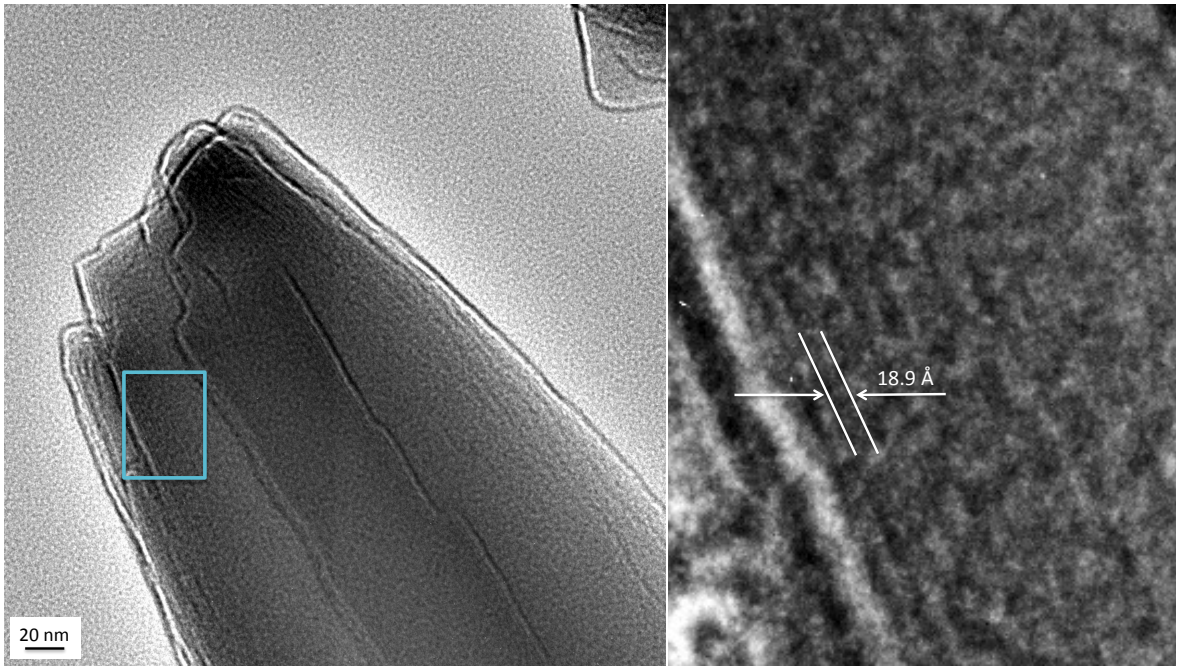

Fig. 4.44 | TEM image of **10** recorded in the diffraction contrast regime, showing layered arrangement (left). The blue square marks the area, which has been enlarged and presented on the right-hand site.

4.4.2. Thermal decomposition of **10** and the formation of calcium carbonate

As presented in Fig. 4.40 (p. 146), the thermal degradation of **10** is a multi-step process, which leads to distinct in different degradation products that are depending on the temperature applied. An analytical sample of **10** was heated in the air atmosphere and the heating ratio was set to 0.35 °C/min. When the sample reached the temperature of 520 °C the source of heat was disengaged and the sample was allowed to cool subsequently. The residues were divided into two separate samples. The first was crushed in a mortar and analysed using

the P-XRD pattern. This allowed determining the phase of $CaCO_3$. The second sample was dispersed in anhydrous methanol. Then a 20 µl droplet of the dispersion was placed on the silicon surface, dried and coated with a thin layer of a Pd/Au alloy. The sample was subsequently imaged using SEM in an attempt to determine the morphology of the residual calcium carbonate.

The results of the P-XRD analysis, presented in Fig. 4.45, confirm that the residues are composed of calcite. Crystals of $CaCO_3$ are the only crystalline phase present within the sample.

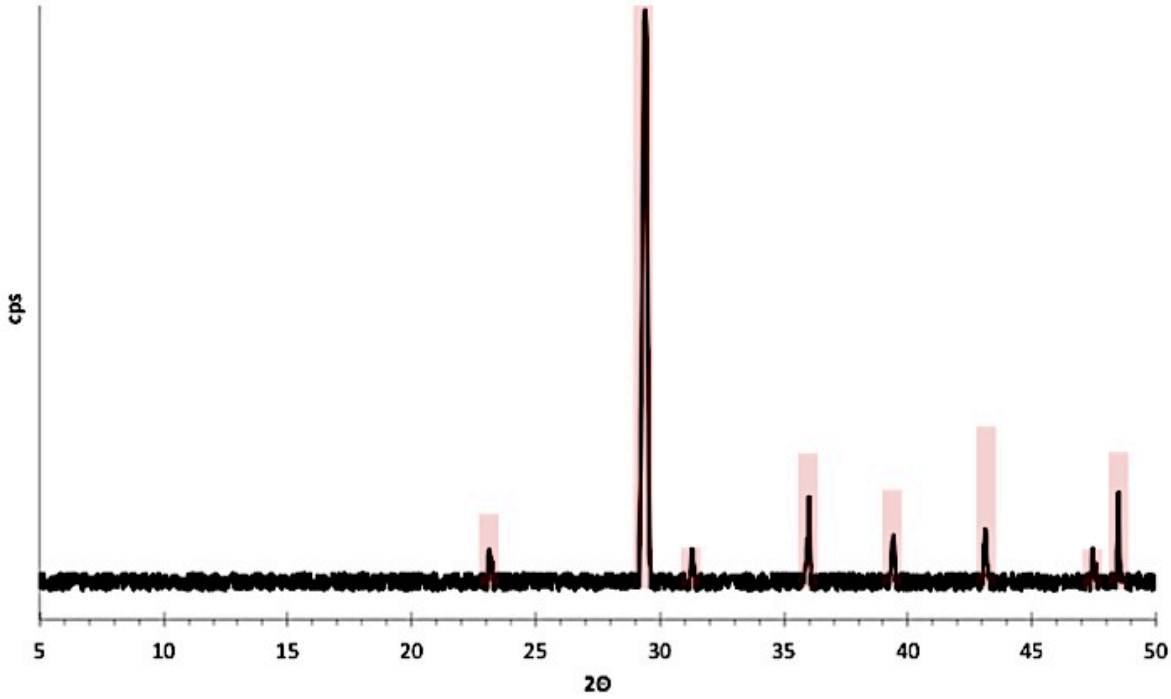

Fig. 4.45 | P-XRD pattern recorded for a sample of **10**. The highlighted areas mark the typical positions and intensities of reflections observed for calcite.[178]

The morphology of the calcite crystals was studied using SEM. As presented in Fig. 4.46, the morphology does not differ from the morphology of the precedent coordination network **10**. Needle-like crystals, *ca.* 200 nm thick and 20 µm long, aggregate to form bunches. Most of the crystals within the same bunch are aligned in the same direction.

Higher magnification imaging (Fig. 4.46e-f) reveals the each needle-like crystals are in fact polycrystalline material, composed of small (~100 nm), irregular nanoparticles that stick together to form a dense three-dimensional solid. These nanocrystals do not display the layered imprint, which was observed previously for the crystals of CuO. Although a selection of nanoparticles is locally organised into a hierarchical layered structure, most of them are randomly orientated.

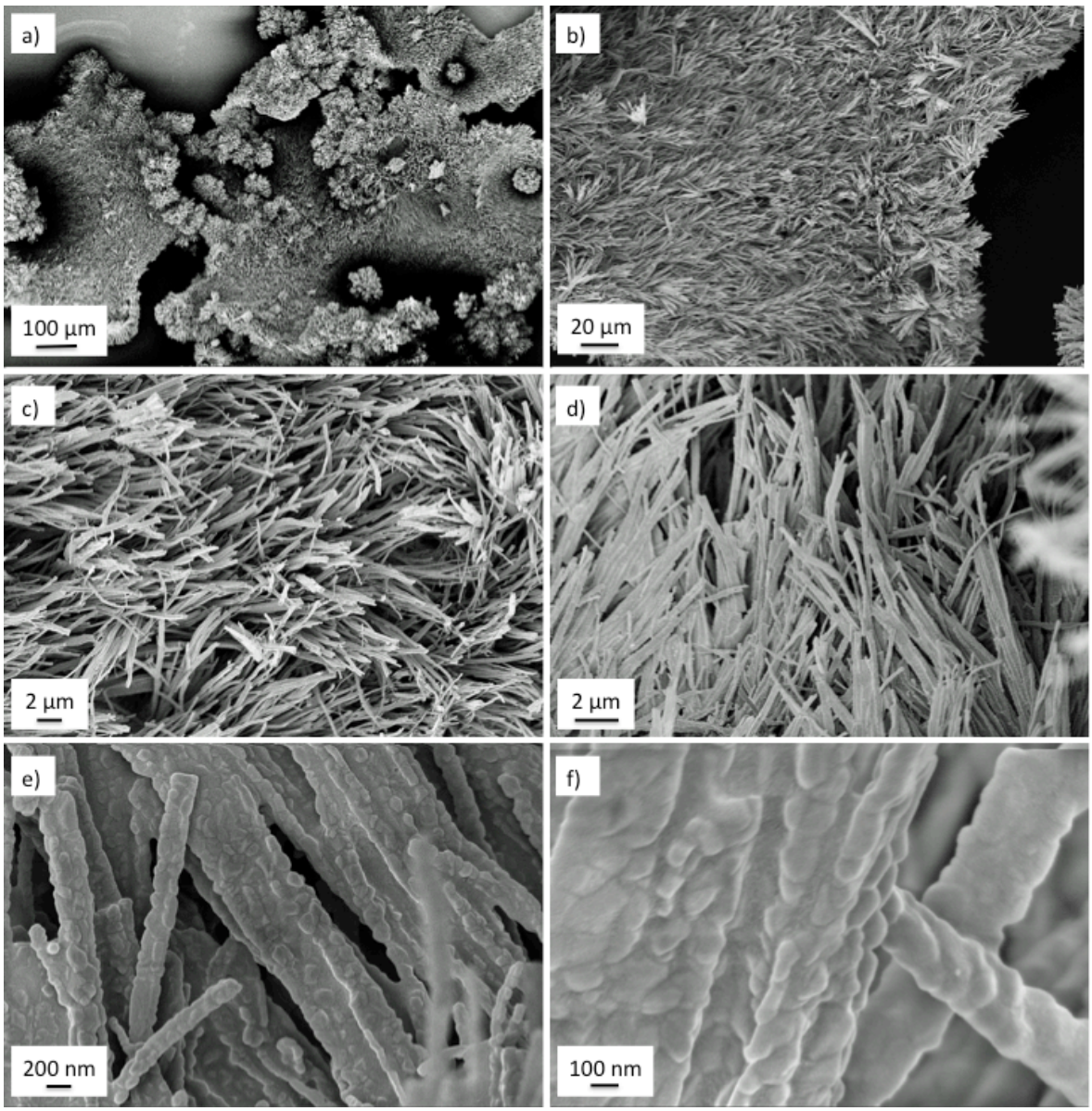

Fig. 4.46 | Calcite crystals formed during the oxidation of **10** in air at 520°C. Imaging performed on a Pd/Au alloy coated sample. **a-b)** overview; **c-d)** magnification showing bunches of fibrous crystals; **e-f)** higher magnification reveals that each single fibre is composed of small nanoparticles sticking together.

In the next step it was decided to reproduce the thermal degradation experiment in the nitrogen atmosphere. An analytical sample of **10** was heated from 30 °C to 520 °C. The heating rate was set to 0.35 °C/min. At 520 °C the residues were allowed to cool down and were subsequently analysed using the P-XRD to determine their chemical identity, and then were imaged using SEM to investigate their morphology.

The P-XRD pattern for the residues is presented in Fig. 4.47. All of the visible reflections are associated with calcite. This proves that the formation of $CaCO_3$ is rather an internal rearrangement of the calcium ion coordination environment than an oxidation, which would require an external source of oxygen.

The mass of the residues recorded at 520 °C equals 28.2% of the mass of the original coordination network. As the theoretical mass of calcium carbonate is 20.4% of the initial weight, the remaining 7.8% may be associated with the amorphous carbon remaining within the sample. This indicates that the residual amorphous carbon constitutes 27.7% (by weight)

of the post-pyrolytic residues. The elemental analysis experiment, which was performed on the post-pyrolytic residues, confirms the above calculations. The presence of hydrogen or nitrogen atoms was not detected in the sample, what ultimately confirms that the additional mass may be associated with amorphous carbon.

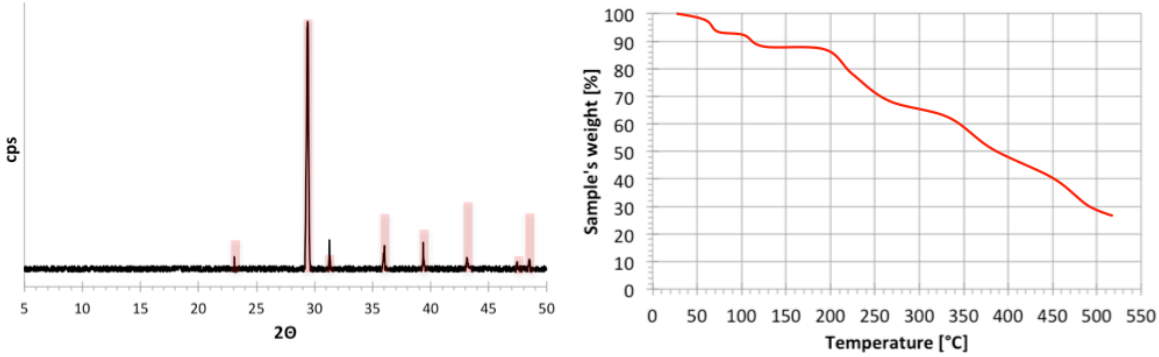

Fig. 4.47 | P-XRD pattern obtained for the residues remaining after the pyrolysis of **10** in nitrogen. The highlighted areas correspond to the typical positions and intensities of signals calculated for calcite crystals.[178]

The morphology of the residues was determined using SEM. In order to prepare an analytical sample, the residues were transferred to a clean sample tube and immersed in ethanol. During this process the solid divided into two parts: the black dust (which was believed to be the post-pyrolytic carbon) and the white crystalline material, which was further imaged. The pictures presented in Fig. 4.48 reveal that the residual calcite crystals display two distinct levels of organisation. The first level is observed on the nanoscale, where small (~150 nm) particles stick together to form elongated polycrystalline particles that are about 15 μm in length. The internal arrangement of these nanoparticles seems to be more ordered than it was observed for the crystals obtained in the air atmosphere. They appear to have a layered organisation (see Fig. 4.48g-h), where each nanoparticle serves as a brick, which builds up the three-dimensional solid. This may be the residual imprint of the layered organisation of the preceding coordination network.

The second level of organisation is observed on the microscale, where the polycrystalline particles further assemble into bunches (Fig. 4.48b-d). Each bunch contains several hundreds of polycrystalline particles, which are aligned in a similar direction and seem to grow from a common centre.

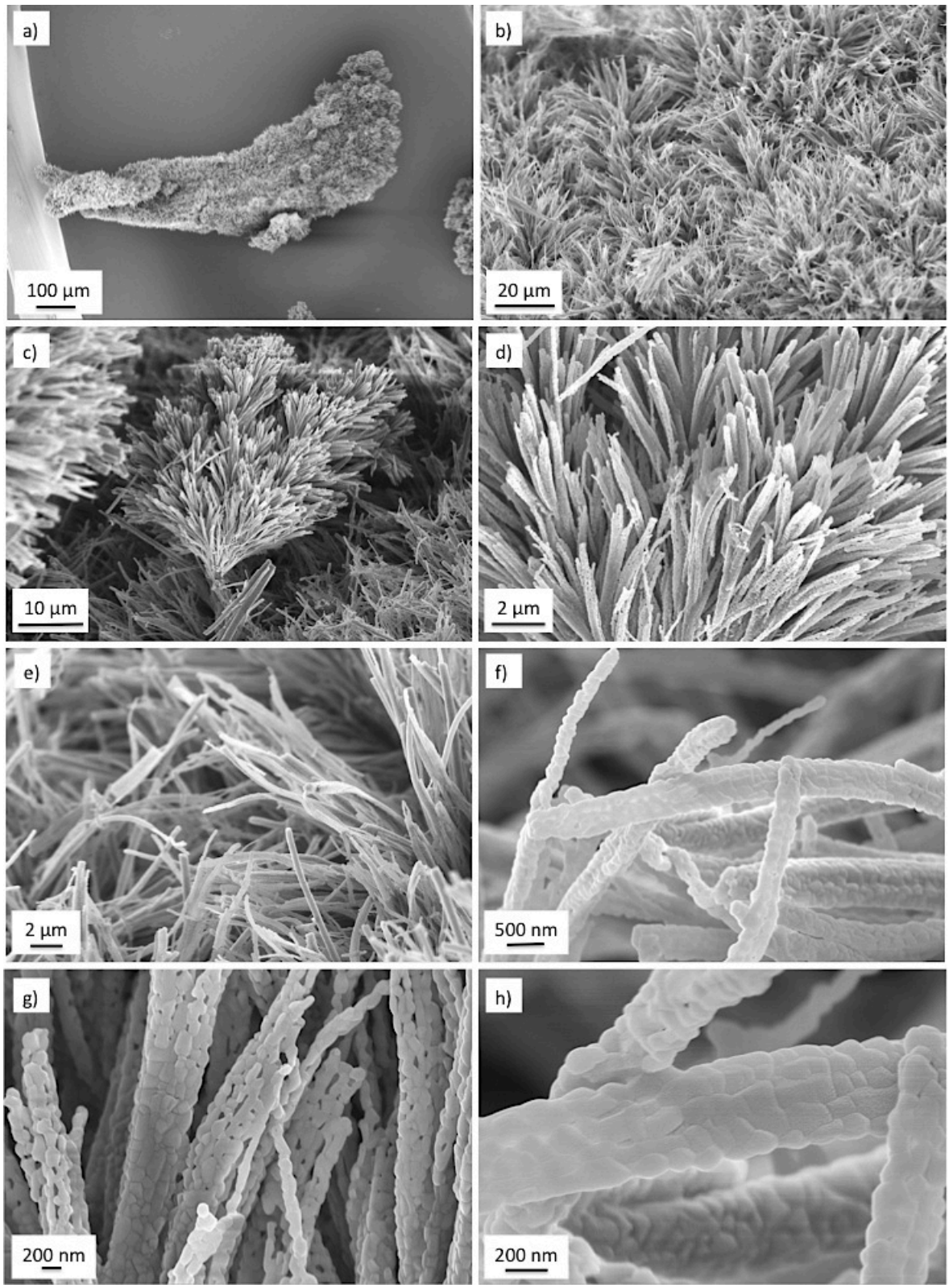

Fig. 4.48 | Calcite crystals formed during the pyrolysis of **10** in nitrogen at 520°C.

4.5. Compound [Ca(C_{10}vda)(H_2O)$_2$] (**11**)

The successful characterization of compound **10** provided us with the inspiration to explore a system where the C_{10}vda ligand, which is equipped with a longer aliphatic chain, is reacted with calcium ions. The implementation of this change allowed us to further investigate how the extend of the aliphatic chain influences the self-assembly process of the metal-organic complexes. Moreover, it gave us the opportunity to answer the question if the extended hydrophobic chain changes the morphology of the post-thermolytic and post-pyrolytic ceramic materials.

4.5.1. Characterization

Compound **11**, with the chemical formula [Ca(C_{10}vda)(H_2O)$_2$], forms when the C_{10}vda ligand reacts with $CaCl_2$ in a water/methanol (1:1 v/v) mixture. Triethylamine is used to deprotonate the ligand. The formation of a white precipitate is observed within 15 seconds of combining the reagents.

The reaction conditions (solvents' ratio, pH, temperature) were varied in order to obtain a single-crystalline material, however, all attempts were unsuccessful. Due to this, the structure of **11** had to be determined indirectly, with a combination of spectroscopy and microscopy techniques.

We assumed that the increase in the length of the hydrophobic chain affects only the solid-state packing structure and that the coordination mode observed within the complex remains the same. This assumption was based on observations from the previously described compound **10** and the crystallographic structures of compounds **8** and **9**, where the hydrophobic parts of the structures were separated from the N- and O-donors surrounding the metal ion.

We predicted that the coordination environment of the calcium ion in **11** would not differ much from the coordination spheres observed in compounds **8**-**10**. It should consist of one N-donor and three carboxylic O-donors of the iminodiacetic acid moiety (two groups from one C_{10}vda ligand molecule and one bridging group from a symmetry equivalent ligand molecule), one aromatic hydroxyl O-donor and two coordinating water molecules. As the metal ion should be surrounded by seven donors, the coordination geometry could vary from irregular to distorted pentagonal bipyramide.

One carboxylate group of the ligand molecule should form a bridge between two neighbouring metal ions. Therefore, it was expected that the complexes should self-assemble into 1D chains linked with coordination bonds. These structural motifs might be further cross-linked *via* hydrogen bond interactions. Finally, hydrophobic interactions and van der Waals forces might be the driving force causing the self-assembly of the resulting layers into three-dimensional lamellar material, where the hydrophilic parts sandwich between the hydrophobic ones.

Elemental analysis

In order to confirm the chemical formula of **11**, an elemental analysis experiment was conducted. The theoretical elemental composition was calculated for the formula of the complex described above, which is $C_{23}H_{37}CaNO_{10}$. Tab. 4.6 shows a good correlation between the theoretical and experimental values, proving that the assumed formula is correct.

Tab. 4.6 | Elemental analysis of compound **11**.

Element	Theoretical abundance [%]	Elemental analysis result [%]
C	52.36	**52.18**
H	7.07	**7.16**
N	2.65	**2.52**
Ca	7.60	**7.44**

Thermogravimetry

Thermogravimetric analysis of compound **11** was performed in an air atmosphere. The heating rate was set to 1 °C/min and the change of weight was recorded in the range between 30 and 900 °C. As presented in Fig. 4.49, the initial weight loss occurs following exposure of the sample to the flow of dry air. The dehydrated product forms at 75 °C and remains stable up to 210 °C (*experimental weight loss*: 7.4%, *theoretical*: 6.8%). Above this temperature a rapid oxidation of the organic ligand occurs. Between 360 and 450 °C a *plateau* is observed, which appears to be associated with the formation of calcium iminodiacetate (*experimental weight loss*: 63.8%, *theoretical*: 67.6%). Further heating leads to the formation of calcium carbonate at 515 °C (*experimental weight loss*: 81.7%, *theoretical*: 81.0%). This compound is stable up to 630 °C. The final product of the oxidation is calcium oxide, observed above 650 °C (*experimental weight loss*: 92.1%, *theoretical*: 89.4%).

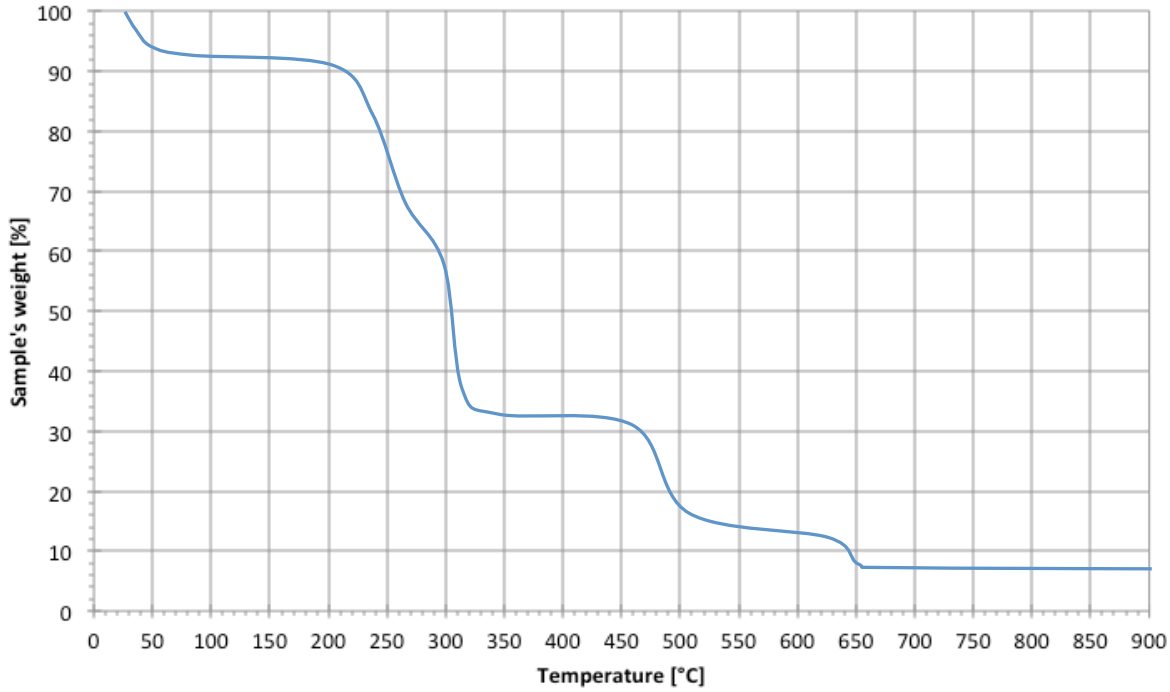

Fig. 4.49 | TGA analysis of **11** performed in air, at 1 °C/min.

IR analysis

After the chemical formula of 11 has been successfully established, the IR spectroscopy was used to determine the binding mode of the C_{10}vda ligand. The resulting spectrum, presented in Fig. 4.50, show four signals that may be associated with the carboxylate functional groups. The first set of vibrations occurs at the frequencies of 1638.00 cm^{-1} and 1603.33 cm^{-1} and may be assigned to the asymmetric stretching. Two following signals that are attributed to the asymmetric stretching frequencies are observed at 1404.94 cm^{-1} and 1336.02 cm^{-1}.

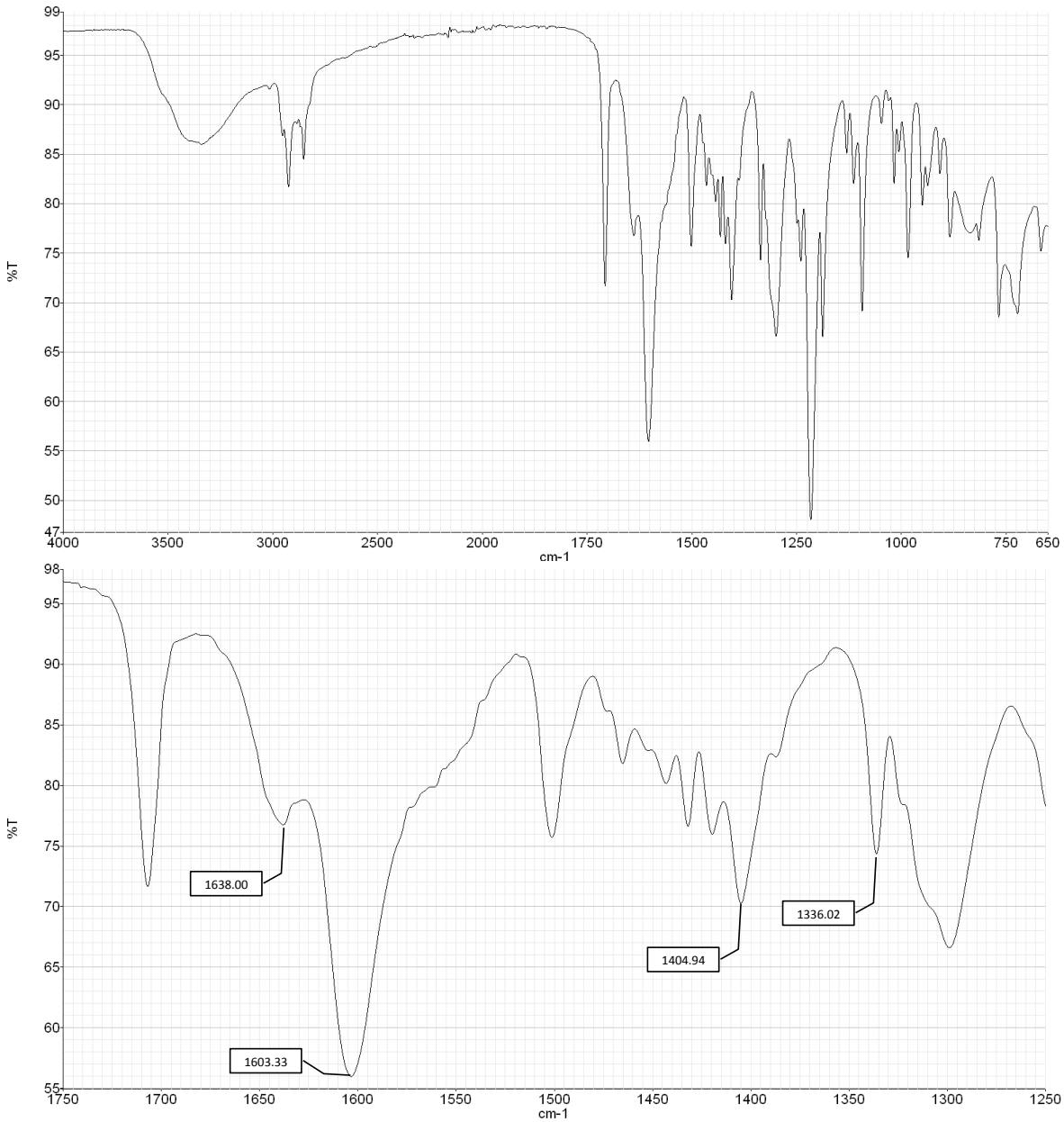

Fig. 4.50 | (**top**) the FT-IR spectrum of **11**; (**bottom**) magnification on the range displaying carboxylate signals.

As it was discussed previously (see p. 137), the differences in the frequencies of the asymmetric and symmetric stretching within the carboxylate group (Δν) may be used to determine the binding mode of this particular functionality. In case of **11**, there are two signals originating from the asymmetric and symmetric stretching vibrations, this suggests

that each carboxylate group of the iminodiacetic acid functionality adopts a different binding mode. The first difference, Δv_1, is 301.98 cm^{-1} and it indicates that one of the carboxylate functional groups adopts the *unidentate* binding mode. The second difference, Δv_2, which equals 198.39 cm^{-1} confirms that the second carboxylate functionality binds to two symmetry equivalent calcium ions in the bridging mode and therefore is responsible for the formation of a 1D coordination chain that links neighboring mononuclear complexes. This observation is in agreement with the binding modes observed in previous structures **8**-**10**.

Electron microscopy

The morphology of **11** was investigated using SEM. The images, presented in Fig. 4.51, show that **11** self-assembles into sheet-like belts or ribbons. The material appears to be soft; ribbons appear to be twisted, bent or folded. This may be a result of the weak, hydrophobic interactions that occur between the aliphatic chains of the organic ligand molecules.

The lengths of the ribbons vary. The shortest belts are ~2 μm long while the length of the longest ribbons can exceed 100 μm. The belts are between 200 nm and 5 μm wide. The material appears to be relatively thin (less than 100 nm) in the third direction.

The ribbons may cover large areas of the sample and are not aligned in any specific direction. Their surface is smooth and do not display any other morphological features.

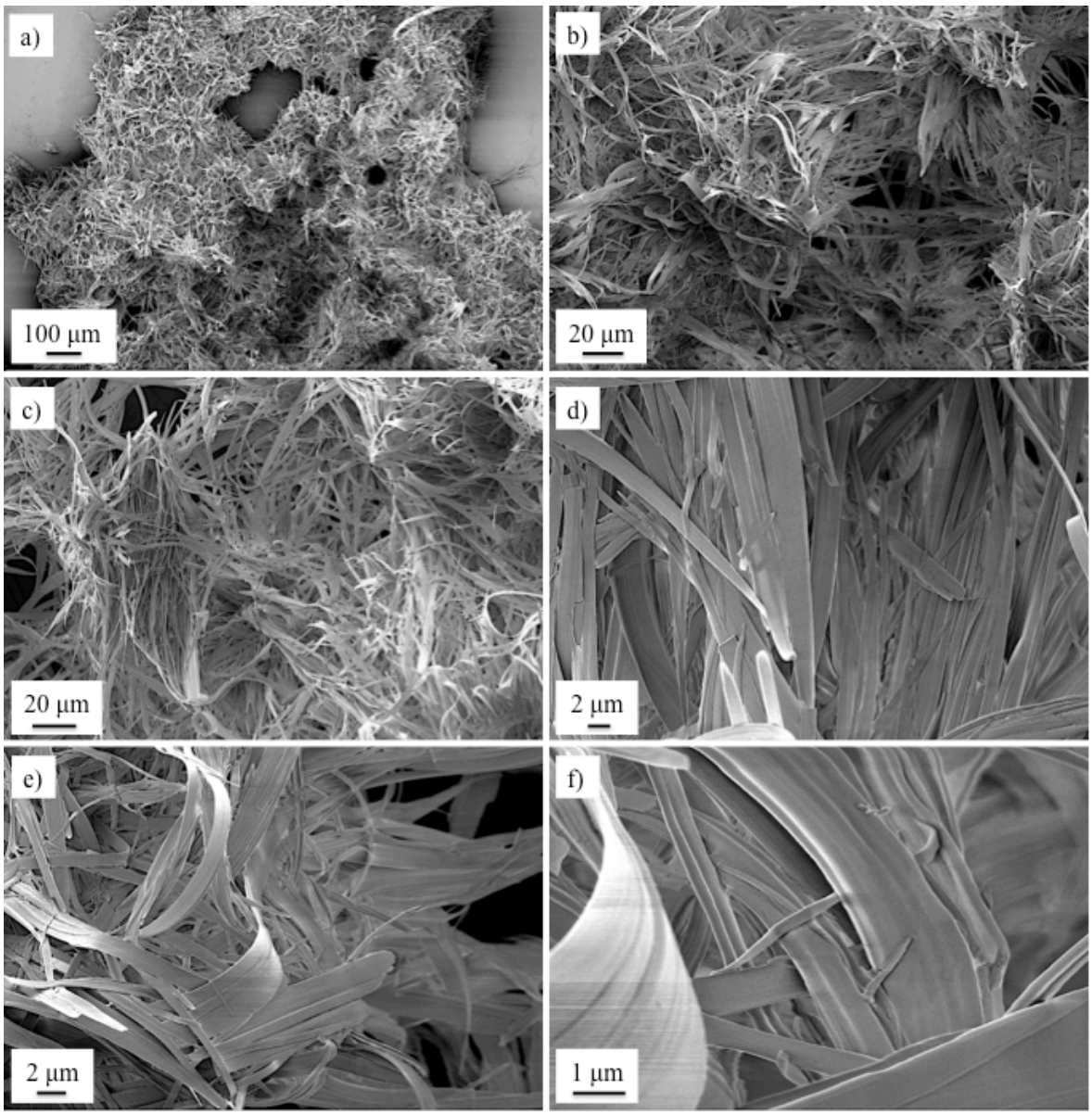

Fig. 4.51 | SEM images of **11**. **a-b)** overview; **c-f)** higher magnification imaging showing individual ribbon-like assemblies.

The SEM imaging provided an opportunity to employ the EDX analysis. The resulting spectrum, presented in Fig. 4.52, shows that carbon, nitrogen, oxygen and calcium are the only elements present within the sample (hydrogen cannot be detected with this method). This result is in agreement with the elemental analysis and proves that the composition of the compound agrees with the assigned formula. Moreover, it confirms that **11** does not contain any major impurities.

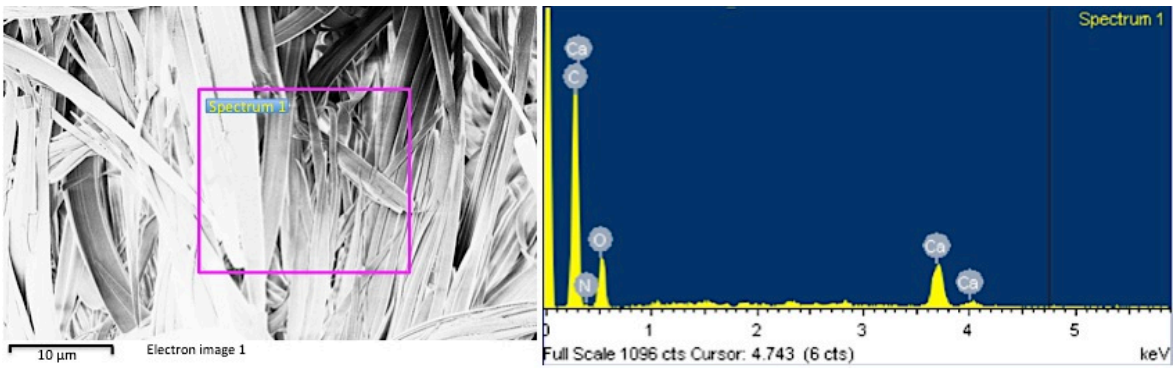

Fig. 4.52 | EDX analysis of the ribbon-like assemblies of **11**. The electron image (left) and the X-ray energy spectrum (right).

The thinness of the ribbons enabled us to perform TEM imaging on an analytical sample of **11**. The coordination compound appears to be stable in the electron beam. The images, presented in Fig. 4.53, ultimately confirm the layered lamellar arrangement of the molecular structure of **11**. The lattice separation distance is *ca.* 2.3 nm. This value is in agreement with the crystallographically determined lattice separation distance in corresponding copper complex $[Cu(C_{10}vda)(H_2O)_2]$ (**5**), which equals 2.28 nm. It is also about 0.45 nm larger than the corresponding distance observed in the C_6vda-containing compound **10**; this is not surprising as the hydrophobic chain in **11** is four carbon atoms longer.

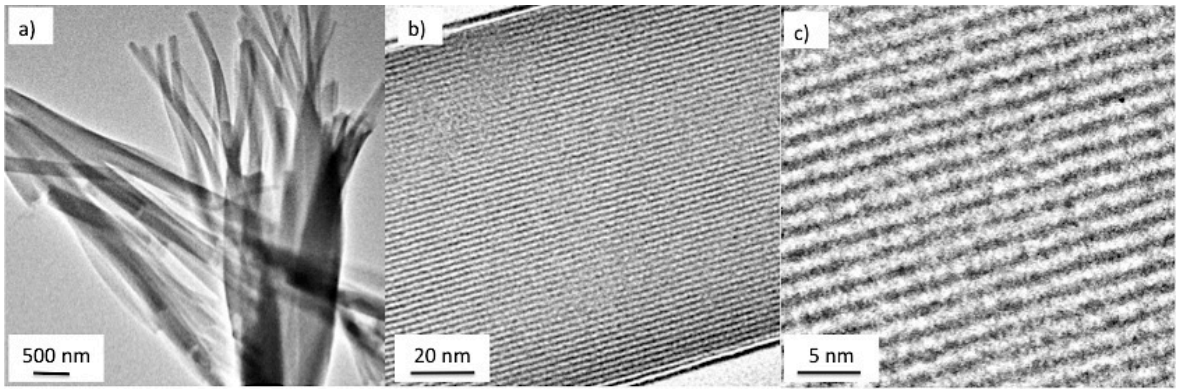

Fig. 4.53 | TEM images of **11** recorded in the diffraction contrast regime. **a)** Overview picture of the individual ribbon-like assemblies; **b)** and **c)** HR imaging reveals the layered lamellar arrangement in **11** allowing the measurement of the lattice separation distance.

4.5.2. Results of the thermal degradation

Thermolysis in an air atmosphere

As it was mentioned before, upon heating, **11** undergoes a multi-step decomposition. At 515 °C it forms calcium carbonate. To investigate the morphology of thermolysed products, a sample of **11** was heated from 30 °C up to 520 °C at a heating rate of 0.35 °C/min. After reaching the target temperature the sample was allowed to cool to room temperature. Then the residues were analysed using P-XRD and they were imaged using SEM in order to investigate their morphology.

The P-XRD pattern, presented in Fig. 4.54, confirms that calcite is the only crystalline phase present within the residues.

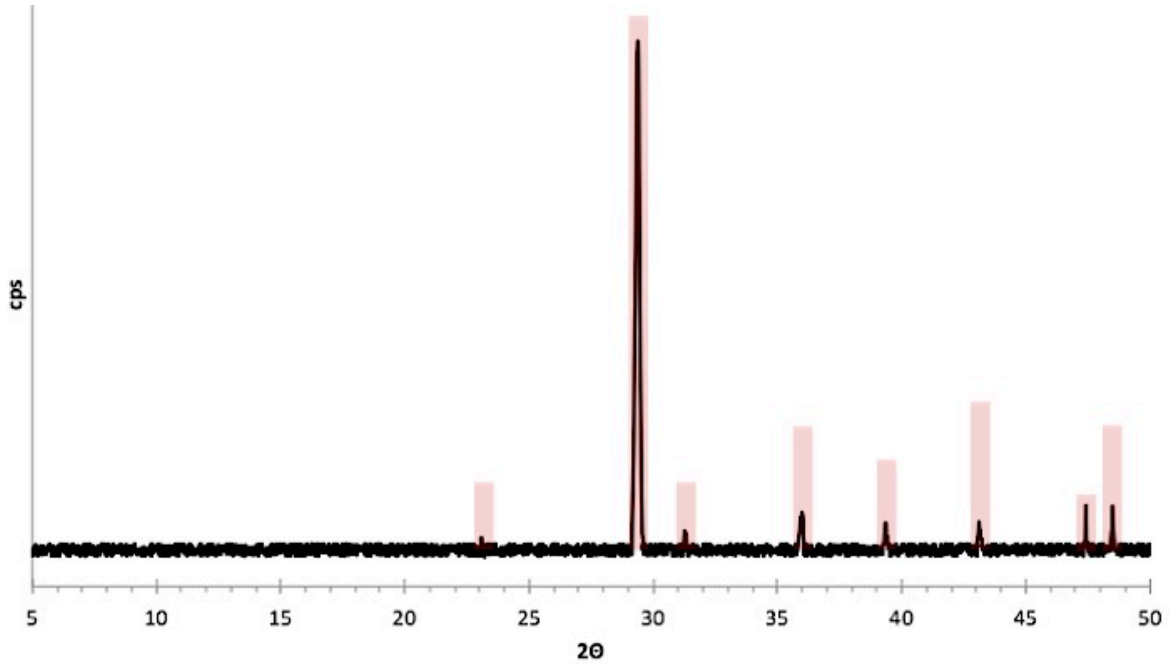

Fig. 4.54 | P-XRD pattern of the residues obtained by the thermolysis of **11** in an air atmosphere. The highlighted areas correspond to the position and intensities calculated for calcite crystals.[178]

The SEM images, presented in Fig. 4.55, show that the morphological appearance of the thermolised material largely corresponds to that of the preceding coordination compounds. Elongated, 1D agglomerates of calcite crystals, are randomly orientated. Their length does not exceed 50 μm, however they appear much thicker than the ribbon-like assemblies of **11**. It is possible that during the thermolysis several ribbons fuse together and form thicker $CaCO_3$ morphologies.

Higher magnification images (Fig. 4.55f-h) reveal that these elongated morphologies are in fact polycrystalline, and composed of small (less than 200 nm) nanocrystals. These nanoparticles agglomerate and give rise to a dense, solid aggregation.

The nanocrystals have irregular faces and do not adopt preferential orientation upon aggregation as observed for **10**. On the nanoscale it is not possible to observe any templating effects of the molecular structure of **11** on the morphology of the residual $CaCO_3$.

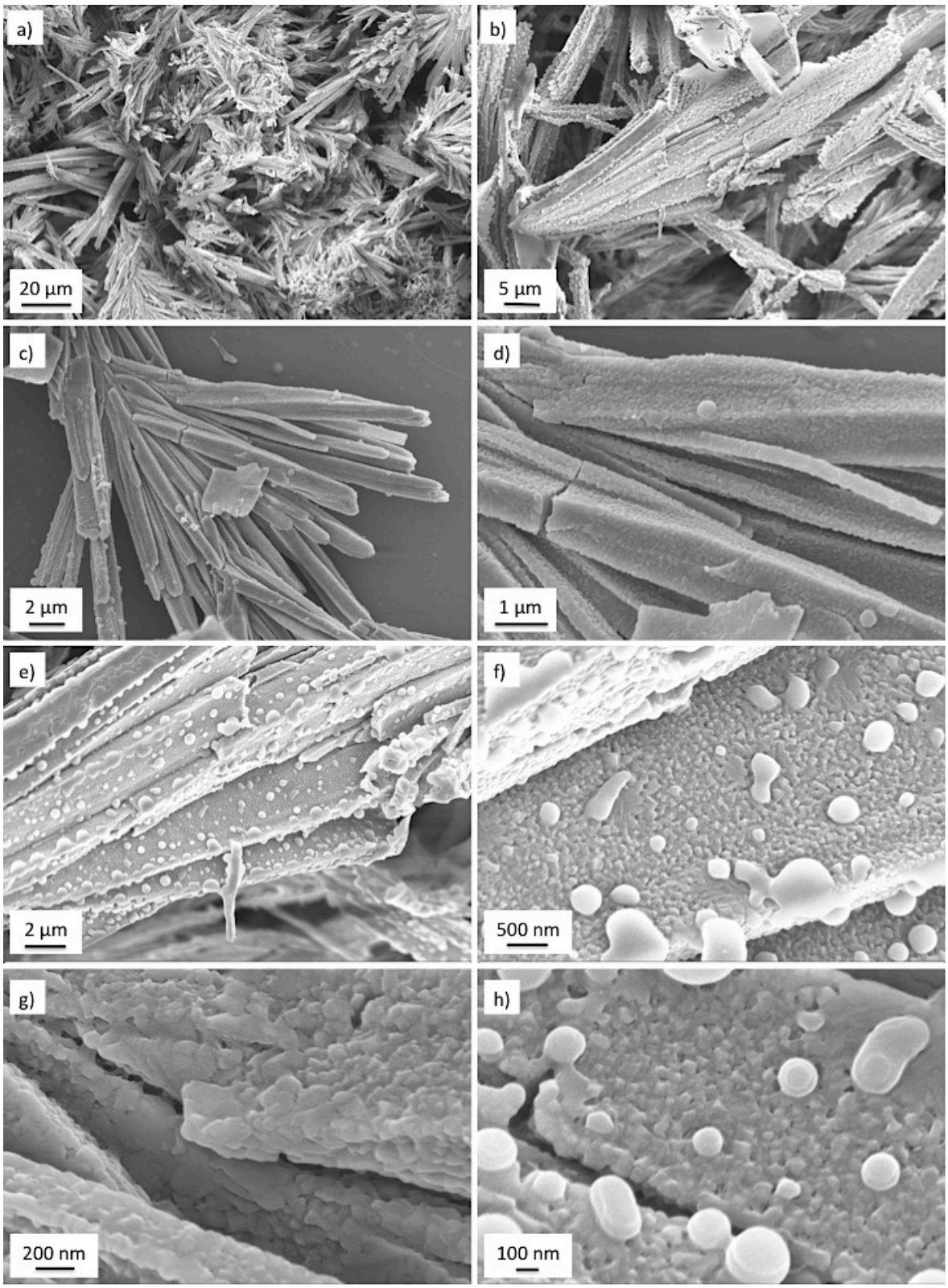

Fig. 4.55 | Calcite crystals formed by thermolysis of **11** in air at 520°C.

Pyrolysis in a nitrogen atmosphere

In a successive experiment the compound was pyrolysed in a nitrogen atmosphere. An analytical sample was heated from 30 °C to 520 °C and the heating rate was kept constant at 0.35 °C/min. The residues were analysed using the P-XRD and further imaged using SEM.

The P-XRD pattern of the residues is presented in Fig. 4.56 (left). All of the reflections are associated with the calcite phase and no other crystalline phase was detected.

The mass of the pyrolysed residues equals 24.2% of the initial compound (Fig. 4.56 right). As the theoretical mass of $CaCO_3$ is estimated to be 19.0% of the starting material, the remaining 5.2% corresponds to the mass of amorphous carbon present within the residues. Further calculations indicate that the mass of the carbon is equal to 21.5% of the total mass of the residues. These calculations are further supported by the results of the elemental analysis experiment.

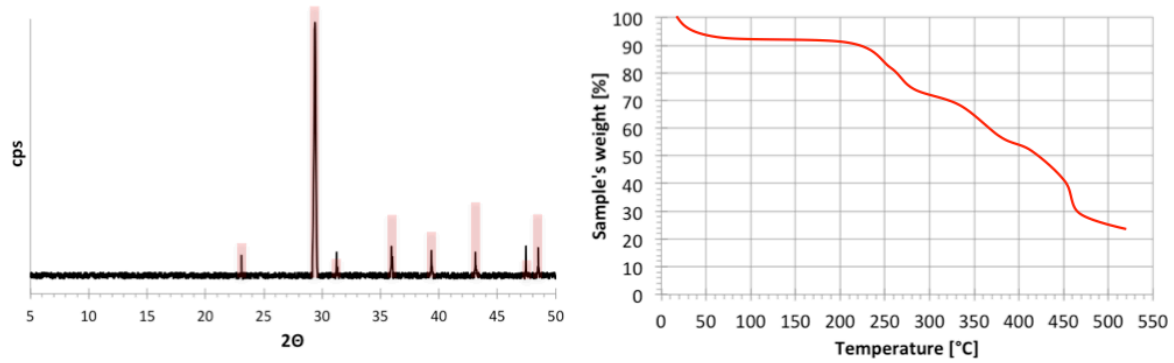

Fig. 4.56 | (**left**) P-XRD pattern of the residues obtained by slow pyrolysis of **13** in the nitrogen atmosphere. The highlighted areas correspond to the positions and intensities calculated for calcite crystals.[178] (**right**) The TGA curve corresponding to the pyrolysis process.

The morphology of the post-pyrolytic residues was studied using SEM. For this purpose the black residues were transferred to a sample tube and immersed in ethanol. It was noticed that once in ethanol, the residues separated into two solids: black, which was believed to be the remaining carbon and white, which was placed on a silicon surface and imaged.

The images, presented in Fig. 4.57a-b, show that the sample is composed of polycrystalline material. Elongated, block-shaped polycrystalline particles aggregate together to form irregular bunches. The shape of these agglomerates resembles the appearance of the ribbon-like assemblies of **11** and also the shape of the calcite crystals obtained in air.

As it is presented in Fig. 4.57c-e, each block-shaped, elongated polycrystalline particle of $CaCO_3$ is *ca.* 25 μm long, while the thickness varies from several hundreds of nanometers to *ca.* 3 μm.

Higher magnification imaging (Fig. 4.57f-h) reveals that the polycrystalline particles are composed of small nanocrystals. There are two different classes of these nanocrystals observed within the sample. The first class contains relatively large (~150 nm) crystalline grains, while the second class consist of very small (less than 10 nm) particles (see Fig. 4.57h). In the images it appears that the larger crystals are immersed in the matrix composed of those very small particles. One may speculate that the initial smaller crystallites form during the pyrolysis process. They fuse together at elevated temperatures and recrystallise to form larger crystals. This kind of morphological transition is explained by the Ostwald ripening process and was observed previously in many systems involving calcium carbonate crystals.[143, 145]

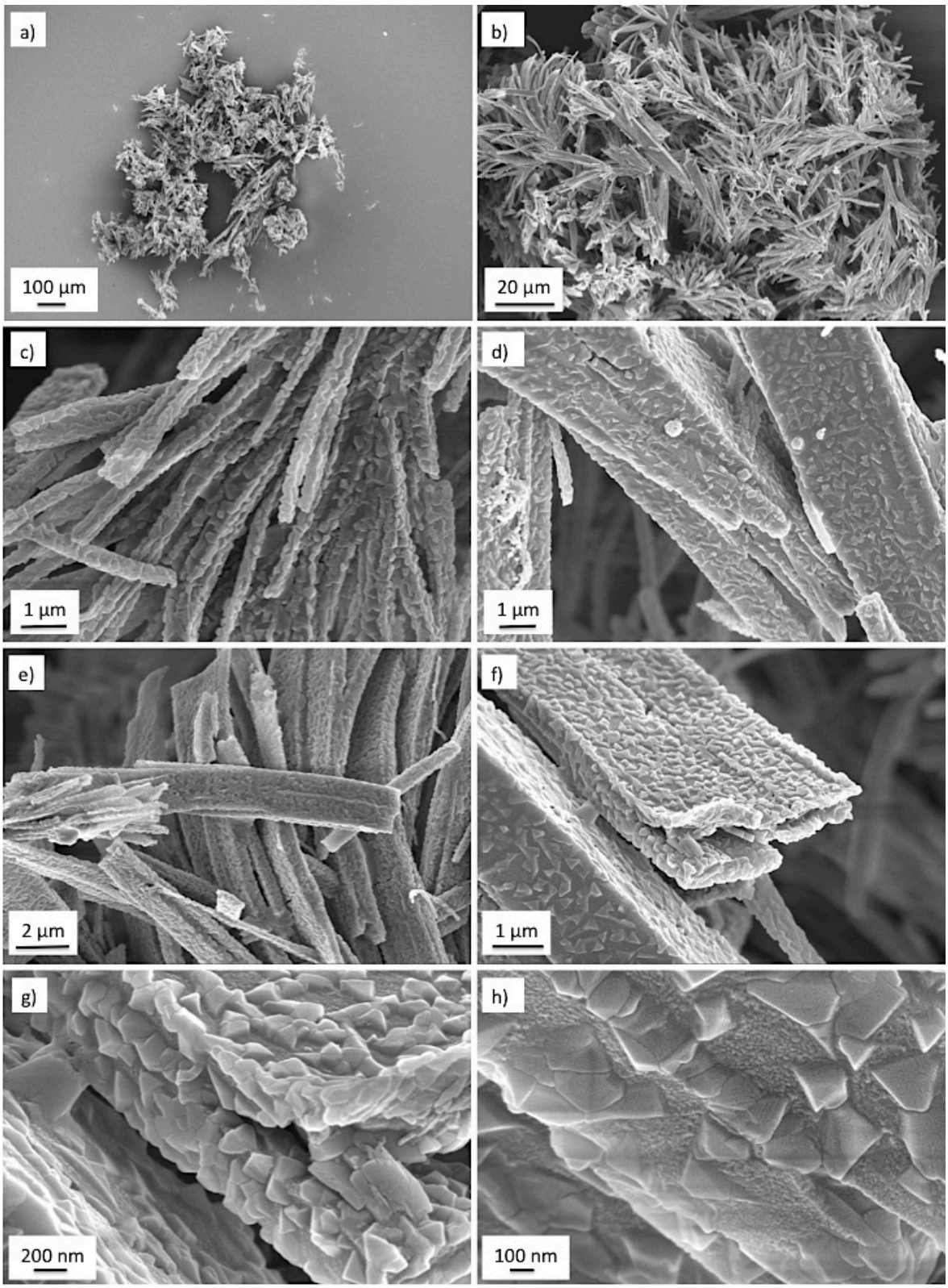

Fig. 4.57 | Crystals of calcite formed during the pyrolysis of **11** in a nitrogen atmosphere at 520°C.

4.6. Compound $[Ca(C_{12}hda)(H_2O)_2] \cdot H_2O$ (**12**)

The successful characterization of the previous calcium-containing compounds encouraged the synthesis of another novel coordination network, which would contain a hda-type ligand substituted with a *n*-C_{12} dodecyl chain, C_{12}hda. It was expected that this compound would adopt a layered lamellar packing structure, similar to those observed for compounds **8-11**. The incensement in the length of the aliphatic chain could further reinforce the hydrophobic interactions and van der Waals forces that occur within the hydrophobic parts of the structure and therefore could alter the self-assembly of the complexes. It may also have an influence on the morphologies of the post-thermolytic and post-pyrolytic ceramic residues.

These predictions were founded on the fact that the C_{12}hda ligand was synthesised before and its complexes with transition metal ions (e.g. Fe^{3+}) were confirmed to adopt hierarchical packing structures. The C_{12}hda ligand was used to prepare the corresponding Ca compound, **12**, which was the subject of extensive studies, including the structure characterization, studies on the self-assembly process, determination of mechanical properties, investigation of the ageing behaviour and the templating effect on residual calcium carbonate.

4.6.1. Characterization of the compound

Compound **12** with the chemical formula $[Ca(C_{12}hda)(H_2O)_2] \cdot H_2O$ forms when calcium ions react with one equivalent of the C_{12}hda ligand under conditions similar to those that led to the formation of compounds **7-11**. A 1:1 (v/v) water/methanol mixture was used and two molar equivalents of triethylamine were added in order to facilitate the deprotonation of the ligand molecules. **12** rapidly precipitates from the solution and despite many attempts it was not possible to obtain a single-crystalline material, which would be suitable for the single crystal X-ray diffraction analysis.

Elemental analysis

Based on our experience with the previously described compounds, it was anticipated that **12** forms 1D coordination chains that consist of mononuclear units, where the ligand molecule provides three O-donors and one N-donor and the coordination sphere surrounding the metal ion is completed with two coordinating water molecules and an additional O-donor originating form a carboxylate group of a neighbouring unit. It was assumed that similarly to structures **8-11**, one of the carboxylate groups of the iminodiacetic acid functionality binds to the calcium ion in the *unidentate* mode, while the second one adopts a bridging mode and therefore connects two neighbouring calcium ions.

It is justified to assume that the neighbouring 1D chain motifs are cross-linked through hydrogen bonding interactions, what results in the formation of 2D sheets. Further self-assembly of these 2D structural motifs is realised *via* hydrophobic interactions and van der Waals forces to give a layered, lamellar solid.

The chemical formula of the mononuclear unit can be written as $[Ca(C_{12}hda)(H_2O)_2]$. An elemental analysis experiment was performed on a dried sample in order to confirm if the

proposed formula is right. The results, presented in Tab. 4.7, show that there is a correlation between the calculated and experimental values.

Tab. 4.7 | Elemental analysis results for compound **12**.

Element	Theoretical composition [%]	Elemental analysis result [%]
C	58.27	**57.92**
H	8.15	**8.71**
N	2.83	**2.81**
Ca	8.10	**8.05**

Thermal analysis

In order to determine the quantity of the constitutional water molecules within **12** and in order to analyse its thermal degradation pathway a TGA experiment was performed. An analytical sample of **12** was placed in a ceramic crucible and heated. The temperature range varied between 30ºC and 900ºC and a linear heating rate of 0.5 ºC/min was applied. The resulting graph is presented in Fig. 4.58.

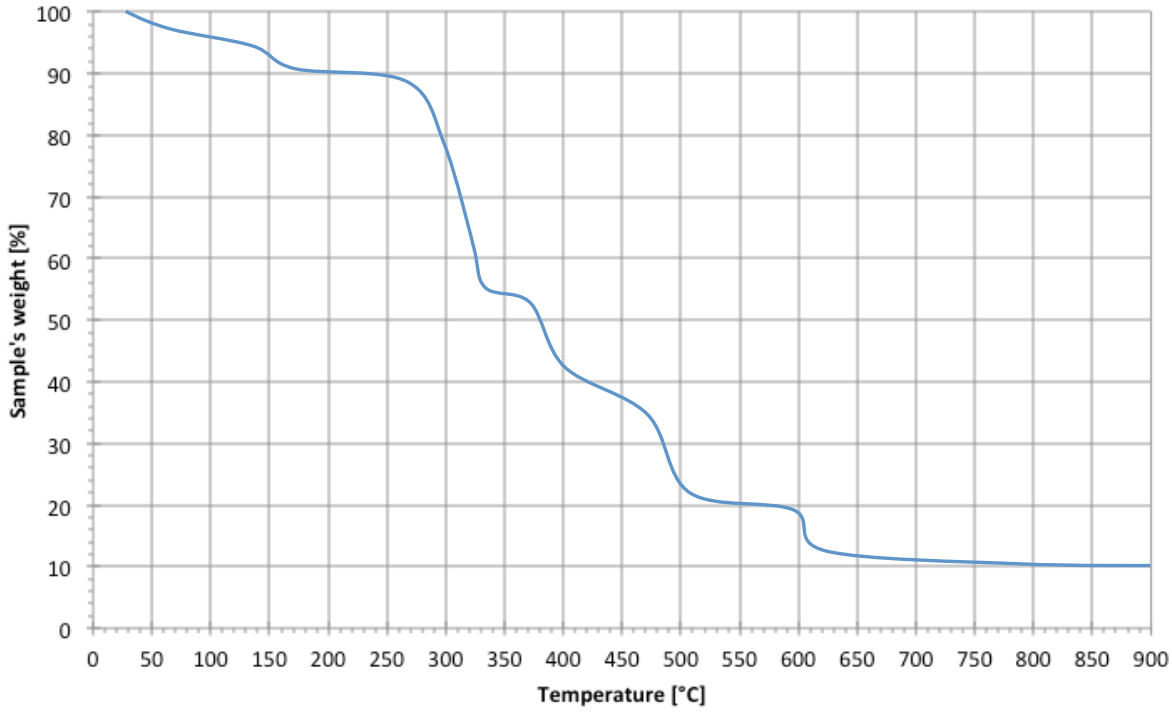

Fig. 4.58 | TGA analysis of **12** performed in air at 0.5 ºC/min.

The initial weight loss is recorded immediately after exposing the sample to the flow of dry air and is associated with the loss of one constitutional water molecule (*experimental weight loss*: ~3%, *theoretical*: 3.5%).

The coordinating water molecules are lost at *ca.* 130 ºC and the completely dehydrated product is stable up to 240 ºC (*experimental weight loss*: ~9.5%, *theoretical*: 10.5%). Above this temperature a rapid oxidation of the organic ligand is observed. Calcium carbonate forms at *ca.* 500 ºC (*experimental weight loss*: ~80%, *theoretical:* 80.5%). The final product of the

degradation, calcium oxide, starts forming at *ca.* 585 ºC and remains stable up to 900 ºC (*experimental weight loss*: ~89%, *theoretical*: 89.1%).

The TGA confirmed that **12** is composed of one ligand molecule, one calcium ion and three water molecules. Two of the water molecules are expected to be involved in coordinative bonds to calcium ions and one might be considered as constitution water molecule. Thus, the TGA of **12** is in agreement with the chemical formula $[Ca(C_{12}hda)(H_2O)_2] \cdot H_2O$.

IR spectroscopy

After the chemical formula of **12** was successfully established, the IR spectroscopy was used to gather information about the binding mode of the C_{12}hda ligand. The IR spectrum of compound **12** was compared with the spectrum of compound **8**. As the only difference between the Me_2hda and C_{12}hda molecules is the presence of the long, *n*-dodecyl chain, it was expected that both spectra would be similar.

Indeed, as presented in Fig. 4.59, the IR spectra of **8** and **12** are very similar. The presence of intense signals at 2918.08 cm^{-1} and 2848.82 cm^{-1} in the spectrum of **12** can be attributed to the asymmetric and symmetric C-H stretching modes arising from the long aliphatic chains. Even the fingerprint areas of the spectra show very similar signals, however, their intensities differ slightly.

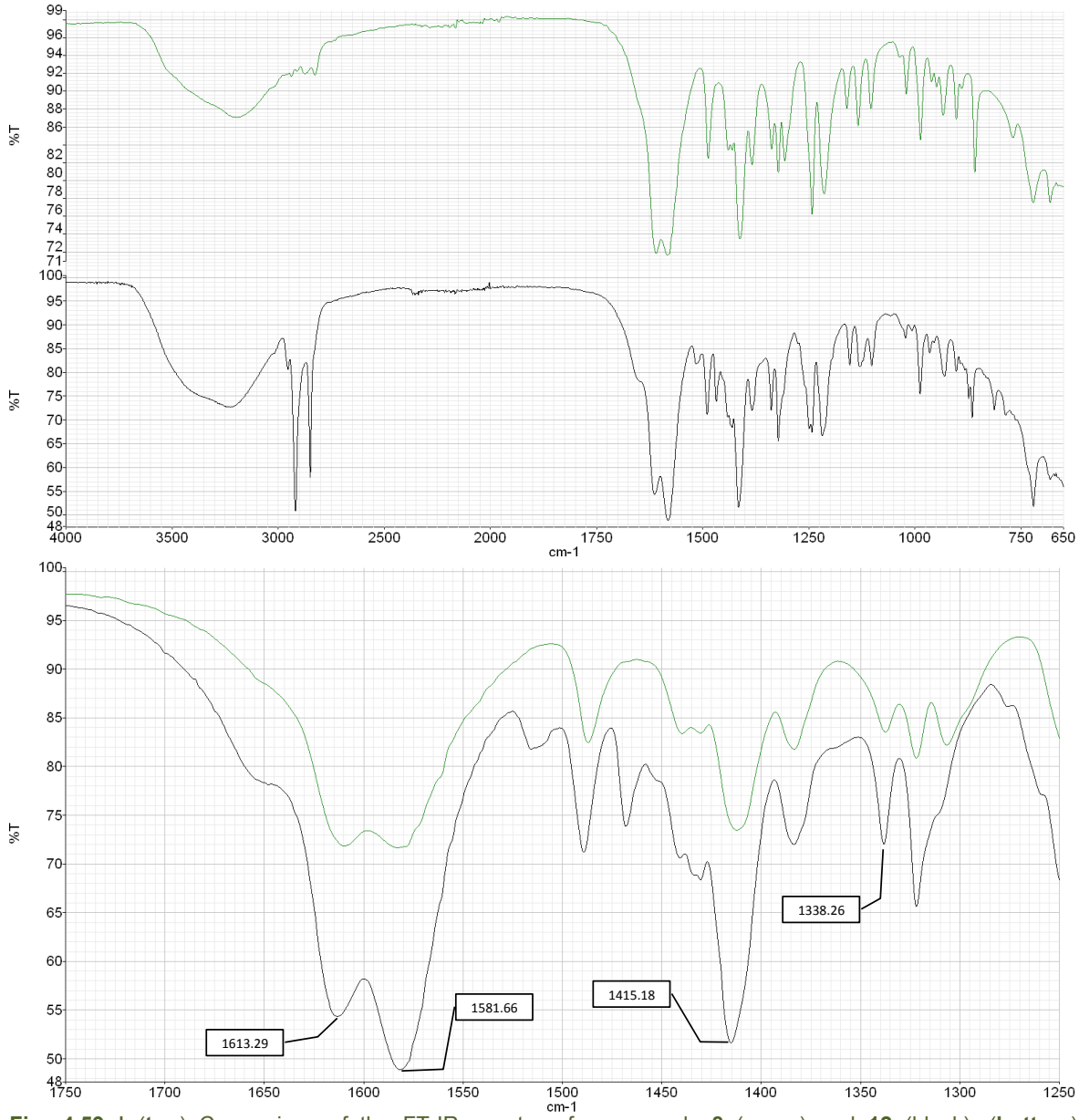

Fig. 4.59 | (**top**) Comparison of the FT-IR spectra of compounds **8** (green) and **12** (black); (**bottom**) magnification on the range showing carboxylate signals.

The frequencies of the signals attributed to the carboxylate groups in **8** and **12** are summarised in Tab. 4.8. The positions of the corresponding signals are not shifted by more than 4 cm^{-1}.

Tab. 4.8 | Characteristic frequencies of the carboxylate groups vibrations observed in the IR spectra of **8** and **12**.

Compound	ν_{as1} (COO)	ν_{as2} (COO)	ν_{s1} (COO)	ν_{s2} (COO)	$\Delta\nu_1$	$\Delta\nu_2$
8	1609.87 cm^{-1}	1582.95 cm^{-1}	1412.19 cm^{-1}	1338.31 cm^{-1}	170.79 cm^{-1}	271.56 cm^{-1}
12	1613.29 cm^{-1}	1581.66 cm^{-1}	1415.18 cm^{-1}	1338.26 cm^{-1}	166.48 cm^{-1}	275.03 cm^{-1}

In both cases the differences between the asymmetric and symmetric stretching ($\Delta\nu$) frequencies of the carboxylate groups are similar.

As it was observed for the previously described compounds, one difference ($\Delta\nu_1$) corresponds to the carboxylate group that binds in the bridging mode to two neighboring

calcium ions, while the second one ($\Delta\nu_2$) can be attributed to the remaining carboxylate group of the iminodiacetic acid moiety which adopts the *unidentate* binding mode. It is therefore believed that the C_{12}hda ligand molecules are responsible for linking neighboring complexes into 1D chains, which further assemble *via* hydrogen bond interactions and form 2D layers. These observations are in agreement with the crystallographic information obtained for compound **8** and with the tendencies observed for **9**-**11**.

Electron microscopy

SEM was used to study the morphology of the self-assembled material. Fig. 4.60 shows that the Ca complex forms fibrous- or belt-like structures that are randomly orientated on the surface.

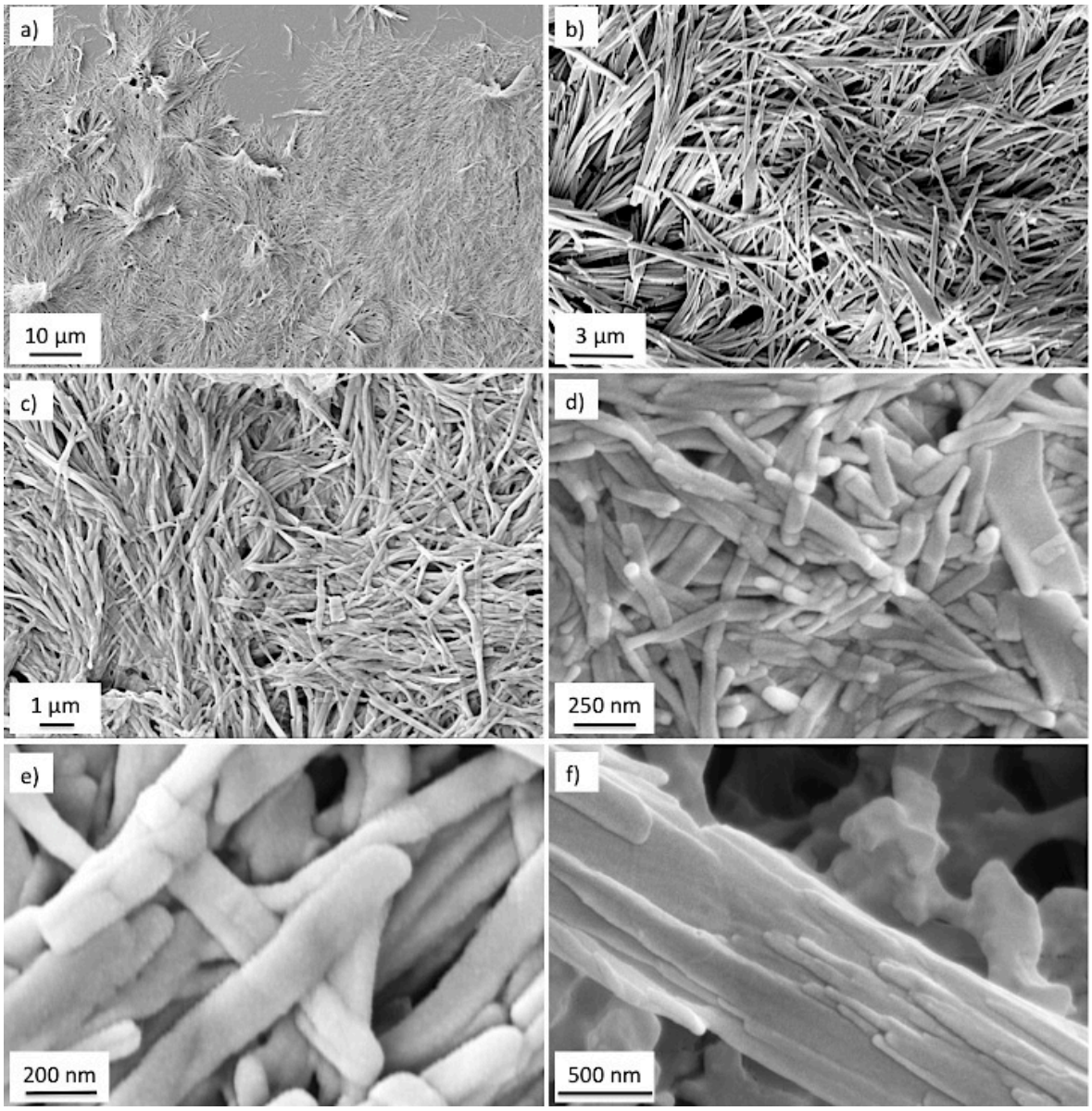

Fig. 4.60 | SEM micrographs of the assemblies of **12**. **a)** overview picture; **b-d)** higher magnification showing randomly orientated assemblies; **e-f)** imaging on the nanoscale shows individual fibres.

The average length of a single fibre is ~5 µm, while the width does not exceed 300 nm. A selection of fibres agglomerates but most remain separated. Similar to the assemblies of **10**

and **11**, the material appears to be soft. Individual fibres can be twisted, folded or bent (see Fig. 4.60e). Although the surface of the majority of fibres is smooth, some of them further assemble to give larger and thicker objects (Fig. 4.60f).

The SEM imaging allowed for the employment of the EDX analysis. The X-ray energy spectrum presented in Fig. 4.61 confirms that the fibres are composed of carbon, oxygen and calcium (the abundance of the nitrogen atoms is below detectable levels and the hydrogen atoms cannot be detected with this technique). There are no other elements present; this confirms that the coordination complex, as predicted, does not contain any impurities.

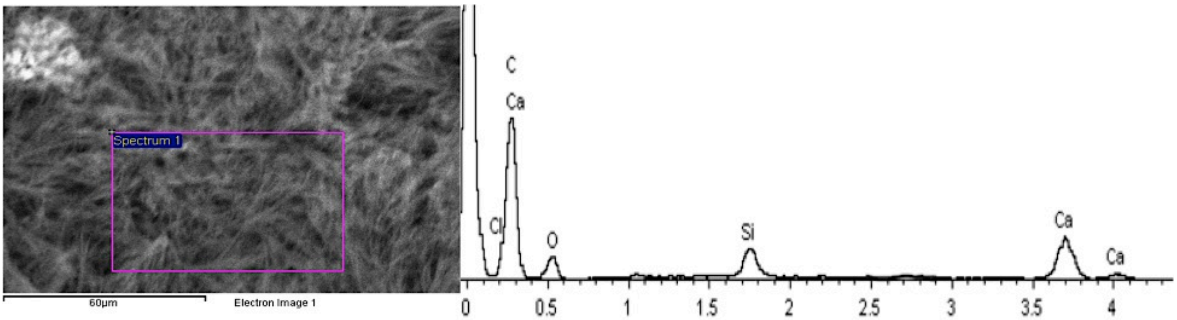

Fig. 4.61 | EDX analysis of compound **12**. The SEM image (left) and the corresponding X-ray energy spectrum (right).

The fibrous assemblies are thin enough to allow for TEM studies. Fig. 4.62 confirms that **12** adopts layered, lamellar structure. The lattice separation distance measured with this technique is 2.51(±0.15) nm. This value is 0.19 nm larger than it was observed for compound **11**, which contains a decyl chain attached through an ester moiety.

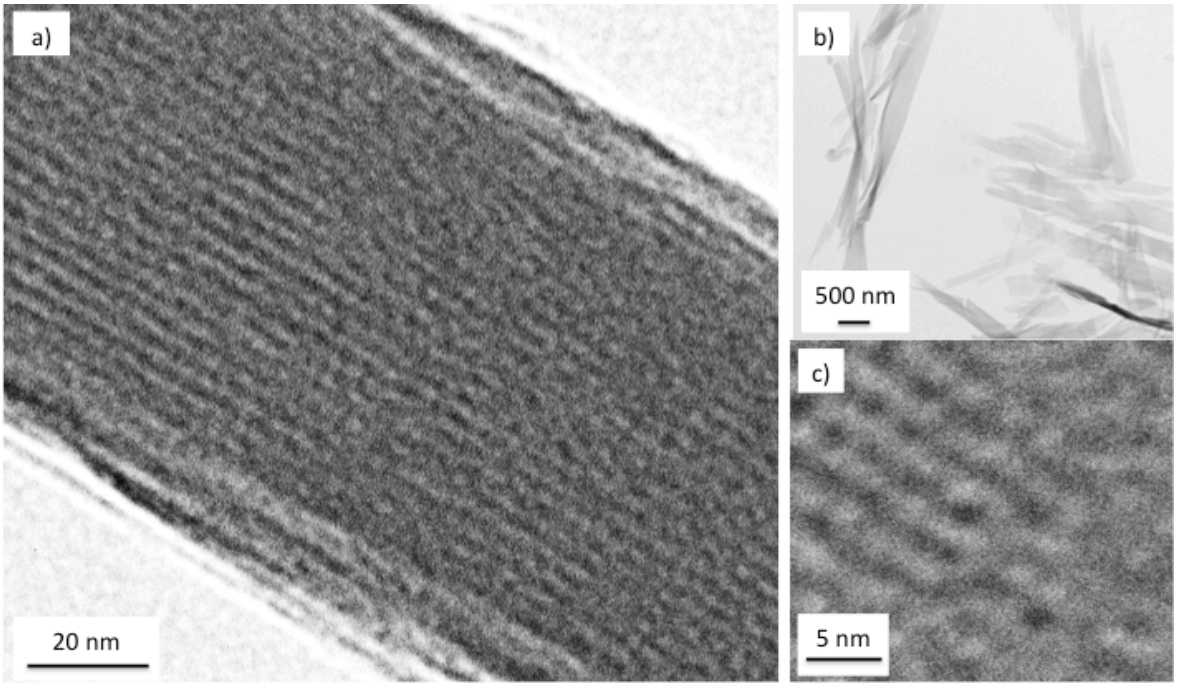

Fig. 4.62 | TEM imaging performed on the assemblies of **12** in the diffraction contrast regime. **a)** layered, lamellar packing motif is observed within the assemblies; **b)** overview; **c)** higher magnification allows to calculate the lattice separation distance.

A model of the packing structure of the self-assembled belt-shaped particles of **12** can be proposed, based on the information provided by the SEM and TEM imaging. As presented in Fig. 4.63a-b, neutral layers in **12** extend parallel to the longest belt axis and stack across

the width of the belt with a separation distance of *ca.* 2.5 nm, which is very well in agreement with the extent of alkyl moieties of the organic ligands. The corresponding supramolecular interactions are coordination bonds, which link mononuclear units located parallel to the longest belt axis, and hydrophobic interactions along with van der Waals forces that act parallel to the middle-length belt axis. Hydrogen bond interactions dominate along the shortest belt axis.

As presented in Fig. 4.63b, within the terminal sides of the belt, which are defined by the shortest and the longest belt axes, coordinating water molecules are expressed towards the external environment. Hydrogen bond interactions link these O-donors with solvent water molecules, therefore, it is justified to say that the surface of these sides is entirely covered by water.

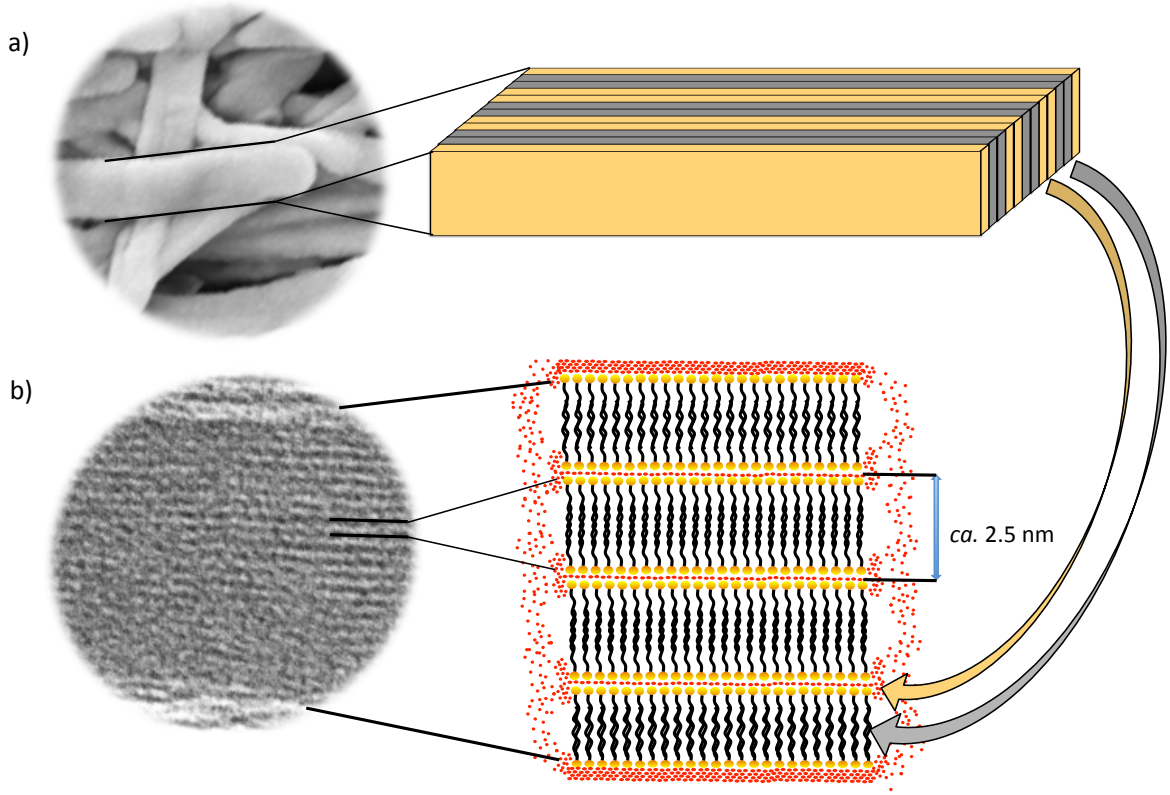

Fig. 4.63 | A model of the solid-state packing structure of **12** synthesised in an aqueous environment. **a)** SEM image shows that **12** self-assembles into belt-shaped objects, which can be considered as blocks consisting of the near 2D H-bound layers; **b)** the layered arrangement in **12** is confirmed by TEM. Colour code: black – aliphatic chains, red - water molecules, yellow – Ca along with its coordination sphere. Within the model blocks, the yellow colour corresponds to the hydrophilic areas and the grey colour represents the hydrophobic areas.

Ageing process

During the SEM investigations, it was noticed that the amphiphilies in as-prepared solid samples are capable of undergoing morphological rearrangements at room temperature. It was observed that meshes of entangled belts amalgam to produce homogenous films that extend over the surface of the sample. This effect is a continuous process, which may be associated with a slow loss of constitutional solvent molecules. In contrast, dried or heated samples of **12** retain their fibrous, entangled structure.

The images obtained after one week from the deposition of **12** on a Si surface, which are presented in Fig. 4.64, suggest that the rearrangement is initiated in the thinner, outer edges of the sample and involves the formation of crossbar or grid motifs whereby single belts are crossed at *ca.* 90° angles.

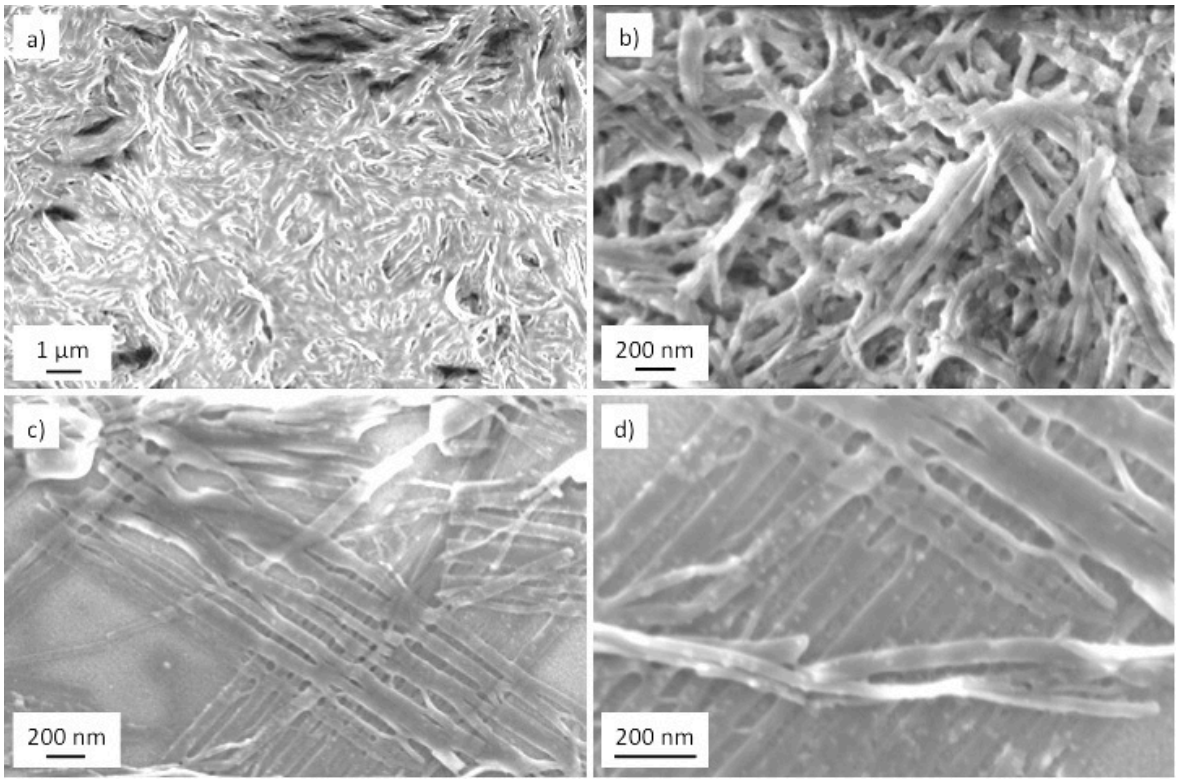

Fig. 4.64 | Surface of **12** imaged after one weak from preparation. SEM images obtained for an uncoated sample.

When the same sample was imaged after two weeks (Fig. 4.65), the obtained micrographs revealed that the whole surface of the sample was taking part in the rearrangement process. It was noticed that the surface of the sample seemed to display two different morphologies: a clearly visible grid-like motif and several extended film areas (max. observed dimension 0.3 mm x 0.5 mm), which appeared to form on the previously mentioned grid-like architecture.

In the SEM images presented in Fig. 4.65, the areas covered by the film appear darker, while the brighter parts adopt the grid-like arrangement. It is almost impossible to observe the meshes of belt-like assemblies, which were the original morphology noted for a fresh sample of **12**.

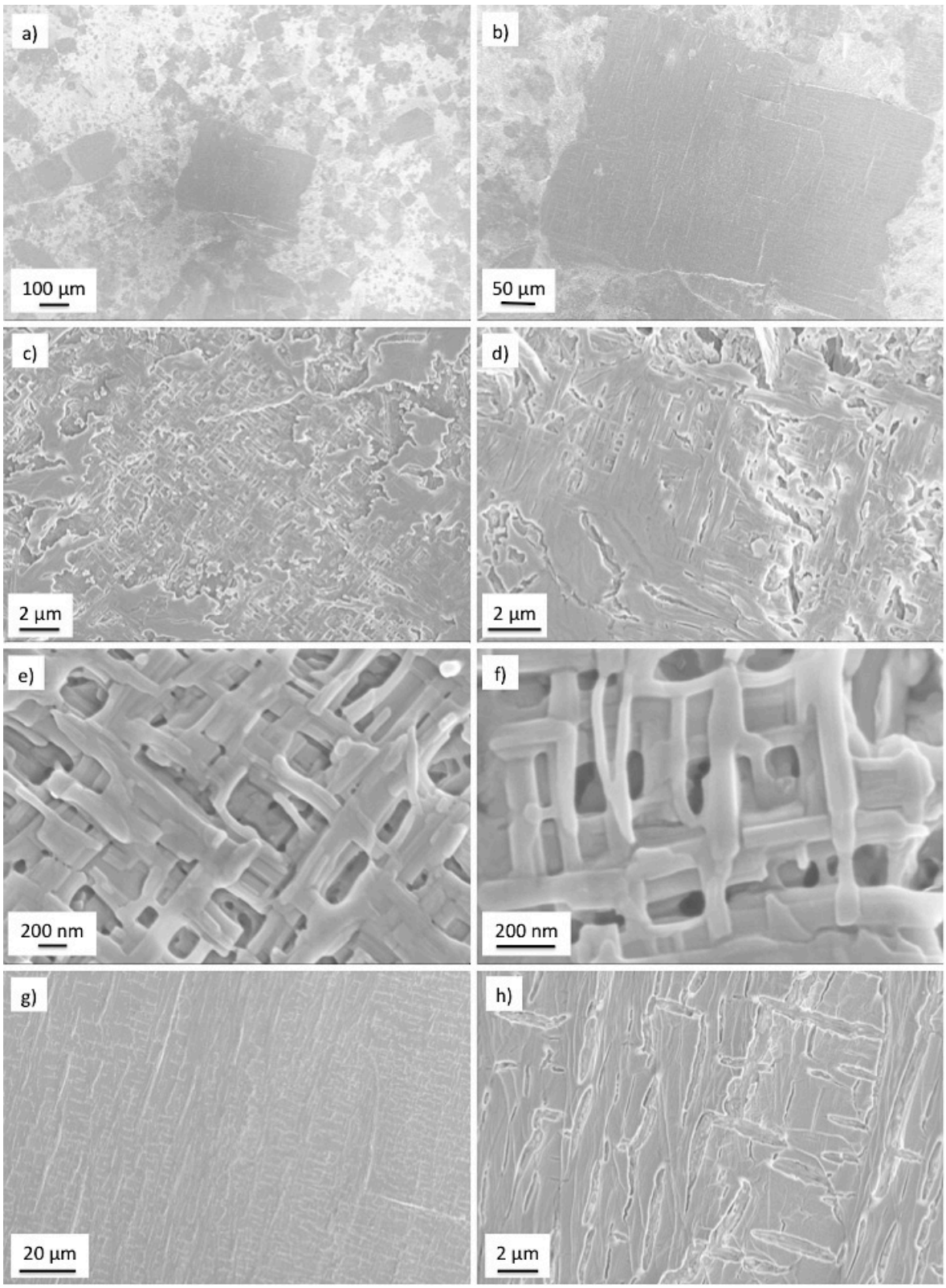

Fig. 4.65 | A sample of **12** deposited on a Si surface and imaged after 2 weeks from the preparation. **a)** overview picture; **b)** magnification on a smooth area (which appears darker on the SEM pictures); **c-d)** higher magnification images showing the grid-like motif and the smooth film formation on the top of the grid; **e-f)** magnification on the grid-like motif; **g-h)** magnification on the smooth area reveals the surface details.

The final result of the morphological rearrangement was the formation of a film on the surface of the sample. It was noticed that in one month the entire area (*ca.* 0.5 x 1.0 cm) of the sample was completely covered by the film. As visualised in Fig. 4.66, the surface of the film appeared to be smooth.

Higher magnification imaging (Fig. 4.66e-f) revealed that the surface of the film displayed a layered imprint, which extended in the horizontal direction (with respect to the image). The thickness of the visible layers was *ca.* 300 nm. This value can be compared with the width of the original belt-like assemblies that was measured along their middle-length axis.

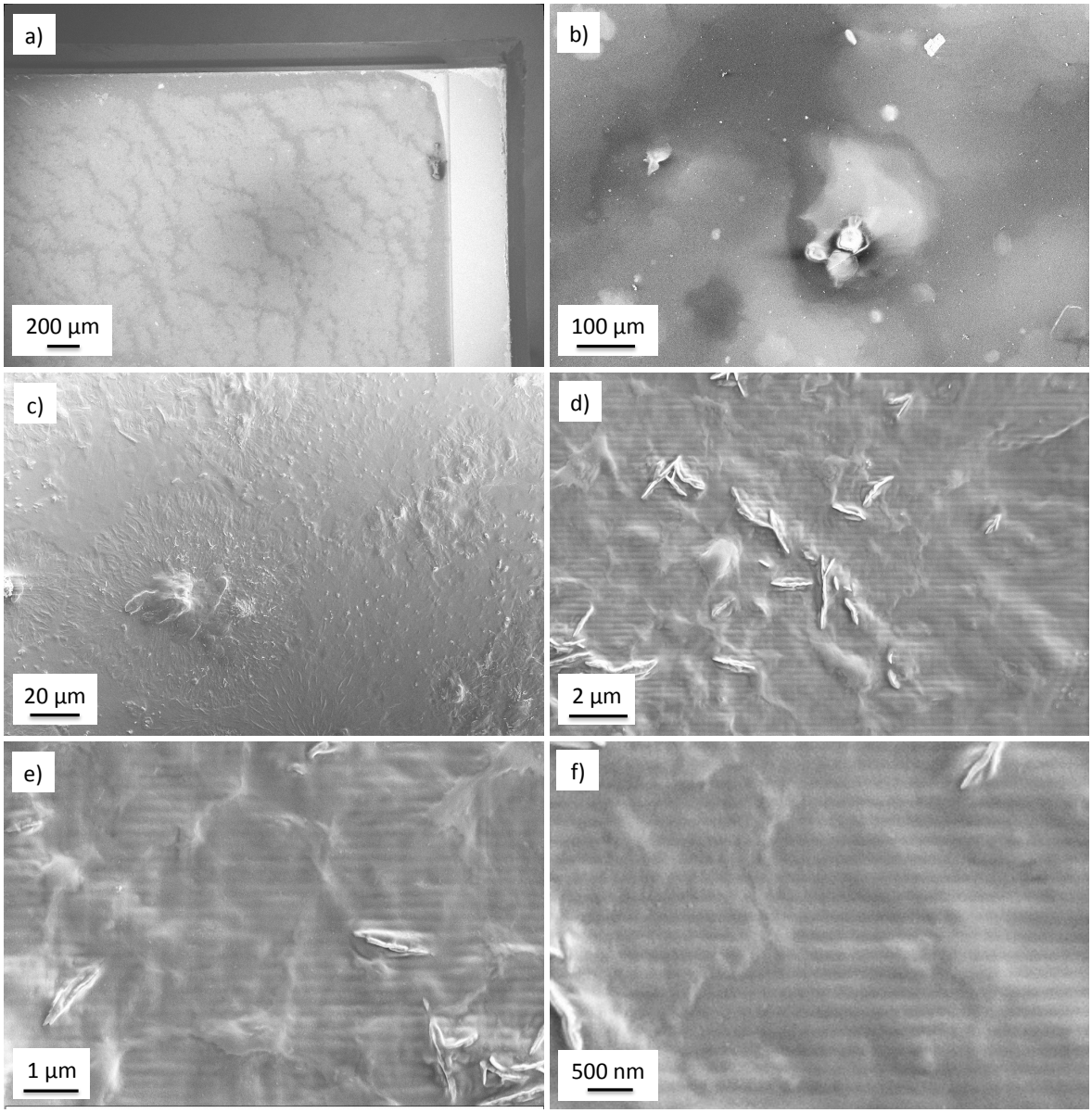

Fig. 4.66 | The surface of **12** imaged after 4 weeks.

These observations suggest that the fibrous morphology observed for the fresh samples of **12** is a kinetic product of the self-assembly process. In time, the fibres rearrange to form a thermodynamically stable product, which appears to be the film. This morphological rearrangement may be a result of a two-dimensional crystallisation process, which could be driven by the drying effect and the necessity to fill the resulting vacant coordination sites of the Ca ions.

The rearrangement was also observed in other samples of **12**, which were placed on the surface of a polycarbonate membrane (SEM images are not presented as they have poor

quality due to the charging effects), thus, this effect cannot be considered as a result of the epitaxial growth of the crystalline phase on the (101) silicon surface.

Mechanical properties

It was observed that the freshly prepared self-assembled belts of **12** can be processed into films. In order to do so, a dried sample of **12** was immersed in dichloromethane and sonicated in the ultrasound bath to form a homogenous suspension. Then few drops of the suspension were filtered using a polycarbonate membrane filter. The sample located on the surface of the membrane dried and formed a thin film, as presented in Fig. 4.67.

In collaboration with Prof. Biqiong Chen from the TCD School of Engineering, a nanoindentation experiment was performed to determine the mechanical properties of this film. The calculated elastic modulus for this thin structure was 0.142 (±0.011) GPa, what indicated that the mechanical properties of the film could be compared with rubber (which exhibits the elastic module of 0.01-0.1 GPa) or nylon fibres (2-4 GPa).[180] The corresponding load vs. displacement chart is presented in Appendix A.2.1 on page 259.

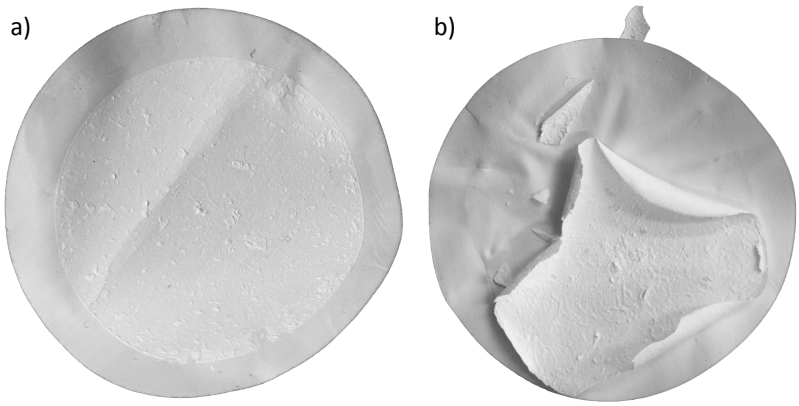

Fig. 4.67 | Thin film of **12** formed on a polycarbonate membrane by filtering a dispersion of the self-assembled material in CH_2Cl_2. **a)** fresh sample; **b)** the dried film separates from the membrane.

After confirming that **12** is indeed a soft material, it was decided to test if it can reinforce the mechanical properties of polymeric composite materials. It was decided to test if a small addition of **12** can elevate the elastic modulus of poly(acrylic acid), which is often used as a dental filling material. This research was performed in collaboration with the TCD Dental Hospital and the detailed methodology can be found in the PhD thesis written by Dr. Adam Dowling.[181] From the mechanical point of view, for a successful nanoadditive the shape of the particles is as important as their composition. The polymer chains can interact *via* non covalent bonds with the thin and flexible particles characterised by nanometric dimensions, thus any occurring crack has a chance to stop propagating when it reaches the fibres.[182-184]

Small amounts of freshly prepared fibres of **12** (1, 2 and 3% by weight) were dried in ambient conditions and mixed with poly(acrylic acid) (Mn = 80.8 kDa, $\boldsymbol{P}$ = 1.65). Then the composite material was processed into small discs characterised by an average diameter of 3.84 mm. Finally, the necessary force required to break these discs was measured and from its values the elastic modulus was calculated. The highest increase in the elastic modulus of the

composite material, 25%, was observed when 2% (by weight) of **12** was added to the polymer matrix. This number is comparable to values noted for other commercially accessible nanoadditives, e.g. montmorylonite or SiO_2.[185]

4.6.2. **12** as a template for the formation of calcium carbonate

The degradation pathway of **12**, which was investigated using TGA, indicates that one of the degradation products is calcium carbonate, forming at *ca.* 500 °C (see Fig. 4.58 on page 165). In order to investigate the templating effect, which the supramolecular structure of **12** may have on the residual $CaCO_3$ crystals, the TGA experiment was repeated. The heating rate was set to 0.35 °C/min and an analytical sample of **12** was heated from the room temperature up to 520 °C. The residues were allowed to cool to room temperature and were collected and analysed using the IR, P-XRD pattern and SEM techniques.

The P-XRD analysis (Fig. 4.68) confirms that calcite is the only crystalline phase present within the sample.

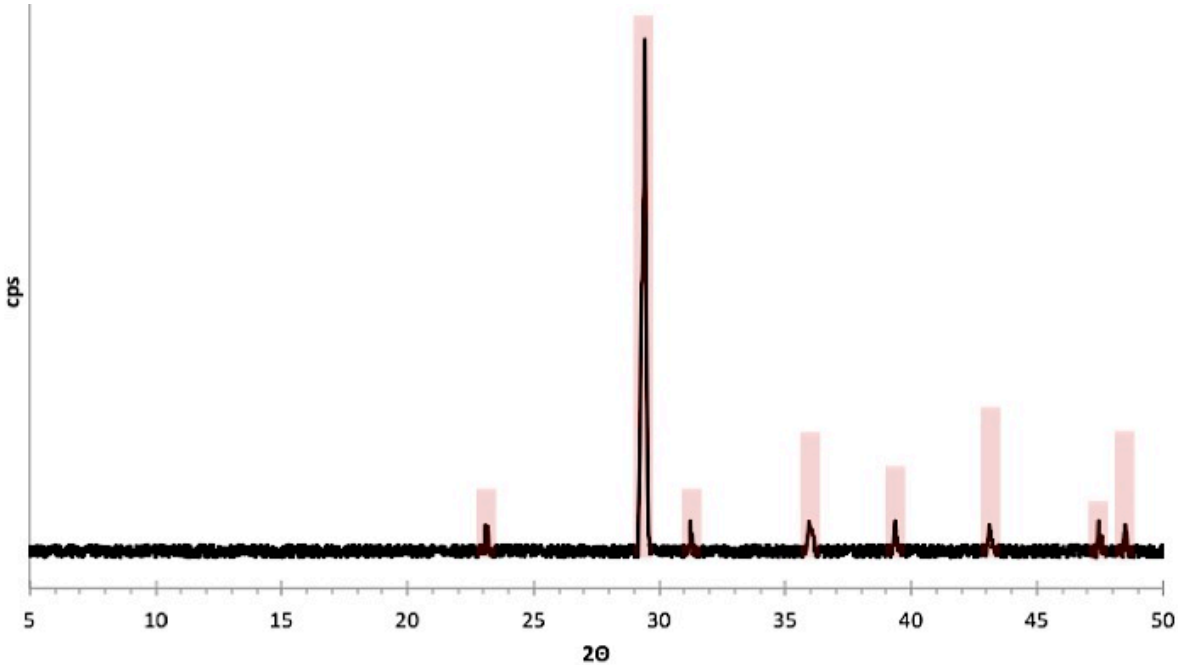

Fig. 4.68 | P-XRD pattern obtained for the residual $CaCO_3$ crystals remaining after the thermolysis of **12** in air. The highlighted areas correspond to the calculated positions and intensities of calcite crystals.[178]

The thermal degradation process was traced using IR analysis. A small sample of the residues was collected each time when the sample reached a certain temperature. The results, presented in Fig. 4.69, show that along with the increase of the temperature the relative intensity of the signals that origin from the organic ligands decreases. At 130 °C the broad band between 3800 and 3400 cm^{-1} is no longer present, due to the loss of the constitutional moisture. The relative intensity of the asymmetric and symmetric $–CH_2-$ stretches also decreases as the long hydrophobic chain degrades. The low intensities of the bands observed at 350 °C may suggest that calcium iminodiacetate is the thermolysys product which directly precedes the formation of $CaCO_3$.

The fingerprint region of the spectra recorded for the samples that had been heated at 30 °C, 130 °C and 210 °C is almost similar. Above this temperature the organic ligand rapidly decomposes, this is reflected in the IR spectrum obtained at 290 °C, where the fingerprint area is flatten and many signals are missing. The spectrum recorded at 500 °C is identical to a reference spectrum of $CaCO_3$.

The IR spectroscopy results are in agreement with the calculations performed for the TGA analysis and with the behavior of the previously described compounds **8**-**11**.

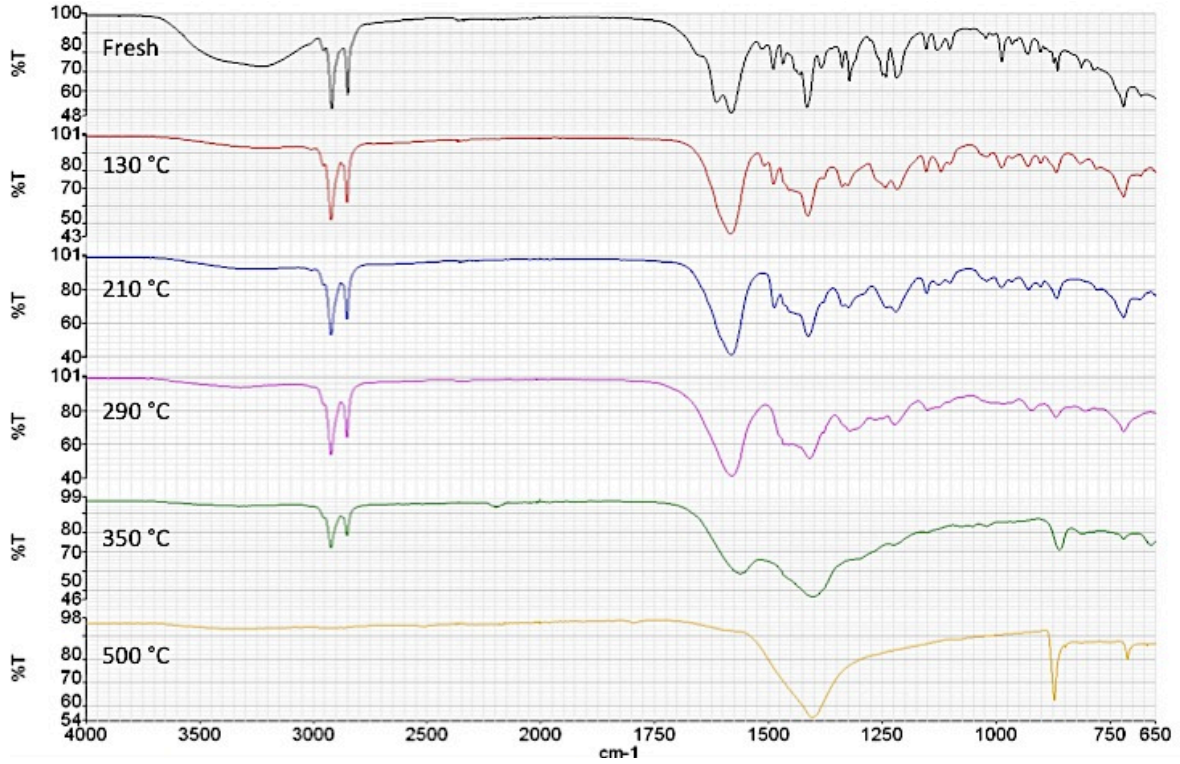

Fig. 4.69 | IR spectra of the residues of **12** obtained in different temperatures. **Black**) fresh sample; **red**) 130 °C; **blue**) 210 °C; **pink**) 290 °C; **green**) 350 °C; **yellow**) 500 °C.

The residues remaining after the thermolysis were imaged using SEM to determine their morphology. As presented in Fig. 4.70a-b, the residual crystals of $CaCO_3$ form large (*ca.* 200 μm), polycrystalline agglomerates that adopt an irregular shape. Their edges are highly defected what suggest that they had been a part of a more unified structure that cracked during the drying process/thermolysis. Higher magnification images (Fig. 4.70c-d) show that the agglomerates are composed of small crystalline particles, which stack in random directions and form a dense solid. Their sizes range between a few hundred nanometers and 3 μm. The orientation of these crystallites is rather random and they do not seem to prefer any specific direction.

Imaging performed on the nanoscale reveals that each crystallite displays a distinct layered imprint. Fig. 4.70e-h shows clearly that the particles do not look like typical rombohedral calcite crystals, but may be viewed as composed of almost flat, two-dimensional layers that stack to give rise to a 3D object. The observed thickness of these layers varies between ~5 and 40 nm. The crystallites may contain layered features that are smaller and

that may correlate to the molecular structure of the hybrid organic-inorganic precursor, however, the resolution of the applied SEM technique did not allow us to confirm this.

This morphology is similar to the layered arrangement observed for the Cu-containing structures **1**-**5**. Although the thickness of the layers exceeds the previously determined lattice separation distance, the formation of the layered motif may be a result of the layered, lamellar arrangement observed within the packing structure of **12**.

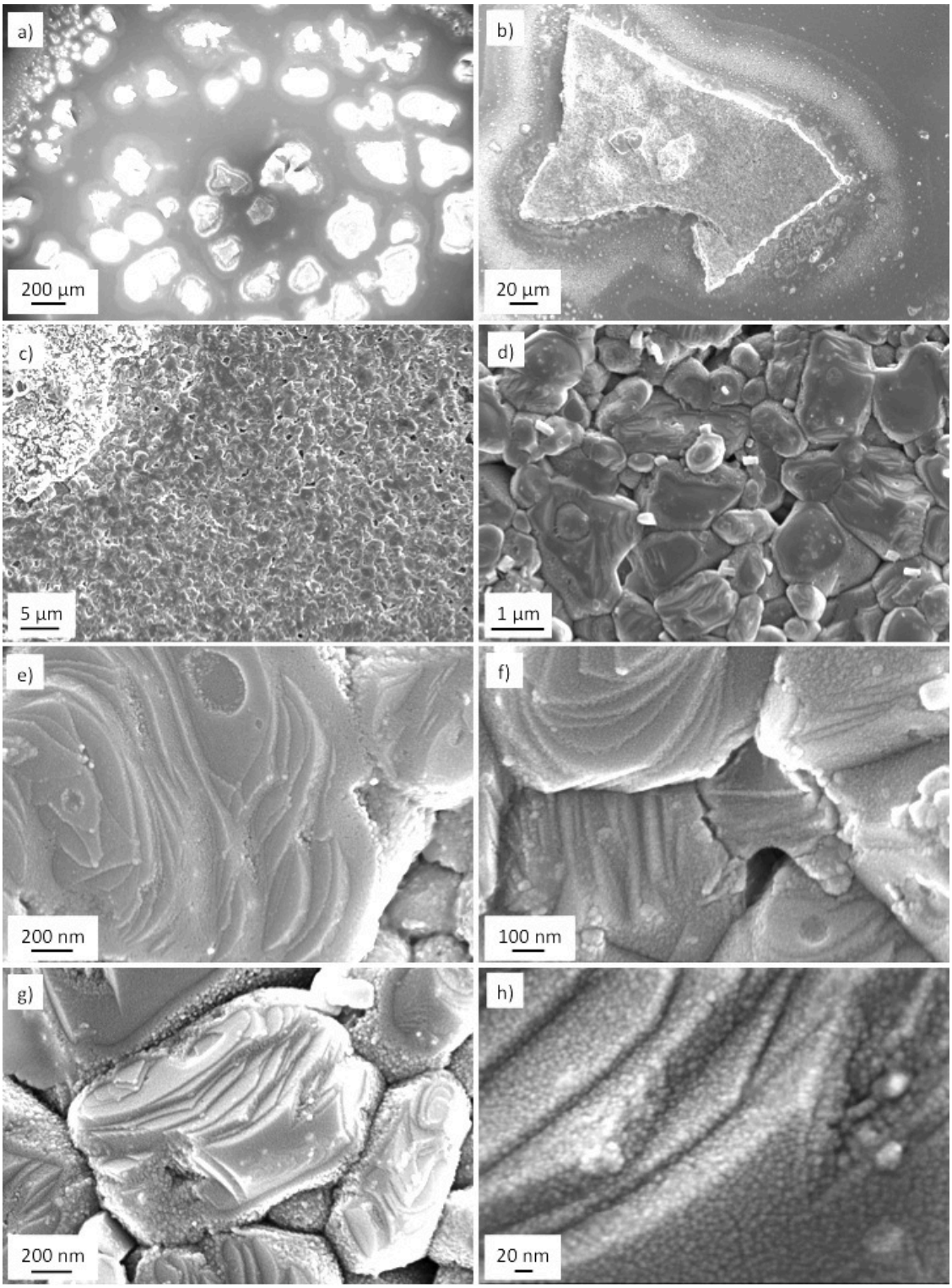

Fig. 4.70 | SEM images of the residual calcite crystals obtained in the thermolysis process of **12**. Imaging performed on a Au-coated sample. **a)** overview; **b)** magnification on an individual polycrystalline particle; **c-d)** the polycrystalline particle is composed of small crystals; **e-h)** these small crystals display hierarchical layered organisation.

It was decided to reproduce the thermolysis experiment in an nitrogen atmosphere to check if the lack of oxygen may enhance the potential templating effect of **12** on the formation of $CaCO_3$.

An analytical sample of **12** was placed in a ceramic crucible and heated from 30 °C to 520 °C. The heating rate of 0.35 °C/min used previously was not changed. The residues were collected and analysed using the P-XRD and SEM techniques.

The P-XRD pattern, presented in Fig. 4.71, confirms that calcite is the only crystalline product of the pyrolysis process. It also shows that no other crystalline impurities are present within the residues.

The quantity of amorphous carbon remaining in the sample can be calculated from the corresponding TGA curve (Fig. 4.71, right). At 520 °C the remaining mass of the sample equals 29.4% of the original weight. As the theoretical mass of $CaCO_3$ is 19.5% of the initial mass, the remaining 9.9% corresponds to the excess of carbon. This means that the mass of the amorphous carbon residues represents 33.7% of the total mass of the residues. These calculations have been further confirmed by the results of the elemental analysis experiment, which was performed on the post-pyrolytic residues.

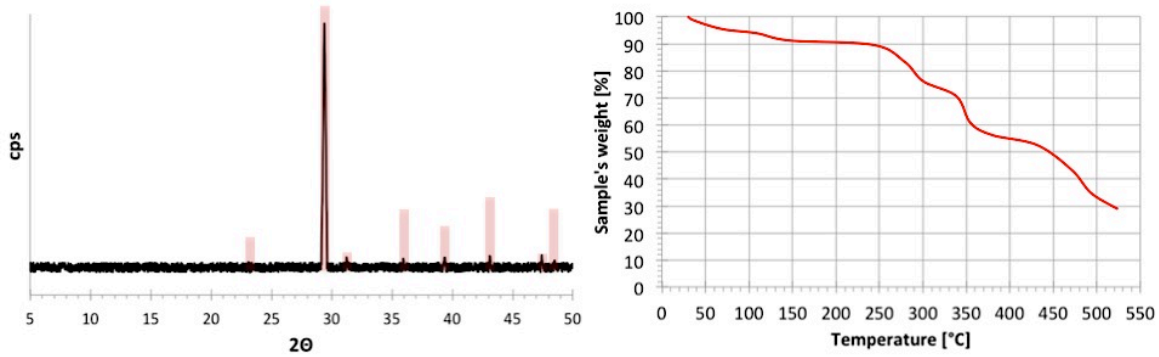

Fig. 4.71 | (**left**) P-XRD pattern recorded for the residues remaining after the pyrolysis of **12** in nitrogen. The highlighted areas correspond to the positions and intensities calculated for calcite crystals.[178] (**right**) The TGA curve corresponding to the pyrolysis process.

The SEM images of the residues, presented in Fig. 4.72, show that the whole Si surface is covered with an irregular, rather thick layer of small, irregular particles. Some of these particles form thicker agglomerates, which are presented in Fig. 4.72b. High magnification images (Fig. 4.72c-d) reveal that in contrast to the calcite crystals obtained in an air atmosphere, these crystallites do not display the layered imprint. Moreover, they do not have sharp crystal faces and aggregate to an extend that their borders cannot be clearly defined.

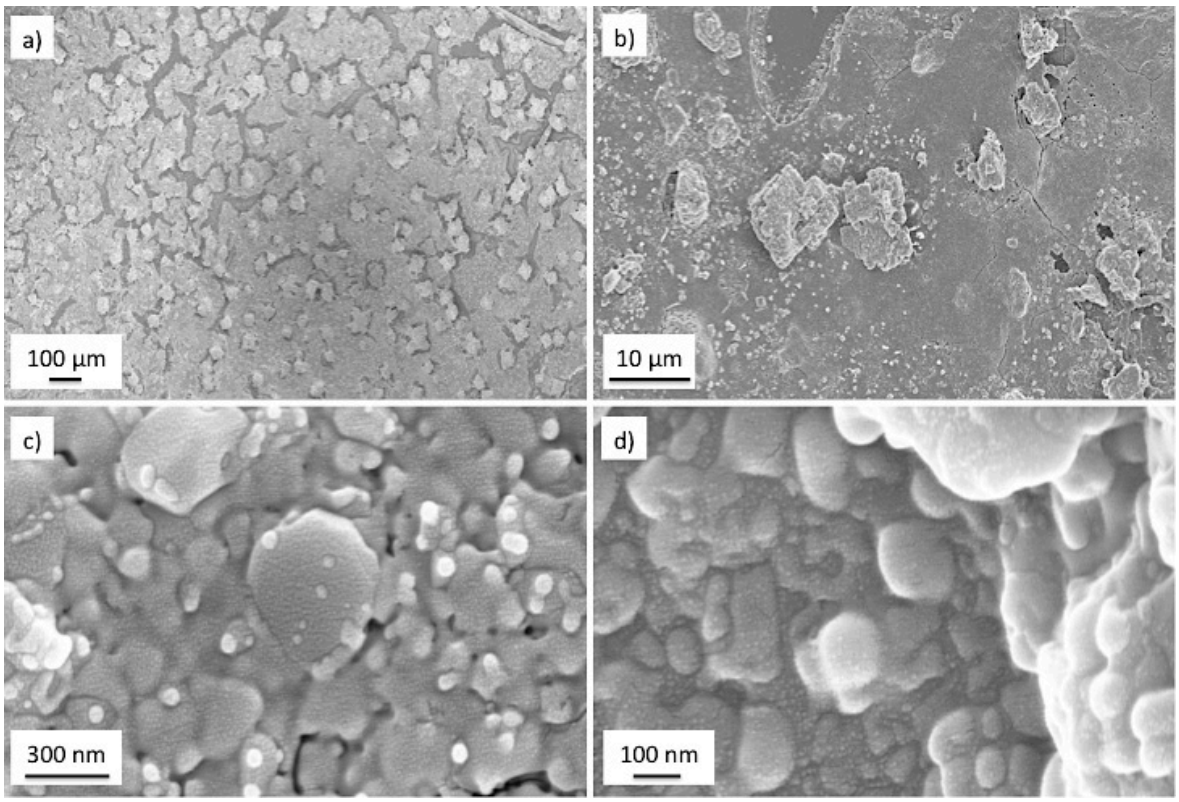

Fig. 4.72 | SEM images of the residual $CaCO_3$ remaining after the pyrolysis of **12** performed in nitrogen. **a-b)** overview pictures; **c-d)** higher magnification imaging reveals that the surface of the material is highly irregular and the layered imprint does not prevail in this solid.

These observations indicate that the pyrolysis of **12** results in the formation of calcite crystals that adopt a morphology that is different to the one observed for the crystals obtained in an air atmosphere. According to the previous assumptions and observations, the growth of $CaCO_3$ crystals is initiated within the hydrophilic parts of the structure. As presented in Fig. 4.73a, in an air atmosphere, the organic ligand is completely oxidised and leaves the crystallising system as H_2O and CO_2. The calcite crystals, which might have initially grown in two directions, can easily come into contact with each other in the third direction. The observed layered imprint on the residual calcite crystals may confirm this growth mechanism.

Fig. 4.73b represents what may happen when the thermolysis is performed in a nitrogen atmosphere. Although the coordination sphere surrounding the calcium ions contains enough oxygen atoms to initiate the nucleation of $CaCO_3$ crystals, it cannot provide enough oxygen to fully oxidise the remaining organic material. In this case, some carbon atoms of the ligand molecules can react with the excess of oxygen atoms (the formation of calcite requires only three oxygen atoms while the mononuclear unit in **12** contains seven of them) and the remaining nitrogen atom. This may result in the generation of volatile organic compounds that leave the reacting mixture. The remaining carbon stays trapped within the sample, obstructing the growth of the resulting calcite crystals in the third direction. It is possible that the thickness of the obtained calcite crystals may be comparable with the thickness of the hydrophilic areas in **12**, however, the resolution limit of the SEM has not allowed us to make any final conclusion.

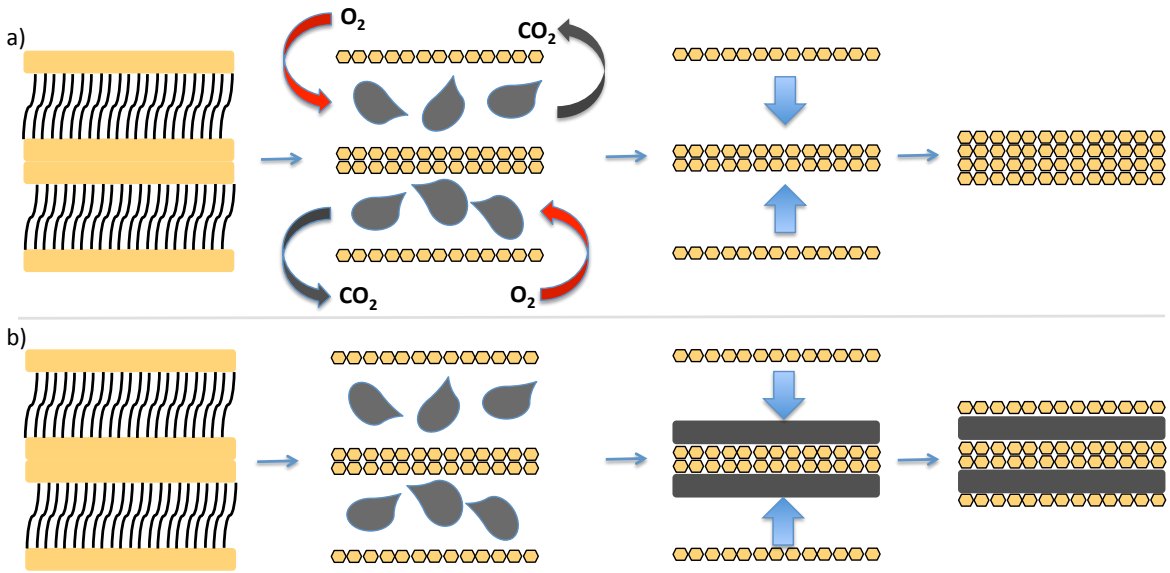

Fig. 4.73 | A proposed mechanism of the thermal degradation of **12** in an air (**a**) and a nitrogen (**b**) atmosphere. The yellow areas correspond to the polar parts of the self-assembled structure of **12** while the black regions correspond to the carbon-containing parts of **12**.

4.7. [Ca(*t*-Bu$_2$hda)(H$_2$O)$_2$] · 3H$_2$O (**13**)

In the previous structures, **8**-**12**, the length of the aliphatic chain located in the *para* position, with respect to the aromatic hydroxyl group, was modified in an attempt to study the influence of the amphiphilicity of the ligand on the self-assembly process. Simultaneously, the *ortho* position (again, with respect to the aromatic hydroxyl group) was substituted with a methyl or a methoxy functional group.

In a consecutive experiment, it was decided to modify the hydrophobicity of both substituents, which were located in the *ortho* and *para* positions. The first ligand used in these investigations was *t-Bu$_2$hda*, containing two *t*-Bu functional groups. The aim of this modification was to investigate how this change in the ligand molecule affected the self-assembly process when *t-Bu$_2$hda* was reacted with calcium ions. The secondary objective was to determine if the resulting self-assembled, Ca-containing coordination compound imposes a templating effect on the post-thermolytic or post-pyrolitic residual calcite crystals.

4.7.1. Characterization

Compound **13**, with the chemical formula [Ca(*t*-Bu$_2$hda)(H$_2$O)$_2$] · 3H$_2$O, forms when the *t*-Bu$_2$hda ligand reacts with a stoichiometric amount of CaCl$_2$ in a 1:1 (v/v) water/methanol mixture. Two equivalents of triethylamine were added to deprotonate the carboxylic acid groups.

The reaction temperature, the ratio of the solvent mixture and the pH were varied in an attempt to obtain a single-crystalline material. Unfortunately, this task was not successful. A white precipitate of **13** forms almost instantly after the reactants are combined. The composition and structure of this compound, including the supramolecular packing mode, was investigated using indirect analyses, namely CHN, TGA, IR and TEM.

The characterization of **13** is based on the assumption that the *t*-Bu functional groups do not have any significant influence on the binding mode of the ligand and the overall coordination sphere around the Ca^{2+} cation. This is justified by the structures of the compounds **3, 5, 6** and **8**-**12**, where the coordination environments and packing motifs are similar, despite the differences of the aromatic phenol substituents.

It is predicted that the calcium ion should be surrounded by two water molecules and donors provided by the *t-Bu$_2$hda* ligand. This ligand can supply one N-donor, one O-donor of the aromatic hydroxyl group and two O-donors of the two carboxylate groups. It is expected that one carboxylate group of the iminodiacetic acid moiety binds to the metal ion in the *unidentate* mode while the second one adopts the bridging mode and links neighbouring metal ions. The chemical formula of this compound is C$_{19}$H$_{31}$CaNO$_7$. In order to confirm that, elemental analysis was performed. The results, presented in Tab 4.9, show that there is a good correlation between the theoretical and experimental values, thus suggesting that the constitutional formula is correct.

Tab. 4.9 | Elemental analysis of **13**.

Element	Theoretical composition [%]	Elemental analysis result [%]
C	53.63	**52.98**
H	7.34	**7.51**
N	3.29	**3.06**
Ca	9.42	**9.23**

The exact number of the constitutional water molecules within **13** was calculated from the TGA results.

Thermogravimetric analysis

A sample of **13** was heated in an air atmosphere in the temperature range between 30 and 900 °C. The heating rate was adjusted to 1 °C/min and the corresponding weight loss was recorded. The results are presented in Fig. 4.74.

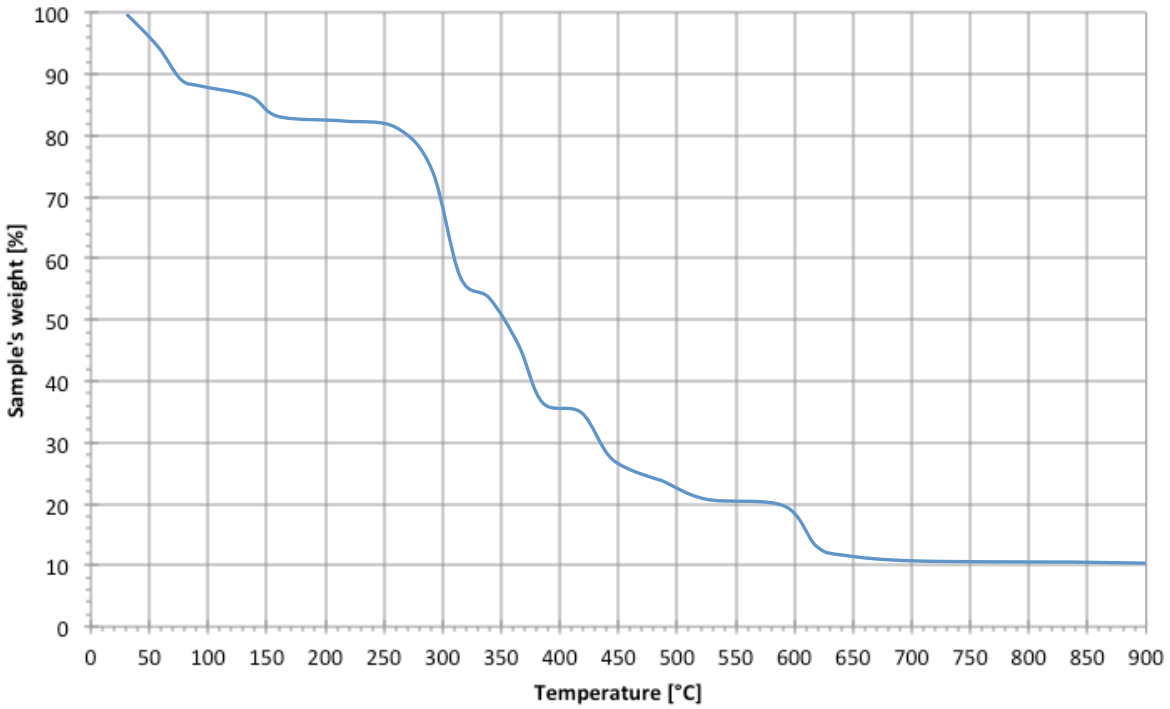

Fig. 4.74 | TGA analysis of **13** performed in air at 1 °C/min.

The initial weight loss occurs almost instantly after exposing the sample to the flow of dry air. Three constitutional water molecules are lost at 50 °C (*experimental weight loss*: ~12%; *theoretical:* 11.3%). This is followed by the loss of two coordinating water molecules and the formation of an anhydrous product at 130 °C (*experimental weight loss*: 18.2%; *theoretical*: 18.8%). This compound is stable up to 230 °C. Above this temperature a rapid oxidation occurs. A plateau observed between 365 °C and 405 °C corresponds to calcium iminodiacetate (*experimental weight loss*: 63.6%; *theoretical*: 64.3%) and indicates that at *ca.* 365 °C the aromatic part of the ligand is completely oxidised. Further heating leads to the formation of calcium carbonate at 515 °C (*experimental weight loss*: 79.8%, *theoretical*: 79.1%). Calcium

oxide is the final oxidation product, which forms around 610 °C (*experimental weight loss*: ~89.5%; *theoretical*: 88.3%).

IR spectroscopy

After the chemical formula of **13** was confirmed, it was necessary to explore that the coordination environment in **13** is in agreement with the proposed model. Therefore, IR spectroscopy was used to study the coordination mode of the iminodiacetic acid carboxylate groups. The resulting IR spectrum, presented in Fig. 4.75, was also compared with the spectra of compounds **8** and **12** that contain similar hda-type ligands.

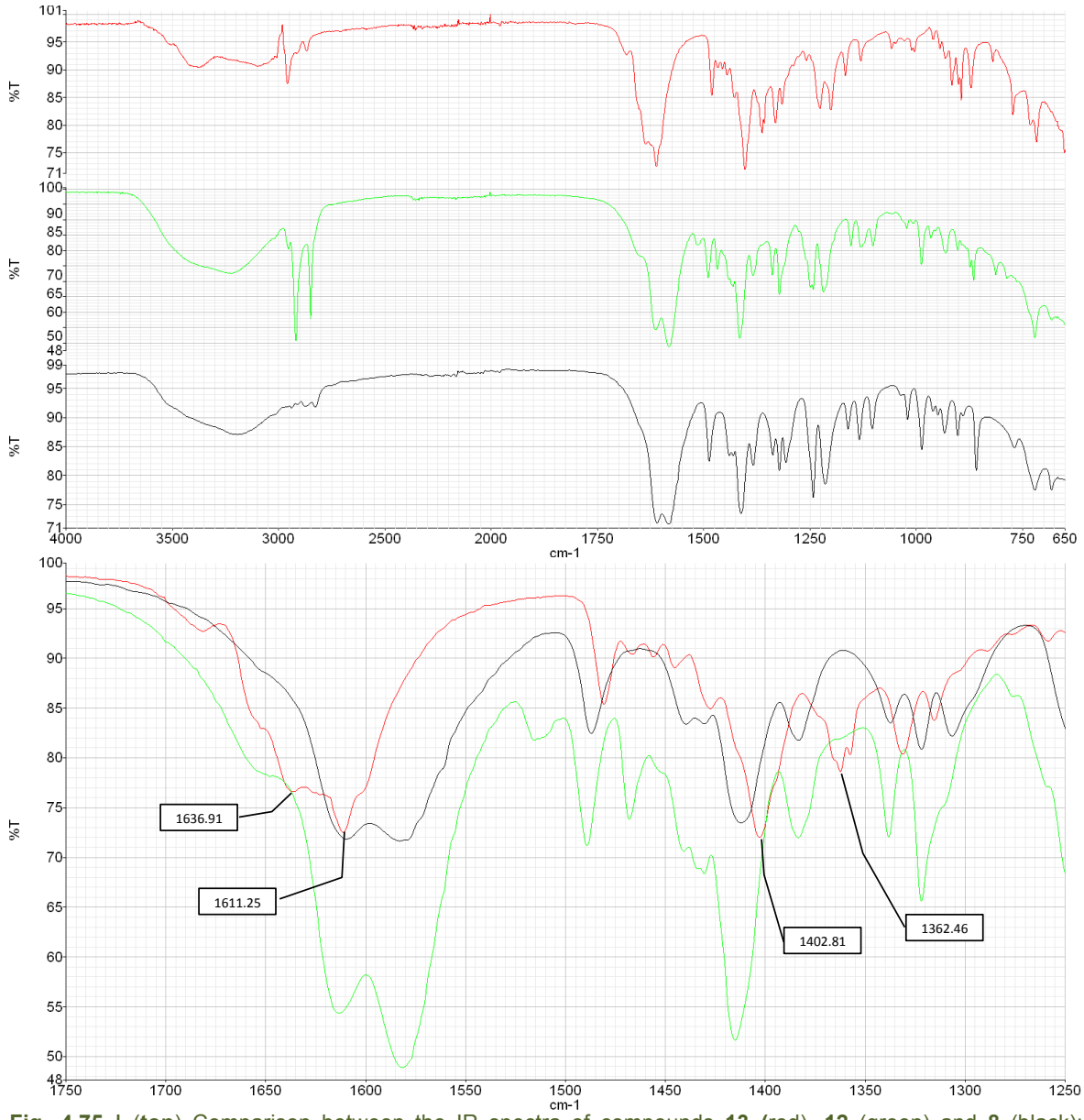

Fig. 4.75 | (**top**) Comparison between the IR spectra of compounds **13** (red), **12** (green) and **8** (black); (**bottom**) magnification between 1750 and 1250 cm^{-1}.

The IR spectrum of compound **13** is similar to the spectra of the other hda-type ligand-containing compounds. A slight shift of the signals towards the higher wavenumber values may be explained by the presence of three constitutional water molecules that are involved in

hydrogen bonding interactions with the iminodiacetic acid carboxylate groups. The frequencies of the signals, which originate from the carboxylate groups, are summarised in Tab. 4.10.

The $\Delta\nu_1$ value of 208.44 cm^{-1} is slightly higher than 200 cm^{-1}, indicating that the carboxylate functionality adopts a bridging mode and links two calcium ions into a 1D chain.

Tab. 4.10 | The frequencies of the carboxylate group signals in the IR spectra for compounds **13**, **8** and **12**.

Compound	ν_{as1} (COO)	ν_{as2} (COO)	ν_{s1} (COO)	ν_{s2} (COO)	$\Delta\nu_1$	$\Delta\nu_2$
13	1636.91 cm^{-1}	1611.25 cm^{-1}	1402.81 cm^{-1}	1362.46 cm^{-1}	208.44 cm^{-1}	274.45 cm^{-1}
8	1609.87 cm^{-1}	1582.95 cm^{-1}	1412.19 cm^{-1}	1338.31 cm^{-1}	170.79 cm^{-1}	271.56 cm^{-1}
12	1613.29 cm^{-1}	1581.66 cm^{-1}	1415.18 cm^{-1}	1338.26 cm^{-1}	166.48 cm^{-1}	275.03 cm^{-1}

The $\Delta\nu_2$ value, observed for the second carboxylate group of the iminodaicetic moiety, is 274.45 cm^{-1} and indicates the *unidentate* binding mode. These values indicate that the coordination environment of the metal ion in **13** is similar to previously discussed structures. It is probable that one of the iminodiacetic acid carboxylate groups forms a bridge between two calcium ions and is further responsible for the formation of a coordination chain. This one-dimensional structural motif may be cross-linked with its neighbouring equivalents *via* hydrogen bond interactions to give neutral layers, which self-assemble *via* hydrophobic interactions and van der Waals forces into a layered, lamellar material.

Electron microscopy

The morphology of **13** was studied using SEM. The images, presented in Fig. 4.76a-c, show that **13** self-assembles into spherical particles. The diameter of the particles ranges between 15 and 25 μm. There was no other phase observed within the sample.

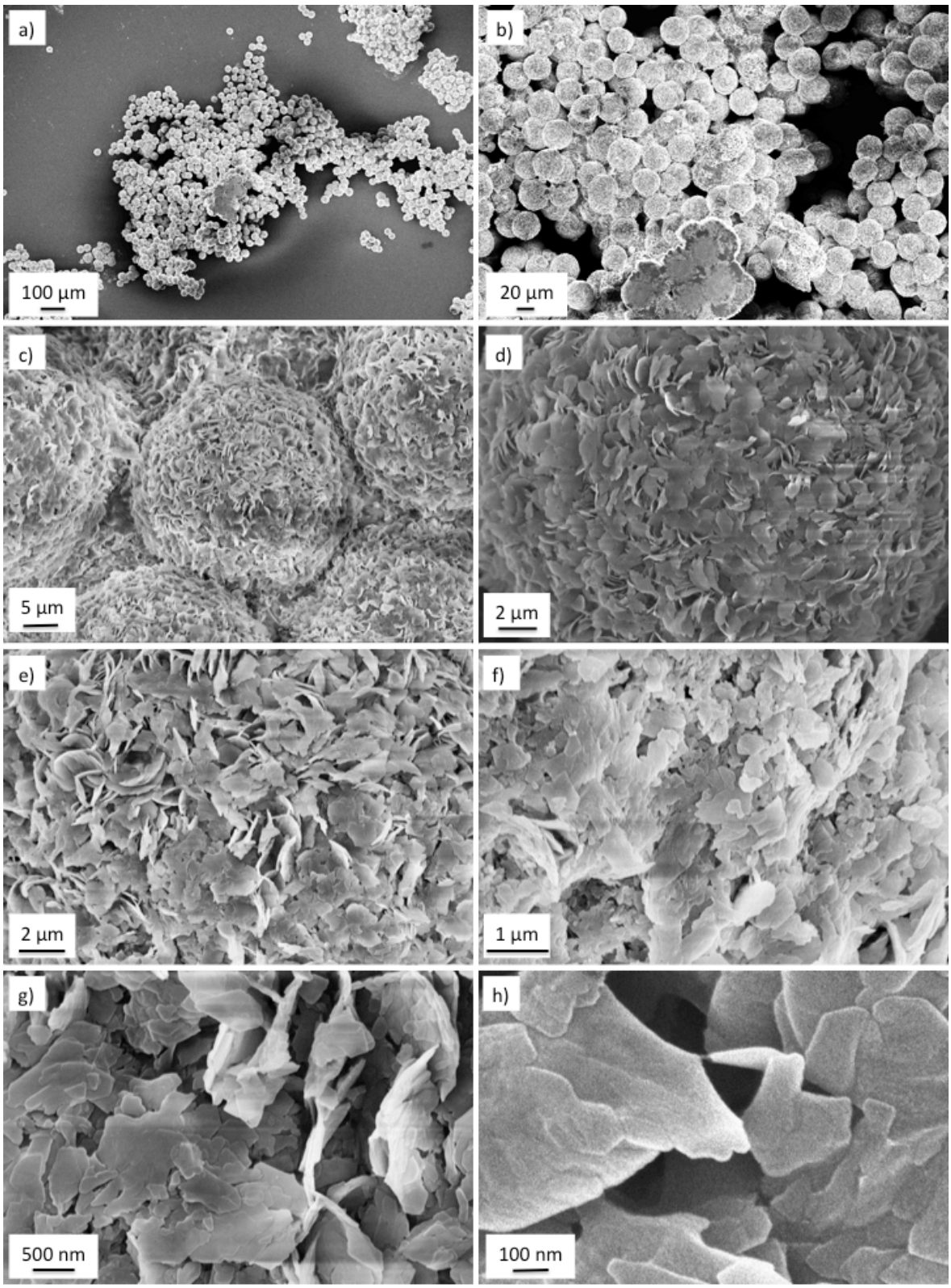

Fig. 4.76 | SEM images of **13**. **a-b)** overview; **c-d)** magnification showing separate ball-like assemblies; **e-h)** higher magnification revealing the almost flat, plate-like aggregating flakes.

Higher magnification imaging (Fig. 4.76d-g) reveals that the surface of the assemblies is highly irregular. It consists of a vast number of thin, flake-like particles, which aggregate in a random manner. High-resolution imaging (Fig. 4.76h) shows that each flake is composed of very thin (~10 nm) and small (~100 nm) plate-like crystals.

Some of these nanocrystals were further imaged using TEM. The images, presented in Fig. 4.77, suggest that **13** adopts the proposed layered lamellar arrangement with the lattice separation distance of 2.5 (±0.2) nm. A similar distance of 2.35 nm was crystallographically determined for the corresponding Fe-containing coordination compound [Fe(*t*-Bu$_2$hda)(H$_2$O)$_2$]·3H$_2$O.[186]

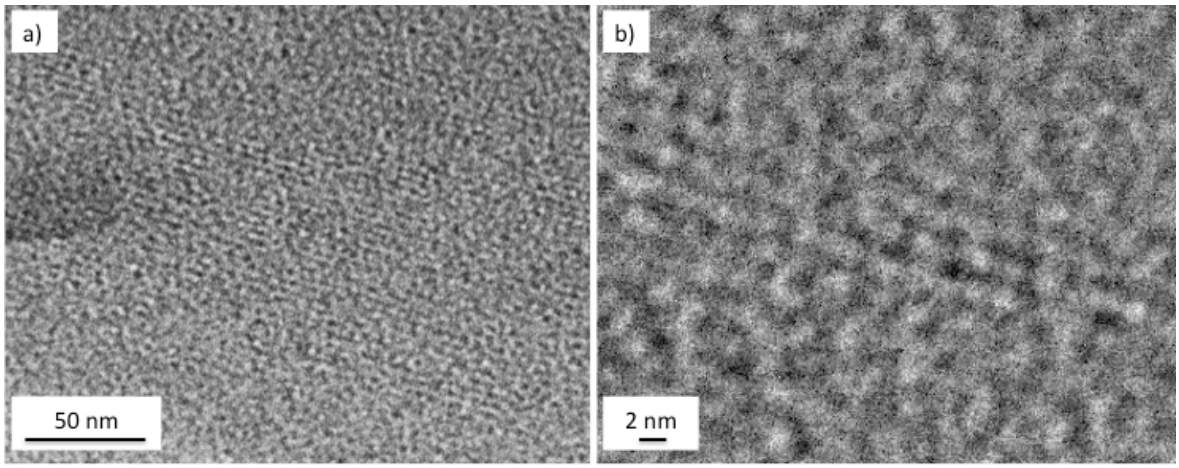

Fig. 4.77 | TEM images of the assemblies of **13** recorded in the diffraction contrast regime. **a)** overview; **b)** HR imaging is in agreement with a layered, lamellar structure.

The SEM imaging provided an opportunity to utilise the EDX analysis to confirm the elemental composition of **13**. The results, presented in Fig. 4.78, show that carbon, nitrogen, oxygen and calcium are the only non-hydrogen elements present within the sample (hydrogen cannot be detected using this technique) agreeing well with the proposed composition of **13**.

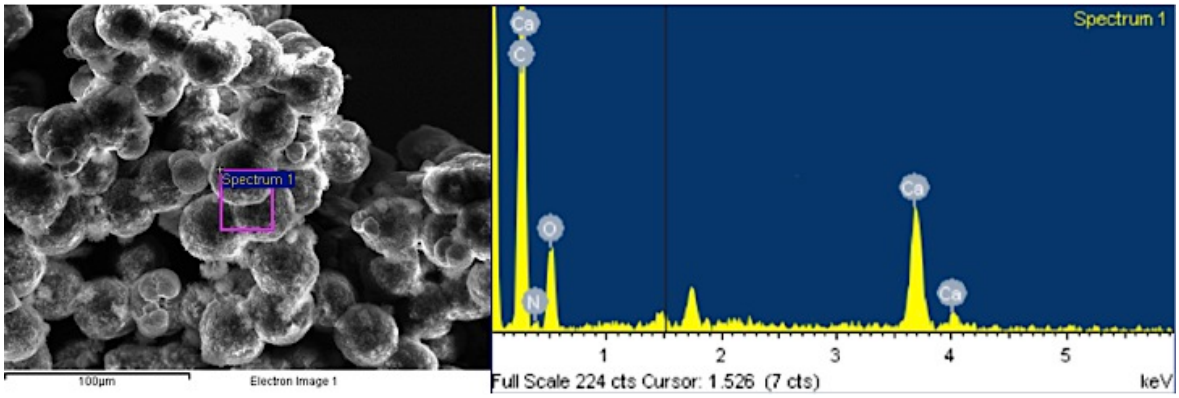

Fig. 4.78 | EDX analysis of **13**. Electron microscopy image (left) and the X-ray energy spectrum (right). The signal at 1.75 keV originates from the Si surface on which the sample was placed.

4.7.2. Results of the calcification

The degradation pathway of **13** was monitored using TGA and is presented in Fig. 4.74. It was confirmed that $CaCO_3$ is one of the intermediate products of the oxidation process. In order to investigate if the observed three-dimensional packing arrangement of **13** templates the formation of calcium carbonate, the TGA experiment was reproduced and the heating rate was decreased to 0.35 °C/min. A sample of **13** was heated up to 540 °C and the residual solid was collected and analysed using P-XRD and SEM.The P-XRD pattern, presented in Fig. 4.79, shows that calcite is the only crystalline phase present within the sample. All of the reflections are visible and located in the predicted positions.[178]

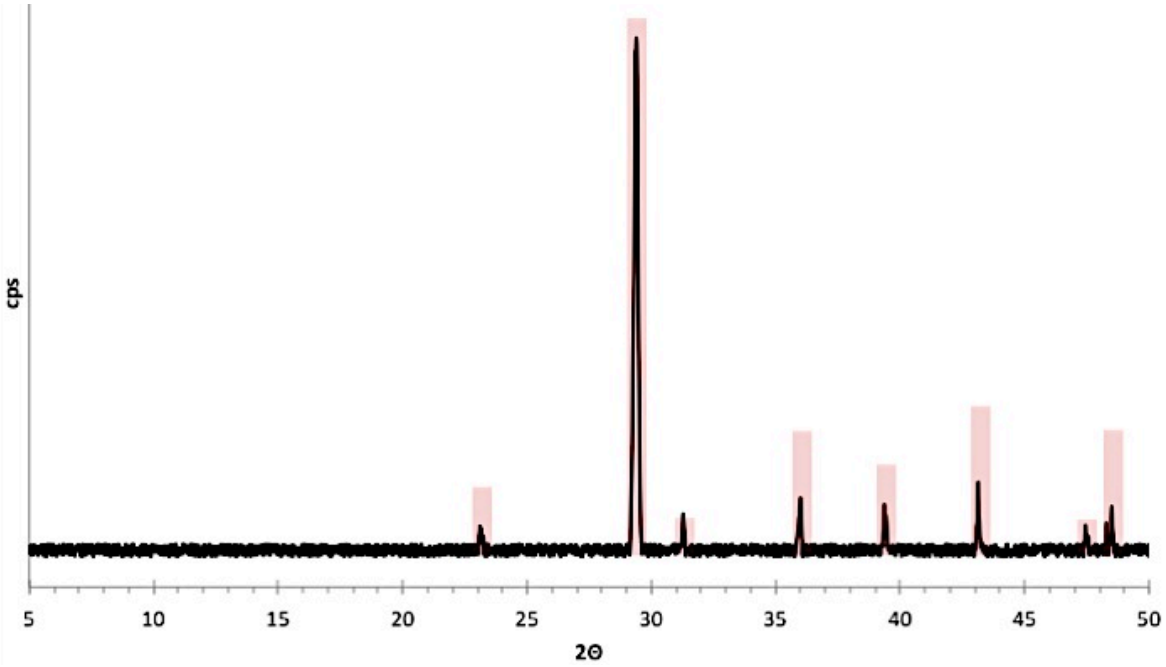

Fig. 4.79 | P-XRD pattern obtained for the residues remaining after the slow thermolysis of **13** in an air atmosphere. The highlighted areas correspond to the typical positions and intensities of the calcite reflections.[178]

SEM was used to determine the morphology of the resulting calcite crystals. The overview pictures, presented in Fig. 4.80a-c, show that the shape of the calcite particles is similar to the ball-like assemblies of **11**. Their average diameter of ~12 μm is slightly smaller than that observed for the original material. Higher magnification images that show the surface of the spherical particles (Fig. 4.80e-f) reveal that their morphology is highly irregular. The surface consists of small (~50 nm), almost flat materials, which agglomerate in a random mode to form fibrous micromorphologies.

In rare cases (less than 3% of particles), the thermolysis leads in significantly lower yields to the formation of dumbbell-like particles (see Fig. 4.80g-h). In contrast to the other spherical morphologies these appear to be composed of small, elongated, block-shaped crystals of calcite, which agglomerate in a highly organised manner.

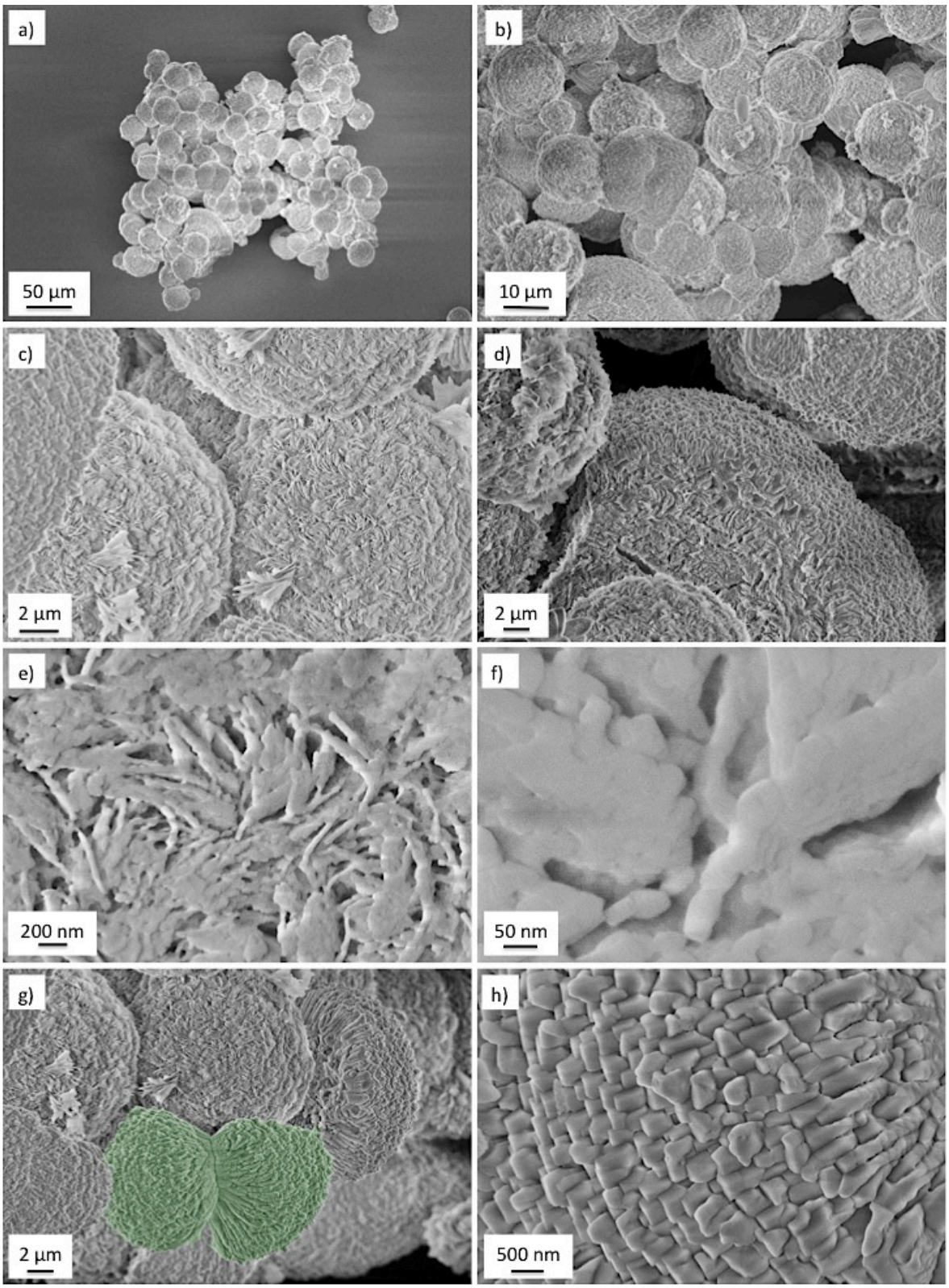

Fig. 4.80 | SEM images of the residual calcite crystals remaining after the thermolysis of **13** in air. **a-b)** overview; **c-d)** higher magnification showing irregular surface of the spheres; **e-f)** higher resolution imaging reveals the existence of plate-like nanocrystals; **g)** a dumbbell-like particle observed within the sample; **h)** magnification showing the regular and ordered surface of the dumbbell-like particle.

In a consecutive experiment an analytical sample of **13** was pyrolised in the nitrogen atmosphere. The heating rate was kept at 0.35 °C/min and the target temperature was 540 °C. The residues were collected and analysed using P-XRD and SEM techniques.

The P-XRD pattern, presented in Fig. 4.81, shows that the only crystalline phase present within the sample is calcite.

The amount of the amorphous carbon remaining within the residues can be calculated from the TGA curve corresponding to the pyrolysis process (Fig. 4.81 right). The weight of the sample recorded at 540 °C equals 35.2% of the weight of the original coordination compound. As the theoretical weight of calcium carbonate is equal to 20.9% of the starting material, the remaining 14.3% may be associated with the carbon present within the residues. This indicates that the amount of additional amorphous carbon equals 40.6% of the total mass of the residues. The TGA results were further confirmed using the elemental analysis of the residues.

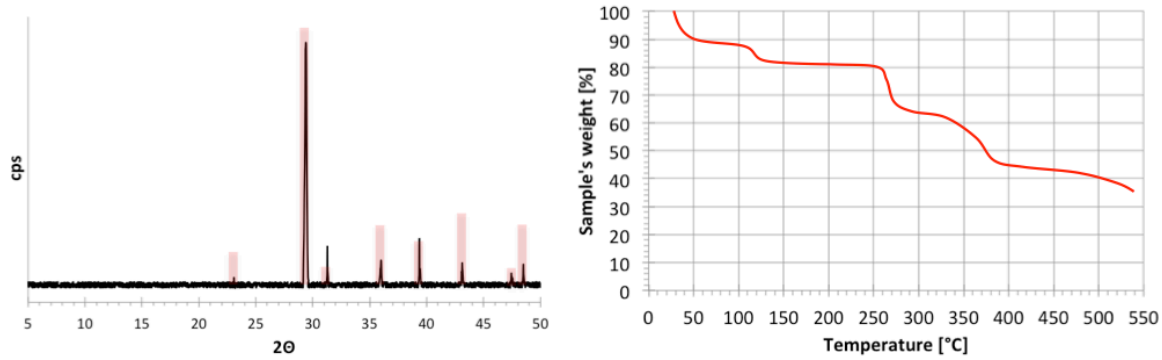

Fig. 4.81 | (**left**) P-XRD pattern of the residues remaining after thermolysis of **11** in the nitrogen atmosphere. The highlighted areas correspond to the typical positions and intensities of calcite crystals.[178] (**right**) The TGA curve that corresponds to the pyrolysis experiment.

SEM microscopy was used to investigate the morphology of the post-pyrolitic calcite crystals. Suspending the residues in ethanol and placing a number of drops of the suspension on the Si surface allowed us to prepare a SEM sample. The residual carbon was washed away and removed from the calcite material in this process. The overview pictures, shown in Fig. 4.82a-b, illustrate that the spherical morphology of the original coordination compound is retained within the residual material. It is possible to notice that calcite forms two types of particles that adopt two distinct morphologies.

The first type of morphology, which can be termed as 'micro-morphology', may be described as polycrystalline spherical agglomerates and can be observed in Fig. 4.82a-b. The average diameter of these spherical $CaCO_3$ agglomerates is *ca.* 10 μm. Higher magnification images, presented in Fig. 4.82e-f, show that the surface of these particles is rough. It is composed of small (less than 100 nm in size) agglomerates that form a porous, highly defected solid.

A second 'nano-morphology' is observed in the sample: The larger micros-agglomerates are covered by a large number of small, polycrystalline calcite spheres. In contrast to the previously described agglomerates, their surface appears to be smooth. It is interesting to note the narrow size distribution of these particles. Their average diameter is *ca.* 400 nm (Fig. 4.82c-d).

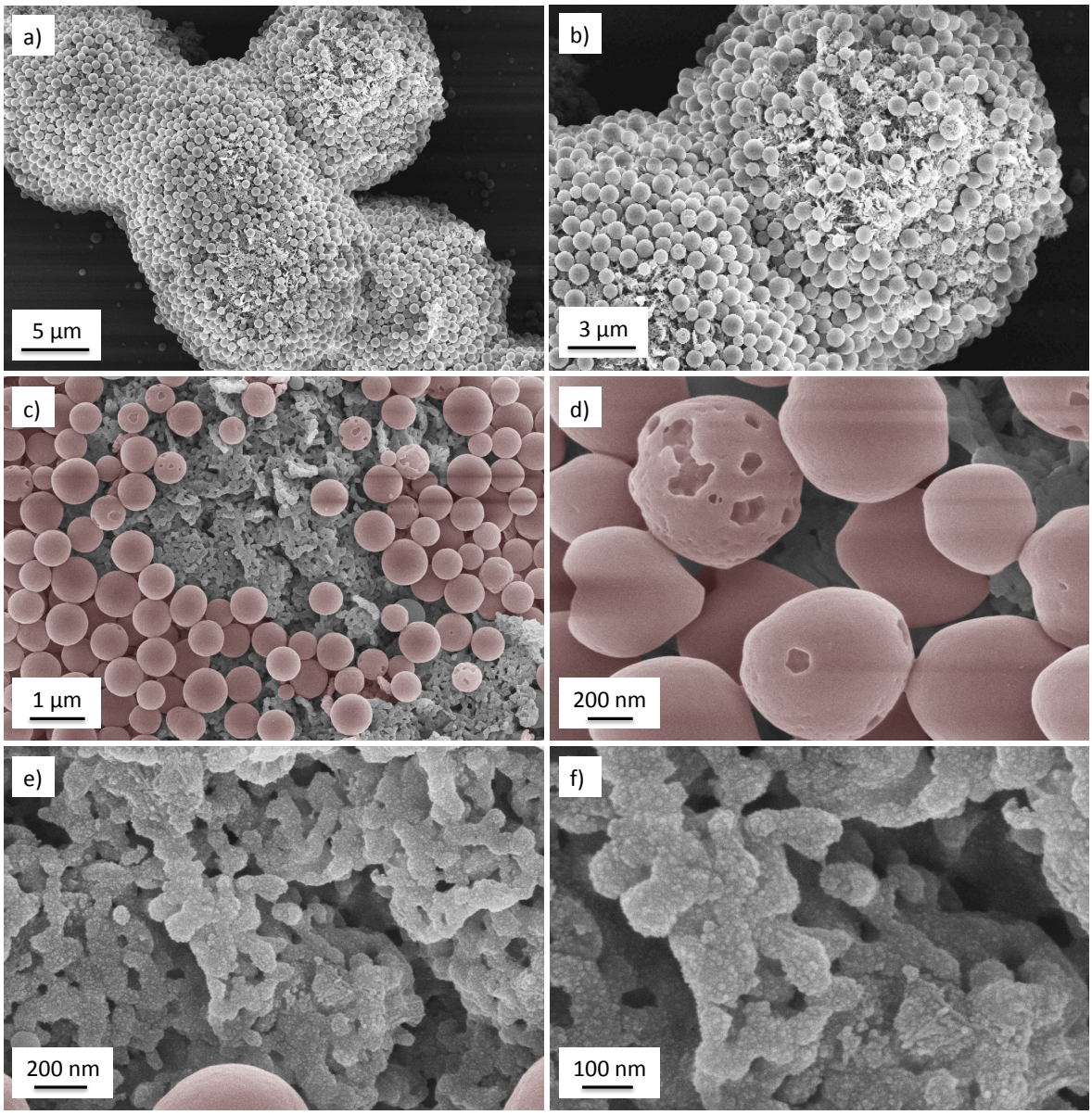

Fig. 4.82 | False colour SEM images of calcite samples obtained by the thermolysis of **13** in a nitrogen atmosphere. **a-b)** Overview pictures showing the spherical aggregates; **c-d)** magnification on the spheres (highlighted in red colour); **e-f)** magnification on the surface of the microsized calcite agglomerates.

As the smooth surface and spherical shape of the observed calcite particles is highly unusual for this mineral, further experiments were performed in order to confirm their chemical identity. The study included TEM imaging along with EDX analysis.

The TEM micrographs of the residual $CaCO_3$ spheres are presented in Fig. 4.83. They show the smaller spheres that are located on the surface of the large 'micro' agglomerates. Although in the low magnification mode the 'nano' spheres also appear to be smooth, high-resolution imaging reveals that they are indeed composed of small crystals of calcite (*ca.* 5 nm in size), which do not adopt any preferred orientation (Fig. 4.83c). The lattice separation distance measured using TEM (Fig. 4.83d) is 3.0 (±0.3) Å; this value corresponds to the *d*-spacing between the (104) faces, which are predominantly expressed in calcite crystals.[149] The electron diffraction pattern, presented in Fig. 4.83d, confirms the polycrystalline nature of the particles.

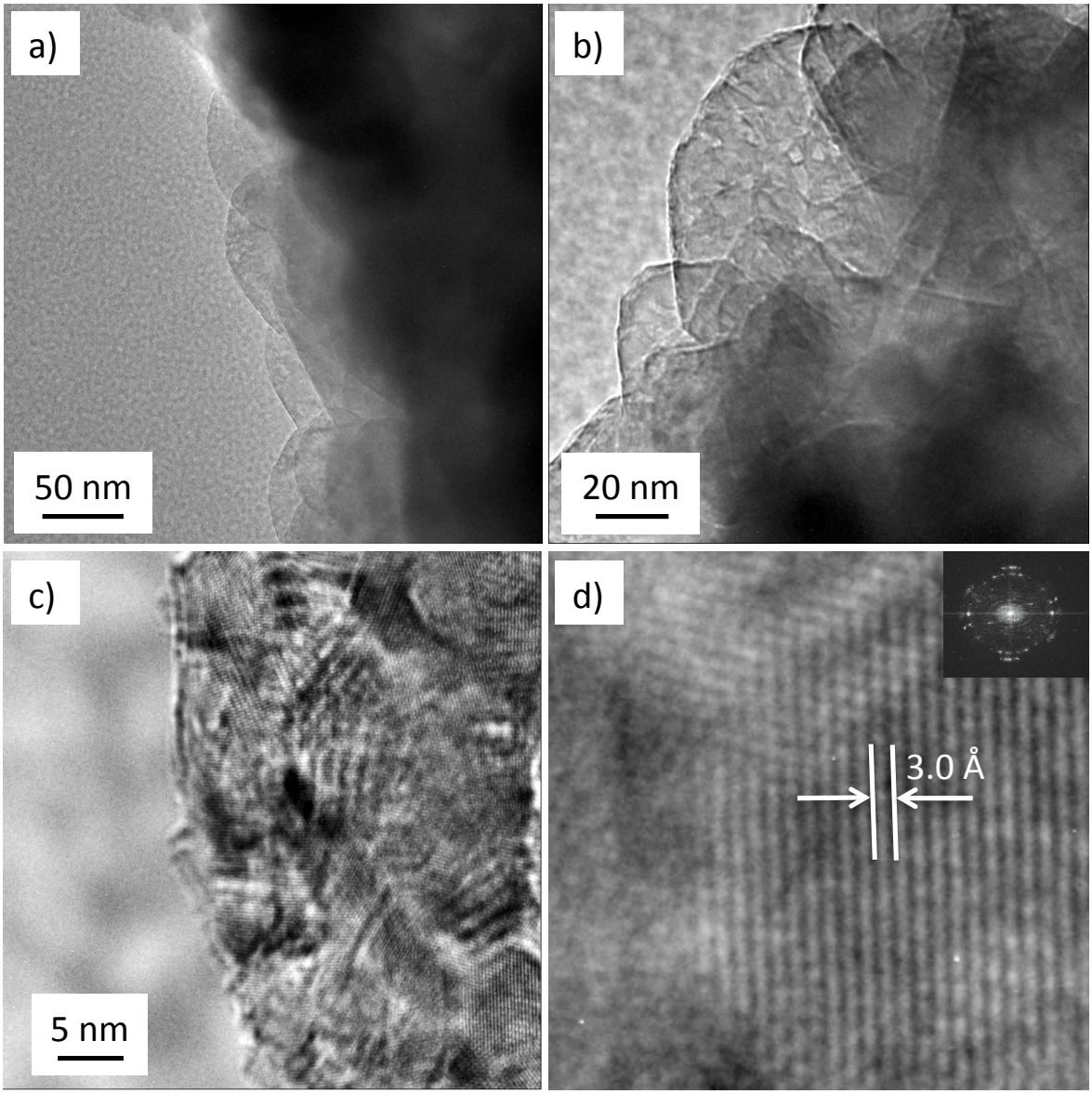

Fig. 4.83 | TEM images of the small spherical particles observed on the surface of the large agglomerates. All images were recorded in the phase contrast regime. The inset in (**d**) shows the corresponding electron diffraction pattern.

Once the sample was imaged using TEM, the EDX analysis was performed selectively on the 'nano' spheres. The spectrum, presented in Fig. 4.84, shows signals that are associated with carbon, oxygen and calcium. The signals attributed to copper originate from the carbon-coated copper TEM support grid.

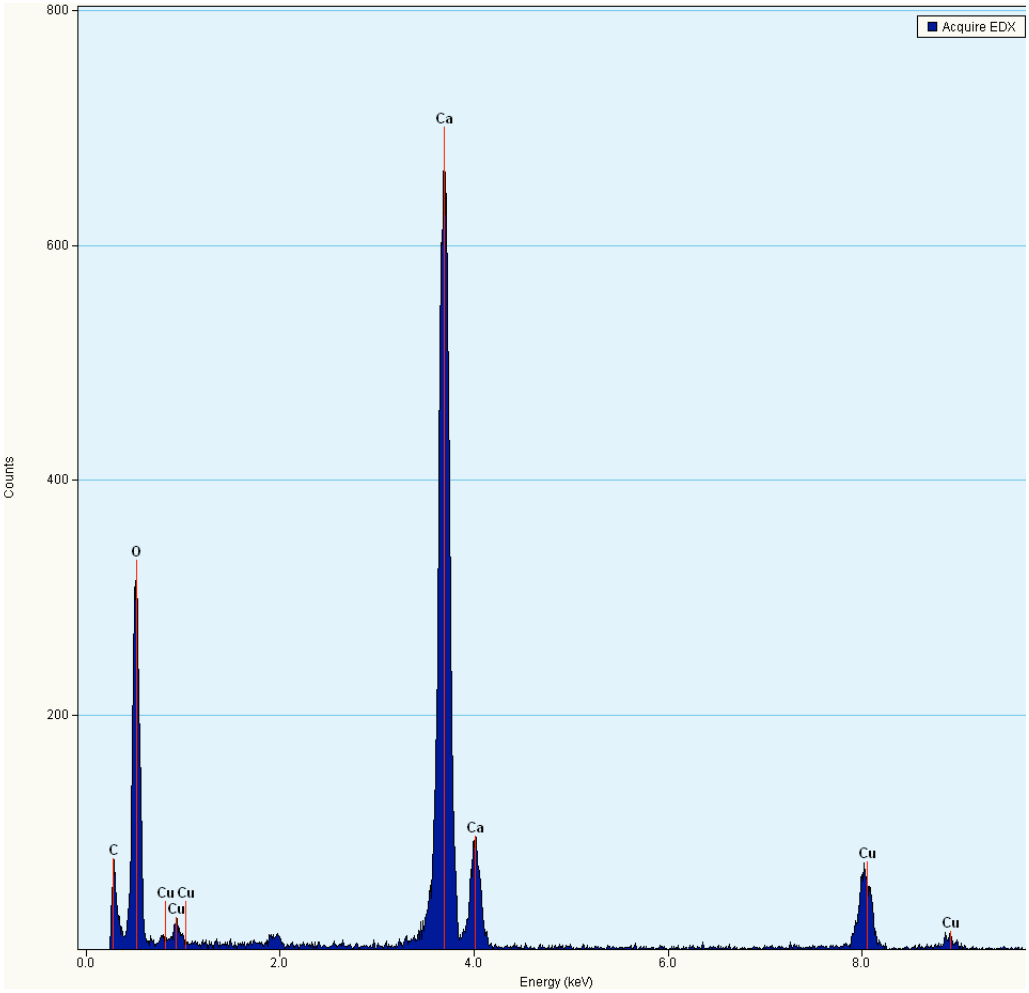

Fig. 4.84 | TEM-EDX spectrum obtained for the small spheres observed on the surface of the large polycrystalline agglomerates. The signals attributed to copper originate from the TEM grid.

The quantitative analysis of the EDX spectrum, which is presented in Tab. 4.11, confirms that the small 'nano' spheres are composed of calcium carbonate.

Tab. 4.11 | Quantitative results of the EDX experiment performed on the 'nano' spheres, which remained after the pyrolysis of **13**.

Element	Experimental composition	Theoretical composition
Ca	42.23	40.04
C	10.89	12.00
O	44.74	47.96

Additional TEM images of the post-pyrolytic residues revealed that in many areas the 'nano' spheres display further organisation on a scale above 1 nm. As presented in Fig. 4.85a, in several parts of the sample it is possible to observe a layered arrangement. The lattice separation distances are not constant and vary between 1.1 nm and 1.6 nm. These values are too high to be considered as the interference fringes.

The corresponding electron diffraction pattern, shown in Fig. 4.85b, displays three regular, circular signals that may be attributed to polycrystalline calcite particles. As summarised in Tab. 4.12, further calculations allowed us to assign the *hkl* indexes to these signals.

In the area close to the incident beam (Fig. 4.85c), within the low scattering angle range, there are reflections that do not appear to be circular or even regular. These correspond to *d*-spacings larger than 1 nm and therefore cannot originate from calcite crystals. Their occurrence may be in agreement with the features previously observed in the TEM images (Fig. 4.85a).

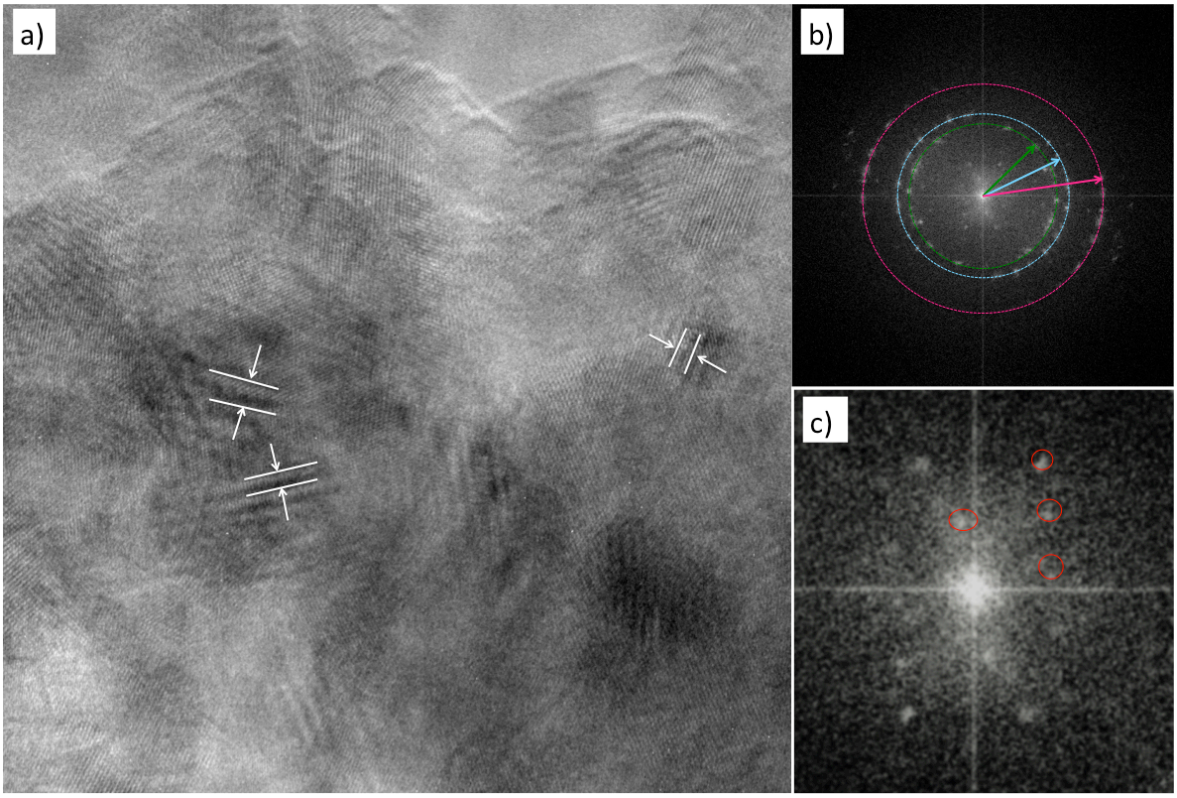

Fig. 4.85 | TEM analysis of the residues remaining after the thermolysis of **13** in a nitrogen atmosphere. **a)** TEM image highlighting large lattice separation distances; **b)** a corresponding electron diffraction pattern obtained by performing a Fourier transformation on fig. (**a**); **c)** magnification on the low-angle scattering area of the electron diffraction pattern (**b**), the highlighted reflections originate from lattice separation distances larger than 1 nm and cannot be attributed to calcite crystals.

Tab. 4.12 | The assignment of the circular signals observed in the electron diffraction pattern presented in Fig. 4.85b.

Circle no.	Measured *d*-spacing	(*hkl*)	Theoretical *d*-spacing in calcite
1 (green)	3.0 Å	(104)	3.037 Å
2 (blue)	2.5 Å	$(2\bar{1}0)$	2.448 Å
3 (red)	1.9 Å	$(10\bar{8})$	1.939 Å

These features may originate from layers and appear locally throughout the sample (areas of *ca.* 3 nm x 5 nm). They may indicate that the structure of **13** imparts a local templating effect on the morphology of the post-pyrolytic crystals of calcite. It is possible that the pre-organisation of the starting materials within the initial coordination compound contributes to the growth of thin, nearly 2D inorganic crystals. A small amount of carbon can be trapped between these structures, giving rise to the layered arrangement observed in TEM.

4.8. Compound $K_2(H_2O)_5[Ca(H_2Bc_2hda)(HBc_2hda)(H_2O)_4]Cl{\cdot}H_2O$ (**14**)

After the successful synthesis and characterization of compound **13** ([Ca(*t*-Bu$_2$hda)]·3H$_2$O) it was decided to explore the self assembly process that occurs when calcium ions react with the Bc$_2$hda ligand, which contains dimethyl-benzyl moieties located in the *ortho* and *para* positions (with respect to the aromatic hydroxyl group). Surprisingly, the behaviour of this ligand in Ca-complexes was different to the previously investigated vda- and hda-type ligands.

Despite several attempts to obtain a single-crystalline material in conditions similar to that which were previously applied for the Ca-containing compounds **7**-**13** (water/methanol mixture, pH adjusted with TEA), it was not possible to obtain a single crystal of this new compound. Therefore, it was decided to change the crystallisation conditions by decreasing the polarity of the solvent mixture and by adjusting the pH with a mineral base.

Single crystals of the new compound with the chemical formula $K_2(H_2O)_5[Ca(H_2Bc_2hda)(HBc_2hda)(H_2O)_4]Cl{\cdot}H_2O$ (**14**) formed when the Bc$_2$hda ligand was reacted with a stoichiometric amount of calcium chloride in a 1:1 (v/v) ethanol/methanol mixture. Two equivalents of potassium hydroxide were added to facilitate the deprotonation of the ligand molecules. Colourless block-shaped crystals formed on the walls of the sample tubes that contained the reaction mixture after 5 days of slow evaporation of the solvent at ambient conditions. A single crystal X-ray diffraction experiment was performed to determine the solid-state structure of **14**. It revealed that the asymmetric unit in **14** contains a partially hydrated calcium ion, two symmetry independent, partially hydrated potassium ions and two symmetry independent Bc$_2$hda ligand molecules. Water molecules and carboxylate functionalities of the ligand molecules interact with the metal ions *via* coordination bonds and dipole-cation interactions, bridging between the metal ions, giving rise to 2D sheets in the crystallographic *ab*-plane.

The hydrophilic, inner core of these sheets contains the positively charged Ca^{2+} and K^+ metal ions, coordinating water molecules and deprotonated carboxylate functionalities. The outer surface consists of aromatic rings of the Bc$_2$hda ligand. The self-assembly in the crystallographic *c*-direction is realised through hydrophobic interactions, van der Waals forces and π-π stacking interactions between the neighbouring ligand molecules. This results in the formation of a three-dimensional structure, where the hydrophilic, metal ions-containing layers sandwich between the hydrophobic, ligand-containing parts.

Asymmetric unit

In addition to the previously mentioned ligand molecules and metal ions, the asymmetric unit in **14** also contains a chlorine anion and ten water molecules. As presented in Fig. 4.86, the mutual orientation of atoms within the asymmetric unit is highly complex.

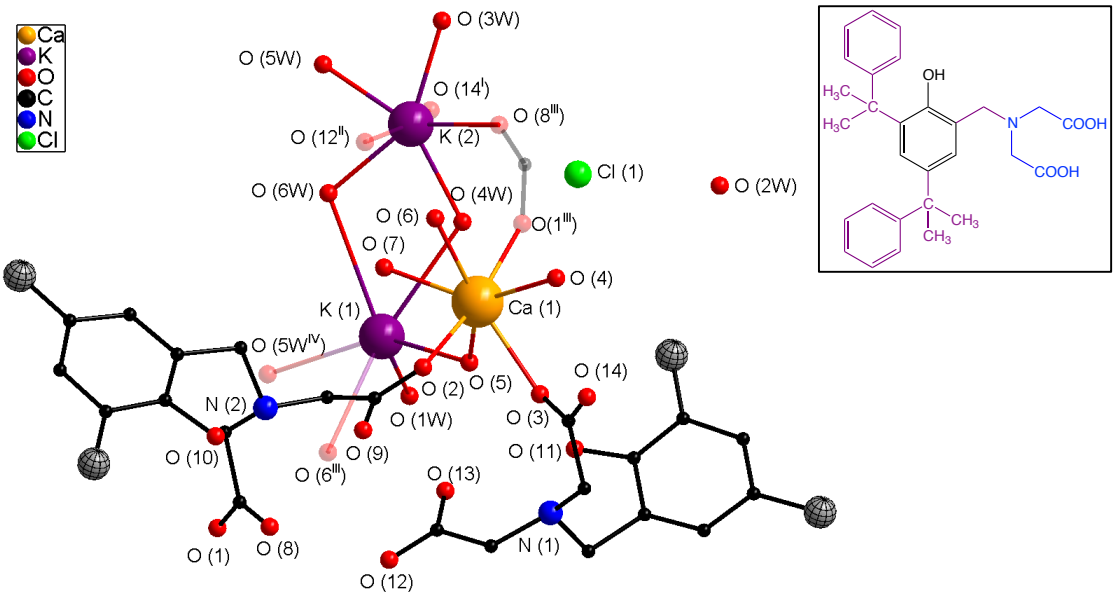

Fig. 4.86 | Asymmetric unit in **14**. Symmetry codes: (I): -1+x, y, z; (II): 1-x, 0.5+y, 1-z; (III): 1-x, -0.5+y, 1-z; (IV): -x, -0.5+y, 1-z. The artificial grey atoms correspond to the $–C(CH_3)_2Ph$ substituents. Hydrogen atoms were omitted for clarity. Inset: structure of the Bc_2hda ligand.

As visualised in Fig. 4.86, the Bc_2hda ligand molecules bind to the calcium ions in two different modes. The first mode is observed for the ligand, which contains the N(1) nitrogen atom. In this case, the O-donor O(3) of the iminodiacetic acid carboxylate functionality coordinates to the Ca(1) ion in the *unidentate* mode and the corresponding bond length is 2.433(9) Å. The second oxygen atom of this functional group, O(14), binds to K(2). The bond distance is 2.352(7) Å. The second carboxylate group binds to another symmetry equivalent of the K(2^{I}) ion through the oxygen atom O(12). The K(2^{I})-O(12) bond distance is 2.376(7) Å. The remaining oxygen atom of this functionality, O(13), does not bind to any metal ion.

The second binding mode is observed for the ligand, which contains the N(2) atom (again, see Fig. 4.86). In this case, the ligand binds to the calcium ion through the O-donor O(2) of the iminodiacetic acid carboxylate functionality. The bond distance is 2.358(7) Å. The second oxygen atom of this functional group, (O(9)), does not bind to metal ions. The O-donor O(1) of the second carboxylate group binds to the calcium ion with a distance of 2.353(7) Å. The last oxygen atom of this carboxylate group, O(8), binds to the ion K(2). Therefore, the carboxylate group bridges in a μ_2 syn-anti fashion between the calcium ion and the potassium ion K(2) (see Fig. 4.86 and Fig. 4.90).

The coordination sphere surrounding the calcium ion is a highly distorted 7 coordinate one. The bond distances and the exact coordination geometry are presented in Fig. 4.87.

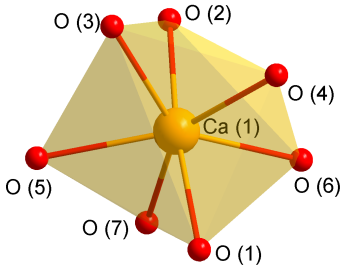

Atom 1	Atom 2	Symmetry code for atom 2	Bond lenght [Å]
Ca(1)	O(1)	x, y, z	2.353(9)
Ca(1)	O(2)	x, y, z	2.358(7)
Ca(1)	O(4)	x, y, z	2.380(9)
Ca(1)	O(5)	x, y, z	2.404(8)
Ca(1)	O(7)	x, y, z	2.415(8)
Ca(1)	O(3)	x, y, z	2.433(9)
Ca(1)	O(6)	x, y, z	2.442(8)

Fig. 4.87 | Coordination environment of the Ca(1) ion in **14**. The table presents the corresponding bond distances.

As shown in Fig. 4.87, the oxygen atoms surrounding both potassium ions adopt irregular geometries. The O-donor O(5) of the coordinating water molecule forms a μ_2 type bridge between the Ca(1) and K(1) ions. The O-atoms of two water molecules O(4W) and O(6W) interact with the potassium counter ions *via* dipole-cation interactions and form two μ_2 bridges between K(1) and K(2). These bridges along with the bridge formed by one of the carboxylate functional groups are responsible for the formation of an 8-membered ring motif within **14** (see Fig. 4.88 for clarity). The distance between the two potassium ions is 4.773(4) Å. The K(1) ion is located 4.937(3) Å from the calcium ion, while for the K(2) ion this distance is 5.312(3) Å.

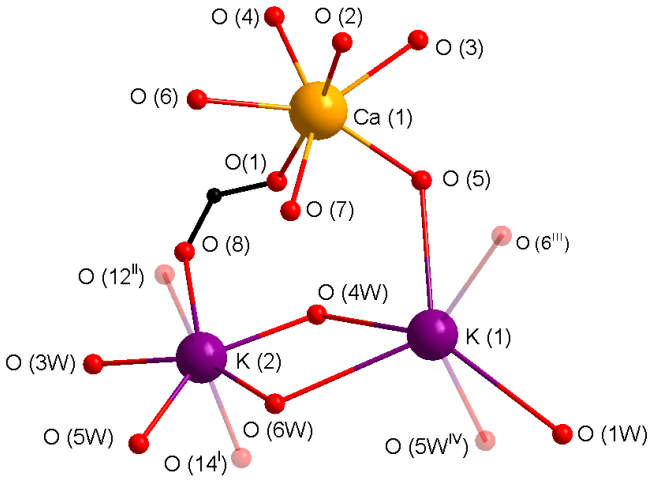

Fig. 4.88 | Metal ions in **14**. Symmetry codes: (I): -1+x, y, z; (II): 1-x, 0.5+y, 1-z; (III): 1-x, -0.5+y, 1-z; (IV): -x, -0.5+y, 1-z.

Connectivity

As discussed above, the N(1)-containing ligand molecule binds to one Ca^{2+} ion, while the N(2) containing Bc_2hda molecule binds to two symmetry equivalent calcium ions through the O-donors O(1) and O(2) of two different iminodiacetic acid carboxylate functionalities. Thus, with respect to the Ca^{2+} ions, only the N(2)-containing ligand is responsible for the formation of a 1D chain motif, which extends parallel to the crystallographic *b*-axis *via* coordination bonds (see Fig. 4.89).

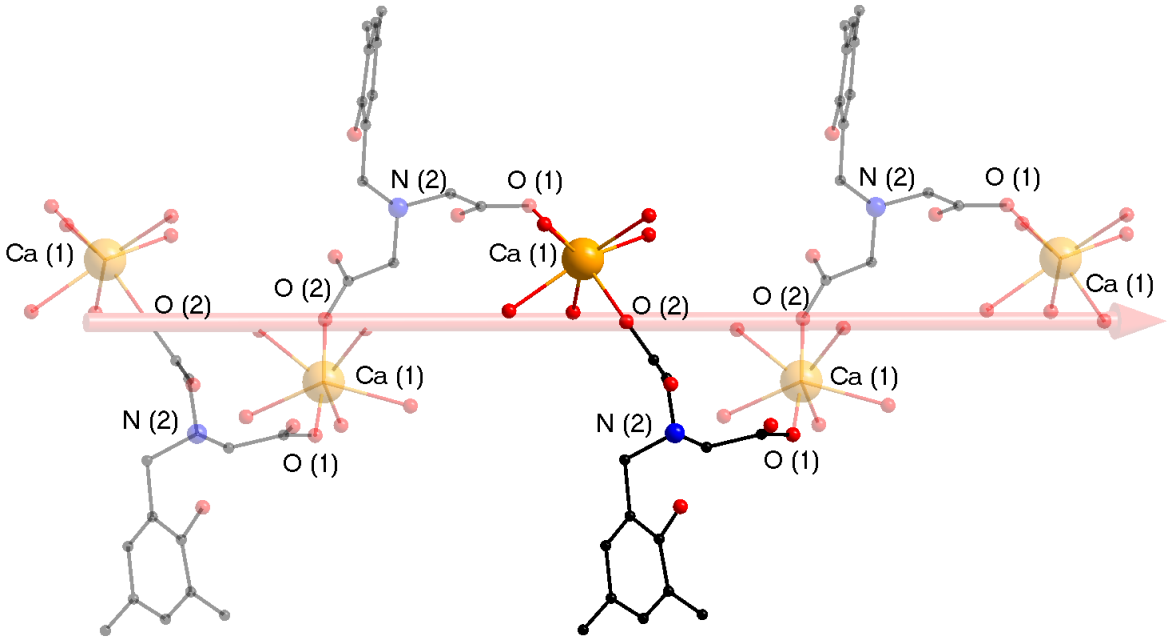

Fig. 4.89 | 1D coordination chain motif that extends in the direction of the crystallographic b-axis (indicated by the red vector). Potassium ions, non-Ca-coordinating and constitutional water molecules, hydrogen atoms, chlorine anions and the N(1)-containing ligand molecules were omitted for clarity. For the same reason the dimethyl-benzyl substituents of the phenol ring are not shown.

In addition to the bond involving the Ca ions that occur along the crystallographic *b*-axis, the potassium ions facilitate the cross-linking between the 1D chain motifs in the direction of the *a*-axis. As presented in Fig. 4.90, the N(1)-containing ligand molecule binds to the calcium ion Ca(1) and to two symmetry equivalent counter ions: K(2^{III}) and K(2^{V}). The N(2)-containing ligand binds to two symmetry equivalent calcium ions (Ca(1) and Ca(1^{II})) and to the counter ion K(2^{III}). One of the carboxylate groups of the N(1)-containing ligand molecule forms a μ_2 syn-anti type bridge between the K(2) counter ion and the symmetry generated calcium ion Ca(1). Therefore, it is justified to say that the Ca(1) ion is linked to its symmetry equivalent Ca(1^{VI}) ion. Ca(1) and Ca(1^{VI}) are located 11.855(4) Å from each other.

The afore-mentioned K(2^{V}) ion and the symmetry generated calcium ion Ca(1^{V}) are bridged with one of the carboxylate groups of the N(1)-containing ligand (O(8^{V}) and O(1^{V})). The distance between the symmetry equivalent calcium ions Ca(1) and Ca(1^{V}) is 10.585(4) Å.

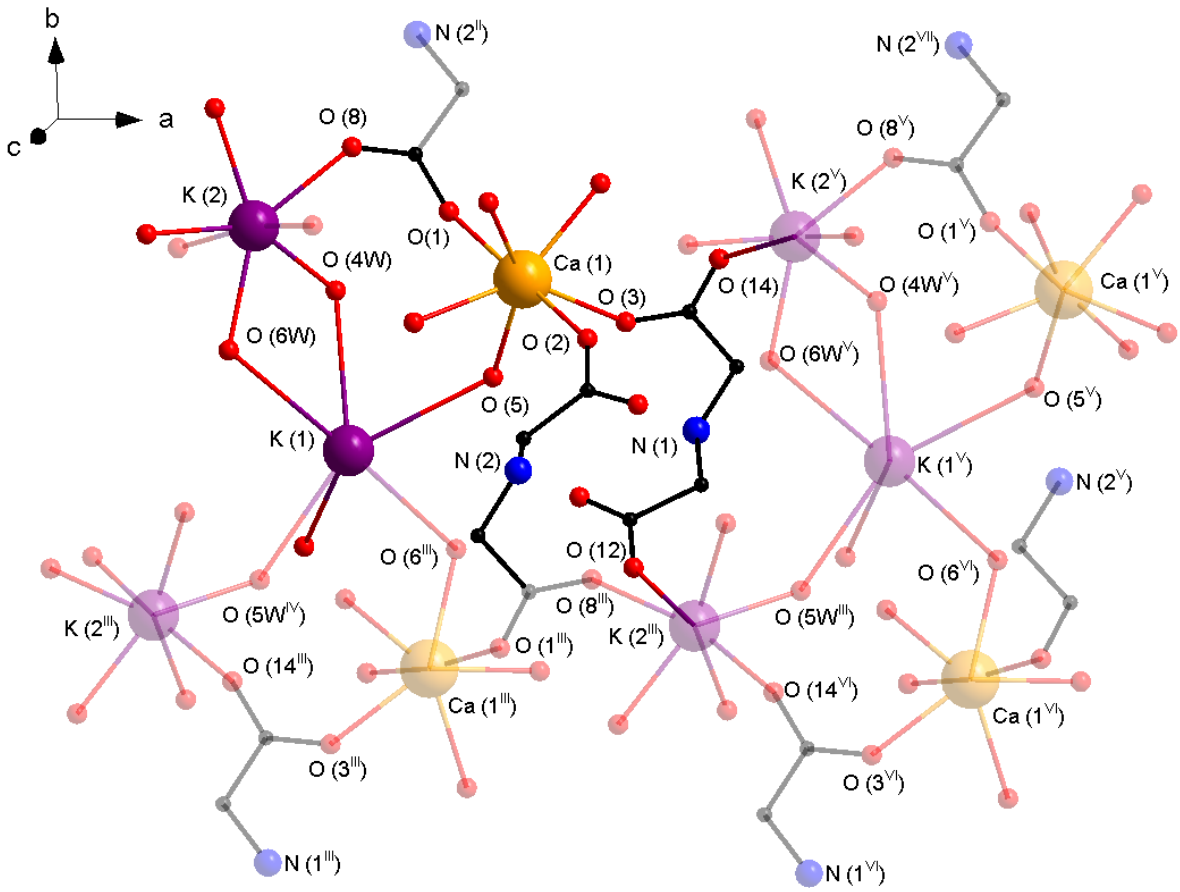

Fig. 4.90 | Potassium counter-ions facilitate the cross-linking between the 1D coordination chain motifs in the direction of the crystallographic *a*-axis. Hydrogen atoms and ligand molecules are omitted for clarity; only the iminodiacetic acid carboxylate groups are shown. Symmetry codes: (II): 1-x, 0.5+y, 1-z; (III): 1-x, -0.5+y, 1-z; (IV): -x, -0.5+y, 1-z; (V): 1+x, y, z; (VI): 2-x, -0.5+y, 1-z; (VII): 2-x, 0.5+y, 1-z.

Both symmetry equivalent ions K(2^{III}) and K(2^{V}) are linked through μ_2 syn-syn type oxygen bridges to the K(1^{V}) potassium counter ion (Fig. 4.90). This ion (K(1^{V})) interact with the oxygen atoms O(5^{V}) and O(6^{VI}) of the coordination spheres of the Ca(1^{V}) and Ca(1^{VI}) ions, respectively.

The Ca-O bonds that extend in the direction of the *b*-axis along with the ion-dipole interactions observed along the crystallographic *a*-axis give rise to a neutral sheet that extends in the crystallographic *ab*-plane (Fig. 4.91). Its core is composed of metal ions, chlorine anions and constitutional and coordinating water molecules. The thickness of the core is *ca.* 9.9 Å (measured as a distance between the opposite aromatic hydroxyl groups O(10) and O(11)). The outer area of the layer is composed of ligand molecules, which interact through weak π-π interactions that provide additional stabilisation to the structure. The thickness of the layer is *ca.* 22.5 Å (largest distance between two opposite carbon atoms of the organic ligand).

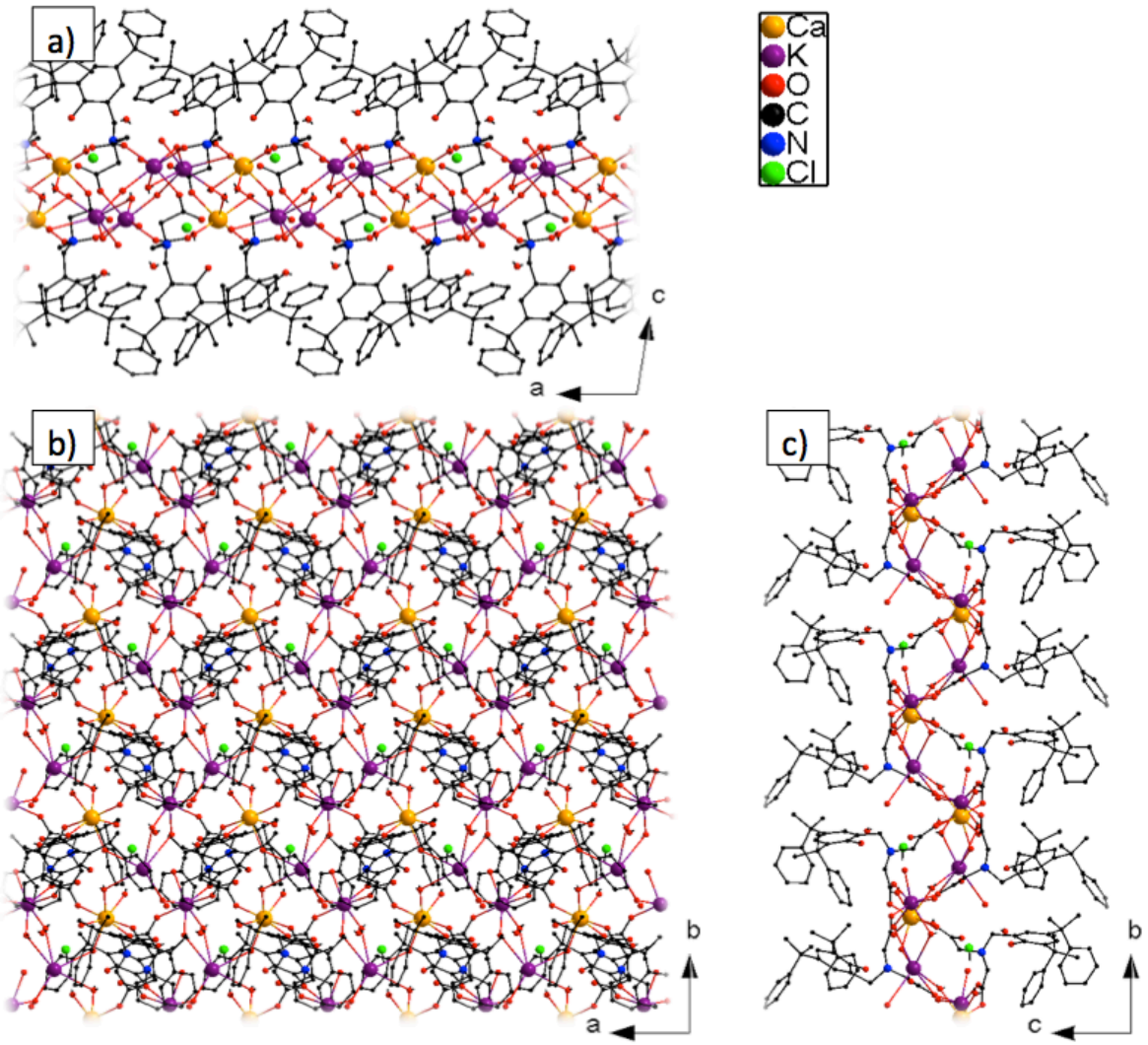

Fig. 4.91 | A 2D sheet in **14**. View in the direction of the crystallographic *b*-axis (**a**), *c*-axis (**b**) and *a*-axis (**c**). Hydrogen atoms were omitted for clarity.

Packing

The previously discussed neutral layers pack in the direction of the crystallographic *c*-axis. This process is facilitated by hydrophobic interactions, van der Waals forces and weak π-π stacking interactions that occur between the aromatic functionalities of the ligand molecules.

As visualised in Fig. 4.92, **14** adopts a lamellar organisation, where the hydrophilic areas sandwich between the hydrophobic parts of the structure. The thickness of the hydrophobic parts is *ca.* 12.5 Å, while the thickness of the hydrophilic areas corresponds to the thickness of the hydrophilic cores of the 2D sheets (*ca.* 9.9 Å).

As the hydrophobic moieties of the organic ligand molecules do not interdigitate with their symmetry equivalents, the lattice separation distance (measured along the crystallographic *c*-direction) is a sum of the thickness of the hydrophilic and the hydrophobic areas and equals *ca.* 22.4 Å. This value is in a good agreement with the unit cell parameters of **14** (c = 22.459(5) Å).

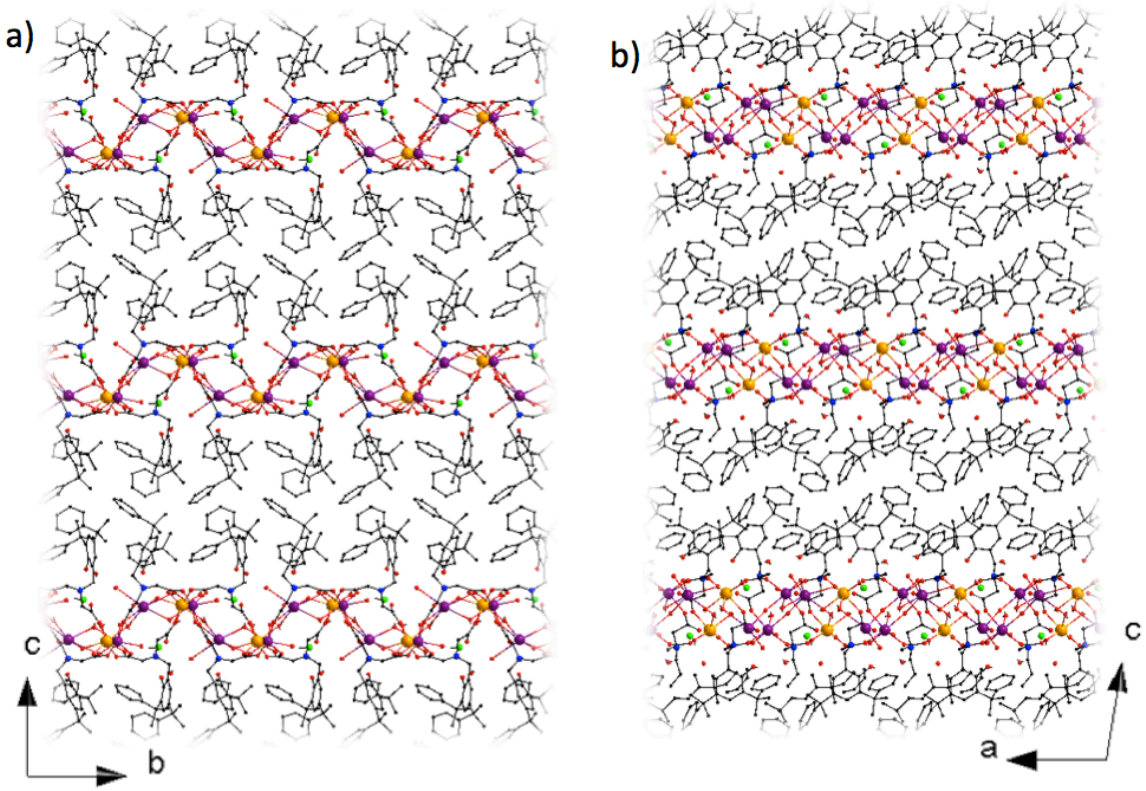

Fig. 4.92 | Packing structure of **14**. The layered lamellar arrangement is visible when the structure is viewed along the crystallographic *a*-axis (**a**) and *b*-axis (**b**).

The packing structure of **14** resembles to some extent the previously discussed Ca-containing compounds **8** - **13**. The presence of additional counter ions has a significant effect on the connectivity of the structure; however, the overall packing motif still displays the separation between hydrophilic and hydrophobic areas of the sample.

Refinement details

The refinement parameters are presented in Tab. 4.13

Tab. 4.13 | Refinement parameters for compound **14**.

Identification code	**14**
Empirical formula	$C_{58}H_{71}CaClK_2N_2O_{20}$
Formula weight	1269.90 g/mol
Temperature	150(2) K
Wavelength	0.71073 Å
Crystal system	Triclinic
Space group	*P*1
Unit cell dimensions	a = 10.585(2) Å α = 90.00° b = 13.702(3) Å β = 98.99(3)° c = 22.459(5) Å γ = 90.00°
Volume	3217.2(11) $Å^3$
Z	2
Density (calculated)	1.312 g/cm^3

Absorption coefficient	0.340 mm^{-1}
F(000)	1338
Crystal size	0.1 x 0.1 x 0.05 mm^3
Theta range for data collection	0.92 to 24.99°
Index ranges	-12<=h<=12, -14<=k<=16, -26<=l<=26
Reflections collected	25867
Independent reflections	9746 [R(int) = 0.1119]
Completeness to theta = 31.06°	99.3%
Absorption correction	Semi-empirical from equivalents
Refinement method	Full-matrix least-squares on F^2
Data / restraints / parameters	9746 / 18 / 770
Goodness-of-fit on F^2	1.165
Final R indices [I>2sigma(I)]	R1 = 0.1119, wR2 = 0.2843
R indices (all data)	R1 = 0.1354, wR2 = 0.3201
Largest diff. peak and hole	1.198 and -1.567 e.$Å^{-3}$

The refinement parameters indicate that the quality of the obtained dataset is not very good. The measurement was particularly difficult to perform due to the appearance of the crystals, which formed on the walls of a sample tube, within a drop of evaporating solvent. Each attempt to detach the crystals from the wall and to mount them on a glass fibre caused them to redissolve in the remaining solvent mixture.

The unit cell parameters strongly suggest that the structure should be solved in a monoclinic space group, however, despite many attempts, it was not possible to establish a comprehensive model of **14** in a higher symmetry space group. Our approaches to solve this problem included integrating the dataset in a monoclinic crystal system, using XPREP software to determine the space group and using Platon software to change the space group after the refinement.[187, 188] Unfortunately, all of these methods failed.

Additional analyses

It was difficult to isolate a single crystal of **14**, and it was confirmed that these crystals readily decompose after removing from the reaction mixture and loose their crystallinity. This is not surprising, as the asymmetric unit of **14** contains ten water molecules, which are involved in crucial bridging interactions between metal ions. Due to this fact, other analyses, such as the powder XRD, elemental analysis or thermogravimetric analysis were not performed on **14**.

Single crystal X-ray diffractometry revealed that **14** is a substantially different structure when compared with the previous Ca-containing compounds based on the iminodiacetic acid-containing ligands. Although the observed lamellar packing arrangement seems similar to the layered lamellar compounds **7**-**13**, the coordination environment of the Ca^{2+} ions and the Bc_2hda ligand binding modes are significantly different. This may be caused

by the introduction of potassium ions that compete with calcium ions in gaining the affinity of the carboxylic acid functionalities of the ligand molecules. It is worth to remember, that in the Cu-containing structures the addition of an inorganic base, such as potassium hydroxide, had always altered the formation of regular, mononuclear units and either the potassium ions or the chlorine anions were present within the structure (see compounds **2** and **4** for reference). This regularity seems to be valid also for the Ca-containing compounds.

–– CHAPTER V ––

Morphogenesis of calcium carbonate crystallised in the presence of the hda- and vda- type ligands

One aspect of the research described in Chapters III and IV was concerned with the development of synthetic methodologies, where inorganic compounds, such as carbonates and oxides, were derived from pre-existing organic-inorganic coordination networks. The formation of inorganic residues was a result of thermolysis or pyrolysis processes.

Naturally occurring biominerals are not usually formed at elevated temperatures. Their crystallisation occurs predominantly in ambient conditions. This is possible due to unique crystallisation strategies observed in nature. These are genetically controlled processes, refined through 500 million years of evolution. Living organisms have developed extraordinary abilities to preserve highly unstable transient phases, such as amorphous calcium carbonate (ACC), which are used as the starting materials for crystal growth. Therefore, naturally occurring crystallisation very often be described as a secondary phase change, where the amorphous phase is rearranged into an ordered crystalline material. This is possible due to non-covalent interactions and highly selective molecular recognition processes, which occur between the ACC moieties and specific protein residues preventing direct nucleation of the crystalline phases. As ACC is more susceptible to biological transport than the parent crystalline phases, it can be transported directly to a confined space, where nucleation may occur.

In order to mimic natural crystallisation processes, a vast number of organic molecules has been used to template the growth of inorganic crystals. The primary role of these molecules was to disturb the classical crystallisation process either through interactions with the crystal nucleus, selective inhibition of crystal faces or stabilising the amorphous phases (see sub-chapter 1.2.2 on p. 18). Most of these molecules contain a carboxylate group or an amine functionality as these functionalities have a high affinity to stabilise calcium ions, preventing condensation and hydrolysis reactions.

The hda- and vda-type ligands were not explored in this context before. The formation of network structures discussed in Chapter IV proved that both classes of ligands have the ability to interact with calcium ions, therefore, it was decided to study the possibility of using them as habit modifiers during the crystallisation processes of $CaCO_3$.

Based on the elucidated crystal structures, we anticipated that these ligands could potentially be good habit modifiers as their chelating ability gives rise to partially hydrated complexes. This binding ability might give rise to a directional growth of condensed phases.

Experimental methodology

In all of the performed experiments, aqueous solutions of calcium chloride and sodium bicarbonate were reacted, according to the following reaction equation:

$$CaCl_{2(aq)} + 2NaHCO_{3(aq)} \rightleftharpoons CaCO_{3(s)} + 2NaCl_{(aq)} + H_2O + CO_2\uparrow$$

The ratio between the Ca^{2+} ions and the HCO_3^- anions was kept constant at 1:2 [mol/mol]. The reaction was performed in a 50 ml beaker by mixing 5 ml of 0.1 M aqueous solution of $NaHCO_3$ and 10 ml of 0.025 M aqueous solution of $CaCl_2$. The reactants were further stirred for 1 minute; then the magnetic stirrer was removed and the breaker was covered with parafilm. In a reference experiment, when no ligand was used and the reaction was performed in ambient conditions, the formation of calcium carbonate was observed within the first 5 minutes after the addition of all reagents. A small sample of the precipitate was analysed using P-XRD (in order to determine the phase purity) and SEM (to investigate the morphology of the $CaCO_3$ crystals).

P-XRD confirmed that calcite is the predominant phase that forms in this process (Fig. 5.2). As expected, the SEM images presented in Fig. 5.1 show that the calcite crystals form regular, mainly rhombohedral blocks. Their dimensions vary between 2 and 10 μm.

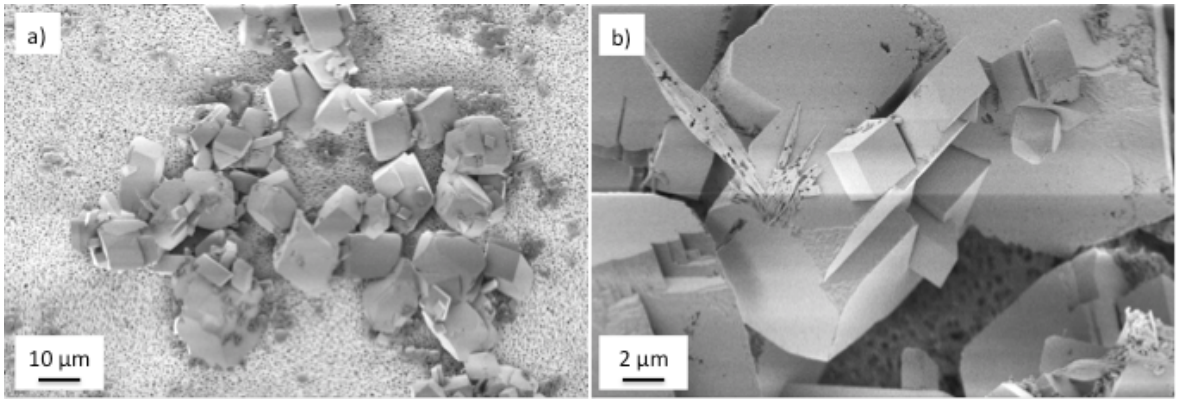

Fig. 5.1 | SEM micrographs of calcite crystals obtained from the reaction between sodium bicarbonate and calcium chloride in water without the presence of templating agents.

The formation of the rhombohedral crystals was disturbed when an organic templating agent was present in the reaction mixture. Also the reaction conditions, such as temperature or pH, were confirmed to be important parameters influencing the morphology of growing $CaCO_3$ crystals.

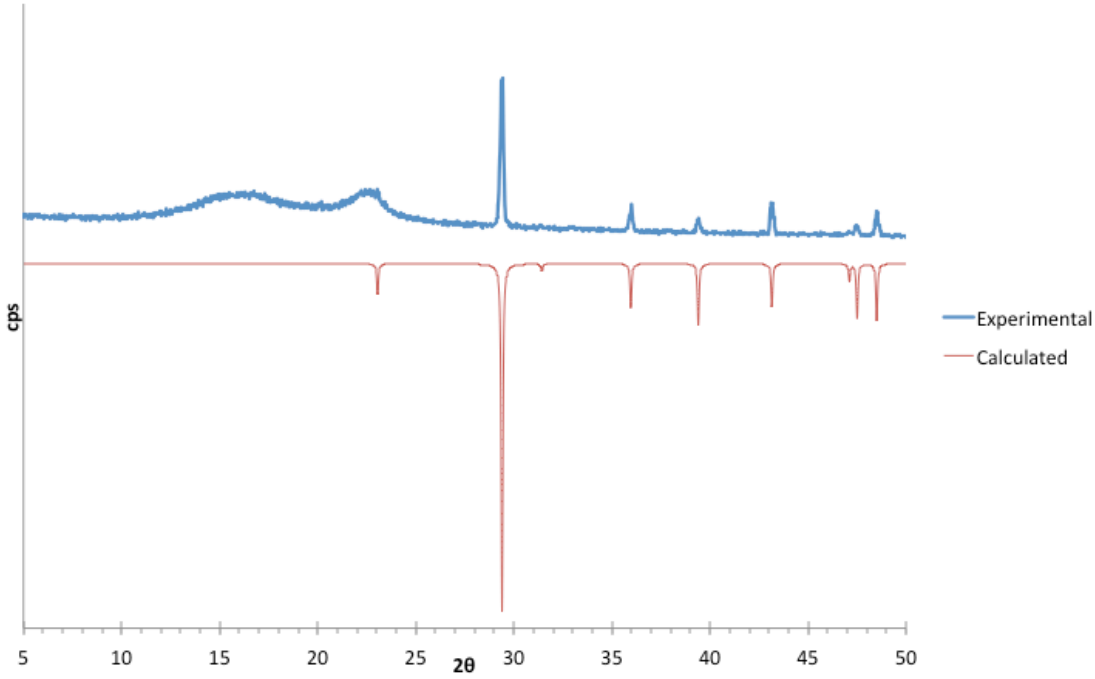

Fig. 5.2 | P-XRD pattern obtained for the crystals of $CaCO_3$ synthesised in the absence of an organic habit modifier (**blue**) compared with a reference P-XRD pattern for calcite (**red**).[178]

5.2. Me_2hda as the habit modifier for the crystallisation of $CaCO_3$

The first ligand used in an attempt to change the morphology of growing calcium carbonate crystals was Me_2hda. It is the most hydrophilic ligand within the hda-class and its binding mode to Ca^{2+} ions has been investigated in compound **8** (p. 114).

Four samples were prepared, where the calcium to ligand mole ratio was set to 50:1, 25:1, 10:1 and 5:1 under the previously described conditions. After one day the samples were filtered and washed with deionised water. The samples were then imaged using SEM to determine their morphology. A small amount of each sample was also analysed using P-XRD. The comparison of the P-XRD patterns, presented in Fig. 5.3, show that at lower concentrations of the ligand (50:1 and 25:1) calcite is the only phase observed. This is confirmed by the presence of the characteristic reflections at 29.4°, 35.9°, 39.4°, 43.2°, 47.5° and 48.5°. Surprisingly, when the concentration of the ligand increases to 10:1, only a residual pattern of calcite is observed. All major reflections (5.3°, 11.5°, 14.7°) originate from the $[Ca(Me_2hda)(H_2O)_3]\cdot½H_2O\cdot½MeOH$ (**8**) complex (see Fig. 4.18 on page 122). Further increase in the Me_2hda concentration (5:1) leads to the formation of phase pure compound **8**.

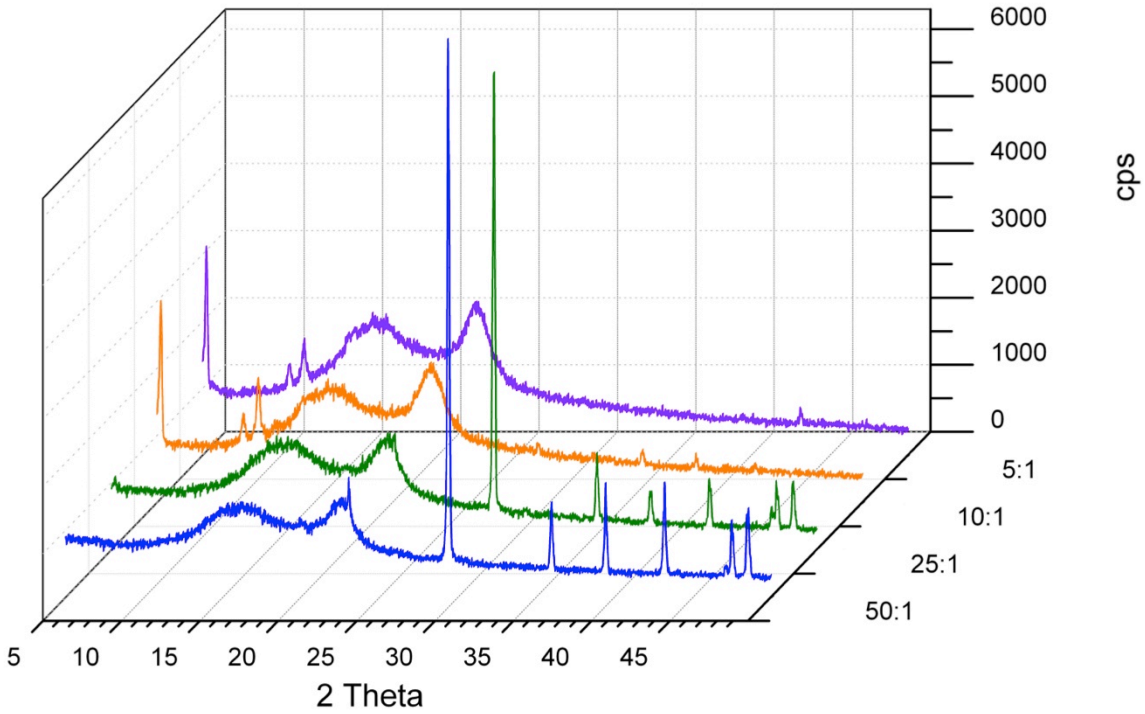

Fig. 5.3 | P-XRDs recorded for the samples of calcium carbonate formed in the presence of Me_2hda. The concentrations are as follows: 50:1 (**blue**), 25:1 (**green**), 10:1 (**orange**), 5:1 (**violet**).

The morphology of calcite crystals that grow in the presence of Me_2hda is different to the ordinary rhombohedrical blocks observed in a reference experiment. SEM imaging shows that when the calcium/ligand ratio is 50:1 the crystals are severely defected (Fig. 5.4). Although the hexagonal shape is still recognizable, the crystals adopt irregular geometries. Their length ranges between 10 and 12 μm.

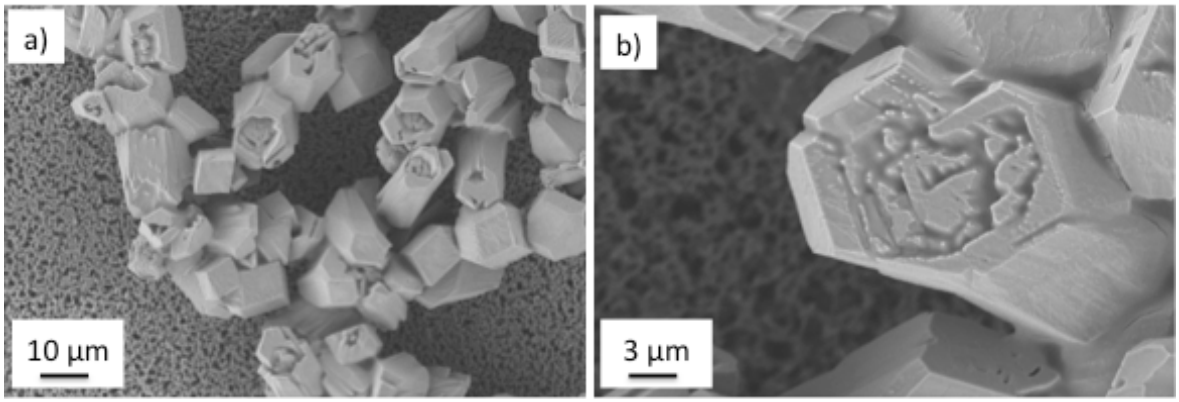

Fig. 5.4 | SEM micrograph of the crystals of calcite, which were grown in the presence of Me_2hda. calcium/ligand ratio: 50:1.

When the concentration of the ligand increases to a 25:1 mole ratio, three different type of morphologies are observed within the sample. As presented in Fig. 5.5, $CaCO_3$ crystals may grow as heavily defected rhombohedrons, irregular disks or dumbbell-like particles.

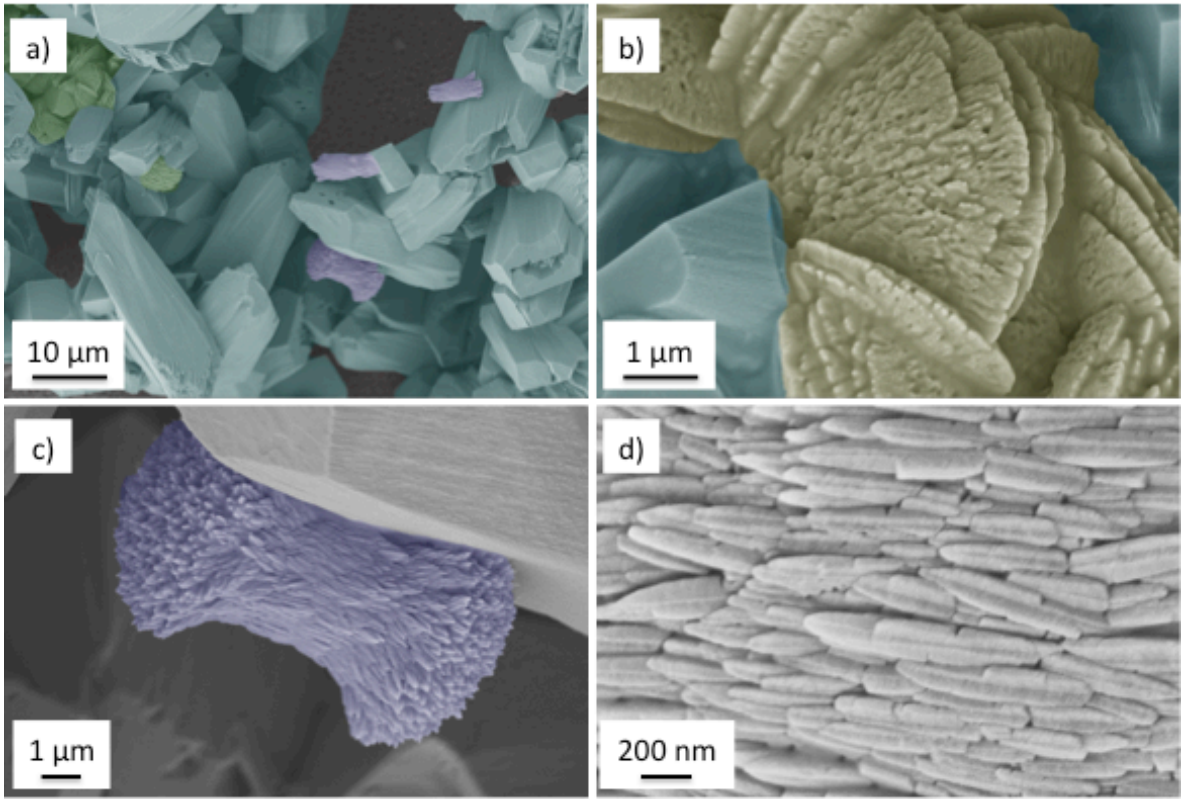

Fig. 5.5 | False colour SEM micrographs of $CaCO_3$ crystals grown in the presence of Me_2hda. Calcium/ligand ratio: 25:1. **a)** overview; **b)** disk-like crystals; **c)** dumbbell particles; **d)** magnification on the dumbbell-like crystal.

The dumbbell-like calcite morphology has already been described in the literature. It was obtained by crystallising $CaCO_3$ in the presence of magnesium ions or malic acid.[189, 190] Although the shape of the dumbbells is slightly different to those synthesised before, they are composed of similar small, coffee grain-like crystals, elongated along their longest axes (Fig. 5.5d). As Me_2hda is equipped with a dicarboxylic acid moiety, the mechanism of formation of the dumbbell-like particles may be similar to that reported before by Mann *et al.* for α,ω-dicarboxylic acids.[191] According to this explanation, dicarboxylates have the ability to bind to these faces of calcite crystals which comprise carbonate moieties oriented perpendicular to the

crystal surface. The nature of this interaction is purely electrostatic. According to the reported formation processes, when the crystal nucleus is formed and the growth is initiated, Me_2hda molecules are expected to form a monolayer on the hydrophilic faces (i.e. $(1\bar{1}0)$) of calcite. Further growth along these faces is obstructed, thus propagation along the elongated *c*-axis becomes kinetically favourable. Sasaki *et al.* showed that the following nucleation of new crystals is favoured on the solvent-particle interface of existing crystals.[192] Because a large number of new crystals nucleate at the same time, not all of them align in the same direction due to space restrictions. Each newly formed particle is slightly shifted in respect to the previous one by a certain angle (Fig. 5.6). As this angle is usually very small it does not significantly affect local structures of the crystal, however, it may change the morphology on a larger scale.

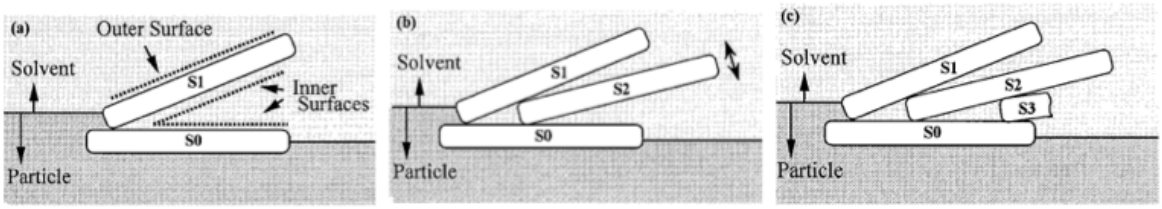

Fig. 5.6 | Explanation of the formation of the dumbbell-like particles of calcite.[192]

The disk-shaped particles, presented in Fig. 5.5b, consist of small crystalline particles that agglomerate to form round polycrystalline objects. Similar morphologies were observed and described before by Li *et al.*, however, they were attributed to the vaterite phase.[193] It is possible that the disks obtained in the experiment consist of vaterite and the P-XRD analysis does not show vaterite reflections due to the low abundance of this phase (when compared with calcite).

When the ligand/calcium mole ratio is increased to 1:10 the coordination compound **8** is the main product of the reaction. As we observed lower intense calcite reflections present in the P-XRD pattern, the sample was imaged using SEM. The pictures presented in Fig. 5.7 show aggregates of irregular $CaCO_3$ crystals. In contrast to the calcite crystals observed at lower ligand/calcium ratios, these crystals have smoother surfaces and seem to be composed of smaller, plate-like, aggregating particles (Fig. 5.7c). The average length of the crystals is *ca.* 45 μm, while the thickness ranges between 10 and 15 μm. Dumbbell-type particles also form under these conditions, however, they seem to be incorporated into the dominant, irregular calcite crystals.

Fig. 5.7d shows a dumbbell-like particle of calcite that grew on the surface of another crystal. Its morphology and dimensions resemble the dumbbell particles observed at the ligand to calcium ratio 1:25.

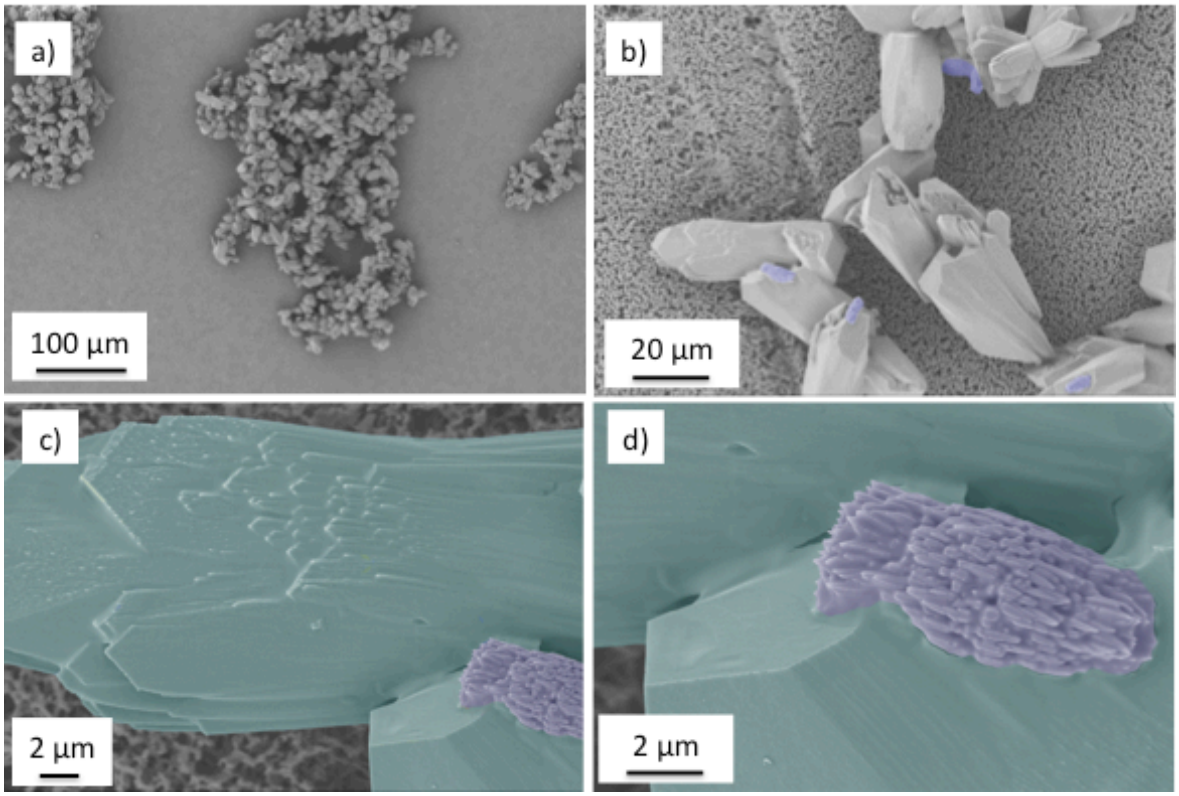

Fig. 5.7 | False colour micrographs of the calcite and compound **8** crystals formed in the presence of Me_2hda. Ligand/calcium ratio: 1:10. **a)** overview; **b-c)** higher magnification showing crystals of the coordination compound **8** and dumbbell-like particles of calcite; **d)** magnification showing a dumbbell-like particle attached into another crystal.

Further increase of the ligand/calcium ratio led to the formation of higher yields of plate-like crystals of **8**, which tend to aggregate into bunch-like structures (Fig. 5.8). The individual plates are *ca.* 40 µm long and 5 µm thick. The morphology of **8** obtained under these conditions is in agreement with that described in section 4.2.1 (see Fig. 4.19c on p.123). As no other types of crystals were observed one can conclude that calcium carbonate does not form under these conditions.

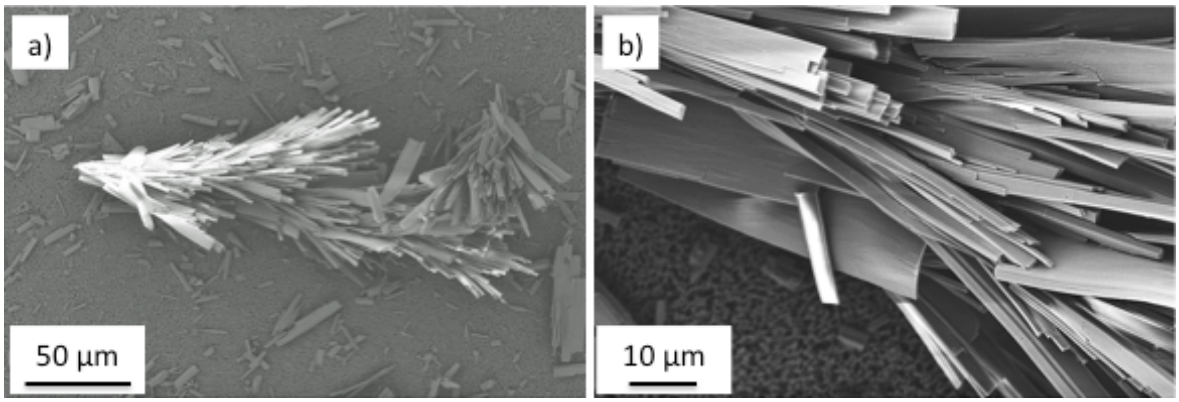

Fig. 5.8 | SEM images of the crystals of coordination network **8** formed when the calcium to ligand ratio was set to 5:1. **a)** Overview; **b)** magnification.

5.3. Calcium carbonate crystals templated using the C_{12}hda ligand

After the influence of the Me_2hda ligand on the $CaCO_3$ morphology was investigated, it was decided to test C_{12}hda as a habit modifier for $CaCO_3$. Based on the previously determined X-ray structures, it was assumed that the dodecyl chain would not interact with the crystal nucleus and ligand-crystal interactions would primarily be limited to the iminodiacetic acid moiety and the aromatic hydroxyl group.

5.3.1. Ligand/metal ratio dependence

In order to improve the solubility of C_{12}hda, these experiments were performed at 30°C. Tab. 5.1 presents the exact mole ratio between the ligand and the calcium ions that were investigated in these studies.

Tab. 5.1 | Molar ratios between the ligand molecules and the metal ions investigated in these studies

Sample no.	Mole ratio		
	C_{12}hda	Ca^{2+}	HCO_3^-
1	0.01	1	2
2	0.01	0.5	1
3	0.01	0.25	0.5
4	0.01	0.1	0.2
5	0.01	0.05	0.10

The P-XRD pattern of each obtained sample is presented in Fig. 5.9. In every case, calcite was the only $CaCO_3$ phase that was detected. For the relatively low ligand/Ca^{2+} ratio (Fig. 5.9d-e) all of the signals expected for the calcite phase were visible in the P-XRD pattern.

The increase of the ligand concentration results in less intense signals at higher 2θ values, above 30°. For samples obtained at the 1:10 mole ratio (Fig. 5.9b), the characteristic signal observed at 29.5° and attributed to the (104) plane is the only visible reflection. For the highest studied ligand/Ca^{2+} mole ratio, 1:5, the (104) signal is most intense (Fig. 5.9a). In addition, the pattern contains a broad signal that corresponds to the $(10\bar{2})$ crystal face.

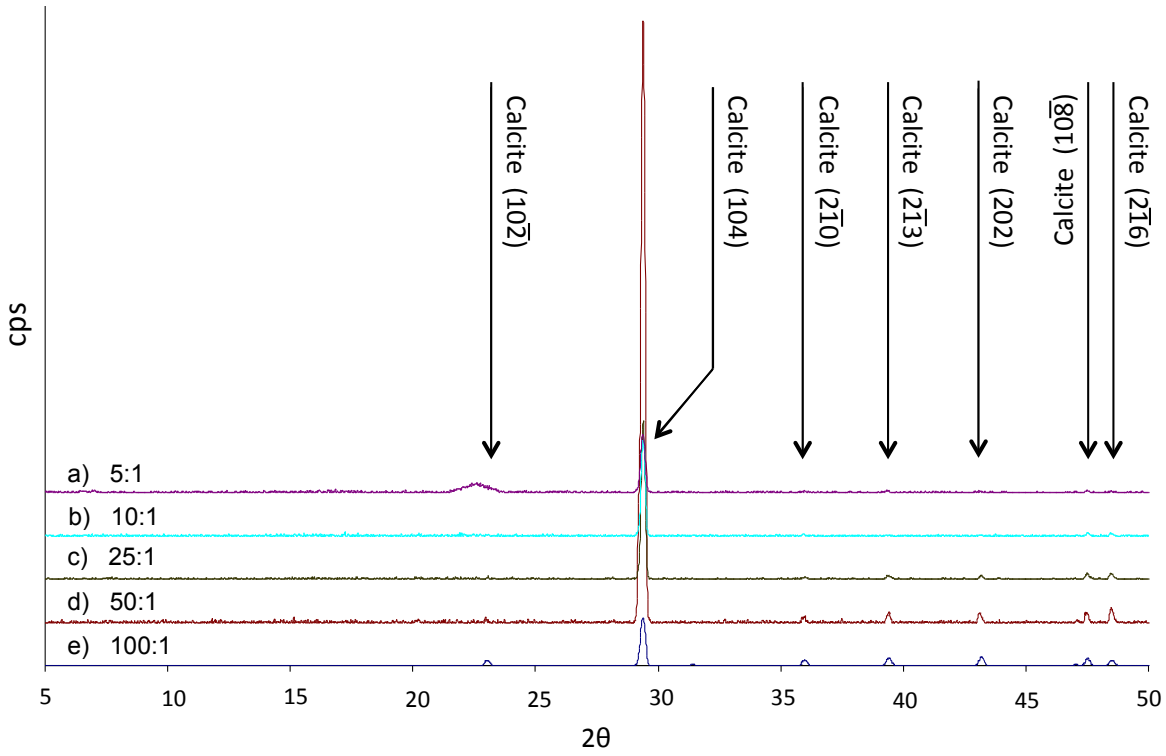

Fig. 5.9 | Comparison of the P-XRD patterns of the calcium carbonate samples prepared in the presence of the C_{12}hda ligand in different concentration.

The pattern of a sample obtained at the 1:25 ligand/Ca^{2+} mole ratio, which is presented in Fig. 5.9c, appears to reflect a transition where the reflections at higher 2θ values are still observed, but their relative intensities compared to the signal at 29.5° is lowest. This result suggests that at this ratio, the ligand starts to have a visible effect on the crystallisation process. It is worth noting that the same mole ratio of 1:25 had an impact on the morphology of the calcite crystals when Me_2hda was used as a habit modifier. The morphology of the crystals was monitored with SEM and the results are shown in Fig. 5.10. In all examined cases, the samples did not contain a single pure morphology. Some elongated crystals of calcite, with a high length to width aspect, were visible in the background in all examined samples.

A sample obtained at a ligand/Ca^{2+} mole ratio of 1:100 (Fig. 5.10a-b) is predominantly composed of well-defined rhombohedral calcite crystals. When the ligand/Ca^{2+} mole ratio increases to 1:50 these crystals are still visible, however it is possible to identify an increased number of cracks and defects on their surface (Fig. 5.10c-d). The further increase of the ligand/metal ratio to 1:25 resulted in the formation of discs of calcite, which contain a hole in the middle (Fig. 5.10e-f). This is a highly unusual morphology for a synthetic sample. When the ligand/calcium mole ratio was further increased to 1:10 the entire sample was composed of long and thin crystals. As visualised in Fig. 5.10g-h, only a few residual rhombohedra were observed. Finally, at 1:5 ligand/metal ratio, only the flake-like crystals that display a vague similarity to the morphology of **12** (Chapter 4.6) were obtained (Fig. 5.10i-j).

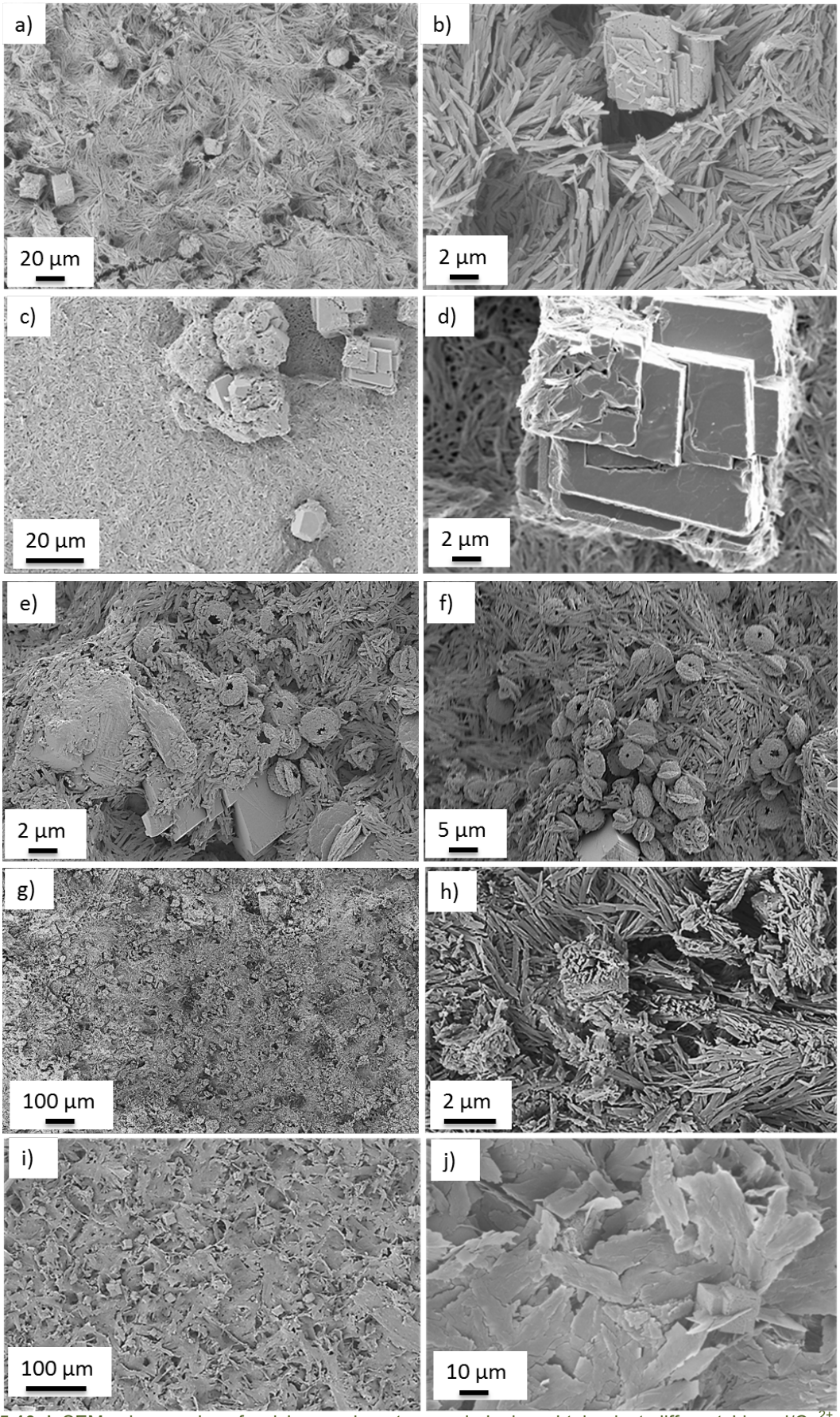

Fig. 5.10 | SEM micrographs of calcium carbonate morphologies obtained at different Ligand/Ca^{2+} ratio. **a-b)** 1:100; **c-d)** 1:50; **e-f)** 1:25; **g-h)** 1:10; **i-j)** 1:7.

For the consecutive experiments, the ligand to metal ratio was kept at 1:25. This approach was justified as we observed pronounced changes of the P-XRD patterns of samples

that form at the same ratio. In addition, these samples are composed of unusual disk-like calcite morphologies. This ratio is also in good agreement with the literature reports that describe a similar research methodology, which exploits ligands with iminodiacetic acid moieties as habit modifier.[194]

5.3.2. Temperature dependence

The influence of the reaction temperature on the crystallisation process was investigated. The outlined sample preparation was repeated at different temperatures, ranging from 40°C to 90°C (10°C increments). The samples were primarily investigated using the P-XRD analyses. The results presented in Fig. 5.11 reveal that at elevated temperatures (80-90°C) the formation of aragonite is favoured. Calcite seems to be stable up to 60°C. At 70°C both phases are observed. This data are consistent with literature reports that describe the $CaCO_3$ crystallisation experiments in the absence of any additives.

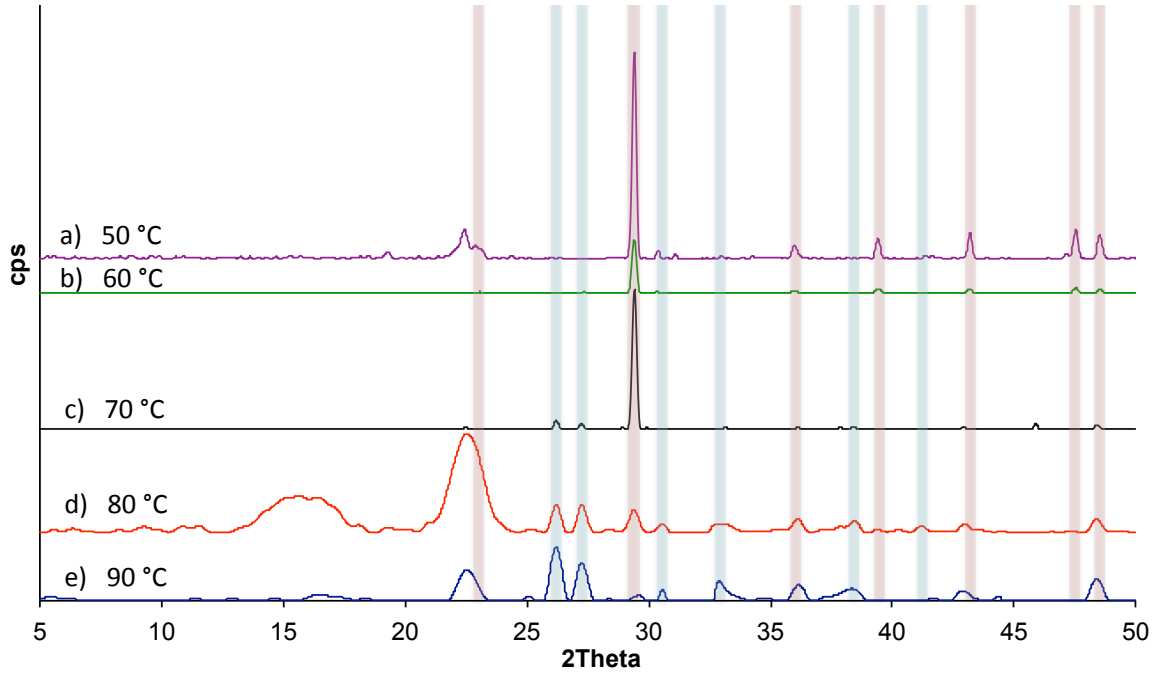

Fig. 5.11 | P-XRD patterns recorded for calcium carbonate crystals that were obtained in the presence of the C_{12}hda at different temperatures. The highlighted areas correspond to the positions of reflections: calcite – red, aragonite – blue.[178]

As all samples were kept in the reaction mixture for 1 day prior to the filtration, it is not surprising that the presence of the thermodynamically unstable vaterite phase was not detected.

The morphologies corresponding to the experiments performed in elevated temperatures are presented in Fig. 5.12.

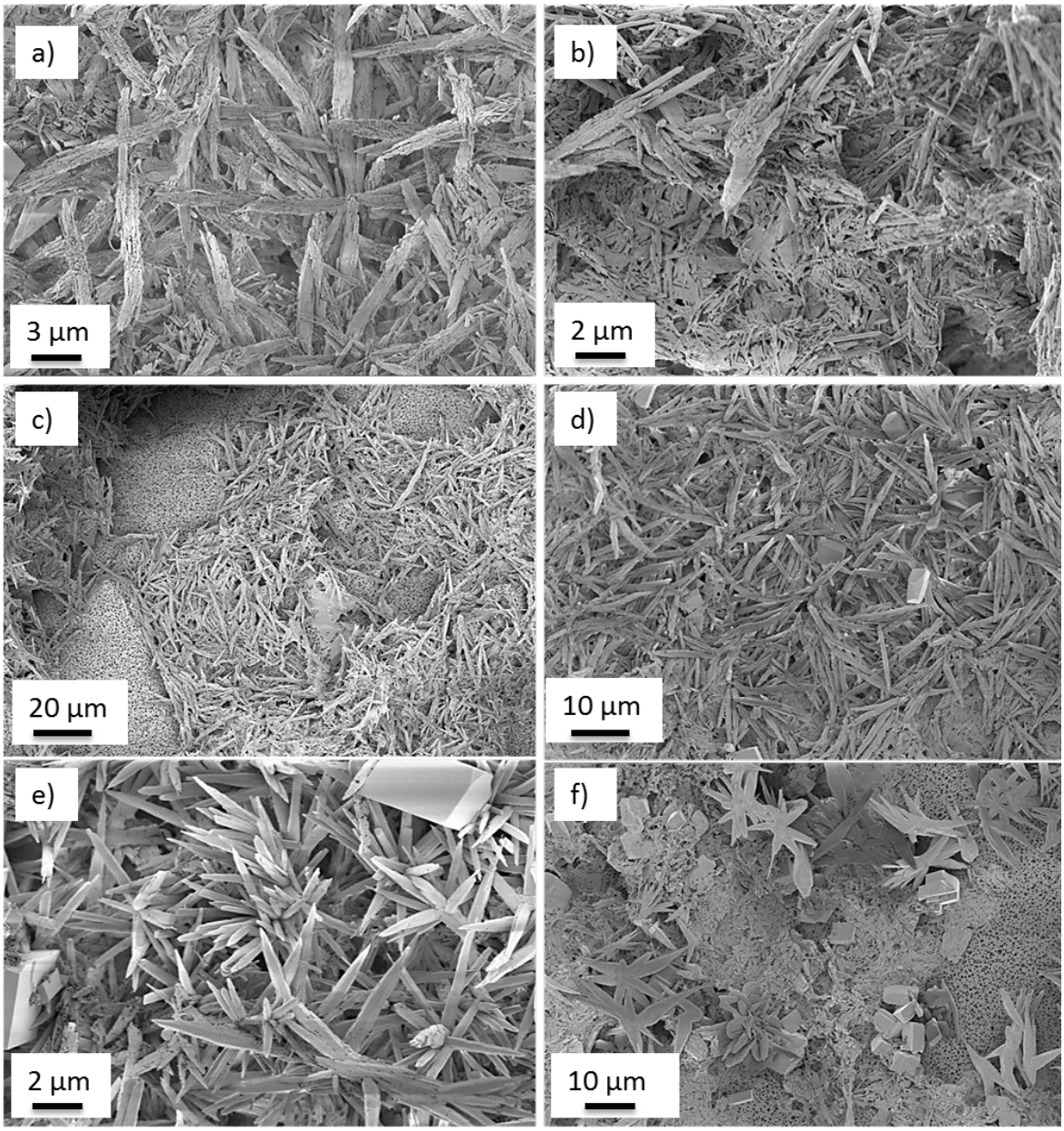

Fig. 5.12 | Dependence of the $CaCO_3$ morphology on the temperature. **a-b)** 90°C; **c)** 80°C; **d)** 70°C; **e)** 60°C; **f)** 50°C

Aragonite crystals that form at elevated temperatures (above 70°C) adopt typical needle-like morphologies (Fig. 5.12a-d).[189] When the reaction mixture is heated at 60°C both phases, calcite and aragonite, are formed. The blocks of calcite and needles of aragonite are visible in Fig. 5.12e. At 50°C the formation of calcite is favoured; irregular block-shaped crystals dominate over aragonite needles (Fig. 5.12f).

At temperatures below 50°C only calcite phases were observed. As mentioned previously, samples prepared at 30°C formed calcite discs assemblies that have a hole in their geometric centres (Fig. 5.10g-h). This morphology was further explored and the results are presented in section 5.3.4 on page 216.

5.3.3. Time dependence

A sample of $CaCO_3$ was synthesised as outlined above in the presence of C_{12}hda (ligand/metal mole ratio 1:25) and small portions of the white precipitate were collected after certain periods of time, dried and kept under a nitrogen atmosphere. The $CaCO_3$ phase changes occurring within the sample were then resolved using the P-XRD pattern. Our initial observations revealed that three phases of calcium carbonate are involved in the crystallisation process that occurs under the outlined conditions. Fig. 5.13 shows that the first initial phase that precipitates from the reaction mixture is amorphous calcium carbonate. The P-XRD patterns obtained from a sample collected 1 minute after combining the reactants looks flat and no major signals are observed. The next sample, collected after five minutes is composed of vaterite (and possibly remaining ACC). This result suggests that the first crystalline product of the reaction is a kinetically favoured phase, which has the potential to undergo further rearrangements.

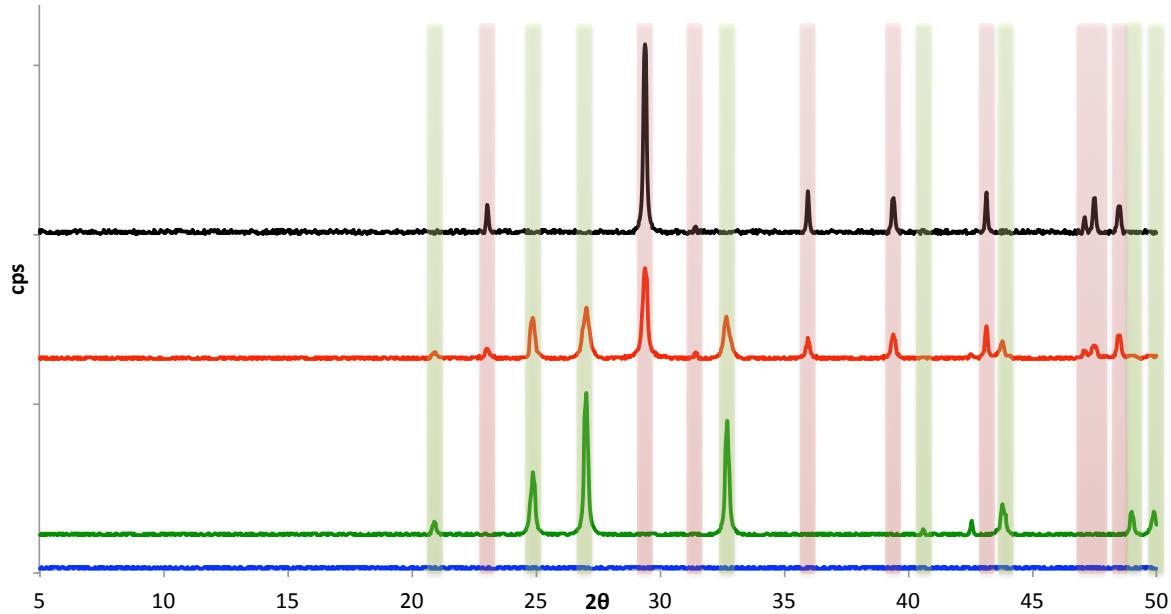

Fig. 5.13 | P-XRD patterns recorded for the sample of calcium carbonate that forms in the presence of the C_{12}hda ligand after: 1 minute from preparation (**blue**); 5 minutes from preparation (**green**); 15 minutes from preparation (red) and 1 hour from preparation (**black**). The highlighted areas correspond to the typical positions of calcite (red) and vaterite (green) reflections.[178]

When the P-XRD pattern is obtained form a sample of $CaCO_3$ that was collected after 15 minutes after combining the reactants, two crystalline phases are detected. As presented in Fig. 5.13 (red line), the powder XRD pattern demonstrates that the sample is composed of calcite and vaterite. The presence of calcite may be explained by the recrystallisation of the thermodynamically unstable vaterite crystals, which is known to occur under similar conditions.[195, 196]

The P-XRD patterns (Fig. 5.13, black line) demonstrate that calcite is the only present phase when precipitates are left for 1 hour and more in the reaction mixture. The vaterite crystals are not observed any more suggesting that they recrystallise and transform into calcite phase. This phase transition is well described in the literature and is applicable to $CaCO_3$ of synthetic and biological origin.[195, 197, 198]

5.3.4. Spherical aggregates

As previously stated, when the ligand to metal mole ratio was kept at 1:25 and the reaction was performed at 40°C, calcite was the only phase observed within samples that were left for 1 day in the reaction mixture. The morphology of this phase was studied using SEM. The imaging revealed that $CaCO_3$ particles adopt various shapes – from regular cuboids to flower-like assemblies (Fig. 5.14). Disks observed at 30°C are also present, however, this time they aggregate to form empty spheres.

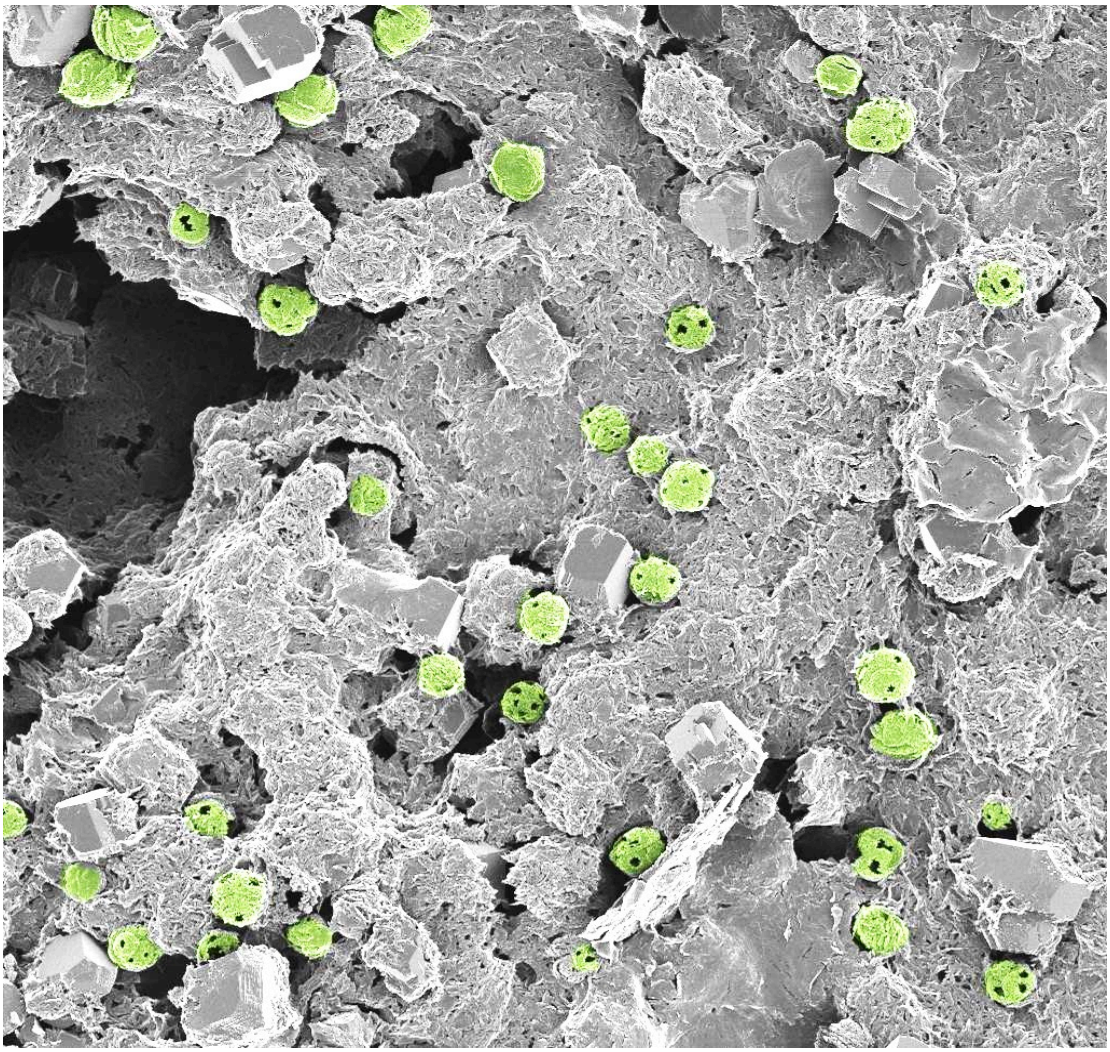

Fig. 5.14 | False colour HeIM micrograph showing the morphology of the calcite crystals obtained at 40°C and the ligand to metal ratio of 1:25. The green colour highlights the spherical aggregates of calcite disks.

A magnification on these aggregates reveals details of their microstructure (Fig. 5.15). The diameter of each particle is in a range between 5 and 8 μm and the average number of the disks involved in the formation of the structure varies between 7 and 12. The diameter of a single disk does not exceed 3μm and the diameter of the hole typically situated in the centroid of each disk is smaller than 1 μm. The thickness of the disks measured close to their centre is about 500 nm.

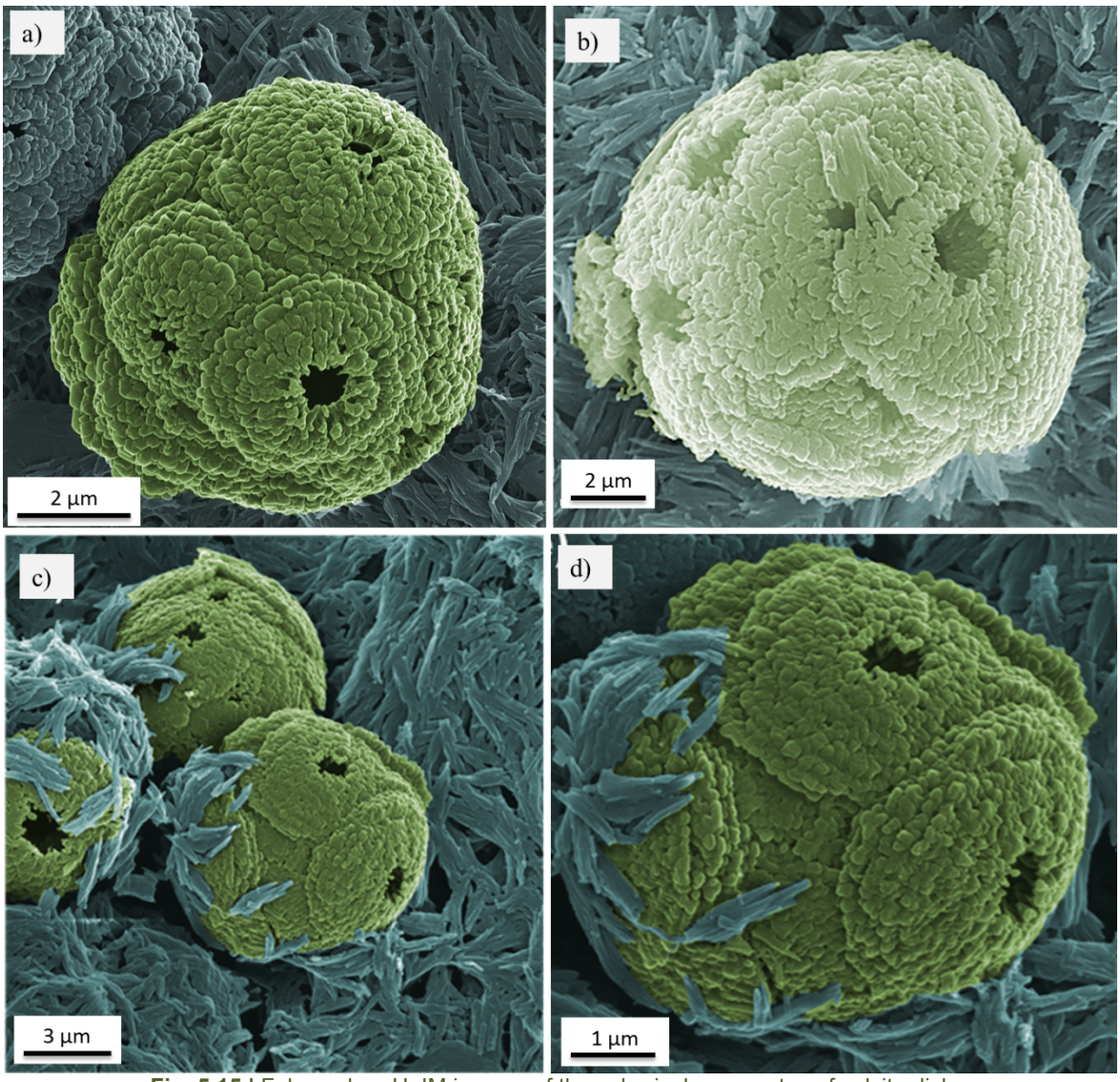

Fig. 5.15 | False colour HeIM images of the spherical aggregates of calcite disks.

The calcite disks were thin enough to attempt TEM imaging in order to determine the growth direction of individual calcite crystals. Fig. 5.16 shows a TEM image of a single calcite disk and an electron diffraction pattern obtained for crystals located on the outer edge of the disk. There is a correlation between the recorded diffraction pattern and a pattern simulated for a calcite crystal viewed in the direction of the crystallographic *c*-axis. This result indicates that the small crystals of calcite, which form the disks, grow primarily in the crystallographic (001) plane.

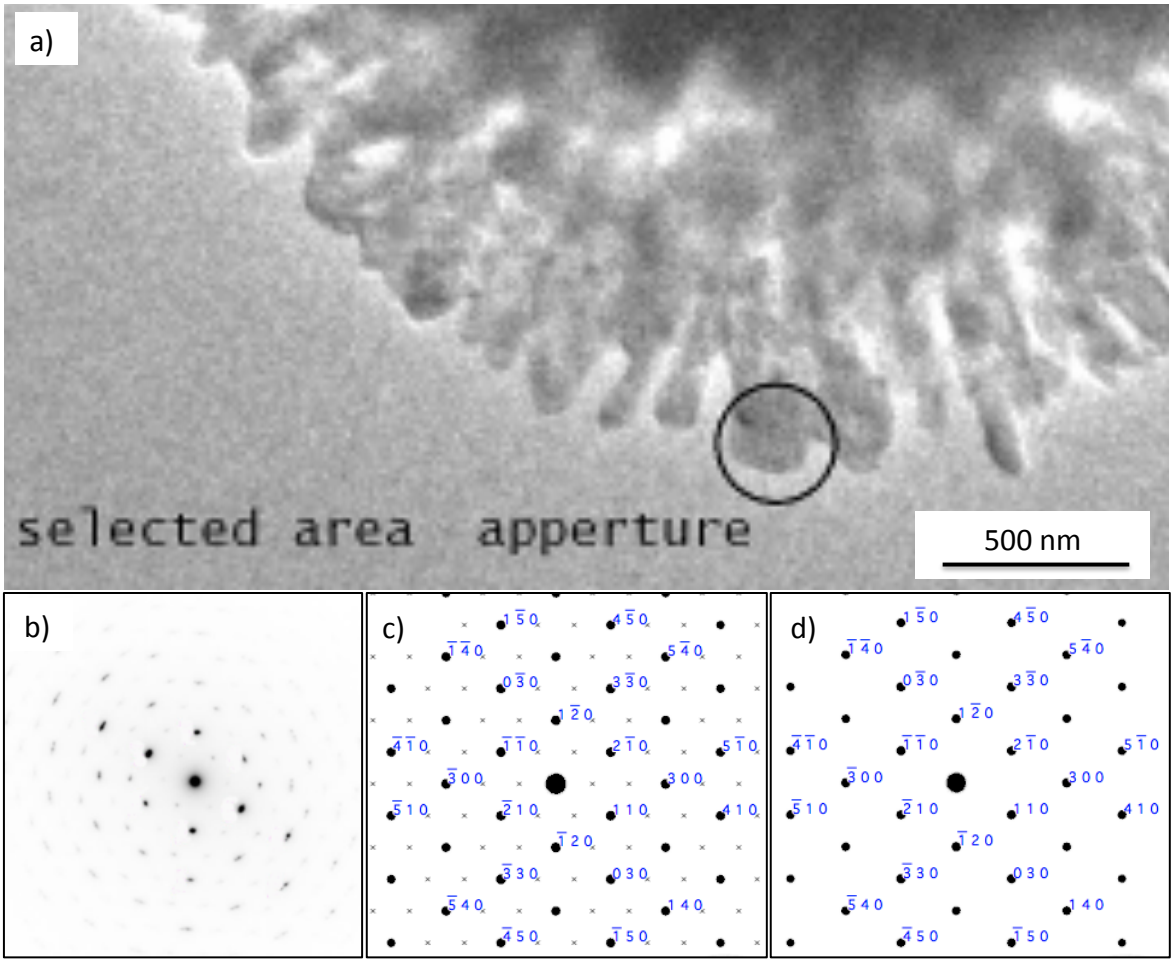

Fig. 5.16 | a) TEM image of a single disc from a spherical particle observed within the sample; **b)** corresponding electron diffraction pattern (negative image); **c)** electron diffraction pattern simulated and indexed for a calcite crystal viewed in the crystallographic *c*-direction; **d)** simplified calculated electron diffraction pattern, where the forbidden reflections (lattice and space group absences) were omitted for clarity.

Establishing the mechanism responsible for the formation of the spherical aggregates described above is a challenging task. Calcite particles displaying a vaguely related morphology were reported before, however, their formation is associated with biological processes that occur in living cells. Several marine algae, which are called coccolithophores, have the ability to produce exoskeletons that are made of calcite and comprise several (15-20) round disks-shaped polycrystalline particles agglomerating into a sphere. The spheres, presented in Fig. 5.17, are named coccospheres while each individual polycrystalline plate is called a coccolith. The formation of these discs starts in the Golgi body of a living cell. When complete, they fuse with the cell wall and are further exocytosed towards the external environment. Finally, they agglomerate and surround the cell, providing shelter from zooplankton and maintaining the buoyancy. The morphology of the coccoliths is highly complex. Each coccolith has an oval or round shape and a hole in its geometric centre. It is possible to observe that the discs are composed of highly organised single-crystalline plates, which form a chiral pattern on the surface. Despite several attempts it was not possible to develop a synthetic approach that would allow obtaining similar particles.

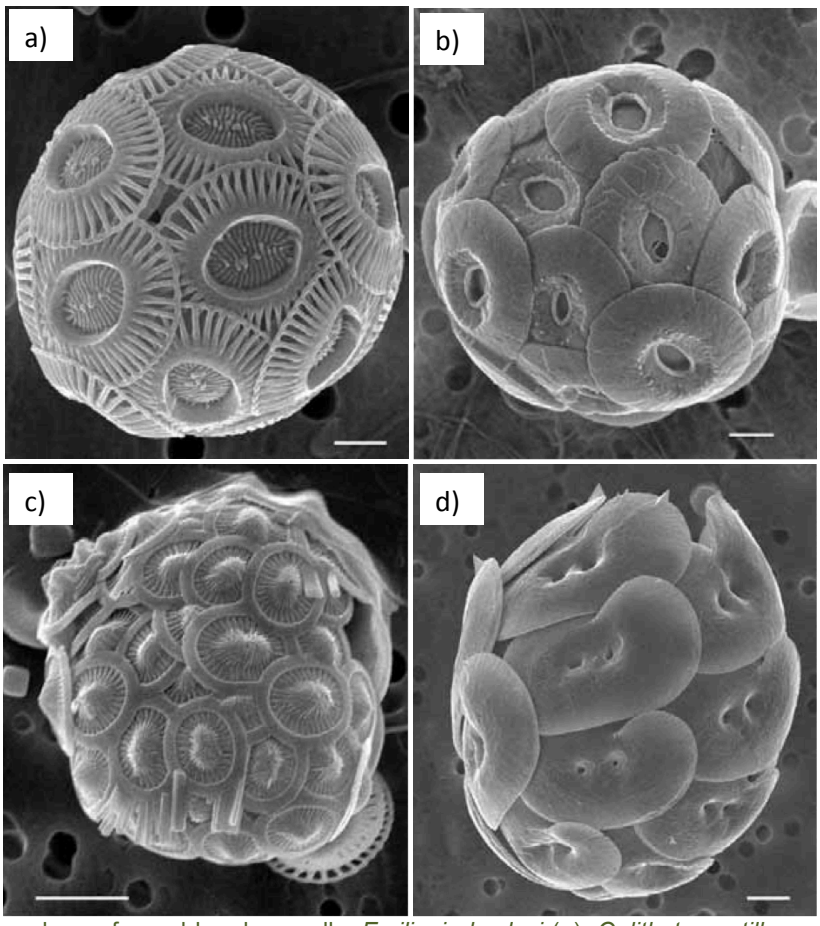

Fig. 5.17 | Coccospheres formed by algae cells: *Emiliania huxleyi* (**a**), *Oolithotus antillarum* (**b**), *Acanthoica acanthifera* (**c**), *Helicosphera carteri* (**d**). The scale bars correspond to 1 μm.[199]

The spheres obtained in the experiment, which consist of agglomerating calcite disks, resemble to some extent the morphology of the coccospheres. However, they do not exhibit chiral motifs and the single-crystalline particles forming the disks adopt random orientation. Although the biological processes are clearly not relevant for the formation of these particles, elementary processes of self-organisation may be observed on two levels:

1. The small, single-crystalline particles organise into discs that have a hole in the middle;
2. The disks agglomerate into spherical particles

The key question to answer is if the observed spherical disks are formed separately and aggregate into the sphere or do they form *in situ* on the surface of pre-formed spheres or some other template. There are two pathways established in the literature that seem to some extend be applicable to the observed process.

The first pathway may be associated with the aggregation of C_{12}hda-stabilised ACC particles at the underside of CO_2 droplets trapped at the meniscus at the air/water interface. This behaviour was previously observed by Rudloff *et al.* for vaterite crystals.[200] As presented in Fig. 5.18, the process starts when the CO_2 bubbles, which are a by-product of the reaction, reach the surface of the reaction mixture. They form a droplet at the solid-liquid interface, which attracts the ACC particles. These particles further aggregate and when their mass exceeds a certain limit, they sink into the bottom of a sample tube. As the bubble starts to

sink, further discs are formed and tessellate the surface. This pathway explains the distinct curved shape of the observed disks.

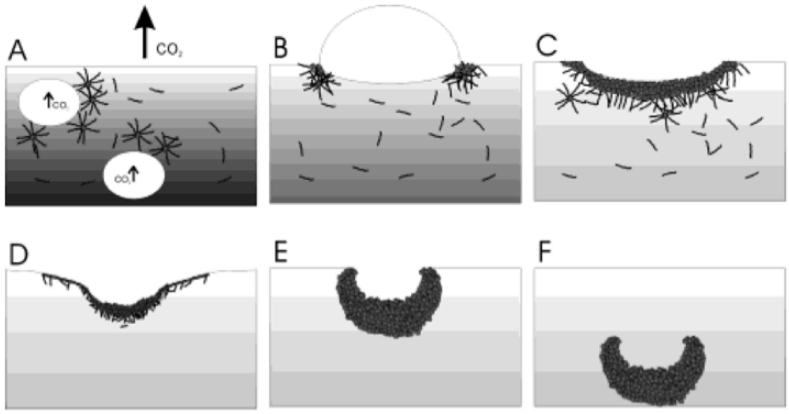

Fig. 5.18 | Schematic growth mechanism of CO_2 bubble templated $CaCO_3$ nanoparticle superstructure formation.[200]

An alternative pathway relies on the self-transformation of an C_{12}hda-stabilised ACC phase of solid microspheres *via* surface-directed Ostwald ripening to form hollow vaterite spheres, as it was reported by Yu *et al.*[145] The authors of this research paper concluded that surfactant-stabilised ACC may aggregate into spherical particles, which undergo further rearrangements. As presented in Fig. 5.19, due to the Ostwald ripening process, the cores of these particles become depleted as they recrystallise to give hollow vaterite spheres. The further surface patterning may be directed by the CO_2 outgassing, a process similar to the one observed by Walsh *et al.* for hollow aragonite particles.[201, 202]

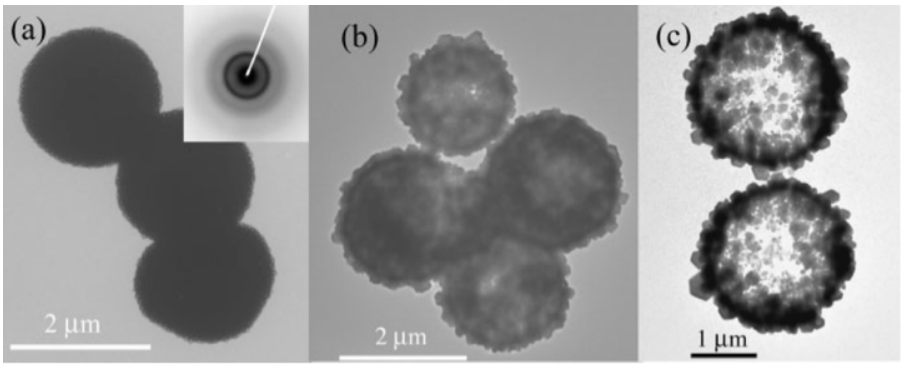

Fig. 5.19 | TEM images. The Ostwald ripening process is responsible for the transformation of spherical aggregates of sodium dodecyl sulphate-stabilised ACC aggregates (**a**) to hollow, spherical polycrystalline particles of vaterite (**c**).[145]

The pathway of the formation of the coccosphere-like particles within our investigated regime could not be resolved in detail. The best strategy that could be applied to determine the mechanism of their formation would require a direct observation of the sample using low-vacuum environmental scanning electron microscope techniques (ESEM).

5.4. Templating effect of the vda-type ligands family

5.4.1. Calcium carbonate crystals grown in the presence of the C_2vda ligand

Following the characterization of the morphology of the calcite microspheres obtained in the presence of C_{12}hda, it was decided to investigate the effect that the vda-class ligands may have on the morphology of $CaCO_3$. Although these molecules are similar to the previously used hda-class, they contain an additional ester functionality, which provides two additional O-atoms that could potentially interact with the calcium ions. As presented in chapter 4.3, these oxygen atoms do not bind directly to calcium ions, however, this may not necessarily be applicable for systems that contain an excess of metal ions. One O-donor of the ester functionality was confirmed to coordinate to copper ions in **1**; this had a recognizable effect on the solid-state structure of this compound. It is possible that the presence of the ester group may disturb the observed stabilisation effect of the vaterite phase.

The conditions that had the most influential effect on the $CaCO_3$ morphology in the hda-system (metal/ligand ratio of 25:1, 40 °C) were also applied in corresponding reaction systems that contained vda-type molecules.

The first species of this class to be applied as a potential habit modifier was C_2vda. The resulting white residues that formed under the outlined conditions were collected 24 hours after combining the reactants. They were analysed using the P-XRD to determine the phase and SEM was applied to investigate their morphology.

The P-XRD pattern, presented in Fig. 5.20, confirmed that calcite was the only crystalline phase present within the sample.

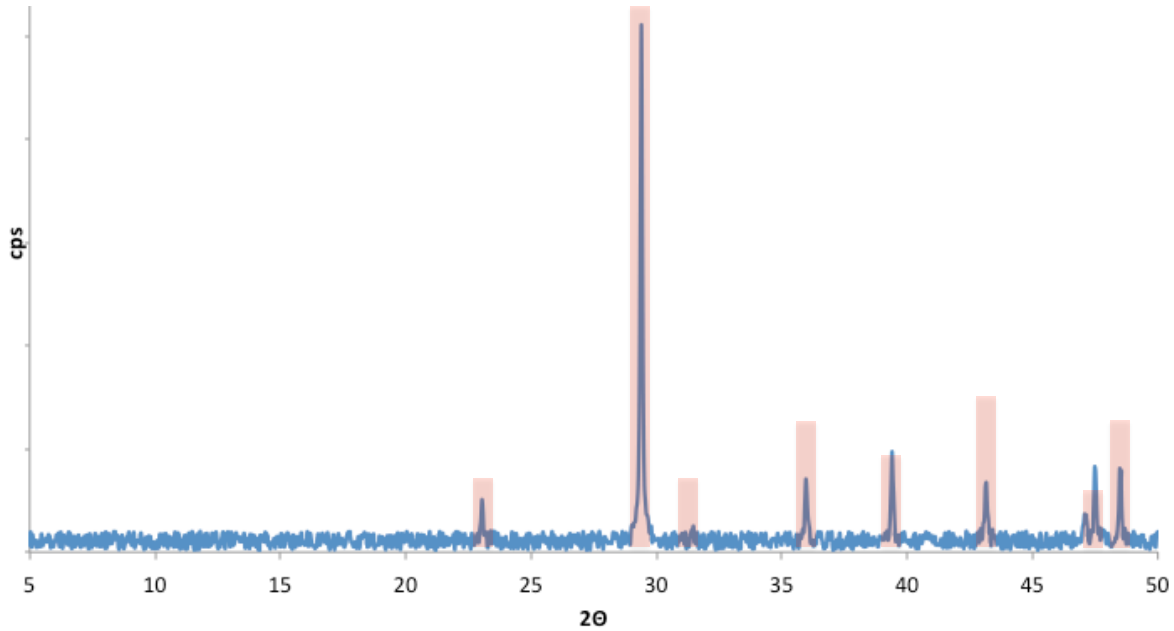

Fig. 5.20 | P-XRD pattern recorded for a sample of $CaCO_3$ synthesised in the presence of C_2vda. The highlighted areas correspond to the typical positions and intensities of calcite reflections.[178]

The SEM images, presented in Fig. 5.21a-b, show crystals of calcite randomly orientated on the surface. Their dimensions range between 10 and 20 μm. Higher

magnification imaging (Fig. 5.21c-d) reveals that the crystals do not adopt a typical rombohedral shape, moreover their morphology is highly irregular whereby individual crystallites appear to agglomerate.

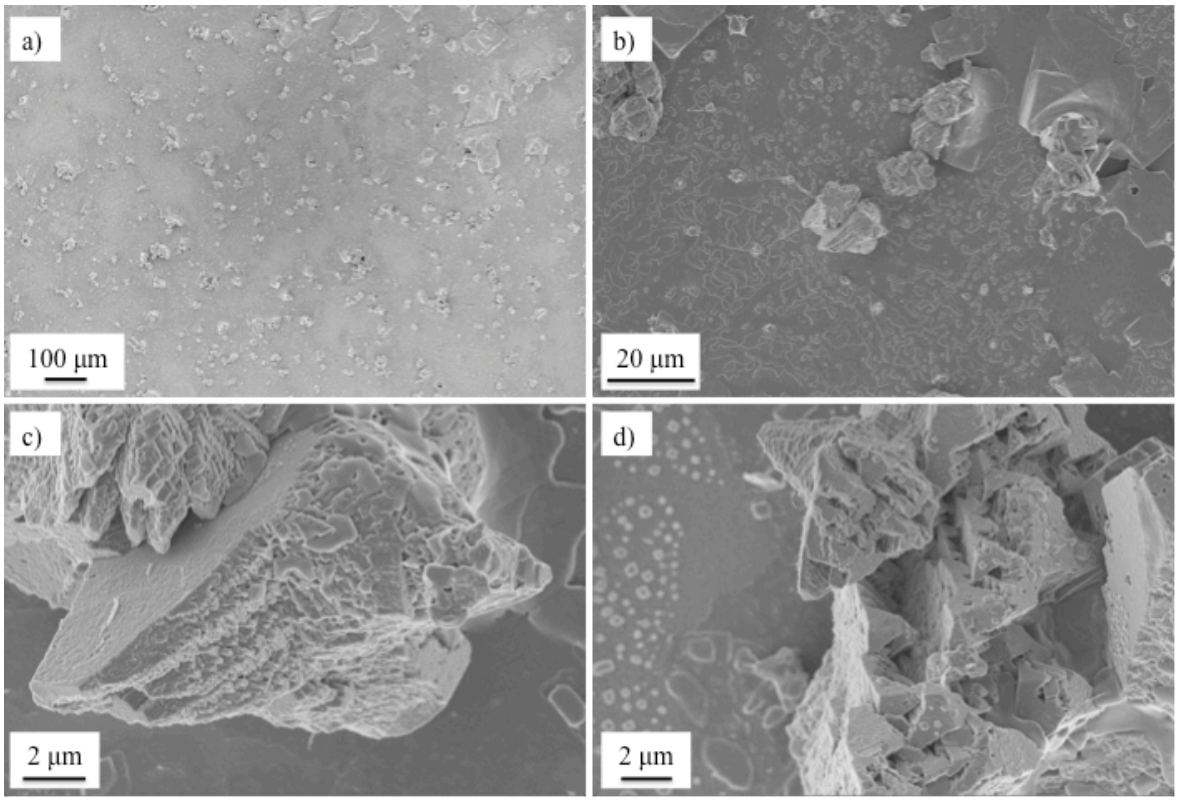

Fig. 5.21 | SEM micrographs of the calcite crystals grown in the presence of the C_2vda ligand. **a)** an overview picture; **b)** irregular crystals of calcite visible on the surface; **c-d)** higher magnification images reveal the details of the morphology.

The morphology of the calcite crystals obtained in the presence of C_2vda differs dramatically to the morphology of the crystals modified with Me_2hda. All of the observed crystals that form in the presence of C_2vda are highly defected and it is not possible to define a singular shape. In contrast, the sample obtained using Me_2hda as the habit modifier in majority consisted of regular, pseudo-hexagonal crystals (see Fig. 5.4 and Fig. 5.5 on page 207).

It is noteworthy that Me_2hda and C_2vda promote the formation of different calcite morphologies when used as habit modifiers. This effect is attributable to the different functionalities of the organic compounds. C_2vda contains additional oxygen atoms arising from the ester and methoxy moieties. These potential O-donors may interfere with binding characteristics of this complexing agent. In addition the structural arrangement of the ethyl moiety may influence the assembly process of individual C_2vda molecules. Indeed the crystallographic studies of corresponding Cu(II) complexes support this assumption (see **1** on page 41 and the dinuclear complex $[Cu^{II}(Me_2hda)(H_2O)]_2 \cdot H_2O$ reported by La Spina).[203]

5.4.2. Calcium carbonate crystals grown in the presence of the C_6vda ligand

It was decided to explore the influence of the length of the hydrophobic chain on the morphology of $CaCO_3$ crystals. The C_6vda compound was added to the reaction, which was carried out under the same conditions that were applied in previous experiments (metal/ligand ratio of 25:1, 40 °C). The resulting carbonate precipitation was analysed using powder X-ray diffraction and SEM techniques.

The P-XRD data recorded for the sample are presented in Fig. 5.22. All of the reflections can be associated with calcite crystals, confirming that this is the only crystalline phase present in the sample.

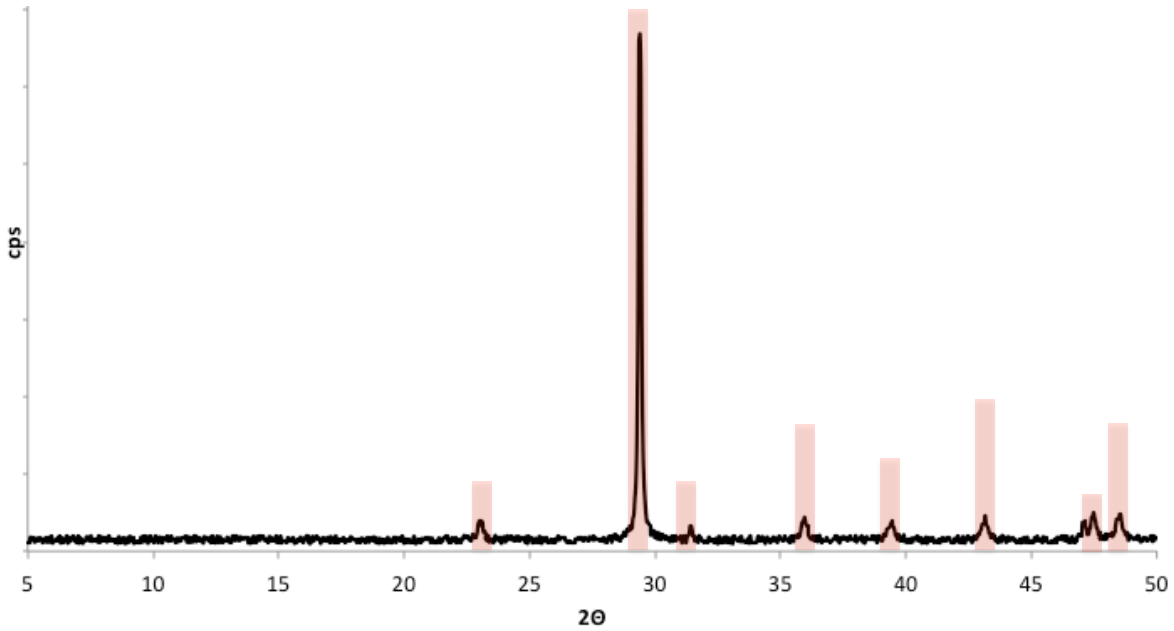

Fig. 5.22 | P-XRD pattern recorded for a $CaCO_3$ sample synthesised in the presence of C_6vda. The highlighted areas correspond to the positions and intensities of calcite reflections.[178]

The SEM images, presented in Fig. 5.23, show that polycrystalline calcite particles adopt an irregular shape. Their dimensions are *ca.* 50 μm and the higher magnification pictures reveal that the morphology of the crystals is highly complex. They appear to be formed by a vast number of thin, fibrous crystallites, which align in the same direction and agglomerate to form a dense solid. Their thickness is *ca.* 100 nm and their length uniformly matches the length of the entire polycrystalline particle. This material displays an ordered, hierarchical architecture; the fibrous crystallites are aligned in the same direction and seem to fuse at the solid-liquid interface. The morphology of the crystallites may be compared (to some extent) with the fibrous crystallites of Na_2CO_3 that were reported by Schmitt *et al.*[204]

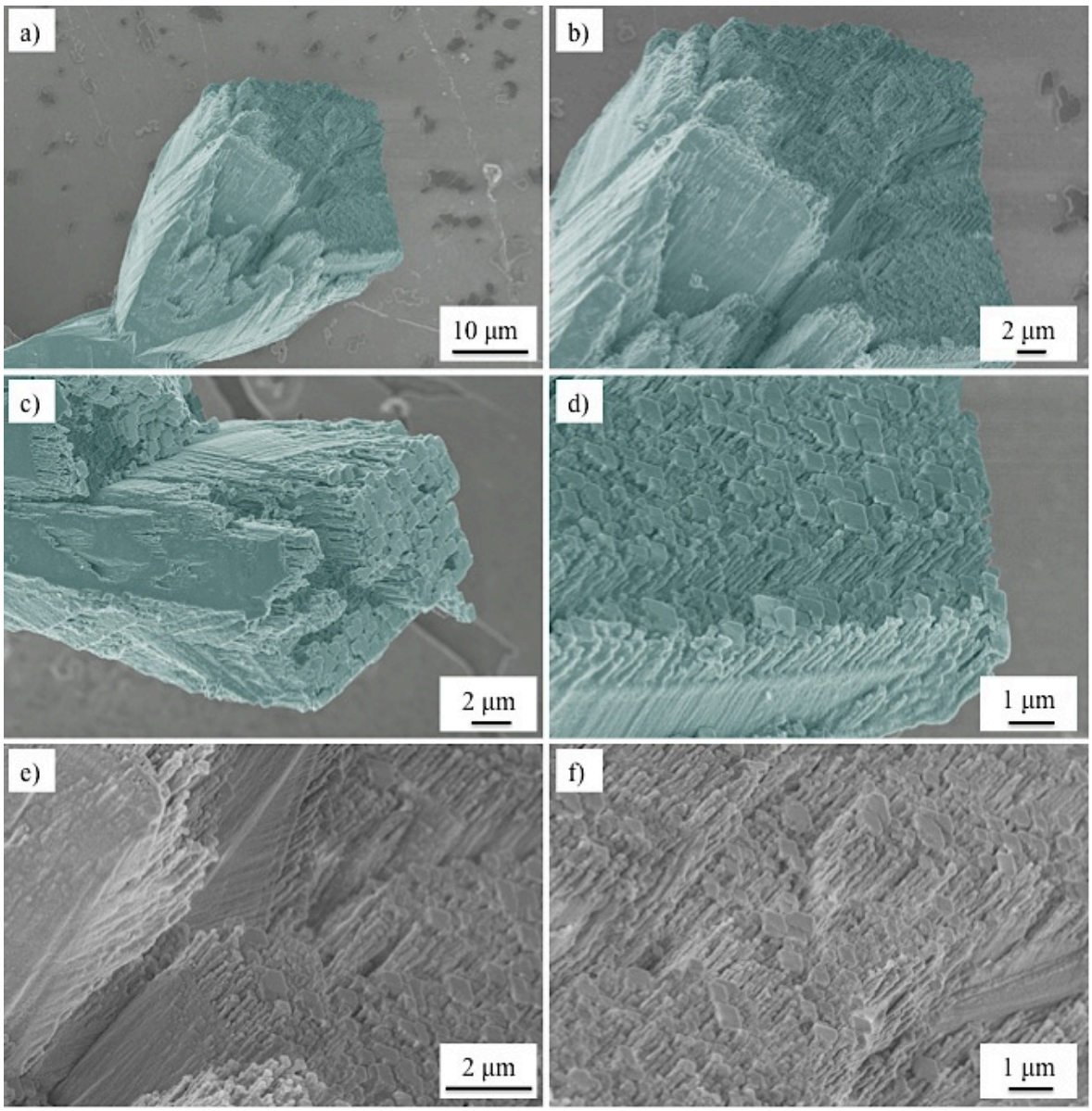

Fig. 5.23 | False colour SEM images of the calcium carbonate crystals obtained in the presence of the C_6vda molecules. **a-b)** overview; **c-f)** magnification showing fibrous arrangement.

The formation of these particles that relies on the presence of C_6vda, has to be enabled by the presence of the hexyl chain. It is possible that the chains interact *via* hydrophobic interactions and van der Waals forces, as observed for the C_{12}hda molecules; this leads to the formation of a pre-arranged precursor phase, which further rearranges and gives rise to the observed polycrystalline agglomerates.

The fibrous shape of the crystals suggests that the ligand inhibits the crystal growth in two crystallographic directions by interacting with at least two different crystal faces. Thus, the growth of $CaCO_3$ is promoted in one direction only, leading to the formation of the fibrous crystallites.

5.4.3. Calcium carbonate crystals grown in the presence of the C_{10}vda ligand

In an attempt to investigate the effect of a longer aliphatic chain, the C_{10}vda ligand was used in a consecutive experiment. The conditions of the reaction were the same as for the previously used vda-type compounds. The obtained crystals were filtrated and analysed using the P-XRD and SEM techniques.

Unsurprisingly, the obtained powder X-ray diffraction pattern, which is presented in Fig. 5.24, confirms that the sample is composed of calcite.

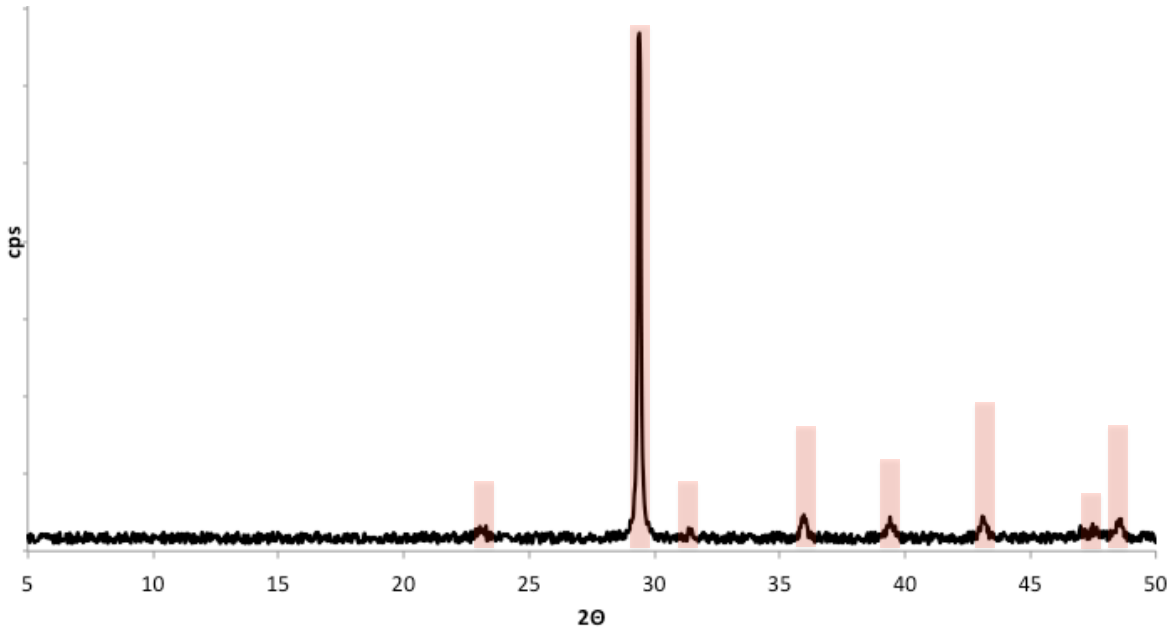

Fig. 5.24 | P-XRD data recorded for a $CaCO_3$ sample synthesised in the presence of C_{10}vda. The highlighted areas correspond to the positions and intensities of calcite reflections.[178]

The SEM images, presented in Fig. 5.25a, show that the resulting samples consist irregular, polycrystalline calcite particles. The largest dimension of the calcite particles that form under these conditions does not exceed 100 μm. Higher magnification images (Fig. 5.25b-d) show that the surface of each polycrystalline particle is covered with thin, plate-shaped crystallites that may be a result of the drying effect. However, in the areas below, which are not covered by these crystals, it is possible to observe partially aligned calcite features (see Fig. 5.25d for a magnification of this area). Undoubtedly the presence of C_{10}vda disturbs the growth of typical calcite rombohedrons, however, under the applied conditions it does not promote the formation of any specific, homogeneous morphology.

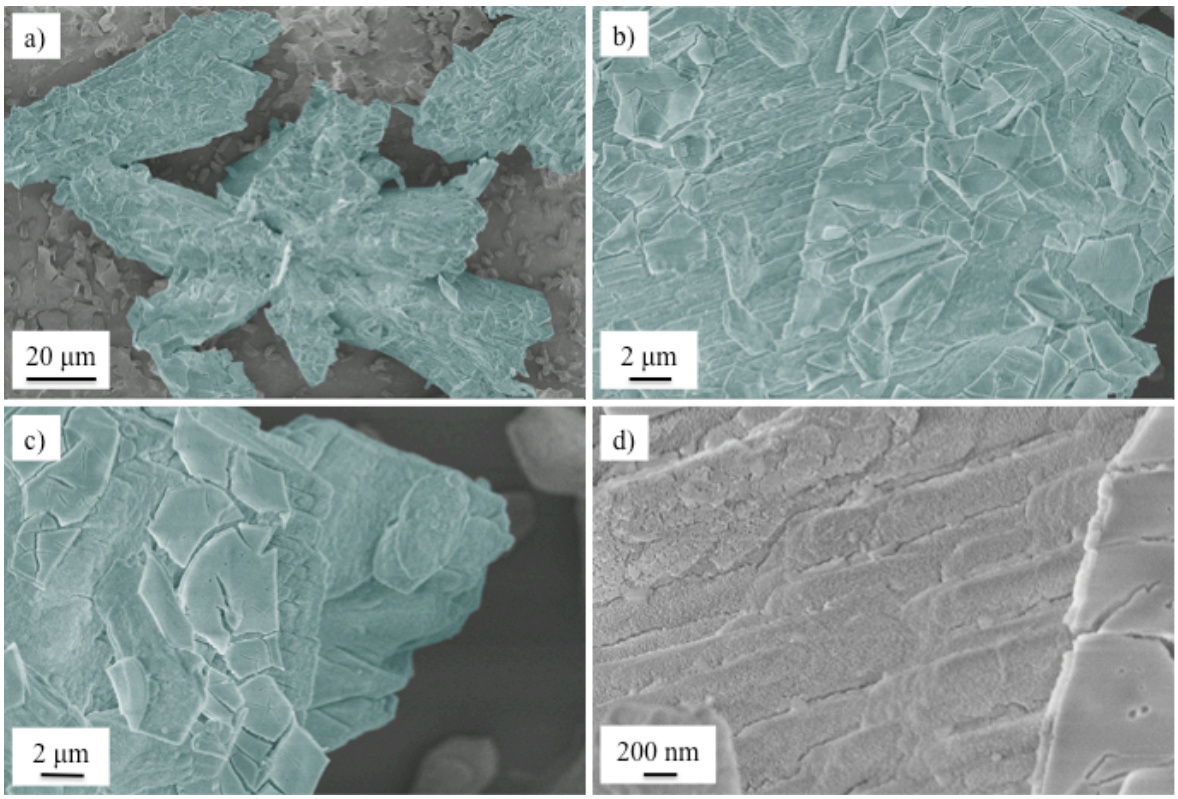

Fig. 5.25 | SEM micrographs of the polycrystalline calcite particles synthesised in the presence of the C_{10}vda ligand. **a)** overview picture; **b-d)** higher magnification images reveal hierarchical organisation of the small nanocrystals within the particles.

–– CHAPTER VI ––

Conclusions and future work

6.1. Conclusions

The general aim of this research thesis was to explore the synthetic methodologies, chemical properties and degradation pathways of a series of coordination compounds based on the iminodiacetic acid-substituted aromatic ligands.

At the initial stage of the project a methodology for new, amphiphilic, aromatic ligands, which are based on the iminodiacetic acid and vanillic acid moieties (vda-type ligands), was developed. The resulting complexing agents contain an ester functionality, which allows the introduction of aliphatic alkyl residues that are characterised by different chain lengths. Eight compounds containing this ligand class were successfully synthesised and characterised (**1**-**5**, **9**-**11**)

Six new coordination complexes containing transition metal ions and iminodiacetic acid-based ligands were presented in Chapter III; five of them contain Cu^{2+} metal ions and one accommodates Zn^{2+} ions. The complexes were synthesized under ambient conditions, crystallised *via* the slow evaporation technique and extensively characterised using the single crystal X-ray diffraction method. These analyses provided a fundamental understanding of the formation of the coordination compounds and the of the coordination behaviour of the complexing agents. The structural analysis provided knowledge about the solid-state structure of these compounds allowing one to understand the nature of the supramolecular interactions observed within these complexes.

In case of the complexes containing Cu^{2+} ions and vda-type ligands, the following general tendencies were observed:

1. The vda-type ligands react with a stoichiometric amount of copper(II) to produce coordination compounds.
2. All coordination networks containing the vda-type ligands adopted to a certain extent layered lamellar topologies. This result is in agreement with previously reported observations for Fe(III) complexes containing iminodiacetic acid-substituted phenols and naphthols as ligands.[61]
3. Jahn-Teller-type distortions are observed for all of the presented structures containing Cu(II) ions (**1**-**5**).
4. The length of the alkyl chain attached to the ester functionality determines the nature of the interactions between the ligand molecules in the solid state structure. In case of the ethyl chains, hydrophobic interactions and van der Waals forces play a minor role whilst higher homologues, e.g. hexyl and decyl substituents, enable these types of interactions.

5. The length of the aliphatic chain determines the thickness of the hydrophobic areas of the structures. No direct influence of the length of the aliphatic chain on the coordination environment of the metal ions was observed.
6. The nature of the base used to deprotonate the ligand molecules has indirectly an influence on the coordination environment of the metal ions. When triethylamine was used, the compounds tended to form mononuclear complexes. In case of inorganic bases, such as KOH, charges metal complexes were produced and chlorine anions were observed within the complexes, bridging between metal ions. In case of **4**, a potassium counter ion was detected in the asymmetric unit in order to balance the total charge. This observation may also be applicable to calcium-containing compounds, which formed mononuclear complexes in the presence of triethylamine, while using KOH gave a potassium ion-mediated structure (**14**).
7. All Cu-containing complexes display similar thermal degradation behaviour. They decompose to give phase pure copper(II) oxide materials at *ca.* 300 – 320 ºC. This temperature range is elevated when the coordination compounds contain additional elements, such as chlorine or potassium counter ions. The observed morphology of the residual CuO residues generally resembles the shape of the preceding crystals of the precursor coordination compounds. In most cases it was possible to observe a layered imprint on the CuO crystallites. This might be a result of the layered lamellar packing mode observed in the coordination assemblies.

The Zn^{2+}-containing compound **6** is characterised by a coordination environment similar to those observed for the Cu^{2+}-containing structures.

The thermal degradation of **6** resulted in polycrystalline ZnO crystallites, which retained the macroscopic fibrous shape of the original crystals of the coordination compound. Higher magnification imaging revealed that on the nanoscale the residues are composed of small nanoparticles that display a layered imprint, similar to that previously observed for the CuO residues remaining after the thermolysis of compounds **1**-**5**. This might be a sign of a templating effect whereby the molecular structure influences the morphology of the thermal decomposition product.

Coordination complexes containing the hda or vda-type ligands and calcium ions were described in Chapter IV. Eight new compounds were successfully synthesised and characterised. The analysis of these compounds gives rise to the following conclusions:

1. Calcium ions reacted with the hda- and vda-type ligands form coordination compounds that further organise into coordination assemblies and networks. The topologies of these networks vary from dense, three-dimensional networks (**7**) to layered, lamellar materials (**8**-**14**) depending on the nature and functional groups attached to the aromatic ligands.
2. The networks, which do not contain extensive hydrophobic areas and long alkyl residues (**7**, **8**, **9**), can be crystallised using slow evaporation techniques. The single crystal X-ray

diffraction analysis was applied to investigate their molecular structures and solid-state packing arrangements.

3. In case of the structures containing ligands with longer alkyl moieties (**10**, **11**, **12**) it was not possible to obtain single-crystalline materials. Electron microscopy techniques along with spectroscopic methods were used to investigate the layered, lamellar packing modes of the compounds.
4. The molecular self-assembly of amphiphilic complexes was investigated. The calcium-containing complexes containing alkyl moieties, generally tend to self-assemble into fibrous materials. It was possible to observe that the stiffness of these fibrous assemblies decreased with increasing length of the aliphatic chain. For example, compounds **8** and **9**, which contain only short substituents in the *para* position (in respect to the aromatic phenol hydroxyl group) form needle or fibrous crystals, while the long-chain containing compounds **11** or **12** assembled into soft hierarchical assemblies including ribbons or fibres which bent or twist.
5. **12** is a soft material, which over time undergoes a morphological change when deposited on a Si surface. This change was observed with SEM and described. The mechanical properties of compound **12** were studied underlining its soft nature.
6. The thermal degradation pathways of the neutral, Ca compounds **8**-**13** are rather similar; after the initial loss of constitutional and coordinating water molecules, the organic ligand moieties undergo oxidation resulting in calcium iminodiacetate. This compound further decomposes to form calcium carbonate at *ca.* 520 ºC and calcium oxide above 650 ºC.
7. P-XRD experiments confirmed that calcite is the only crystalline phase that forms during the thermolysis processes. The residual $CaCO_3$ retained the macroscopic shape of the preceding crystals of the precursor compounds. Imaging on the nanoscale confirmed that the residues generally are composed of polycrystalline nanoparticles. When the thermolysis was performed in an air atmosphere, these nanoparticles generally did not adopt any preferential orientations. When the experiment was performed in a nitrogen atmosphere, the nanoparticles seemed to aggregate into a more ordered fashion often resulting in hierarchical assemblies.
8. A layered imprint in the resulting $CaCO_3$ crystallites was only observed for the material derived from the C_{12}-long aliphatic chain-containing complex.

The final aspect of this work explored the usage of selected hda- and vda-type ligands or their Ca complexes as habit modifiers during the crystallisation process of calcium carbonate. The results, presented in Chapter V, proved that the hda and vda ligand families have the ability to influence the morphology of $CaCO_3$ crystals. The influence can be attributed to the co-ordinating ability of the ligand and the ability of the aphiphilic ligands to self-organise into hierarchical assemblies in polar solutions.

The C_{12}hda ligand had the most remarkable effect on the morphology of crystallising $CaCO_3$. It led to the formation of hollow spherical particles, which are composed of 7-9 polycrystalline disks. Each disk has a hole in the middle. This morphology resembles to some extend the coccospheres, which are naturally occurring, biogenic calcite minerals produced by marine algae, e.g. *Emiliania huxleyi*.

Although the vda-type ligands are very similar to the hda-type family, the introduction of two more potential O-donors changed the effect that both families have on the morphology of calcite. The vda-type ligands tend to produce polycrystalline materials, while the hda-type molecules give coccolith-like particles or previously discovered dumbbell-like agglomerates. These results demonstrate that even small changes of the chemical structures of the organic habit modifiers result in distinctly different $CaCO_3$ morphologies.

6.2. Recommended directions of future research

There are several promising directions in which the presented research can be continued to potentially generate further outstanding results.

Regenerative medicine

Future research activities may be related to the self-assembly processes, observed for the presented copper and calcium ions-containing complexes. As it was discussed in the chapter 1, molecular self-assembly concepts have gained significant attention in the field of regenerative medicine. Stupp *et al*. have developed class of self-assembled amphiphilic organic compounds known as the polyamphiphiles.[14, 16, 78] It was proven that the hydrophilic part of these molecules could be modified to incorporate an additional drug molecule (i.e. nabumetone, 4-(6-methoxy-2-naphthyl)-2-butanone, see Sch. 6.1), which acts as a non-inflammatory agent and reinforces the naturally occurring healing processes when introduced into a human body.[205] In water solutions, these molecules self-assemble and fold to form soft, fibrous materials, which express their drug-containing, hydrophilic outer part to the environment. Stupp and co-workers have proven that these materials have the potential to significantly enhance the natural healing processes that occur within the hard tissues of a human body.[206]

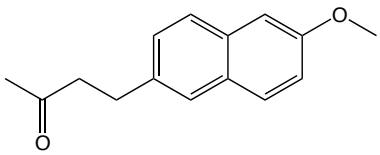

Sch. 6.1 | Chemical structure of nabumetone.

The amphiphilic system presented in this research thesis shows important similarities to Stupp's system. It may even offer important advantages. Most of the self-assembled complexes presented in chapters III and IV form soft materials that adopt fibrous morphology. However, in contrast to the polyamphiphilic fibres, the compounds presented in this thesis contain also additional metal ions, especially biologically essential Ca^{2+} ions. These cations are an important building block for hard tissues (i.e. bones, teeth) and the self-assembled materials have the potential to deliver both, the metal ions and drug molecules simultaneously to the desired place in a body. It is anticipated that the presence of calcium ions could enhance the effectiveness of the healing processes that occur within damaged (through an accident or illness) tissues.

A feasible synthetic pathway to incorporate nabumetone into the vda-type ligand family can be proposed. It involves the usage of a ligand, where the methoxy group is substituted with a halogen atom (for instance chlorine). As presented in Sch. 6.2, this atom may be further exchanged for a hydrazine functional group.

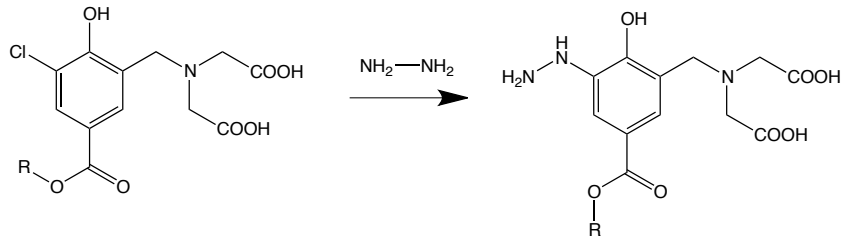

Sch. 6.2 | A reaction with hydrazine replaces the chlorine atom with the hydrazine functionality.

Finally, the hydrazine functional groups should have undergone a condensation reaction with the ketone functionality of the nabumetone molecules. This should have led to the formation of a hydrazone bridge liking these two molecules, as presented in Sch. 6.3. As confirmed by Matson *et al*., the hydrazone linker undergoes a slow hydrolysis when placed in a human body, leading to the release of the attached drug molecule.[168]

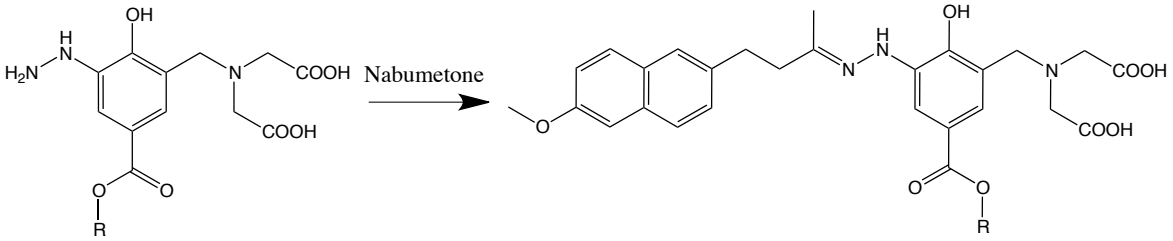

Sch. 6.3 | The final compound forms when the hydrazine functionality undergoes a condensation reaction with the ketone functional group of the drug molecule.

Topology of the residual carbon

While observing the formation of inorganic residues during the thermolysis processes that occur in a nitrogen atmosphere one may become interested in the morphology of carbon residues. Although this research topic was not investigated in this thesis, it may be an interesting research direction leading to the discoveries of new methods of influencing carbon morphology. One may speculate that the layered arrangement of ligand molecules may result in the formation of graphene upon the thermolysis, which was performed in specifically adjusted conditions (temperature, heating rate). Similarly, open-framework or honeycomb coordination networks may degrade to give single-walled or multi-walled carbon nanotubes when thermolysed. These carbon morphologies have been proven to be useful for electronic applications, however their large-volume synthesis is challenging. Supramolecular approach may contribute to the development of new synthetic methods that allow producing high volumes of these carbon-based materials.

Further modifications of the iminodiacetic acid-containing ligands

The vda-type ligand family presented in this research thesis relies on the esterification reaction, where a primary alcohol reacts with the carboxylic acid group, which is located on the aromatic ring. The potential of the esterification reaction is genuinely unlimited allowing the introduction of different residues containing a variety of functionalities. The approach my be expanded to amides. Future research direction may include the introduction of peptide residues in this position. Residues that contain more than one aliphatic chain attached to the β-carbon may affect the formation of the lamellar topology, as the chains may enhance

interactions with neighbouring molecules in more than one direction. The applied pathway to modify the ligands may even provide a way to produce conductive materials, where the conductance is realised *via* conjugated π-π systems located within hydrophobic part of the solid-state structure.

Changes to the coordinating arm

As discussed in the Introduction, the iminodiacetic acid functionality has been extensively used in coordination chemistry to form complexes with many different metal ions.

The substitution of iminodiacetic acid moiety with another aminoacid, such as (S)-aspartic acid (Sch. 6.4), could change the coordination behaviour; in addition to that, it could be a simple way of introducing chirality into the overall packing motifs observed within the hda and vda-type coordination compounds.

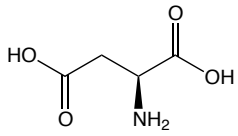

Sch. 6.4 | The structure of (S)-aspartic acid, a potential substituent for the hda- and vda-type ligands.

Assuming that the degradation pathway of the resulting Ca complexes containing related aspartic acid based ligands resembles the degradation of compounds **8**-**12**, the formation of calcium aspartate should precede the formation of $CaCO_3$. If a similar pathway was observed in a biodegradation process, the presence of the aspartates may enhance the biocompatibility and self-healing phenomena of the system. This ligand type could be further modified by a nabumetone drug molecule and explored in regenerative medicinal applications.

–– CHAPTER VII ––

Experimental procedures

7.1. Materials and methods

7.1.1. Reagents

All chemicals were purchased from Sigma Aldrich, Fluka or TCI Europe in a high purity grade (>97%) and were used without further purification. Solvents were of reagent grade (unless otherwise stated) and purchased from local solvent suppliers. Water was deionised before use.

7.1.2. Nuclear magnetic resonance spectroscopy.

^{1}H-NMR spectra were recorded on a Bruker Avance 400 machine operating at 400 MHz for ^{1}H by either Dr. John O'Brien or Dr. Manuel Ruether. Samples were run in deuterated solvents (D_2O, d^6-DMSO, $CDCl_3$, CF_3COOD) and signal assignments are listed for each spectrum. Standard abbreviations for ^{1}H spectra: s – singlet, d – doublet, t – triplet, m – multiplet, m.m. – multiplet of multiplets, J - coupling constant.

Where appropriate, the 2D NMR analyses were performed on a Bruker Avance II spectrometer operating at 600 MHz for ^{1}H. The obtained FID datasets were processed with the Bruker TopSpin v. 2.0 software or the MNova 7 package.

7.1.3. Mass spectrometry

Mass spectrometry experiments were performed by using the GCT Premier GC/MS System. In a typical case the electrospray ionization technique was preferred.

Small quantities of samples (less than 1 mg) were placed in 2 ml vials (APEX Scientific) and dissolved in appropriate solvents (water, alcohols, ACN, DCM, $CHCl_3$). Small amounts of formic acid were added to facilitate the ionization of organic molecules.

7.1.4. Elemental analysis

Elemental Analysis was carried out at University College Dublin by Ms. Anne Connelly using a Carlo Erba 1006 automatic analyser.

7.1.5. Infrared spectroscopy.

Infrared spectra were recorded in the range 4000-650 cm^{-1} on a Perkin Elmer Spectrum One FTIR spectrometer using a diffuse reflectance sampling accessory. The scan rate was 8 scans per minute with a resolution of 4 scans/cm^{-1}. The following abbreviations were used to describe the intensities: vs - very strong, s – strong, m – medium, w – weak, vw - very weak, br - broad.

7.1.6. Thermogravimetric Analysis (TGA).

Thermogravimetric analyses were carried out using a Perking Elmer Pyris 1 TGA under both nitrogen and air flow using a ceramic crucible. The instrument was calibrated to In and Ni standards in air atmosphere. Typical operating parameters for the thermal degradation studies were as follows: temperature range from 30 °C to 900 °C, heating rate: 3 °C/min. For obtaining the inorganic residues from preceding crystal of a coordination compound the heating rate was significantly decreased (usual value: 0.35 °C/min) and the investigated temperature range was adjusted depending on the desired inorganic material (30 – 520 °C for $CaCO_3$).

7.1.7. P-XRD analysis

P-XRD experiments were performed using a Siemens D500 diffractometer with a Cu-$K\alpha_1$ radiation with a wavelength of λ = 1.54056 Å. Samples were analysed in 2θ range from 5º to 50º or 60º in room temperature. Where it was necessary, results were compared with the reference patterns obtained from the American Mineralogist Crystal Structure Database (available on-line free of charge at http://rruff.geo.arizona.edu/AMS/amcsd.php).[178]

The obtained patterns were processed with the OriginPro 7® software for the baseline corrections, Fourier shifts and intensity adjustments.[207]

7.1.8. Single X-ray diffraction.

Single crystal analyses were performed at 150 K with a Bruker SMART APEX CCD diffractometer using graphite monochromated Mo-Kα radiation (λ = 0.71073 Å). A full sphere of data was obtained using the ω scan method. Data were collected, processed, and corrected for Lorentz and polarization effects using SMART and SAINT-NT software. The structures were solved using direct methods and refined with the Bruker SHELXTL® software package.[187]

Images based on the refined datasets were produced with the Diamond 3® and CrystalMaker® software packages.[208, 209]

Where appropriate, bond valence sum analysis was performed with the VaList software package.[210]

7.1.9. SEM Microscopy.

Scanning electron micrographs were obtained using either the Zeiss Supra Variable Pressure Field Emission Scanning Electron Microscope or the Zeiss Ultra Plus Scanning Electron Microscope. In a typical case, samples were placed on a silicon surface and evaporated or filtered through a polycarbonate membrane and dried. In order to prevent the charging effects and to obtain a good quality image it was necessary to coat samples with a thin (about 4 nm) layer of gold/palladium or platinum/palladium alloy. Imaging was performed in a low-kV mode (typically 2 kV) by using the In-Lens (Carl Zeiss) detector. Good depth of field was achieved by using small apertures (7.5 μm and 20 μm).

The images were processed with the Adobe Photoshop Elements 10® software.[211] The contrast, brightness and shadow highlights were optimised in order to get the most representative pictures.

Electron Dispersive X-ray Spectroscopy was generally conducted on uncoated samples. In some cases it was necessary to coat a sample with a thin (~10nm) layer of carbon. The operating voltage was increased to 20 kV and the SE2 (Carl Zeiss) and EDX (Oxford Instruments) detectors were used.

7.1.10. Helium Ion Microscopy (HeIM)

Helium ion microscopy images were obtained using the Zeiss Orion HeIM microscope operating at 37 kV accelerating voltage and using the SE2 (Carl Zeiss) detector. The working distance was in the range between 5 and 7 mm. All samples were coated with a thin (below 4 nm) layer of palladium, gold, gold/palladium alloy or palladium/platinum alloy.

Images were corrected for the brightness, contrast and shadow highlights with the Adobe Photoshop Elements 10® software.[211]

7.1.11. TEM Microscopy.

TEM images were obtained using the FEI Titan G2 Transmission Electron Microscope, equipped with the field emission gun operating at 300 kV. Unless stated otherwise, the diffraction contrast regime was preferred (objective aperture size of 50 μm). Samples were placed on the Carbon/Formvar coated copper grid (200 - 400 mesh) and dried in a high vacuum. Images were recorded using a CCD camera. The diffraction analysis relied on the observation of the back-focal plane; the Fast Fourier Transform (FFT) generated electron diffraction patterns were not used. Unless stated otherwise, the obtained images were not processed. In case of diffraction patterns, the diffraction spots were assigned by comparison with a pattern simulated with the CrystalDiffract® software.[209]

When the phase contrast regime was used, the objective aperture was removed completely and the resulting HR interference pattern was compared with the d-spacing value for the analysed material.

7.2. Synthesis of the ligands

7.2.1. Synthesis of 2,2'-(2-hydroxy-3,5-dimethylbenzylazanediyl)diacetic acid (Me_2hda)

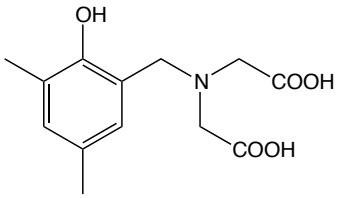

The compound was synthesised by following a modified literature procedure.[166] 5 g (0.041 moles) of 2,4-dimethylphenol was placed in the round bottom flask. 100 ml of 1:1 (v/v) mixture of methanol/water was added. This was stirred and heated at 55ºC. In a separate beaker 3.36 g (0.084 moles) of sodium hydroxide was dissolved in 10 ml of water and 5.46 g (0.041 moles) of iminodiacetic acid was added to this solution. After the iminodiacetic acid dissolved, the content of the beaker was added to the flask that contained the phenol. 3.32 ml (0.041 moles) of a 37 wt. % solution of formaldehyde was added dropwise and the mixture was heated at 85ºC for 4 hours.

The mixture was cooled down and acidified with 7.5 ml of 32% hydrochloric acid. Methanol was removed from the mixture with a rotary evaporator. This caused immediate formation of a white precipitate. This solid was washed with 500 ml of water and dried in an oven at 50ºC overnight. Yield: 8.67 g (79%).

Mass spectrometry: Exact mass: 267.11 g/mol, observed: (M-H)/q: 266.09

CHN analysis: Formula: $C_{13}H_{17}NO_5$; Calculated: C: 58.42%, H: 6.46%, N: 5.24%; Found: C: 58.16%, H: 6.39%, N: 5.17%

^{1}H NMR δ_H (400 MHz, DMSO): 6.84 (s, 1H), 6.61 (s, 1H), 3.78 (s, 2H), 3.41 (s, 4H), 2.14 (s, 3H), 2.10 (s, 3H).

^{13}C NMR δ_C (101 MHz, DMSO): 172.47 (q), 152.60 (q), 130.68 (=CH-), 127.63 (=CH-), 126.61 (q), 123.67 (q), 120.94 (q), 55.01 (-CH_2-), 53.20 (-CH_2-), 20.01 (-CH_3), 15.74 (-CH_3).

IR/cm^{-1}: 3307 (w), 3073 (w), 1677 (s), 1608 (sh), 1488 (s), 1418 (s), 1298 (m), 1197 (s), 1016 (br), 1116 (w), 968 (s), 853 (s, br).

7.2.2. Synthesis of 2,2'-((3,5-di-*tert*-butyl-2-hydroxybenzyl)azanediyl)diacetic acid (*t*-Bu_2hda)

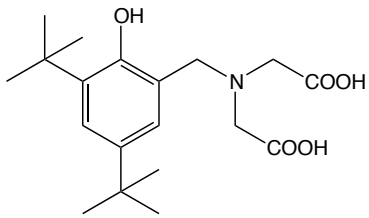

5.00 g (0.024 moles) of 2,4-di-*tert*-butylphenol was placed in a 250 ml round bottom flask and dissolved in 100 ml of acetic acid at 50 ºC. In a separate beaker 1.94 g (0.049 moles) of sodium hydroxide was dissolved in 30 ml of water. Then 3.23 g (0.024 moles) of iminodiacetic acid was dissolved in this basic solution and poured slowly into the flask.

The temperature was set to 95 ºC and 1.97 ml (0.024 moles) of a 37 wt. % water solution of formaldehyde was added drop-wise to the reaction mixture.

After 4 hours the heating was turned off and the content of the flask was allowed to cool down to the room temperature. A 5% water solution of hydrochloric acid was added to the flask, causing the formation of a white precipitate. This was filtered off, washed three times with water and cold ethanol, and dried. Yield: 7.45 g (88%).

Mass spectrometry: Exact mass: 351.4373 g/mol, observed: (M-H)/q: 350.4717

CHN analysis: Formula: $C_{19}H_{29}NO_5$; Calculated: C: 64.93%, H: 8.32%, N: 3.99%; Found: C: 64.79%, H: 8.24%, N: 3.86%.

^{1}H NMR δ_H (400 MHz, DMSO): 7.18 (s, 1H, Ar), 6.88 (s, 1H, Ar), 3.70 (s, 4H, iminodiacetic acid -CH_2-), 3.32 (s, 2H, methylene -CH_2-), 1.44 - 1.16 (m.m., 18H, -CH_3 groups).

IR/cm^{-1}: 3637 (w), 3010 (s), 2975 (s), 2654 (w), 1737 (w), 1708 (s), 1580 (m), 1505 (m), 1464 (m), 1410 (s), 1378 (s), 1243 (s), 1071 (m), 1007 (m), 913 (m), 898 (m), 807 (m), 757 (m), 700 (w), 690 (m).

7.2.3. Synthesis of 2,2'-((2-hydroxy-3,5-bis(2-phenylpropan-2-yl)benzyl)azanediyl)diacetic acid (Bc$_2$hda)

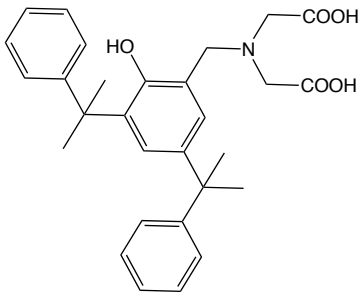

5.00 g (0.015 moles) of 2,4-*bis*-(2-phenylpropan-2-yl)phenol was placed in a 250 ml round bottom flask and dissolved in 100 ml of methanol at 50 ºC. In a separate beaker 1.24 g (0.031 moles) of sodium hydroxide was dissolved in 30 ml of water and 2.01 g (0.015 moles) of iminodiacetc acid was dissolved in this basic solution. The content of the beaker was poured into the flask. 1.23 ml (0.015 moles) of a 37 wt. % solution of formaldehyde was added to the flask and the reaction mixture was refluxed for 3 hours.

After that time the flask was allowed to cool down and a 5% water solution of hydrochloric acid was added, causing instant precipitation of grey, glue-like compound. This was collected and placed in a clean beaker, where it was allowed to dry. Yield: 5.22 g (73%).

Mass spectrometry: Exact mass: 475.2359 g/mol, observed: (M-H)/q: 474.2401

CHN analysis: Formula: $C_{29}H_{33}NO_5$; Calculated: C: 73.24%, H: 6.99%, N: 2.95%; Found: C: 72.92%, H: 6.85%, N: 2.88%.

^{1}H NMR δ_H (400 MHz, DMSO): 7.55 – 7.34 (m.m, 10H, phenyl substituents), 7.29 (s, 1H, Ar), 7.14 (s, 1H, Ar), 4.48 (s, 2H, methylene bridge), 3.50 (s, 4H, iminodiacetic acid -CH_2-), 1.72 (s, 6H, -CH_3 groups), 1.28 (s, 6H, -CH_3 groups).

IR/cm^{-1}: 3484 (br), 3289 (br), 3023 (w), 2965 (s), 2588 (br), 1754 (s), 1723 (s), 1601 (w), 1493 (m), 1479 (m), 1445 (s), 1406 (w), 1382 (w), 1362 (m), 1274 (vw), 1255 (w), 1229 (s), 1193 (vs), 1155 (m), 1095 (w), 1076 (m), 1029 (m), 1008 (m), 950 (w), 966 (w), 938 (w), 899 (m), 876 (m), 828 (m), 788 (w), 763 (s), 722 (vw), 700 (vs).

7.2.4. Synthesis of 2,2'-((3-carboxy-2-hydroxynaphthalen-1-yl)methylazanediyl)diacetic acid (Chnida)

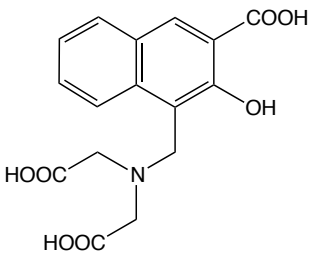

2.16 g (0.054 moles) of sodium hydroxide was placed in a beaker and dissolved in 10 ml of water. Then 3.59 g (0.027 moles) of iminodiacetic acid was dissolved in this solution. 2.19 ml (0.027 moles) of a 37 wt. % formaldehyde solution was added to the beaker and the mixture was put into ice for 15 minutes. In the meantime 5 g (0.027 moles) of 3-hydroxy-2-naphthoic acid was put in a round bottom flask and dissolved in 100 ml of acetic acid. The temperature was set to 105 ºC. Then the iminodiacetic acid solution was dropped in slowly through the dropping funnel. The

reaction mixture was left for 2 hours.

After that time a yellow precipitate was observed inside the flask. The mixture was cooled down using the ice bath and the yellow solid was filtered and washed with large amounts of cold water. Then the sample was dried in an oven for 14 hours at 80ºC. Yield: 8.22 g (91%).

Mass spectrometry: Exact mass: 333.08 g/mol, observed: (M-H)/q: 332.09

CHN analysis: Formula: $C_{16}H_{15}NO_7$; Calculated: C: 57.56%, H: 4.54%, N: 4.20%; Found: C: 57.54%, H: 4.51%, N: 4.23%

^{1}H NMR δ_H (400 MHz, DMSO): 3.34 (s, 4H), 3.69 (s, 2H), 7.00 (d, 1H, J = 9.0 Hz), 7.22 (d, 1H, J = 7.5 Hz), 7.43 (d, 1H, J = 8.0 Hz), 7.70 (m, 2H), 7.93 (d, 1H, J = 8.0 Hz).

IR/cm^{-1} : 3062 (vw), 3023 (w), 2975 (w), 1699 (m), 1628 (s), 1604 (m), 1519 (m), 1479 (m), 1427 (sw), 1370 (w), 1258 (br), 1324 (m), 1258 (s), 1211 (m), 1157 (sh), 1075 (m), 979 (m), 949 (w), 901 (s), 823 (s).

7.2.5. Synthesis of ethyl 4-hydroxy-3-methoxybenzoate (ethyl vanillate)

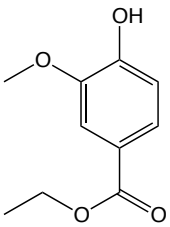

4-Hydroxy-3-methoxybenzoic acid (vanillic acid) (5.00 g; 29.74 mmol) was dissolved in absolute ethanol (40 ml). The mixture was heated to 55°C, then 95-97% sulphuric acid (4ml) was added drop-wise with stirring. The temperature was raised to 95°C and the reaction mixture was refluxed at this temperature for 24 hours. Ethanol was removed using the rotary evaporator. Ethyl acetate (100 ml) was added to dissolve the residues. A 10% aqueous solution of sodium bicarbonate was added dropwise until the acid was neutralised. The ethyl acetate organic layer was separated and dried using anhydrous magnesium (II) sulfate. The solvent was evaporated, leaving a viscous dark red oil. Yield: 5.11 g (88%).

Mass spectrometry: Exact mass: 196.0736 g/mol, observed: (M-H)/q: 195.1241

CHN analysis: Formula: $C_{10}H_{12}O_4$; Calculated: C: 61.22%, H: 6.16%; Found: C: 60.99%, H: 6.24%

^{1}H NMR δ_H (400 MHz, DMSO) 7.47 (1 H, Ar, d, *J*=8.2 Hz), 7.44 (1 H, Ar, s), 6.87 (1 H, Ar, d, *J*=8.2 Hz), 4.26 (2 H, ethyl -CH_2-, q, *J*=7.1 Hz), 3.82 (3 H, methoxy -CH_3, s), 1.25 (3 H, ethyl –CH_3, t, *J*=7.1 Hz).

^{13}C NMR δ_C (101 MHz, DMSO) 165.56 (Ar, q), 151.41 (q), 147.31 (Ar, q), 123.33 (Ar, =CH-), 120.72 (Ar, q), 115.11 (Ar, =CH-), 112.38 (Ar, =CH-), 60.19 (ethyl, -CH_2-) , 55.54 (ethyl, -CH_3), 14.25 (methoxy, -O-CH_3).

7.2.6. Synthesis of 2,2'-(5-(ethoxycarbonyl)-2-hydroxy-3-methoxybenzylazanediyl)diacetic acid (C_2vda)

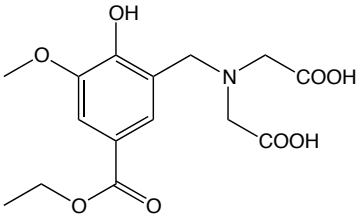

Ethyl vanillate (4.50 g; 22.93 mmol) was dissolved in 100% acetic acid (70 ml) and heated to 55°C. In a separate beaker, sodium hydroxide (1.88 g; 47.01 mmol) was dissolved in deionised water (15 ml), after which iminodiacetic acid was added (3.05 g; 22.93 mmol). Once a clear solution was obtained, the contents of the beaker were added to the ethyl vanillate solution. A 37% aqueous solution of formaldehyde (1.86 ml; 22.93 mmol) was added drop-wise with stirring. The temperature was elevated to 85°C and the reaction mixture stirred for 3 hours. The reaction mixture was allowed to cool, the acetic acid was evaporated and the residues dissolved in a 1:1 (v/v) mixture

of ethyl acetate and water. 34% aqueous hydrochloric acid solution (4.32 ml; 47.01 mmol) was added to neutralise the mixture. After 12 hours, the white precipitate was filtered, washed with water and left in the oven at 50°C to dry overnight. Yield: 2.76 g (40%).

Mass spectrometry: Exact mass: 340.1158 g/mol, observed: (M-H)/q: 339.1488

CHN analysis: Formula: $C_{16}H_{20}O_8$; Calculated: C: 56.47%, H: 5.92%; Found: C: 56.33%, H: 5.86%

^{1}H NMR δ_H (400 MHz, DMSO) 7.41 (1 H, Ar, s), 7.40 (1 H, Ar, s), 4.26 (2 H, ethyl –CH_2-, q, *J*=7.1 Hz), 3.89 (2 H, methylene –CH_2-, s), 3.82 (3 H, methoxy -CH_3, s), 3.43 (4 H, iminodiacetic acid -CH_2-, s), 1.30 (3 H, ethyl –CH_3, t, *J*=7.1 Hz).

^{13}C NMR δ_C (101 MHz, DMSO) 172.45 (iminodiacetic acid moiety, -COOH), 165.57 (q), 150.58 (Ar, q), 147.27 (Ar, q), 123.74 (Ar, =CH-), 122.83 (Ar, q), 119.97 (Ar, q), 111.63 (Ar, =CH-), 60.29 (ethyl, -CH_2-), 55.66 (methoxy, -O-CH_3), 53.53 (methylene, –CH_2-), 53.46 (iminodiacetic acid moiety, -CH_2-), 14.28 (ethyl, -CH_3).

HMBC See **Fig.** on page 255 (Appendix A.2.1.)

IR/cm^{-1} : 3540 (w, br), 2992, 2972, 2942 (w), 1683 (s, br), 1600 (m), 1509 (m), 1451 (w), 1390 (m), 1362 (m), 1305 (s), 1220 (s), 1201 (s), 1185 (s), 1095 (s), 1020 (s), 955 (s), 867 (s), 762 (s), 707, 684, 658 (s).

7.2.7. Synthesis of hexyl 4-hydroxy-3-methoxybenzoate (hexyl vanillate)

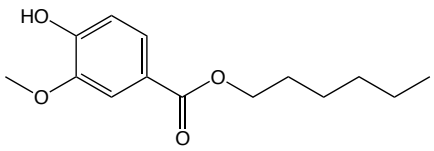

5 g (29.74 mmol) of 4-hydroxy-3-methoxybenzoic acid (vanillic acid) was placed in a 100 ml round-bottom flask and dissolved in 40 ml of hexanol. The mixture was heated to 60ºC and 4 ml of 98% sulfuric acid was added dropwise. The temperature was elevated to 95ºC and the mixture was refluxed for 18 hours. After that time the reaction mixture was poured into a separating funnel that contained 100 ml of a 10% aqueous solution of sodium bicarbonate and 100 ml of ethyl acetate. The organic phase was collected. It was washed 3 times with deionised water and dried with anhydrous magnesium (II) sulphate. The solvent was evaporated to give a dark red oil. Yield: 5.84 g (78%).

Mass spectrometry: Exact mass: 252.1362 g/mol, observed: (M-H)/q: 251.1544

CHN analysis: Formula: $C_{14}H_{20}O_4$; Calculated: C: 66.65%, H: 7.99%; Found: C: 66.31%, H: 7.85%

^{1}H NMR δ_H (400 MHz, DMSO + residual H_2O) 9.84 (1 H, hydroxyl –OH, s), 7.46 (1 H, Ar, d, *J*=8.0 Hz), 7.45 (1 H, Ar, s), 6.85 (1 H, Ar, d, *J*=8.0 Hz), 4.19 (2 H, hexyl -CH_2-, t, *J*=6.6 Hz), 3.82 (3 H, methoxy –O-CH_3, s), 3.52 – 0.76 (11 H, hexyl chain, m.m.).

7.2.8. Synthesis of 2,2'-(5-(hexyloxycarbonyl)-2-hydroxy-3-methoxybenzylazanediyl)diacetic acid (C_6vda)

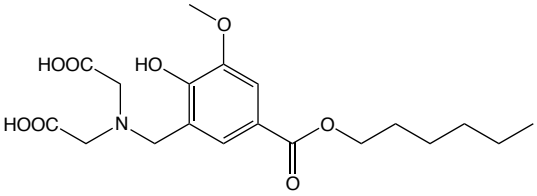

5 g (19.82 mmol) of hexyl vanillate was placed in a 250 ml round bottom flask and dissolved in 75 ml of acetic acid at 65ºC. In a separate beaker 1.63 g (40.63 mmol) of sodium hydroxide was dissolved in 15 ml of water and 2.64 g (19.82 mmol) of iminodiacetic acid was added to the base's solution. When the iminodiacetic acid was completely dissolved the content of the beaker was poured into the flask and 1.61 ml (19.82 mmol) of 37 wt. % aqueous solution of formaldehyde was added dropwise. The temperature

was set to 95ºC and the mixture was stirred for 2.5 hours.

After that time the reaction mixture was cooled down and the solvent was evaporated using a rotatory evaporator. The residues were dissolved in a 5% HCl/ethyl acetate mixture (1:1, v/v). The presence of hydrochloric acid caused slow precipitation of a white solid. This was filtered off after *ca.* 12 hours and washed with deionised water and ethyl acetate. Yield: 2.44 g (31%).

Mass spectrometry: Exact mass: 397.1737 g/mol, observed: (M-H)/q: 396.1495

CHN analysis: Formula: $C_{19}H_{27}NO_8$; Calculated: C: 57.42%, H: 6.85%, N: 3.52%; Found: C: 57.16%, H: 6.92%, N: 3.84%

^{1}H NMR δ_H (400 MHz, DMSO) 7.41 (1 H, Ar, d, *J*=2.0 Hz), 7.40 (1 H, Ar, d, *J*=2.0 Hz), 4.21 (2 H, hexyl moiety, t, *J*=6.7 Hz), 3.89 (methylene, -CH_2-), 3.82 (3 H, methoxy –O-CH_3, s), 3.43 (4 H, iminodiacetic acid –CH_2-, s), 3.56 – 0.45 (11 H, hexyl chain, m.m.).

^{13}C NMR δ_C (101 MHz, DMSO) 172.84 (iminodiacetic acid moiety, -COOH), 166.09 (q), 151.11 (Ar, q), 147.76 (Ar, q), 124.20 (Ar, =CH-), 123.11 (Ar, q), 120.47 (Ar), 112.19 (Ar, =CH-), 64.77 (hexyl, -O-CH_2-), 56.16 (methoxy, -O-CH_3), 54.08 (methylene, -CH_2-), 53.98 (iminodiacetic moiety, -CH_2-), 31.29 (hexyl, -CH_2-), 28.62 (hexyl, -CH_2-), 25.55 (hexyl, -CH_2-), 22.41 (hexyl, -CH_2-), 14.28 (hexyl, -CH_3).

HMBC See **Fig.** on page 256 (Appendix A.2.2.)

IR/cm^{-1} : 3247 (w, br), 3078 (w), 2957 (w), 2956 (w), 2870 (w), 1715 (m), 1689 (m), 1603 (w), 1509 (m), 1462 (m), 1416 (m), 1367 (m), 1307 (s), 1218 (s), 1185 (s), 1113 (s), 1096 (s), 1013 (m), 990 (m), 957 (s), 886 (s), 849 (m, br), 769 (m), 751 (m).

7.2.9. Synthesis of decyl 4-hydroxy-3-methoxybenzoate (decyl vanillate)

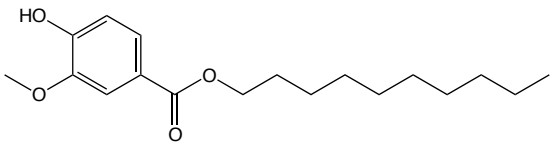

5 g (29.74 mmol) of 4-hydroxy-3-methoxybenzoic acid (vanillic acid) was placed in a 100 ml round bottom flask and dissolved in 40 ml of *n*-decanol at 90ºC. Then 4 ml of sulfuric acid was added dropwise and the reaction mixture was stirred and heated for 20 hours.

After that time the flask was cooled to room temperature and the excess of alcohol was removed on a rotatory evaporator. The reaction mixture was dissolved in a 1:1 (v/v) mixture of water and ethyl acetate and placed in a separator. Sodium bicarbonate was added until the pH of the water phase reached neutral levels. Then the organic phase was separated and washed three times with deionised water. It was dried upon addition of anhydrous magnesium sulfate. In the final step the solvent was evaporated to give an almost black solid (r.t.). Yield: 7.22 g (79%).

Mass spectrometry: Exact mass: 308.1988 g/mol, observed: (M-H)/q: 307.1771

CHN analysis: Formula: $C_{18}H_{28}O_4$; Calculated: C: 70.10%, H: 9.15%; Found: C: 69.84%, H: 9.02%

^{1}H NMR δ_H (400 MHz, DMSO) 7.44 (1 H, Ar, d, *J*=8.1 Hz), 7.43 (1 H, Ar, s), 6.84 (1 H, Ar, d, *J*=8.1 Hz), 4.16 (2 H, decyl –O-CH_2-, t, *J*=6.5 Hz), 3.80 (3 H, methoxy, -O-CH_3, s), 3.37 – 0.50 (19 H, m.m.).

^{13}C NMR δ_C (101 MHz, DMSO) 165.39 (q), 151.49 (Ar, q), 147.23 (Ar, q), 123.18 (Ar, =CH-), 120.66 (Ar, q), 114.90 (Ar, =CH-), 112.36 (Ar, =CH-), 60.74 (decyl –O-CH_2-), 55.33 (methoxy, -O-CH_3), 39.55, 32.60, 31.42, 29.27, 29.15, 28.87, 25.59, 22.15, 13.69.

7.2.10. Synthesis of 2,2'-(5-(decyloxycarbonyl)-2-hydroxy-3-methoxybenzylazanediyl)diacetic acid (C_{10}vda)

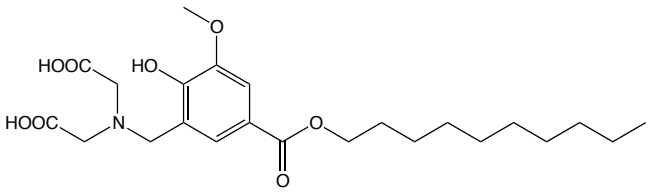

5 g (16.21 mmol) of decyl vanillate was placed in a round bottom flask and dissolved in 75 ml of acetic acid at 85°C. In a separate beaker 1.33 g (33.23 mmol) of sodium hydroxide was dissolved in 15 ml of water and 2.16 g (16.21 mmol) of iminodiacetic acid was added to this mixture. When the acid completely dissolved the content of the beaker was poured into the flask and 1.31 ml (16.21 mmol) of formaldehyde was added dropwise. The reaction mixture was stirred and heated at 85°C for 3 hours.

After that time the content of the flask was cooled and the solvent was evaporated on a rotatory evaporator. The residues were dissolved in a water/ethyl acetate mixture (1:1 v/v) and 3.05 ml (33.23 mmol) of 34% hydrochloric acid was added to the mixture. This initiated the formation of white precipitate that was collected after 12 hours and washed with deionised water and ethyl acetate. Yield: 1.96 g (27%).

Mass spectrometry: Exact mass: 453.2363 g/mol, observed: (M-H)/q: 452.1856

CHN analysis: Formula: $C_{23}H_{35}NO_8$; Calculated: C: 60.91%, H: 7.78%, N: 3.09%; Found: C: 60.65%, H: 7.52%, N: 3.01%

^{1}H NMR δ_H (600 MHz, DMSO) 7.42 (1 H, Ar, s), 7.40 (1 H, Ar, s), 4.20 (2 H, decyl O-CH_2-, t, *J*=6.6 Hz), 3.92 (2 H, methyl –CH_2-, s), 3.82 (3 H, methoxy, -O-CH_3, s), 3.46 (4 H, iminodiacetic acid methyl –CH_2-, s), 1.73 – 0.75 (19 H, m.m.).

^{13}C NMR δ_C (151 MHz, DMSO) 172.27 (iminodiacetic acid carboxyl, q), 165.59 (ester group –COO-, q), 150.77 (Ar, q), 147.36 (Ar, q), 123.94 (Ar, =CH-), 122.53 (Ar, q), 120.09 (Ar, q), 111.88 (Ar, =CH-), 64.29 (decyl –O-CH_2-), 55.72 (methoxy, -O-CH_3), 53.76 (methyl –CH_2-), 53.52 (iminodiacetic acid methyl –CH_2-), 31.35, 28.98, 28.74, 28.70, 28.29, 25.49, 22.14, 13.94 (decyl –CH_3).

HSQC See **Fig.** on page 257 (Appendix A.2.3.)

HMBC See **Fig.** on page 258 (Appendix A.2.3.)

IR/cm^{-1} : 3218 (w, br), 3072 (w), 2958 (w), 2922 (m), 2854 (m), 1716 (s), 1684 (s), 1602 (m), 1508 (m), 1461 (m), 1429 (w), 1417 (m), 1385 (w), 1367 (m), 1304 (s), 1218 (s), 1184 (s), 1112 (m), 1094 (m), 1050 (w), 1005 (w), 986 (w), 956 (s), 922 (m), 878 (w), 841 (m, br), 769 (m), 751 (m).

7.2.11. Synthesis of 2,2'-((5-dodecyl-2-hydroxy-3-methylbenzyl)azanediyl)diacetic acid (C_{12}hda)

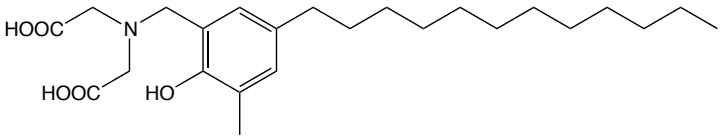

The compound was prepared by following a modified literature procedure.[166, 212] 5 g. (0.018 moles) of 4-dodecyl-2-methylphenol was placed in a round-bottom flask and was dissolved in 50 ml of ethanol at 50 °C. In a separate beaker 2.40 g (0.018 moles) of iminodiacetic acid was dissolved in 10 ml of water after the addition of 1.44 (0.036 moles) of sodium hydroxide. Then 20 ml of ethanol was poured into the

beaker and 1.46 ml (0.018 moles) of a 37 wt. % formaldehyde solution was added. The solution of iminodiacetic acid was slowly added through the dropping funnel into the flask and the temperature was increased to 95ºC. The reaction was carried out for 6 hours. After that time 3.65 ml (0.036 moles) of hydrochloric acid was added to the flask to neutralise the solution. When the flask was cooled down, a white precipitate formed. It was filtered out and washed with cold water and ethanol. Then it was dried in the oven at 60ºC for 16 hours. Total yield: 7.12 g (94%).

Mass spectrometry*:* Exact mass: 421.28 g/mol, observed: (M-H)/q: 420.22

CHN analysis*:* *Formula:* $C_{24}H_{39}NO_5$; *Calculated:* C: 68.38%, H: 9.32%, N: 3.32%; *Found:* C: 68.17%, H: 9.36%, N: 3.37%

^{1}H NMR δ_H (400 MHz, DMSO): 6.80 (s, 1H, ArH), 6.58 (s, 1H, ArH), 3.77 (s, 2H, CH_2), 3.39 (s, 4H, $(CH_2)_2$), 1.20 (m.m., 25H, n-$C_{12}H_{25}$), missing –CH_3 signal overlaps with the long chain multiplets

IR/cm^{-1}: 3294 (w, br), 3092 (w), 3009 (w), 2958 (w), 2915 (s), 2848 (m), 1677 (s), 1488 (m), 1421 (m), 1377 (w), 1196 (w), 959 (w), 834 (w, br), 719 (w)

7.3. Synthesis of the complexes

7.3.1. Synthesis of $[Cu^{II}(C_2vda)(H_2O)]\cdot 2H_2O\cdot 2MeOH$ (1)

35 mg (0.1 mmol) of the C_2vda ligand was placed in a sample tube along with 17 mg (0.1 mmol) of $CuCl_2\cdot 2H_2O$. 10 ml of methanol was added into the sample tube and the content was stirred vigorously. The presence of the two positive copper ions facilitated the dissolution of the ligand. The mixture was further stirred for *ca.* 10 minutes. After that time it was filtrated, the solution was placed in a sampletube sealed with a parafilm and left in ambient conditions. Blue, needle-shaped crystals of **1** formed after 2 weeks of slow evaporation. Yield: 42 mg (83%).

CHN analysis: Formula: $[Cu(C_2vda)(H_2O)]$; *Calculated*: C: 45.34%, H: 4.82%, Ca: 10.09%, N: 3.52%; *Found*: C: 45.28%, H: 4.79%, Ca: 10.10%, N: 3.48%.

IR/cm^{-1}: 3207 (m, br), 2988 (w), 1696 (m), 1586 (s), 1515 (m), 1461 (m), 1426 (m), 1408 (w), 1371 (w), 1353 (w), 1303 (s), 1221 (s, br), 1184 (w), 1099 (m), 1032 (w), 1026 (m), 992 (w), 949 (w), 925 (m), 871 (w), 722 (m), 710 (w), 683 (w).

7.3.2. Synthesis of $[Cu^{II}_3(\mu\text{-}Cl)_2(\mu\text{-}C_2vda)(C_2vda)(H_2O)_4]\cdot H_2O$ (2)

35 mg (0.1 mmol) of the C_2vda ligand was placed in a sample tube and immersed in 8 ml of methanol. Then 1 ml of 0.1 M methanol solution of KOH was added, causing immediate dissolution of the ligand. In the final step 1 ml of 0.1 M methanol solution of $CuCl_2\cdot 2H_2O$ was added. The resulting blue-green solution was filtered and left to slowly evaporate in ambient conditions. Blue rectangular plates of **2** formed after ca. 14 days. Yield: 27 mg (52%).

CHN analysis: Formula: $[Cu_3(\mu\text{-}Cl)_2(\mu\text{-}C_2vda)(C_2vda)(H_2O)_4]$; *Calculated*: C: 35.60%, H: 4.18%, Cl: 7.01%, Cu: 18.83%, N: 2.77%; *Found*: C: 35.47%, H: 4.26%, Cl: 6.92%, Cu: 18.69%, N: 2.63%.

IR/cm^{-1}: 3112 (w, br), 2992 (w), 1690 (s), 1596 (s), 1503 (m), 1468 (m), 1388 (s), 1371 (m), 1306 (s), 1225 (s), 1185 (m), 1115 (m), 1091 (s), 1027 (s), 1002 (m), 953 (w), 925 (m), 911 (w), 886 (m), 871 (m), 807 (w), 762 (m), 740 (m), 669 (w).

7.3.3. Synthesis of $[Cu^{II}(C_6vda)(H_2O)_2]$ (3)

40 mg (0.1 mmol) of the C_6vda ligand was placed in a sample tube along with 17 mg (0.1 mmol) of $CuCl_2\cdot 2H_2O$. 10 ml of methanol was poured into the sample tube and the resulting mixture was stirred vigorously. The presence of the Cu^{2+} ions caused the dissolution of the ligand. The obtained blue solution was filtered and placed in a sample tube, sealed with a parafilm and left in ambient conditions. The formation of blue, block-shaped crystals of **3** was observed after 4 days of slow evaporation. Yield: 42 mg (74%).

CHN analysis: Formula: $[Cu(C_6vda)(H_2O)_2]$; *Calculated:* C: 46.10%, H: 5.91%, N: 2.83%; Cu: 12.84%; *Found*: C: 46.06%, H: 5.88%, N: 2.81%, Cu: 12.82%.

IR/cm^{-1}: 3324 (m, br), 2953 (m), 2862 (w), 1703 (s), 1631 (w), 1598 (vs), 1521 (m), 1473 (w), 1451 (w), 1425 (w), 1411 (m), 1343 (m), 1312 (s), 1226 (vs), 1192 (m), 1135 (w), 1120 (w), 1097 (s), 1016 (w), 988 (m), 969 (w), 941 (w), 912 (w), 901 (w), 845 (w, br), 771 (m), 737 (m, br), 682 (w).

7.3.4. Synthesis of $K_2[Cu_2(\mu\text{-}Cl)_2(C_6vda)_2]\cdot 4H_2O$ (**4**)

40 mg (0.1 mmol) of the C_6vda ligand was placed in a sample tube and immersed in 8 ml of methanol. Then 1 ml of 0.1M methanol solution of KOH was added causing immediate dissolution of the ligand. Finally, 1 ml of a 0.1 M methanol solution of $CuCl_2 \cdot 2H_2O$ was added. The resulting blue-green solution was filtered into a clean sample tube and left to slow evaporate in ambient conditions. Square blue plates of **4** were obtained after 7 days. Yield: 12 mg (21%).

CHN analysis: Formula: $K(H_2O)_2[Cu(C_6vda)Cl]$; *Calculated*: C: 40.07%, H: 5.13%, Cl: 6.22%, Cu: 11.16%, K: 6.86%, N: 2.46%; *Found*: C: 39.94%, H: 5.18%, Cl: 6.13%, Cu: 11.08%, K: 6.77%, N: 2.31%.

IR/cm^{-1}: 3468 (w, br), 2958 (w), 2934 (w), 2870 (w), 1693 (m), 1624 (s), 1599 (s), 1507 (w), 1463 (w), 1454 (w), 1392 (m), 1327 (s), 1300 (s), 1221 (s), 1181 (m), 1113 (m), 1094 (m), 1096 (m), 1010 (m), 958 (m), 918 (m), 915 (m), 773 (m), 770 (m), 743 (m), 674 (m).

7.3.5. Synthesis of $[Cu^{II}(C_{10}vda)(H_2O)_2]$ (**5**)

45 mg (0.1 mmol) of the C_{10}vda ligand was placed in a sample tube and immersed in 9 ml of methanol. Then 1 ml of a 0.1 M methanol solution of $CuCl_2 \cdot 2H_2O$ was added. The reagents were stirred and the presence of $CuCl_2$ caused slow dissolution of the ligand. After *ca.* 30 minutes the sample was filtered and placed in a clean sample tube. The formation of blue, needle-like crystals of **5** was observed after 5 days of slow evaporation. Yield: 38 mg (69%).

CHN analysis: Formula: $[Cu(C_{10}vda)(H_2O)_2]$; *Calculated*: C: 50.13%, H: 6.77%, Cu: 11.53%, N: 2.54%; *Found:* C: 49.87%, H: 6.85%, Cu: 11.45%, N: 2.48%.

IR/cm^{-1}: 3560 (w), 3483 (w), 3165 (w, br), 2924 (m), 2848 (w), 1713 (m), 1672 (m), 1645 (m), 1604 (m), 1579 (m), 1506 (w), 1483 (w), 1465 (w), 1436 (m), 1395 (s), 1320 (m), 1304 (s), 1280 (m), 1225 (s), 1200 (s), 1114 (m), 1093 (m), 1074 (m), 1048 (w), 1007 (m), 994 (w), 957 (m), 916 (m), 904 (m), 887 (m), 877 (m), 768 (m), 741 (m), 678 (m).

7.3.6. Synthesis of $[Zn(Me_2hda)(H_2O)_2]\cdot H_2O$ (**6**)

27 mg (0.1 mmol) of the Me_2hda ligand was dissolved in a mixture of 5 ml of water and 4.5 ml of methanol and the solution was heated to 60ºC. Then 32 µl (0.23 mmol) of triethylamine was injected into the mixture. In the next step 0.5 ml of 0.1 M $Zn(ClO_4)_2$ methanol solution was added slowly. The reagents were further stirred for 30 minutes. After that time the mixture was cooled and filtrated. Thin, colourless, needle-like crystals of **6** were collected after 12 days of slow evaporation. Yield: 17.6 mg (66%).

CHN analysis: Formula: $[Zn(Me_2hda)(H_2O)_2]\cdot H_2O$; *Calculated*: C: 40.69%, H: 5.25%, N: 3.65%, Zn: 17.04%; *Found*: C: 40.76%, H: 5.21%, N: 3.62%, Zn: 16.89%

IR/cm^{-1}: 3003 (br), 2942 (vw), 2919 (vw), 1584 (m), 1393 (s), 1134 (w), 858 (w), 682 (w).

7.3.7. Synthesis of $[Ca_2(Chnida)_2(H_2O)_2]\cdot 4H_2O$ (**7**)

33.3 mg (0.1 mmoles) of the Chnida ligand was placed in a glass tube (25x75 mm). Then 5 ml of methanol and 4.5 ml of water were added and the mixture was stirred and heated to 50 ºC. 27 µl (0.193 mmol) of triethylamine (TEA) was injected into the mixture

causing slow dissolution of the ligand. When the solution became clear, 0.5 ml of the 0.1 M aqueous $CaCl_2$ solution was added causing colour transition from slightly yellow to light orange. Then the mixture was filtered through a paper filter into a sample tube and left in ambient conditions. Thin, yellow, plate-like crystals of **7** formed after 5 days of slow evaporation. Yield: 21 mg (54%).

CHN analysis: Formula: $[Ca_2(Chnida)_2(H_2O)_2]$; *Calculated:* C: 49.10%, H: 4.38%, Ca: 10.24%, N: 3.58%; *Found*: C: 48.96%, H: 4.41%, Ca: 10.13%, N: 3.64%

IR/cm^{-1}: 3281 (w), 2980 (br), 1739 (w), 1660 (s), 1514 (m), 1456 (s), 1289 (m), 1210 (s), 1164 (m), 1096 (m), 945 (m), 890 (m), 796 (s)

7.3.8. Synthesis of $[Ca(Me_2hda)(H_2O)_3]\cdot\frac{1}{2}H_2O\cdot\frac{1}{2}MeOH$ (8)

27 mg (0.1 mmol) of the Me_2hda ligand was dissolved in a 1:1 (v/v) mixture of water and methanol. The reagents were heated to 50°C and stirred. Then 30 µl (0.215 mmol) of triethylamine was added. This step was followed by the addition of 50 µl of 1 M aqueous $CaCl_2$ solution. The reaction mixture was further stirred for 15 minutes; after that time it was allowed to cool and filtrated through filter paper into a sample tube. Colourless crystals of **8** formed after *ca.* 7 days of slow evaporation. Yield: 14.5 mg (44%).

CHN analysis: Formula: $[Ca(Me_2hda)(H_2O)_3]$; *Calculated:* C: 43.45%, H: 5.89%, Ca: 11.15%, N: 3.90; *Found:* C: 43.22%, H: 5.96%, Ca: 11.01%, N: 3.79%

IR/cm^{-1}: 2923 (m), 2852 (m), 1586 (s), 1410 (m), 1325 (s), 1246 (s), 1221 (s), 1152 (s), 990 (s), 867 (s), 721 (m)

7.3.9. Synthesis of $[Ca(C_2vda)(H_2O)_2]\cdot H_2O$ (9)

30 mg (0.1 mmol) of the C_2vda ligand was placed in a sample tube and immersed in a mixture of 5 ml of methanol and 4.5 ml of water. Then 30 µl (0.215 mmol) of triethylamine was added resulting in the slow dissolution of the ligand. In the next step 0.5 ml of a 0.1 M aqueous solution of $CaCl_2$ was added and the reagents were stirred for *ca.* 30 minutes. Then the mixtre was filtrated into a clean sample tube, sealed with parafilm and left in ambient conditions. Yellow, block-shaped crystals of **9** were observed after 30 days. Yield: 13 mg (37%).

CHN analysis: Formula: $[Ca(C_2vda)(H_2O)_2]\cdot H_2O$; *Calculated:* C: 43.37%, H: 5.10%, Ca: 9.65%, N: 3.37; *Found:* C: 43.24%, H: 5.17%, Ca: 9.61%, N: 3.32%

IR/cm^{-1}: 3223 (m, br), 2984 (w), 1693 (m, br), 1614 (m), 1571 (vs), 1506 (m), 1456 (m), 1422 (m), 1399 (w), 1367 (w), 1344 (w), 1323 (w), 1297 (s), 1215 (s, br), 1179 (w), 1109 (w), 1093 (m), 1026 (w), 1013 (m), 987 (w), 946 (w), 921 (m), 886 (w), 865 (w), 764 (m), 741 (w), 714 (w), 676 (w).

7.3.10. Synthesis of $[Ca(C_6vda)(H_2O)_2]\cdot H_2O$ (10)

40 mg (0.1 mmol) of the C_6vda ligand was placed in a sample tube. Then a mixture of 5 ml of methanol and 4.5 ml of water was added and the content of the sample tube was stirred. In a following step 30 µl (0.215 mmol) of triethylamine was added, which caused the slow dissolution of the ligand. Finally, 0.5 ml of 0.1 M aqueous $CaCl_2$ solution was added causing formation of a white precipitate of **12**. This was filtrated off, dried and analysed. Yield: 32.2 g (81%).

CHN analysis: Formula: [Ca(C_6vda)(H_2O)$_2$]; *Calculated:* C: 48.40%, H: 6.20%, N: 2.97%; Ca: 8.50%; *Found*: C: 47.95%, H: 6.31%, N: 2.93%, Ca: 8.44%.

IR/cm^{-1}: 3337 (m, br), 2956 (m), 2868 (w), 1707 (s), 1639 (w), 1604 (vs), 1500 (m), 1464 (w), 1442 (w), 1431 (w), 1421 (w), 1405 (m), 1336 (m), 1303 (s), 1238 (w), 1219 (vs), 1185 (m), 1130 (w), 1111 (w), 1092 (s), 1010 (w), 992 (w), 982 (m), 960 (w), 936 (w), 906 (w), 887 (w), 836 (w, br), 767 (m), 732 (m, br), 669 (w).

7.3.11. Synthesis of [Ca(C_{10}vda)(H_2O)$_2$] (**11**)

45 mg (0.1 mmol) of the C_{10}vda ligand was placed in a sample tube and dissolved in a mixture of 5 ml of methanol and 4.5 ml of water. Then 30 µl (0.215 mmol) of triethylamine was added, facilitating the dissolution of the ligand molecules. In the final step 0.5 ml of 0.1 M aqueous $CaCl_2$ solution was added, causing rapid precipitation of **13**. The precipitate was filtered off, dried and analysed. Yield: 36 mg (85%).

CHN analysis: Formula: [Ca(C_{10}vda)(H_2O)$_2$]; *Calculated:* C: 52.36%, H: 7.07%, N: 2.65%; Ca: 7.60%; *Found*: C: 52.18%, H: 7.16%, N: 2.52%, Ca: 7.44%.

IR/cm^{-1}: 3338 (m, br), 2924 (m), 2852 (w), 1707 (s), 1638 (w), 1603 (vs), 1501 (m), 1465 (w), 1443 (w), 1431 (w), 1419 (w), 1405 (m), 1336 (m), 1299 (s), 1240 (w), 1215 (vs), 1188 (m), 1130 (w), 1113 (w), 1094 (s), 1047 (w), 1017 (w), 1005 (w), 984 (m), 949 (w), 937 (w), 907 (w), 884 (w), 814 (w), 767 (w), 722 (m, br), 667 (w).

7.3.12. Synthesis of [Ca(C_{12}hda)(H_2O)$_2$] · H_2O (**12**)

42 mg (0.1 mmol) of the C_{12}hda ligand was dissolved in a mixture of 4.5 ml of water and 5 ml of methanol. The mixture was stirred and heated. When the temperature reached 65ºC, 30 µl (0.215 mmol) of triethylamine was added. In the next step 0.5 ml of the 0.1M aqueous $CaCl_2$ solution was added causing instant formation of a white precipitate of **14**. The mixture was left to cool down in ambient conditions. The precipitate was filtered of and analysed. Total yield: 40 mg (84%).

CHN analysis: Formula: [Ca(C_{12}hda)(H_2O)$_2$]; *Calculated*: C: 58.27%, H: 8.15%, Ca: 8.10%, N: 2.83%; *Found*: C: 57.92%, H: 8.71%, Ca: 8.05%, N: 2.81%.

IR/cm^{-1}: 3853 (vw), 3225 (s, br), 2918 (s), 2848 (s), 2368 (vw), 1655 (m), 1613 (m), 1582 (s), 1489 (w), 1415 (m), 1338 (w), 1322 (w), 1241 (w), 1217 (w), 988 (w), 865 (w), 721 (m).

7.3.13. Synthesis of [Ca(*t*-Bu_2hda)(H_2O)$_2$]·3H_2O (**13**)

35 mg (0.1 mmol) of the *t*-Bu_2hda ligand was placed in a sample tube and dissolved in a mixture of 5 ml of methanol and 4.5 ml of water. An addition of 30 µl (0.215 mmol) of triethylamine facilitated this process. In a following step 0.5 ml of a 0.1 M aqueous solution of $CaCl_2$ was added, causing the instant formation of a white precipitate of **11**. This was filtered off, dried and analysed. Yield: 29 mg (77%).

CHN analysis: Formula: [Ca(*t*-Bu_2hda)(H_2O)$_2$]; *Calculated:* C: 53.63%, H: 7.34%, N: 3.29%; Ca: 9.42%; *Found*: C: 52.98%, H: 7.51%, N: 3.06%, Ca: 9.23%.

IR/cm^{-1}: 3388 (m, br), 2981 (s), 2971 (w), 2904 (w), 1760 (w), 1714 (w), 1637 (w), 1611 (vs), 1483 (w), 1463 (w), 1429 (w), 1403 (m), 1396 (w), 1362 (w), 1331 (m), 1290 (w), 1241 (w), 1210 (w), 1195 (w), 1125 (w), 1085 (w), 1022 (w), 968 (m), 930 (w), 911 (w), 879 (s), 779 (w), 761 (w).

7.3.14. Synthesis of $K_2(H_2O)_5[Ca(H_2Bc_2hda)(HBc_2hda)(H_2O)_4]Cl{\cdot}H_2O$ (**14**)

47.5 mg (0.1 mmol) of the Bc_2hda ligand was placed in a sample tube. 5 ml of water and 3.5 ml of methanol were added and the mixture was stirred vigorously. Then 1 ml of a 0.2 M methanol solution of KOH was added causing immediate dissolution of the ligand. In a following step 0.5 ml of 0.1 M methanol solution of $CaCl_2$ was added. The reaction mixture was further stirred for *ca.* 30 minutes. After that time the content of the flask was filtrated through filter paper into a sample tube, covered with a parafilm and left in ambient conditions. Colourless, block-shaped crystals of **10** formed on the walls of the sample tube, above the surface of the reaction mixture, after 14 days of slow evaporation. Yield: 6 mg (~10%).

CHN analysis: Formula: $K[Ca(Bc_2hda)_2(H_2O)_4]Cl_2$; *Calculated:* C: 59.53%, H: 6.12%, N: 2.39%, Ca: 3.42%, Cl: 6.06%, K: 3.34%; *Found*: C: 53.01%, H: 6.66%, N: 2.12%, Ca: 3.06%, Cl: 5.38%, K: 2.98% (see p. 201 for additional comments).

IR/cm^{-1}: not available.

7.4. $CaCO_3$ morphogenesis

7.4.1. General synthetic procedure

The synthetic procedure for $CaCO_3$ materials relates to the following reaction equation:

$$CaCl_2(aq) + 2\ NaHCO_3(aq) \rightleftharpoons CaCO_3\ (s) + 2\ NaCl\ (aq) + H_2O\ (l) + CO_2\uparrow$$

In a typical experiment a specific mass of a chosen ligand was dissolved in 10 ml of an aqueous solution containing 0.043 g (0.5 mmol) of $NaHCO_3$. The temperature of this mixture was adjusted to a desired value. After the organic ligand was completely dissolved, 5 ml of an aqueous solution containing 0.037 g (0.25 mmol) of $CaCl_2 \cdot 2H_2O$ was injected and the mixture was further stirred for one minute. After that time the beaker was sealed with a parafilm and left for 24 hours. Depending on the chosen ligand, the formation of $CaCO_3$ crystals was observed between a few seconds (vda-type ligands) and 15 minutes (Me_2hda).

7.4.2. Sample preparation and methods

SEM and HeIM microscopy

Samples for the SEM analysis were collected 24 hours after the preparation by filtration using a hydrophilic polycarbonate membrane (Millipore – Isopore 0.4 μm membrane). Samples were then placed on aluminum sample holders, coated with 3 nm layer of platinum and imaged using a Zeiss Ultra Plus Scanning Electron Microscope. Helium Ion Microscope images were obtained with a Zeiss Orion Plus microscope operating at 37kV acceleration voltage and 15.1 mm working distance. Samples were coated with 6 nm layer of Pt/Pd alloy prior to imaging.

TEM microscopy

Calcite samples were filtered on a membrane filter (as for SEM) and the solid was used to create a suspension in chloroform. Then 1 drop of the suspension was placed on a Formvar/Carbon 200 Mesh TEM grid and imaged in 300kV mode with FEI Titan microscope.

X-ray powder diffraction

Room temperature X-ray powder diffraction was performed on the precipitates using a Siemens D500 diffractometer with Cu-$K\alpha_1$ radiation with a wavelength of $\lambda = 1.54056$ Å.

References

1. J.-M. Lehn, *Angew. Chem. Int. Ed.*, 1990, **29**, 1304-1319.
2. J.-M. Lehn, *Science*, 1993, **260**, 1762-1763.
3. W. Lu and C. M. Lieber, *Nat. Mater.*, 2007, **6**, 841-850.
4. E. Baeuerlein, in *Biomineralization - From Biology to Biotechnology and Medical Application*, ed. E. Baeuerlein, Wiley-VCH, Editon edn., 2000.
5. S. A. Davis, S. Mann and E. Dujardin, *Curr. Opin. Solid State Mater. Sci.*, 2003, **7**, 273–281.
6. W. Schmitt, P. A. Jordan, R. K. Henderson, G. R. Moore, C. E. Anson and A. K. Powell, *Coord. Chem. Rev.*, 2002, **228**, 115-126.
7. W. L. Murphy and P. B. Messersmith, *Polyhedron*, 2000, **19**, 357–363.
8. X. Wang and W. E. G. Müller, *Trends Biotechnol.*, 2009, **27**, 375-383.
9. M. Murugesu, M. Habrych, W. Wernsdorfer, K. A. Abboud and G. Christou, *J. Am. Chem. Soc.*, 2004, **126**.
10. J. Kim, B. Chen, T. M. Reineke, H. Li, M. Eddaoudi, D. B. Moler, M. O'Keeffe and O. M. Yaghi, *J. Am. Chem. Soc.*, 2001, **123**, 8239-8247.
11. N. L. Rosi, J. Eckert, M. Eddaoudi, D. T. Vodak, J. Kim, M. O'Keeffe and O. M. Yaghi, *Science*, 2003, **300**, 1127-1130.
12. J. L. C. Rowsell and O. M. Yaghi, *Microporous Mesoporous Mater.*, 2004, **73**, 3-14.
13. S. Pellet-Rostaing, A. Favre-Reguillon and M. Lemaire, *Actual. Chim.*, 2005, **290-291**, 98-107.
14. J. D. Hartgerink, E. Beniash and S. I. Stupp, *Science*, 2001, **294**, 1684-1688.
15. J. D. Hartgerink, E. Beniash and S. I. Stupp, *Proc. Natl. Acad. Sci. U. S. A.*, 2002, **99**, 5133-5138.
16. G. A. Silva, C. Czeisler, K. L. Niece, E. Beniash, D. A. Harrington, J. A. Kessler and S. I. Stupp, *Science*, 2004, **303**, 1352-1355.
17. K. Biradha, *CrystEngComm*, 2003, **5**, 374-384.
18. C. J. Pedersen, *J. Amer. Chem. Soc.*, 1967, **89**, 7017-7036.
19. C. Dosi, E. Giglio, V. Pavel and C. Quagliata, *Acta Cryst. A*, 1973, **29**, 644-650.
20. M. Kolbe, H. Besir, L.-O. Essen and D. Oesterhelt, *Science*, 2000, **288**, 1390-1396.
21. C. Janiak, *Dalton*, 2000, 3885-3896.
22. H. W. Roesky and M. Andruh, *Coord. Chem. Rev.*, 2003, **236**, 91-119.
23. B.-H. Ye, M.-L. Tong and X.-M. Chen, *Coord. Chem. Rev.*, 2005, **249**, 545-565.
24. S. Grimme, *Angew. Chem. Int. Ed.*, 2008, **47**, 3430-3434.
25. K. J. M. Bishop, C. E. Wilmer, S. Soh and B. A. Grzybowski, *Small*, 2009, **5**, 1600-1630.
26. D. Chandler, J. D. Weeks and H. C. Andersen, *Science*, 1983, **220**, 787-794.
27. J. G. Angyan, *J. Chem. Phys.*, 2007, **127**, 24108-24101.
28. K. A. Dill, *Biochemistry*, 1990, **29**, 7133-7155.
29. T. P. Silverstein, *J. Chem. Ed.*, 1998, **75**, 116-118.
30. G. Gilli, P. Gilli and Editors, *The Nature of Hydrogen Bond: Outline of a Comprehensive Hydrogen Bond Theory*, Oxford University Press, 2009.
31. T. Steiner, *Angew. Chem., Int. Ed.*, 2002, **41**, 48-76.
32. A. U. Czaja, N. Trukhan and U. Muller, *Chem. Soc. Rev.*, 2009, **38**, 1284-1293.
33. P. Gilli, V. Bertolasi, V. Ferretti and G. Gilli, *J. Am. Chem. Soc.*, 1994, **116**, 909-915.
34. C. L. Perrin and J. B. Nielson, *Annu. Rev. Phys. Chem.*, 1997, **48**, 511-544.
35. R. Hubbard and J. Garratt, *Chem. Rev.*, 1991, **1**, 25-27.
36. J. D. Watson and F. H. C. Crick, *Nature*, 1953, **171**, 737-738.
37. G. Maga, *DNA Replication, Repair and Recombination at the Crossroad Between Genome Integrity and Genomic Instability: A Biochemical Perspective*, Research Signpost, 2008.
38. L. V. Yakushevich, *Int. J. Quantum Chem.*, 2011, **111**, 2482-2489.
39. L. E. Kay and Editor, *Who Wrote the Book of Life? A History of the Genetic Code*, Stanford University Press, 2000.

40. http://www.academic.brooklyn.cuny.ed.
41. C. Sanchez, S.-I. G. J. de, F. Ribot, T. Lalot, C. R. Mayer and V. Cabuil, *Chem. Mater.*, 2001, **13**, 3061-3083.
42. C. Sanchez, B. Julian, P. Belleville and M. Popall, *J. Mater. Chem.*, 2005, **15**, 3559-3592.
43. O. H. Van, *Science*, 1966, **154**, 645-646.
44. M. Jose-Yacaman, L. Rendon, J. Arenas and M. C. S. Puche, *Science*, 1996, **273**, 223-225.
45. S. Mann, S. L. Burkett, S. A. Davis, C. E. Fowler, N. H. Mendelson, S. D. Sims, D. Walsh and N. T. Whilton, *Chem. Mater.*, 1997, **9**, 2300-2310.
46. E. Ruiz-Hitzky, *Adv. Mater.*, 1993, **5**, 334-340.
47. E. P. Giannelis, *Appl. Organomet. Chem.*, 1998, **12**, 675-680.
48. F. Leroux and J.-P. Besse, *Chem. Mater.*, 2001, **13**, 3507-3515.
49. G. Fornasieri, L. Rozes, C. S. Le, B. Alonso, D. Massiot, M. N. Rager, M. Evain, K. Boubekeur and C. Sanchez, *J. Am. Chem. Soc.*, 2005, **127**, 4869-4878.
50. C. G. Goltner and M. Antonietti, *Adv. Mater.*, 1997, **9**, 431-436.
51. C. T. Kresge, M. E. Leonowicz, W. J. Roth, J. C. Vartuli and J. S. Beck, *Nature*, 1992, **359**, 710-712.
52. N. Steunou, S. Foerster, P. Florian, C. Sanchez and M. Antonietti, *J. Mater. Chem.*, 2002, **12**, 3426-3430.
53. S. Harrisson, G. L. Drisko, E. Malmstrom, A. Hult and K. L. Wooley, *Biomacromolecules*, 2011, **12**, 1214-1223.
54. H. Li, M. Eddaoudi, M. O'Keeffe and O. M. Yaghi, *Nature*, 1999, **402**, 276-279.
55. H. Cui, M. J. Webber and S. I. Stupp, *Biopolymers*, 2010, **94**, 1-18.
56. T. Kokubo, H.-M. Kim and M. Kawashita, *Biomaterials*, 2003, **24**, 2161-2175.
57. R. K. Iha, K. L. Wooley, A. M. Nystrom, D. J. Burke, M. J. Kade and C. J. Hawker, *Chem. Rev.*, 2009, **109**, 5620-5686.
58. H.-C. Zhou, J. R. Long and O. M. Yaghi, *Chem. Rev.*, 2012, **112**, 673-674.
59. L. Zhang, B. Marzec, R. Clerac, Y. Chen, H. Zhang and W. Schmitt, *Chem. Commun.*, 2013, **49**, 66-68.
60. C. Yang, X. Wang and M. A. Omary, *Angew. Chem. Int. Ed.*, 2009, **48**, 2500-2505.
61. W. Schmitt, J. P. Hill, M. P. Juanico, A. Caneschi, F. Costantino, C. E. Anson and A. K. Powell, *Angew. Chem. Int. Ed.*, 2005, **44**, 4187-4192.
62. C. Banglin, N. Ockwig, W., A. R. Millward, D. S. Contreras and O. M. Yaghi, *Angew. Chem. Int. Ed.*, 2005, **44**, 4745 –4749.
63. H. Furukawa, N. Ko, Y. B. Go, N. Aratani, S. B. Choi, E. Choi, A. O. Yazaydin, R. Q. Snurr, M. O'Keeffe, J. Kim and O. M. Yaghi, *Science*, 2010, **329**, 424-428.
64. A. E. Platero-Prats, l. P.-O. s. V. A. de, N. Snejko, A. Monge and E. Gutierrez-Puebla, *Chem.--Eur. J.*, 2010, **16**, 11632-11640.
65. A. Sigel, H. Sigel and R. K. O. Sigel, *Biomineralization : from nature to application*, John Wiley & Sons, Chichester, 2008.
66. W. Maret and Y. Li, *Chem. Rev.*, 2009, **109**, 4682-4707.
67. F. Heylighen, *The Science of Self-organization and Adaptivity*, Publishers Co. Ltd, 1999.
68. J. P. Hill, W. Jin, A. Kosaka, T. Fukushima, H. Ichihara, T. Shimomura, K. Ito, T. Hashizume, N. Ishii and T. Aida, *Science*, 2004, **304**, 1481-1483.
69. J.-M. Lehn, *Supramolecular Chemistry - Concepts and Perspectives*, VHC, New York, 1995.
70. K. Konstas, S. J. Langford and M. J. Latter, *Int. J. Mol. Sci.*, 2010, **11**, 2453-2472.
71. D. T. Bong, T. D. Clark, J. R. Granja and M. R. Ghadiri, *Angew. Chem., Int. Ed.*, 2001, **40**, 988-1011.
72. E. H. C. Bromley, K. Channon, E. Moutevelis and D. N. Woolfson, *ACS Chem. Biol.*, 2008, **3**, 38-50.
73. S. Zhang, D. M. Marini, W. Hwang and S. Santoso, *Curr. Opin. Chem. Biol.*, 2002, **6**, 865-871.
74. S. Ghanaati, M. J. Webber, R. E. Unger, C. Orth, J. F. Hulvat, S. E. Kiehna, M. Barbeck, A. Rasic, S. I. Stupp and J. C. Kirkpatrick, *Biomaterials*, 2009, **30**, 6202–6212.
75. L.-s. L. Wei-Wen Tsai, Honggang Cui, Hongzhou Jiang, *Tetrahedron*, 2008, **64**, 8504-8514.

76. M. J. Webber, J. Tongers, M.-A. Renault, J. G. Roncalli and D. W. Losordo, *Acta Biomater.*, 2010, **6**, 3-11.
77. M. T. McClendon and S. I. Stupp, *Biomaterials*, 2012, **33**, 5713-5722.
78. M. J. Webber, J. B. Matson, V. K. Tamboli and S. I. Stupp, *Biomaterials*, 2012, **33**, 6823-6832.
79. M. J. Webber, J. Tongers, C. J. Newcomb, K.-T. Marquardt, J. Bauersachs, D. W. Losordo and S. I. Stupp, *Proc. Natl. Acad. Sci. U. S. A.*, 2012, **109**, 9220.
80. D. J. Toft, T. J. Moyer, S. M. Standley, Y. Ruff, A. Ugolkov, S. I. Stupp and V. L. Cryns, *ACS Nano*, 2012, **6**, 7956-7965.
81. E. D. Spoerke, S. G. Anthony and S. I. Stupp, *Adv. Mater.*, 2009, **21**, 425–430.
82. P. Zhang, Y. Li, F. Z. Wang and Q. Yang, *Russ. J. Coord. Chem.*, 2009, **35**, 784-788.
83. K. Chen, S. P. Wathen and A. W. Czarnik, *Tetrahedron Lett.*, 1992, **33**, 6303-6306.
84. Z. R. Ratkovic, L. Somsak, K. Micskei, C. Zucchi and G. Palyi, *J. Organomet. Chem.*, 2001, **637-639**, 813-819.
85. Z.-Y. Fu, X.-T. Wu, J.-C. Dai, S.-M. Hu and W.-X. Du, *Jiegou Huaxue*, 2002, **21**, 296-298.
86. K. Micskei, Z. Juhasz, Z. R. Ratkovic and L. Somsak, *Tetrahedron Lett.*, 2006, **47**, 6117-6120.
87. A. R. Samakaeva and R. K. Samakaev, *Estestv. Tekh. Nauki*, 2007, 119-122.
88. Y. Liu, Q.-H. Pang, X.-G. Meng, F.-R. Liu, J.-M. Li, J. Du and C.-W. Hu, *J. Appl. Polym. Sci.*, 2010, **118**, 2043-2049.
89. S. Mukhopadhyay, P. B. Chatterjee, D. Mandal, G. Mostafa, A. Caneschi, J. van Slageren, T. J. R. Weakley and M. Chaudhury, *Inorg. Chem.*, 2004, **43**, 3413-3420.
90. G. Schwarzenbach, *Helv. Chim. Acta*, 1952, **35**, 2344-2359.
91. E. Zhang, H. Hou, H. Han and Y. Fan, *J. Organomet. Chem.*, 2008, 1927-1937.
92. W. Schmitt, P. A. Jordan, R. K. Henderson, G. R. Moore, C. E. Anson and A. K. Powell, *Coord. Chem. Rev.*, 2002, **228**, 115-126.
93. S. L. Heath and A. K. Powell, *Angew. Chem. Int. Ed. Engl.*, 1992, **31**, 191-193.
94. S. L. Heath, P. A. Jordan, I. D. Johnson, G. R. Moore, A. K. Powell and M. Helliwell, *J. Inorg. Biochem.*, 1995, **59**, 785-794.
95. I. McKeogh, J. Hill, E. Collins, T. McCabe, A. Powell and W. Schmitt, *New J. Chem.*, 2007, **31**, 1882 - 1886.
96. W. Schmitt, C. E. Anson, J. P. Hill and A. K. Powell, *J. Am. Chem. Soc.*, 2003, **125**, 11142-11143.
97. W. Schmitt, J. P. Hill, S. Malik, C. A. Volkert, I. Ichinose, C. E. Anson and A. K. Powell, *Angew. Chem. Int. Ed.*, 2005, **44**, 7048-7053.
98. G. La Spina, R. Clerac, E. S. Collins, T. McCabe, M. Venkatesan, I. Ichinose and W. Schmitt, *Dalton Trans.*, 2007, **45**, 5248-5252.
99. S. Mann and G. Ozin, *Nature*, 1996, **382**, 313-318.
100. L. Gago-Duport, M. J. I. Briones, J. B. Rodriguez and B. Covelo, *J. Struct. Biol.*, 2008, **162**, 422-435.
101. Y. Politi, T. Arad, E. Klein, S. Weiner and L. Addadi, *Science*, 2004, **306**, 1161-1164.
102. Y. Politi, Y. Levi-Kalisman, S. Raz, F. Wilt, L. Addadi, S. Weiner and I. Sagi, *Adv. Funct. Mater.*, 2006, **16**, 1289-1298.
103. S. Mann, D. D. Archibald, J. M. Didymus, T. Douglas, B. R. Heywood, F. C. Meldrum and N. J. Reeves, *Science*, 1993, **261**, 1286-1292.
104. F. C. Meldrum, *Int. Mater. Rev.*, 2003, **48**, 187-224.
105. C. P. Van, *Rev. Mineral. Geochem.*, 2003, **54**, 357-381.
106. A. Ridgwell, *Mar. Geol.*, 2005, **217**, 339-357.
107. H. H. Teng, P. M. Dove, C. A. Orme and Y. J. J. De, *Science*, 1998, **282**, 724-727.
108. H. Pauly, *Arctic*, 1963, **16**, 263-264.
109. J. L. Bischoff, J. A. Fitzpatrick and R. J. Rosenbauer, *J. Geol.*, 1993, **101**, 21-33.
110. J. L. Bischoff, S. Stine, R. J. Rosenbauer, J. A. Fitzpatrick and T. W. Stafford, Jr., *Geochim. Cosmochim. Acta*, 1993, **57**, 3855-3865.
111. T. Ogino, T. Suzuki and K. Sawada, *Geochim. Cosmochim. Acta*, 1987, **51**, 2757-2767.
112. D. Kralj, L. Brecevic and A. E. Nielsen, *J. Cryst. Growth*, 1990, **104**, 793-800.
113. Y. Levi, S. Albeck, A. Brack, S. Weiner and L. Addadi, *Chem.--Eur. J.*, 1998, **4**, 389-396.
114. L. Wang, I. Sondi and E. Matijevic, *J. Colloid Interface Sci.*, 1999, **218**, 545-553.
115. H. Hull and A. G. Turnbull, *Geochim. Cosmochim. Acta*, 1973, **37**, 685-694.

116. H. Effenberger, *Monatsh. Chem.*, 1981, **112**, 899-909.
117. K. Fukushi, T. Munemoto, M. Sakai and S. Yagi, *Sci. Technol. Adv. Mater.*, 2011, **12**, 64701-64712.
118. T. Wang, D. Porter and Z. Shao, *Adv. Funct. Mater.*, 2012, **22**, 435-441.
119. D. Rautaray, A. Banpurkar, S. R. Sainkar, A. V. Limaye, N. R. Pavaskar, S. B. Ogale and M. Sastry, *Adv. Mater.*, 2003, **15**, 1273-1278.
120. E. M. Flaten, M. Seiersten and J.-P. Andreassen, *J. Cryst. Growth*, 2009, **311**, 3533-3538.
121. L. Fernandez-Diaz, J. M. Astilleros and C. M. Pina, *Chem. Geol.*, 2006, **225**, 314-321.
122. F.-W. Yan, S.-F. Zhang, C.-Y. Guo, X.-H. Zhang, G.-C. Chen, F. Yan and G.-Q. Yuan, *Cryst. Res. Technol.*, 2009, **44**, 725-728.
123. P. Braillon and J. Serughetti, *Phys. Status Solidi A*, 1976, **33**, 405-413.
124. V. C. Hover, L. M. Walter and D. R. Peacor, *Chem. Geol.*, 2001, **175**, 221-248.
125. K. Henriksen, S. L. S. Stipp, J. R. Young and M. E. Marsh, *Am. Mineral.*, 2004, **89**, 1709-1716.
126. A. Berman, L. Addadi, A. Kvick, L. Leiserowitz, M. Nelson and S. Weiner, *Science*, 1990, **250**, 664-667.
127. J. Seto, Y. Ma, S. A. Davis, F. Meldrum, A. Gourrier, Y.-Y. Kim, U. Schilde, M. Sztucki, M. Burghammer, S. Maltsev, C. Jaeger and H. Coelfen, *Proc. Natl. Acad. Sci. U. S. A.*, 2012, **109**, 3699-3704.
128. T. Sugimoto, *Adv. Colloid Interface Sci.*, 1987, **28**, 65-108.
129. G. Shen, Y. Bando and D. Golberg, *Int. J. Nanotechnol.*, 2007, **4**, 730-749.
130. J. Aizenberg, G. Lambert, L. Addadi and S. Weiner, *Adv. Mater.*, 1996, **8**, 222-226.
131. E. Loste, R. M. Wilson, R. Seshadri and F. C. Meldrum, *J. Cryst. Growth*, 2003, **254**, 206-218.
132. F. Nudelman, E. Sonmezler, P. H. H. Bomans, W. G. de and N. A. J. M. Sommerdijk, *Nanoscale*, 2010, **2**, 2436-2439.
133. S. E. Wolf, J. Leiterer, V. Pipich, R. Barrea, F. Emmerling and W. Tremel, *J. Am. Chem. Soc.*, 2011, **133**, 12642-12649.
134. D. C. Bassett, B. Marelli, S. N. Nazhat and J. E. Barralet, *Adv. Funct. Mater.*, 2012, **22**, 3460-3469.
135. A.-W. Xu, Q. Yu, W.-F. Dong, M. Antonietti and H. Coelfen, *Adv. Mater.*, 2005, **17**, 2217-2221.
136. S. Mann, *Nature*, 1993, **365**, 499-505.
137. M. Li and S. Mann, *Adv. Funct. Mater.*, 2002, **12**, 773-779.
138. M. Li, B. Lebeau and S. Mann, *Adv. Mater.*, 2003, **15**, 2032-2035.
139. I. M. Weiss, *Nat. Chem. Biol.*, 2011, **7**, 192-193.
140. L. Addadi, S. Raz and S. Weiner, *Adv. Mater.*, 2003, **15**, 959-970.
141. M. Cusack and A. Freer, *Chem. Rev.*, 2008, **108**, 4433-4454.
142. J. Donners, E. W. Meijer, R. J. Nolte, C. Roman, A. Schenning, N. Sommerdijk and B. R. Heywood, *Chem. Commun.*, 2000, 1937-1938.
143. W. Ostwald, *Lehrbuch der allgemeinen Chemie. Second edition*, W. Engelmann, 1896.
144. A.-W. Xu, M. Antonietti, H. Coelfen and Y.-P. Fang, *Adv. Funct. Mater.*, 2006, **16**, 903-908.
145. J. Yu, H. Guo, S. A. Davis and S. Mann, *Adv. Funct. Mater.*, 2006, **16**, 2035-2041.
146. S.-H. Yu, H. Coelfen and M. Antonietti, *J. Phys. Chem. B*, 2003, **107**, 7396-7405.
147. H. Colfen, *Macromol. Rapid Commun.*, 2001, **22**, 219-252.
148. M. Sedlak, M. Antonietti and H. Coelfen, *Macromol. Chem. Phys.*, 1998, **199**, 247-254.
149. H. Coelfen and S. Mann, *Angew. Chem. Int. Ed.*, 2003, **42**, 2350-2365.
150. S. Wohlrab, N. Pinna, M. Antonietti and H. Coelfen, *Chem.--Eur. J.*, 2005, **11**, 2903-2913.
151. R.-Q. Song, H. Coelfen, A.-W. Xu, J. Hartmann and M. Antonietti, *ACS Nano*, 2009, **3**, 1966-1978.
152. T. Wang, H. Coelfen and M. Antonietti, *J. Am. Chem. Soc.*, 2005, **127**, 3246-3247.
153. N. Gehrke, H. Coelfen, N. Pinna, M. Antonietti and N. Nassif, *Cryst. Growth Des.*, 2005, **5**, 1317-1319.
154. R. L. Penn, *J. Phys. Chem. B*, 2004, **108**, 12707-12712.
155. D. Walsh, B. Lebeau and S. Mann, *Adv. Mater.*, 1999, **11**, 324-328.
156. S. Mann, B. R. Heywood, S. Rajam and J. D. Birchall, *Nature*, 1988, **334**, 692-695.

157. J. M. Didymus, S. Mann, W. J. Benton and I. R. Collins, *Langmuir*, 1995, **11**, 3130-3136.
158. A. L. Litvin, S. Valiyaveettil, D. L. Kaplan and S. Mann, *Adv. Mater.*, 1997, **9**, 124-127.
159. L. Addadi, J. Moradian, E. Shay, N. G. Maroudas and S. Weiner, *Proc. Natl. Acad. Sci. U. S. A.*, 1987, **84**, 2732-2736.
160. D. Walsh and S. Mann, *Nature*, 1995, **377**, 320-323.
161. Y. Kitano, K. Park and D. W. Hood, *J. Geophys. Res.*, 1962, **67**, 4873-4874.
162. Z. Mao and J. Huang, *J. Solid State Chem.*, 2007, **180**, 453-460.
163. F. Massimino, M. Bruno, M. Rubbo and D. Aquilano, *Cryst. Res. Technol.*, 2011, **46**, 789-794.
164. S. Babu Mukkamala and A. K. Powell, *Chemical Communications*, 2004, 918-919.
165. C. Mannich and W. Kroesche, *Arch. Pharm.*, 1912, **250**, 647-667.
166. V. Y. Temkina, M. N. Rusina, G. F. Yaroshenko, M. Z. Branzburg, L. M. Timakova and N. M. Dyatlova, *Zh. Obshch. Khim.*, 1975, **45**, 1564-1570.
167. M. Rodriguez, A. Llobet and M. Corbella, *Polyhedron*, 2000, **19**, 2483-2491.
168. J. B. Matson and S. I. Stupp, *Chem. Commun.*, 2011, **47**, 7962-7964.
169. C. Boehm, F. Leveiller, D. Jacquemain, H. Moehwald, K. Kjaer, J. Als-Nielsen, I. Weissbuch and L. Leiserowitz, *Langmuir*, 1994, **10**, 830-836.
170. D. F. Sibley and T. A. Vogel, *Science*, 1976, **192**, 551-553.
171. A. Lerman and F. T. Mackenzie, *Aquat. Geochem.*, 2005, **11**, 345-390.
172. A. R. Couto and M. A. Brown, *Curr. Rheumatol. Rep.*, 2007, **9**, 231-236.
173. P. V. Monje and E. J. Baran, *Plant Physiol.*, 2002, **128**, 707-713.
174. A. J. Mieszawska, L. D. Nadkarni, C. C. Perry and D. L. Kaplan, *Chem. Mater.*, 2010, **22**, 5780-5785.
175. M. A. Guino-o, J. S. Alexander, M. L. McKee, H. Hope, U. B. Englich and K. Ruhlandt-Senge, *Chem.--Eur. J.*, 2009, **15**, 11842-11852.
176. G. La Spina, R. Clerac, E. S. Collins, T. McCabe, M. Venkatesan, I. Ichinose and W. Schmitt, *Dalton Trans.*, 2007, 5248-5252.
177. I. McKeogh, J. P. Hill, E. S. Collins, T. McCabe, A. K. Powell and W. Schmitt, *New J. Chem.*, 2007, **31**, 1882-1886.
178. American Mineralogist Crystal Structure Database, http://rruff.geo.arizona.edu/AMS/amcsd.php.
179. G. B. Deacon and R. J. Philips, *Coord. Chem. Rev.*, 1980, **33**, 227.
180. H. Saechtling and M. Kaufmann, *International plastics handbook : for the technologist, engineer and user*, 2nd edn., Hanser, München, 1987.
181. A. H. Dowling, University of Dublin, 2010.
182. M. Bogun, T. Mikolajczyk and S. Rabiej, *J. Appl. Polym. Sci.*, 2009, **114**, 70-82.
183. M. Bogun, E. Stodolak, E. Menaszek and A. Scislowska-Czarnecka, *Fibres Text. East. Eur.*, 2011, **19**, 17-21.
184. C. Hartmann-Thompson, A. Merrington, P. I. Carver, D. L. Keeley, J. L. Rousseau, D. Hucul, K. J. Bruza, L. S. Thomas, S. E. Keinath, R. M. Nowak, D. M. Katona and P. R. Santurri, *J. Appl. Polym. Sci.*, 2008, **110**, 958-974.
185. M. S. Soh, A. Sellinger and A. U. J. Yap, *Curr. Nanosci.*, 2006, **2**, 373-381.
186. W. Schmitt, M. Murugesu, J. C. Goodwin, J. P. Hill, A. Mandel, R. Bhalla, C. E. Anson, S. L. Heath and A. K. Powell, *Polyhedron*, 2001, **20**, 1687-1697.
187. Bruker AXS Inc., Madison, Wisconsin, USA, 2002.
188. A. L. Spek, *J. Appl. Cryst.*, 2003, **36**, 7-13.
189. F. C. Meldrum and S. T. Hyde, *J. Cryst. Growth*, 2001, **231**, 544-558.
190. Y. Dauphin, A. D. Ball, M. Cotte, J.-P. Cuif, A. Meibom, M. Salome, J. Susini and C. T. Williams, *Anal. Bioanal.Chem.*, 2008, **390**, 1659-1669.
191. S. Mann, J. M. Didymus, N. P. Sanderson, B. R. Heywood and E. J. A. Samper, *J. Chem. Soc., Faraday Trans.*, 1990, **86**, 1873-1880.
192. N. Sasaki, Y. Murakami, D. Shindo and T. Sugimoto, *J. Colloid Interface Sci.*, 1999, **213**, 121-125.
193. Q. Li, Y. Ding, F. Li, B. Xie and Y. Qian, *J. Cryst. Growth*, 2002, **236**, 357-362.
194. S. Babu Mukkamala and A. K. Powell, *Chemical Communications*, 2004, 918-919..
195. A. G. Turnbull, *Geochim. Cosmochim. Acta*, 1973, **37**, 1593-1601.
196. S. S. Berdonosov, I. V. Znamenskaya and I. V. Melikhov, *Inorg. Mater.*, 2005, **41**, 1308-1312.
197. P. Davies, D. Dollimore and G. R. Heal, *J. Therm. Anal.*, 1978, **13**, 473-487.

198. C. Barriga, J. Morales and J. L. Tirado, *J. Mater. Sci.*, 1986, **21**, 947-952.
199. L. Cros and J. M. Fortuño, *Sci. Mar.*, 2002, **66**, (S1) 7-182.
200. J. Rudloff and H. Colfen, *Langmuir*, 2004, **20**, 991-996.
201. D. Walsh and S. Mann, *Nature*, 1995, **377**, 320-323.
202. D. Walsh and S. Mann, *Adv. Mater.*, 1997, **9**, 658-662.
203. G. La Spina, University of Dublin, 2012.
204. W. Schmitt, J. P. Hill, S. Malik, C. A. Volkert, I. Ichinose, C. E. Anson and A. K. Powell, *Angew. Chem., Int. Ed.*, 2005, **44**, 7048-7053.
205. J. B. Matson and S. I. Stupp, *Chem. Commun.*, 2011, **47**, 7962-7964.
206. J. B. Matson, C. J. Newcomb, R. Bitton and S. I. Stupp, *Soft Matter*, 2012, **8**, 3586-3595.
207. OriginLab Corporation, One Roundhouse Plaza, Suite 303, Northampton, MA 01060, USA, 2008.
208. K. Brandenburg, H. Putz and M. Berndt, Crystal Impact, Kreuzherrenstr. 102, D-53227 Bonn, Germany, 2011.
209. CrystalMaker Software Limited, Centre for Innovation & Enterprise, Oxford University Begbroke Science Park, Woodstock Road, Begbroke, Oxfordshire, OX5 1PF, UK, 2012.
210. A. S. Wills, VaList- Bond Valence Calculating and Listing, 1999.
211. Adobe Systems Incorporated, 345 Park Avenue, San Jose, CA 95110-2704, USA, 2011.
212. W. R. Harris, R. J. Motekaitis and A. E. Martell, *Inorganic Chemistry*, 1975, **14**, 974-978.

Appendixes

A.1. 2D NMR results

A.2.1. HMBC spectrum of 2,2'-(5-(ethoxycarbonyl)-2-hydroxy-3-methoxybenzylazanediyl)diacetic acid (C_2vda)

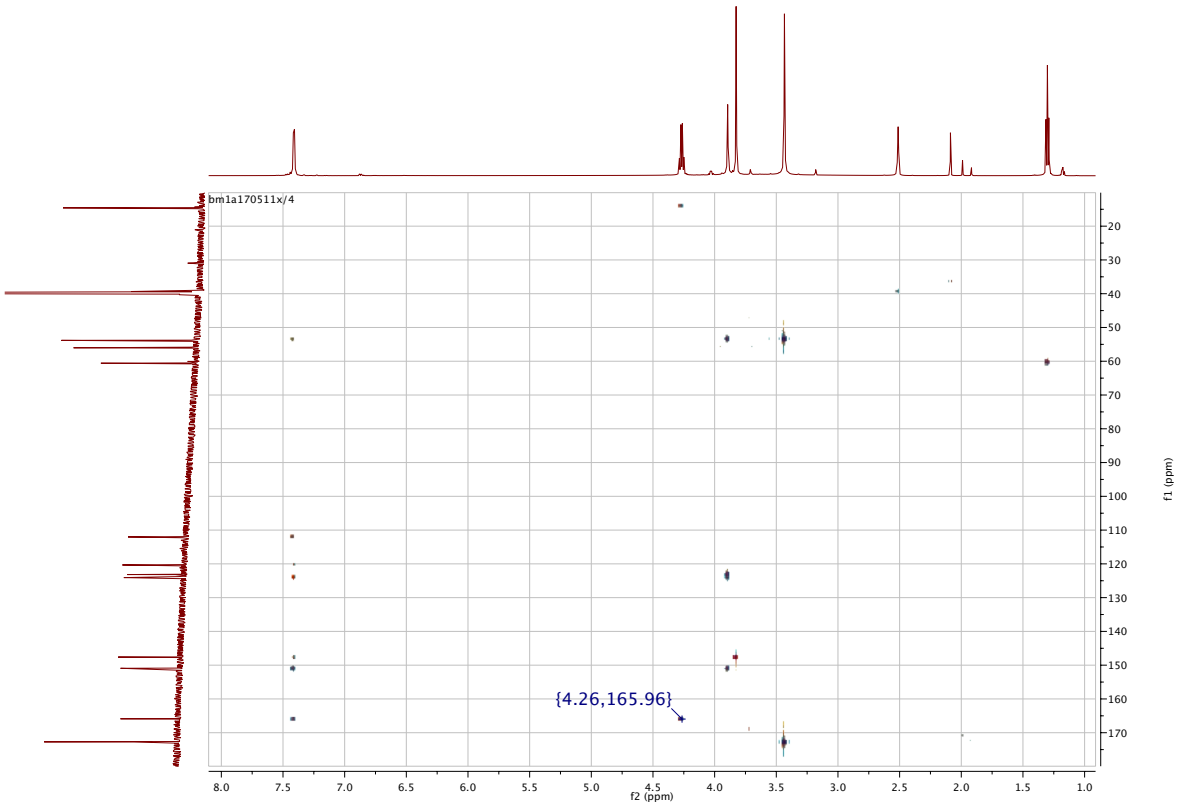

Fig. A.1 | HMBC spectrum of C_2vda.

^{13}C-^{1}H HMBC spectrum confirms that C_2vda is an ester. A correlation exists between the quaternary carbon (165.96 ppm) that belongs to the carboxylic group and the quartet (4.26 ppm) assigned as the two hydrogen atoms that are a part of the ethyl moiety.

A.2.2. HMBC spectrum of 2,2'-(5-(hexyloxycarbonyl)-2-hydroxy-3-methoxybenzylazanediyl)diacetic acid (C_6vda)

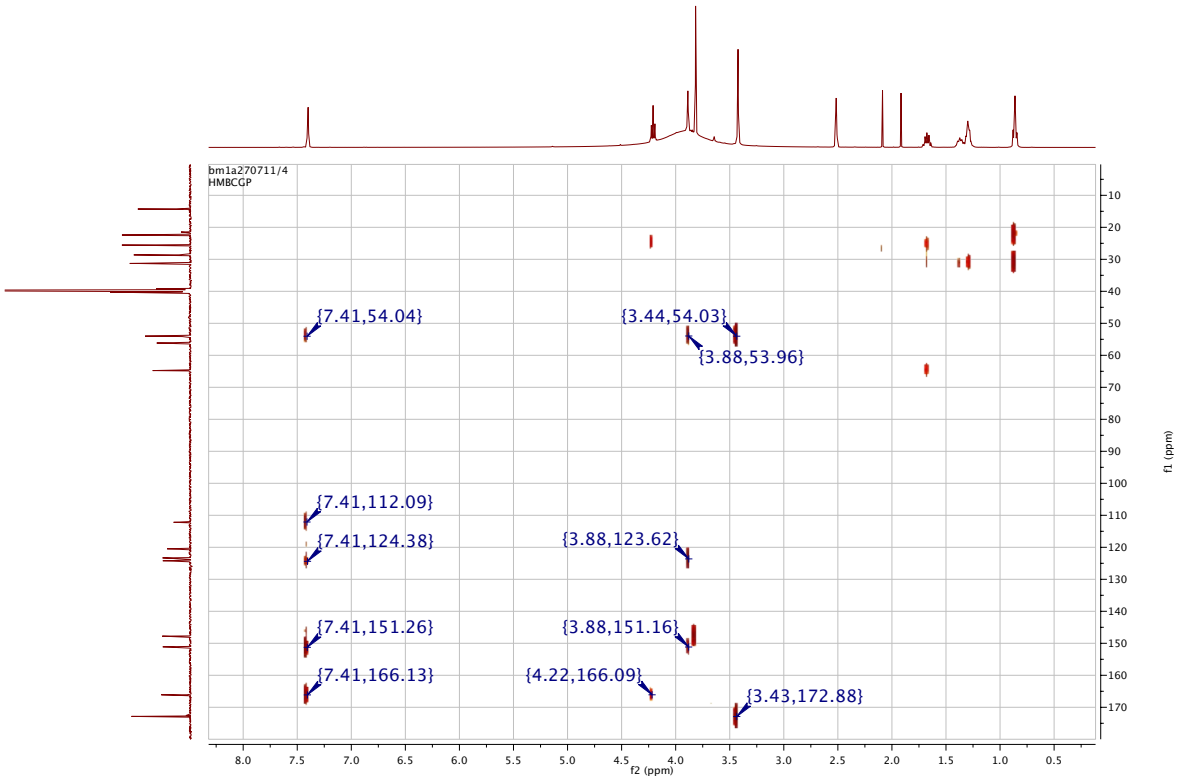

Fig. A.2 | HMBC spectrum of C_6vda.

^{13}C-^{1}H HMBC spectrum confirms that the C_6vda molecule was successfully synthesised. A correlation exists between the quaternary carbon (166.09 ppm) that belongs to the carboxylic group and the quartet (4.22 ppm) assigned as the two hydrogen atoms that are a part of the ethyl moiety. Moreover, there is a correlation between the methylene bridge singlet (3.88 ppm) and three aromatic carbons (151.16 ppm, 124.20 ppm, 123.62 ppm). The methylene bridge hydrogens are also correlated with the carbons that originate from the iminodiacetic acid –CH_2- methylene group (54.03 ppm).

A.2.3. HSQC and HMBC spectra of 2,2'-(5-(decyloxycarbonyl)-2-hydroxy-3-methoxybenzylazanediyl)diacetic acid (C_{10}vda)

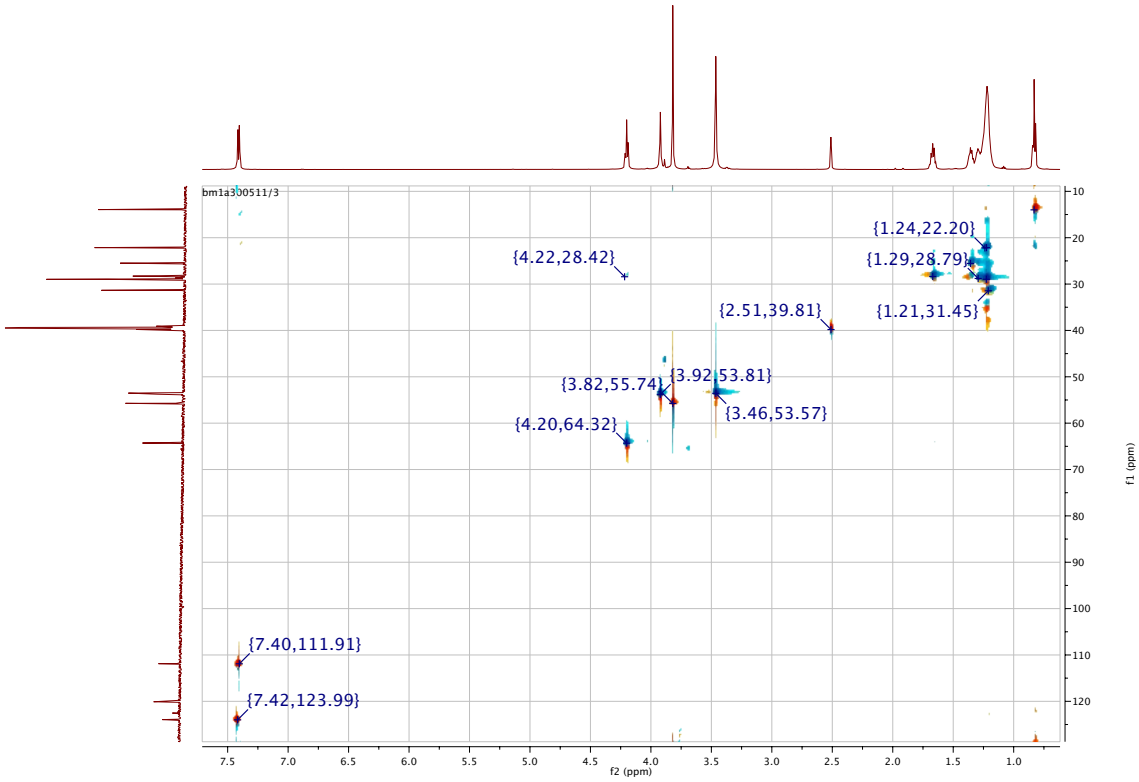

Fig. A.3 | HSQC spectrum of C_{10}vda.

Correlation table:

Carbon [ppm]	Hydrogen [ppm]	Carbon [ppm]	Hydrogen [ppm]
123.99	7.42	**31.45**	1.21
111.91	7.40	**28.96**	1.23
64.32	4.20	**28.79**	1.29
55.74	3.82	**28.42**	4.22
53.81	3.92	**28.37**	1.67
53.57	3.46	**25.55**	1.36
39.81	2.51	**22.20**	1.24

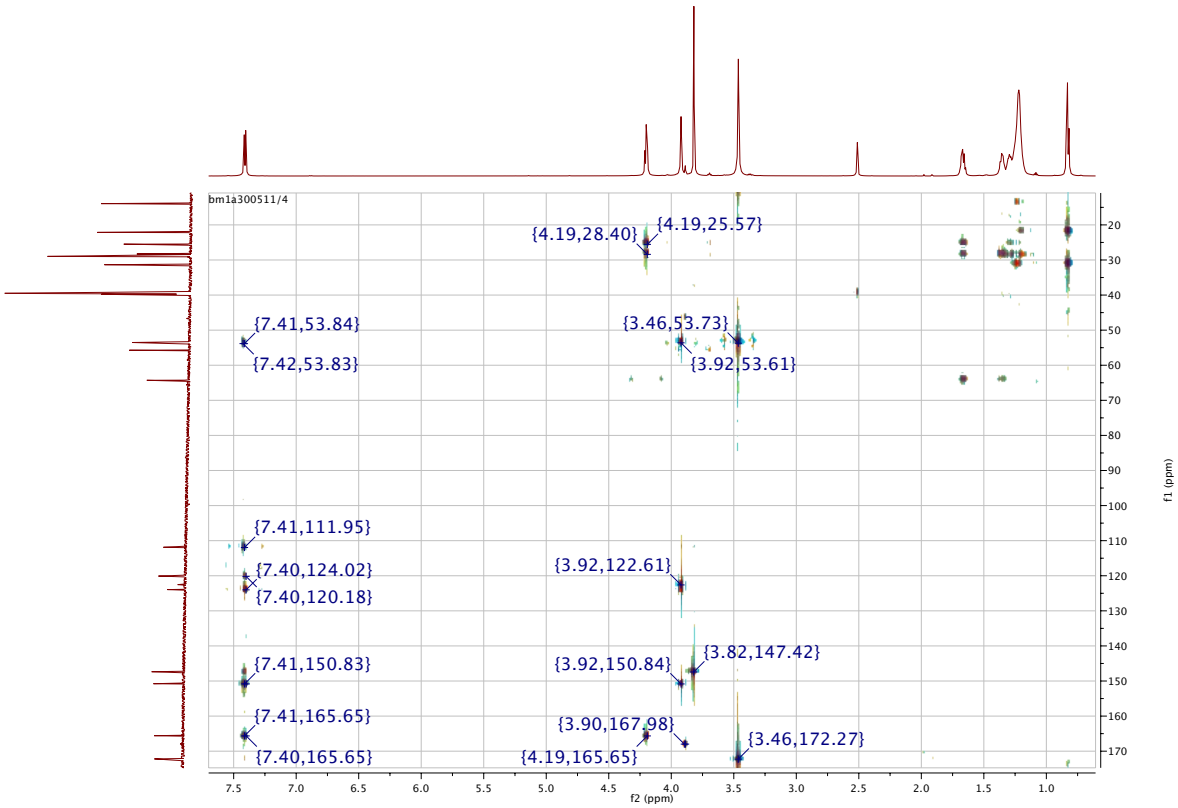

Fig. A.4 | HMBC spectrum of C_{10}vda.

^{1}H-^{13}C HMBC proves that all parts of the C_{10}vda molecule are properly bound. The ester bond links the decyl originating hydrogen atoms (-CH_2-O, triplet, 4.19 ppm) and the ester quaternary carbon atom (165.65 ppm). The iminodiacetic acid methylene hydrogen atoms (-CH_2-, singlet, 3.46 ppm) are coupled with the methylene bridge carbon (53.73 ppm). Moreover, the methylene bridge hydrogen atoms (3.92 ppm) are coupled with the carbons that belong to the aromatic ring (122.61 ppm, 150.84 ppm).

A.2. Mechanical measurements results

A.2.1. The nanoindentation experiment on compound **12**

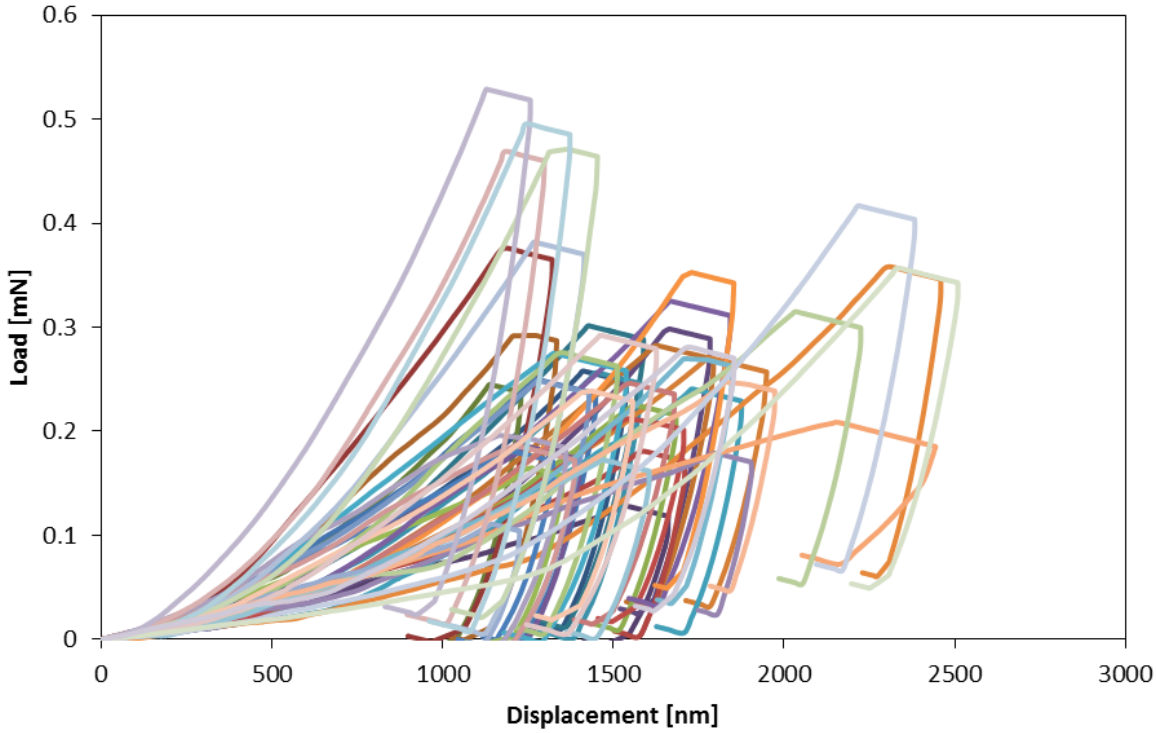

Fig. A.5 | Load *vs*. displacement graph for the nanoindentation experiment performed on a thin film of compound **12**.

7.5. Content of the attached CD

The attached CD contains the following:

- The electronic version of the thesis (in the MS Word 2007/2010/2011 and Adobe Portable Document formats - .docx and .pdf files, respectively)
- The crystallographic information files (CIF) for compounds **1**-**14**. These files may be opened using Mercury software, which is available to download free of charge at http://www.ccdc.cam.ac.uk/free_services/mercury/downloads/.